Edited by
L.Kubin and J.P. Hirth

Dislocations in Solids

Volume 16

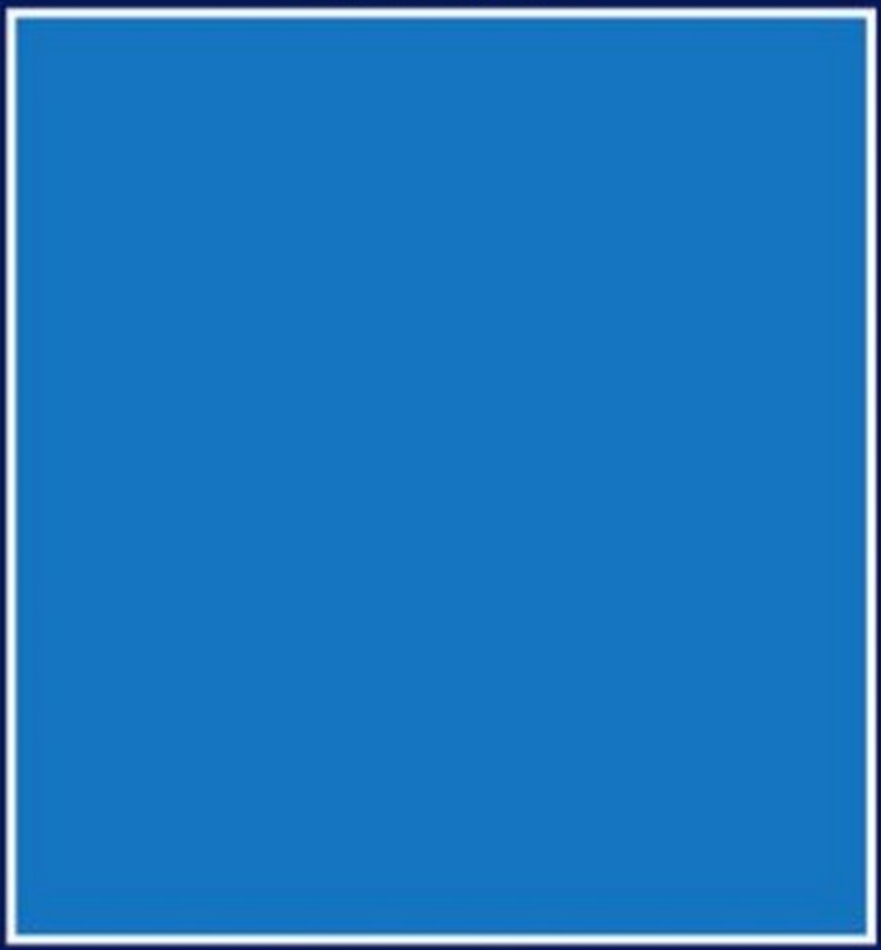

North-Holland

Dislocations in Solids

Volume 16

The 30th Anniversary Volume

Edited by

J. P. HIRTH

Hereford, AZ, USA

and

L. KUBIN

Laboratoire d'Étude des Microstructures,
CNRS-ONERA, Chatillon Cedex, France

ELSEVIER

Amsterdam • Boston • Heidelberg • London • New York • Oxford
Paris • San Diego • San Francisco • Singapore • Sidney • Tokyo

North-Holland is an imprint of Elsevier

North-Holland is an imprint of Elsevier
Radarweg 29, PO Box 211, 1000 AE Amsterdam, The Netherlands
Linacre House, Jordan Hill, Oxford OX2 8DP, UK

First edition 2010

Library of Congress Cataloging-in-Publication Data
A catalog record for this book is available from the Library of Congress

British Library Cataloguing in Publication Data
A catalogue record for this book is available from the British Library

ISBN: 978-0-444-53443-9
ISSN: 1572-4859

Preface

This 30th Anniversary Volume brings the series to a close. The intent of the series as initiated by F.R.N. Nabarro was to feature incisive position papers and to extend the treatment of dislocations to new materials. The success of the series in doing so is extended in the present volume. New materials addressed for the first time include the chapters on minerals by Barber et al. and the chapter on dislocations in colloidal crystals by Schall and Spaepen. The latter was an area of interest for Nabarro late in his career. Moriarty et al. extend the first principles calculations of kink configurations in bcc metals to high pressures, including the use of flexible boundary conditions to model dilatational effects. Rabier et al. clarify the issue of glide-shuffle slip systems in diamond cubic and related III–V compounds. Metadislocations, discussed by Feuerbacher and Heggen, represent a new type of defect in multicomponent metal compounds and alloys. Thus, as with other recent volumes in the series, this volume includes chapters on a wide range of topics, all at the leading edge of new research in the dislocation area.

J.P. Hirth
L. Kubin

CHAPTER 92

Dislocations and Plasticity in bcc Transition Metals at High Pressure

LIN H. YANG, MEIJIE TANG, AND JOHN A. MORIARTY

Lawrence Livermore National Laboratory, Livermore, CA 94551-0808, USA

1572-4859, DOI: 10.1016/S1572-4859(09)01601-5

Dislocations in Solids
Edited by J. P. Hirth and L. Kubin

Contents

1. Introduction 3
2. Computational approach 6
   2.1. First-principles electronic-structure methods 6
   2.2. Quantum-based interatomic potentials 7
   2.3. Green's function atomistic simulation 8
   2.4. Dislocation dynamics simulation 10
3. Salient high-pressure mechanical properties of bcc transition metals 12
   3.1. Bulk and shear elastic moduli 12
   3.2. Ideal shear strength 15
   3.3. Generalized stacking-fault (γ) energy surfaces 17
4. $a/2\langle 1\,1\,1\rangle$ screw dislocation properties at high pressure 22
   4.1. Equilibrium core structure and energy 22
   4.2. Low shear stress limit: kink-pair formation energy 27
   4.3. High shear stress limit: Peierls stress 29
   4.4. Activation enthalpy 31
   4.5. Dislocation mobility near and above the Peierls stress 34
5. Multiscale modeling of single-crystal plasticity 36
   5.1. Analytic representations of dislocation velocity 37
   5.2. Temperature- and pressure-dependent plastic flow 39
6. Summary and conclusions 44
Acknowledgements 44
References 44

1. Introduction

The intriguing possibility of modeling across length scales all the way from the atomic level to the continuum level to achieve a physics-based multiscale description of mechanical properties such as plasticity and strength has attracted widespread research interest in the last decade [1–8]. To be sure, the predictive multiscale materials modeling of plasticity and strength requires an in-depth theoretical understanding and quantum-based calculation of fundamental dislocation and other defect processes at the atomic length scale [9–19] as essential input into higher length scale simulations such as 3D dislocation dynamics (DD) of single-crystal plasticity at the microscale [20–31]. Especially important is the accurate atomistic modeling of the structure, motion, and interaction of individual dislocations, as well as the accurate modeling of the relevant aspects of elasticity, including elastic moduli and the limits of elastic stability. To accomplish this task fully, one not only needs to understand the underlying *qualitative mechanisms* that control plastic deformation, but also needs to be able to calculate the *quantitative parameters* that will allow a predictive description of plasticity and strength properties in real materials under various conditions. The latter is particularly important in regimes where experimental data are scarce or nonexistent such as under the extreme conditions of pressure, temperature, strain, and strain rate of current interest to many modern applications. Especially interesting in this regard is the regime of high pressure, a regime in which dislocation-driven plasticity has been heretofore largely unexplored from a fundamental perspective. The objective of the present paper is to help fill that void. Specifically, we elaborate here a predictive multiscale description of dislocation behavior and single-crystal plasticity in bcc transition metals over a wide range of pressures, ranging from ambient all the way up to many hundreds of gigapascals (GPa). In this process we build upon and greatly extend the multiscale dislocation work on these materials previously reported by the present authors and their collaborators [13,14,16,19].

In recent years since the mid-1990s, there has been considerable renewed interest in understanding dislocation behavior and plastic deformation in bcc metals [1–6, 9–19,21–23,27–32], where even at ambient pressure much remains unknown at the atomistic level about the fundamental mechanisms and quantitative parameters of dislocation motion. The numerous studies published on these materials over the years, especially the pioneering papers by Vitek and Duesbery [32–36], have identified many of the basic characteristics of dislocation behavior in bcc metals and have laid the groundwork for our investigations. In particular, at ambient pressure the low-temperature and high-strain-rate plastic behaviors of these metals are controlled by the intrinsic core properties of screw dislocations with Burgers vector

$\boldsymbol{b} = a/2\langle 1\,1\,1\rangle$, where a is the bcc lattice constant. Unlike the highly mobile edge dislocations in bcc metals, the motion of the $a/2\langle 1\,1\,1\rangle$ screw dislocations is severely restricted by the nonplanar atomic structure of its core, resulting in low intrinsic mobility, the formation of thermally activated kinks on the dislocation line at finite temperature, and a temperature-dependent yield stress. Since these unique qualitative characteristics are closely tied to the bcc structure itself, we expect them to remain in effect at high pressure as well. We will, therefore, concentrate here on pressure-dependent $a/2\langle 1\,1\,1\rangle$ screw dislocation behavior in the bcc lattice and the single-crystal plasticity that it drives.

At the same time, an important general consideration is the identification and separation of purely *generic* behavior representative of bcc metals as a whole from *materials-specific* behavior representative of chemical differences and environmental factors such as high pressure. The historical perspective has been to assume that bcc dislocation behavior and plasticity is highly generic in character. The expectation of possible materials-specific behavior under high pressure, however, underscores the importance of chemical bonding, in addition to crystal symmetry, in elaborating dislocation and strength properties. In bcc metals, chemical bonding ranges from nondirectional, nearly free-electron sp bonding in the alkali metals (e.g., Na, K) to directional d-electron bonding in transition metals (e.g., Ta, Mo, Fe). The latter also depends strongly on pressure-sensitive d-electron occupation, which can vary significantly within nonmagnetic group-VB (e.g., V, Ta) and group-VIB (e.g., Mo, W) elements, as well as between these elements and magnetic group-VIII elements (e.g., Fe). Here we will focus on a small subset of the nonmagnetic materials as prototypes, namely V, Ta, and Mo, and examine in detail how their mechanical properties vary under the influence of high pressure. These materials have different ranges of bcc stability, as well as different high-pressure elastic behavior. While Ta is predicted to remain stable in the bcc phase up to at least 1000 GPa [37], Mo and V undergo high-pressure phase transitions, which are predicted above 500 GPa in the case of Mo [38,39] and observed near 69 GPa in the case of V [40]. The latter transition has also been confirmed theoretically [41]. The phase transitions in Mo and V are closely coupled, respectively, with the elastic softening of the C' and the C_{44} shear modulus in the compressed bcc lattice prior to the transitions.

Large-scale computer simulation is the enabling tool of multiscale modeling and is at the heart of the present investigation. This approach is not entirely unique, however, and involves a number of important strategic, physical, and computational issues and choices. Here we have adopted an information passing strategy to the multiscale modeling of single-crystal plasticity across three overlapping length scales: electronic, atomic, and micro- or mesoscopic. Crystal elastic moduli and the basic core properties of dislocations at the electronic length scale are governed by the laws of quantum mechanics, which can be implemented from first principles via modern density functional theory (DFT) [42–44] in both full-potential (FP) and pseudopotential (PP) electronic-structure methods [37–39,44–48]. We use DFT electronic-structure calculations to establish the pressure dependence of certain key mechanical properties, including the shear elastic moduli, the ideal shear strength, and the generalized stacking-fault (γ) energy surface. On the other hand, one can

study the structure, motion, and interaction of individual dislocations in much greater detail at the atomic length scale through static and dynamic atomistic simulations, using suitable quantum-based *interatomic potentials* that encode the necessary quantum information. For transition metals, DFT-based generalized pseudopotential theory (GPT) [49] provides a rigorous approach to obtain the required potentials. In our present multiscale strategy, we perform additional DFT electronic-structure calculations to establish a large database of fundamental pressure-dependent properties of the zero-temperature bcc phase of each metal of interest, and then use this database to constrain and validate simplified *model* GPT (or MGPT) multi-ion potentials [50], which in turn permit efficient atomistic simulations with full quantum realism. In particular, the MGPT potentials encode the fundamental directional bonding of central transition metals through explicit three- and four-ion angular-dependent terms, and can be used to make predictive calculations of high-pressure dislocation properties.

Atomistic simulations of point and extended defects are performed on a specified finite collection of atoms contained within a chosen computational cell of variable shape and size to which specific boundary conditions and other constraints such as temperature, stress, and strain rate are applied. Both molecular statics (MS) techniques, which seek to minimize the total energy of the system at zero temperature, and finite-temperature molecular dynamics (MD) techniques can be used. The simulation of individual dislocations requires special treatment due to the long-ranged ($\sim 1/r$) elastic field associated with them. Traditionally, fixed boundary conditions have been most often used in such dislocation simulations, where exterior atoms are frozen at their bulk lattice positions, and distant atomic positions in the computational cell are established by the conditions of linear anisotropic elasticity. This requires very large simulation cells in practice, but this method is always problematic with respect to force buildup between fixed and relaxed atomic regions. An elegant and practical solution to the latter problem is to use the so-called flexible boundary conditions. In particular, Rao et al. [51,52] have developed an advanced Green's function version of such conditions for both 2D and 3D dislocation simulations, denoted as Green's function boundary conditions (GFBC). In this method, a buffer layer is introduced between the fixed outer and inner relaxed atomistic regions of the simulation cell, allowing one to dynamically update the boundary conditions of the simulation, while dramatically reducing the size of the atomistic region. Using the GFBC approach, we subsequently developed a specialized Green's function atomistic simulation method to implement multi-ion MGPT potentials and calculate the pressure-dependent properties of $a/2\langle 1\,1\,1\rangle$ screw dislocations through MS and MD simulations [13]. These properties include the core structure and energy, the kink-pair formation energy, and the Peierls stress τ_P, as well as the full activation enthalpy below τ_P and the phonon-drag mobility above τ_P needed to describe dislocation motion in DD microscale simulations.

At the microscale, dislocation dynamics simulations implement the equations of continuum elasticity theory to track the motion and interaction of individual dislocations under an applied stress, leading to the development of a dislocation microstructure and single-crystal plastic deformation. In our multiscale modeling

strategy for bcc transition metals, the primary atomistic input supplied to the DD simulations is the dislocation mobility of individual $a/2\langle 1\,1\,1\rangle$ screw dislocations. For a given material, this input takes the form of an activation enthalpy versus shear stress curve and phonon-drag coefficients calculated for each pressure under consideration. Here full activation enthalpy curves have been calculated at selected pressures in Ta, Mo, and V, and phonon drag has been studied as a function of pressure and temperature in the case of Ta. These results have been fitted and modeled in suitable analytic forms to interface smoothly with the DD simulation codes. Detailed DD simulations have then been carried out in Ta and Mo as a function of pressure, temperature, and strain rate. Our DD simulations have been performed in part with the pioneering lattice-based serial code developed for bcc metals [21,22] but even more extensively with the general node-based Parallel Dislocation Simulator (ParaDiS) code recently developed at the Lawrence Livermore National Laboratory [27–30].

2. Computational approach

We begin by introducing and briefly discussing the specific computational methods we have used in the present work to implement our multiscale modeling strategy for bcc transition metals.

2.1. First-principles electronic-structure methods

The first-principles DFT electronic-structure results used below to constrain and validate MGPT potentials, and to calculate basic high-pressure properties have been obtained with either the full-potential linear muffin-tin orbital (FP-LMTO) method [37–39,44,45,47] or the plane-wave pseudopotential method [44–46,48]. The FP-LMTO method was used previously to study basic structural and mechanical properties in Ta to 1000 GPa (10 Mbar) [37], as well as in Mo [38,39] and V [47] to 600 GPa (6 Mbar). These data are used here in establishing the zero-temperature equation of state (cold EOS or pressure vs. volume curve) and the high-pressure shear elastic moduli. The FP-LMTO and PP methods were also used previously to study vacancy-formation energetics in bcc metals including Ta, Mo, and V [45]. Together with the cold EOS and shear elastic moduli, FP-LMTO and PP data on the vacancy formation energy are used to constrain the MGPT potentials. To help further validate the potentials at high pressure for the present dislocations studies, entirely new PP results have been obtained here on the ideal shear strength and high-symmetry features of the $\{1\,1\,0\}$ and $\{2\,1\,1\}$ γ surfaces to 400 GPa in Ta and Mo, and 140 GPa in V.

The FP-LMTO and PP methods have been implemented from first principles within the DFT and require only the atomic number and an assumed functional form for the exchange and correlation energy of the electrons as input. Historically, the latter functional has been treated within both the standard local-density

approximation (LDA) [43,44] and the more modern generalized gradient approximation (GGA) [44]. In general, the GGA is believed to provide the more accurate treatment for central transition metals and has been used in all of the FP-LMTO and PP results discussed here. In both the FP-LMTO and PP approaches, the electron charge density and potential are allowed to have any geometrical shape and are calculated self-consistently. In the FP-LMTO method all electrons are treated, including tightly bound inner-core, loosely bound outer-core, and itinerate valence electrons, to ensure that their rapidly changing character under pressure is fully accommodated. One incorporates non-sphericity to the charge density and potential by representing the crystal with nonoverlapping spheres (of a variable, optimum size) surrounding each atomic site and a general-shaped interstitial region between the spheres. Inside the spheres, the wave functions are represented as Bloch sums of linear muffin-tin orbitals and are expanded by means of structure constants. The kinetic energy is not restricted to be zero in the interstitial region and the wave function expansion contains Hankel or Neumann functions (depending on sign of the kinetic energy) together with Bessel functions. Also in the FP-LMTO method, all relativistic terms, including the spin–orbit coupling, can be included in the Hamiltonian as necessary, and this has been done in the results used here in the case of Ta. The metals V and Mo have been treated in a semi-relativistic fashion without the spin–orbit coupling.

In the PP method applied to transition metals one normally treats only the valence s, p, and d electrons, which total five per atom in V and Ta, and six per atom in Mo. Here special pseudopotentials in the Troullier–Martins form [48] have been constructed from scalar-relativistic atomic calculations to be accurate in the pressure range below 400 GPa. An important advantage of the PP method is that it provides accurate forces so that fully relaxed atomic configurations can be considered. We have used this capability here to obtain accurate relaxed $\{1\,1\,0\}$ and $\{2\,1\,1\}$ γ surfaces for Ta, Mo, and V. It is also possible to use relaxed PP configurations to perform validating FP-LMTO calculations on relaxed defects and γ surfaces, as was done previously at ambient pressure [13,45].

2.2. Quantum-based interatomic potentials

Within DFT quantum mechanics, first-principles GPT provides a fundamental basis for *ab initio* interatomic potentials in metals and alloys. In the GPT applied to transition metals [49], a mixed basis of plane waves and localized d-state orbitals is used to self-consistently expand the electron density and total energy of the system in terms of weak sp pseudopotential, d–d tight-binding, and sp–d hybridization matrix elements, which in turn are all directly calculable from first principles. For a bulk transition metal, one obtains the real-space total-energy functional

$$E_{\mathrm{tot}}(R_1 \ldots R_N) = NE_{\mathrm{vol}}(\Omega) + \frac{1}{2}{\sum_{i,j}}' v_2(ij;\Omega) + \frac{1}{6}{\sum_{i,j,k}}' v_3(ijk;\Omega) + \frac{1}{24}{\sum_{i,j,k,l}}' v_4(ijkl;\Omega). \tag{1}$$

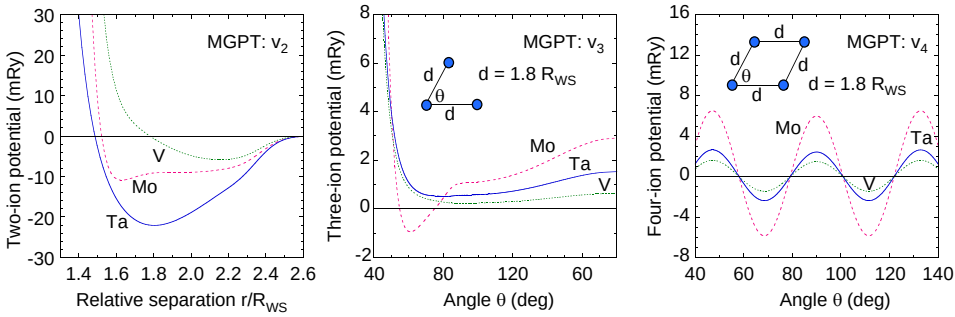

Fig. 1. Present advanced generation MGPT multi-ion potentials v_2, v_3, and v_4 for Ta, Mo, and V calculated at their respective equilibrium volumes.

The leading volume term in this expansion, E_{vol}, as well as the two-, three-, and four-ion interatomic potentials, v_2, v_3, and v_4, are volume-dependent, but *structure-independent* quantities and thus *transferable* to arbitrary bulk ion configurations. The angular-force multi-ion potentials v_3 and v_4 reflect directional-bonding contributions from partially filled d bands and are important for mid-period transition metals. In the full GPT, however, these potentials are multidimensional functions, so that v_3 and v_4 cannot be readily tabulated for application purposes. This has led to the development of a simplified MGPT, which achieves short-ranged, analytic potential forms that can be applied to large-scale atomistic simulations [50].

The MGPT is derived from the GPT through a series of systematic approximations applicable to central transition metals. Canonical d bands are introduced to express the d-state components of v_2 and the multi-ion potentials v_3 and v_4 analytically in terms of a single radial function and three universal angular functions that depend only on d symmetry and apply to all transition metals and all volumes. To compensate for the approximations introduced into the MGPT, the d-state potential coefficients in v_2, v_3, and v_4 together with E_{vol} are constrained by fundamental theoretical and/or experimental data. In our current preferred scheme for bcc metals, we fit a combination of first-principles DFT calculations and experimental data on the cold equation of state, shear elastic moduli, unrelaxed vacancy formation energy, and Debye temperature over a prescribed volume or pressure range. Advanced generation MGPT potentials have been so obtained in Ta to 1000 GPa [13,14], in Mo to 400 GPa [16,53], and in V to 230 GPa [53]. Representative results for these three metals are displayed in Fig. 1 at their respective equilibrium volumes.

2.3. Green's function atomistic simulation

Previously, the flexible GFBC method of Rao et al. [51,52] for dynamically updating the boundary conditions used in atomistic simulations was implemented for MGPT potentials and applied to study Ta dislocation properties at ambient

pressure [13]. This same approach has been used here to study $a/2\langle 1\,1\,1\rangle$ dislocation core structure and mobility at high pressure in Ta, Mo, and V. The GFBC approach extends the 2D lattice Green's function boundary relaxation method originated by Sinclair et al. [54] for treating rigid, straight dislocations to 3D simulations, including kink and kink-pair formation. The boundary conditions for 2D and 3D defect simulations cells are evaluated using line [55] and point [56] force distributions, respectively. In the flexible GFBC method, the simulation cell is divided into three regions, denoted as atomistic, Green's function (GF), and continuum. In the outer continuum region, the atomic positions are initially determined according to the anisotropic elastic displacement field [55] for a dislocation line defect at the center of the atomistic region, and then are relaxed by GF methods according to the forces in GF region. Complete atomistic relaxation is performed in the atomistic region according to the interatomic forces generated from Eq. (1). Forces developed in the GF region, as relaxation is achieved in the atomistic region, are then used to relax those atoms in *all three* regions by the 2D or 3D elastic and lattice GF solutions for line or point forces. The atomistic and GF relaxations are iterated until all force components on each atom are sufficiently small (10^{-4} eV/Å or less), and the final few steps must also be performed by direct atomistic relaxation for the atomistic and GF regions to ensure there is no force buildup in these two regions.

In our GFBC/MGPT simulation code, a spatial domain decomposition scheme is implemented for all three calculational regions, as illustrated schematically in Fig. 2. The small domain cells defined in this scheme are connected via a cell-linked-list method such that each cell has a fixed number of neighboring cells. This reduces the number of unnecessary interatomic separations considered in evaluating the MPGT potentials, which is crucial to their efficient application. In general, there are three major computational issues that need to be addressed: (1) the geometry of the simulation cell, which is purely cylindrical for a straight dislocation and in the form of a series of displaced cylindrical disks for a kink; (2) the fact that there are three regions in the full simulation cell, so that a connectivity algorithm for information passing between different regions is therefore necessary; and (3) the large effective cutoff radius $R_{\mathrm{cut}} = 4.25R_{\mathrm{WS}}$ for the MGPT potentials, which means there is a large overhead associated with the number of atoms per cell if the conventional domain-cell partition is considered (i.e., if each cell covers a volume R_{cut}^3, which then contains about 16 atoms). To solve these problems, a so-called layered-cake decomposition is used to split the three regions in the full simulation cell, so that each region has its own domain-cell-linked list. To reduce the overhead associated with the number of atoms per cell, the cell sizes are reduced by a factor of eight, therefore the average number of atoms per cell is about two. In addition, this approach allows a better description of the cylindrical geometry involved in the simulation when a cubic domain decomposition is used. As shown previously [13], the performance of our GFBC/MGPT simulation code is thereby increased by an order of magnitude as compared to conventional domain decomposition methods.

To take advantage of the scalable architectures of modern state-of-the-art computer platforms, a mapping algorithm was also developed for massively parallel

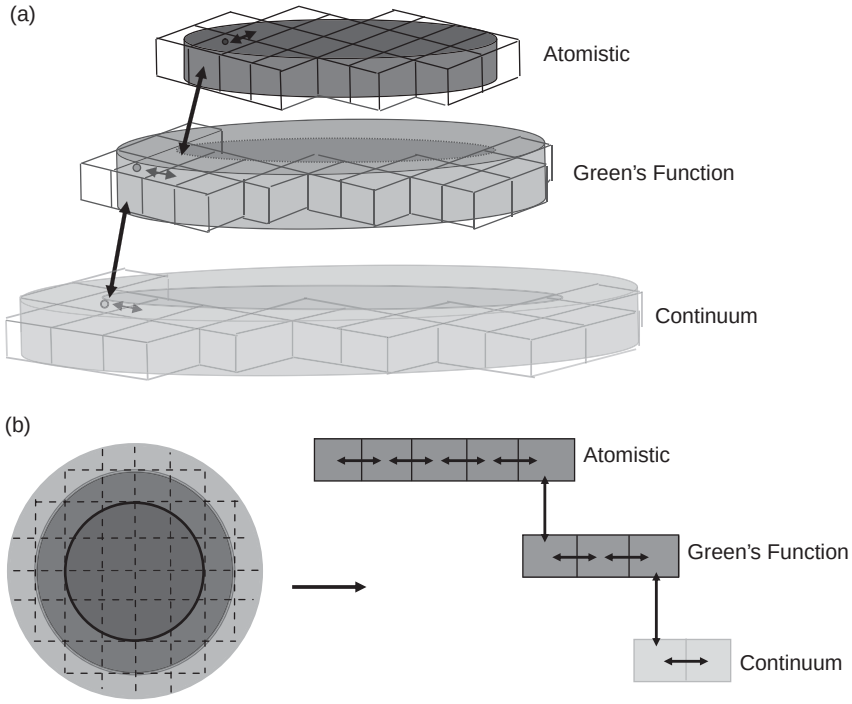

Fig. 2. Schematic representation of the domain decomposition scheme used to implement flexible Green's function boundary conditions in our GFBC/MGPT atomistic simulation code for dislocation calculations. (a) The three main computational regions separated into a layered-cake structure for a cylindrical coordinate system such that each region has its own domain decomposition. (b) To ensure the connectivity between regions and compatibility with parallel computing platforms, the domain cells are mapped into three one-dimensional arrays with cell-linked pointers between the cells and overlap regions.

computers. A 3D to 1D mapping list is built at the beginning of the simulation. This mapping list ensures the connectivity between different regions, so that no information is lost during the simulation. The logic behind this algorithm is that our simulation is always performed in a 1D computational domain regardless of the physical geometry involved. This is particularly useful when dealing with complicated geometries such as kinked dislocation structures or dislocation–dislocation interactions.

2.4. Dislocation dynamics simulation

DD simulation methods provide a numerical tool to directly connect the physics of individual dislocations to the strength properties of a crystalline material. These methods simulate explicitly the motion, multiplication, and interaction of collective dislocation lines in response to an applied load. A number of DD simulation

methods have been developed and reported over the past two decades [20–26]. Although they differ in their detailed approach, these methods share common basic features of dislocation motion and interaction. In this paper, we focus mainly on a general new node-based DD method developed at Lawrence Livermore National Laboratory called ParaDiS that allows efficient large-scale DD simulations on parallel computing platforms [27–30]. This approach complements the original lattice-based method for bcc metals of Tang et al. [21,22] and here we have performed DD simulations with atomistic input using both methods.

In ParaDiS, the dislocation lines are discretized by an assembly of nodes with straight-line dislocation segments connecting individual nodes [30]. The driving force for dislocation motion is calculated at each node. The force comes from various contributions including the dislocation self-energy change, dislocation–dislocation interaction forces, the external loading, and surface traction forces when applicable [31]. The dislocation–dislocation interactions are treated by isotropic linear elasticity theory and the latest development of non-singular stress expressions [29] has been implemented. A fast multiple method has also been implemented to gain computational efficiency for the force calculations. A detailed description of the ParaDiS method can be found in Ref. [30].

With the nodal forces determined, we calculate the nodal velocities by specifying the response of the nodes to the driving forces through the individual dislocation mobility functions. These mobility functions are very material and environment specific. They require specific parameters obtained from the lower length scale atomistic calculations performed at the single dislocation level. The mobility functions also depend on the character of the dislocations. In the case of bcc transition metals, the screw and edge mobility functions are defined differently. The screws move primarily by a thermally activated kink mechanism, and the edges move primarily by a phonon-drag mechanism. The specific functional forms and parameters of the mobility functions used in our DD simulations are discussed in Section 5.1 In the earlier lattice-based DD method, only screw and edge dislocation segments are considered. This method does not provide an accurate description of the dislocation line motion in general, and is only valid for conditions when the screws move much faster than the edges, as occurs in bcc metals at low and moderate temperature. In the current ParaDiS method, on the other hand, we have general line segments connecting the nodes with segment character of all types including screw, edge, and mixed segments. The mobility of the mixed segments is derived from that of both screw and edge.

The major material inputs to the DD simulations include the elastic constants and the Burgers vector at the chosen pressure and temperature conditions, as well as the pressure-dependent parameters used in the mobility functions. All of these quantities are explicitly calculated at the atomistic level, as described in Sections 3 and 4 of this paper. The loading condition for the DD simulations is typically constant strain rate. The major outputs are stress–strain response and the dislocation density changes. In Section 5.2, we discuss the details of the simulation of high-pressure yield strengths for Ta and Mo single crystals.

3. Salient high-pressure mechanical properties of bcc transition metals

We next discuss some important basic high-pressure mechanical properties of bcc transition metals that underpin our treatment of both dislocations and plasticity, and that can be obtained directly from first-principles electronic-structure calculations. These properties include the bulk and shear elastic moduli, the ideal shear strength, and generalized stacking-fault or γ energy surfaces. The pressure-dependent elastic moduli of a material establish the detailed character of the elasticity field in which individual dislocations move and interact, as well as serve as fundamental constraints on our MGPT interatomic potentials. The ideal shear strength provides a fundamental upper bound on material strength in the absence of dislocations and is a basic validation test of the potentials. The relevant low-energy γ surfaces for the $\{1\,1\,0\}$ and $\{2\,1\,1\}$ slip planes of interest in bcc plastic flow impose general constraints on dislocation character and are very useful validation tests for the MGPT potentials.

3.1. Bulk and shear elastic moduli

In our treatment of high-pressure mechanical properties, we assume that the bcc solid is subject to a stress tensor of the general form

$$S_{ij} = -P\delta_{ij} + \tau_{ij}, \tag{2}$$

where P is the uniform isotropic pressure in the material and τ_{ij} is a small additional applied deviatoric stress. In this regard, we assume that the loading path is such that the material is first uniformly compressed to pressure P through either static (e.g., diamond-anvil cell) or dynamic (e.g., shock) means, and then τ_{ij} is applied in some unspecified manner. In transition metals, the pressure $P = P(\Omega, T)$ has a strong dependence on the atomic volume Ω of the metal, but a relatively weak dependence on temperature T. For the purposes of this paper, it is adequate to replace P with the zero-temperature equation of state $P_0(\Omega)$. Calculated MGPT results for $P_0(\Omega)$ and the pressure dependence of the corresponding bulk modulus,

$$B_0(P) = -\Omega \left.\frac{\partial P_0(\Omega)}{\partial \Omega}\right|_{P=P_0(\Omega)}, \tag{3}$$

for Ta, Mo, and V up to 400 GPa are displayed in Fig. 3. By construction, these results are consistent with both room-temperature experimental data [40,57–59] and high-pressure FP-LMTO calculations [37,38,47]. At the observed room-temperature equilibrium volume Ω_0, $P_0(\Omega_0)$ is necessarily slightly negative (~ -1 GPa), as indicated in Table 1 for Ta, Mo, and V, since the compensating positive thermal pressure is neglected. In some of our later results we will refer to $P_0(\Omega_0)$ as ambient pressure. Also up to 400 GPa in Ta and Mo, and 200 GPa in V, the bulk modulus B_0 is nearly linear in pressure, so that $B_0' = \partial B_0/\partial P$ is approximately constant over the pressure ranges of interest in this paper. Consistent with the above assumptions and with the usual convention in high-pressure physics,

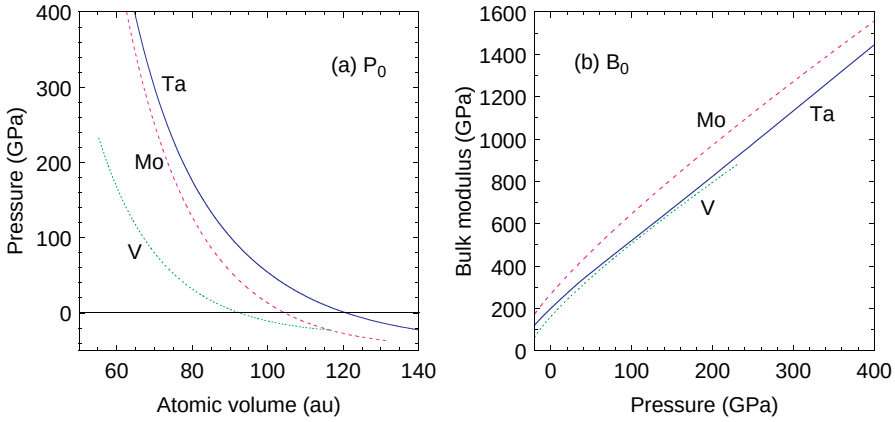

Fig. 3. Present calculated zero-temperature equations of state for Ta, Mo, and V. (a) Pressure versus atomic volume and (b) bulk modulus versus pressure.

Table 1
Observed equation of state (EOS) and elasticity properties in Ta, Mo, and V at their respective equilibrium volumes [58], with volume in atomic units (a.u.) and stress values in GPa

Quantity	Ta	Mo	V
EOS			
Ω_0	121.6	105.1	93.23
$P_0(\Omega_0)$	−1.1	−1.2	−1.1
B_0	196	263	157
B_0'	3.77	4.44	4.26
Elasticity			
C_{44}	82.5	109.0	43.4
C'	52.5	152.0	55.4
G_{111}	62.5	137.8	51.4
A	1.57	0.72	0.78

Note: These data are fully reflected in the present MGPT potentials.

we define individual elastic moduli C_{ij} as stress–strain relations relative to the current compressed state [60]. The corresponding MGPT-calculated shear elastic moduli $C' = (C_{11} - C_{12})/2$ and C_{44} are displayed in Fig. 4 for Ta to 1000 GPa, Mo to 400 GPa, and V to 250 GPa together with constraining FP-LMTO and experimental data, with equilibrium values listed in Table 1. The experimental data include ultrasonic measurements of the moduli and their pressure derivatives at ambient conditions [58] and high-resolution inelastic X-ray scattering (HRIXS) measurements at 37 GPa in Mo [59]. The shear moduli generally increase with increasing pressure, except for C' in Mo above 300 GPa and C_{44} in V above 20 GPa. The latter behavior reflects nearby phase transitions: bcc to close-packed phases

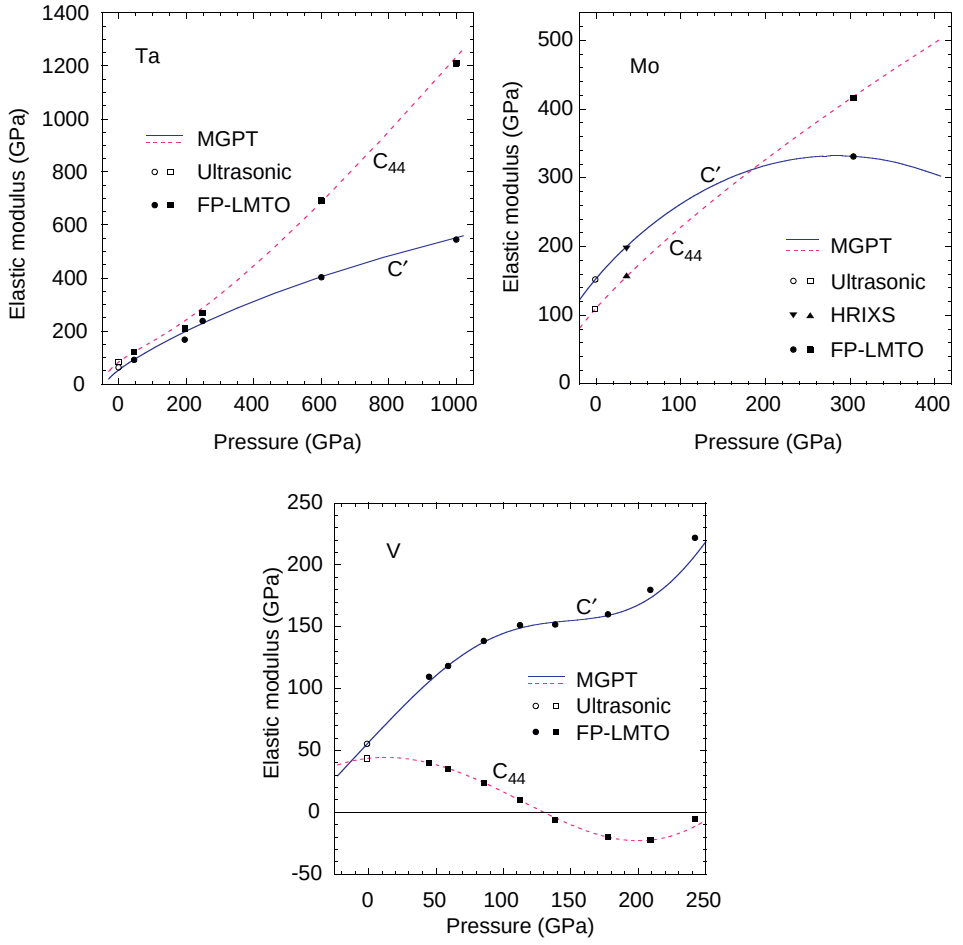

Fig. 4. Present MGPT-calculated high-pressure shear elastic moduli in Ta, Mo, and V together with constraining FP-LMTO and experimental data.

above 500 GPa in Mo [38,39] and bcc to a rhombohedral phase at 69 GPa in V [40]. In the case of V, C_{44} becomes negative and the bcc structure is mechanically unstable above 120 GPa.

Of special interest here to bcc screw dislocation motion is the effective shear modulus along the $\langle 1\,1\,1 \rangle$ slip direction,

$$G_{111} = \frac{2C' + C_{44}}{3}, \tag{4}$$

and the corresponding anisotropy ratio,

$$A = \frac{C_{44}}{C'}, \tag{5}$$

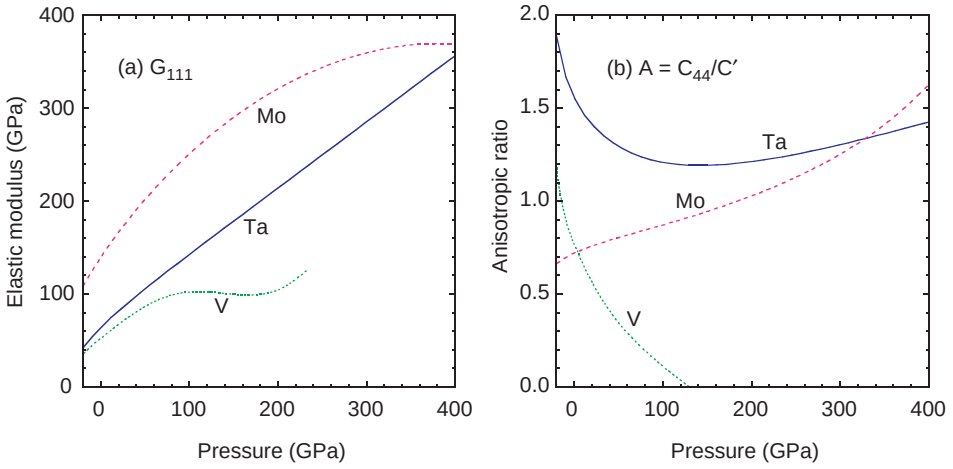

Fig. 5. Present calculated high-pressure behavior of the $\langle 1\,1\,1\rangle$ shear modulus G_{111} [panel (a)] and the anisotropic ratio A [panel (b)] for Ta, Mo, and V.

where a value of $A = 1.0$ would denote an elastically isotropic solid. MGPT-calculated results on the pressure dependence of these quantities for Ta, Mo, and V up to 400 GPa are displayed in Fig. 5. Over this pressure range, G_{111} is nearly linear in pressure for the case of Ta, but has a more complex behavior for Mo and V due to the proximity of the noted phase transitions in these metals. The pressure dependence of A over the same range also shows somewhat complex behavior, with a minimum of about 1.2 in the case of Ta near 140 GPa, a substantial increase with pressure from a value of 0.72 at ambient to about 1.6 at 400 GPa in Mo, and a very rapid decrease with pressure from a value of 0.78 at ambient to zero near 120 GPa in V.

3.2. Ideal shear strength

The next fundamental mechanical property we consider is the ideal shear strength of a bcc metal, as defined by Paxton et al. [61] and as previously discussed in the case of Ta [13,37]. At constant pressure, the ideal strength of the uniformly compressed perfect crystal is identified with the maximum shear stress τ_c required for a continuous homogeneous deformation of the crystal into itself via the observed twinning mode. For bcc metals, this mode can be specified by a shear direction $\eta = [\bar{1}\,\bar{1}\,1]$ and a normal plane $\mathrm{K} = (1\,1\,2)$. In the absence of tensile relaxation normal to K, which has been shown to be small for bcc transition metals [61,62], the atomic positions during the deformation can be directly related to the relative amount of shear x/s along the twinning path, where $s = 1/\sqrt{2}$ is maximum shear displacement along η per unit length along the $[1\,1\,2]$ direction. In particular, the unrelaxed ideal strength calculation may be carried out entirely using a single atom per unit cell and periodic boundary conditions, allowing for easy application

of full DFT electronic-structure methods. Previously for Ta, self-consistent FP-LMTO calculations of the unrelaxed ideal shear strength were performed at a few selected volumes in the 0–1000 GPa pressure range [37] and also later repeated at the observed equilibrium volume Ω_0 for comparison with corresponding MGPT calculations [9]. In the present work we have supplemented these results with extensive PP and MGPT calculations as a function of pressure over the range of 0–400 GPa in Ta and Mo, and 0–100 GPa in V.

In all cases we calculate a symmetric energy barrier along the twinning path at constant volume,

$$W(x,\Omega) = \frac{E_{\rm tot}[x,\Omega] - E_{\rm tot}[0,\Omega]}{N}, \tag{6}$$

where the barrier height is $W_{\rm c}$ at $x = s/2$. The corresponding stress along this path is given by

$$\tau(x,\Omega) = \frac{1}{\Omega}\frac{\partial W(x,\Omega)}{\partial x}. \tag{7}$$

The ideal shear strength is then defined as the maximum calculated stress along the twinning path, $\tau_{\rm c} = \tau(x_{\rm c},\Omega)$, where $x_{\rm c}$ is the critical shear separating regimes of elastic and plastic deformation of the crystal. In the present PP calculations, $W(x,\Omega)$ has been calculated at intervals of $x/s = 0.025$ in the range $0 \le x \le s/2$ and the curve extended to $x = s$ by symmetry. The result has then been fitted and differentiated analytically to obtain $\tau(x, \Omega)$ via Eq. (7). In the present MGPT calculations, $W(x, \Omega)$ has been calculated at smaller intervals of 0.01 over the full range $0 \le x \le s$, and then a smooth $\tau(x, \Omega)$ curve has been obtained directly from numerical differentiation. The present PP and MGPT results for Ta at $\Omega = \Omega_0$ are plotted and compared in Fig. 6. Present and previous calculated values of the barrier height $W_{\rm c}$, critical stress $\tau_{\rm c}$, and relative critical shear $x_{\rm c}/s$ at ambient pressure are listed and compared in Table 2. The overall agreement among the PP, FP-LMTO, and MGPT results is reasonable and adequate for the present purposes, although the MGPT values of $W_{\rm c}$ and $\tau_{\rm c}$ are systematically larger than the corresponding DFT electronic-structure values, and for Mo and V in better agreement with the FP-LMTO results than the PP results.

Under high pressure, the MGPT potentials for Ta, Mo, and V also fully capture the qualitative behavior of the ideal strength in these metals, with approximately the same level of quantitative agreement with the DFT electronic-structure calculations as at ambient pressure. In the left panel of Fig. 7, we compare MGPT, FP-LMTO, and PP results for the critical stress $\tau_{\rm c}$ in Ta as a function of pressure to 400 GPa. All three results show an approximate linear dependence of $\tau_{\rm c}$ on pressure, as one expects from the linear variation of G_{111} with pressure for Ta displayed in Fig. 5. The MGPT-calculated scaling behavior of $\tau_{\rm c}/G_{111}$ with pressure for Ta and Mo to 400 GPa, and V to 100 GPa is plotted in the right panel of Fig. 7. In contrast to the case of Ta, where $\tau_{\rm c}/G_{111}$ remains nearly constant at a value of about 0.12, $\tau_{\rm c}/G_{111}$ for Mo and V shows a noticeable decrease with increasing pressure. In part this reflects the nonlinear variation of G_{111} with pressure for these

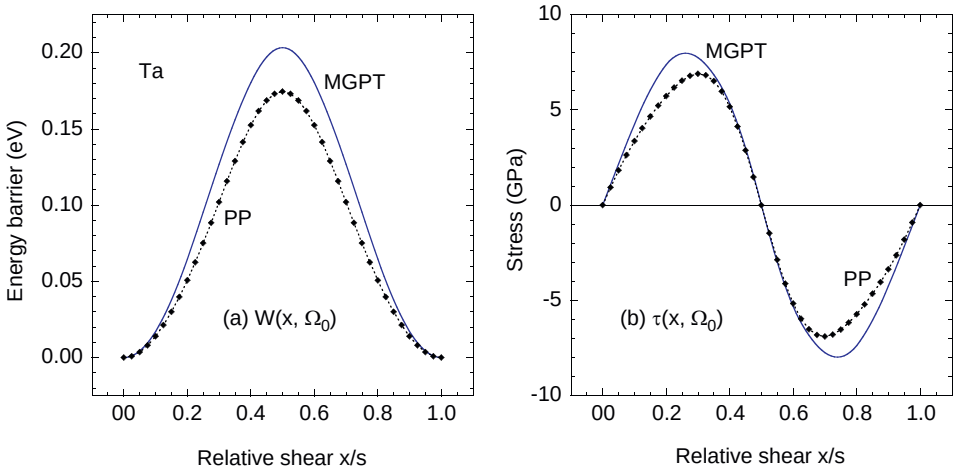

Fig. 6. Ideal shear strength of Ta at its observed equilibrium volume Ω_0, as calculated by the PP and MGPT methods. (a) Symmetric energy barrier $W(x, \Omega_0)$ and (b) corresponding shear stress $\tau(x, \Omega_0)$.

Table 2
Calculated ideal shear strength properties of Ta, Mo, and V at their observed equilibrium volumes, as obtained with the MGPT, FP-LMTO, and PP methods

Metal	Method	W_c (eV)	x_c/s	τ_c (GPa)
Ta	MGPT	0.20	0.26	8.0
	FP-LMTO[a]	0.18	0.26	6.5
	PP	0.17	0.30	6.9
Mo	MGPT	0.46	0.27	21.6
	FP-LMTO[b]	0.42	0.26	19.2
	PP	0.34	0.25	16.0
V	MGPT	0.15	0.28	7.9
	FP-LMTO[b]	0.15	0.26	7.3
	PP	0.09	0.30	5.0

[a]Ref. [13].
[b]Ref. [61].

metals (Fig. 5), although in both Mo and V the variation with pressure is clearly somewhat different for τ_c and G_{111}. At the same time, the variations in τ_c/G_{111} from one material to another as well as under high pressure for a given material are confined to the small range from 0.12 to 0.16 for all three metals.

3.3. Generalized stacking-fault (γ) energy surfaces

For accurately modeling bcc screw dislocation behavior, an even more important validation test concerns the generalized stacking-fault or γ energy surfaces for the

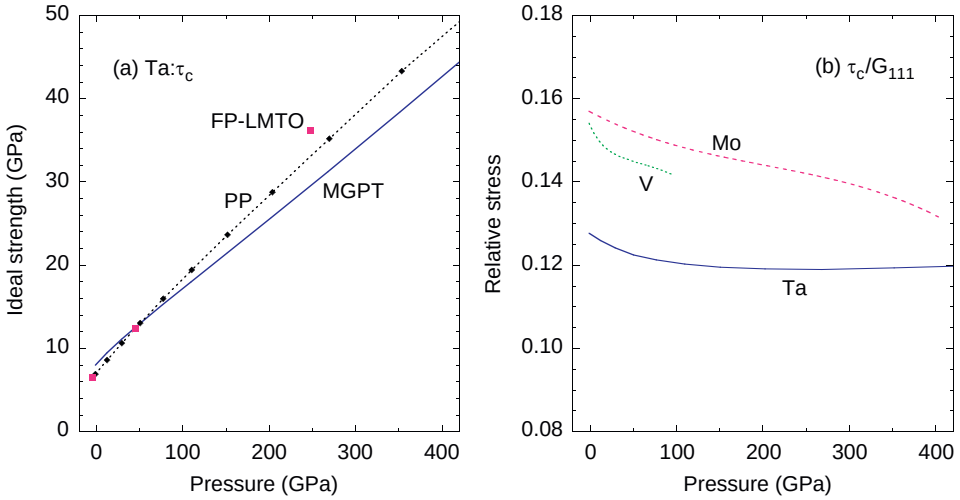

Fig. 7. Calculated ideal shear strength in bcc metals at high pressure. (a) Critical stress τ_c in Ta, as obtained with the MGPT, FP-LMTO, and PP methods and (b) relative stress τ_c/G_{111} for Ta, Mo, and V, as obtained with the MGPT method.

{1 1 0} and {2 1 1} slip planes. As first defined by Vitek [33], the γ surface is an energy profile of two semi-infinite blocks of bulk crystal rigidly displaced relative to each other by a vector $\boldsymbol{u}$ in a chosen fault plane, with atomic relaxation allowed only perpendicular to the plane. One can calculate high-pressure γ-surface energies at constant atomic volume using an appropriate computational super-cell with periodic boundary conditions. If desired, this can be done using two fault surfaces per super-cell, so that the full translational symmetry of the bulk crystal is preserved. Alternately, one can use one fault surface per triclinic super-cell with two constant lattice translation vectors and a variable vector inclined along the displacement direction $\boldsymbol{u}$. In this way, the number of atoms needed to define the super-cell is reduced by half, making first-principles DFT electronic-structure calculations of high-symmetry features of the γ surface much more tractable. As previously done in the case of Ta at ambient pressure [13], we follow here the latter approach and use a super-cell consisting of at least 12 atomic planes perpendicular to the fault surface and with one half of the cell shifted by the displacement vector $\boldsymbol{u}$. In the $\langle 1\,1\,1 \rangle$ direction, $\boldsymbol{u} = \alpha \boldsymbol{b}$, where $0 \leq \alpha \leq 1.0$. The same approach can then be applied to MGPT, FP-LMTO, or PP calculations at any pressure.

Complete {1 1 0} and {2 1 1} γ surfaces calculated for bcc Ta at its equilibrium volume with the present MGPT potentials are displayed in Fig. 8. Super-cell size is not a limitation in the MGPT calculations, and larger cells consisting of 32 planes (96 atoms) for the {1 1 0} surface and 96 atomic planes (96 atoms) for the {2 1 1} surface were used to ensure full convergence. Qualitatively, the calculated γ surfaces display the well-known general features expected for bcc metals [33]. In particular, the {1 1 0} surface is fully symmetric, while the {2 1 1} surface reveals

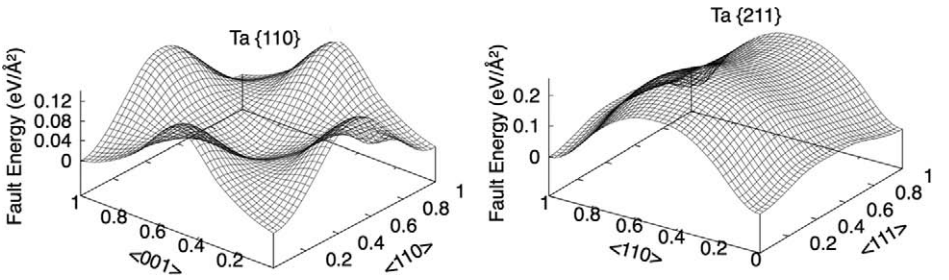

Fig. 8. Calculated γ surfaces for Ta at its equilibrium volume $\Omega = \Omega_0$ obtained by the MGPT method. Left panel: the $\{1\,1\,0\}$ surface; right panel: the $\{2\,1\,1\}$ surface.

the well-known twinning–anti-twinning asymmetry along the $\langle 1\,1\,1 \rangle$ direction characteristic of bcc materials. No stable stacking faults in the form of local minima are found on either surface, and all extrema are either maxima or saddle points. These same qualitative features are also maintained in Ta at high pressure to at least 400 GPa, as well as in Mo to 400 GPa and V to 100 GPa.

In order to validate the MGPT potentials quantitatively for high-pressure dislocation studies, we have calculated high-symmetry slices of the $\{1\,1\,0\}$ and $\{2\,1\,1\}$ γ surfaces along the $\langle 1\,1\,1 \rangle$ direction in Ta, Mo, and V using both the MGPT and PP methods. In particular, such calculations along $\langle 1\,1\,1 \rangle$ provide a very sensitive test of the quality of the MGPT potentials because the stacking-fault energies involved are small and similar in magnitude to those encountered in the formation and motion of $a/2\langle 1\,1\,1 \rangle$ screw dislocations. Calculated MGPT and PP results at selected pressures for Ta, Mo, and V are shown in Figs 9–11, respectively. Here the displacement parameter α can be conveniently written as x/b, where b is the magnitude of the Burgers vector. In the cases of Ta and Mo, the maxima in these curves at $x = b/2$, which is commonly defined as the unstable stacking-fault energy $\gamma_{\rm us}$, increase monotonically with pressure. This is shown more directly in Fig. 12(a) where complete MGPT results for $\gamma_{\rm us}^{110}$ and $\gamma_{\rm us}^{211}$ are plotted as a function of pressure up to 400 GPa. At each of the selected pressures in Figs 9 and 10, the MGPT curves conform to the PP points very closely and the quantitative agreement is everywhere within 7%. In this regard, on the $\{2\,1\,1\}$ γ surface of Mo the expected twinning–anti-twining asymmetry is clearly evident in both the MGPT and PP results, and is very accurately predicted by the MGPT potentials. We conclude, therefore, that the present MGPT potentials should be reliable for the calculation of the $a/2\langle 1\,1\,1 \rangle$ screw dislocation properties for Ta and Mo up to at least 400 GPa.

The case of V shows somewhat more complicated behavior. In this metal the calculated PP and MGPT stacking-fault energies increase monotonically with pressure only up to about 80 GPa such that above that point the γ surface actually lies lower in energy than that at 53 GPa. This is shown more clearly in Fig. 12(a), where the complete set of MGPT unstable stacking-fault energies $\gamma_{\rm us}^{110}$ and $\gamma_{\rm us}^{211}$ for V up to 230 GPa are plotted. In addition, up to at least 53 GPa, the calculated PP stacking-fault energies are systematically higher than those obtained with the MGPT potentials by 10–25%, as shown in Fig. 11. This makes the MGPT

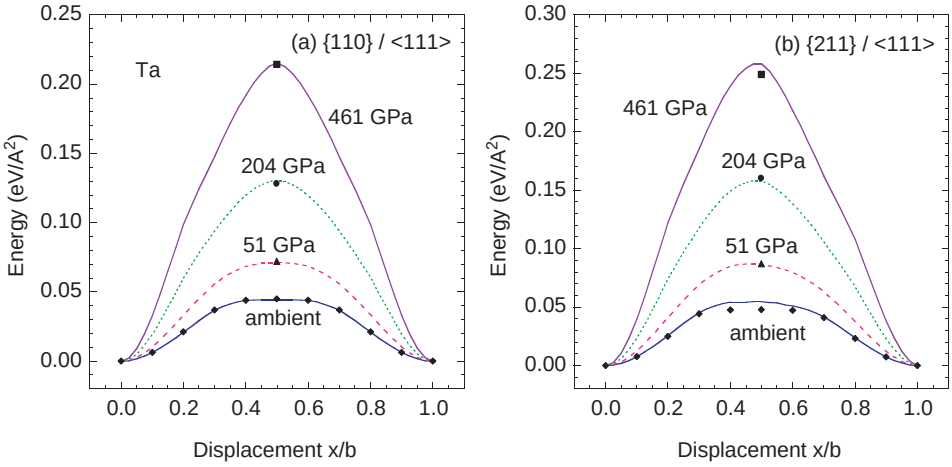

Fig. 9. Calculated slices of the {1 1 0} and {2 1 1} γ surfaces in Ta at four selected pressures obtained using the MGPT (solid, dashed, and dotted lines) and PP (solid points) methods. (a) The {1 1 0} surface along the $\langle 1\,1\,1 \rangle$ direction and (b) {2 1 1} surface along $\langle 1\,1\,1 \rangle$.

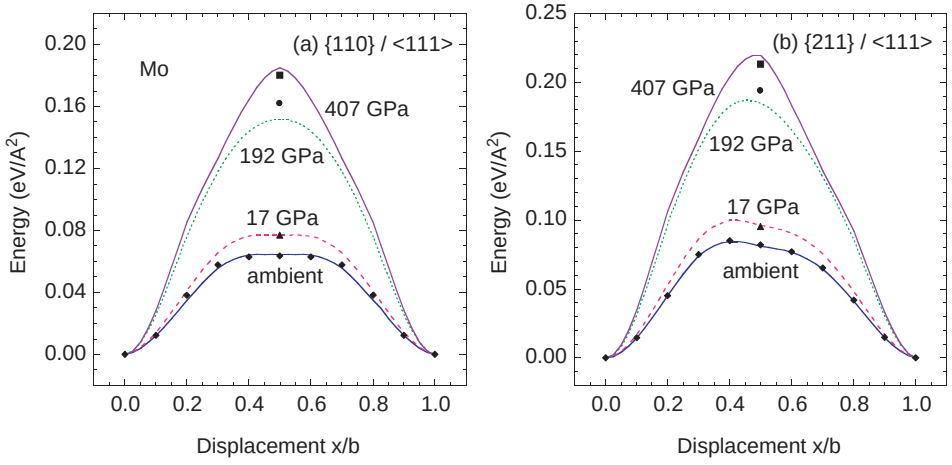

Fig. 10. Calculated slices of the {1 1 0} and {2 1 1} γ surfaces in Mo at four selected pressures obtained using the MGPT (solid, dashed, and dotted lines) and PP (solid points) methods. (a) The {1 1 0} surface along the $\langle 1\,1\,1 \rangle$ direction and (b) {2 1 1} surface along $\langle 1\,1\,1 \rangle$.

calculation of $a/2\langle 1\,1\,1 \rangle$ dislocation properties in V somewhat less certain quantitatively than in either Ta or Mo.

Fig. 12(a) further shows that the {1 1 0} unstable stacking-fault energy $\gamma_{\rm us}^{110}$ is systematically smaller than the {2 1 1} fault energy $\gamma_{\rm us}^{211}$ for all pressures up to 400 GPa in Ta and Mo, and up to 230 GPa in V. This has important implications for the motion of $a/2\langle 1\,1\,1 \rangle$ screw dislocations on {1 1 0} and {2 1 1} slip planes. At all

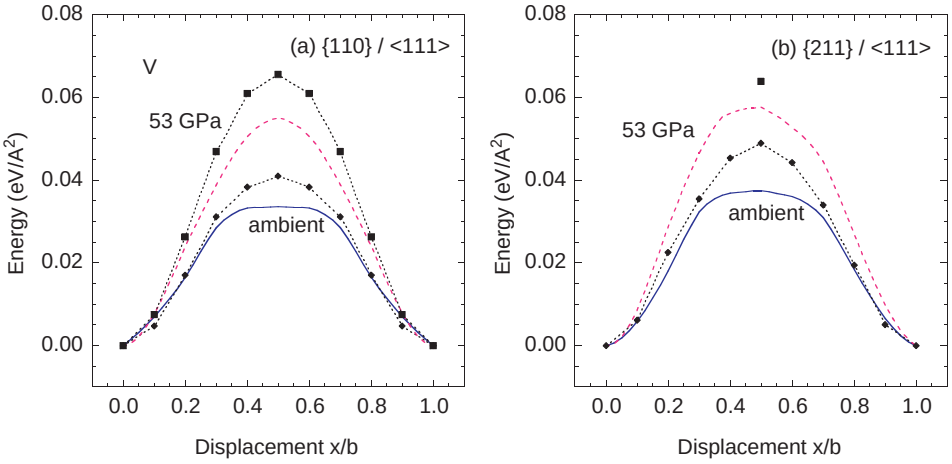

Fig. 11. Calculated slices of the {1 1 0} and {2 1 1} γ surfaces in V at two selected pressures obtained using the MGPT (solid and dashed lines) and PP (dotted lines and solid points) methods. (a) The {1 1 0} surface along the $\langle 1\,1\,1 \rangle$ direction and (b) {2 1 1} surface along $\langle 1\,1\,1 \rangle$.

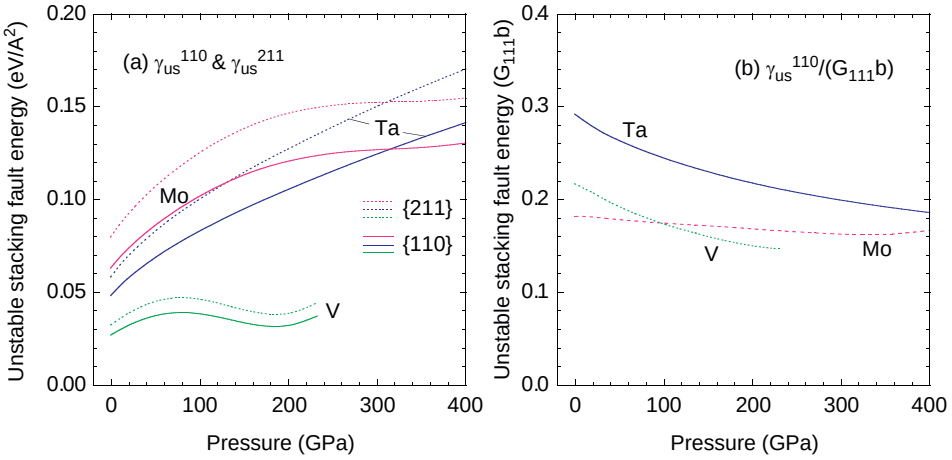

Fig. 12. Unstable stacking-fault energies for Ta, Mo, and V, as calculated with the MGPT method. (a) Energies γ_{us}^{110} and γ_{us}^{211} for the {1 1 0} and {2 1 1} γ surfaces, respectively and (b) scaled energy $\gamma_{us}^{110}/(G_{111}b)$ for the {1 1 0} surface.

pressures considered here, the screw dislocations in Ta, Mo, and V prefer to move on {1 1 0} planes although, as previously discussed [13], this can happen in more than one way, such that at larger length scales slip may effectively appear to occur on either {1 1 0} or {2 1 1} planes. Also the scaled fault energy $\gamma_{us}^{110}/(G_{111}b)$ displays scaling properties similar to those found for the scaled ideal strength τ_c/G_{111}, except that the roles of Ta and Mo are reversed, as shown in Fig. 12(b).

In particular, the scaled unstable stacking-fault energy is nearly constant as a function of pressure in the case of Mo, but clearly decreases with pressure for Ta and V.

4. a/2⟨111⟩ screw dislocation properties at high pressure

As first pointed out by Hirsch [63], the mobility of an $a/2\langle 1\,1\,1\rangle$ screw dislocation in a bcc lattice is severely restricted by the atomic structure of its core. Around a given $\langle 1\,1\,1\rangle$ direction, the bcc structure has three-fold symmetry. Each such $\langle 1\,1\,1\rangle$ zone contains three $\{1\,1\,0\}$ and three $\{1\,1\,2\}$ planes that are potential slip planes in the bcc structure, as well as admitting the possibility of a three-dimensional spreading of the core structure along $\langle 1\,1\,2\rangle$ directions on the $\{1\,1\,0\}$ planes when the screw dislocation is formed. Detailed descriptions of extended core structures in bcc metals have been obtained from many previous atomistic studies [9–19,32–36,64] and have indicated a core extension of a few Burgers vectors in length and a high Peierls stress associated with its movement under an applied load. In this section, we discuss our atomistic simulations of basic $a/2\langle 1\,1\,1\rangle$ screw dislocation core properties at both ambient and high pressures in bcc Ta, Mo, and V, using the MGPT potentials and Green's function methodology discussed above. Our focus will be on the zero-temperature calculation of core properties that are fundamental to an understanding of dislocation structure and mobility. The properties considered include the atomic structure and energy of the equilibrium dislocation core in the absence of any additional shear stress, the nature and energetics of isolated kinks and mobile kink pairs that can be formed from this core in the low shear stress limit, and the magnitude and orientation dependence of the Peierls stress required to move the rigid dislocation in the high shear stress limit. To link directly to corresponding DD simulations of plasticity, we also consider the full activation enthalpy associated with activated screw dislocation motion as a function of applied shear stress, as well as dislocation motion above the Peierls stress in the phonon-drag regime.

4.1. Equilibrium core structure and energy

The $a/2\langle 1\,1\,1\rangle$ screw dislocation has one or more stable core configurations located at the center of gravity of three $\langle 1\,1\,1\rangle$ atomic rows forming a triangular prism. Around these three rows the near-neighbor atoms are located on a helix that winds up in a clockwise or counterclockwise manner, depending on the location of the elastic center and the sign of the Burgers vector, so that two different types of core configurations can be obtained [9]. One configuration is isotropic and of high energy, and may or may not be stable. This is usually referred to as the ''hard'' core. The other configuration is of low energy and is normally the stable ground-state structure. This is the so-called ''easy'' core. In general, the ''easy'' core can exhibit three-fold $\langle 1\,1\,2\rangle/\{1\,1\,0\}$ directional spreading in two geometrically distinct, but

energetically equivalent ways, resulting in a doubly degenerate ground-state core structure with two possible orientations. Under certain circumstances, however, this directional spreading may vanish and an isotropic nondegenerate core with a higher, but still three-fold, symmetry results. In the present work, we have studied the pressure dependence of the ''easy'' core ground-state in bcc Ta, Mo, and V up to very high pressure.

As done previously [13,14,16,19], we have simulated the stable ground-state screw dislocation core structure using a two-dimensional GFBC/MGPT technique in cylindrical geometry, with periodic boundary conditions and a period of $b = \sqrt{3}a/2$ along the z-axis ($\langle 1\,1\,1 \rangle$ direction) at constant atomic volume $\Omega = a^3/2$ in the bcc structure. In this procedure, an infinite $a/2\langle 1\,1\,1 \rangle$ screw dislocation is first introduced by displacing all atoms in the simulation according to anisotropic elasticity solutions using Stroh's sextic formalism [55]. The atomic positions of the core atoms are then allowed to relax within the GFBC simulation cell. Radially outward from the cylinder axis, the inner atomistic region of the simulation cell is surrounded by GF and continuum regions (see Fig. 2) each with a shell thickness of $R_{\mathrm{cut}} = 4.25R_{\mathrm{WS}}$, the effective cutoff radius for the MGPT potentials. A radius for the atomistic region of about $20b$ is needed to accurately characterize the fully relaxed core structure.

The qualitative aspects of the calculated core structures are most easily displayed and discussed using the standard differential displacement method of Vitek [33]. In this method, the $\langle 1\,1\,1 \rangle$ screw components of the relative displacement of neighboring atoms due to the dislocation (i.e., the total relative displacement in the z direction less that in the perfect lattice) is represented by an arrow between the two atoms. The calculated screw-component differential displacement maps for Ta at two widely different pressures are shown in Fig. 13. The left panel of that figure displays the nearly isotropic core structure of Ta that we calculate at ambient pressure, while the right panel shows the strong directional spreading obtained in the same metal at a pressure of 1000 GPa. In both cases, the length of the arrows is normalized by $b/3$, the magnitude of the separation of neighboring atoms along the $\langle 1\,1\,1 \rangle$ direction. A corresponding differential displacement map can also be constructed for the edge components of the dislocation as well, but the magnitude of the edge displacements is found to be 10–100 times smaller than that of the screw components [13], and we do not consider these further in this paper.

Qualitatively, the core structures displayed in Fig. 13 are representative of the isotropic and the spread core structures we have obtained for Ta, Mo, and V. The degree of three-fold directional spreading of the core can be directly quantified by its so-called polarization $\boldsymbol{p}$, which measures the simultaneous translation of the three central atoms nearest to the core center [64,65]. This translation is parallel to the dislocation line but in the opposite sense for the two different core orientations, usually denoted as positive p and negative n. By symmetry, the magnitude of p can only vary from zero to $b/6$. At $p = 0$, the two core configurations coincide and a fully symmetric or isotropic core structure with a higher three-fold symmetry is obtained. At $p = b/6$, on the other hand, a fully polarized core is obtained with a maximum three-fold spreading along $\langle 2\,1\,1 \rangle$ directions. Our calculated core

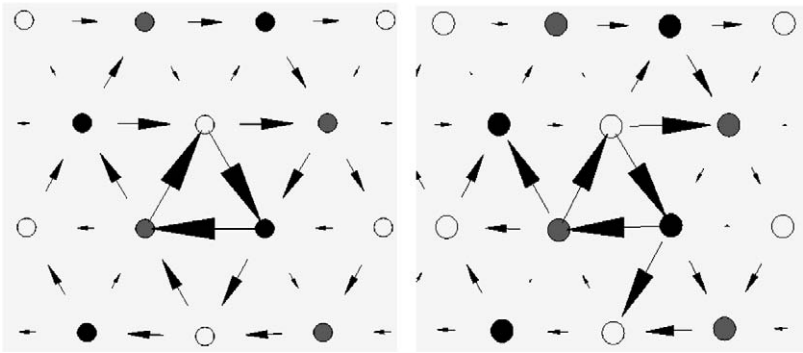

Fig. 13. Differential displacement maps of the relaxed core structures of Ta at low and high pressures as calculated with GFBC/MGPT atomistic simulations. Left panel: isotropic core structure at ambient pressure; right panel: spread core structure at 1000 GPa.

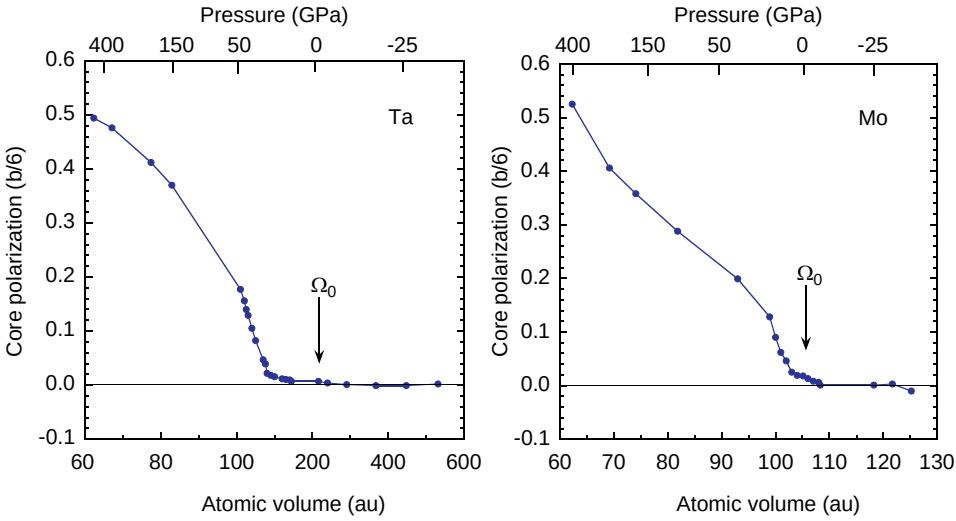

Fig. 14. Calculated volume and pressure dependence of the core polarization for Ta and Mo, as obtained from the present GFBC/MGPT atomistic simulations.

polarization as function of atomic volume and pressure is plotted in Fig. 14 for Ta and Mo to 400 GPa, and in Fig. 15 for V to 75 GPa. In the cases of Ta and Mo near equilibrium ($\Omega = \Omega_0$) and at expanded volumes corresponding to negative pressures, the calculated core polarization is less than $0.02b/6$, the approximate level of accuracy of our results, and thus consistent with a nondegenerate isotropic core structure. Under compression, however, the polarization rises rapidly in both cases and attains a value of $0.5b/6$ near pressures of 400 GPa. In contrast to Ta and Mo, the dislocation core of V is already significantly polarized near equilibrium and

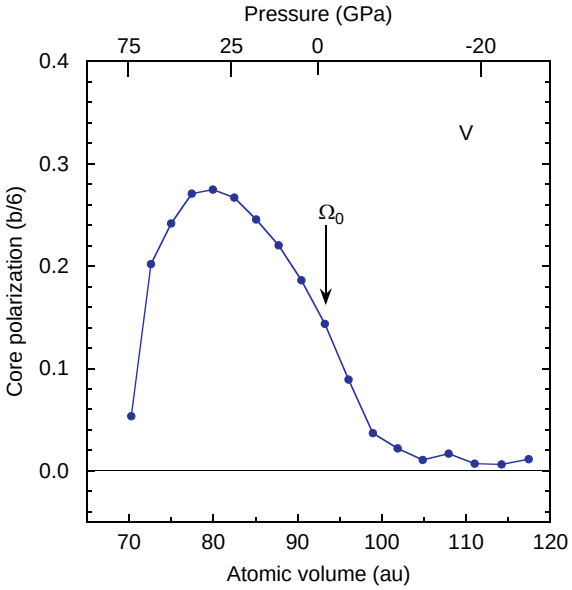

Fig. 15. Calculated volume and pressure dependence of the core polarization for V, as obtained from the present GFBC/MGPT atomistic simulations.

p rises only to a maximum of about $0.275b/6$ near 32 GPa and then descends rapidly toward zero close to the bcc→rhombohedral phase transition observed at 69 GPa [40]. As in Ta and Mo, at sufficiently expanded volumes and negative pressure in V, the polarization p does tend toward zero. In all three metals, the transition between an isotropic core with $p = 0$ and a spread core with finite p appears to be continuous and not a first-order phase transition. Calculated values of p at $\Omega = \Omega_0$ for Ta, Mo, and V are listed in Table 3.

The above results show clearly that the screw dislocation core structure in bcc metals is a materials-specific property that depends on both chemical element and environmental factors such as pressure. Near ambient pressure, our predictions of a nearly isotropic core structure in Ta and Mo are consistent with recent first-principles DFT electronic-structure calculations of core structure using small computational cells and a variety of boundary conditions [10,11,17,66], as well as with quantum-based bond-order potential (BOP) calculations on Mo using fixed boundary conditions [18]. In contrast to our results for Mo and V, an earlier systematic study of the group-VB and -VIB metals using empirical radial-force potentials [29] found isotropic cores for the VB metals, including V and Ta, and three-fold spread cores for the VIB metals, including Mo. Our present result for Mo at ambient pressure is also in contrast to previous results [9,12], which found a strong three-fold spreading of the core structure using the earlier generation 1994 MGPT potentials for that metal [50].

In addition to its atomic structure, it is also of interest to calculate the effective size and energy associated with the equilibrium core, as done previously for Ta at

Table 3
Basic $a/2\langle 1\,1\,1\rangle$ screw dislocation properties in bcc Ta, Mo, and V at their respective equilibrium atomic volumes [58]

Quantity	Ta	Mo	V
Structure			
Ω_0 (Å^3)	18.02	15.57	13.82
a (Å)	3.303	3.146	3.023
b (Å)	2.861	2.725	2.618
p (b/6)	0.007	0.018	0.144
Energy			
R_c/b	1.75	1.75	2.0
E^f_{core} (eV/Å)	0.22	0.30	0.11
$A_{elastic}$ (eV/Å)	0.25	0.50	0.17
Mobility			
E^f_{kp} (eV)	0.96	1.15	0.68
τ_P (GPa)	0.577	0.860	0.360
τ_P/G_{111}	0.00923	0.00625	0.00701

Note: Included quantities are the atomic volume Ω_0, bcc lattice constant a, magnitude of the Burgers vector b, core polarization p, core radius R_c, core energy E^f_{core}, elastic energy $A_{elastic}$, kink-pair formation energy E^f_{kp}, and Peierls stress τ_P.

ambient pressure [13]. In continuum elasticity theory, the formation energy E^f_{screw} of a screw dislocation (per unit length) in a cubic crystal is a linear function of $\ln(R/R_c)$, where R is the outer radius of a cylinder that contains the dislocation core at its center and R_c is the core radius. The formation energy E^f_{screw} includes the core energy stored inside R_c, E^f_{core}, plus the elastic energy stored in the region between R_c and R, such that

$$E^f_{screw} = E^f_{core} + A_{elastic}\ \ln\left(\frac{R}{R_c}\right), \tag{8}$$

where the elastic energy coefficient $A_{elastic}$ can be directly calculated from the elastic moduli of the material [9]. The main unknown in Eq. (8) is the minimum core radius R_c that will satisfy that equation. One can find by iteration, starting with a trial value of R_c, and calculating E^f_{core} and E^f_{screw} via atomistic simulation as a function of R. An essentially equivalent procedure that is sometimes useful in the context of GFBC/MGPT simulations is to define R_c to be the minimum radius at which the 2D elastic and lattice Green's functions become equal [13]. Either procedure results in some uncertainty in determining optimum values of R_c, but here we have used the former approach and thereby calculated E^f_{core} for selected pressures in Ta, Mo, and V. In all three metals, we determine R_c/b to be in the range 1.75–3.0, with R_c increasing with increasing pressure up to 400 GPa. Our calculated results for E^f_{core} and $A_{elastic}$ are plotted in Fig. 16 with the ambient-pressure results for R_c/b, E^f_{core}, and $A_{elastic}$ given in Table 3.

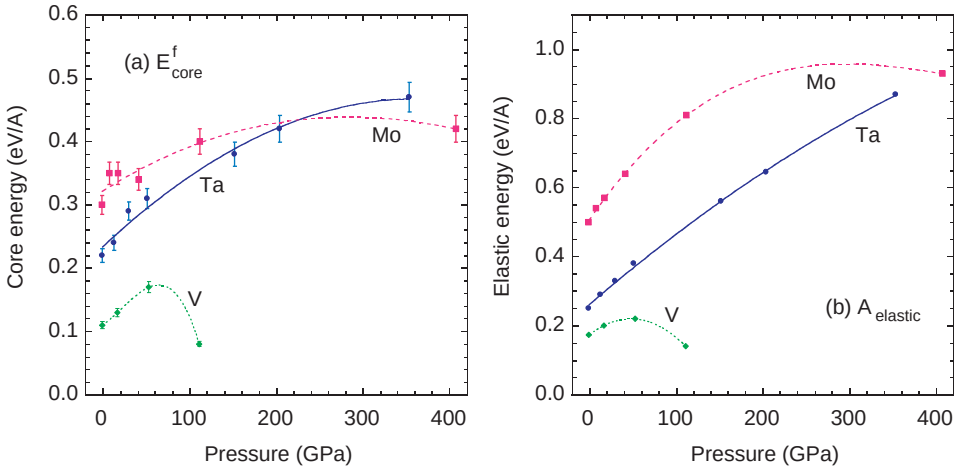

Fig. 16. Core and elastic contributions to the screw dislocation formation energies [Eq. (8)] in Ta, Mo, and V as function of pressure. (a) Core formation energy $E^{\mathrm{f}}_{\mathrm{core}}$ as obtained from GFBC/MGPT atomistic simulations and (b) elastic coefficient A_{elastic} determined from MGPT elastic moduli.

As seen in Fig. 16, the uncertainty in R_{c} results in some fluctuations in the calculated values of $E^{\mathrm{f}}_{\mathrm{core}}$.

4.2. Low shear stress limit: kink-pair formation energy

At finite temperature, the motion of the screw dislocations in the bcc lattice normally occurs by the thermally assisted formation and migration of kink pairs. For low shear stress conditions, the individual kinks in a kink pair are well separated and weakly interacting, so kink-pair formation can be modeled by just looking at isolated left- and right-kink formation. In this limit, the nature and atomic structure of the possible kinks is closely related to the unstressed dislocation core, which we assume here is of doubly degenerate form. As we have discussed above, the doubly degenerate core structure of the rigid $a/2\langle 1\,1\,1\rangle$ screw dislocation can have two energetically equivalent configurations with opposite polarizations denoted as positive p and negative n. As a result, there are different possible kinks and kink-pair configurations involving p and n segments that can be formed. In addition, p and n segments can coexist on the same dislocation line in the form of a so-called anti-phase defect (APD). This further increases the multiplicity of possible kinks and kink pairs, as we have previously elaborated in the case of Ta [13].

Here we assume that an isolated left (l) or right (r) kink of a kink pair consists of two semi-infinite segments of p or n orientation separated by a kink height h. The symmetry of the bcc lattice allows six distinct and nondegenerate kinks [34]. These are of character *nln* (degenerate with *plp*), *nrn* (degenerate with *prp*), *nlp*, *nrp*, *pln*, and *prn*. As previously demonstrated in the case of Ta [13], the lowest energy kink pair in the absence of a preexisting APD has the character *pln–nrp*. In Ta at

ambient pressure and zero applied shear stress, this kink pair has a calculated formation energy $E^{\mathrm{f}}_{\mathrm{kp}}$ of 0.96 eV, which is in close agreement with the empirically derived zero-stress activation enthalpy of 1.02 eV used in microscale DD simulations to account for the observed yield stress [21]. For this reason, we have adopted the *pln–nrp* kink pair as the appropriate model for kink-pair formation in bcc transition metals, and used it here for Ta, Mo, and V at both ambient and high pressures.

To model an isolated *pln* or *nrp* kink accurately, we work at constant volume and set up the GFBC simulation cell in the form of a long compliant cylinder made up of unit disks of width b and radius $20b$ (for the atomistic region), and a total length $60–80b$ centered on the dislocation line. A transition region of $10–15b$ is allowed across the kink height h, where the kink is fully relaxed in the GFBC/MGPT simulation. To form a closed 3D cage, the two ends of the cylinder are capped with GF and continuum regions. The z-axis of the compliant cylinder is taken parallel to a [1 1 1] dislocation line direction, while the y-axis is taken parallel to [1 $\bar{1}$ 0] and the x-axis to [$\bar{1}$ $\bar{1}$ 2]. The smallest repeat translation vector for the rigid screw dislocation core in the bcc lattice is $(a/3)[\bar{1}\,\bar{1}\,2]$ on a {1 1 0} plane, and this defines the elementary kink height h with magnitude $\sqrt{6}a/3$. We have considered only kinks formed within this geometry. Kinks formed on other planes such as {2 1 1} have significantly larger kink heights and therefore either are unstable or have much larger kink-formation energies [9,67].

We further assume that the process of kink-pair formation is limited by the isolated kink-formation energies E^{f}_{pln} and E^{f}_{nrp}, as opposed to the competing process of kink migration, which is controlled by the secondary Peierls stresses needed to move the left- and right-hand kinks. As shown previously in the case of Ta at ambient pressure [13], the secondary Peierls stresses are one to two orders of magnitude smaller than the corresponding Peierls stress for the rigid screw dislocation itself, so both kinks are expected to be mobile with the left kink moving faster than the right kink. Consequently, we expect the dislocation velocity at low shear stress τ to be controlled by the kink-pair formation energy $E^{\mathrm{f}}_{\mathrm{kp}}$ rather than any small kink migration barriers. In the $\tau = 0$ limit, the former is calculated as a sum of left- and right-kink-formations energies:

$$E^{\mathrm{f}}_{\mathrm{kp}} = E^{\mathrm{f}}_{pln} + E^{\mathrm{f}}_{nrp}. \tag{9}$$

The individual left- and right-kink-formation energies are most efficiently calculated by summing the unit disk contributions in our GFBC compliant cylinder across the transition region in the kink. That is, in each unit disk we subtract from the atomistic total energy with the kink present the corresponding total energy for the perfect straight dislocation. This procedure provides a cancellation of total-energy errors and leads to kink-formation energy values that are typically accurate to 0.05–0.10 eV or 5–10%. We have so calculated $E^{\mathrm{f}}_{\mathrm{kp}}$ at selected pressures in Ta, Mo, and V. These results are plotted in Fig. 17(a) with ambient-pressure values listed in Table 3. As expected, $E^{\mathrm{f}}_{\mathrm{kp}}$ is monotonically increasing with pressure, but in a significantly nonlinear way in each case. The scaled kink-formation energy

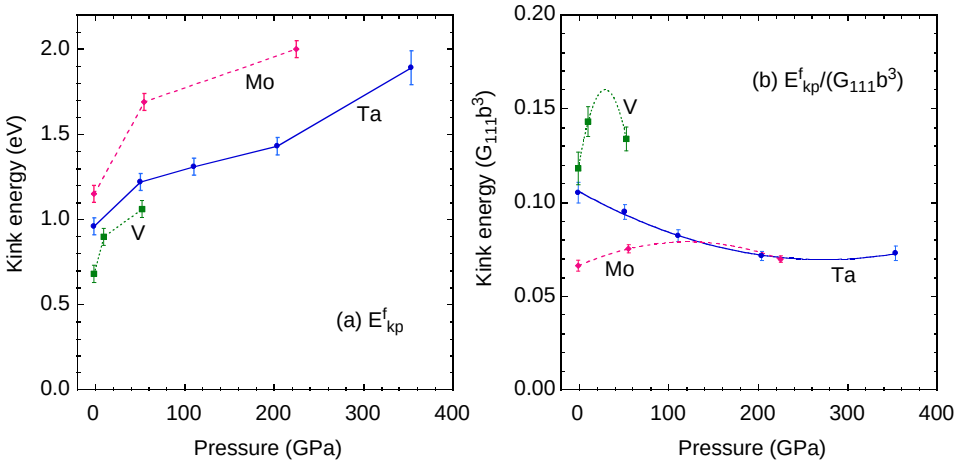

Fig. 17. Pressure dependence of the *pln–nrp* kink-pair formation energies for Ta, Mo, and V, as calculated from GFBC/MGPT atomistic simulations. (a) Full energy $E^{\mathrm{f}}_{\mathrm{kp}}$ and (b) scaled energy $E^{\mathrm{f}}_{\mathrm{kp}}/(G_{111}b^3)$.

$E^{\mathrm{f}}_{\mathrm{kp}}/(G_{111}b^3)$ displays a somewhat soother and slowly varying pressure dependence in the cases of Ta and Mo, as shown in Fig. 17(b). In any case, the calculated values of $E^{\mathrm{f}}_{\mathrm{kp}}$ constrain the low shear stress limit of the full stress-dependent activation enthalpy for dislocation motion, which is considered below in Section 4.4.

4.3. High shear stress limit: Peierls stress

Next we turn to the high stress limit and the calculation of the Peierls stress τ_{P} for the rigid $a/2\langle 1\,1\,1\rangle$ screw dislocation. Bcc metals are known to slip predominantly on {1 1 0} and/or {1 1 2} planes at low temperatures, but this slip does not follow the familiar Schmid law [68] and, in fact, a rather complex orientation dependence of the slip geometry and the yield stress is experimentally observed [69]. Consequently, one expects that there is a strong dependence of the critical resolved shear stress (CRSS) needed to move the rigid screw dislocation on the orientation of the applied stress. In the context of GFBC/MGPT simulations, this orientation dependence was previously investigated in bcc Ta at ambient pressure [13] by applying both pure glide shear stresses and selected shears with a uniaxial stress component. For applied stresses either on a {1 1 0} plane or in the twinning direction of a {1 1 2} plane, it was found that the addition of a uniaxial stress component in either compression or tension always raises the CRSS. For this reason, we have confined our attention here to only applied shear stresses and have examined the CRSS in both Ta and Mo at ambient pressure. For our present purposes we identify the Peierls stress τ_{P} with the minimum CRSS as a function of shear stress orientation and then calculate the pressure dependence of τ_{P} for that orientation.

In order to determine the Peierls stress in a self-consistent and accurate manner, our GFBC/MGPT simulations of the CRSS have been performed at conditions of constant stress, rather than constant volume, and start from the relaxed equilibrium core structure as determined above. The simulations do utilize periodic boundary conditions along the screw axis, however, so they are strictly 2D zero-temperature calculations. For a given applied stress orientation, the CRSS is assumed to be reached when the dislocation moves at least one lattice spacing on the maximum resolved shear stress plane. In a bcc crystal along a given $\langle 1\,1\,1 \rangle$ direction, there are three $\{1\,1\,0\}$ planes and three $\{1\,1\,2\}$ planes, mutually intersecting at every 30°. Because of the twinning–anti-twinning asymmetry in the bcc lattice, unique values of the CRSS can exist on different planes ranging in orientation from $\chi = -30^\circ$ (twinning orientation on $\{2\,1\,1\}$) to $\chi = 30^\circ$ (anti-twinning orientation on $\{2\,1\,1\}$), with χ being the angle measured from a given $\{1\,1\,0\}$ slip plane. The CRSS over this orientation range has been calculated in Ta and Mo at ambient pressure, and the results are presented in Fig. 18. In the case of Ta, these results are the same as those reported previously [13] except at $\chi = 0$, where the CRSS is calculated slightly lower in value. Both Ta and Mo display a significant twinning–anti-twinning asymmetry with the minimum CRSS occurring at $\chi = 0^\circ$. These latter results are our defined values of τ_P at ambient pressure and are also listed in Table 3.

Also plotted for comparison in Fig. 18 are experimental estimates of the CRSS or Peierls stress based on the observed yield stress at the indicated stress orientations [70–72]. In the case of Ta at $\chi = -10^\circ$ and Mo at $\chi = -30^\circ$, our calculated CRSS values are nearly a factor of two greater than the experimental estimates, while in Mo at $\chi = 0^\circ$ our result is only about 20% higher. However, experiment here does not represent a direct measurement of the Peierls stress, and consequently, the

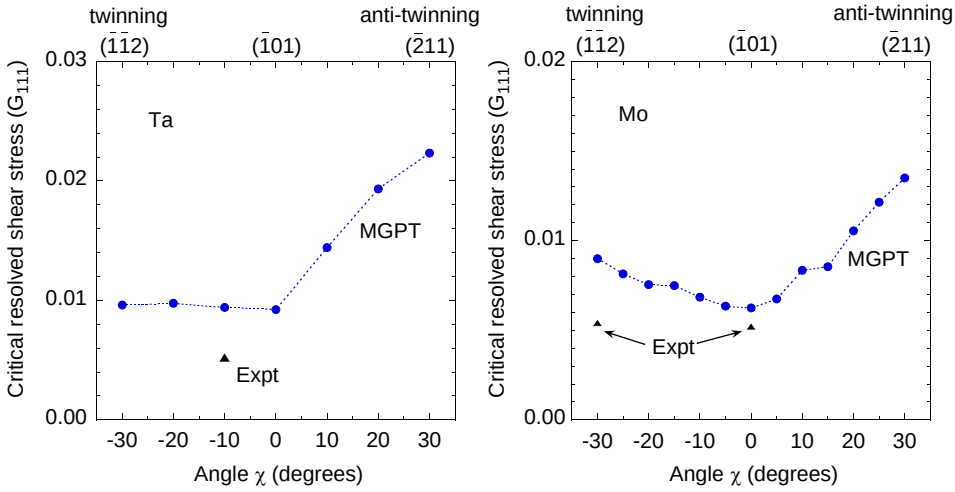

Fig. 18. Orientation dependence of the critical resolved shear stress (CRSS) in Ta and Mo at ambient pressure, as calculated with the present MGPT potentials and compared with experimental estimates based on the observed yield stress [70–72].

relationship between theory and experiment remains an open and somewhat controversial question [13,16]. Also in this regard, other recent quantum-based calculations of the same CRSS in Ta and Mo produce generally higher values than ours [15,16,18]. These include small-cell DFT calculations using Green's function boundary conditions [15] as well as larger-cell BOP calculations with fixed boundary conditions [18]. Whether or not these differences represent a sensitivity of the calculations to cell size and/or boundary conditions also remains an open question.

We have obtained the pressure dependence of the Peierls stress by performing GFBC/MGPT simulations of the $\chi = 0^\circ$ CRSS for selected pressures to 1000 GPa in Ta, 400 GPa in Mo, and 53 GPa in V. The resulting scaled Peierls stress τ_P/G_{111} is plotted for Ta and Mo in Fig. 19, and for V in Fig. 20. Shown for comparison in these figures are the corresponding average values of τ_P/G_{111}, which are 0.0102 in Ta, 0.0059 in Mo, and 0.0068 in V. Although there are significant fluctuations from these constant values in Ta and Mo at pressures below 150 GPa, overall they are fairly representative over the entire pressure range in each case. Also shown in Figs 19 and 20 are the corresponding values of the scaled ideal strength τ_c/G_{111}, which is more than an order of magnitude larger for each metal.

4.4. Activation enthalpy

The pressure- and shear-stress-dependent activation enthalpy $\Delta H(P,\tau)$ for dislocation motion provides the necessary connection between the $\tau = 0$ kink-pair formation energy E_{kp}^{f} and the high shear stress $\tau = \tau_P$ limit where the rigid screw

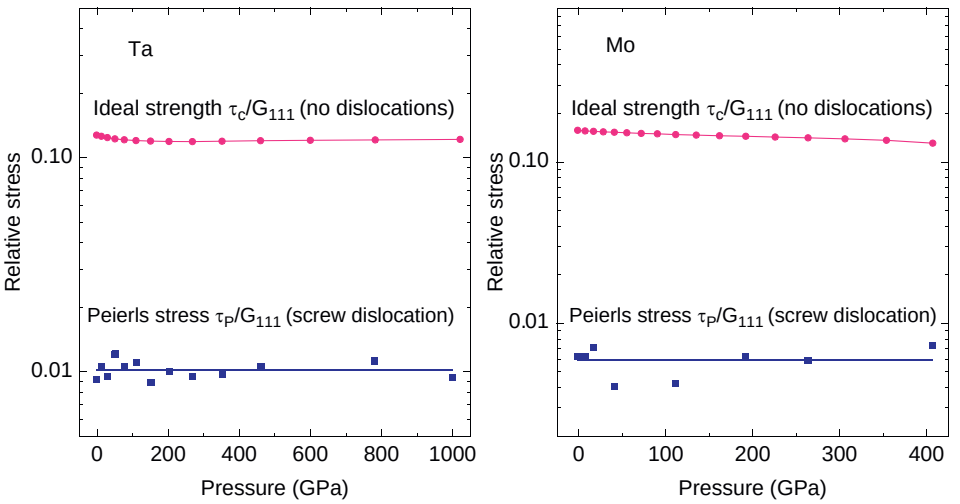

Fig. 19. Pressure dependence of the scaled Peierls stress τ_P/G_{111} in Ta and Mo, as calculated from GFBC/MGPT atomistic simulations (solid square points) and compared with a constant average (solid line below). Also shown for comparison is the corresponding scaled ideal strength τ_c/G_{111} (solid circles and solid line above).

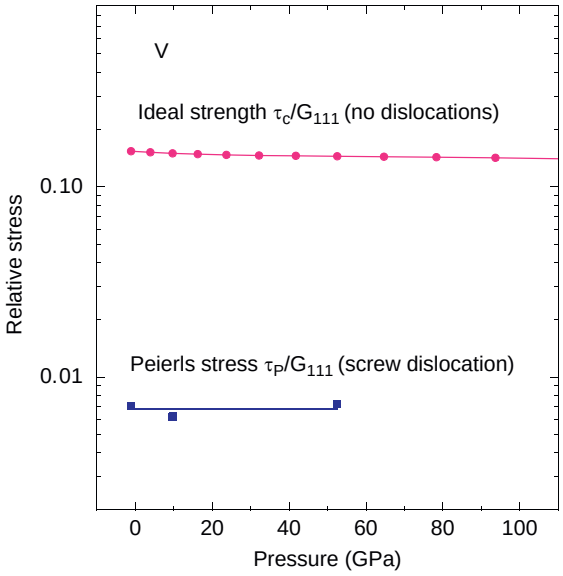

Fig. 20. Pressure dependence of the scaled Peierls stress τ_P/G_{111} in V, as calculated from GFBC/MGPT atomistic simulations (solid square points) and compared with a constant average (solid line below). Also shown for comparison is the corresponding scaled ideal strength τ_c/G_{111} (solid circles and solid line above).

dislocation moves without kink formation. The calculation of $\Delta H(P, \tau)$ requires an atomistic simulation of kink formation under both pressure and shear stress, which is convenient to perform at constant atomic volume rather than constant total stress. To do so, we first consider the thermodynamic enthalpy of N simulation atoms at zero temperature, $H = N(E + P\Omega)$, and manipulate the required enthalpy change into a useful form for constant-volume calculations. In this regard, Hirth has argued [73] that at high pressure there should be an explicit contribution to the activation enthalpy at constant pressure arising from the "$P\Omega$" term in H, but as we show below such a contribution drops out in a constant-volume formulation.

We begin in the $\tau = 0$ limit, where the change in enthalpy to form either a kinked or unkinked screw dislocation at constant pressure P can be written as

$$\Delta H(P) = N[E_2(\Omega_2) - E_1(\Omega_1) + P\Delta\Omega], \tag{10}$$

with E the average energy per atom and $\Delta\Omega = \Omega_2 - \Omega_1$. Here the subscript "1" refers to the initial state and the subscript "2" to the final state. While the total volume change $N\Delta\Omega$ may be significant if N is large, the average change in atomic volume $\Delta\Omega$ is small, so that one may perform a Taylor series expansion of the term $E_2\Omega_2$ about the volume Ω_1:

$$\begin{aligned} E_2(\Omega_2) &= E_2(\Omega_1) + \frac{\partial E_2(\Omega_1)}{\partial\Omega}\Delta\Omega + \cdots \\ &= E_2(\Omega_1) - P\Delta\Omega + \cdots \end{aligned} \tag{11}$$

To obtain the second line of Eq. (11), we have re-expanded the derivative term in the first line about Ω_2 and noted that at constant pressure

$$P = -\frac{\partial E_1(\Omega_1)}{\partial \Omega} = -\frac{\partial E_2(\Omega_2)}{\partial \Omega}. \tag{12}$$

Using Eq. (11) in Eq. (10), one finds that the pressure terms cancel and one is left with the result, correct to first order in $\Delta\Omega$,

$$\Delta H(P) = N\Delta E(\Omega_1) = N[E_2(\Omega_1) - E_1(\Omega_1)]. \tag{13}$$

The leading correction to this result is of the order $(\Delta\Omega)^2$ and negligible.

Eq. (13) can be immediately connected with the two important limiting cases already considered above. First, in the formation of the rigid screw dislocation from the perfect bcc lattice, we identify $N\Delta E$ with the formation energy at constant volume $E^{\mathrm{f}}_{\mathrm{screw}}$ in Eq. (8). Second, in the formation of an isolated pair of kinks on the screw dislocation line, we identify $N\Delta E$ with the kink-pair formation energy at constant volume $E^{\mathrm{f}}_{\mathrm{kp}}$ in Eq. (9). In the latter case, we may generalize Eq. (13) to the case of two attractively interacting kinks separated by a distance λ and held in (unstable) equilibrium under an applied shear stress τ to obtain the desired total activation enthalpy:

$$\Delta H(P,\tau) = E^{\mathrm{f}}_{\mathrm{kp}}(\Omega) + E_{\mathrm{int}}(\lambda) - \tau(\lambda)\lambda h b, \tag{14}$$

where $E^{\mathrm{f}}_{\mathrm{kp}}$ remains the constant-volume kink-pair formation energy at infinite separation and E_{int} is the additional interaction energy at separation λ. In the small shear stress limit $\tau < 0.2\tau_{\mathrm{P}}$, the kink–kink separation λ is larger than the kink width ($\sim 7b$ for Ta), and $E_{\mathrm{int}}(\lambda)$ varies as λ^{-1} and $\tau(\lambda)$ varies as $\lambda^{-1.5}$ [13], making it possible to evaluate the final two terms in Eq. (14).

For larger shear stresses $\tau > 0.2\tau_{\mathrm{P}}$, a special atomistic simulation procedure has been developed to evaluate $\Delta H(P,\tau)$. In the procedure, a self-consistent 3D atomistic model of kink-pair formation and migration is constructed involving three new steps in our GFBC/MGPT simulations: First, a straight $a/2\langle 1\,1\,1\rangle$ screw dislocation is constructed and is then fully relaxed under a trial applied shear stress. The straight screw dislocation line is lifted in energy above the valley of the Peierls potential, and the degree of lifting depends on the magnitude of the applied shear stress. Next, a 3D kink-pair model is constructed from this reference configuration. In this construction, the kink separation distance λ is treated as a fixed parameter, which is chosen to approximate the separation distance at which the kink pair is just balanced by the applied stress. Under the constraint of fixed λ, the kink-pair configuration is then fully relaxed. The total energy is calculated by summing over the atom-to-atom energy difference between the relaxed 3D configuration and the straight screw dislocation under the same applied shear stress. This produces the sum of the first two terms on the right-hand side of Eq. (14). Finally, the shear stress τ for kink-pair formation at the separation λ and the work done by that stress is calculated from the trapezoid model of Koizumi et al. [74]. This gives the final term in Eq. (14). This approach has been successfully applied here to calculate $\Delta H(P, \tau)$ for shear stresses up to $0.9\tau_{\mathrm{P}}$.

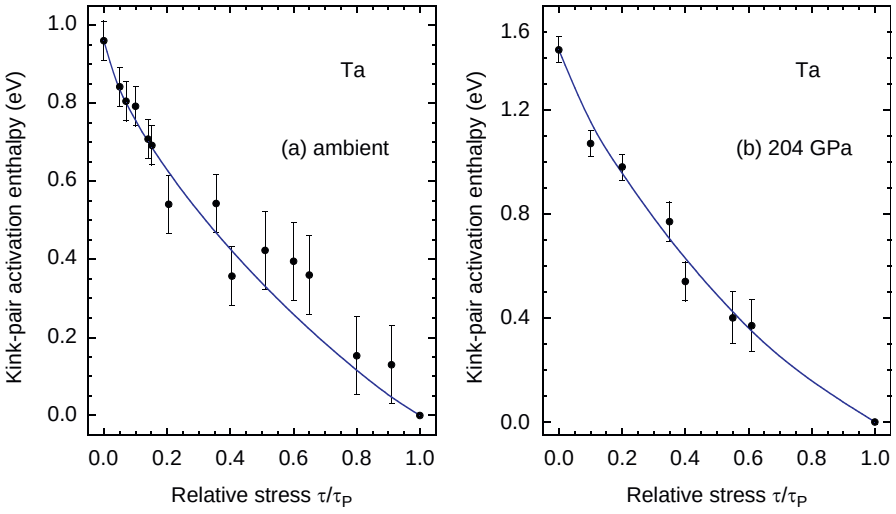

Fig. 21. Activation enthalpy for Ta at two selected pressures, as calculated from GFBC/MGPT atomistic simulations (solid points) and from an analytic fit [Eq. (15)] to these data (solid lines). (a) Ambient pressure and (b) $P = 204$ GPa.

Using this procedure, we have calculated a full kink-pair activation enthalpy curve at a total of four selected pressures in Ta, and three pressures each in Mo and V. Representative results for Ta and Mo are displayed in Figs 21 and 22, respectively. In these figures we have plotted both individual points obtained from GFBC/MGPT atomistic simulations and smooth analytic fits to the results. The latter provide a means to directly input atomistic activation enthalpy data into DD plasticity and yield strength simulations, and is discussed further below in Section 5.2. The individual simulation points at shear stresses above $0.2\tau_P$ have significant error bars of up to 0.1 eV, but the high stress part of the curve is well constrained by the requirement that $\Delta H(P, \tau)$ vanishes at $\tau = \tau_P$, so quite regular fits can be obtained.

4.5. Dislocation mobility near and above the Peierls stress

At finite temperature, a dislocation moves under the influence of thermal fluctuations and as the temperature rises the possibility of forming kink pairs is increased [75]. When the applied shear stress is high and approaches τ_P, multiple kinks begin to be formed and it actually becomes possible to see them in dynamic atomistic simulations. To investigate this phenomenon in bcc transition metals, we have preformed a large-scale finite-temperature MD GFBC/MGPT simulation of $a/2\langle 1\,1\,1\rangle$ screw dislocation motion in Ta under pure shear loading at a stress level about 10% below the Peierls stress. Here the simulation cell was constructed in a cylindrical geometry with periodic boundary conditions along the $\langle 1\,1\,1\rangle$

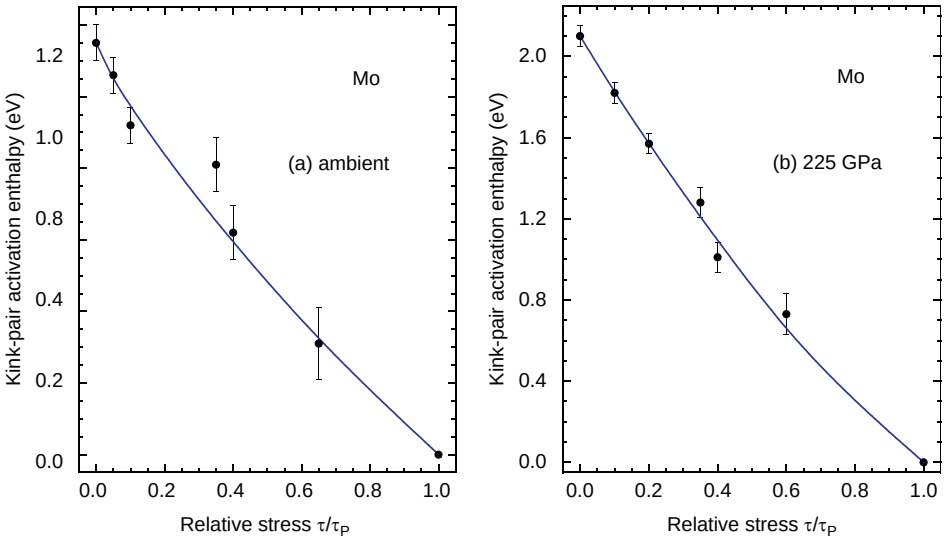

Fig. 22. Activation enthalpy for Mo at two selected pressures, as calculated from GFBC/MGPT atomistic simulations (solid points) and from an analytic fit [Eq. (15)] to these data (solid lines). (a) Ambient pressure and (b) $P = 225\,\mathrm{GPa}$.

dislocation line direction. The atomistic region of the cell had a radius of $40b$ and was $200b$ in length, containing over 1.3 million atoms. The simulation was performed at 300 K and ambient pressure with the shear stress applied on a $(\bar{1}\,1\,0)$ plane in a $\langle 1\,1\,1 \rangle$ direction. Our simulation results indeed reveal kink formation along the screw dislocation line, and a snapshot of the kink structure is displayed in Fig. 23.

For shear stresses $\tau > \tau_P$, the resistance to dislocation motion comes entirely from thermal vibrations and the screw dislocation velocity $v_s(P, T, \tau)$ becomes linear in the applied stress with a phonon-drag mobility that depends on pressure and temperature. To study dislocation motion above the Peierls stress at a given pressure and temperature, similar large-scale MD GFBC/MGPT simulations have been performed in Ta as a function of applied shear stress. The cylindrical simulation cell geometry used was the same as just described above, except that the atomistic region of the cylinder was chosen to be somewhat larger with a radius of $50b$ and length of $400b$, so that about 4 million atoms were simulated in each case. In these simulations the screw dislocation was initially placed at the center of the simulation box. The simulation cell was then pre-strained at the plastic strain corresponding to the applied shear stress τ, so that the simulation could be run at constant volume rather than constant total stress [67]. The molecular dynamics was carried out by integrating Newton's equations of motion for the atoms in the atomistic region using a time step of 1 fs at constant temperature, which was maintained using a Nosé–Hoover thermostat [76,77]. The displacements of the atoms in the Green's function region of the simulation cell were updated every 10 MD time steps while the atoms in the continuum region were kept fixed.

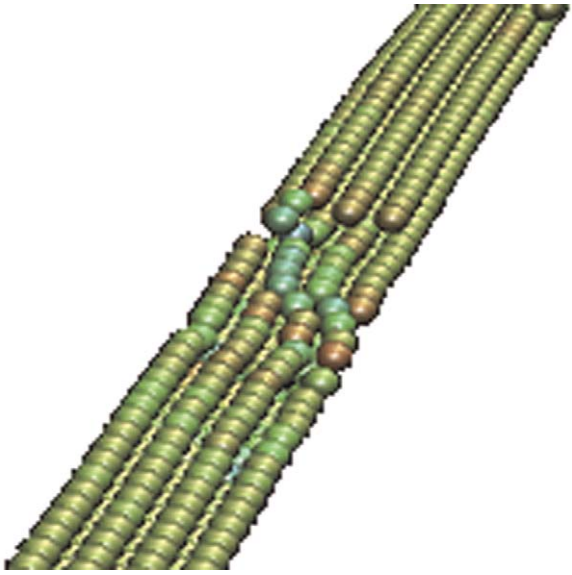

Fig. 23. A snapshot of kink formation on a $\langle 1\,1\,1 \rangle$ screw dislocation along the $\langle \bar{1}\,\bar{1}\,2 \rangle$ direction on the $(\bar{1}\,1\,0)$ plane in Ta at 300 K, ambient pressure, and an applied shear stress $\tau = 0.9\tau_P$, as obtained with an MD GFBC/MGPT simulation.

Using this computational scheme, we have focused our MD GFBC/MGPT simulations on bcc Ta within the applied stress range from $1.05\tau_P$ to $1.25\tau_P$ and the pressure range from ambient to 400 GPa. Within these ranges we found that the phonon-drag mobility was approximately linear in the scaled temperature, $T/T_m(P)$, where $T_m(P)$ is the pressure-dependent melt temperature as determined from previous MGPT calculations on Ta [14]. Consequently, at each pressure treated we considered only temperatures of approximately $0.3T_m(P)$ and $0.6T_m(P)$ in our MD simulations. The actual temperature values were 900 and 1800 K at ambient pressure, 1545 and 3090 K at 50 GPa, and 2580 and 5200 K at 230 GPa. The results of these simulations for $v_s(P, T, \tau)$ are plotted in Fig. 24 together with least-squared linear analytic fits to the simulation data. In these simulations the screw dislocation was found to glide on a $\{1\,1\,0\}$ plane at all pressures, temperatures, and applied stress levels considered. The analytic fits in Fig. 24 show that the velocity data are well represented by a form that is linear in the pressure P as well as in $T/T_m(P)$ and τ/τ_P. These fits will be discussed further in Section 5.1 below and used to provide an analytic form of the phonon-drag mobility suitable for DD simulations.

5. *Multiscale modeling of single-crystal plasticity*

As a practical matter, all computational dislocation dynamics methods require a robust analytic representation of the mobility of individual dislocation segments.

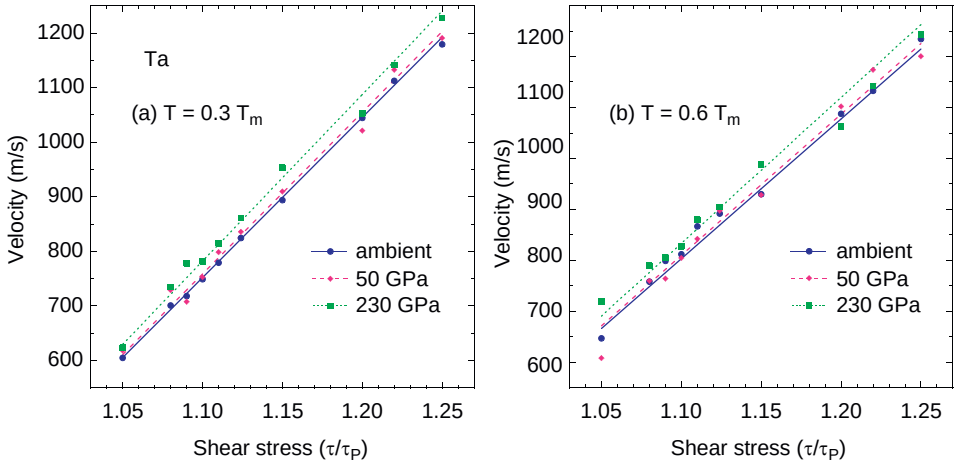

Fig. 24. Screw dislocation velocity above the Peierls stress in the phonon-drag regime for Ta, as calculated by MD GFBC/MGPT simulations (points) with linear analytic fits [Eqs (20)–(21)] to the simulation data (lines). Temperatures (a) $0.3T_m(P)$ and (b) $0.6T_m(P)$.

In this section we first consider appropriate analytic forms to represent the atomistic results for $a/2\langle 1\,1\,1\rangle$ screw dislocations discussed above in Section 4 within both the legacy lattice-based DD code [21,22] and the modern node-based ParaDiS code [27–30]. Using these analytic functions, we then discuss atomistically informed DD simulations of yield stress and plasticity for Ta and Mo as a function of pressure, temperature, and strain rate to complete our multiscale modeling of these materials.

5.1. Analytic representations of dislocation velocity

As shown in Fig. 21 for Ta and Fig. 22 for Mo, the activation enthalpy for $a/2\langle 1\,1\,1\rangle$ screw dislocation motion below the Peierls stress in the thermally activated regime is accurately represented by the following well-known analytic form:

$$\Delta H(P,\tau) = \Delta H_0(P)\left[1 - \left(\frac{\tau}{\tau_P}\right)^p\right]^q, \tag{15}$$

where $\Delta H_0(P)$ and τ_P are calculated atomistic quantities, and p and q are additional parameters that have been determined by a least-squares fit to the atomistic simulation data for $\Delta H(P,\tau)$. As can be inferred from Eq. (14), $\Delta H_0(P)$ is just the kink-pair formation energy at $\tau = 0$:

$$\Delta H_0(P) = E^f_{kp}(\Omega)\Big|_{P=P_0(\Omega)}. \tag{16}$$

Values of the parameters $\Delta H_0(P)$, τ_P, p, and q are listed in Table 4 for the 10 cases for which full activation enthalpy curves for Ta, Mo, and V have been calculated.

Eq. (15) is used in both the lattice-based and ParaDiS DD codes although with different treatments of the internal parameters $\Delta H_0(P)$, τ_P, p, and q. In the lattice-based code, the parameters in Table 4 have been used directly, except for τ_P in Ta, which has been scaled by a factor of 0.5 to account for the apparent overestimate of the Peierls stress relative to experiment noted in Fig. 18. In ParaDiS, however, additional modeling has been introduced to smooth the pressure dependence of the internal parameters. First, p and q are assumed to be universal constants, which have been fixed in our ParaDiS simulations at $p = 0.50$ and $q = 1.23$. In addition, $\Delta H_0(P)$ and τ_P are assumed to obey the high-pressure scaling laws

$$\Delta H_0(P) = a_0 G_{111}(P)[b(P)]^3, \tag{17}$$

and

$$\tau_P = b_0 G_{111}(P), \tag{18}$$

where the constants a_0 and b_0 are determined at ambient pressure from our atomistic results, with the caveat that τ_P in Ta is again scaled by a factor of 0.5. Specifically, we have taken a_0 to be 0.11 eV/GPa Å^3 in Ta and 0.066 eV/GPa Å^3 in Mo, and b_0 to be 0.0051 in Ta and 0.0062 in Mo.

In the lattice-based DD code, the screw dislocation velocity below the Peierls stress in the thermally activated regime is calculated as

$$v_s(P, T, \tau) = v_0(P) \exp\left[-\frac{\Delta H(P, \tau)}{k_B T}\right], \tag{19}$$

where $v_0(P)$ is a constant velocity computed in terms of the pressure-dependent Debye frequency and Burgers vector of the bcc lattice, and the length of the screw dislocation [21]. In this case, dislocation motion above the Peierls stress is not treated explicitly, so for $\tau > \tau_P$ one takes $v_s = v_0$.

Table 4
Calculated (ΔH_0, τ_P) and fitted (p, q) parameters entering the activation enthalpy $\Delta H(P, \tau)$ of Ta, Mo, and V, as represented by Eq. (15)

Metal	P (GPa)	ΔH_0 (eV)	p	q	τ_P (GPa)
Ta	Ambient	0.96	0.71	1.10	0.577
	51	1.22	0.85	1.34	1.283
	204	1.43	0.81	1.27	2.158
	354	1.89	0.84	1.31	3.139
Mo	Ambient	1.15	0.84	1.06	0.860
	55	1.69	0.93	1.14	1.349
	225	2.10	0.97	1.23	2.035
V	Ambient	0.68	0.74	1.12	0.360
	9.7	0.90	0.78	1.10	0.369
	53	1.06	0.82	1.14	0.633

In the ParaDiS code, on the other hand, a modified form of Eq. (19) is used in the thermal activation regime, as described below, and above the Peierls stress in the phonon-drag regime, the screw dislocation velocity is modeled by the linear equations used to fit the Ta data in Fig. 24, which have the form

$$v_s(P,T,\tau) = M_s(P,T)\left(A\frac{\tau}{\tau_P} - B\right), \tag{20}$$

where

$$M_s(P,T) = C_0\left(1 - C\frac{T}{T_m} + DP\right). \tag{21}$$

where C_0 is the shear sound speed at ambient pressure, and A, B, C, and D are constants determined by the least-squares fit to the Ta data. The latter have values $A = 1.525$, $B = 1.28625$, $C = 0.20323$, and $D = 1.627 \times 10^{-4}\,\mathrm{GPa}^{-1}$, and here these values have been used for both the Ta and Mo DD simulations with ParaDiS discussed in Section 5.2. Regarding the material-dependent shear sound speed, in Ta we have used $C_0 = 2048\,\mathrm{m/s}$ and in Mo we have used $C_0 = 3496\,\mathrm{m/s}$.

The modified form of Eq. (19) used in ParaDiS for the screw dislocation velocity in the thermally activated regime below τ_P is of the form

$$v_s(P,T,\tau) = M_s(P,T)(A - \beta B)\frac{\tau}{\tau_P}\exp\left[-\frac{\Delta H(P,\tau)}{k_B T}\right], \tag{22}$$

where the pre-exponential terms have been chosen to provide approximate continuity of v_s and its first stress derivative across the Peierls stress τ_P with Eq. (20) for the phonon-drag contribution. The choice $\beta = 1$ in Eq. (22) gives continuity of v_s at $\tau = \tau_P$, but a discontinuity in the first derivative. However, by matching Eqs (20) and (22) at a shear stress τ slightly below τ_P, one can maintain continuity of both v_s and its first derivative for a value of β near 1.

In addition to a velocity function for the screw dislocations, a velocity function for the edge dislocations is also required in the DD codes. Here simplifying assumptions are made without any specific guidance from atomistic calculations [21,22,27–30]. In the lattice-based DD code, these functions are used directly for the screw and edge dislocation segments. In ParaDiS, after the basic segment velocity functions are established, the code utilizes the screw and edge segment mobilities to obtain a general velocity at each dislocation node by mixing the two mobility functions. The details of this mixing and the resulting nodal velocity are given in Ref. [30].

5.2. Temperature- and pressure-dependent plastic flow

Using the ParaDiS simulation code and the above described velocity functions, we have carried out DD simulations in Ta and Mo for a range of pressure and temperature conditions. In the case of Ta, we have also carried out the simulations at different strain rates, as well as simulations with the lattice-based DD code over a

wider range of pressures. The simulations focus on the initial yield behavior rather than later stage strain hardening. The ParaDiS simulations start with an initial dislocation configuration consisting of screw lines with the total density of $5 \times 10^{12}\,\mathrm{m}^{-2}$ in a cubic 5-μm simulation box with periodic boundary conditions along all directions. The simulations are carried out under a constant strain rate. The flow stress response is initially elastic until dislocations start to move. When the plastic strain rate reaches the applied strain rate, the flow stress shows a steady state behavior, as shown in the stress–strain response curves. The yield stress is thus obtained at the end of the simulations when the flow stress reaches a nearly steady value. The loading is uniaxial tension and the orientation is along [1 2 3]. Under this single slip orientation, the Schmid factor is 0.467. The resolved yield stress is obtained from the flow stress multiplied by the Schmid factor.

The simulated ParaDiS stress–strain curves for Ta are shown in Fig. 25 at ambient pressure and at 30 GPa, for temperatures of 300, 600, and 1000 K, and at strain rates of 1 and $1000\,\mathrm{s}^{-1}$. All simulated responses show an initial elastic behavior, then plastic deformation when the flow stress is high enough to move the dislocations. The dislocation densities also go through orders of magnitude increase in these simulations. The corresponding resolved yield stress values obtained are shown in Fig. 26. The resolved yield stresses clearly show a strong dependence on strain rate, pressure, and temperature. The higher the strain rate, the higher the pressure, and the lower the temperature, the higher the yield stress. This is expected for plastic deformation process dominated by thermally activated dislocation motion. The pressure dependence comes from the fact that both the activation enthalpy and the Peierls stress are higher at higher pressures. The temperature

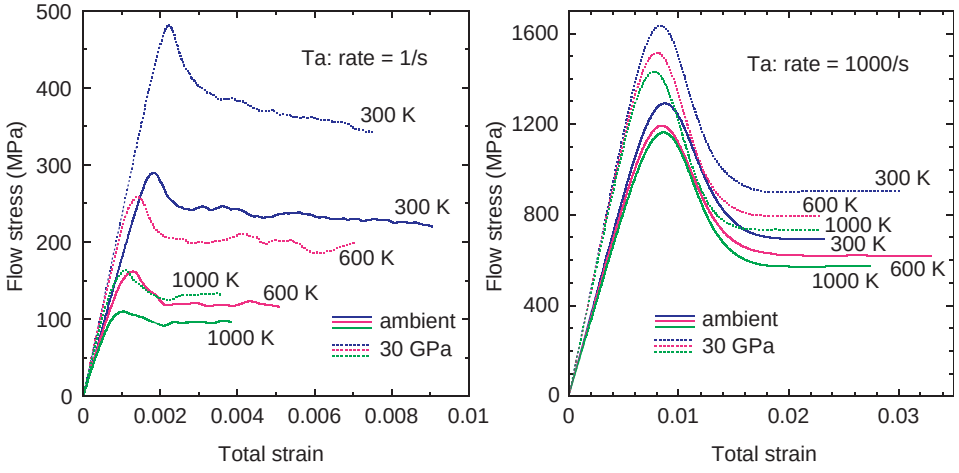

Fig. 25. Simulated stress–strain curves of single-crystal Ta, as obtained with the ParaDiS DD code. The left panel shows the results at a strain rate of $1\,\mathrm{s}^{-1}$, and the right panel results at a strain rate of $1000\,\mathrm{s}^{-1}$. For each strain rate, the simulations were performed at two pressures values, ambient and 30 GPa, and for temperatures of 300, 600, and 1000 K. The nearly steady state flow stress values at the end of the simulations are used to obtain the resolved yield stress values in Fig. 26.

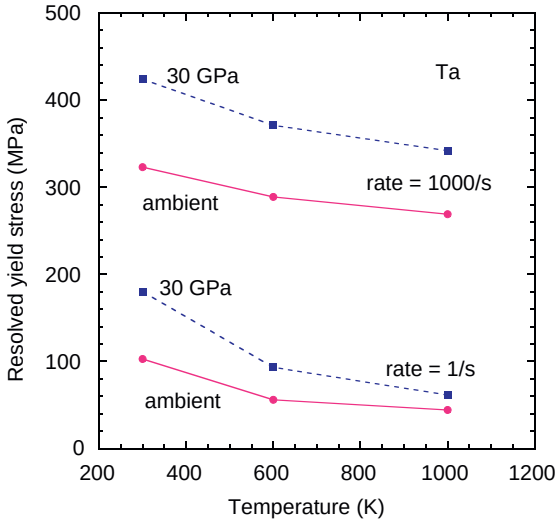

Fig. 26. The resolved yield stress values for single-crystal Ta corresponding to the stress–strain curves in Fig. 25. The solid square symbols are values at 30 GPa, and the solid circles values at ambient pressure. The upper curves are results obtained at a strain rate of $1000\,s^{-1}$, while the lower curves were obtained at $1\,s^{-1}$.

dependence is direct through the dislocation velocity functions [Eqs (20) and (22)]. As for the strain rate dependence, higher stress is required to move the dislocations with a higher deformation rate. The dislocations multiply faster and also move faster at higher strain rate. The simulations show that the dislocation density at yield for the higher strain rate is about 25 times the density at the lower strain rate. This means the main effect responding to the high strain rate is through the velocity speedup rather than density multiplication alone.

In the case of Ta, calculations of the temperature dependence of the yield stress have also been performed over a wider pressure range using the lattice-based DD code. These results are plotted in Fig. 27 and cover pressures as high as 204 GPa. These simulations were performed at a quasi-static strain rate of $10^{-3}\,s^{-1}$, which for ambient pressure allows a close comparison with accurate experimental data [78]. While our factor of two scaling down of the Peierls stress was motivated in part by a desire to normalize to experiment at one point on the ambient-pressure curve, the full temperature dependence of the experimental data is nonetheless well captured by our simulation. Using ParaDiS, we performed verification simulations at ambient pressure using the same parameters and loading conditions and obtained reasonable consistency when compared with the results obtained using the lattice-based DD code.

We have also carried out ParaDiS simulations for single-crystal Mo at ambient pressure for temperatures of 300, 600, and 1000 K, and at 225 GPa for temperatures of 600 and 1000 K. These simulations were all carried out at a strain rate of $1\,s^{-1}$ and the simulated stress–strain curves are shown in Fig. 28. An attempt to simulate

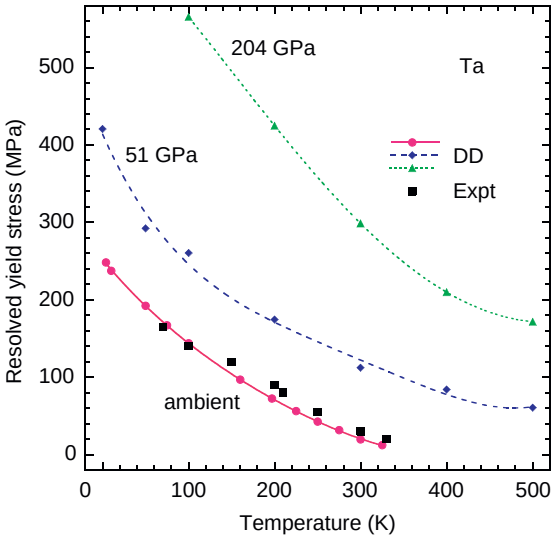

Fig. 27. Temperature dependence of the resolved yield stress at three pressures in single-crystal Ta, as obtained using the legacy lattice-based DD code at a quasi-static strain rate of $10^{-3}\,s^{-1}$. Experimental data at ambient pressure and the same strain rate (solid squares) are from Ref. [78].

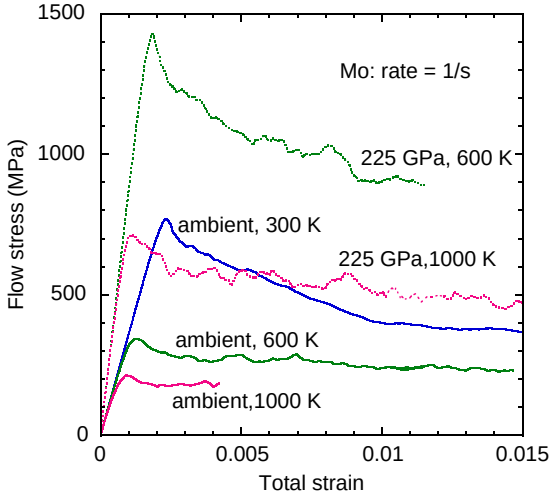

Fig. 28. Simulated stress–strain curves for single-crystal Mo at a strain rate of $1\,s^{-1}$, as obtained with the ParaDiS DD code. The solid lines are results obtained at ambient pressure for temperatures of 300, 600, and 1000 K. The dashed lines are results obtained at 225 GPa for temperatures of 600 and 1000 K. As in the case of Ta, the nearly steady state flow stress values at the end of the simulations were used to obtain the resolved yield stresses plotted in Fig. 29.

the additional point at 225 GPa and 300 K was made, but due to the extremely large activation enthalpy and low temperature, the DD time step required was too small to obtain meaningful results. We have, however, estimated the resolved yield stress for this point in the following manner. Using the rate equation, $\dot{\varepsilon} = \rho b v_s = \text{constant}$, we first used the simulated dislocation density ρ at 225 GPa and 600 K to estimate its value at 300 K. Then combining this rate equation and the velocity function in Eq. (22) we obtained an estimate of the resolved yield stress. This value, together with the resolved yield stresses obtained directly from the stress–strain curves in Fig. 28, is shown in Fig. 29. Again, one sees a strong dependence on pressure and temperature in these results. For comparison we also show in Fig. 29 ambient pressure and temperature experimental data for the resolved yield stress in Mo from the Seeger group in Germany [70,71] and from the Aono group in Japan [79]. We note, however, that these data were measured at quasi-static strain rates as opposed to the $1\,s^{-1}$ strain rate in our simulations. Since the resolved shear stress value is expected to decrease with decreasing strain rate, the data should be lower in magnitude than the simulation, which they are. However, the two experimental data points themselves have a rather large discrepancy. This shows the sensitivity of the experimental measurement to sample conditions.

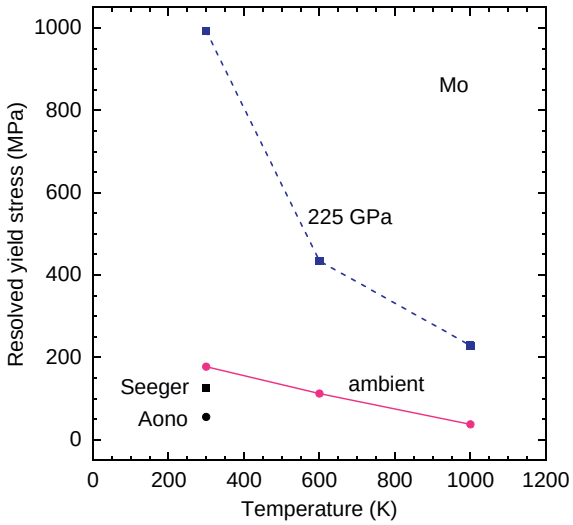

Fig. 29. Resolved yield stresses of single-crystal Mo obtained at ambient pressure (solid circles and solid lines) and at 225 GPa (solid squares and dashed lines). Except for the estimated point at 225 GPa and 300 K (see text), the remaining results were obtained from the stress–strain curves in Fig. 28 obtained at a strain rate of $1\,s^{-1}$. For comparison, ambient temperature and pressure experimental data points from the Seeger group [70,71] and the Aono group [79] at lower quasi-static strain rates are also shown.

6. Summary and conclusions

In this paper we have successfully combined first-principles PP and FP-LMTO electronic-structure calculations, quantum-based GFBC/MGPT atomistic simulations, and atomistically informed lattice-based and ParaDiS dislocation dynamics simulations at the microscale to study the fundamental properties of $a/2\langle 1\,1\,1\rangle$ screw dislocations and the plasticity that they drive in the bcc transition metals Ta, Mo, and V over a wide range of pressure. Within this information-passing approach to the multiscale modeling of mechanical properties, the electronic-structure calculations have allowed us to accurately calculate the *material-specific* high-pressure elasticity and range of bcc mechanical stability in these metals, and to provide fundamental bcc data on the equation of state, ideal strength, and γ surfaces needed to validate multi-ion MGPT interatomic potentials. In particular, we have shown that the present MGPT potentials for Ta and Mo predict very accurately the $\{1\,1\,0\}$ and $\{2\,1\,1\}$ γ surfaces relevant to screw dislocation structure and motion over pressures ranging from ambient to 400 GPa. With the GFBC/MGPT atomistic simulations, we have studied in detail the pressure-dependent properties of the $a/2\langle 1\,1\,1\rangle$ screw dislocations, including the core structure and energy, the Peirels stress τ_P and its orientation dependence, the kink-pair formation energy E_{kp}^{f} and the activation enthalpy $\Delta H(P, \tau)$ for dislocation motion below τ_P, and the dislocation velocity $v_s(P, T, \tau)$ in the phonon-drag regime above τ_P. These properties exhibit a complex blend of both material-specific and generic scalable behavior. The core structure is materials specific and varies qualitatively with material and pressure, while the Peierls stress τ_P is always minimized for $\langle 1\,1\,1\rangle$ shear stresses on $\{1\,1\,0\}$ slip planes and scales reasonable well with the G_{111} shear modulus to 1000 GPa in Ta, 400 GPa in Mo, and 53 GPa in V. The kink-pair formation energy E_{kp}^{f} is less robust in its scaling properties but varies approximately as $G_{111}b^3$ at high pressure. The activation enthalpy $\Delta H(P, \tau)$ and phonon-drag velocity $v_s(P, T, \tau)$ lend themselves to analytic fits as a function of pressure, temperature, and shear stress that can be used directly in the DD simulations to quantify the motion of individual dislocation segments. Using these analytic functions, we have successfully performed predictive lattice-based and ParaDiS simulations of flow stress and resolved yield stress in Ta and Mo as a function of pressure, temperature, and strain rate.

Acknowledgements

This work was performed under the auspices of the U.S. Department of Energy by the Lawrence Livermore National Laboratory in part under Contract W-7405-Eng-48 and in part under Contract DE-AC52-07NA27344. We would like to thank A. Arsenlis, R. Becker, G. Hommes, and M. Rhee for helpful discussions related to the ParaDiS simulations.

References

[1] S. Yip (Ed.), Modeling Industrial Materials: Connecting Atomistic and Continuum Length Scales, special issue of J. Comput. Aided Mater. Des., vol. 3 (1–3) 1996.

[2] H.M. Zbib, J.P. Hirth, T. Khraishi, R. Thomson (Eds.), Multi-Scale Modeling of Deformation and Fracture, special issue of J. Eng. Mater. Technol., vol. 121 (2) 1999.
[3] V.V. Bulatov, T. Diaz de la Rubia, R. Phillips, E. Kaxiaras, N. Ghoniem (Eds.), Multiscale Modelling of Materials, MRS Symposium Proceedings, vol. 538, Materials Research Society, Warrendale, 1999.
[4] L. Levine, L. Kubin, R. Becker (Eds.), Dislocations 2000: An International Conference on the Fundamentals of Plastic Deformation, special issue of Mater. Sci. Eng. A, vols. 309–310, 2001.
[5] E.A. Chandler, T. Diaz de la Rubia (Eds.), Bodega Bay International Workshop on Multiscale Modeling of Material Strength and Failure, special issue of J. Comput. Aided Mater. Des., vol. 9 (2) 2002.
[6] B. Devincre, D. Rodney, P. Veyssiere (Eds.), Dislocations 2004, special issue of Mater. Sci. Eng. A, vols. 400–401, 2005.
[7] Z. Xiao Guo (Ed.), Multiscale Materials Modeling, Woodhead Publishing, Abington, 2007.
[8] P. Gumbsch (Ed.), Third International Conference on Multiscale Materials Modelling, MMM 2006, J. Comput. Aided Mater. Des., vol. 14 (Suppl. 1) 2007.
[9] W. Xu, J.A. Moriarty, Phys. Rev. B 54 (1996) 6941;
Comput. Mater. Sci. 9 (1998) 348.
[10] S. Ismail-Beigi, T.A. Arias, Phys. Rev. Lett. 84 (2000) 1499.
[11] C. Woodward, S.I. Rao, Philos. Mag. A 81 (2001) 1305.
[12] S.I. Rao, C. Woodward, Philos. Mag. A 81 (2001) 1317.
[13] L.H. Yang, P. Söderlind, J.A. Moriarty, Philos. Mag. A 81 (2001) 1355.
[14] J.A. Moriarty, J.F. Belak, R.E. Rudd, P. Söderlind, F.H. Streitz, L.H. Yang, J. Phys. Condens. Matter 14 (2002) 2825 and references therein.
[15] C. Woodward, S.I. Rao, Phys. Rev. Lett. 88 (2002) 21642.
[16] J.A. Moriarty, V. Vitek, V.V. Bulatov, S. Yip, J. Comput. Aided Mater. Des. 9 (2002) 99 and references therein.
[17] S.L. Frederiksen, K.W. Jacobsen, Philos. Mag. 83 (2003) 365.
[18] M. Mrovec, D. Nguyen-Manh, D.G. Pettifor, V. Vitek, Phys. Rev. B 69 (2004) 94115.
[19] J.A. Moriarty, L.X. Benedict, J.N. Glosli, F.H. Streitz, M. Tang, L.H. Yang, J. Mater. Res. 21 (2006) 563 and references therein.
[20] L. Kubin, G. Canova, M. Condat, B. Devincre, V. Pointikis, Y. Brechet, Solid State Phenom. 23–24 (1992) 455.
[21] M. Tang, L.P. Kubin, G.R. Canova, Acta Mater. 46 (1998) 3221.
[22] M. Tang, in: S. Yip (Ed.), Handbook of Materials Modeling, vol. 1, Springer, Amsterdam, 2005, p. 827.
[23] M. Rhee, H. Zbib, H. Huang, T. Diaz de la Rubia, Modell. Simul. Mater. Sci. Eng. 6 (1998) 467.
[24] K. Schwarz, J. Appl. Phys. 85 (1999) 108.
[25] N. Ghoniem, L. Sun, Phys. Rev. B 60 (1999) 128.
[26] D. Weygand, L. Friedman, E. Van der Giessen, A. Needleman, Modell. Simul. Mater. Sci. Eng. 10 (2002) 437.
[27] V.V. Bulatov, W. Cai, Computer Simulations of Dislocations, Oxford Press, Oxford, 2006.
[28] V.V. Bulatov, L.L. Hsiung, M. Tang, A. Arsenlis, M.C. Bartelt, W. Cai, J.N. Florando, M. Hiratani, M. Rhee, G. Honnes, T.G. Pierce, T. Diaz de la Rubia, Nature 440 (2006) 1174.
[29] W. Cai, A. Arsenlis, C. Weinberger, V. Bulatov, J. Mech. Phys. Solids 54 (2006) 561.
[30] A. Arsenlis, W. Cai, M. Tang, M. Rhee, T. Oppelstrup, G. Hommes, T.G. Pierce, V.V. Bulatov, Modell. Simul. Mater. Sci. Eng. 15 (2007) 553.
[31] M. Tang, G. Xu, W. Cai, V. Bulatov, Simul. Mater. Sci. Eng. 14 (2006) 1139.
[32] M.S. Duesbery, V. Vitek, Acta Mater. 46 (1998) 1481.
[33] V. Vitek, Cryst. Lattice Defects 5 (1974) 1.
[34] M.S. Duesbery, Acta Metall. 31 (1983) 1747 and 1759.
[35] M.S. Duesbery, Proc. R. Soc. Lond. A 392 (1984) 145 and 175.
[36] M.S. Duesbery, in: F.R.N. Nabarro (Ed.), Dislocations in Solids, Elsevier, Amsterdam, 1989, p. 67.
[37] P. Söderlind, J.A. Moriarty, Phys. Rev. B 57 (1998) 10340.
[38] P. Söderlind, R. Ahuja, O. Eriksson, B. Johansson, J.M. Wills, Phys. Rev. B 49 (1994) 9365.
[39] N.E. Christensen, A.L. Ruoff, C.O. Rodriguez, Phys. Rev. B 52 (1995) 9121.
[40] Y. Ding, R. Ahuja, J. Shu, P. Chow, W. Luo, H.-K. Mao, Phys. Rev. Lett. 98 (2007) 85502.

[41] B. Lee, R.E. Rudd, J.E. Klepeis, P. Söderlind, A. Landa, Phys. Rev. B 75 (2007) 180101.
[42] P. Hohenberg, W. Kohn, Phys. Rev. 136 (1964) B864.
[43] W. Kohn, L. Sham, Phys. Rev. 140 (1965) A1133.
[44] R.M. Martin, Electronic Structure: Basic Theory and Practical Methods, Cambridge Press, Cambridge, 2004, and references therein.
[45] P. Söderlind, L. Yang, J.A. Moriarty, J.M. Wills, Phys. Rev. B 61 (2000) 2579.
[46] L. Yang, in: A. Koniges (Ed.), Industrial Strength Parallel Computing, Morgan Kaufmann, San Francisco, 2000, p. 297.
[47] A. Landa, J. Klepeis, P. Söderlind, I. Naumov, O. Velikokhatnyi, L. Vitos, A. Ruban, J. Phys. Chem. Solids 67 (2006) 2056.
[48] N. Troullier, J.L. Martins, Phys. Rev. B 43 (1991) 1993.
[49] J.A. Moriarty, Phys. Rev. B 38 (1988) 3199.
[50] J.A. Moriarty, Phys. Rev. B 42 (1990) 1609;
49 (1994) 12431.
[51] S. Rao, C. Hernandez, J. Simmons, T. Parthasarathy, C. Woodward, Philos. Mag. A 77 (1998) 231.
[52] S. Rao, T.A. Parthasarathy, C. Woodward, Philos. Mag. A 79 (1999) 1167.
[53] J.A. Moriarty, J.N. Glosli, R.Q. Hood, J.E. Klepeis, D.A. Orlikowski, P. Söderlind, L.H. Yang, in: TMS 2008 Annual Meeting Supplemental Proceedings Volume I: Materials Processing and Properties, TMS, Warrendale, PA, 2008, p. 313.
[54] J. Sinclair, P. Gehlen, R. Hoagland, J. Hirth, J. Appl. Phys. 49 (1978) 3890.
[55] A.N. Stroh, Philos. Mag. 3 (1958) 625;
J. Math. Phys. 41 (1962) 77.
[56] P.H. Dederichs, G. Leibfried, Phys. Rev. 188 (1969) 1175.
[57] H. Cynn, C.-S. Yoo, Phys. Rev. B 59 (1999) 8526.
[58] K.W. Katahara, M.H. Manghnani, E.S. Fisher, J. Phys. F: Met. Phys. 9 (1979) 773.
[59] D.L. Farber, M. Krisch, D. Antonangeli, A. Beraud, J. Badro, F. Occelli, D. Orlikowski, Phys. Rev. Lett. 96 (2006) 115502.
[60] D.C. Wallace, Thermodynamics of Crystals, Wiley, New York, 1972. Our present elastic moduli C_{ij} are the stress–strain coefficients B_{ij} defined by Wallace.
[61] A.T. Paxton, P. Gumbsch, M. Methfessel, Philos. Mag. Lett. 63 (1991) 267.
[62] J.W. Morris Jr., C.R. Krenn, D. Roundy, M.L. Cohen, in: P.E. Turchi, A. Gonis (Eds.), Phase Transformations and Evolution in Materials, TMS, Warrendale, PA, 2000, p. 187.
[63] P.B. Hirsch, in: Proceedings of the Fifth International Conference on Crystallography, Cambridge Press, Cambridge, 1960.
[64] M.S. Duesbery, V. Vitek, D. Bowen, Proc. R. Soc. Lond. A 332 (1973) 85.
[65] A. Seeger, C. Würthrich, Nuovo Cim. B 33 (1976) 38.
[66] B. Sadigh, W. Cai, V. Bulatov, 2002 (private communication and unpublished).
[67] M.S. Duesbery, 1999 (private communication and unpublished).
[68] K. Ito, V. Vitek, Philos. Mag. A 81 (2001) 1387.
[69] S. Takeuchi, E. Kuramoto, T. Suzuki, Acta Metall. 20 (1972) 909.
[70] A. Seeger, L. Hollang, Mater. Trans. JIM 41 (2000) 141.
[71] L. Hollang, M. Hommel, A. Seeger, Phys. Status Solidi A 160 (1997) 329.
[72] T. Suzuki, Y. Kaminura, H.O.K. Kirchnner, Philos. Mag. A 79 (1999) 1629.
[73] J.P. Hirth, in: S. Yip (Ed.), Handbook of Materials Modeling, vol. 1, Springer, Amsterdam, 2005, p. 2879.
[74] H. Koizumi, H.O.K. Kirchner, T. Suzuki, Philos. Mag. A 69 (1994) 805.
[75] J.P. Hirth, J. Lothe, Theory of Dislocations, Wiley-Interscience, New York, 1982.
[76] S. Nosé, Mol. Phys. 52 (1984) 255.
[77] W.G. Hoover, Phys. Rev. A 31 (1985) 1695.
[78] W. Wasserbach, Philos. Mag. A 53 (1986) 335.
[79] Y. Aono, E. Kuramoto, K. Kitajima, in: R.C. Gifkins (Ed.), Strength of Metals and Alloys, vol. 1, Pergamon Press, Oxford, 1982, p. 9.

CHAPTER 93

Dislocations in Silicon at High Stress

J. RABIER, L. PIZZAGALLI, AND J.L. DEMENET

PHYMAT, Université de Poitiers, CNRS UMR 6630, Boîte Postale 30179, F-86962 Futuroscope Chasseneuil Cedex, France

1572-4859, DOI: 10.1016/S1572-4859(09)01602-7

Dislocations in Solids
Edited by J. P. Hirth and L. Kubin

Contents

1. Introduction 49
   1.1. Crystal structure and dislocations in silicon 49
   1.2. The dissociation of dislocations 51
   1.3. Bond reconstruction in the dislocation cores 54
   1.4. Dislocation mobility 55
2. High-stress deformation: experimental features 58
   2.1. Deformation experiments at high stress 59
      2.1.1. Dislocation microstructures after indentation 59
      2.1.2. High-stress plastic deformation under a confining pressure up to 1.5 GPa 59
   2.2. Evidence of the nucleation of perfect dislocations at high stresses 62
      2.2.1. Plastic deformation under 5 GPa 62
      2.2.2. Plastic deformation in the metallic phase 64
      2.2.3. Dislocation microstructure resulting from surface scratches 65
      2.2.4. Deformation substructure in Si indented at low temperature 65
   2.3. What is the transition stress? 66
      2.3.1. Stress measurements using TEM 66
      2.3.2. Stress measurements using X-ray diffraction 67
      2.3.3. The transition stress 68
   2.4. The dislocation microstructures at high stress 68
      2.4.1. The signature of low temperature, high-stress deformation 68
      2.4.2. The signature of low temperature, high-stress deformation: revisiting previous works 69
   2.5. Dislocation core structure and transformation 70
      2.5.1. From dissociated glide dislocations to perfect dislocations 70
      2.5.2. From perfect dislocations to dissociated glide dislocations 71
      2.5.3. Conclusions about the evidences of dislocation core transformations 72
   2.6. Physical signatures associated to perfect dislocations 73
3. The core structure and mobility of perfect dislocations 75
   3.1. General features of perfect dislocations in the shuffle plane: a geometrical analysis 78
   3.2. Atomistic calculations 79
      3.2.1. Perfect dislocation structure and stability 79
         3.2.1.1. Screw dislocations 79
         3.2.1.2. 60° dislocations 81
      3.2.2. Dislocation mobility 82
         3.2.2.1. Perfect screw dislocation: Peierls stress and energy 82
         3.2.2.2. Perfect screw dislocation: mobility by formation and migration of kinks 84
         3.2.2.3. Mobility of 60° dislocations 89
      3.2.3. Effect of pressure on the core structure of perfect dislocations 90
      3.2.4. Nucleation of non-dissociated dislocations 93
4. Discussion 96
   4.1. Summary of experimental and numerical results 96
      4.1.1. Results 96
      4.1.2. Current limitations 98

4.2. Transition between two regimes: a core structure transformation? 98
4.3. Are non-dissociated dislocations in the glide or the shuffle set? 101
4.4. Other semiconductor materials 102
4.5. Perspectives 103
4.6. Concluding remarks 104
References 104

1. Introduction

The study of dislocations in semiconductors is strongly connected to the advent and development of the electronics industry. Indeed, it was very soon observed that the presence of crystalline defects, including dislocations, was detrimental to the processing and service life of devices. Thus, the very early research focused on the link between dislocation properties and their influence on the potential applications of semiconductors.

Silicon is obtained from silica, the main component of the Earth's crust; it was quickly used in electronics due to its natural abundance. As a consequence, many efforts were devoted to understanding the nature and properties of defects in this material. In addition, silicon appeared as, and is still nowadays, a model material for plasticity investigations because it is an elemental material with a crystal structure that is rather common among semiconducting materials. This material is also obtained as single crystals with zero dislocation content, which allows one to study dislocation nucleation.

This chapter aims at giving a comprehensive view about the structure and properties of dislocations obtained at high stress in silicon, which have been proved to have a different core structure from what was believed before.

Although many review papers or book chapters have been published on structures and properties of dislocation in semiconductors (see, e.g., [1–6]), the first part is devoted to present the context, ideas, and milestones that are necessary for understanding the subject of this chapter. The second part deals with the experimental works that have contributed to point out that different dislocation mechanisms and dislocation core structures are found at high stress in silicon: results of recent experiments are reported together with those of early experiments. These results, which reveal the existence of a different dislocation core structure at high stress, have promoted core structure analysis and numerous atomistic computations that are the subject of the third part. Finally, the results of experiments and computations are confronted in order to obtain a comprehensive view of the high-stress deformation regime existence. The transition between the two deformation regimes is also discussed.

1.1. Crystal structure and dislocations in silicon

Studies of the plasticity of semiconductors started at the beginning of the 1950s, with experiments on germanium and silicon, which were reported to be ductile above approximately 500 and 900 °C, respectively [7,8]. Seitz [8] explained Gallagher's measurements of plastic flow in germanium and silicon [7] in terms of

the theory of dislocations: the dislocations move by glide in {1 1 1} planes and have a Burgers vector equal to the ⟨1 1 0⟩-type translations in these planes. Besides, Seitz considered as improbable a dissociation of the dislocations into partials.

Shockley [9] was the first to describe the diamond-cubic structure of silicon and possible dislocations in this structure, followed by Hornstra [10], Haasen and Seeger [11], and Hirth and Lothe [12]. The structure is characterized by a tetrahedral environment of each atom. It can be represented as two face-centered cubic (fcc) sublattices shifted with respect to each other by a quarter of the ⟨1 1 1⟩ diagonal (Fig. 1).

Representing the atoms of one sublattice by capital letters and those of the other sublattice by small letters, one can describe the structure as an alternating stacking of close-packed layers of both types, …AaBbCcAaBbCc…. Fig. 2 shows a classical representation of the structure in projection along ⟨1 1 0⟩. In this figure, and by analogy with the fcc structure where the glide planes are {1 1 1} planes and the shortest translation vector of the lattice is 1/2⟨1 1 0⟩, there are two possible ways to produce a shear and, thus, for a dislocation to move (Fig. 2): between two widely spaced planes (e.g., Bb) of type I, or between two narrowly spaced planes (e.g., bC) of type II. Later, Hirth and Lothe [12] called these planes the shuffle set and the glide set, respectively. According to this terminology, which is still in use, dislocations lying on these planes are called shuffle dislocations and glide dislocations.

Hornstra [10] discussed several possible structures of dislocations in the diamond-cubic lattice. Starting from the fact that "an arbitrary direction in the crystal may be considered as the sum of steps in ⟨1 1 0⟩ directions," he considered that "the only simple dislocations that need to be studied are those along ⟨1 1 0⟩ directions." Then, it appears that the dislocation segments can be of type screw, edge, or 60° [Figs 3(a) and 3(b)].

Dash's observations [13] of Frank-Read sources in silicon, revealed by the copper decoration technique, showed that the dislocations have a pronounced tendency to

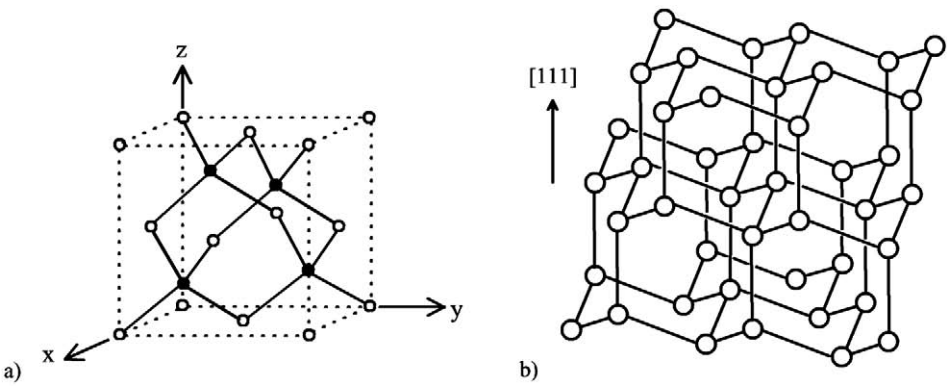

Fig. 1. The diamond structure. (a) The nodes of the two sublattices correspond to the white and black atoms, respectively and (b) view along ⟨1 1 0⟩.

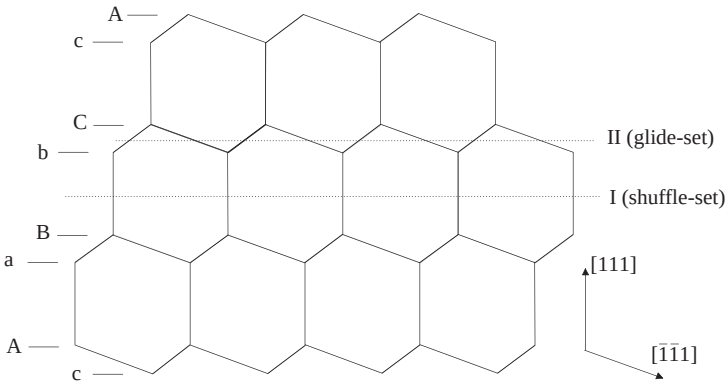

Fig. 2. The diamond structure viewed in projection along [1 $\bar{1}$ 0]. The (1 1 1) glide plane is horizontal, and the two possible shear locations I (shuffle set) and II (glide set) are indicated.

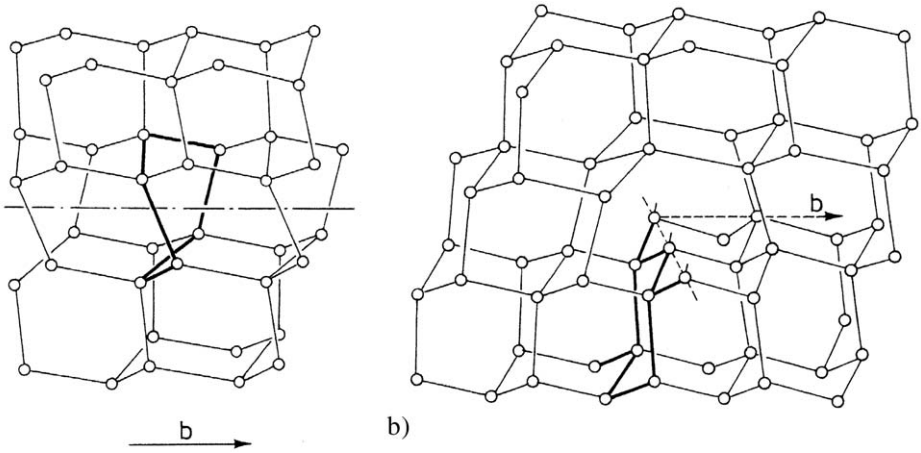

Fig. 3. Perfect dislocations in the diamond structure (after Hornstra [10]). (a) Screw dislocation and (b) 60° dislocation.

be predominantly of screw or 60° character. Later on (see, e.g., [1,14]), it was observed that, after a significant plastic deformation, dislocations are curved at high temperatures, but are aligned along the low-energy ⟨1 1 0⟩ directions when the temperature decreases and/or the stress increases.

Till the end of the 1960s, dislocations were thought to glide as perfect dislocations between the planes of type I (shuffle set). Indeed, the movement of a perfect dislocation in the shuffle set requires the breaking of one bond per atom, whereas three bonds must be broken in the glide set. In addition, the generally accepted view according to which shear is favored by a larger distance between slip planes is

consistent with a lower Peierls stress in the shuffle set and dislocations lying in this set.

1.2. The dissociation of dislocations

The dissociation of a perfect dislocation in its glide plane into partial dislocations of the 1/6⟨1 1 2⟩ Shockley-type was also an important domain of investigation. It was shown that the dissociation modes between two planes of type I or type II exhibit marked differences (Figs 4 and 5; see, e.g., Refs [12,15,16] for a detailed discussion). In short, the dissociation between planes of type II (glide set) leads to the formation of an intrinsic stacking fault and the distortions of the bonds remain confined in the cores of the partial dislocations. A glissile dissociation between planes of type I cannot be envisaged because the bonds between atoms in the stacking fault would be severely distorted.

Although the dissociation of a shuffle dislocation is unlikely *stricto sensu*, a dissociation involving shuffle dislocations was studied from a theoretical viewpoint by different authors [10–12,15]. This dissociation leads to a stacking fault between type II planes, bounded at one end by a glissile Shockley dislocation and at the

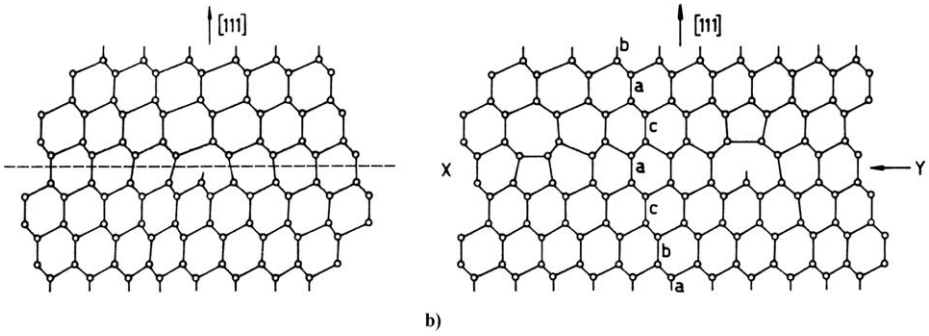

Fig. 4. 60° dislocation in the type I glide plane (shuffle set), after Amelinckx [16]. (a) Undissociated and (b) dissociated with formation of an intrinsic stacking fault. In that case, the stacking fault is of type II and is associated to a dislocation dipole at its right end (see Ref. [16]).

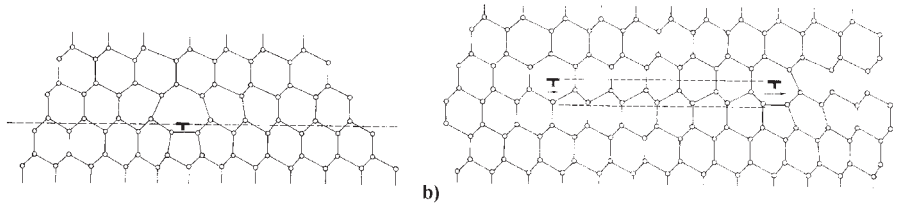

Fig. 5. 60° dislocation in the type II glide plane (glide set), after Amelinckx [16]. (a) Undissociated and (b) dissociated with formation of an intrinsic stacking fault.

other end by a sessile partial dislocation. The motion of this last partial requires a nonconservative atomic rearrangement. This type of rearrangement is called a shuffling and, for that reason, Hirth and Lothe [12] called the set of type I planes the shuffle set and the dislocations lying in these planes shuffle dislocations.

The dissociated shuffle dislocation, called ''extended shuffle dislocation'' by Alexander [1], can be described in two ways: either as a stacking-fault ribbon bounded by two Shockley dislocations of opposite sign associated with a shuffle dislocation, or as a dissociated glide (DG) dislocation that has emitted or absorbed a line of vacancies or interstitials in the core of one of its partials.

An essential contribution to the knowledge of dislocation cores in semiconductors was brought by the weak-beam technique, which was developed by the end of the 1960s (see Refs [17–19] for the case of Si). This transmission electron microscopy (TEM) technique allowed obtaining a finer image of the region of the crystal close to the actual position of dislocations. In silicon, the dislocations generated by deformation at 850 and 1200 °C were found to be dissociated in the (1 1 1) plane according to the reaction:

$$\frac{a}{2}[1\,\bar{1}\,0] \rightarrow \frac{a}{6}[2\,\bar{1}\,\bar{1}] + \frac{a}{6}[1\,\bar{2}\,1] \tag{1}$$

These observations confirmed previous observations of extended nodes in silicon made by Aerts et al. [20]. Dislocation dissociation was also observed in germanium using the same technique [19]. Later, Meingast and Alexander [21], showed that dislocations also moved in dissociated form in germanium thin foils locally heated in the electron microscope. Regarding the $\langle 1\,1\,0 \rangle$ low-energy directions, the perfect screw dislocation is dissociated into two 30° partial dislocations, and the 60° perfect dislocation is dissociated into a 30° partial dislocation and a 90° partial dislocation (Fig. 6).

From the observation of the dissociation of dislocations, both at rest and moving, it was concluded that dissociated dislocations belong to the glide set. In principle, TEM examinations of edge-on dislocation lines at high resolution and of the associated simulated contrasts should allow one to distinguish the dissociation modes.

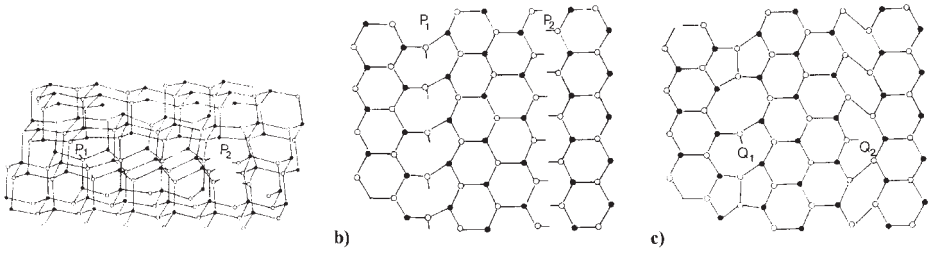

Fig. 6. (a) A 60° dislocation dissociated in the glide set into 30° (P_1) and 90° (P_2) partial dislocations. (b) Same configuration projected on the (1 1 1) glide plane. Partial dislocations are not reconstructed. (c) Partial dislocations are reconstructed. A reconstruction defect (soliton) is shown on each partial. After George and Rabier [2].

In practice, the occurrence of defects along the dislocation lines (kinks, jogs, point defects, …) makes the interpretation of high-resolution micrographs difficult and hazardous.

Although most of the dislocations are seen to be dissociated at the scale of transmission electron microscopy, constrictions were also observed on dislocation segments in silicon [19] as well as in germanium [22,23]. These constrictions are particularly numerous after high-temperature deformation, around 520 °C for germanium and 800 °C for silicon. Packeiser and Haasen [22,23] showed, in germanium, that they are formed on jogs with a height larger than the spacing between glide planes. The same explanation could apply to silicon. A link between point defects and local modifications of dislocation splitting observed by TEM was suggested in order to explain that jogs were able to move along the dislocation lines. They were assumed to do so by an exchange of point defects between the dislocation and the lattice [1]. Moreover, it was not excluded that these constricted segments could belong to the shuffle set [15]. This can be related to the work of Louchet and Thibault-Desseaux [24], who discussed the possible coexistence of glide and shuffle partial dislocations. These authors considered that dissociation is not restricted to the glide set and that the core structure is not unique along a given partial. Partial dislocations have complex cores with an average glide character but they contain a number of shuffle sites due to point defects, the nature of which depends on the character of the dislocations.

1.3. Bond reconstruction in the dislocation cores

The possible occurrence of bond reconstruction in the dislocation cores became quickly an open issue, in particular for researchers working in the electronics industry. Shockley [9] was the first to notice that the unsaturated bonds appearing at edge dislocation cores in semiconductors could form a one-dimensional energy band partially filled with electrons. After this seminal work, other authors showed that acceptor and recombination centers were introduced during plastic deformation. This effect was presumably connected to dangling bonds present in dislocation cores, the carrier lifetime being inversely proportional to the dislocation density. For more details, the reader is referred to a recent and well-documented historical summary published by Figielski [5] on dislocations considered as electrically active centers. At the same time microstructural studies were devoted to electrical and optical properties of dislocations, using different techniques like electronic paramagnetic resonance (EPR), deep level transient spectroscopy (DLTS), electron beam induced current (EBIC), and photo- or cathodo-luminescence. The influence of dislocations on electrical properties, namely the density, mobility, and lifetime of electrical carriers was studied as a subject of basic research as well as a critical point to obtain reliable devices.

Most of these studies were performed on samples deformed between 650 and 850 °C, which are temperatures easily accessible in laboratory and for which silicon still presents some ductility. The Alexander group in Köln [25,26] and the Ossipyan

group in Chernogolovka [27] investigated the dislocation cores using EPR. Indeed, this technique is sensitive to unpaired electrons in the core of dislocations and thus to the presence of dangling bonds. EPR spectra are different according to the deformation temperature between 850 and 420 °C, and more resonance peaks are observed at high temperature. However, the existence of a recombination center not associated with a particular type of dislocation seemed to indicate that the movement of dislocations is correlated with the existence of point defects in the dislocation cores. This point is still a matter of debate, and it is not clear whether point defects are dragged by dislocations during their motion or left behind by the dislocations. The recent observation of dislocation trails revealed by selective chemical etching and possibly associated with EBIC and DLTS signals stirred up a renewal of interest to this question [28]. Besides, EPR experiments showed that the number of dangling bonds is small as compared to the number of sites on the dislocation line, less than 5%. Thus, most of the dislocations should be reconstructed.

Because of the strong covalent bonding, one can imagine that relaxation involving bond rearrangements can occur and dislocation cores should be reconstructed. A 60° dislocation dissociates into 30° and 90° partials with dangling bonds almost parallel to the slip plane [Figs 6(a) and 6(b)]. Those dangling bonds may disappear pairwise by core reconstruction. The calculations of reconstructed core structures in silicon were essentially made on the 30° and 90° partials. The full reconstruction of a 30° partial leads to the unique possibility of a double-period (DP) core [Fig. 6(c)]. On the other hand, a 90° partial can be reconstructed in two ways, leading to a single-period (SP) core [Fig. 6(c)] or a DP core. The SP reconstruction was independently proposed by Hirsch [29] and Jones [30], and further discussed by Bennetto et al. [31]. The DP reconstruction proposed in Ref. [31] doubles the period along the dislocation line. Calculations using various approaches and potentials slightly favor this DP core reconstruction [32]. However, the occurrence of defects along the dislocation line (impurities, reconstruction defects, or solitons, vacancies, interstitials, …) could affect locally the reconstruction mechanism. Energy values associated to these defects were calculated and can be found in Ref. [32].

1.4. Dislocation mobility

The mobility of the dislocations was for a long time another important theoretical and experimental topic. Dislocation motion can be assisted by temperature and the external stress. The critical stress for the movement of a dislocation at 0 K is defined as the Peierls stress. At finite temperatures, the motion of a dislocation from a low-energy valley to the next one occurs by the local nucleation of short segments, the kink pairs, which cross the energy barrier in the direction of dislocation motion. Then, each kink propagates sideways along the dislocation line, which transfers the latter as a whole into the neighboring low-energy valley. These two elementary mechanisms are associated with an energy barrier. The energy necessary to

overcome a Peierls potential of the first kind and nucleate a kink pair is $2F_k$, where F_k is the formation energy of a single kink. W_m, the migration energy, is the energy to overcome the Peierls potential of the second kind, which allows a kink to propagate along the line. Contrary to ''usual'' fcc metals, where W_m is negligible, both energies could be high and of the same order in semiconductors. These mechanisms of kink pair nucleation and kink migration were studied by Hirth and Lothe [12] in crystals with a high Peierls relief, taking into account the number of nucleation sites and the length of the free segments. The mean free path of a kink along the dislocation line is limited by the presence of another kink of opposite sign, with which it annihilates, or by the presence of a pinning obstacle. In steady-state conditions, a dislocation moves with a constant velocity, which implies that each pinning or annihilation event is compensated by a nucleation event. This kink-diffusion model leads to two regimes: a regime where the dislocation velocity depends on the length of segments because the kink can propagate all along the line, and a regime where the dislocation velocity is independent from the length of segments because of the kink–kink collisions.

The reconstruction of core bonds leads to the existence of various types of kinks according to the nature of the partial (30° or 90°) and the position of the kink, at the right or left side of its companion. The different types of kinks were classified and analyzed by atomistic simulations for determining their energy and their probability of occurrence. In the case of a 90° partial, the unreconstructed configuration is symmetric and both right and left kinks are identical. Due to the reconstructed nature of the dislocation core, many different topological kinks can be formed. In the case of the 30° partial the number of reconstructed kinks is even more important since, there are two different kink structures in the unreconstructed configuration due to the intrinsic left–right asymmetry of a kink pair [33].

The partial reconstruction of bonds can occur along the line as well as at a kink, leading to the existence of reconstruction defects, or solitons, as mentioned above. The formation of these reconstruction defects is thermically activated and their low migration energy makes them highly mobile. This description is the basis of the model initially proposed by Jones [34] and Heggie and Jones [35], which was further developed by Bulatov et al. [33]. Solitons facilitate the nucleation and the migration of the kink pairs by locally restoring the covalent bonding. Within the framework of this model, it seems reasonable to think that the energies associated to the first and second kinds of Peierls potentials are of the same order.

Attempts to determine experimentally the values of F_k and W_m were carried out using various techniques: internal friction [36,37], deformation under load pulse sequence [38], and TEM. There are very few internal friction experiments on semiconductors. The reason is the brittleness of these materials and the need to work at very low frequencies in order to get a relaxation peak at moderate temperatures. The direct observation of kink motion was realized by TEM, either by studying the relaxation of out-of-equilibrium dissociated dislocations [39], by *in situ* deformation [40], or by using forbidden reflections in the high-resolution mode [41,42]. These various experiments were analyzed within the framework of the kink-diffusion model of Hirth and Lothe [12], which does not take into account

the dissociation of the dislocations. The applied stress can lead to different Peach–Koehler forces on the partials, so that the dissociation width depends on the applied stress. Thus, under low stresses, the nucleation of kink pairs on both partials can be correlated. Using atomic-resolution electron microscopy, Kolar et al. [42] analyzed recordings of kinks moving on partial dislocations and obtained the values $F_k = 0.73\,\text{eV}$ and $W_m = 1.24\,\text{eV}$ at 600 °C. The various results obtained by different techniques show that, in contrast to the case of metals, the Peierls potential of the second kind is important with a value of W_m around 1.2 eV. This is in agreement with the first calculations of Jones [43]. The Hirth and Lothe model predicts the occurrence of a transition between the length-dependent and the kink-collision regimes characterized by a change in the kink formation energy. The two regimes of kink motion were observed by TEM [39,40], with a critical segment length of about 0.4 μm at the transition, but without any change in activation energy. The entropy term contribution, which is not taken into account in the model, should exhibit unrealistically high values to yield a good agreement between theory and experiment. It appears, thus, that the length-independent regime found experimentally should not be a kink-collision regime. This is also supported by other experimental results obtained by intermittent pulse loading [38] or by monitoring the motion of a threading dislocation in strained thin films [44]. Then, kink motion may be limited by obstacles like point defects along the dislocation lines.

The dislocation velocities can also be measured on macroscopic specimens. Double etch pits and X-ray topography are the most common techniques used for this purpose. The dislocation velocities v were measured by different authors as a function of temperature T and stress τ; the results were analyzed using the phenomenological law:

$$v = v_0 \left(\frac{\tau}{\tau_0}\right)^m \exp\left(-\frac{Q}{kT}\right), \tag{2}$$

where v_0 and τ_0 are constants, k is the Boltzmann's constant, the exponent m is usually between 1 and 2, and Q is the total activation energy. In the most explored range of intermediate stress and temperature values, 1–50 MPa and 600–800 °C, respectively, experimental results on pure silicon lead to $m = 1$ and $Q \sim 2.2\,\text{eV}$. This seems to confirm that only one of the two predicted regimes is observed.

To summarize this brief history of dislocations in silicon, it appears that some points are well established. In particular, at high and medium temperatures, which are the best documented domains, dislocations lie in the glide set where they are dissociated both at rest and when they move. They have to overcome high Peierls potentials of the first and second kinds. However, several questions remain a matter of debate: what is the mean free path of kinks? What is the density of localized obstacles along the dislocation lines? What is the role of point defects on dislocation mobility?

In 1996, Duesbery and Joós [45] determined that in "usual stress conditions," dislocations should belong to the glide set. Using Peierls barriers deduced from atomistic computations, these authors calculated the kink pair activation energies

for perfect shuffle (PS) screw dislocations and for the 30° glide partial. The activation energy for screw shuffle dislocations was the highest in the whole stress range, but the difference was found to decrease with increasing stress. Extrapolating these results to high stresses, it was predicted that a transition should occur from plastic deformation carried out by glide dislocations to plastic deformation carried out by shuffle dislocations around $\tau/\mu = 0.01$ (μ is the shear modulus). This has constituted the motivation for revisiting the plastic deformation of silicon at high stress, both experimentally and theoretically. The results of these investigations are described in the following parts of this chapter.

2. High-stress deformation: experimental features

Low-temperature high-stress deformation tests in silicon allowed investigating extreme mechanical conditions such as those encountered in the machining of wafers, in deformation regimes controlled by decorrelated partial motion or mechanical twinning, and in the deformation mechanisms involved in the brittle to ductile transition (BDT). The effect of electronic doping was also investigated, since it is expected to be more important when the deformation temperature is low. Indeed, the BDT temperature was found to depend on doping, in good agreement with the dependence of dislocation velocities on dopant concentration [46,47]. Furthermore, renewed interest on high-stress deformation mechanisms was stimulated in the last decade by investigations of the plastic properties of nanostructured materials. These small-scale objects exhibit a high strength that is due to size effects. For example, it was shown that silicon nanopillars could sustain stresses that are much higher than the ones encountered in bulk materials at the BDT [48]. In this context, understanding the nucleation of dislocations as well as the elementary deformation mechanisms at high stress not only is a challenge in defects physics but becomes a critical issue for nanostructural engineering.

In order to achieve such high stresses in low temperature deformation regimes, two main techniques can be used, which superimpose a hydrostatic component to an applied shear stress: microindentation and deformation under a confining pressure. The hydrostatic component limits cracks extension and induces a shift in the BDT toward low temperatures. Microindentation (or nanoindentation) tests are very easy to perform but they suffer from two main drawbacks: the stress tensor is not known and the plastic region is confined to a very small volume of the specimen, which makes TEM observations of the deformation substructure quite difficult.

Deformation under hydrostatic pressure is less easy to carry out, but it allows one to perform TEM observations in larger areas. Although the hydrostatic pressure can be controlled quite accurately, the main drawback – that depends on the experimental setup – can be the measurement of the uniaxial stress. In the range of pressures suited for studying the plasticity of silicon, this problem can now be solved using deformation apparatuses devised to function in synchrotron beamlines (see Section 2.3.2).

In what follows, we report on experiments on the deformation of silicon, which were designed to shed light into the main features of high-stress dislocation mechanisms.

2.1. Deformation experiments at high stress

2.1.1. Dislocation microstructures after indentation

Indentation techniques were widely used for a long time to investigate the plasticity of silicon at low temperature. However, a difficulty arises because silicon shows a phase transition from diamond-cubic structure to β-Sn metallic Si at a pressure of about 12 GPa [49]. As the shear stress increases during an indentation test, the hydrostatic component simultaneously increases and the critical pressure for the phase transition can be reached. In such conditions, the hardness values and dislocation microstructures cannot be representative of dislocation-induced plasticity mechanisms. Indeed, the occurrence of the phase transition under indentation was found to explain the observed saturation of hardness values below 400 °C ([50,51]; see also Fig. 8). Dislocations were nevertheless observed after indentation at temperatures lower than 400 °C, but their possible connection with the phase transition was not investigated.

After indentation at room temperature, dislocations are not mobile and stay in the close vicinity of the indentation site. This results in a very high local density of dislocations, which are difficult to resolve individually [52,53]. For that reason, most of the observations of dislocations were performed after indentation at a medium temperature or after a room temperature anneal of the microstructure, in order to promote dislocation nucleation or the propagation of the dislocations at some distance from the imprints (see, e.g., [52]). After anneals at typically 400 °C, the dislocation configurations are similar to the ones found in usual conditions, that is, dislocations with $\langle 1\,1\,0 \rangle$ Burgers vectors, {1 1 1} glide planes, and glide dislocation loops exhibiting a hexagonal shape with segments lying along the $\langle 1\,1\,0 \rangle$ directions. In one of the many works performed on silicon indentation, Hill and Rowcliffe [53] were able to derive original results from the observation of dislocations after indentation at room temperature and at 300 °C. These authors noticed that ‘‘indentation at room temperature produces shear loops composed of long 30° dislocations and short 60° dislocations segments.’’ Specimens indented at 300 °C contained the same type of dislocations but the 30° dislocations were not straight anymore. Hill and Rowcliffe [53] concluded that the types of dislocations and their arrangements differ considerably from those observed in silicon at elevated temperature. They proposed a mechanism in which the theoretical shear strength being locally exceeded, the dislocations resulted from the accommodation of displacements by non-dislocation-mediated block slip.

2.1.2. High-stress plastic deformation under a confining pressure up to 1.5 GPa

The first work on the deformation of silicon under hydrostatic pressure as a way to reach high stresses was performed by Castaing et al. [54], using a Griggs apparatus

dedicated to the deformation of minerals under pressure. In this experimental setup, confining pressures are produced by a solid confining medium. The accuracy of applied stress measurements suffers from the friction stress exerted by the solid confining medium on the moving deformation rams. Single crystals of silicon with ⟨1 2 3⟩ (oriented for single slip) and ⟨1 0 0⟩ compression axes were deformed under a pressure of 1.5 GPa between 450 and 275 °C at imposed strain rates ranging from 2×10^{-5} to $2 \times 10^{-6}\,s^{-1}$. Without prestrain, the lowest temperature at which plastic deformation occurred under a strain rate of $2 \times 10^{-6}\,s^{-1}$ was 450 °C. At the same strain rate and after a prestrain at 450 °C, the lowest temperature at which macroscopic plasticity could be obtained was 275 °C.

Fig. 7 shows a stress–strain curve obtained at low temperature on a virgin silicon crystal [54,55]. The yield point usually found at medium temperatures is still present. This behavior is characteristic of a low initial dislocation density followed by a multiplication stage and an overshoot of the dislocation density after the multiplication stage.

The temperature dependence of the yield stress was analyzed using the rate equation:

$$\dot{\gamma} = \dot{\gamma}_0 \exp\left(-\frac{\Delta G}{kT}\right), \tag{3}$$

where $\dot{\gamma}$ and $\dot{\gamma}_0$ are, respectively, the resolved imposed strain rate and a reference strain rate. The stress dependence of the activation free energy was determined by stress relaxation tests and was found to be logarithmic. The temperature dependence of the yield stress can then be written in the form:

$$\ln(\tau) = \ln(\tau_0) + \beta T, \tag{4}$$

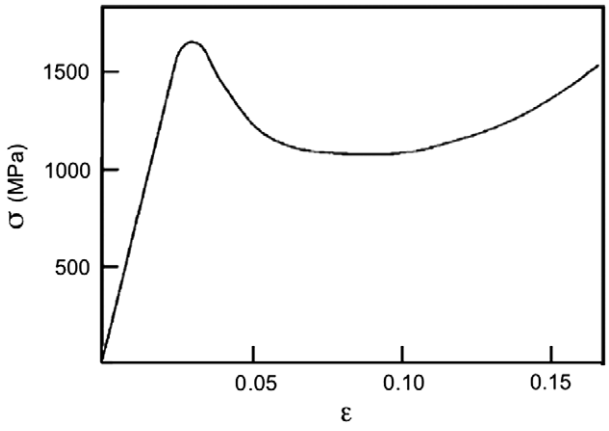

Fig. 7. Stress–strain curve of a ⟨1 2 3⟩ Si crystal deformed at $T = 425$ °C under a strain rate of $2 \times 10^{-6}\,s^{-1}$ and a confining pressure of 700 MPa. After Demenet [55].

where the strain rate dependence is accounted for by the coefficient β. The flow stress extrapolated at 0 K, τ_0, is between 100 and 200 GPa, that is, it is comparable to the shear modulus. A large value was found for the ratio $\Delta G/kT = c$ ($c = 36$); this value is surprising since c should in principle lie between 20 and 30 [56]. These two unexpected experimental results imply that either the above analysis is questionable or there are several controlling deformation mechanisms in the small temperature interval investigated (250–450 °C).

The temperature dependence of the yield stress obtained in Si down to 275 °C was compared with microhardness data obtained down to room temperature (Fig. 8) [51]. In contrast to microhardness data, the yield stress values do not level off below 400 °C, which is consistent with the occurrence under the microindenter of the phase transition mentioned in Section 2.1.1 [50,52]. In the compression tests, the pressure was kept below the critical value for the onset of this transition.

The temperature dependencies of the yield stresses are similar for samples deformed along the ⟨1 2 3⟩ and ⟨1 0 0⟩ compression axes [54,55,58]. However, the deformation microstructures look very different. This feature is related to the resolved applied stresses on the active slip planes. These stresses are such that, for dissociated glide dislocations, they increase the dissociation width for the ⟨1 2 3⟩ loading axis and decrease it for the ⟨1 0 0⟩ loading axis.

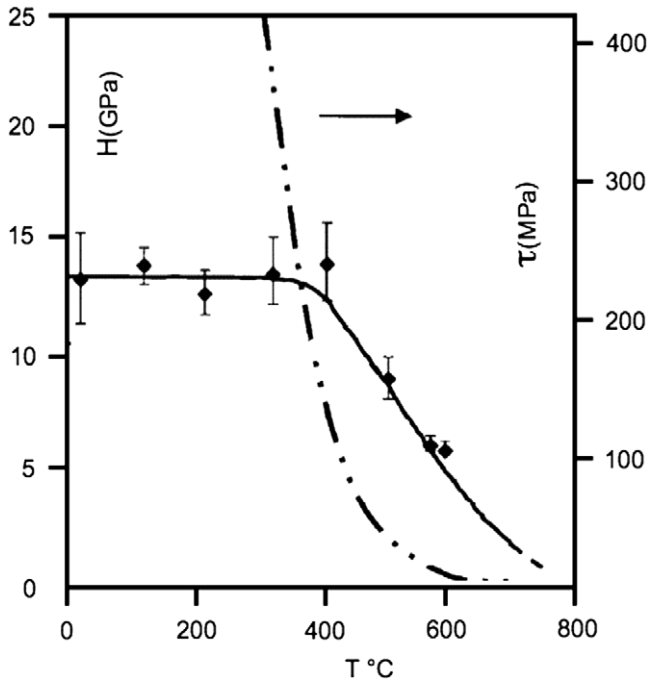

Fig. 8. Hardness (H) as a function of temperature (from Suzuki and Ohmura [51]). The temperature dependence of the yield stress is also schematically drawn (from Castaing et al. [54]). After Rabier and Demenet [57].

Fig. 9(a) shows the microstructure obtained after deformation of a ⟨1 2 3⟩ sample; when observed in the primary glide plane, it consists of dissociated dislocations. There is a tendency for the screw segments to be longer than the other ones. However, this microstructure is not very different from what is found at higher temperatures under standard deformation conditions. Moreover, although the stress tensor favors the narrowing of the stacking fault, no perfect dislocations are obtained. The deformation microstructure of samples deformed along the ⟨1 0 0⟩ compression axis is quite different. It consists of extended stacking faults that point at a deformation mechanism controlled by the movement of decorrelated partials [Fig. 9(b)].

Although the deformation microstructures are different in these two orientations, the analysis of surface source nucleation mechanisms in silicon led to the conclusion that the activation energies for the movement of decorrelated partials and of dissociated dislocations should be the same at high stresses, in agreement with the apparent macroscopic response [57].

These experiments under hydrostatic pressure allowed the study of silicon plasticity under high stresses in the absence of a phase transition. However, although stresses as high as 2 GPa were reached in the plastic regime, the dislocation microstructures were not found to significantly differ from those found in usual low-stress deformation conditions where dissociated dislocations control plasticity. This may relate to the prestrain that was needed to increase substantially the range of experimental conditions leading to plastic behavior (see Ref. [57] for more detail and discussion).

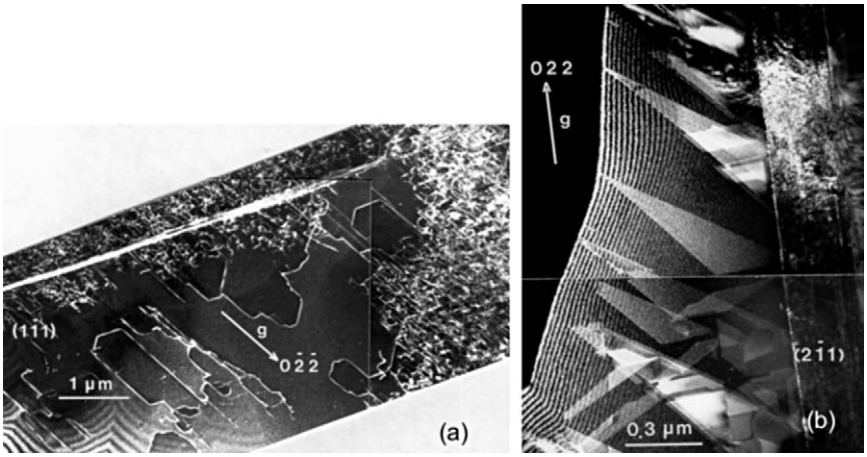

Fig. 9. Dislocation microstructures in silicon crystals after high-stress deformation. (a) ⟨1 2 3⟩ crystal deformed up to the upper yield stress ($\tau = 800$ MPa) at $T = 425\,^{\circ}$C under a strain rate of $2 \times 10^{-6}\,s^{-1}$ and a confining pressure of 700 MPa (after Demenet [55]). (b) ⟨1 0 0⟩ crystal deformed at $T = 450\,^{\circ}$C under a strain rate of $2 \times 10^{-6}\,s^{-1}$ and a confining pressure of 1.5 GPa (after Castaing et al. [54]).

2.2. Evidence of the nucleation of perfect dislocations at high stresses

2.2.1. Plastic deformation under 5 GPa

In order to obtain plasticity at lower temperatures and larger yield stresses, an increase of the confining pressure is required, especially for dislocation-free materials. Yet, the confining pressure has to be maintained below 12 GPa in order to avoid the phase transition artefacts encountered during indentation below 400 °C (Section 2.1.2). Since the highest pressure that can be achieved with a standard Griggs apparatus is 1.5 GPa, experiments at higher pressures require another deformation setting that is routinely used in the field of geophysics: the multi-anvil apparatus. This deformation machine makes it possible to apply pressures up to 25 GPa on ''large'' volumes of materials, but in this type of experiments the yield stress cannot be measured during the mechanical test. A multi-anvil apparatus dedicated to plastic deformation, in which the confining medium was designed to produce an additional uniaxial stress during pressure application [59], was used by Rabier et al. [60,61] to deform virgin Si single crystals. Plastic deformation could be obtained under a hydrostatic pressure of 5 GPa at temperatures as low as room temperature and 150 °C. The applied pressure around the sample was raised at a rate of 1 GPa/h. As a consequence of the design of the solid confining medium, a uniaxial stress also builds up during the pressure application. In such conditions, the deformation rate can be roughly estimated to be $5 \times 10^{-5}\,s^{-1}$ and a permanent strain of several percent is obtained in these tests.

The analysis of the deformed samples shows that the macroscopic deformation results from crack generation as well as from dislocation nucleation and motion. TEM investigations of the deformation microstructure show dislocations that were nucleated at the lateral surfaces of cracks and others that propagated in the bulk material and accumulated in areas with very high dislocation densities. The dislocation loops emitted from the crack surfaces are elongated along specific crystallographic directions [Fig. 10(a)] and so are the dislocation loops that

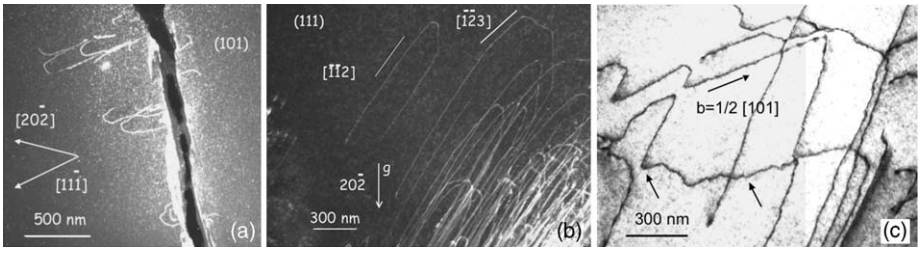

Fig. 10. Deformation microstructures containing perfect dislocations (the confining pressure is 5 GPa). (a) Deformation temperature: $T = 293$ °C; (1 0 1) foil plane, weak-beam dark field (4.1g, $g = 2\,0\,\bar{2}$). The dislocations nucleated at crack edges are of $1/2[1\,0\,\bar{1}](1\,\bar{1}\,1)$ type. These half-loops are elongated along the [3 2 1] direction (after Rabier and Demenet [62]). (b) In the bulk, the same dislocations tend to be aligned along several Peierls valleys: $\langle 1\,1\,2\rangle/30°$, $\langle 1\,2\,3\rangle/41°$, and screw orientation (after Rabier et al. [62]). (c) Deformation temperature: $T = 150$ °C. Same Peierls valleys as at room temperature; some strong pinning points are indicated by arrows (after Rabier et al. [61]).

propagated in the bulk of the sample [Fig. 10(b)]. Strong pinning points are evidenced together with wavy, unstable orientations that result from the presence of very short segments with different orientations [Fig. 10(c)]. Weak-beam dark field contrast studies revealed, that these dislocations are perfect dislocations with the usual $1/2\langle 1\,1\,0\rangle$ Burgers vectors and $\{1\,1\,1\}$ glide planes. The straight segments were found to lie along the screw orientation, as well as along $\langle 1\,1\,2\rangle/30^\circ$ and $\langle 1\,2\,3\rangle/41^\circ$ which can be assumed to be Peierls valleys. These Peierls valley directions were not reported before and differ from the usual $\langle 1\,1\,0\rangle$ ones that characterize dissociated glide dislocations. The density of pinning points was found to be the largest at the deformation temperature of 150 °C [Fig. 10(c)].

These observations were made in samples deformed in compression along the $\langle 1\,2\,3\rangle$ orientation, for which one usually finds dissociated glide dislocations with a small dissociation width (Section 2.1.2). In order to confirm the occurrence of perfect dislocations, a compression axis with a $\langle 1\,0\,0\rangle$ orientation was selected to check whether or not extended stacking faults are nucleated under large stresses. In contrast to what is found at higher deformation temperatures (Section 2.1.2), extended stacking faults were not evidenced. Instead, the microstructure was of same type as in the $\langle 1\,2\,3\rangle$ samples and contained perfect dislocations. This result confirmed the occurrence of a new deformation mechanism involving perfect dislocations, in a stress range where dissociated glide dislocations would no longer have a stable, finite dissociation width. Owing to the apparently perfect nature of the dislocations, cross slip is expected to be an efficient relaxation mechanism. Evidence of this mechanism was looked for in TEM samples, but, surprisingly, it was quite difficult to find any trace of cross slip at this scale of observation.

In this context, various high-stress deformation conditions were tested, with the aim of producing other deformation microstructures containing perfect dislocations. The results are discussed in the next section.

2.2.2. Plastic deformation in the metallic phase

Since a phase transformation as well as dislocations can be evidenced simultaneously after indentation tests at room temperature, the deformation of silicon under a pressure of 15 GPa, that is, in the β-Sn metallic phase, was investigated at 293 K using the same device as in previous tests [62]. In such conditions, silicon deformed along $\langle 1\,0\,0\rangle$ showed an exceptional ductility: a macroscopic strain of more than 20% was obtained without major failure. The *postmortem* observations showed silicon high-pressure phases (Si III, Si XII). These phases were characterized by their Raman spectra on the surfaces of sections extracted from the specimen (unpublished) and by TEM on grains of the different phases. No amorphous phase was evidenced. In addition to these high-pressure phases, a large fraction of the specimen recovered the diamond-cubic phase Si I after the deformation test. TEM observations of this recovered phase showed evidence for an intense plastic activity. Perfect dislocations were found, emerging from dense glide bands, as well as isolated defects in less dislocation-dense areas [Figs 11(a) and 11(b)]. Deformation bands containing mechanical twins were also evidenced (J. Rabier et al., unpublished data). The characteristic features of isolated

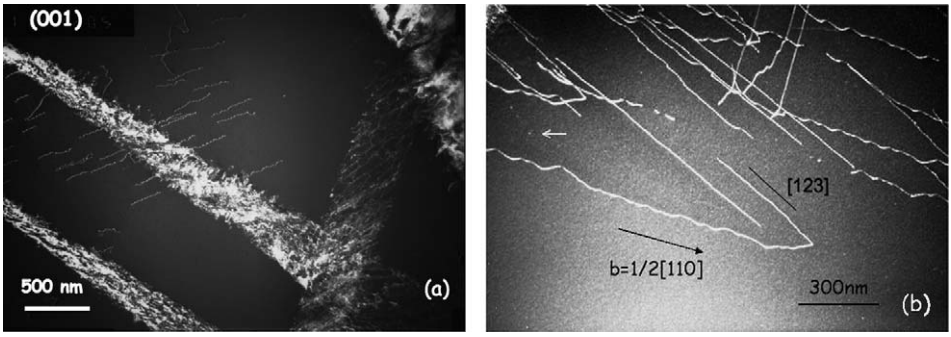

Fig. 11. Silicon deformed in the metallic phase (confining pressure: 15 GPa, $T = 293\,^{\circ}C$). Deformation microstrutures in the diamond-cubic Si I phase. (a) Glide bands with a high dislocation density and isolated perfect dislocations. Weak-beam dark field $2g$, $g = 0\,4\,0$. (b) Isolated perfect dislocations with $\langle 1\,2\,3\rangle/41^{\circ}$ orientation (straight lines) and unstable 1/2[1 1 0] screw segments. After Rabier et al. [62].

dislocations escaping from dense dislocation bands were investigated [62]. The dislocation lines contained segments with average screw orientation and $\langle 1\,2\,3\rangle/41^{\circ}$ segments. The screw orientation appeared to be unstable and was composed of $\langle 1\,2\,3\rangle/41^{\circ}$ segments. Segmented small loops built up with these segments were found to result from dislocation dipole annihilations [62].

2.2.3. *Dislocation microstructure resulting from surface scratches*

Scratching at room temperature followed by annealing at about 800 °C under a bending stress was widely used to nucleate dislocations in silicon. As an example, small densities of large dislocation loops suited for X-ray topography observations could be produced by this method in order to study dislocation mobility as a function of stress and temperature [63,64]. However, although extensive work was performed using this technique for dislocation characterization and properties, analyses are lacking on the nature of dislocations nucleated at scratch sites at room temperature and without subsequent annealing treatment.

Fig. 12 shows the microstructure of a Si sample resulting from a scratch on a {0 0 1} surface along a $\langle 1\,1\,0\rangle$ direction, with an applied load of 0.45 N [61,65]. No additional stress was applied and no subsequent annealing was performed on that sample. Usually, after annealing, such a scratch orientation is found to produce glide set dislocations mainly on the two {1 1 1} planes having a common direction perpendicular to the scratch. Thin foils parallel to one of these planes were extracted from the specimen in order to study the deformation microstructure generated by a room temperature scratch. Large perfect glide loops with $1/2\langle 1\,1\,1\rangle$ Burgers vectors were found in the two {1 1 1} glide planes. They consisted of segments aligned along directions varying between $\langle 1\,1\,2\rangle/30^{\circ}$ and $\langle 1\,2\,3\rangle/41^{\circ}$, plus a few screw segments. When expanding in the glide plane, these loops kept these two low-energy directions, so that the resulting segments with average 60° and 90° orientations exhibited irregular sawtooth shapes. The junctions between

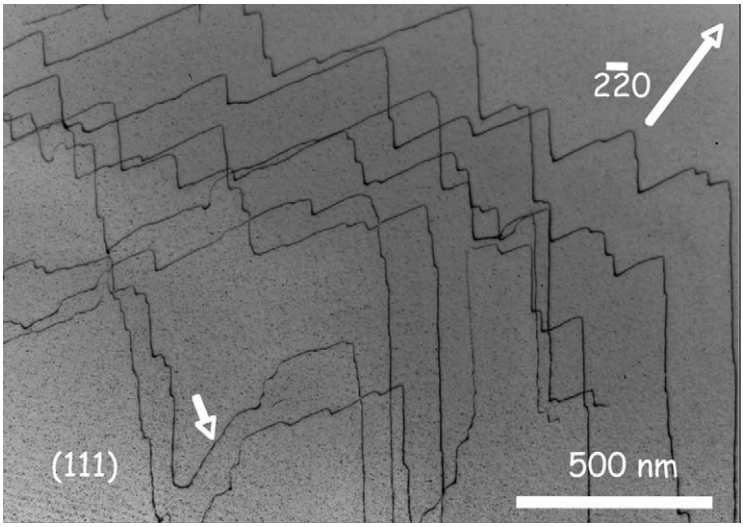

Fig. 12. Microstructure resulting from a scratch at room temperature. Note the roughness of the dislocation lines. Dislocations are aligned along $\langle 1\,1\,2 \rangle$ and $\langle 1\,2\,3 \rangle$ directions. One segment (arrowed) has a screw orientation. After Rabier et al. [65].

two $\langle 1\,1\,2 \rangle/30^\circ$ segments located in two Peierls valleys at an angle of 60° acted as strong pinning points.

2.2.4. Deformation substructure in Si indented at low temperature

Asaoka et al. [66] recently revisited the indentation of silicon with the aim of deforming it plastically below room temperature. These authors indented silicon at 77 K and showed that it can be deformed plastically. TEM observations of the microstructure showed dislocations aligned along the $\langle 1\,1\,0 \rangle$ and $\langle 1\,1\,2 \rangle$ directions. Weak-beam dark field showed these dislocations were perfect ones and had $a/2\langle 1\,1\,0 \rangle$ Burgers vectors. A HREM observation was also performed on a dislocation seen edge-on, which was shown to have an undissociated core. The exact location of this core, in a glide plane or a shuffle plane, could not be determined.

2.3. What is the transition stress?

Since it appears that two types of dislocations are nucleated in two very different temperature and stress regimes, it is of interest to derive the transition stress at which the nature of the nucleated dislocations change from dissociated to perfect. For that purpose, it is necessary to compare deformation tests performed in very different experimental conditions. In particular, the deformation conditions that produce deformation microstructures containing undissociated dislocations are such

that it is usually difficult to measure the uniaxial yield stress. Thus, two types of stress measurements were performed using TEM and X-ray diffraction.

2.3.1. Stress measurements using TEM

Postmortem TEM characterization of the deformation substructures can be performed after any type of mechanical tests. Such characterizations can be used to determine the stresses experienced by dislocations that were frozen in at the end of a test. In the local line tension approximation and for elastically isotropic materials, the dislocation curvature R under a stress τ can be derived from [67]:

$$\tau = \frac{T(C_{ij}, \alpha)}{bR}, \tag{5}$$

where T is the line tension that depends on the elastic constants C_{ij} and the character α of the dislocation line. Gottschalk [68] showed that this expression could be used in the case of dislocations experiencing high Peierls potentials. In such conditions, the information relevant to the measure of the applied stress is localized in the bends connecting two straight segments that are lying in different Peierls valleys. The curvature radii of these bends are inversely proportional to stress, which makes measurements all the more difficult as the stress is high. This method was applied to different deformation microstructures containing glide dislocations and perfect dislocations. The deformation conditions investigated were chosen in such a way that dislocations were nucleated during mechanical testing without any prestrain. In some tests, the applied stress was measured by usual methods during deformation and a high temperature test was used to check the calculation parameters. For each test several curvature radii were measured and the local stress was estimated using eq. (5). The average curvature radii of dislocations and the resulting stresses are given in Table 1.

From the results given in Table 1, one can see the nature of the observed dislocations is changing for an applied stress value within the interval from 560 to 1100 MPa. Obviously, these data are very scarce and more deformation tests have to be performed to further reduce this stress interval.

Table 1
Stress measurements from curvature radii of dislocations under various deformation conditions of confining pressure (CP) and testing temperature

T, CP	τ (MPa) applied	$\bar{R}$ (nm) measured	$\bar{\tau}$ (MPa) calculated	Nature of dislocations
700 °C, (1)	50	800	×	DG
450 °C, 1.5 GPa (2)	700	75	560	DG
150 °C, 5 GPa (3)	?	40	1100	PD
20 °C, 5 GPa (3)	?	25	1600	PD

Note: DG: dissociated glide dislocation; PD: perfect dislocation. (1) Standard test [55], (2) Griggs apparatus [70], and (3) multi-anvil apparatus [60,61].
Source: After Ref. [69].

2.3.2. Stress measurements using X-ray diffraction

More recently, it became possible to obtain stress–strain curves under pressure in the range of deformation controlled by perfect dislocations and at the transition [71]. This was performed using a deformation apparatus (called D-DIA) that is designed to operate in a synchrotron beamline and allows applying separately the confining pressure and the applied stress [72]. In this experimental setup, the specimen length is monitored by X-ray radiography using platinum foils placed at the specimen ends that are opaque to the X-ray beam. The applied stresses are measured through the shift of X-ray diffraction peaks of polycrystalline alumina rams. Yield stresses were then measured between room temperature and 425 °C under an average strain rate of $2 \times 10^{-5}\,s^{-1}$. Plotting the obtained resolved yield stress versus temperature together with data extracted from several other experimental studies one generates a master curve (Fig. 13), which clearly exhibits an inflection. This inflection is correlated with the occurrence of a deformation controlled by perfect dislocations and occurs at a stress of about 1.5 GPa and a temperature of about 300 °C.

Interestingly, an extrapolation of the yield stresses controlled by dissociated glide dislocations leads to a yield stress $\tau_0 = 15 \pm 5$ GPa $(0.3 \pm 0.1\mu)$ at 0 K [51], whereas an extrapolation of the data obtained in the domain controlled by perfect dislocations yields a flow stress $\tau_0 = 1.5 \pm 0.4$ GPa $(0.03 \pm 0.008\mu)$ at 0 K.

2.3.3. The transition stress

TEM experiments allow one to measure the local stress the dislocations were submitted to when the microstructure was frozen in at the end of the deformation test. Yield stresses can be measured during the tests but, then, they include not only the local stress but also the internal stress. One concludes that perfect dislocations are nucleated at stresses larger than 1.1–1.5 GPa, which corresponds to temperatures

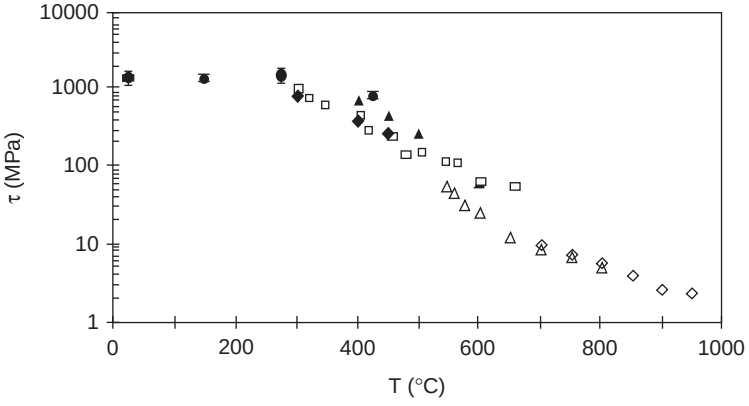

Fig. 13. Logarithm of the resolved yield stress as a function of temperature for Si single crystals, showing a transition around 300 °C. (●) Rabier et al. [71], (♦ and ▲) Castaing et al. [54], (◇ and Δ) Omri [73], and (□) Demenet [55]. After Rabier et al. [71].

lower than 300 °C. An extrapolation of the data of Duesbery and Joós [45] to high stresses predicts that the transition between the deformation mechanisms controlled by dissociated glide dislocations and perfect shuffle dislocations should occur at a stress far lower than the measured ones: about 680 MPa (close to 0.01μ). Such stresses were reached in experiments on virgin materials (see the stress–strain curve at 450 °C in Fig. 7) and dissociated glide dislocations were evidenced. Thus, Duesbery and Joós correctly predicted a change in mechanism at high stresses, but the value of the transition stress should be reconsidered in the light of experimental results.

2.4. The dislocation microstructures at high stress

2.4.1. The signature of low temperature, high-stress deformation

The previous sections clearly show that the low temperature, high-stress deformation microstructures nucleated under resolved shear stresses larger than 1 GPa have particular signatures as compared to usual ones. At the resolution of the weak-beam dark field images, dislocations are found to be perfect ones and they lie in uncommon Peierls valleys like $\langle 1\,1\,2\rangle/30^\circ$ and $\langle 1\,2\,3\rangle/41^\circ$. Strong pinning points are also found along their lines. These features bring evidence of the nucleation of dislocations with different core structures at high stress and low temperature.

The nature of the dislocations not depends only on the applied stress but also on other thermomechanical conditions imposed to the material. Indeed, the same resolved shear stress (about 2 GPa) induces the formation of largely dissociated dislocations when reached after a prestrain ([54]; see Section 2.1.1) and of perfect dislocations when applied to virgin crystals below 400 °C. In these two cases, the dislocations were submitted to stresses larger than the stress for partial decorrelation, since decorrelated partials were observed after a prestrain. This is in agreement with the fact that the perfect dislocations found at high stresses and low temperatures are not glide set dislocations.

2.4.2. The signature of low temperature, high-stress deformation: revisiting previous works

Keeping in mind the striking features of high-stress dislocations, which clearly emerge from the investigations reported above, we reexamine relevant studies published some time ago in a different context.

Hill and Rowcliffe reported dislocations features of the high-stress type after indentation at 300 °C, as can be seen in Fig. 6 of Ref. [53]. These dislocations were not thought to be associated to the deformation process itself; they were assumed to be geometrically required at the ends of block slip displacements of the material under large stresses, close to the theoretical shear stress value. Similar dislocation types were also found by another group after room temperature indentation in the 1970s, but they were assumed to be irrelevant (V.G. Eremenko, private communication).

Most of the high-stress dislocations features can be found in the TEM pictures of published research works on the micromachining of silicon surfaces. Although the mechanism of material removal in the ductile mode must be related to the formation of an amorphous phase, dislocations with average properties looking like those of perfect dislocations were observed in some grinding conditions (see, e.g., [74]). Using cross-sectional TEM, Johansson et al. [75] were also able to image perfect dislocations, besides the presence of cracks, in the vicinity of silicon surfaces polished with 6 μm diamond paste. Their published micrographs show dislocations exhibiting the same original characteristics as those discussed above.

This rapid overview shows that perfect dislocations are systematically present in high-stress dislocation deformation processes. Saka et al. [76] also found out a large dislocation activity resulting from some fatigue process at room temperature. However, the TEM micrographs do not allow one to draw a conclusion about the nature of these dislocations.

2.5. Dislocation core structure and transformation

Since two types of dislocations exist in silicon, namely dissociated and undissociated ones, it is of interest to determine whether they are nucleated in separate temperature and stress domains, or could result from a transformation from one form to the other upon switching from one stress and temperature domain to the other one.

The various authors who observed perfect dislocations assumed that they were located in the shuffle set, as follows from the calculations of Duesbery and Joós [45]. However, there is yet no *direct* experimental evidence about the nature of the plane, glide, or shuffle, in which the core of these perfect dislocations is located.

Several experiments were conducted in order to check the ability of the dislocation cores to undergo transformations. These experiments consist in nucleating dislocations of one type under their specific nucleation conditions and submitting this microstructure to experimental conditions where the other type of core is observed.

2.5.1. From dissociated glide dislocations to perfect dislocations

A specific experiment was designed to check whether dissociated glide dislocations could be transformed into undissociated dislocations [77]. A sample was deformed at room temperature after having been previously deformed in the athermal regime at 1050 °C. It is well known that such a high temperature prestrain leads to a microstructure of weakly dissociated dislocations, mainly of edge character, but that does not contain straight crystallographic segments [78].

The microstructure obtained after room temperature deformation is complex. Nevertheless, several features can be evidenced. In some areas of the thin foil, the microstructure is not different from what is observed in an initially dislocation-free sample. It consists of undissociated dislocations with $a/2\langle 1\,1\,0\rangle$ Burgers vectors elongated along the $\langle 1\,2\,3\rangle$ direction. However, the more frequently observed

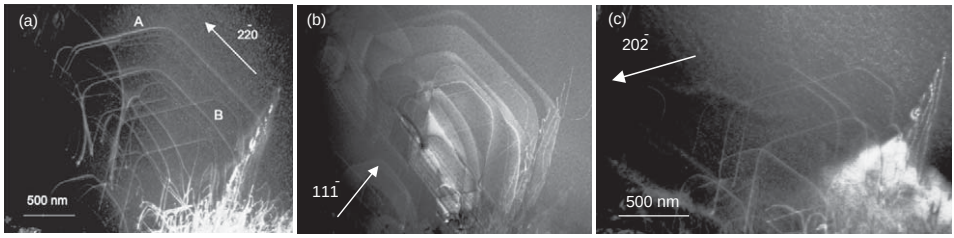

Fig. 14. Dissociated dislocations in the (1 1 1) glide plane of a crystal prestrained at 1050 °C and further deformed at 293 °C under 5 GPa. There are two slip systems, A and B. (a) Weak-beam dark field (2.2g, $g = 2\,\bar{2}\,0$); A and B are in contrast. (b) Weak-beam dark field (7.1g, $g = 1\,\bar{1}\,1$); the stacking fault of A is in contrast, B is in contrast. (c) Weak-beam dark field (3.1g, $g = 2\,0\,\bar{2}$); A is out of contrast, B is in contrast. After Rabier and Demenet [77].

microstructure is made of hexagonal loops of partial dislocations or widely dissociated dislocations. Extra diffraction spots associated to twin bands can also be evidenced in some areas. Examples of hexagonal dislocation loops are shown in Fig. 14. Two glide systems A and B are associated to these loops, which are lying in {1 1 1} planes and are composed of $\langle 1\,1\,0 \rangle$ segments. Contrast analysis (Fig. 14) shows that slip system A contains only one type of partial dislocations, with Burgers vector $a/6[1\,\bar{2}\,1]$. These partial dislocations arise from the dissociation of dislocations with $a/2[1\,\bar{1}\,0]$ Burgers vector into $a/6[1\,\bar{2}\,1] + a/6[2\,\bar{1}\,\bar{1}]$. The dislocations found in slip system B have a Burgers vector $a/2[0\,\bar{1}\,1]$ and are dissociated into $a/6[1\,\bar{2}\,1] + a/6[\bar{1}\,\bar{1}\,2]$. Hence, there is a large difference in splitting widths between the two systems.

Clearly, the hexagonal loops, widely dissociated half-loops, and twin bands are related to dislocations created during the high temperature prestrain. From their initial dissociated configurations, these dislocations moved under the high stress applied at room temperature and were blocked into $\langle 1\,1\,0 \rangle$ Peierls valleys. The latter are the signature of dissociated dislocations of the glide set [2,14]. Furthermore, the application of a high stress can lead to the motion of uncorrelated partials, partial dislocation sources as well as to twinning. These results show that it is also difficult to transform dissociated glide dislocations into perfect dislocations. In short, at room temperature and under high stress, mobile dislocations of the glide set have the same $\langle 1\,1\,0 \rangle$ Peierls valleys as at high temperature and remain dissociated.

2.5.2. *From perfect dislocations to dissociated glide dislocations*

Rabier and Demenet [69] performed *in situ* annealing in a transmission electron microscope in order to promote the transformation of perfect dislocations into dissociated glide dislocations. A low-deformation microstructure was obtained at room temperature and under a pressure of 5 GPa in the conditions described in Section 2.2.1. It contained perfect dislocations with their usual character, like $\langle 1\,1\,2 \rangle/30°$, as well as cracks. This sample was annealed in the heating stage of a

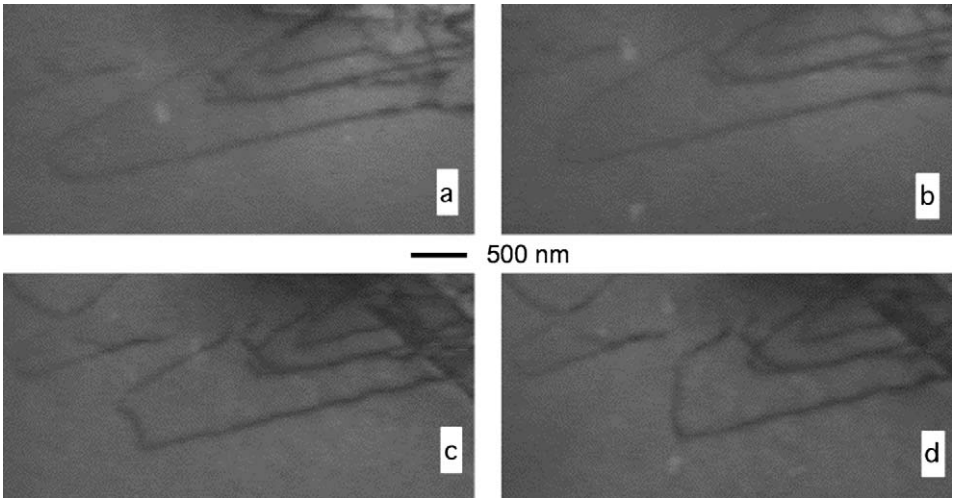

Fig. 15. Snapshots taken during an *in situ* anneal of undissociated dislocations up to 685 °C in the TEM. After Rabier and Demenet [69].

JEOL 200CX electron microscope at temperatures up to 685 °C. The evolution of the microstructure was recorded with a video camera.

Fig. 15 shows snapshots of a recording that was taken during an annealing time of 90 min. Evidently, there is no major evolution in the shape of the perfect dislocation glide loops. Only the front of the loops moves, dislocation segments staying locked in the $\langle 1\,1\,2\rangle/30^\circ$ and screw Peierls valleys. This shape evolution provides no evidence of a transformation. However, in an area of the same thin foil that initially looked free of dislocations (but not of cracks), the annealing treatment induced the nucleation at crack edges of glide loops with hexagonal shapes characteristic of the glide set dislocations (Fig. 16).

This experiment reveals no evidence of a massive transformation of preexisting perfect dislocations. It rather shows nucleation events of glide dislocations from lateral crack surfaces, where undissociated dislocations are nucleated at room temperature and under high stresses.

Asaoka et al. [66] also performed TEM *in situ* annealing on thin foils cut from indented samples at 77 K. Annealing the microstructure of perfect dislocations at 673 K produced no change in the dislocation configurations. At 973 K, different dislocation configurations were evidenced, in which dislocations were dissociated and the lines were either curved or lying along $\langle 1\,1\,0\rangle$ directions. These dislocations of the glide set were connected to perfect dislocations that were assumed to be shuffle dislocations. In parallel, the initial microstructure of shuffle dislocations was not significantly modified. The authors concluded that shuffle dislocations are still immobile at 973 K.

Saka et al. [76] used a FIB-machined sample designed in such a way as to be saturated with interstitials, in order to study the possible shuffle to glide

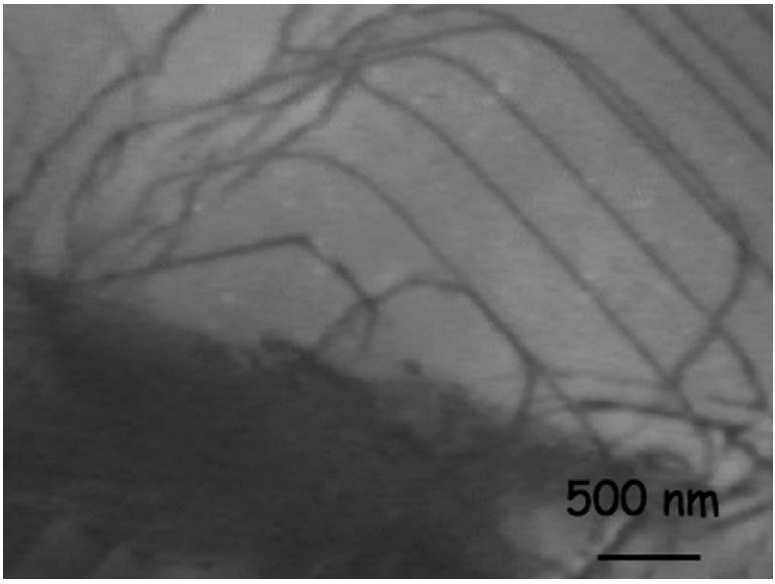

Fig. 16. Nucleation of dislocations having the signature of glide set dislocations from lateral surfaces of cracks during *in situ* annealing. After Rabier and Demenet [69].

transformation in the presence of point defects. A transformation started after annealing at around 400 °C and seemed to be initiated at, or at least near, sharp bends of the preexisting shuffle set dislocations. In the place of perfect dislocations, which had moved away, faint contrast effects were found that were attributed to debris or dislocation loops.

Hill and Rowcliffe [53] have annealed *in situ* a sample indented at room temperature and found analogous features. The effect of annealing could be distinguished after 30 min at 550 °C, but became substantial only after 1 h at 600 °C. These annealing experiments show that 30° dislocations do not move at high temperature under the residual stress present in indented samples. Rather, bowed-out non-screw segments are seen to move rapidly, trailing long screw segments.

2.5.3. Conclusions about the evidences of dislocation core transformations

These experiments, which were aimed at changing the nature of the core structure of dislocations, provide the following evidence:

- Dissociated glide dislocations do not transform into perfect dislocations at low temperature and high stress. The dissociation widths increase under the application of a high stress, which prevents the occurrence of any transformation. In the case where the applied stress induces a narrowing of the splitting width, Demenet [55] and Grosbras et al. [79] demonstrated that it is impossible to recombine a dissociated configuration.

- Perfect dislocations resulting from high-stress deformation do not move significantly in the temperature range where glide dislocation usually nucleate.
- There is no massive transformation of perfect dislocations. Rather, some nucleation events occur, from which glide dislocation can move away and multiply contribute to relax the initial microstructure. In these experiments, no external stress was applied: the driving forces were either the residual mechanical stresses resulting from the previous treatments or the chemical forces built up from a supersaturation of interstitials.

2.6. Physical signatures associated to perfect dislocations

More insight about the actual core structure of perfect dislocations can be obtained from their influence on the physical properties of the material. For these reasons, physical characterizations of samples deformed at high stress and low temperature were performed.

Experiments were designed to compare by means of positron annihilation the defect populations after plastic deformation at high and low temperatures, which are expected to contain different populations of point defects [80]. After room temperature deformation, rather stable vacancy clusters appear and no evidence is found for positron capture by dislocations. In contrast, after high-temperature deformation (800 °C), positrons are trapped in large vacancy clusters and dislocations acting as combined traps. These point defects signatures show clearly that the deformation mechanisms depend on temperature and stress. However, the way the different dislocation structures formed during high-stress deformation at room temperature influence point defect generation is an open question.

The physical properties of perfect dislocations, which are assumed to be shuffle ones, were mainly probed through photoluminescence (PL) measurements. Pizzini et al. [81] performed PL measurements on samples that were deformed following the procedures reported in Section 2.2.1.

Typical PL spectra of samples deformed at room temperature and 150 °C are shown in Fig. 17. They are rather different from those typical of glide dislocations. The canonical emission related to glide dislocations, which consists of a quartet of lines conventionally labeled D1–D4, at about 0.807, 0.877, 0.945, and 1.00 eV [82], is in fact absent. The PL spectrum of the sample deformed at room temperature presents instead a broad emission at about 0.8–0.9 eV, whose shape is influenced by the detector cutoff, and three narrow peaks at 0.973, 1.003, and 1.023 eV that emerge from the background.

In the sample deformed at 150 °C [Fig. 17(b)], the narrow peak intensities are strongly reduced and an additional contribution to the background is observed around the Si free-exciton emission at 1.1 eV. In addition, an asymmetric and broad emission peaked at 1.029 eV is replacing the sharp peak at 1.023 eV that is observed in the sample deformed at room temperature [Fig. 17(a)]. It was suggested that the peak at 1.029 eV is the superimposition of two different spectral contributions.

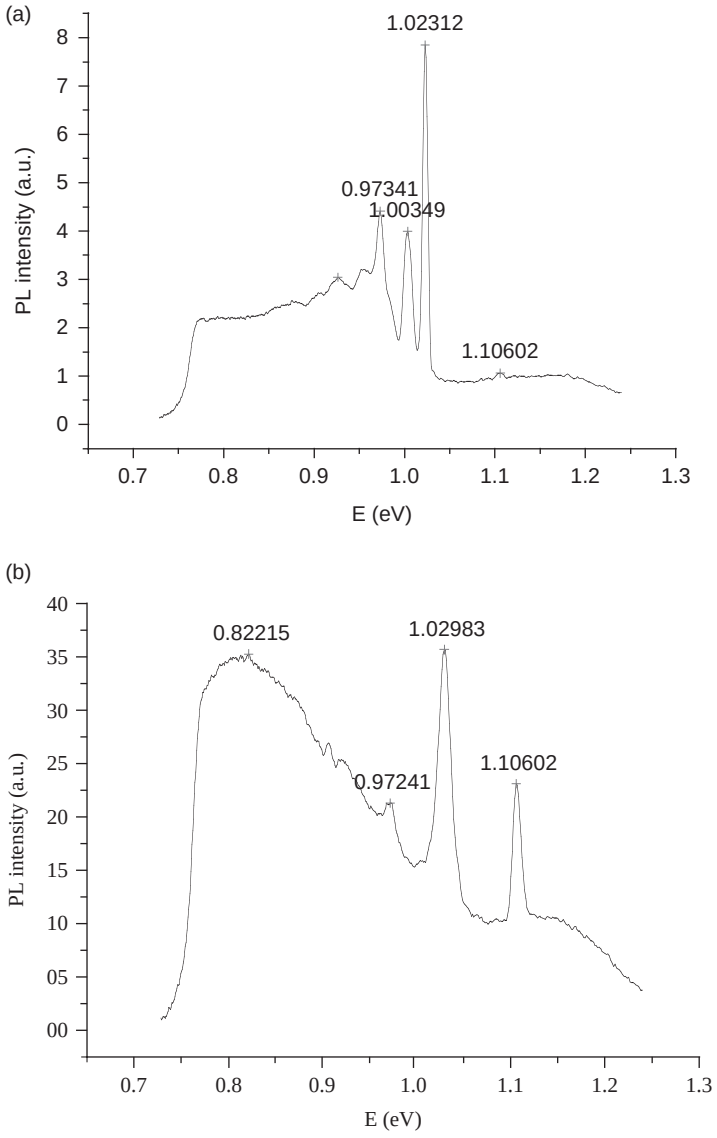

Fig. 17. Photoluminescence spectra of deformed silicon. (a) At room temperature, under 5 GPa and (b) at 150 °C, under 5 GPa. After Pizzini et al. [81]. See text for detail.

Since the PL spectra do not show any evidence of specific emissions associated to shuffle dislocations, Pizzini et al. [81] concluded that perfect dislocations present a reconstructed core, and their generation is accompanied by the introduction of point defects and point defect clusters. A broad band around 1 eV is the only PL

feature that could be directly related to perfect dislocations; it was explained by the conjecture that gap changes are induced by the dislocation strain fields.

Steinman et al. [83] used samples analogous to those investigated in Ref. [81]. The samples were subjected to isochronous anneals at and above 300 °C. Fig. 18 shows PL spectra of the sample after deformation at room temperature under a hydrostatic pressure of 5 GPa and a subsequent anneal at 300 and 400 °C. After annealing at 300 °C, the PL intensity increases significantly. This can be interpreted as unresolved dislocation-related luminescence (DRL) due to the presence of typical features at D1–D4 line positions. In parallel, the intensity of the band exhibiting a maximum at 1.02 eV rapidly decreases. Further annealing at 400 °C leads to an increase of DRL and a significative increase in the resolution of D4 and D3 bands. As these bands are usually attributed to straight segments of dissociated 60° dislocations, this change in DRL after annealing of a microstructure of perfect dislocations is consistent with the PL signature attributed to dissociated dislocations of the glide set.

These PL experiments indicate some trends about the atomic structure of the perfect dislocations:

- They are likely to be reconstructed.
- Their signatures are convoluted with that of point defects.

As far as core modifications or nucleation of glide dislocation are concerned, it appears that a transition in the signature of PL spectra after annealing gives a

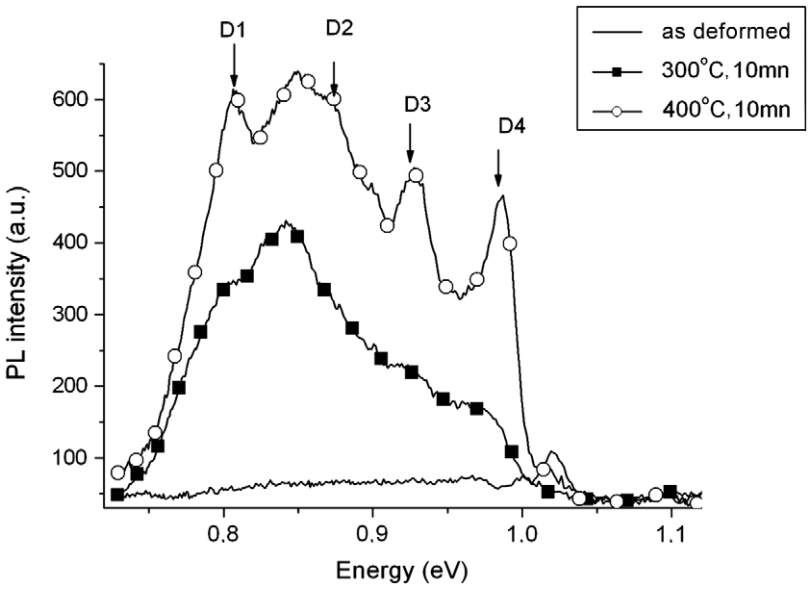

Fig. 18. Photoluminescence spectra of deformed silicon: annealing effects. See text for detail. After Steinman et al. [83].

transition temperature lower than the one found by *in situ* TEM annealing. Two explanations can be put forward for explaining this discrepancy. TEM is able to show up local events with no statistical significance, whereas PL spectra are sensitive to modifications in the bulk material or to premonitory mechanisms associated to the nucleation of glide dislocations. In addition, the PL signatures attributed to perfect dislocations disappear as soon as the transformation occurs, which is not consistent with TEM observations. This could be explained by some modifications in the signatures of perfect dislocations as a function of temperature (see Ref. [81]).

3. The core structure and mobility of perfect dislocations

Understanding the plastic properties and the nucleation of dislocations at high stress requires knowledge of the actual core structure of perfect dislocations. The major problem is to determine the location of those perfect dislocations, that is, whether they are lying in a shuffle plane or a glide plane. Although one expects perfect shuffle dislocations to be found at high stress, from an extrapolation of the calculations by Duesbery and Joós [45], the apparent agreement of experiments with these calculations needs to be confirmed. However, establishing unambiguously the shuffle or glide nature of dislocations proved to be very difficult even for the ''usual'' dislocations. This fed in the past the debate on the actual core structure of dislocations in silicon. The straightforward method for core structure determination is high-resolution electron microscopy (HREM). For usual dislocations, it was necessary to resolve the $\langle 1\,1\,0 \rangle$ dumbbells for a dislocation aligned along $\langle 1\,1\,0 \rangle$ Peierls valleys, that is, to discriminate between two atoms 0.14 nm apart in the crystal projection. Although corrected HREM can nowadays achieve this resolution quite routinely on perfect crystals, the actual structure of dissociated dislocations in silicon has not been revisited and this problem is still open. The same kind of HREM needs to be carried out on undissociated $\langle 1\,1\,2 \rangle/30^\circ$ dislocations, which control the high-stress, low-temperature plastic deformation of silicon. The challenge appears to be far more difficult since $\langle 1\,1\,2 \rangle$ dumbbells need to be resolved, which are composed of two atoms 0.078 nm apart in projection. Recently, such a resolution was achieved on a perfect silicon crystal using a corrected STEM [84], but high-stress dislocated crystals have not yet been investigated by this technique. In this context, and as was previously done for dissociated glide dislocations, only indirect methods are available to check whether those perfect dislocations are in the shuffle set or not.

Analyzing the core geometry is a first step that can also provide useful information on the low-energy configuration of perfect dislocations. Indeed, this was already performed long ago by Hornstra [10], but these results have to be revisited in view of the new data obtained on high-stress microstructures. Furthermore, most of the work done since the advent of the weak-beam technique (see Section 1) has focused on dissociated dislocations in the glide set.

In addition, atomistic studies were performed to calculate how stable core configurations and Peierls stresses of perfect dislocations depend on the atomic

location of the core. Such calculations were also performed to study the nucleation of dislocations from a surface step. Atomistic calculations of dislocation cores in silicon, using interatomic potentials and *ab initio* methods, benefited from most of the simulation techniques available to date. Long-range deformation fields associated to dislocations were tackled using either periodic or cluster-like conditions.

Not only were calculations done for looking at the structural properties of straight dislocations, but elementary kinks of atomic dimension were also investigated. Peierls stresses were determined either by applying a stress on the dislocation core or by using methods like the nudged elastic band (NEB), which are useful for determining transition configurations and energies. These techniques and their limitations are discussed in several papers (see, e.g., [32,85]).

3.1. General features of perfect dislocations in the shuffle plane: a geometrical analysis

The lowest energy partials of the glide type contain lines of atoms with dangling bonds lying almost in the {1 1 1} glide plane and allowing for easy reconstruction. In contrast, shuffle dislocations – besides screw dislocations that are discussed in Section 3.2.1.1 – exhibit dangling bonds, which are parallel and normal to the glide plane. This geometry is *a priori* unfavorable for the pairing of bonds. This is the reason why it is of interest to check the density of dangling bonds along dislocations as a function of their line orientation in the shuffle plane. Hornstra was the first to perform this analysis [10]; he found out that the density of dangling bonds increases from $\langle 1\,1\,2\rangle/30^\circ$ to $\langle 1\,1\,0\rangle/60^\circ$ and $\langle 1\,1\,2\rangle/90^\circ$ for perfect dislocations with 1/2 $\langle 1\,1\,0\rangle$ Burgers vector. This simple analysis is in good agreement with the observation of high-stress microstructures built with $\langle 1\,1\,2\rangle/30^\circ$ perfect dislocations.

However, the variability of dislocation orientations found in experiments between $\langle 1\,1\,2\rangle/30^\circ$ and $\langle 1\,2\,3\rangle/41^\circ$ lines has prompted one of us to consider the geometry of kinks on $\langle 1\,1\,2\rangle/30^\circ$ and the ability for reconstruction of dangling bonds in the dislocation cores [86]. Since the dangling bond density on the $\langle 1\,1\,2\rangle/30^\circ$ dislocation is low, the dangling bonds are far apart and their reconstruction is unlikely. Then, in order to overcome the conflict between a low dangling bond density and reconstruction, such reconstructions could occur on $\langle 1\,1\,2\rangle/30^\circ$ dislocations showing geometrical kinks. Indeed, a dislocation built with $\langle 1\,1\,2\rangle/30^\circ$ and $\langle 1\,1\,0\rangle/60^\circ$ segments can achieve both a dislocation line with a low dangling bond density and the possibility for those dangling bonds to reconstruct. Then a stable $\langle 1\,2\,3\rangle/41^\circ$ segment is obtained, consistent with the observation of such a Peierls valley at high stress (see Fig. 19). Furthermore, the lattice distortions associated with such a reconstruction could be minimized at kink sites.

Such dangling bond geometry appears on {1 1 1} cleaved surfaces, which exhibit a (2×1) reconstruction as was proposed by Pandey [87]. In this surface reconstruction, dangling bonds attach to in nearest neighbors and share π bonding. This

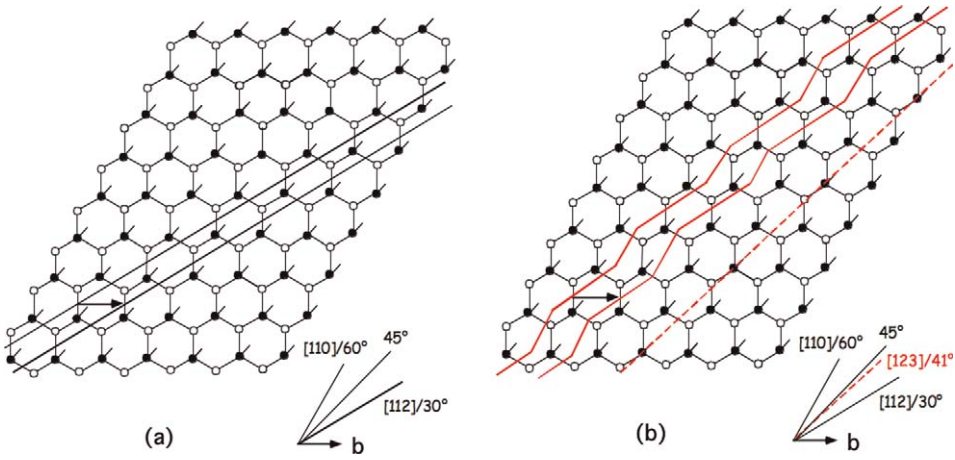

Fig. 19. (1 1 1) glide plane viewed in the shuffle set and showing dangling bonds. The edge of the supplementary plane of a dislocation is indicated. (a) $\langle 1\,1\,2\rangle/30^\circ$ dislocation and (b) $\langle 1\,1\,2\rangle/30^\circ$ dislocation with $\langle 1\,1\,0\rangle$ kinks; this allows for bond pairing and results in a $\langle 1\,2\,3\rangle/41^\circ$ dislocation. After Rabier [86].

surface reconstruction is metastable and is irreversibly transformed into the (7×7) stable configuration by annealing at 600 °C. Such a (2×1) reconstruction was also recently found in *ab initio* calculations [88] during the propagation of a crack in silicon. A reconstruction of this type is exemplified in the case of a $\langle 1\,1\,0\rangle/60^\circ$ dislocation segment located at a kink site in which dangling bonds were put in nearest neighbor positions, as in the case of {1 1 1} surfaces (see Fig. 20). Then a π bond can be formed; this is accompanied by a deformation of the lattice perpendicular to the dislocation line. If such a configuration could be obtained in the case of the $\langle 1\,1\,0\rangle/60^\circ$ dislocation, other line directions would not favor dangling bonds in nearest neighboring positions. However, the strained and "dangling" bonds present in the core of unreconstructed segments could permit the trapping of impurities and intrinsic defects, which may be relevant to the observation of strong pinning points.

3.2. Atomistic calculations

Atomistic computations were performed for 60° and screw dislocations, which are of interest since perfect dislocations of this type appear to be very mobile and are likely to be important in the glide loops development and location. $\langle 1\,1\,2\rangle/30^\circ$ and $\langle 1\,2\,3\rangle/41^\circ$ dislocations were not investigated yet, mainly because calculations are difficult owing to the low periodicity along the dislocation lines.

3.2.1. Perfect dislocation structure and stability

3.2.1.1. Screw dislocations. It is often assumed that screw dislocations govern the plastic behavior in materials with high Peierls stresses, because of their usually low

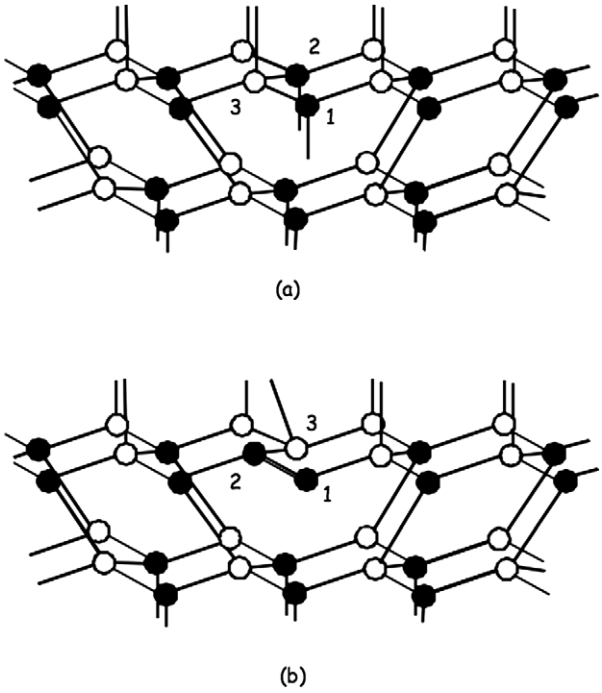

Fig. 20. Possible reconstruction at kinks. (a) Perfect 60° shuffle dislocation with dangling bonds in 1 and 2. (b) Perfect 60° shuffle with a π bond. Dangling bonds have been exchanged between 2 and 3 positions, and pairing of bonds has occurred between 2 and 1. This reconstruction is expected to be feasible at kink sites. After Rabier [86].

mobility related to their ability to dissociate in a sessile way. Their ability to cross slip can also favor a change in core location, for example, between glide and shuffle sets. This explains why several previous investigations were devoted to the structure and stability of the screw dislocation core. From the analysis of the diamond-cubic structure, Hornstra first proposed two possible core structures for the undissociated screw dislocation, located either in a shuffle plane or in a glide plane [10]. The shuffle core was relaxed using first-principles calculations by Arias and Joannopoulos [89]. Another study based on first-principles calculations confirmed that a shuffle core was energetically favored [90]. However, more recently, it was suggested that a glide core reconstructed along the dislocation line is the most stable configuration [91]. Finally, we mention that a new configuration, with a mixed shuffle–glide core at the intersection of the glide and shuffle sets, was proposed by Koizumi et al. on the basis of interatomic potential calculations [92]. Fig. 21 shows all these possible core structures.

The shuffle configuration (A) is characterized by the conservation of the original coordination for atoms in the vicinity of the core, though at the expense of strong bond distortions. For instance, bonds close to the core and linking atoms on both

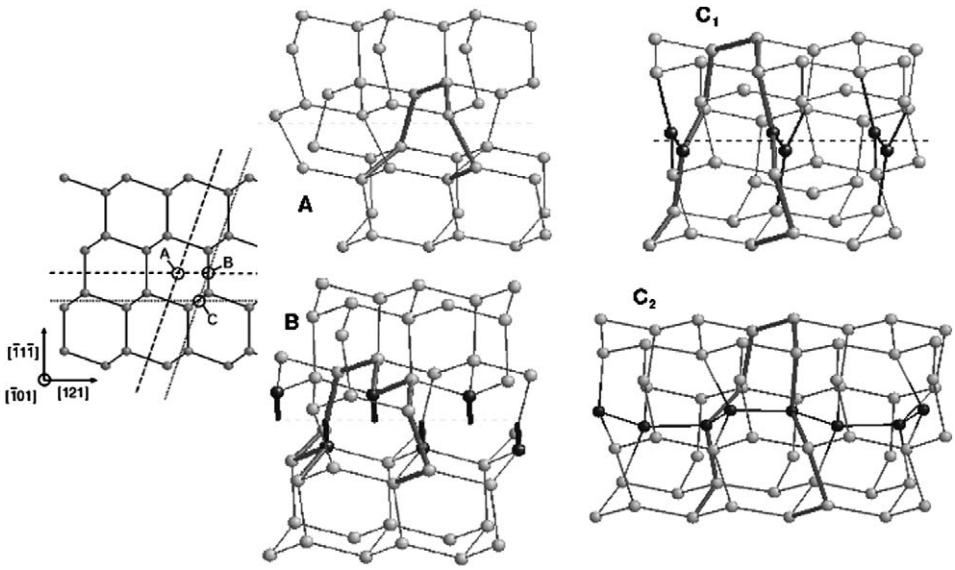

Fig. 21. Possible core configurations for a non-dissociated screw dislocation: shuffle (A), mixed shuffle/glide (B), simple period glide (C_1), and double-period glide (C_2). Thicker dark gray bonds show a Burgers circuit; the dislocation line along $\langle 1\,1\,0 \rangle$ is marked by a dashed line in each case. Atoms located in the immediate vicinity of the core are represented by black spheres. After Pizzagalli et al. [90]. The A, B, C positions for a screw dislocation are shown in the insert on the left side of the figure.

sides of shuffle planes are disoriented by about 20° compared to the bulk [89,90]. The mixed shuffle–glide core (B) involves the breaking of bonds along the dislocation line, apparently resulting in a double row of dangling bonds. As already remarked by Hornstra, such a configuration is likely to be unstable due to symmetry considerations [10]. The simple period glide configuration (C_1) corresponds to a core composed of 3-coordinated atoms, with coplanar bonds and bond–bond angles of approximately 120°, pointing to sp^2 hybridized states. The computed distance between two 3-coordinated atoms is 0.216 nm, to be compared with 0.235 nm, the bulk nearest neighbor distance [93]. Finally, the double-period glide configuration (C_2) allows recovery to a core with only 4-coordinated atoms, after some atomic rearrangements starting from the C_1 glide configuration. The dislocation core is made up of two $\langle 1\,1\,0 \rangle$ rows of dimers, with a dimer length of 0.247 nm, both rows being connected by bonds having a length equal to 0.237 nm.

The relative stabilities of the possible core configurations obtained with different computational methods are reported in Table 2. All performed calculations suggest that the most stable core for a non-dissociated screw dislocation is located in the glide set, with a double period along the dislocation line. The shuffle core A is the second best solution. Electronic structure calculations all indicate that the B core is

Table 2
Relative stabilities of possible core configurations for a non-dissociated screw dislocation (in eV/Burgers vector), computed with different methods

Screw core	Methods						
	Stillinger–Weber potential	Tersoff potential	EDIP	Tight binding DFTB [94]	First principles [91]	Tight binding [91]	First principles [90]
A	0.19	0.31	0.07	0.60	0.54	0.62	0
B	0.05	1.39	0.30	×	×	×	0.32
C_1	1.81	0.85	0.81	×	×	×	0.86
C_2	0	0	0	0	0	0	×

Note: For each column, the zero energy reference is the lowest energy configuration. × means that the value is not available or the considered configuration was found unstable.

unstable, as originally predicted [10]. This casts some doubts on the validity of classical potentials results, especially Stillinger–Weber, for which B is the second best solution, very close to C_2.

Obviously, it is difficult to explain these results by considering the relaxed core structures. Originally, the shuffle core A was thought of as the best option, since the dislocation center is as far as possible from lattice atoms, thus minimizing the deformation. Nevertheless, the reconstruction leading to the glide configuration C_2 apparently allows obtaining a narrow dislocation core with weaker bond distortions.

3.2.1.2. 60° dislocations. The other non-dissociated dislocation that is apparently found to be very mobile during plastic deformation of zinc-blende materials is the 60° dislocation. In his seminal work, Hornstra proposed a possible structure for the 60° dislocation with a core centered in a shuffle plane [10]. This configuration named S_1 here and represented in Fig. 22 has the particularity to include a 3-coordinated atom, with a dangling bond oriented along a $\langle 1\,1\,1 \rangle$ direction. This dislocation core appears to have a high mobility compared to the screw dislocation; it was identified in previous theoretical works with either classical potentials or *ab initio* calculations [95–97]. Nevertheless, the situation is maybe more complex since other possible configurations are stable with a lower core energy. In Fig. 22, we show two of those, obtained from interatomic potential or tight-binding calculations. The glide core G has a very low energy, making it the most stable. The other shuffle core, named S_2, is less stable than the glide core, but still with a lower energy than S_1.

3.2.2. Dislocation mobility

3.2.2.1. Perfect screw dislocation: Peierls stress and energy. There were several early attempts to calculate the Peierls stress of the non-dissociated screw dislocation in silicon [92,98,99]. Empirical potential computations give values ranging from

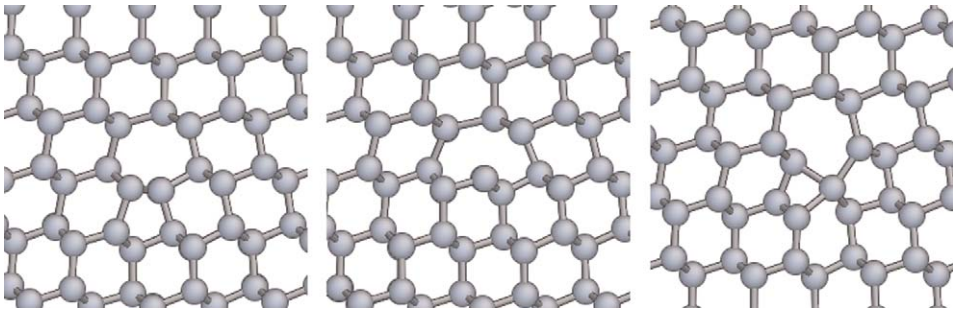

Fig. 22. Three possible core configurations for a non-dissociated 60° dislocation: one glide G (left) and two shuffle, S_1 (middle) and S_2 (right).

0.013 to 0.048 eV/Å^3 (0.03μ to 0.11μ). This large range highlights the difficulty in obtaining accurate values from interatomic potentials in the case of silicon and points at the necessity of using first-principles methods. However, as shown previously, the latter only can be employed in association with small computational systems, for which a careful treatment of boundaries is required. This problem is even more crucial for Peierls stress determination since approaches developed to take boundaries into account are not well suited for treating the displacement of dislocations.

In fact, applying an increasing stress progressively shifts the dislocation, therefore modifying the surface–dislocation interaction in the case of a cluster calculation, or the dislocation–dislocation interaction in the case of periodic boundary conditions. These undesirable effects have to be accounted for if one aims to obtain an accurate value of the Peierls stress in small systems.

This issue has been tackled in the case of the shuffle screw dislocation in silicon [100]. The computed Peierls stress, corrected for spurious boundary interactions, is equal to 0.026 eV/Å^3 or 0.07μ. This value is much lower than measured Peierls stresses for partial dislocations [101]; it can be compared to the Peierls stress of the glide core C_2, which has also been recently computed with a value of about 0.04 eV/Å^3, that is, 0.11μ [91]. The glide configuration appears more difficult to displace under applied stress than the shuffle configuration, possibly because of the presence of reconstructed bonds in its core.

Besides the Peierls stress, a related and interesting quantity for characterizing the mobility of dislocations is the Peierls energy, which is simply the energy barrier to overcome for displacing a straight, infinite dislocation in the lattice. This energy is difficult to compute using standard relaxation techniques, since it is necessarily associated with an unstable dislocation structure. Attempts to extract the relevant information from molecular dynamics simulations have been made [102]. However, the proposed method is tricky and appears more suited for interatomic potentials than for first-principles calculations. Recently, it was proposed to combine both the nudged elastic band method [103] and first-principles calculations performed with periodic boundary conditions, in a way that allows to determine the energy and structure of a dislocation for any migration path [85]. In the case of the non-dissociated screw in

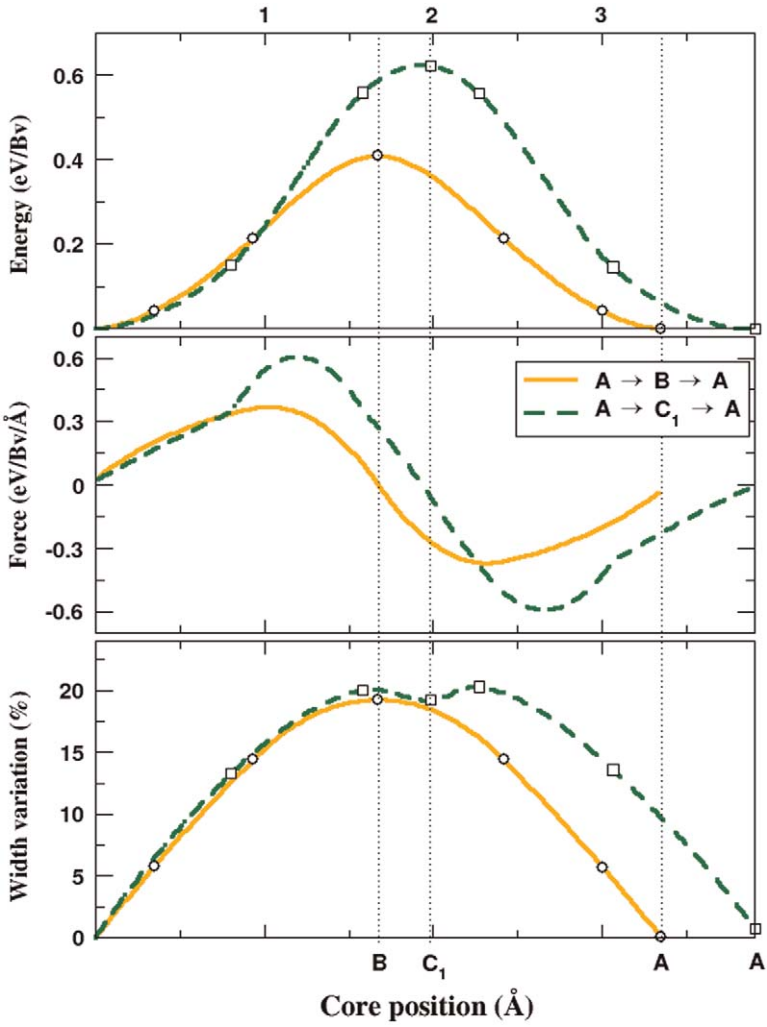

Fig. 23. Variation of dislocation energy (top), its first derivative, that is, the force exerted on the dislocation by the lattice (middle), and dislocation core width (bottom) as a function of the position of a non-dissociated shuffle screw dislocation. The calculations are performed along two possible paths that are indicated in the middle figure. After Pizzagalli et al. [85].

silicon, the computed energy variation as a function of the dislocation position along two possible paths is shown in Fig. 23. The one with the lowest Peierls energy corresponds to the displacement direction previously obtained from calculations using an imposed shear strain [100,104]. The derivative of the calculated energy variation as a function of the dislocation position is the force on the dislocation due to the lattice (Fig. 23). The maximum along the path corresponds to the maximum resistance of the lattice to the dislocation displacement. Converting this force into stress is

straightforward and leads to a value of about $0.025\,eV/Å^3$, in close agreement with previous Peierls stress determinations [100]. Although the computational cost is high due to the use of NEB, there is no need to use boundary corrections with this technique. Another advantage is the possibility to explore high-energy directions for displacing dislocations such as $A \rightarrow C_1 \rightarrow A$, which are not accessible when using imposed shear strain calculations [100].

Finally, information on the structure of a dislocation can be gained from combined NEB and first-principles calculations. For instance, the displacements of core atoms leading to the dislocation migration can be monitored. In the case of the shuffle screw dislocation, the variation of the core width during the displacement was investigated and is represented in Fig. 23. Clearly, the dislocation core expands when the dislocation is centered in an unstable configuration. A possible explanation is that the system gains energy by spreading out atomic displacements, thus minimizing deformation in the dislocation center. Investigations of higher moments of the displacements distribution should provide additional information on the dislocation geometry, such as core asymmetry.

3.2.2.2. Perfect screw dislocation: mobility by formation and migration of kinks. Partial dislocations are known to move at high temperature by the formation and migration of kink pairs, both being thermally activated processes [12]. Non-dissociated perfect dislocations are obtained at lower temperatures and for higher stresses, but since the lattice resistance to dislocation motion is large in silicon, thermal activation is also expected to play a nonnegligible role in that case. Nevertheless, there were very few theoretical studies of kinks on perfect dislocations and those exclusively concern the screw dislocation. Hence, Koizumi and Suzuki investigated the kink velocity as a function of the applied stress and the energy dissipated during kink motion [105]. Their use of a high-energy core configuration does not allow extracting quantitative data regarding the energetics and structure of a single kink.

Recently, Pizzagalli et al. used both interatomic potentials (EDIP, Lenosky) and first-principles methods to study the formation and migration of a kink pair on a perfect shuffle screw dislocation [106,107]. Dislocations and kinks were modeled using silicon clusters (large for potentials, small and passivated with hydrogen atoms for first-principles calculations), one or two kinks being included in the simulation system (Fig. 24). In this work, an unbiased and exhaustive search for all possible configurations of a kink was made initially thanks to the dimer method [108]. This method is particularly useful for studying structural defects with complex reconstructed cores, for which many nonintuitive configurations may exist such as, kinks on partial dislocations in silicon [33]. Thereafter, the migration and formation mechanisms were determined using the nudged elastic band technique. Interestingly, few stable kink configurations were obtained, in contrast with the situation prevailing for partials [33]. This might be explained by the fact that the core of the shuffle screw dislocation is not reconstructed.

Fig. 25 shows two possible structures of a kink. Both are degenerate in energy, at least at the level of the accuracy of first-principles calculations. The first one, called

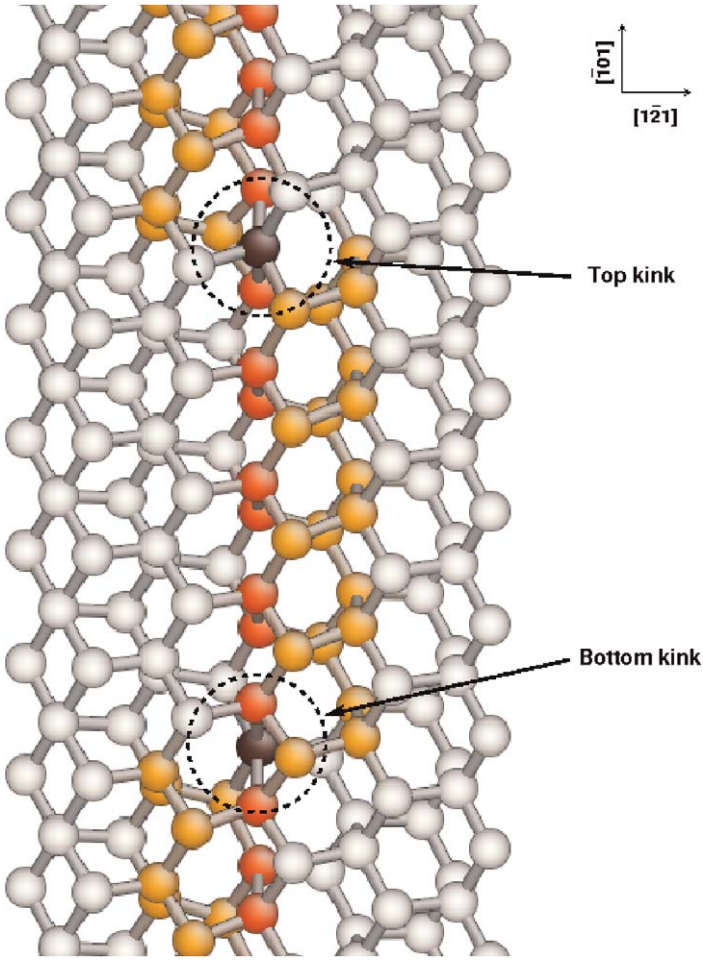

Fig. 24. Ball and stick representation of kinks on a non-dissociated shuffle screw dislocation. Gray atoms indicate screw core atoms while kinks are marked by black atoms. After Pizzagalli et al. [106].

the narrow kink in Ref. [106], is characterized by a 5-coordinated atom in its center, whereas in the second one, called the dangling bond (DB) kink, the central atom is 3-coordinated. Both cores have in common distorted and stretched bonds, with a bond length increasing by 7–13% and an angular deviation greater than 30°. Following a procedure that allows one to obtain the energetics of a single kink in small clusters, the single kink formation energy F_k was determined to be 1.36 eV. With interatomic potentials and EDIP, the narrow kink structure is found to favored. Instead, the Lenosky potential gives the DB kink structure as the most stable configuration. The formation energy of a single kink computed with EDIP is $F_k = 0.91$ eV.

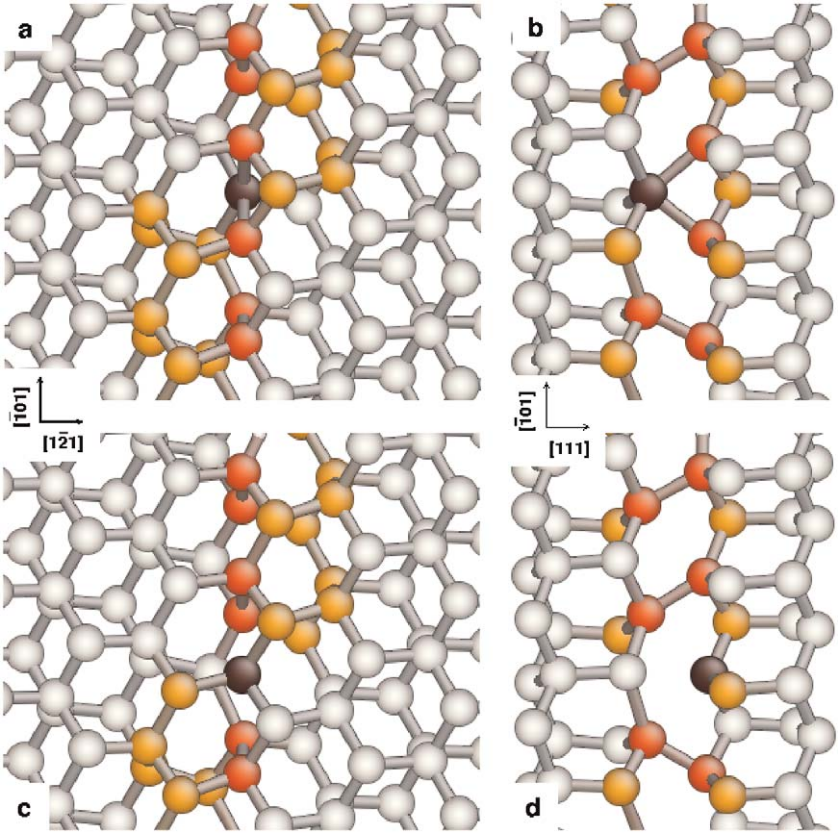

Fig. 25. Ball and stick representations of two possible kink structures shown along two different orientations (left and right). (a and b) Narrow kink and (c and d) DB kink. After Pizzagalli et al. [106].

Nudged elastic band and dimer calculations were also carried out by the same authors in order to investigate the migration of a kink along the shuffle screw dislocation line [106,107]. Fig. 26 shows the migration mechanism corresponding to the displacement of a single DB kink separating from a symmetric kink, using first-principles calculations. Migration of the kink requires first the formation of a bond between the 3-coordinated atom and one of its neighbors, which then becomes 5-coordinated. This configuration is the narrow kink. After the breaking of one bond, the structure recovers the original DB kink configuration, shifted by a Burgers vector b along the dislocation line. Because bonds in the center of the kinks are largely distorted and stretched, the energy variations for forming and breaking bonds are small, yielding a low kink migration energy. Extrapolating values for an infinite kink–kink separation, the first-principles kink migration energy W_m is estimated to be lower than 50 meV. The kink migration mechanism determined with the Lenosky potential is similar, with almost identical migration energy [107]. With EDIP, a slightly different process is obtained since the initial state is the

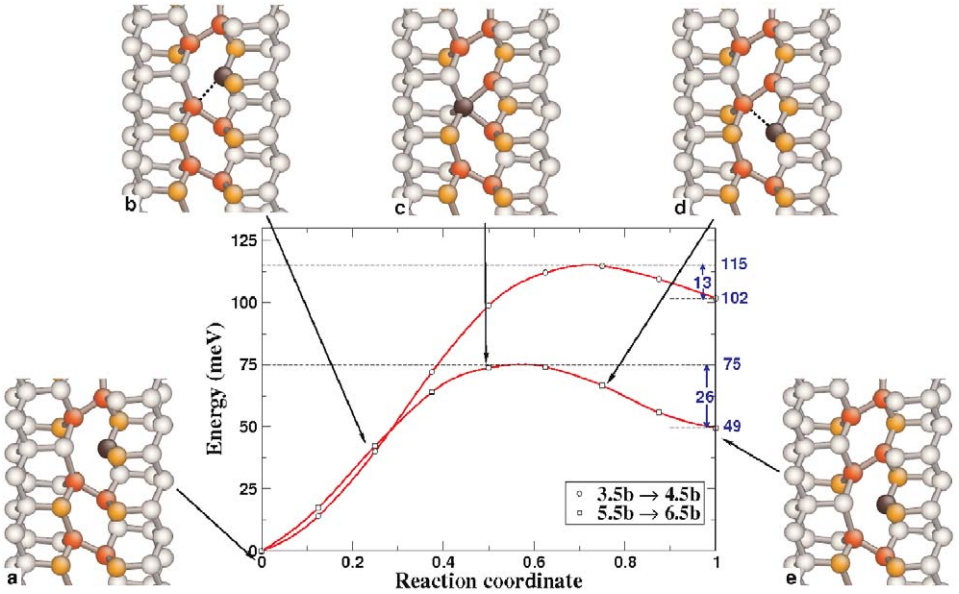

Fig. 26. NEB calculation of excess energy versus reaction coordinate (middle graph) corresponding to the migration of one kink, for two different kink–kink separations, and ball and stick representations of the successive structures (a) to (e) for a separation varying from 5.5*b* to 6.5*b*. After Pizzagalli et al. [106].

narrow kink configuration. During migration, an intermediate stable configuration including three 5-coordinated atoms is formed [106]. However, this migration mechanism appears globally close to the previous ones, with a low associated energy barrier W_m of about 160 meV.

Another important mechanism to be determined relates to the formation of a kink pair. Its theoretical determination brings additional issues, compared to the calculation of kink migration. In fact, it is necessary to consider a system that encompasses two kinks, with a separation distance large enough to prevent spontaneous kink recombination. First-principles NEB simulations of such a system is out of reach of computational facilities for the time being. However, this limitation vanishes for interatomic potential calculations, and the formation mechanism of a kink pair on a shuffle screw dislocation was investigated using both EDIP [106] and the Lenosky potential [107]. In both cases, the results show that the formation occurred following a sequence of structural rearrangements involving the breaking and formation of several bonds. Obviously, the computed mechanisms are somewhat different since the most stable configuration for a kink is different with EDIP and the Lenosky potential. However, the calculated energy barriers for the formation of a kink pair of width 3*b* are in very good agreement, with 1.25 eV for EDIP and 1.19 eV for the Lenosky potential.

Besides thermal activation, the second parameter to take into account for understanding dislocation mobility is stress. In fact, non-dissociated perfect

dislocations are observed in the low temperature, high-stress regime. Large shear stresses, estimated to about one to several GPa, are then required for displacing dislocations. This is very different from the situation occurring for partial dislocations, where thermal activation is the key factor. Despite its importance, very few investigations focused on the effect of the shear stress on kink formation and migration. The only study again concerns the shuffle screw dislocation [106]. The effect of the shear stress on the formation and migration of kinks was computed using the EDIP potential. Fig. 27 represents the energy variation due to the formation and subsequent separation of a kink pair on a perfect shuffle screw for an increasing shear strain. The repeating patterns clearly visible on each curve correspond to the energy variations due to the kink migration. Neglecting the migration, the energy variation as a function of the kink–kink distance d and the shear strain can be fitted by the following elastic expression [12]:

$$\Delta E = -\frac{K}{d} + 2F_{\mathrm{k}} - \tau bhd, \tag{6}$$

where K is an elastic coefficient, h the height of one kink, and τ is the applied shear stress. In case of no applied strain, the energy increases continuously toward the asymptotic value $2F_{\mathrm{k}}$. As expected, a shear stress is required to decrease the energy

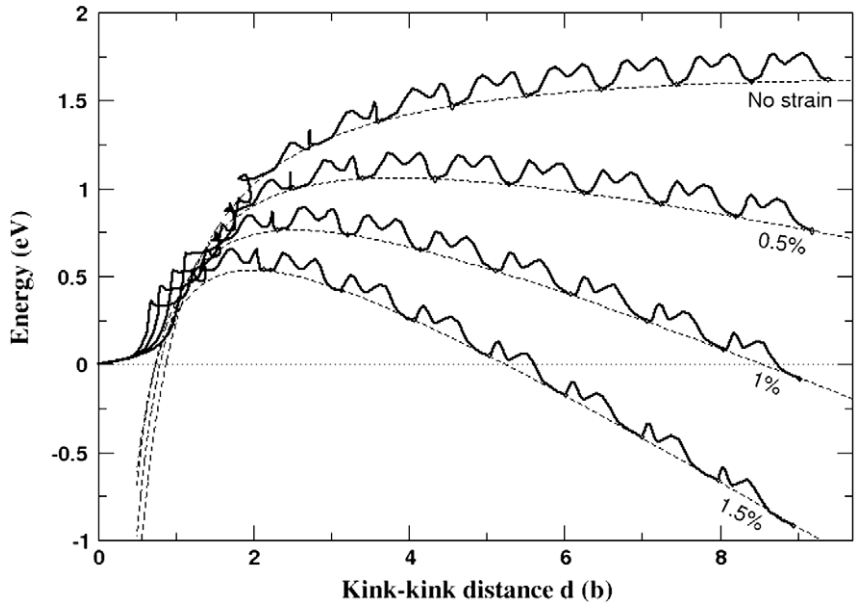

Fig. 27. Kink pair energy as a function of the kink–kink separation d (in Burgers vector unit) for various shear strain values (full lines). Fits from elasticity theory are reported as dashed lines. After Pizzagalli et al. [106].

and for preventing the spontaneous recombination of the two formed kinks. More importantly, the energy barrier to the formation of the stable kink pair, that is the maximum energy on each curve, is strongly dependent on the shear strain. Accurate determinations, taking into account the additional energy barrier due to migration, yield energy barriers of 1.20 eV for a strain of 0.5% (i.e., about 0.28 GPa) and only 0.65 eV for 1.5% (i.e., about 0.85 GPa) [106]. The last value is low enough to suggest that, in silicon, shuffle screw dislocations should be mobile in the range of low temperatures and high stresses involved in the deformation experiments reported in Section 2.

3.2.2.3. Mobility of 60° dislocations. As far as we know, there is little information available regarding the mobility of the various 60° dislocation cores represented in Fig. 22. Using the Stillinger–Weber potential, Li et al. determined a Peierls stress of approximately 1 GPa for the S_1 core [95], confirming that the 60° dislocation is more mobile than the screw dislocation. However, additional investigations of the structural and mobility properties of the 60° dislocation would be welcome. Both core configurations appear to be less mobile than S_1 and additional calculations are needed for a better understanding of the competition between core stability and mobility.

3.2.3. Effect of pressure on the core structure of perfect dislocations

Because perfect dislocations are observed in high-stress conditions where a hydrostatic component is present in the stress tensor, it is of interest to check the effect of such a hydrostatic pressure on their core structure configuration and mobility. One can expect three kinds of effects due to pressure: (i) the material is usually stiffer (this is the case for silicon), with an increase of elastic constants that affect the strain field around the core, (ii) the core structure and its stability could be modified, and (iii) pressure could favor dislocation core mobility along certain directions. One may then wonder whether theoretical investigations of non-dissociated perfect dislocations are really representative of experiments.

One first step toward an improved modeling would consist in taking into account an applied pressure. To our knowledge, there were few investigations of pressure influence on dislocation core properties. Durinck et al. [109] determined how pressure would modify the Peierls stress in olivine, an important compound for geophysicists. These authors showed that in the presence of a pressure of 10 GPa, some slip systems would harden whereas others would become softer, a result that cannot be fully explained by elastic effects. Pressure effects were also considered in the case of screw dislocation in bcc metals such as tantalum ([110]; see also Chapter 92 by Yang et al. in the present volume). It was shown that the structure of a screw dislocation core could be significantly modified upon the application of a 10 MPa pressure. However, no pressure dependence of the Peierls stress, scaled by the shear modulus, was found. Regarding semiconductors, Umeno and Černý [111] recently computed the theoretical shear stress as a function of an applied pressure in diamond, silicon, germanium, and two different silicon carbide polytypes, using first-principles calculations. These authors showed that in silicon, the ideal shear

strength is decreased by compression. This finding cannot be understood with a simple hard-sphere model, for which compression results in the squeezing of the spheres and a larger resistance against shear, a picture well suited for metals.

Recently, we investigated the effect of an applied pressure on the stability and mobility properties of the non-dissociated screw dislocation in silicon [94]. A given pressure is applied by homogeneously straining computational cells before the system is relaxed and core energies are calculated. The variations of core energies for two stable core configurations, the glide C_2 and the shuffle A, are shown in Fig. 28. While the presence of an applied pressure tends to increase the core energy of C_2, it lowers the A core energy. This result indicates that pressure can have either a positive or a negative impact on dislocation stability. It is very tempting to interpret these variations in view of an analysis of the core geometry. In fact, the A configuration is characterized by four largely stretched and distorted bonds. Applying a pressure brings atoms closer together, thus lowering the amplitude of bond stretch and distortion, which decreases the core energy. This would mean that under zero pressure conditions, the shuffle A core is in a tensile state. However, it is difficult to understand why pressure tends to increase the core energy of the C_2 configuration simply in terms of the core geometry. As a consequence, the effect of

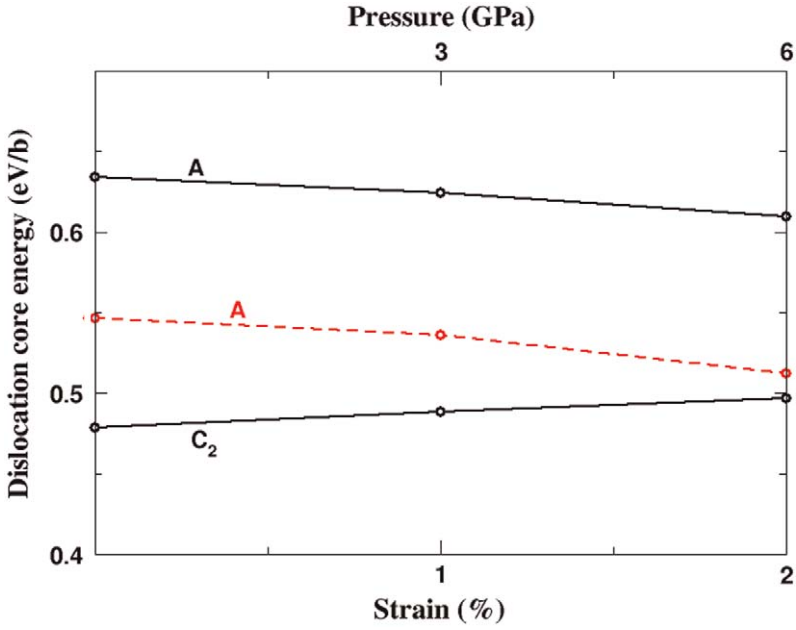

Fig. 28. Dislocation core energies of a screw dislocation as a function of an applied pressure, for shuffle A and glide C_2 cores. Values were determined from tight-binding DFTB (full lines) and DFT-GGA (dashed line) calculations, assuming that the core radius is equal to one Burgers vector *b*. After Pizzagalli et al. [94].

pressure on dislocation core stability is hardly predictable using simple arguments and atomistic calculations are mandatory for its determination.

The pressure tends to favor the shuffle core A for the screw dislocation. However, it remains energetically less favorable than the glide core C_2. Assuming that core energies vary linearly as a function of pressure, one expects a phase transition for an applied strain of about 7%, that is, a pressure of 20 GPa. This is much higher than the pressure corresponding to the phase transition from the cubic-diamond to the β-tin structure, suggesting that the glide core C_2 is the most stable configuration in all the available pressure ranges.

The core energy determination as a function of pressure requires a careful treatment. In the case of dislocation calculations using periodic boundary conditions, the total energy E of the relaxed system including N dislocations can be written

$$E = E_{\text{bulk}} + E_{\text{inter}} + NE_{\text{c}}, \tag{7}$$

where E_{bulk} is the total energy of the same system but with no dislocations, E_{inter} the interaction energy between dislocations, and E_{c} the core energy of a single dislocation. E, E_{bulk}, and E_{inter} all depend on pressure, and have to be correctly determined for an accurate calculation of E_{c}. The largest part of the energy increases in E and E_{bulk} is due to the applied strain. Both terms are obtained using systems with same geometry, thus leading to the cancellation of errors associated with total energy calculations. The last term, E_{inter}, is usually computed in the framework of anisotropic elasticity theory. In the presence of pressure, one has to consider that (i) interactions between dislocations are modified due to the reduction of distances between them and (ii) the elastic constants change as a function of pressure. E_{inter} has to be computed with the appropriate corrections, otherwise errors in core energies variations can be dramatically large [94].

The influence of an applied pressure on the mobility of the core of the non-dissociated screw dislocation was recently studied. Two possible paths were considered: (i) along a $\langle 1\,1\,2 \rangle$ direction for which the dislocation moves in $\{1\,1\,1\}$ shuffle planes and visits alternatively A and B configurations and (ii) along $\langle 1\,1\,0 \rangle$, the dislocation moving in a $\{0\,0\,1\}$ plane and passing through A and C_1 configurations. The dislocation core mobility was determined from computations of energy barriers for cores displacement along the selected directions, using the approach described in Section 3.2.2. The results reported in Fig. 29 show two opposite behaviors. For the first displacement direction, along ABA, an applied pressure leads to a progressive reduction of the Peierls energy. Conversely, the other displacement direction along ACA is increasingly energetically expensive. Therefore, this result indicates that for a given dislocation, slip directions could be hardened or softened in the presence of pressure. As for dislocation core stability, it is difficult to predict whether energy barriers will increase or decrease under pressure without the help of numerical simulations.

The presence of pressure leads to a noticeable modification of the properties of dislocation cores. In fact, both the stability and the mobility of the cores are

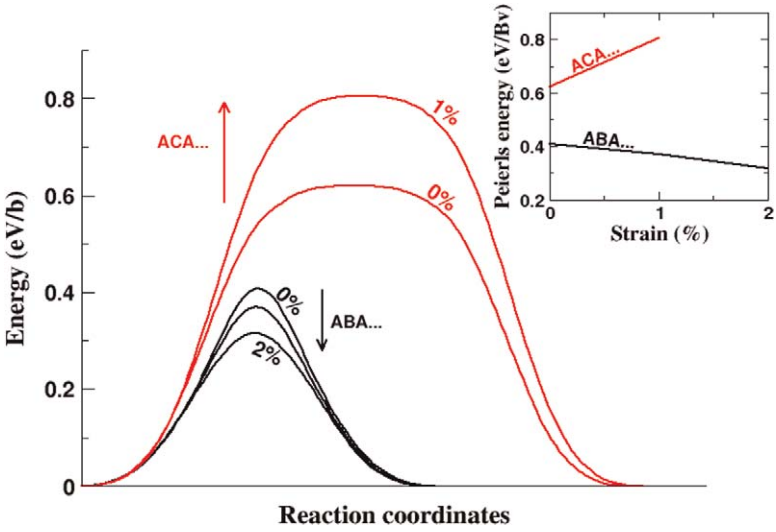

Fig. 29. Screw dislocation gliding along two different directions (see text), as a function of an applied strain. Maximum energies along the MEP are the Peierls energies; they are reported in the inset graph for clarity. After Pizzagalli et al. [94].

modified, either positively or negatively. Although silicon becomes stiffer with pressure, dislocation cores could be more mobile along specific directions. In the specific case of silicon, both the stability of the shuffle core structure A is enhanced and the dislocation displacement in shuffle planes is made easier. This is in agreement with experimental results, which suggest that dislocations are located in shuffle planes.

3.2.4. Nucleation of non-dissociated dislocations

In Section 2.2.1 we showed that in the low temperature, high-stress regime, non-dissociated dislocations were located in the neighborhood of micro-crack surface edges. Defects on these surfaces (steps, ledges) likely act as dislocation sources. Furthermore, dislocation nucleation in silicon deserves a study since there are no preexisting dislocations in virgin crystals and the nucleation and multiplication stages are the signature of macroscopic plasticity.

Compared to investigations of stability and mobility of dislocations, many fewer efforts have been devoted to nucleation. One reason is the extreme difficulty to study experimentally the onset of plasticity, essentially because of the short timescale. Nevertheless, theoretical approaches can allow one to obtain complementary information in that case. From numerical simulations focused on metals, the following conclusions were obtained [112]: (i) the formation of a dislocation from a perfect surface is very unlikely, due to a high-energy barrier and (ii) the presence of a simple defect like a step largely reduces this energy barrier by localizing stresses. Several parameters are expected to have an influence on the

nucleation mechanism, such as the structure of the surface defect (step structure, height), stress orientation, and temperature.

Regarding silicon, investigations of the possible dislocation formation from a surface step were performed by Godet et al. [96,97], from many interatomic potentials and first-principles calculations. Fig. 30 shows how a perfect 60° dislocation is nucleated from a surface step and glides in the shuffle plane passing through the step when the system is uniaxially strained by 13.6%; the stress direction is contained in the surface, at an angle of 22.5° with the step normal. The core of the dislocation is in the S_1 configuration (middle structure in Fig. 22), in agreement with the fact that 60° dislocations are supposed to be more mobile than screw dislocations. The influence of several parameters was studied, leading to the following results:

- 60° dislocations were obtained under both tension and compression, always in shuffle planes.
- No screw dislocations were nucleated.
- The latter point can be explained by considering the Schmid factors and the Peierls stresses for the screw and 60° dislocations.
- In contrast to metals, there is no localized shear in planes close to the step before the onset of plasticity.

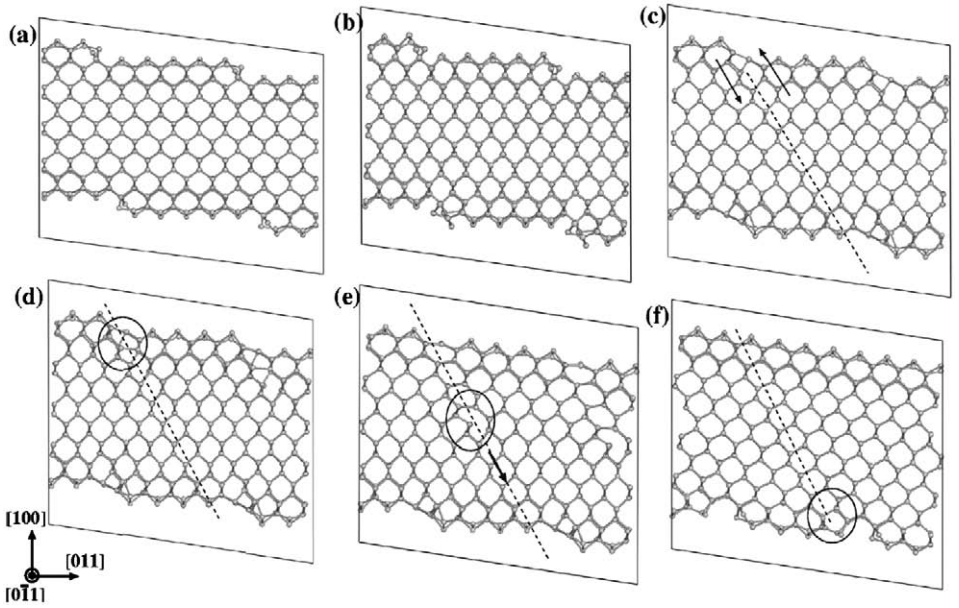

Fig. 30. Successive stages of the formation and propagation of a 60° dislocation from a strained surface, starting from a surface step. (a) Unstrained, and strains of (b) 10.4%, (c) 11.5%, and (d–f) 13.6%.

- The step geometry plays an important role on the nucleation mechanism. That the passivation of silicon surface with hydrogen prevents dislocation formation.
- Higher steps tend to make dislocation formation easier, with lower critical strains.

In the previous calculations, reduced dimensions do not allow for the 3D formation of a dislocation half-loop. This limitation was overcome by Izumi and Yip [113], who examined the nucleation mechanism of a half-loop dislocation from a sharp corner in silicon. These authors performed classical molecular dynamics simulations in high stress, low temperature conditions, which resulted in the formation and propagation in a shuffle plane of a dislocation half-loop composed of two 60° segments and one screw segment. The dislocation core structures were not described, but it is likely that the screw dislocation is in a B configuration, while a S_1 core is obtained for the 60° dislocation, since the Stillinger–Weber potential is used in this work. Configurations extracted from these simulations were then used for determining minimum energy path (MEP) with the NEB method. More recently, Godet et al. performed molecular dynamics simulations of the three-dimensional formation of a dislocation half-loop from a {1 1 1} ledge, considering different stress orientations and temperatures [114]. In the low temperature range, the outcome, shown in Fig. 31, looks very similar to the results of Izumi and Yip [113]. In fact, a half-loop located in a shuffle plane and including two 60° segments and one screw segment is obtained. The dislocation core structures are in agreement with bulk calculations.

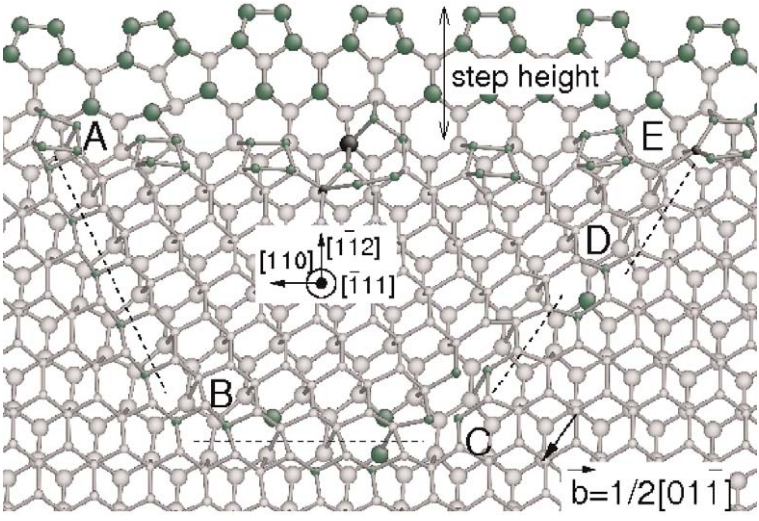

Fig. 31. Dislocation half-loop nucleated from a surface step in silicon at 600 K using the Stillinger–Weber potential. AB and BC are two 60° segments. CD and DE are two screw segments separated by a kink.

In their study, Izumi and Yip [113] indicated that the resolved shear strain for nucleation is 5.1%. In the work by Godet et al. [114], the strain value applied on the system at the onset of plasticity was 13.6%, which corresponds to a resolved shear strain of about 6.2% in the glide plane. The difference between the two values may come from the different geometry of the system, a {1 0 0} sharp corner in one case [113] and a {1 1 1} ledge in the other one [114]. Nevertheless, both values suggest that dislocation nucleation from surfaces requires large stresses, seemingly way too large compared to experimental results. However, two important points have to be considered here. First, the deformation rate in numerical simulations is several orders of magnitude higher than in experiments. It was recently shown that such a difference has a strong effect on critical stresses for dislocation nucleation [115], leading to a reduction by 50% at 300 K. Second, in numerical simulations, the dimensions of the considered systems are at best of several tens of nanometers. At this scale, it was shown experimentally in the case of nanowires and nanopillars that plasticity processes involve stresses substantially larger than in bulk materials.

4. Discussion

Recent experiments reported in Section 2 showed that, in silicon, perfect dislocations control plastic deformation at high stress. Fingerprints of such a regime were also found in some early experimental publications. This evidence motivated theoretical works using atomistic computations, reported in Section 3, in order to sort out core configurations and other properties of such perfect dislocations. The results of these two approaches are compared in this part in order to obtain a comprehensive view of this deformation regime. The transition between this regime and the other one ruled by dissociated dislocations is also discussed, together with the actual location of the dislocation cores.

Results obtained on other semiconductors are finally mentioned for discussing whether a plastic deformation regime controlled by perfect dislocations is a generic property of diamond-cubic semiconductors.

4.1. Summary of experimental and numerical results

4.1.1. Results

What was learnt from both experiments and calculations can be summarized as follows:

1. Non-dissociated dislocations clearly play an important role in the plastic deformation of silicon at low temperature, as shown by many high-stress experiments. This includes deformation experiments under a confinement pressure greater than 1.5 GPa, and scratch and indentation tests. Signatures of such dislocations can also be found during micromachining of silicon surfaces. This regime is definitely different from the high temperature one, where dislocations are dissociated and move under low applied stresses. The stress

required for displacing or nucleating non-dissociated dislocations is estimated to be larger than 1 GPa at room temperature.

2. These non-dissociated dislocations are characterized by $a/2\langle 1\,1\,0\rangle$ Burgers vectors and glide in {1 1 1} planes. Several kinds of dislocations were observed. Typical characters are 30°, 41°, and screw, but short 60° segments were also reported. In one experiment, wavy dislocations, exhibiting an average screw orientation, were found to be constituted of short 41° segments. Very little else is known about the physical signatures of these dislocations, although a few works suggest that these signatures are convoluted with those of point defects.
3. Apparently, partial dislocations obtained by high temperature deformation cannot be transformed into perfect dislocations. Conversely, the transformation of perfect dislocations into dissociated dislocations was observed, but only at a limited rate and in specific regions.
4. There exist several possible stable structures for both the screw and 60° non-dissociated cores, which are located in either glide or shuffle set planes. Glide set configurations seem to have the lowest energies in both cases. No information is available regarding the atomic structure of the 30° and 41° dislocation cores.
5. Regarding mobility, most of the available data concern the non-dissociated screw dislocation. The Peierls stress is known to be 4 and 6 GPa for the shuffle and glide cores, respectively. In the presence of an applied pressure, the mobility of the shuffle screw dislocation is enhanced. From the investigation of kink formation, one expects thermal activation to play a nonnegligible role in the mobility of the shuffle screw dislocation in the high stress, low temperature regime. For the 60° dislocation, the Peierls stress is estimated to be about 1 GPa for the shuffle core, while the undissociated glide core is not glissile.
6. Non-dissociated dislocations can be nucleated from surfaces in the shuffle set under high-stress conditions. The dislocation that is formed the most easily has a 60° orientation. Conversely, at high temperature, partial dislocations are obtained.

Usually, experiments and numerical simulations are rather complementary and it may be difficult to make meaningful comparisons. Nevertheless, there are two cases where this can be done. The first one is related to the mobility of non-dissociated dislocations. The computed Peierls stress for the non-dissociated shuffle screw dislocation is 4 GPa, in good agreement with the order of magnitude of the extrapolation at 0 K of flow stress measurements below 300 °C (Section 2.3.2). In addition, the extrapolation at 0 K of yield stress measurements performed in the medium temperature range fits quite well the computed values of the Peierls stress for glide dislocations. Numerical simulations revealed that the thermally activated motion of non-dissociated screw dislocations was possible at 300 °C under an applied stress of 1.5 GPa, as reported from yield stress measurements (Section 2.3.2). The second case concerns the nucleation of dislocations. Molecular dynamics simulations of the dislocation nucleation from surface steps

suggest that the two types of dislocations, partial or non-dissociated ones, can be generated depending on the applied stress and temperature. This defines two regimes, in agreement with experimental findings.

4.1.2. Current limitations

In spite of numerous studies dedicated to non-dissociated dislocations, there are still many open issues. In fact, there are several limitations to both experiments and numerical simulations, which tend to hinder progress in this domain. Regarding experiments, several limitations are either intrinsic to the techniques or due to the specificity of deformation experiments. First, dislocation observations are performed *postmortem*. Therefore, one may wonder whether the dislocations participating in plastic flow do not experience some modifications before being observed by TEM. In other words, are the dislocations at rest the same as the moving dislocations? *In situ* experiments seem difficult to perform because of complications associated with high-stress requirements. Secondly, although atomic-scale resolution can be achieved by TEM, the determination of the atomic structure of dislocation cores is hardly feasible in silicon using this technique. Finally, non-dissociated dislocations are obtained in a high-stress regime, which usually results in highly damaged samples, containing cracks, point defects, and various micro-structural defects. This makes the analysis all the more difficult.

Numerical simulations suffer from other limitations. Accurate first-principles calculations are very limited in size, as they include usually only a few hundreds of atoms. Given the complexity of dislocation cores and the associated long-range stress fields, first-principles calculations are then restricted to infinite straight dislocations, or to very simple defects along the dislocation lines. Moreover, calculations are essentially static, because computational costs prevent performing dynamical simulations. Another option is the use of classical interatomic potentials, which allow simulating large systems and performing dynamical studies. This provides a way for investigating realistic situations like the thermally activated propagation of curved dislocation segments. However, the reliability of the obtained results is questionable because of the inability of the available potentials for silicon to model reconstructed cores accurately. Tight-binding calculations could be a third viable option, with a good accuracy and a considerable speedup compared to first-principles methods.

4.2. Transition between two regimes: a core structure transformation?

The calculations of Duesbery and Joós [45] fed most of the interpretations about the existence of perfect dislocations at high stress in silicon. This regime can be explained by the fact that perfect shuffle dislocations are the more mobile ones at high stresses. These calculations rely upon dislocation modeling with the Peierls–Nabarro model, using as input gamma surfaces calculated from atomistic computations. Yet, the position of the transition stress is very sensitive to the gamma surface input and to the assumed shape of the kink pairs. Thus, these

calculations cannot be considered as giving reliable transition stress values (P. Carrez, private communication). Furthermore, recent atomistic calculations [116,117] show that a perfect shuffle screw is more mobile than a 30° glide partial in the whole range of stresses. This makes questionable the hypothesis of an intrinsic mechanism responsible for such a transition, unless the mobility of perfect $\langle 1\,1\,2 \rangle$/30° dislocations has to be considered instead that of the screw ones.

Extrinsic factors could also be put forward to explain this transition. Indeed, experimental observations show numerous pinning points on perfect dislocations, whose density increases with temperature. Such pinning points could slow down progressively perfect dislocations to the benefit of partial dislocations.

A point to be clarified is whether the nucleation of partial glide dislocations is assisted when perfect shuffle dislocations preexist. Then, one would have to consider possible mechanisms for core transformation.

The core of PS and DG dislocations can be transformed from one to the other through several elementary mechanisms. The two basic mechanisms that allow dislocations moving over one atomic distance to switch from one set to the other are cross slip and climb (Fig. 32). Some mechanisms that can be involved in such transformations are similar to those proposed in the frame of composite models of dislocation core structures, in which a dissociated dislocation can "move" from glide set to shuffle set in its dissociated form (see, e.g., [1]). However, in composite models, the transformation mechanisms are relevant to the movement of partial dislocations from glide to shuffle positions and a constriction of the parent dislocations is not required. In the present case, the transformation mechanism concerns the change from perfect to dissociated dislocations (as well as the reverse transformation), and a different mechanism can also be involved, namely cross slip [57].

Mechanisms involving the nucleation of fresh dislocations in the stress field of dislocations of another type can also be considered but will not be discussed here.

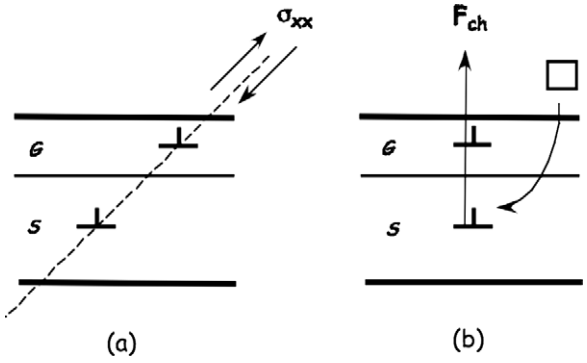

Fig. 32. Transformation from a perfect shuffle dislocation into a dissociated glide dislocation. The perfect dislocation has moved by one interplanar spacing into the glide set by: (a) stress-assisted (shear stress σ_{jj}) cross slip and (b) climb under the action of a chemical force (F_{ch}). After Rabier [86].

Cross slip is a conservative mechanism that occurs under stress with the help of thermal activation. Climb requires point defect annihilations at the dislocation cores and can also be stress-assisted, but to a lesser extent. This indicates that cross slip can be operative at lower temperatures than climb, and points at the core structure of perfect screw dislocations as an important factor determining the stability of perfect shuffle dislocations.

Cross slip is initiated when a critical part of the parent dislocation deviates in the cross slip plane. If the parent dislocation is a perfect one, this can be achieved through local stress concentrations. In the case of a dissociated dislocation, a local constriction of the stacking-fault ribbon is required in a first step to allow for a deviation. Thus, cross slip may be easier from PS to DG than from DG to PS.

Dislocation climb proceeds by point defect absorption or emission at jogs. In the same way, climb mechanisms, which allow transforming a DG into a PS, are less efficient in the presence of a stacking fault. However, point defect absorption can take place either on a preexisting constriction or on one of the glide partials, transforming it into a partial located in the shuffle plane. In this last case, this can help forming a constriction. As compared to previous mechanisms, the transformation PS–DG is trivial: a PS segment climbs over one atomic distance into the glide set; it can then dissociate and form a DG segment.

Thus, mechanisms allowing the transformation from dissociated glide dislocations to perfect shuffle ones are possibly more difficult than the reverse ones. The results of atomistic computations reported in Section 3.2.2 show that it is impossible to move a perfect shuffle dislocation out of its glide plane under the action of a shear stress. Hence, cross slip cannot be considered as a viable mechanism to move a screw dislocation from the shuffle set to the glide set. A climb mechanism is then expected for such a transformation, but it requires a sufficient point defect mobility and concentration.

What was described above about core transformations is relevant to a change of the location of a perfect dislocation core from the shuffle set to the glide set. Another subsequent limiting factor in obtaining a dissociated dislocation in the glide set could be the dissociation process itself. Indeed, starting from a perfect dislocation in the glide set, the incipient partial dislocations are submitted to a Peierls stress in the dissociation (slip) plane. This Peierls stress can be so large as to prevent any gain in elastic energy during the splitting process, unless thermal activation assists the motion of the partial dislocations. Takeuchi [118,119] calculated that a Peierls stress on partial dislocations of the order of 0.02μ to 0.04μ, which is realistic in the case of silicon, could prevent dissociation in the absence of thermal activation.

Following the conclusions of Takeuchi, one may ask whether the transition from a perfect to a dissociated core in silicon could be relevant to the dissociation of a perfect dislocation located in the glide set, which dissociates as soon as temperature and stress allow for the partial dislocations to move. This hypothesis can be ruled out, however, on the basis of the atomistic calculations on dislocation nucleation (Section 3.2.4), where dislocations were found to be nucleated as perfect ones in the shuffle set at high stress and in a dissociated form in the glide set at high temperature.

Are they two different and independent deformation microstructures depending on the thermomechanical conditions? Experimentally, no massive transformation was evidenced from preexisting perfect dislocations to dissociated ones. The interpretations proposed by Rabier and Demenet [69] and Saka et al. [76] seem to be very different, that is, there is no transformation but nucleation of dissociated dislocations, apparently with no relation to preexisting perfect defects [69], or there is a core transformation [76]. The two experiments were performed in very different conditions, but a common interpretation could be that a small critical nucleus of transformed core can provide a source for a new dislocation population [86], leaving unaffected most of the parent dislocation microstructure.

4.3. Are non-dissociated dislocations in the glide or the shuffle set?

Since the pioneering works of Shockley [9] and Hornstra [10], it was always assumed that non-dissociated dislocations would have a shuffle core. In fact, it appeared easier (and less energetically expensive) to break a single bond to form a shuffle core than to break three bonds to form a glide core. However, we know that the covalent nature of silicon bonding tends to favor reconstruction, as is the case for partial dislocation cores. Thus, one may wonder whether the early assumption is still valid in the view of recent results. Considering experimental observations first, it is extremely difficult to reach certainty on this matter although, in principle, it could be possible to perform direct observations of dislocation cores at the atomic-scale level, using for instance corrected HREM.

Numerical simulations should be more appropriate for determining the core structures. All calculations suggest that for screw and 60° orientations, the most stable dislocation cores exhibit a glide character. However, considering first the screw dislocation, the Peierls stress of the reconstructed glide core is 50% larger than that of the shuffle core. Also, due to reconstruction, the kink migration energy is likely to be higher for the glide core than for the shuffle one. Therefore, the glide screw dislocation is expected to be less mobile than the shuffle core, and one may wonder whether the most stable dislocation cores are those that really matter for plastic deformation. This issue is even more critical in the case of the 60° dislocation. The glide core appears to be much more stable than the shuffle core, but it is sessile with a very high Peierls stress. Atomistic simulations also raise another point. The denominations shuffle or glide are related to the type of {1 1 1} plane the center of the dislocation core is located in. In the case of a dislocation core with a complex reconstructed structure, or encompassing two adjacent {1 1 1} planes (see, for instance, the core S_3 for the 60° dislocation), it might be difficult to settle the question in terms of shuffle or glide.

4.4. Other semiconductor materials

From the results obtained about perfect dislocations at high stress in silicon, the question arises of whether this feature is specific to silicon or is generic to

semiconductor materials. As far as the ductile to brittle transition is concerned, the macroscopic behavior of most semiconductors is analogous to that of silicon. This transition was experimentally observed and analyzed on several materials such as, for instance, GaAs [120] and SiC [121]. High-stress microstructures were studied in III–V compounds (GaAs, InSb, InP, …) and in group IV materials.

Using a solid confining pressure of 1.2 GPa, it was possible to extend the usual plastic domain of plasticity and to deform GaAs, InP, and InSb down to 77 K [122]. This increase in the investigated plastic range led to the observation of a hump in the stress versus temperature curves. Furthermore, a transition appeared clearly in a plot of the logarithm of the resolved shear stress as a function of the inverse of temperature. The microstructures, which consisted mainly of perfect screw dislocations below the transition temperature, were interpreted as resulting from a glide to shuffle transition. However, no calculations have been done yet in III–V compounds to confirm the occurrence of this transition. Very recently, indentations on InSb were performed both at room and liquid nitrogen temperatures by Kedjar [123] and Kedjar et al. [124]. At room temperature, the microstructure is made up of partial dislocations, while at 77 K it is made up of perfect screw dislocations. However, no segment was found lying along the $\langle 1\,1\,2 \rangle$ or $\langle 1\,2\,3 \rangle$ directions. This is in agreement with results presented in Ref. [122]. The case of III–V compounds appears to be close to that of silicon, but with some differences in the dislocation microstructures at high stress.

Compression tests at constant strain rate were conducted on 6H- and 4H-SiC, two of the most common polytypes of this material; the plot of the logarithm of the resolved shear stress as a function of the inverse of temperature exhibits a transition associated with two well-defined microstructures [125,126]. At high temperature, dislocations are dissociated into leading-trailing pairs of partials, whereas at low temperature only the leading partial with silicon core is observed together with its associated stacking fault. Other observations on 4H-SiC deformed under a confining pressure of 5 GPa at room temperature and 150 °C, using an anisotropic multi-anvil apparatus, show that the microstructure is composed of both widely dissociated dislocations and undissociated perfect dislocations [127]. The very high density of dislocations after deformation prevented making a fine analysis of the microstructure. It would be of interest to perform high-stress experiments on cubic silicon carbide, which is now available in bulk dimensions.

In Ref. [93], the authors examined the various possible configurations of a perfect screw dislocation in group IV materials by means of first-principles calculations. It appears that the stable screw dislocation is located in the shuffle set for Ge and in the glide set for diamond. No experimental observations were reported yet in Ge. Preliminary experiments on diamond deformed under a pressure of 5 GPa in a multi-anvil apparatus show a high density of dislocations without apparent dissociation, but this result has to be confirmed [128]. In addition, in plastically deformed natural type IIa brown diamonds after high pressure, high temperature annealing, Blumenau et al. [129] found that although most 60° dislocations are found to be dissociated, some appear to be undissociated. This is providing evidence of the existence of two types of dislocations cores.

In conclusion, several semiconductors exhibit the same behavior as silicon under very high stress. This could be a general feature for all semiconducting materials, but with specificities for each material depending on the structure and the covalent versus ionicity balance of the bonding.

4.5. Perspectives

Regarding the issue of glide versus shuffle dislocation cores, experiments are needed to determine the exact location of the perfect dislocations and to establish a correlation between their actual core structures and their physical properties. The investigation of the core structure of dislocations has to be performed using corrected HREM. Clearly, the main difficulty arises from the preparation of an adequate specimen with edge-on dislocations, whose core is not affected by kinks, impurities, or any defect that may blur the structure determination. As far as electron microscopy is concerned, *in situ* nanoindentation experiments can be useful provided this technique can be extended down to atomic scale. This is a technical challenge.

Spatially resolved photoluminescence could help understanding the shuffle–glide transition since it was shown that perfect dislocations have different signatures than dissociated glide dislocations. It would be interesting to follow locally the change in signature of dislocations and, in particular, to check whether some transient core structures or premonitory events are associated to the transition.

Currently, there is a lack of EBIC experiments devoted to the electrical properties of dislocations in silicon. Experiments such as scanning transmission electron beam induced current (STEBIC) could be used to reinvestigate these electrical properties, especially those of perfect dislocations.

EPR is a technique that has been widely used in the determination of the structure of dissociated dislocations (see Section 1.3); this technique would be of interest for determining whether dangling bonds are present in the core of a perfect dislocation.

Concerning numerical simulations, atomistic computations of $\langle 1\,1\,2\rangle/30^\circ$ and $\langle 1\,2\,3\rangle/41^\circ$ dislocations are lacking. Understanding why they are controlling the low temperature deformation microstructures is one of the key issues: the determination of their core configurations and of the structure and mobility of kinks on these dislocations is needed. Nucleation of new dislocations in the stress field of perfect dislocations should also be investigated by atomistic computations. This could shed light on the transition between the two modes of deformation in silicon. The influence of the nature and availability of nucleation sites on dislocation nucleation should also be checked.

Finally, some macroscopic properties should be revisited. As an example, the brittle to ductile transition could be investigated in the light of the existence of perfect dislocations. HREM and TEM experiments should be devoted to examine the very first steps of dislocation nucleation at crack tips. Passivation treatments

should also be used on Si samples in the range of high stress in order to check their influence on mechanical properties, as was done in the other deformation regime (see, e.g., [130]). This could provide information on dislocation mobility as well as on the issue of dangling bonds within the core of perfect dislocation. Finally, the transition between perfect and dissociated dislocations could be reinvestigated by determining the influence of stress and temperature.

4.6. Concluding remarks

In 1996, in their paper dedicated to the mobility of dislocations in silicon, Duesbery and Joós [45] stated that: ''Theoretical arguments, without exception, predict that slip should occur on the shuffle planes. With equal unanimity experimental observations indicate that slip does occur on the glide planes.'' However, a review of the scientific literature clearly indicates that perfect dislocations exist at high stress, bringing back consistency to the former theoretical analyses of the 1950s. Following this argument, the perfect dislocations should glide on the shuffle set planes. Although indirect evidence exists to support this hypothesis, the current state of knowledge does not allow one to draw a clear and definite conclusion on this last point. More has to be done to understand the actual core structure of dislocations in silicon, and the transition between high- and low-stress deformation regimes.

References

[1] H. Alexander, in: F.R.N. Nabarro (Ed.), Dislocations in Solids, vol. 7, North-Holland, Amsterdam, 1986, p. 115.
[2] A. George, J. Rabier, Rev. Phys. Appl. 22 (1987) 941.
[3] J. Rabier, A. George, Rev. Phys. Appl. 22 (1987) 1327.
[4] H. Alexander, H. Teichler, Electronic structure and properties of semiconductors, in: P. Haasen, W. Schröter (Eds.), Materials Science and Technology, vol. 4, 1991, p. 249.
[5] T. Figielski, J. Phys. Condens. Matter 14 (2002) 12665.
[6] D.B. Holt, B.G. Yacobi, Extended Defects in Semiconductors, Cambridge University Press, UK, 2007.
[7] C.J. Gallagher, Phys. Rev. 88 (1952) 721.
[8] F. Seitz, Phys. Rev. 88 (1952) 722.
[9] W. Shockley, Phys. Rev. 91 (1953) 228.
[10] J. Hornstra, J. Phys. Chem. Solids 5 (1958) 129.
[11] P. Haasen, A. Seeger, in: W. Schottky (Ed.), Halbleiterprobleme, vol. IV, Vieweg, Wiesbaden, 1958, p. 68.
[12] J.P. Hirth, J. Lothe, Theory of Dislocations, first ed., MacGraw-Hill, New York, 1968; id. Theory of Dislocations, second ed., MacGraw-Hill, New York, 1982.
[13] W.C. Dash, J. Appl. Phys. 27 (1956) 1193; 31 (1960) 2275.
[14] K. Wessel, H. Alexander, Phil. Mag. 35 (1977) 1523.
[15] H. Alexander, J. Phys. Coll. C7 (1974) 173.
[16] S. Amelinckx, in: F.R.N. Nabarro (Ed.), Dislocations in Solids, vol. 2, North-Holland, Amsterdam, 1979, p. 67.
[17] D.J.H. Cockayne, I.L.F. Ray, M.J. Wheelan, Phil. Mag. A 20 (1969) 1265.

[18] I.L.F. Ray, D.J.H. Cockayne, Phil. Mag. 22 (1970) 853.
[19] I.L.F. Ray, D.J.H. Cockayne, Proc. R. Soc. A 325 (1971) 543.
[20] E. Aerts, P. Delavignette, R. Siems, A. Amelinckx, J. Appl. Phys. 33 (1962) 3078.
[21] R. Meingast, H. Alexander, Phys. Stat. Sol. (a) 17 (1973) 229.
[22] G. Packeiser, P. Haasen, Phil. Mag. 35 (1977) 821.
[23] G. Packeiser, Phil. Mag. A 41 (1980) 459.
[24] F. Louchet, J. Thibault-Desseaux, Rev. Phys. Appl. 22 (1987) 207.
[25] H. Alexander, R. Labusch, W. Sander, Solid State Commun. 3 (1965) 357.
[26] E. Weber, H. Alexander, J. Phys. Coll. 40-C6 (1979) 101.
[27] V.A. Grazhulis, Y.A. Osipyan, Sov. Phys. JETP 31 (1970) 677Sov. Phys. JETP 33 (1971) 623.
[28] V.G. Eremenko, E. Yakimov, N. Abrosimov, Phys. Stat. Sol. (c) 4 (2007) 3100.
[29] P.B. Hirsch, J. Phys. Coll. 40-C6 (1979) 27.
[30] R. Jones, J. Phys. Coll. 40-C6 (1979) 33.
[31] J. Bennetto, R.W. Nunes, D. Vanderbilt, Phys. Rev. Lett. 79 (1997) 245.
[32] W. Cai, V.V. Bulatov, J. Chang, J. Li, S. Yip, in: F.R.N. Nabarro, J.P. Hirth (Eds.), Dislocations in Solids, vol. 12, North-Holland, Amsterdam, 2004, p. 1.
[33] V.V. Bulatov, S. Yip, A.S. Argon, Phil. Mag. A 72 (1995) 453.
[34] R. Jones, J. Phys. Coll. 44-C4 (1983) 61.
[35] M. Heggie, R. Jones, Phil. Mag. B 48 (1983) 365.
[36] H.J. Möller, U. Jenrich, in: R. Tressler, R. Bradt (Eds.), Deformation of Ceramic Materials, Plenum Press, New York, 1984, p. 25.
[37] P. Gadaud, J. Woirgard, P. Mazot, J.L. Demenet, J. de Fouquet, J. Phys. Coll. 48-C8 (1987) 101.
[38] B.Ya. Farber, Yu.L. Iunin, V.I. Nikitenko, Phys. Stat. Sol. (a) 97 (1986) 469.
[39] P.B. Hirsch, A. Ourmazd, P. Pirouz, Inst. Phys. Conf. Ser. 60 (1981) 29.
[40] F. Louchet, Phil. Mag. A 43 (1981) 1289.
[41] H. Alexander, J.C.H. Spence, D. Shindo, H. Gottschalk, N. Long, Phil. Mag. A 53 (1986) 627.
[42] H.R. Kolar, J.C.H. Spence, H. Alexander, Phys. Rev. Lett. 77 (1996) 4031.
[43] R. Jones, Phil. Mag. B 42 (1980) 213.
[44] K. Maeda, Y. Yamashita, Phys. Stat. Sol. (a) 138 (1993) 523.
[45] M.S. Duesbery, B. Joós, Phil. Mag. Lett. 74 (1996) 253.
[46] J. Samuels, S.G. Roberts, Proc. R. Soc. Lond. A 421 (1989) 1.
[47] P.B. Hirsch, S.G. Roberts, Phil. Mag. 64 (1991) 55.
[48] B. Moser, K. Wasmer, L. Barbieri, J. Michler, J. Mater. Res. 22 (2007) 1004.
[49] S. Minomura, H.G. Drickamer, J. Phys. Chem. Solids 23 (1962) 451.
[50] I.V. Gridneva, Yu.V. Milman, V.I. Trefilov, Phys. Stat. Sol. (a) 14 (1972) 177.
[51] T. Suzuki, T. Ohmura, Phil. Mag. A 74 (1996) 1073.
[52] V.G. Eremenko, V.I. Nikitenko, Phys. Stat. Sol. (a) 14 (1972) 317.
[53] M.J. Hill, D.J. Rowcliffe, J. Mater. Sci. 9 (1974) 1569.
[54] J. Castaing, P. Veyssière, L.P. Kubin, J. Rabier, Phil. Mag. A 44 (1981) 1407.
[55] J.L. Demenet, Thèse d'Etat, Université de Poitiers, France, 1987.
[56] M. Cagnon, in: Les Editions de Physique (Ed.), Dislocations et Déformation Plastique, Orsay, 1980, p. 55.
[57] J. Rabier, J.L. Demenet, Phys. Stat. Sol. (b) 222 (2000) 63.
[58] J. Rabier, P. Veyssière, J.L. Demenet, J. Phys. Coll. 44-C4 (1983) 243.
[59] P. Cordier, D. Rubie, Mater. Sci. Eng. A 309–310 (2001) 38.
[60] J. Rabier, P. Cordier, J.L. Demenet, H. Garem, Mater. Sci. Eng. A 309–310 (2001) 74.
[61] J. Rabier, P. Cordier, T. Tondellier, J.L. Demenet, H. Garem, J. Phys. Condens. Matter 12 (2000) 10059.
[62] J. Rabier, M.F. Denanot, J.L. Demenet, P. Cordier, Mater. Sci. Eng. A 387–389 (2004) 124–128.
[63] A. George, G. Champier, Phys. Stat. Sol. (a) 53 (1979) 529.
[64] B. Pichaud, P. Jean, F. Minari, Phil. Mag. A 54 (1986) 479.
[65] J. Rabier, J.L. Demenet, M.F. Denanot, X. Milhet, Mater. Sci. Eng. A 400–401 (2005) 97.
[66] K. Asaoka, T. Umeda, S. Arai, H. Saka, Mater. Sci. Eng. A 400–401 (2005) 93.

[67] G. de Wit, J.S. Koelher, Phys. Rev. 116 (1959) 1113.
[68] H. Gottschalk, J. Phys. Coll. 44-C4 (1983) 69.
[69] J. Rabier, J.L. Demenet, Phys. Stat. Sol. (a) 202 (2005) 944.
[70] J.L. Demenet, J. Rabier, H. Garem, Inst. Phys. Conf. Ser. 87 (1987) 355.
[71] J. Rabier, P.O. Renault, D. Eyidi, J.L. Demenet, J. Chen, H. Couvy, L. Wang, Phys. Stat. Sol. (c) 4 (2007) 3110.
[72] Y. Wang, W.B. Durham, I.C. Getting, D.J. Weidner, Rev. Sci. Instrum. 74 (2003) 3002.
[73] M. Omri, Thèse, INPL, Nancy, France, 1981.
[74] I. Zarudi, L.C. Zhang, J. Mater. Process. Technol. 84 (1998) 149; Int. J. Mech. Sci. 43 (2001) 1985.
[75] S. Johansson, J.Å. Schweitz, K. Peter, O. Lagerlöf, J. Am. Ceram. Soc. 72 (1989) 1136.
[76] H. Saka, K. Yamamoto, S. Arai, K. Kuroda, Phil. Mag. 86 (2006) 4841.
[77] J. Rabier, J.L. Demenet, Scr. Mater. 45 (2001) 1259.
[78] A. Oueldennaoua, R. Allem, A. George, J.P. Michel, Phil. Mag. A 57 (1988) 51.
[79] P. Grosbras, J.L. Demenet, H. Garem, J.C. Desoyer, Phys. Stat. Sol. (a) 84 (1984) 481.
[80] H.S. Leipner, Z. Wang, H. Gu, V.V. Mikhnovich Jr., V. Bondarenko, R. Krause-Rehberg, J.L. Demenet, J. Rabier, Phys. Stat. Sol. (a) 201 (2004) 2021.
[81] S. Pizzini, S. Binetti, A. Le Donne, A. Marzegalli, J. Rabier, Appl. Phys. Lett. 88 (2006) 211910.
[82] N.A. Drozdov, A.A. Patrin, V.D. Tkachev, Pis'ma Zh. Eksp. Teor. Fiz. 23 (1976) 651; Sov. Phys. JETP Lett. 23 (1976) 597.
[83] E.A. Steinman, A.N. Tereshchenko, J. Rabier, Proc. 23rd Int. Conf. ''The Physics of Extreme State of Matter'', Elbrus, Kabardino-Balkaria, Russia, 2008.
[84] P.D. Nellist, M.F. Chisholm, N. Dellby, O.L. Krivanek, M.F. Murfitt, Z.S. Szilagyi, A.R. Lupini, A. Borisevich, W.H. Sides Jr., S.J. Pennycook, Science 305 (2004) 1741.
[85] L. Pizzagalli, P. Beauchamp, H. Jónsson, Phil. Mag. 88 (2008) 91.
[86] J. Rabier, Phys. Stat. Sol. (a) 204 (2007) 2248.
[87] K.C. Pandey, Phys. Rev. Lett. 47 (1981) 1913.
[88] G. Csànyi, T. Albaret, M.C. Payne, A. De Vita, Phys. Rev. Lett. 93 (2004) 175503.
[89] T.A. Arias, J.D. Joannopoulos, Phys. Rev. Lett. 73 (1994) 680.
[90] L. Pizzagalli, P. Beauchamp, J. Rabier, Phil. Mag. A 83 (2003) 1191.
[91] C. Wang, J. Li, K. Ho, S. Yip, Appl. Phys. Lett. 89 (2006) 051910.
[92] H. Koizumi, Y. Kamimura, T. Suzuki, Phil. Mag. A 80 (2000) 609.
[93] L. Pizzagalli, P. Beauchamp, J. Rabier, Europhys. Lett. 72 (2005) 410.
[94] L. Pizzagalli, J.L. Demenet, J. Rabier, Phys. Rev. B 79 (2009) 045203.
[95] C. Li, Q. Meng, G. Li, L. Yang, Superlatt. Microstruc. 40 (2006) 113.
[96] J. Godet, L. Pizzagalli, S. Brochard, P. Beauchamp, Phys. Rev. B 70 (2004) 054109.
[97] J. Godet, S. Brochard, L. Pizzagalli, P. Beauchamp, J.M. Soler, Phys. Rev. B 73 (2006) 092105.
[98] B. Joós, Q. Ren, M.S. Duesbery, Phys. Rev. B 50 (1994) 5890.
[99] Q. Ren, B. Joós, M.S. Duesbery, Phys. Rev. B 52 (1995) 13223.
[100] L. Pizzagalli, P. Beauchamp, Phil. Mag. Lett. 84 (2004) 729.
[101] T. Suzuki, S. Takeuchi, in: S. Takeuchi, T. Suzuki (Eds.), Lattice Defects in Ceramics, Publication Office of Jpn. J. Appl. Phys., Tokyo, 1989, p. 9.
[102] H. Koizumi, H.O.K. Kirchner, T. Suzuki, Phil. Mag. 86 (2006) 3835.
[103] H. Jónsson, G. Mills, K.W. Jacobsen, in: B.J. Berne, G. Ciccotti, D.F. Coker (Eds.), Classical and Quantum Dynamics in Condensed Phases Simulations, vol. 16, World Scientific, Singapore, 1998, p. 385.
[104] M. Miyata, T. Fujiwara, Phys. Rev. B 63 (2001) 045206.
[105] H. Koizumi, T. Suzuki, Mater. Sci. Eng. A 400–401 (2005) 76.
[106] L. Pizzagalli, A. Pedersen, A. Arnaldsson, H. Jónsson, P. Beauchamp, Phys. Rev. B 77 (2008) 064106.
[107] A. Pedersen, L. Pizzagalli, H. Jónsson, J. Phys. Condens. Matter 21 (2009) 084210.
[108] G. Henkelman, H. Jónsson, J. Chem. Phys. 111 (1999) 7010.
[109] J. Durinck, A. Legris, P. Cordier, Phys. Chem. Miner. 32 (2005) 646.
[110] L. Yang, P. Söderlind, J. Moriarty, Mater. Sci. Eng. A 309–310 (2001) 102.
[111] Y. Umeno, M. Černý, Phys. Rev. B 77 (2008) 100101(R).

[112] S. Brochard, P. Beauchamp, J. Grilhé, Phys. Rev. B 61 (2000) 8707.
[113] S. Izumi, S. Yip, J. Appl. Phys. 104 (2008) 033513.
[114] J. Godet, S. Brochard, L. Pizzagalli, J. Appl. Phys. 105 (2009) 026104.
[115] T. Zhu, J. Li, A. Samanta, A. Leach, K. Gall, Phys. Rev. Lett. 100 (2008) 025502.
[116] W. Cai, Ph.D. thesis, Massachusetts Institute of Technology, USA, 2001.
[117] L. Pizzagalli, P. Beauchamp, Phil. Mag. Lett. 88 (2008) 421.
[118] S. Takeuchi, J. Alloys Comp. 378 (2004) 61.
[119] S. Takeuchi, Mater. Sci. Eng. A 400–401 (2005) 84.
[120] S. Wang, P. Pirouz, Acta Mater. 55 (2007) 5515.
[121] M. Zhang, H.M. Hobgood, J.L. Demenet, P. Pirouz, J. Mater. Res. 18 (2003) 1087.
[122] T. Suzuki, T. Yasutomi, T. Tokuoka, I. Yonenaga, Phil. Mag. A 79 (1999) 2637.
[123] B. Kedjar, Thesis, University of Poitiers, France, 2007.
[124] B. Kedjar, L. Thilly, J.L. Demenet, J. Rabier, Mater. Res. Soc. Proc. 1026-C11 (2008) 1.
[125] A.V. Samant, P. Pirouz, Int. J. Refractory Metals Hard Mater. 16 (1998) 277.
[126] J.L. Demenet, M.H. Hong, P. Pirouz, Scr. Mater. 43 (2000) 865.
[127] J.L. Demenet, X. Milhet, J. Rabier, P. Cordier, Mater. Sci. Forum 457–460 (2004) 343.
[128] J. Rabier et al., unpublished data.
[129] A.T. Blumenau, R. Jones, T. Frauenheim, B. Willems, O.I. Lebedev, G. Van Tendeloo, Phys. Rev. B 68 (2003) 014115.
[130] Y. Yamashita, F. Jyobe, Y. Kamiura, K. Maeda, Phys. Stat. Sol. (a) 71 (1999) 27.

CHAPTER 94

Metadislocations

M. FEUERBACHER AND M. HEGGEN

Institut für Mikrostrukturforschung, Forschungszentrum Jülich GmbH, D-52425 Jülich, Germany

1572-4859, DOI: 10.1016/S1572-4859(09)01603-9

Dislocations in Solids
Edited by J. P. Hirth and L. Kubin

Contents

1. Introduction 111
2. Complex metallic alloys 113
   2.1. Structural features 113
      2.1.1. Lattice parameters 113
      2.1.2. Cluster substructure 114
      2.1.3. Disorder 115
      2.1.4. Degree of complexity 116
   2.2. Example: the structure of ε_6-Al–Pd–Mn and the ε-phase family 116
   2.3. Tiling description 118
3. Phason lines and phason planes 121
   3.1. Phason lines 121
      3.1.1. Atomic decoration of a phason line 122
      3.1.2. Movement of a phason line 123
      3.1.3. Kinks in phason lines 125
   3.2. Phason planes 126
      3.2.1. Phason-plane strain field 128
      3.2.2. Related phases and phase transitions in terms of phason planes 129
4. Metadislocations 130
   4.1. History and basic features 130
   4.2. Tiling description 133
   4.3. Burgers vector 135
   4.4. Metadislocation series 136
   4.5. Construction principles 139
      4.5.1. Hexagon column arrangement 139
      4.5.2. Construction via a modified Volterra process 140
      4.5.3. Hyperspace projection 142
5. Further aspects 143
   5.1. Metadislocations as carriers of plastic deformation 143
      5.1.1. Metadislocation loops 143
      5.1.2. Mode of metadislocation motion 145
   5.2. Elastic energy 147
   5.3. Metadislocation reactions 149
   5.4. Metadislocation-based phase boundaries 151
6. Metadislocations in different crystal structures 154
   6.1. Metadislocations in ξ- and monoclinic ε-phases 154
   6.2. Metadislocations in Taylor phases 158
   6.3. Metadislocations in orthorhombic $Al_{13}M_4$ phases 161
   6.4. Comparison of different types of metadislocations 163

Acknowledgments 167

Appendix. Arithmetics of the golden mean τ 167

References 168

1. Introduction

The micrograph shown in Fig. 1(a) was taken in 1998 in the framework of a transmission electron microscopy (TEM) study on the ε_{28}-phase in the system Al–Pd–Mn [1]. The ε_{28}-phase has very large lattice parameters and contains about 1500 atoms in its unit cell. According to the high degree of complexity of the structure, the material is referred to as a complex metallic alloy (CMA).

In the micrograph, a structural defect is seen, which has a remarkable similarity to an edge dislocation in a conventional simple structure. Fig. 1(b), as a typical example, shows a high-resolution TEM micrograph of an edge dislocation in $BaTiO_3$ [2], imaged in end-on orientation. The dislocation core is in the center of the micrograph (arrow) and terminates an inserted halfplane, which extends to the right-hand side. Around the core, the lattice planes are bent on a nanometer scale due to the presence of the dislocation strain field. The defect in the CMA [Fig. 1(a)] shows noticeable similarities, but there are also clear differences. The most obvious one is in the length scale. The lateral extension of the defect in the CMA is larger by about one order of magnitude, and correspondingly a high number of atoms per unit layer, of the order of 10^3, is involved in the defect structure. Also, there are six planar structural features, which apparently terminate at the core (arrow) of the defect.

Defects as shown in Fig. 1(a) are the subject of the present chapter. They are referred to as metadislocations, and occur in numerous structurally complex metallic materials. The concept of metadislocations addresses a central problem in the plasticity of materials with large lattice parameters: In these materials, conventional dislocation-based deformation mechanisms are prone to failure. This is a direct consequence of the elastic strain energy, which, per unit length of dislocation, is given by

$$E_{\mathrm{el}} = \frac{\mu b^2}{4\pi} f \ln\left(\frac{R}{r_0}\right), \tag{1}$$

where b is the length of the dislocation Burgers vector and μ the shear modulus [3]. R and r_0 are the outer and inner cutoff radii for the integration of the strain field, and f is a geometrical factor of the order of unity, which depends on the character of the dislocation. In a typical crystal, $R/r_0 \approx 10^4$ and hence $\ln(R/r_0) \approx 9.2$, so that the energy is approximately μb^2 per unit length [4]. As a result of the proportionality of elastic energy and the square of the Burgers vector length, dislocations with large Burgers vectors are generally energetically unfavorable. Accordingly, in structures with lattice parameters exceeding, say 1.0 nm perfect dislocations are unlikely to form.

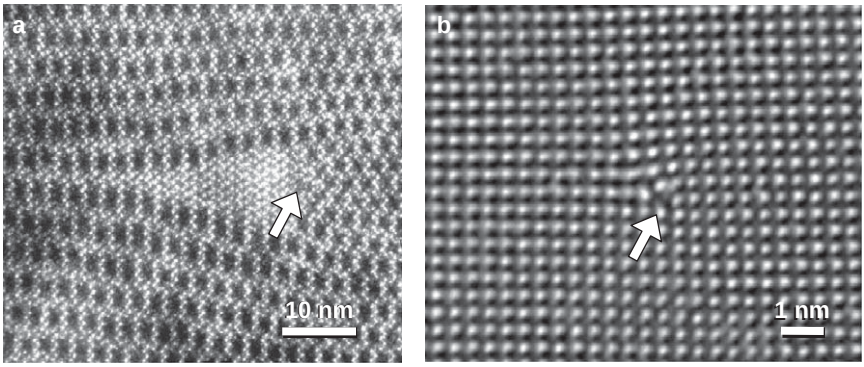

Fig. 1. High-resolution transmission electron micrographs. (a) A metadislocation in the complex metallic alloy (CMA) phase ε_{28}-Al–Pd–Mn [1] and (b) an edge dislocation in $BaTiO_3$ [2] (courtesy of C.L. Jia), both imaged in end-on orientation. The arrows indicate the dislocation cores.

In 1950, Frank [5] approached the problem of dislocations in large-unit-cell structures by introducing the concept of hollow dislocations. He demonstrated that for a dislocation of large Burgers vector, there exists an equilibrium state in which the dislocation core is an empty tube. The idea is that the heavily strained region of matter around the dislocation core is removed, which requires the introduction of internal surfaces. In particular situations outlined by Frank [5], the internal surfaces are energetically less costly than the strained volume and hence the total energy of the system is reduced. Hollow dislocations, with Burgers vector length of 1.5 nm and larger, were experimentally observed in a number of materials, for example in carborundum [5] and SiC [6].

Another system in which perfect dislocations with large Burgers vectors are found are C_{60} crystals. C_{60} crystallizes in a fcc structure with 1.41 nm lattice constant, and perfect dislocations with Burgers vector length of about 1.0 nm were experimentally observed [7]. The structure of these crystals, however, can be understood as a face-centered assembly of C_{60} molecules, that is an upscaled one-to-one replacement of fcc-arranged atoms by C_{60} molecules, connected by van der Waals forces. In these crystals, internal surfaces are of low energy and the shear modulus is very small. Accordingly, in this particular case, the formation of large Burgers vectors is not surprising. This concept, as well as that of hollow dislocations, does not apply to metallic materials with large lattice parameters.

In recent years, CMAs emerged as a novel field in materials science [8]. These materials are intermetallic phases, which possess a highly complex atomic structure. The most prominent feature of CMA phases is that they have large lattice parameters, typically ranging from one up to tens of nanometers. With the advent of this research field, new interest in defects and plasticity of large lattice parameter materials emerged. Indeed, deformation processes involving novel mechanisms and defect types were discovered in CMAs.

Metadislocations, the subject of the present chapter, are among the conceptually most stunning types of defect discovered in CMAs. Their construction is closely

related to the so-called phason defects, which, after a brief recall of the characteristic structural features of CMA materials in Section 2, is introduced in Section 3. The concept of metadislocations is introduced in Section 4. We describe the essential features from the example of a ''basic'' metadislocation, the metadislocation with six associated phason halfplanes in the ''basic'' ε_6-phase, and then proceed to other types that are based on the same concept. In Section 5, we address the question of how metadislocations are involved in plastic deformation mechanisms and finally, in Section 6, we briefly discuss metadislocation types in other crystal structures and generalize their construction principle.

2. Complex metallic alloys

2.1. Structural features

The atomic structure of most CMAs is characterized by the following features, which can be taken as a working definition for this class of materials:

- The lattice parameters are large, exceeding, say, 1.0 nm. Correspondingly, the unit cells are of large volume (frequently referred to as ''giant unit cells'') and contain many tens up to several thousands of atoms.
- The atoms are locally arranged in a cluster substructure, in which icosahedral coordination plays a prominent role.
- A substantial amount of disorder is present in the ideal structure, that is, the structure contains *inherent disorder*.

These criteria are mutually dependent.

2.1.1. Lattice parameters

In metallic systems, the icosahedral atom arrangement due to the high packing density is favorable (see below) but locally involves fivefold rotational axes, which are not compatible with translational periodicity [9,10]. Hence, this type of local order is unfavorable to form in structures with small unit cells, when the lattice parameters are close to or smaller than the diameter of the icosahedral coordination shells. Argued the other way round, if for a given composition of metallic elements the formation of icosahedral clusters is particularly favorable (regarding the atomic radii, the number ratios of atomic species, etc.), long-range order will preferably organize in the form of a structure with large lattice parameters. Indeed, if modulated structures are excluded, the vast majority of phases in metallic systems with large lattice parameters possess an icosahedral-symmetric cluster substructure. In very particular cases, that is, in suitable alloy systems and within limited compositional ranges, the lattice parameters may approach macroscopic dimensions and the translational symmetry is replaced by a scaling symmetry. Such structures, referred to as quasicrystals [11], can hence be formally regarded as special cases of CMAs with infinitely large lattice constants.

2.1.2. Cluster substructure

The tendency to form a cluster substructure is due to a fundamental structural principle for metals and alloys: Generally each atom wants to surround itself by as many neighbors as possible at a maximum packing density. This requirement can be satisfied by atom coordination according to polyhedra of the icosahedral group [12]. These polyhedra include fivefold rotational axes, which are arranged on a periodic lattice with only slight deformation. Icosahedral arrangements of 12 spheres around a central one provide a ''closer packing than closest packing'' [13], that is, closer packing than is possible with spheres of the same size. In the icosahedral configuration, a central atom can be surrounded by 12 atoms of slightly larger diameter (up to 10%) still making contact with it. According to Samson [14], the complexity of the structure probably arises from the difficulty of fitting polyhedra with fivefold axes into a periodic crystal.

In CMAs, the majority of atom coordinations are icosahedrally symmetric. Frequently, one finds a decoration of certain atomic positions with concentric shells of icosahedral polyhedra around a central position. These arrangements are referred to as *cluster substructure* or *clusters* in short. Three types of cluster substructure, based on Bergman, Mackay, and Friauf polyhedra, are found particularly often in CMAs and can be used for a classification of the latter [15].

The Bergman cluster is an icosahedral symmetric arrangement of 116 atoms on 5 concentric shells around one central position. It was firstly identified by Bergman, Waugh, and Pauling [16] in the cubic phase $Mg_{32}(Zn,Al)_{49}$, which has a lattice constant of 1.416 nm and a unit cell comprising 162 atoms. In the Bergman cluster, a central atom is surrounded by an icosahedron of 12 slightly larger atoms. This group of 13 atoms is surrounded by 20 atoms on the corners of a pentagonal dodecahedron. The next 12 atoms lie on the corners of an icosahedron, which is surrounded by a 60-atom shell. The corresponding polyhedron is frequently referred to as a ''soccer ball,'' a truncated icosahedron, which has 20 hexagonal and 12 pentagonal faces. Twelve additional atoms, located out of 12 of the 20 hexagonal faces complete the Bergman cluster.

In the Mackay cluster [17], a central position is surrounded by three concentric shells, an icosahedron, an icosidodecahedron and another, larger icosahedron. These define $12 + 30 + 12 = 54$ atom positions. The Mackay cluster is a basic structural element, for instance of the cubic α-Al–Mn–Si [18]. Clusters referred to as Mackay-type are closely related to Mackay clusters, but may show slight deformation or differing site occupation, in particular of the inner shell, which is frequently not fully occupied due to steric constraints. The ε-phases, which will be discussed extensively below (Section 2.2), are based on Mackay-type clusters.

The Friauf polyhedron consists of a truncated tetrahedron, which has four triangular and four hexagonal faces, around a central position. The next shell is a regular tetrahedron with atom positions out of the hexagonal faces such that the outer shell has 28 triangular faces and 16 corners [12]. Friauf polyhedra are prominent structural elements in the cubic β-Al_3Mg_2 phase, which has a lattice constant of 2.82 nm and 1168 atoms per unit cell [14]. In this structure, the central position is occupied by a Mn atom, the truncated tetrahedron is occupied by 12 Al

atoms and the regular tetrahedron by Mg. Five Friauf polyhedra sharing hexagonal faces can form a larger 47-atom cluster, referred to as the VF-polyhedron [19].

Due to the presence of icosahedral clusters the irrational number of the golden mean plays an important role in CMAs. It is given by $\tau = 1/2(\sqrt{5}+1)$, which numerically amounts to about 1.6180 … (see Appendix). Icosahedral coordination is closely related to the golden mean since the latter is equal to the ratio of next-neighbor and second-next-neighbor distances in a regular pentagon. Also, it can be expressed as $\tau = 2 \cdot \cos(\pi/5)$, which involves the angle of 36°, a prominent angle in pentagonal and icosahedral arrangements.[1]

2.1.3. Disorder

The presence of inherent disorder in CMA structures is closely related to the presence of a cluster substructure. Configurational disorder results from statistically altering orientations of a particular subcluster inside a given cage of atoms. A prominent example is c_2-Al–Pd–Fe [20]. Primary structural building blocks of this structure are edge-sharing icosahedral cages filled by two different cluster motifs. These occur in five different orientations, such that the *average* structure of the different cube arrangements forms a regular dodecahedron.

Chemical or substitutional disorder results from fractional occupancy of certain lattice sites by different elements of similar metallic radius. This causes a variable amount of these elements in the structure and extends the stability range of the corresponding phase in the phase diagram. In $Mg_{32}(Al,Zn)_{49}$, for example, three atom sites can be occupied by either Al or Zn atoms, leading to an extension of the stability range in the Al–Mg–Zn system over a wide spread of values at almost constant Mg content.

Displacement disorder and fractional site occupation arise from steric constraints. High amounts of these types of disorder occur for example in β-Al_3Mg_2 from incompatibilities in the packing of Friauf polyhedra. Split occupation is also caused by geometrical hindrances. In this case, two lattice sites are too close to be occupied simultaneously. Locally, only one site can be occupied, while the other remains empty, which in the average structure corresponds to an occupation factor of 0.5 for both sites.

The presence of disorder can lead to a significant increase of the energetically favored icosahedral coordinated sites. In β-Al_3Mg_2, for example, the disorder is the result of the tendency to maximize the number of icosahedral coordination shells that is compatible with the coordination requirements of the Mg atoms. Introducing disorder by splitting certain Al and Mg sites into such of partial Al/Mg occupancy leads to a gain of 48 icosahedra per unit cell (corresponding to an increase of almost 8%) [14].

[1] At this point, let us make a comment on the phase β-Al–Mg. The exact stoichiometry of this phase is not Al_3Mg_2, as it is commonly referred to. A close look at the phase diagram shows that the composition at the congruent melting point is $Al_{61.5}Mg_{38.5}$, which closely corresponds to the result of the structure model, $Al_{720}Mg_{448}$ [12]. The number ratio between Al and Mg atoms hence amounts to 1.61, and is therefore much closer to the golden mean than to 3/2.

2.1.4. Degree of complexity

The most straightforward means to specify the degree of complexity of a given structure is through the number of atoms in the unit cell. In these terms, the complexity range of CMA phases spreads over several orders of magnitude. The lower limit (which is not rigidly defined) is marked by structures such as cubic $AlTM_{12}$ (TM = Mo, W, Mn, Tc, Re), which have a lattice constant of 0.75 nm and 26 atoms per unit cell, or hexagonal ϕ-$Al_{10}Mn_3$ (lattice constants $a = 0.75$ nm and $c = 0.79$ nm, 28 atoms per unit cell) based on interpenetrating Mackay clusters in different orientations. Among the most complex structures known to date are the cubic β-Al_3Mg_2 phase, which has a lattice constant of 2.82 nm and 1168 atoms per unit cell [14], and ε_{28}-Al–Pd–Mn (*C2mm*, lattice constants $a = 2.389$ nm, $b = 1.656$ nm and $c = 5.80$ nm [21], about 1480 atoms per unit cell).

As seen from the examples given in this section, a wealth of CMA phases exists in Al-based systems. In Al-TM systems (TM = Fe, Mn, Co, Ir, Os, Rh, Re, …) as well as in some Ti-based systems, there are many CMAs with a local structure based on Mackay and Bergman clusters. Various types of CMAs were also found in Zn/Mg-based and Ti-based systems [15].

2.2. Example: the structure of ε_6-Al–Pd–Mn and the ε-phase family

CMA phases frequently exist in close relationship to other phases of similar structure, close or identical composition, which are based on the same cluster substructure but with different lattice parameters. We refer to such groups of related phases as ''phase families.'' A prominent example is the ε-phase family, which is based on the phase ε_6-Al–Pd–Mn.

The ε_6-phase has a composition around $Al_{74}Pd_{22}Mn_4$ and is a ternary extension of the binary phase Al_3Pd. The structure of the latter was firstly solved by Taylor [22], refined by Hiraga [23] and a modified structure model for ε_6-Al–Pd–Mn, which will be discussed in the following, was presented by Boudard et al. [24]. ε_6-Al–Pd–Mn has an orthorhombic structure (space group *Pnma*) and possesses all features typical of a CMA material. The cell parameters are large and amount to $a = 2.389$ nm, $b = 1.656$ nm, $c = 1.256$ nm, and the unit cell contains about 318 atoms. The unit cell is shown in Fig. 2(a) in a perspective view, and in projection along the [0 1 0] and [0 0 1] directions in Figs 2(b) and 2(c), respectively. The phase exhibits a substructure, which is based on Mackay-type clusters (Section 2.1.2). The central position is occupied by a Mn atom and is surrounded by an incomplete Al shell (which in the average structure forms a dodecahedron), an Al icosidodecahedron (30 atoms), and a Pd icosahedron (12 atoms). The cluster, which is frequently referred to as Pseudo-Mackay cluster [25], contains, depending on the occupation of the inner shell, about 52 atoms [Fig. 2(d)].

The structure of ε_6-Al–Pd–Mn can be described by an arrangement of flattened hexagons, on the vertices of which the Mackay-type clusters are arranged (Section 2.3). Adjacent clusters in a layer share three edges. This description comprises about 90% of the atoms in the structure.

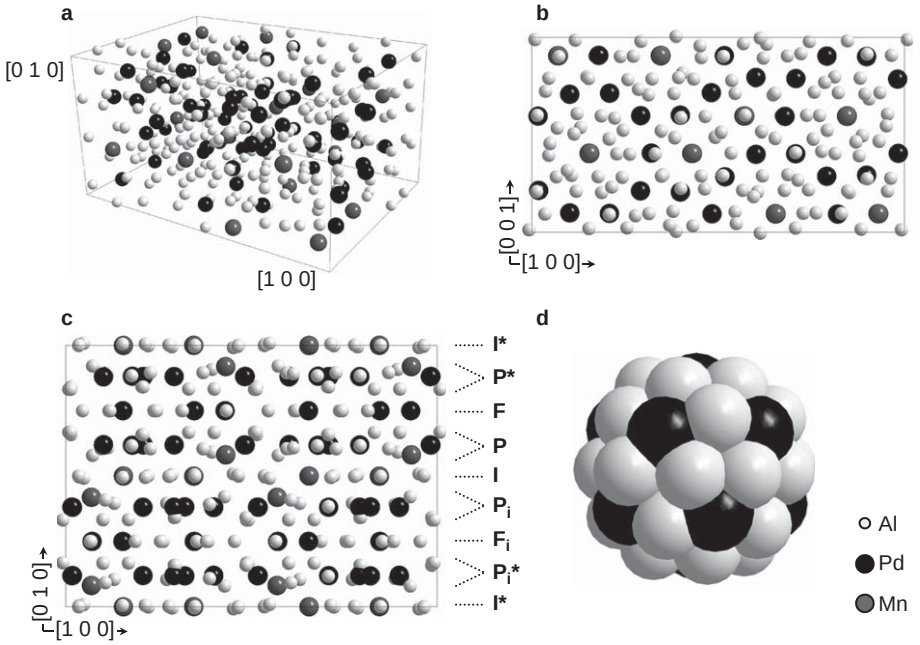

Fig. 2. Structure of ε_6-Al–Pd–Mn. (a) Unit cell in perspective view. (b) Projection along [0 1 0]. (c) Projection along [0 0 1]. (d) Mackay-type cluster.

Perpendicular to the [0 1 0] direction [Fig. 2(c)], the structure can be described as a stacking of eight layers of three different types: A flat layer (F) which is a mirror plane in the structure, a puckered layer (P) and a slightly puckered layer (I) containing the inversion center. Applying the symmetry operations of the *Pnma* space group, the stacking of layers along the [0 1 0] direction is completed by the respective mirror and inversion images F_i, P_i, P^*, I^*, and P_i^* [25]. The subscript "i" stands for inversion images of the respective layers with respect to the inversion center, and the asterisk denotes the mirror images of the respective layers with respect to the F and F_i layers.

The structure of ε_6-Al–Pd–Mn contains a substantial amount of inherent disorder, which in the structure model [24] is reflected by the presence of a high amount of atomic sites with low occupation factors. Of the 48 independent atom positions in the unit cell, only 18 have occupation factors of 100%. While the Mn positions are fully occupied, of the 11 Pd sites, three possess Al/Pd substitutional disorder. Of the Al atoms in the I layers, three have a partial occupation factor. These correspond to interpenetrating icosidodecahedra and form radial pairs between next-neighboring clusters. All Al sites in the P-layers have partial occupancy factors; most of them correspond to the inner Al shells around the cluster centers, which are partially occupied due to steric constraints.

The ε_6-phase and the described cluster substructure form the basis of the other members of the ε-phase family. A sequence of related orthorhombic phases is

referred to as ε_l with $l = 6$, 16, 22, 28, 34 according to the index of the strong diffraction spot (0 0 l), which corresponds to the interplanar spacing of about 0.2 nm occurring in all phases. These phases have identical lattice parameters a and b, and varying c-lattice parameters amounting to 3.24 nm (ε_{16}), 4.49 nm (ε_{22}), 5.80 nm (ε_{28}), and 7.01 nm (ε_{34}) in the Al–Pd–Mn system [26,27]. Note that the orthorhombic ε-phases in the literature are betimes referred to using alternative notations. The ε_6- and ε_{28}-phases are denoted ξ' and Ψ [see 24,28]: others refer to the ε_6-, ε_{16}-, and ε_{28}-phases as ξ', ξ'_1, and ξ'_3 [29] or as ξ', ξ'_1, and ξ'_2 [30].

A further orthorhombic member of the ε-phase family is the ξ-phase. It has lattice parameters $a = 1.9902$ nm, $b = 1.6612$ nm and $c = 1.4460$ nm and can coexist with the other orthorhombic ε-phases taking well-defined orientation relationships [28]. As for ε_6, the structure of the ξ-phase can be described by Mackay-type clusters on the vertices of a lattice of flattened hexagons. However, while flattened hexagons in two alternating orientations are used for the ε_6-phase, for the ξ-phase only hexagon tiles of a single orientation are used, which are arranged in parallel (see Section 2.3).

Further members of the ε-phase family are monoclinic phases, which can be described as local modulations of orthorhombic phases. These were extensively described and classified by Heggen et al. [31].

Phases of the ε-family are found in the alloy systems Al–Pd–(Mn, Fe, Rh, Re, Ru, Co, Ir) and Al–Rh–(Ru, Cu, Ni) [26,32]. The monoclinic and the ξ-structures are found as metastable phases in the Al–Pd–Mn as well as in the Al–Pd–Fe system.

2.3. Tiling description

A highly useful tool for depicting structural features, defects, phase boundaries, etc. in CMAs is the representation in the form of a tiling. A tiling is a two-dimensional projection of a given structure along a specific direction in terms of an area-filling arrangement of polygons, which corresponds to characteristic structural features. A simple (but trivial) example of a tiling is the unit-cell projection, which then, depending on structure type and projection direction, leads to a space-filling pattern of rectangles or rhombohedra.

A straightforward way to construct a useful tiling for a given CMA structure is to connect the centers of its characteristic clusters. This is shown in Fig. 3 for the case of ε_6-Al–Pd–Mn. Fig. 3(a) is a high-resolution transmission electron micrograph along the [0 1 0] direction taken at an overfocus of about 30 nm. Under these conditions, the large spatial frequencies are emphasized, such that the cluster centers are imaged as bright spots while smaller structural features are imaged at weak contrast. A hexagon pattern corresponding to the positions of the cluster centers can directly be seen. Connecting the cluster centers leads to the characteristic tiling shown in the upper right part of the micrograph and in Fig. 3(b).

The tiling consists of flattened hexagons, which are arranged in two different orientations. Neighboring hexagon rows have alternating orientations and equally oriented hexagons are stacked in rows along [0 0 1]. The sequences of alternately

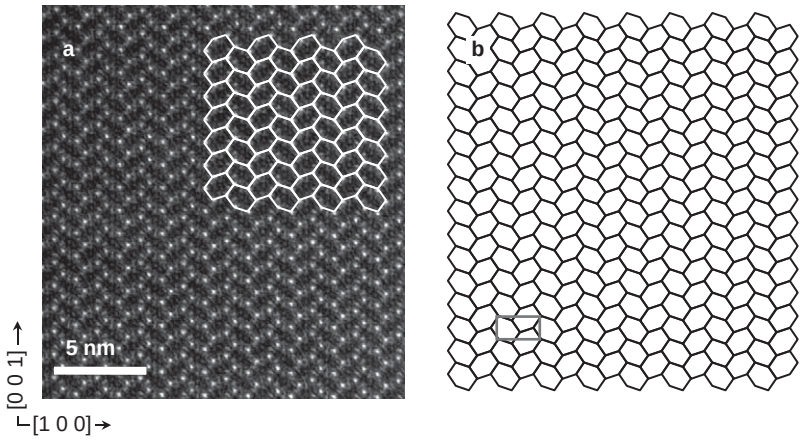

Fig. 3. (a) High-resolution transmission electron micrograph of ε_6-Al–Pd–Mn along the [0 1 0] direction with superposed hexagon tiling. (b) Hexagon tiling.

oriented hexagons along the [1 0 0] direction form puckered (0 0 1) planes with a thickness of one *c*-lattice constant (the unit-cell projection is shown in gray in Fig. 3(b)). These are referred to as hexagon planes in the following.

For a given structure, different tilings may be constructed. For ε_6-Al–Pd–Mn viewed along the [0 1 0] direction, for example, an alternative representation in terms of a rhomb tiling [33] was developed. Which tiling is chosen depends on the structural features under investigation and on the methods applied. For the description of defects in ε_6-Al–Pd–Mn, the hexagon tiling is particularly well suited. It can directly and unambiguously be derived from high-resolution TEM micrographs as shown in Fig. 3(a), and it reproduces all characteristic features of the different defects involved.

The phases related to ε_6-Al–Pd–Mn, that is, the other members of the ε-phase family and the ξ-phase, can be similarly described by tilings. Fig. 4(a) depicts the ε_{28}-phase. For its description, in addition to the hexagon tiles, two other tiles are required – a banana-shaped nine-edge tile and a pentagon. The latter are alternately arranged along the [1 0 0] direction and form (0 0 1) planes regularly stacked perpendicular to the [0 0 1] direction, forming a face-centered lattice. The unit-cell projection is shown in light gray and the lattice directions are parallel to those of the ε_6-phase [Fig. 3(b)]. Fig. 4(b) shows the ε_{16}-phase, which can be described utilizing banana-shaped polygons and pentagons only. The lattice is also face-centered. Fig. 4(c) shows the ξ-phase, which is represented by a parallel arrangement of only one type of hexagon. As indicated by the unit-cell projection, this structure is tilted with respect to the ε_6-phase. Note that the ξ-phase as well as the ε_{16}-phase can alternatively be described in terms of a monoclinic unit cell (dotted). Fig. 4(d) depicts a phase boundary between the ξ- and the ε_6-phase. At the position of the arrow the pattern of parallel hexagons changes to an antiparallel arrangement.

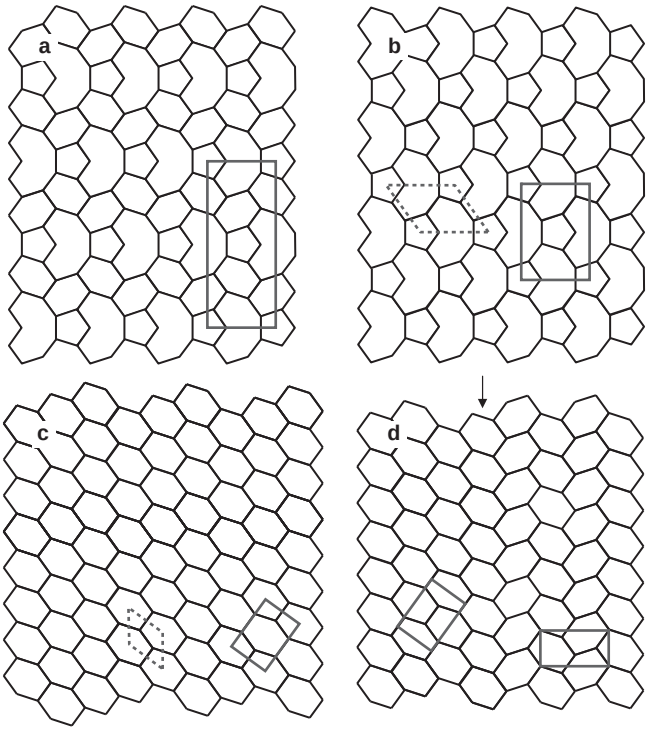

Fig. 4. Tiling representation of (a) the ε_{28}-phase, (b) the ε_{16}-phase, and (c) the ξ-phase. (d) Phase boundary (arrow) between the ξ-phase and the ε_6-phase.

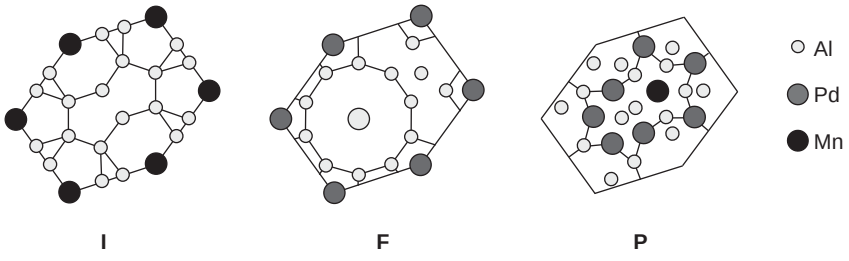

Fig. 5. Atomic decoration of the hexagon tile for the *I*, *F*, and *P* layers.

There exists a one-to-one correspondence between the tiling description and the atomic positions. Similarly to a unit cell, each tile possesses a defined atomic decoration. Fig. 5 shows the decoration of the hexagon tile for the *F*, *I*, and *P* layers. The corresponding tiles for the I^*, P^*, F_i, P_i, and P_i^* layers are related to those shown through the respective symmetry operations (Section 2.2). The corresponding alternately oriented hexagon is obtained via clockwise rotation by 72°.

Hence, with a given atomic decoration, the atom positions in the portion of structure described by a tiling can be unambiguously reconstructed.

3. Phason lines and phason planes

Phason lines and phason planes can assume a dual function in ε-type phases. On the one hand, they are structural defects, for instance in the phases ε_6-Al–Pd–Mn and ξ-Al–Pd–Mn. On the other hand, phason lines and phason planes can arrange regularly, forming a related ε-type phase with larger *c*-lattice constant, and hence become elements of a new ideal structure. Phason lines and phason planes are pivotally connected to metadislocation formation and movement, as well as in phase transitions and formation of ε-phases.

3.1. Phason lines

By means of TEM, Klein et al. [33] first observed a novel defect type in ε_6-Al–Pd–Mn, which they identified as one-dimensional with a [0 1 0] line direction. The new defect has some similarities to phason defects in quasicrystals: If the positions of the atomic structure are described in terms of a higher-dimensional cut-and-projection formalism, all atom displacements associated to the phason line are entirely located in the spatial dimensions perpendicular to the physical real space [25]. According to this analogy, Klein et al. termed this defect ''phason line.'' In a tiling representation, a phason line is depicted by a banana-shaped nine-edge tile with an attached pentagon, which is, as a whole, frequently referred to as ''banana pentagon.'' Fig. 6 shows a phason line, shaded in gray, in a ε_6-Al–Pd–Mn lattice.

Note, however, that phason lines cannot be embedded into an otherwise perfect ε_6-Al–Pd–Mn. The area above the phason line in Fig. 6 contains two hexagon columns, which are turned into their alternate position with respect to the

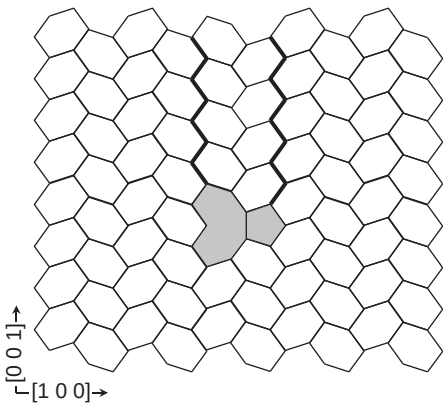

Fig. 6. Phason line (gray) in an ε_6-Al–Pd–Mn tiling.

corresponding hexagon columns below the banana pentagon. Consequently, the area above the banana pentagon contains two boundaries between hexagon columns of parallel orientation (thick lines). These boundaries do not occur in the ideal ε_6-structure, and hence are to be considered planar faults in the latter. The presence of two ''wrong'' hexagon columns is directly related to the mechanism of phason-line movement, which is described in Section 3.1.2.

Note that phason lines, even though they are linear defects, are not dislocations. Analyzing them in terms of ideal tile edges (''modified Burgers circuit,'' see Section 4.3) reveals that they do not possess a Burgers vector.

3.1.1. Atomic decoration of a phason line

Like the flattened hexagons, the tiles representing the phason lines possess a defined atomic decoration. Fig. 7 shows the atomic decoration in the *I*, *F*, and *P* layer. The decoration was developed according to the following criteria:

- Preservation of local order and coordination as in the ideal structure. In each layer the structure, and accordingly the decoration of the hexagon tiles, displays certain preferred local arrangements. This particularly concerns the vertices of the hexagon lattice, i.e. the corners of the hexagon tiles, which correspond to [0 1 0] columns of Mackay-type clusters.
- Compatibility with the model of phason-line movement by Beraha et al. [25]. This model is based on the structure solution by Boudard et al. [24]. It employs shifts in perpendicular space in a higher-dimensional crystallographic approach, as used for quasicrystalline structures, to model the individual atom jumps that make up a vertex flip (Section 3.1.2).
- Compatibility with high-angle annular dark-field (HAADF) images obtained in high-resolution scanning TEM [34]. Applying this technique, one finds that the image intensity is proportional to the square of the atomic number [35]. Hence, the positions of the heavy atoms in the tiling can be directly compared with the model. Fig. 8(a) shows a HAADF micrograph of a phason line in ε_6-Al–Pd–Mn with a superposed banana pentagon. In Fig. 8(b), the same image is seen with superposed projected atom positions for columns containing Pd and/or Mn of all

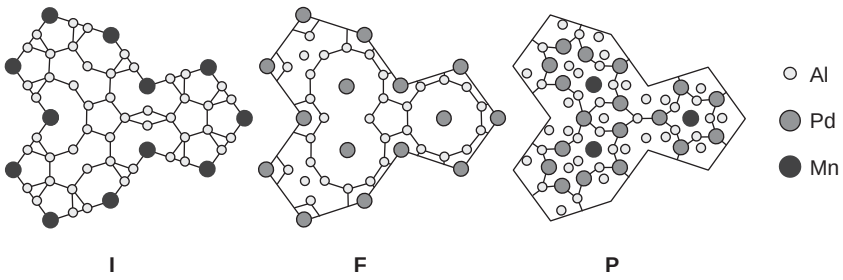

Fig. 7. Atomic decoration of the tile representing a phason line for the *I*, *F*, and *P* layers.

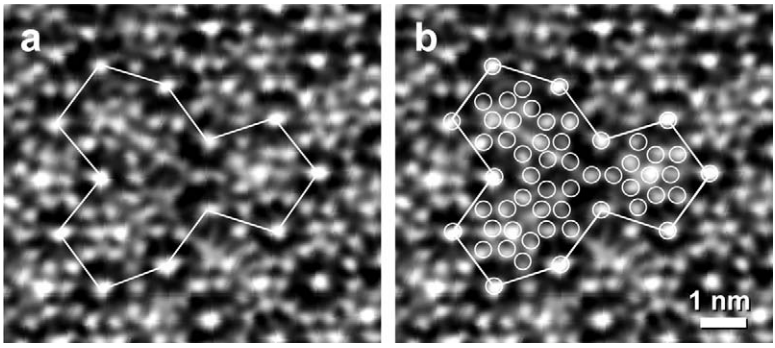

Fig. 8. High-resolution HAADF micrograph of a phason line in ε_6-Al–Pd–Mn. (a) With a superposed phason-line tile. (b) With superposed positions of columns containing Pd and/or Mn atoms (circles).

layers including mirror and inversion images (circles). Clearly, all essential features of the experimental image are well reproduced by the model.

Despite the (0 0 1) mirror symmetry of the tiles representing the phason line, its atomic decoration is not fully symmetric. Small deviations occur for some Al positions in the *P* layer, which are due to the required compatibility with the hexagon tiles. However, according to the structure model [24] the hexagon tiles in the *P* layer by themselves are not symmetric with respect to their long axis (Fig. 5) and the corresponding atom positions exhibit low occupancy factors.

3.1.2. Movement of a phason line

Phason lines can move in the crystal lattice of the ε_6-phase along the [0 0 1] direction. A tiling representation of the mode of movement is given in Fig. 9. Fig. 9(a) shows a phason line in an ε_6-lattice. In this initial position, there are two hexagon planes above the banana pentagon. In Fig. 9(b), the vertex marked by an open circle jumps to the position marked with a solid circle. The hexagon lattice can be redrawn, and a complete hexagon appears at the position given by the dotted line, while the remaining part of the initial banana pentagon together with the hexagon, the corner position of which has moved, form a new banana pentagon [Fig. 9(c)]. The new banana pentagon is located at a lower position along the [0 0 1] direction, and it has an orientation opposite to that in Fig. 9(a). In a subsequent similar step, the phason line can move to the position shown in Fig. 9(d). There are now three hexagon planes above the banana pentagon, that is, the phason line has moved downwards along the [0 0 1] direction by one *c*-lattice constant. Repeating this sequence, the phason line can move over long distances. Analogously, the phason line can move upwards by reverse vertex jumps.

As described in Section 2.3, the hexagon tiling is constructed by drawing lines connecting neighboring cluster centers. This still holds for each individual position of the phason line shown in Figs 9(a)–9(d). However, this does not imply that a vertex jump corresponds to the movement of a complete cluster from the initial to

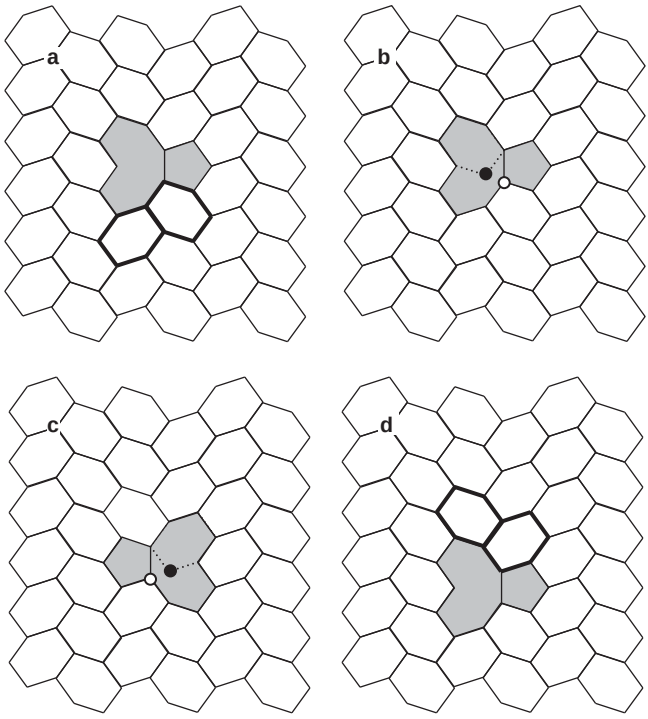

Fig. 9. Tiling representation of the successive steps of phason-line movement along the [0 0 1] direction (see text).

the new vertex position. Physically, only a few atoms move to new positions, which then, together with the present atomic environment at the final position, form a new cluster at the new vertex position. The individual atom movements have been worked out in detail by Beraha et al. [25] for all atomic species and all layers. Fig. 10 illustrates this scenario for the case of the *I* layer in the ε_6-Al–Pd–Mn structure. The cluster positions before and after the jump are indicated by dotted circles. All Al jumps take place within the *I* layer. The Mn atom in the center of the cluster does not directly move from the initial to the final position, but jumps from the initial position to a neighboring *P* or P_i layer, while another Mn atom jumps from the neighboring *P* or P_i layer to the final position. This indirect mechanism reduces the jump distances of the individual atoms to distances of 0.296 nm and below, while the distance between the initial and final cluster position amounts to 0.479 nm. Obviously, the number of atoms involved in the vertex jump (thicker outline) is considerably smaller than the number of atoms being part of the cluster.

In Fig. 6, we have seen that a phason line is connected to two hexagon columns, which are turned into their alternate position with respect to the ideal lattice. Further downwards movement of the phason line as shown in Fig. 9 will lead to elongation of the alternately oriented columns. In other words, passing of a phason

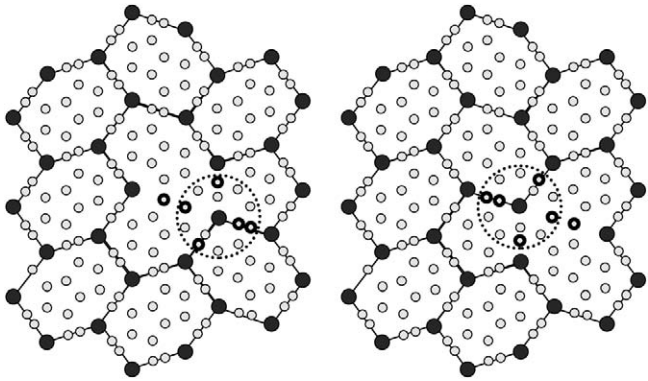

Fig. 10. Individual atomic jumps involved in the *I* layer of ε_6-Al–Pd–Mn during one step of phason-line movement.

line through the ideal ε_6-structure results in the creation of two slabs of twinned ξ-structure, and, accordingly, to two (1 0 0) planar faults in its wake.

3.1.3. Kinks in phason lines

Phason lines are linear defects with a [0 1 0] line direction, which can move along the [0 0 1] direction. It is unlikely, however, that phason lines move as a whole, that is, that the complete line performs a vertex jump in one single step. Although this has not been investigated in detail, it is a plausible assumption that phason lines move by a mechanism involving sequential jumps of small portions of the line, that is, by the formation of kinks and their subsequent movement along the line. This is in full analogy to the Peierls model, which describes dislocation motion by a kink-pair mechanism [36].

Accordingly, it is expected that in a static situation, deviations from the ideal line direction occur. This can indeed be observed in TEM micrographs. Fig. 11 depicts TEM micrographs taken under imaging conditions such that the clusters are imaged as bright spots encircling a dark center. The superposed tiling is constructed by connecting the latter. Fig. 11(a) shows a phason line without a kink. It is represented by a banana pentagon (thick white line) as schematically depicted in Fig. 6. The phason line in Fig. 11(b), on the other hand, cannot be described by a single banana pentagon. In the interior of the defect two overlapping cluster fragments of low contrast are seen, which is interpreted as a phason line with a kink or kink pair. Along the [0 1 0] direction, a part of the phason line has performed a vertex jump, while another part has not. This situation can, therefore, be understood as an intermediate situation between Figs 9(b) and 9(c). Fig. 11(c) accordingly shows a phason line with two kinks or kink pairs.

In TEM practice, it becomes increasingly difficult to find straight phason lines as shown in Fig. 11(a) in thicker specimen areas. One occasionally finds phason lines, which strongly deviate from their ideal line direction, such that no clear inner

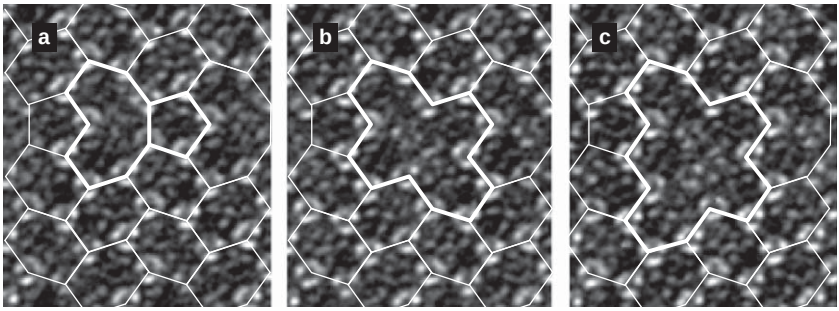

Fig. 11. TEM micrographs and superposed tiling representation of phason lines with different numbers of kinks along the [0 1 0] direction. (a) No kink. (b) One kink. (c) Two kinks.

vertices can be observed over distances up to several nanometers along the [0 0 1] direction.

3.2. Phason planes

If phason lines are present at a certain density in a ε_6-structure, they tend to align along the [1 0 0] direction and form (0 0 1) planes, which are referred to as phason planes.

Fig. 12(a) is a high-resolution HAADF image of a phason plane in ε_6-Al–Pd–Mn and Fig. 12(b) shows the corresponding tiling representation. Since each individual phason line connects two-neighboring hexagon columns with their alternately oriented version (Section 3.1), the phason plane is a (0 0 1) mirror. Accordingly, phason planes can be considered as twin boundaries or inversion boundaries in the ε_6-structure.

Deviations of a phason plane from the (0 0 1) orientation can occur due to the mobility of the individual phason lines along the [0 0 1] direction. Fig. 13 depicts a tiling representation of a tilted phason plane. The [0 0 1] displacement of the phason lines leads to an increase of the fault area and, if the mutual displacement is larger than one *c*-lattice constant, to the occurrence of local (1 0 0) faults (thick line). Hence, alignment of the phason plane along (0 0 1) minimizes the total fault energy and is accordingly considered as the ideal orientation.

Deviations of the phason planes from the ideal orientation may occur in situations where the structure is not fully equilibrated or in internal stress fields, for example, in the vicinity of dislocations or other defects. Fig. 14(a) is a low-resolution bright-field Bragg-contrast TEM image taken along the [0 1 0] direction. Under these conditions, the phason planes are seen edge on and are imaged as dark lines on the light ε_6-Al–Pd–Mn background. The phason planes obviously deviate from their ideal (0 0 1) orientation and can assume substantial curvatures, like in the lower right corner. Fig. 14(b) shows a TEM micrograph at a level of magnification intermediate between that of Figs 12 and 14(a). In the upper left corner is an area of ε_6-structure, in which the alternating hexagons are resolved. The phason lines are

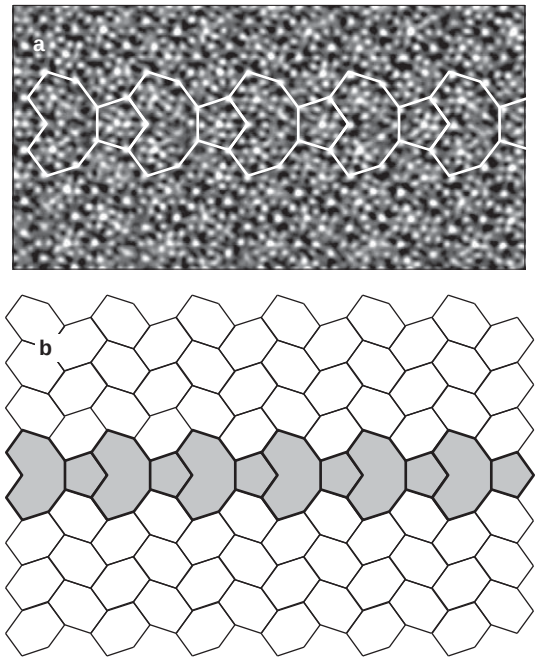

Fig. 12. Phason planes in ε_6-Al–Pd–Mn. (a) High-resolution HAADF image. (b) Corresponding tiling representation (gray).

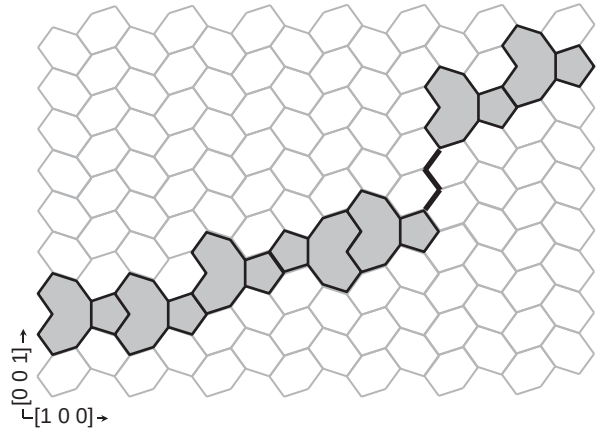

Fig. 13. Tiling representation of a tilted phason plane. Locally, (1 0 0) faults occur (thick line).

imaged as almost rectangular dark areas and the composition of phason planes by individual phason lines is seen. The phason planes show sizeable deviation from their ideal (0 0 1) orientation, and the individual phason lines deviate from their ideal [0 1 0] orientation.

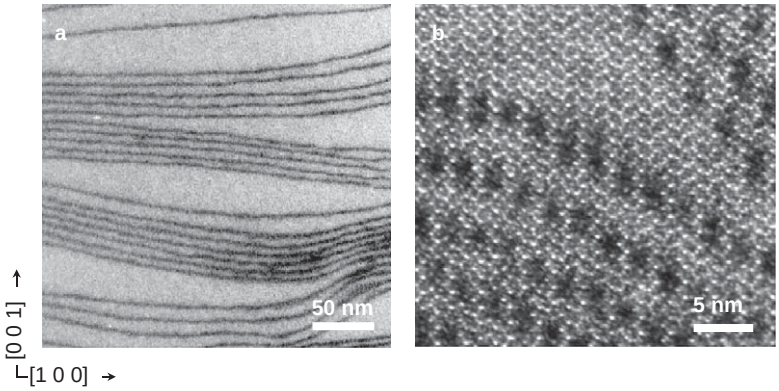

Fig. 14. TEM micrographs along the [0 1 0] direction of tilted phason planes. (a) Under low-resolution bright-field conditions. (b) At higher magnification.

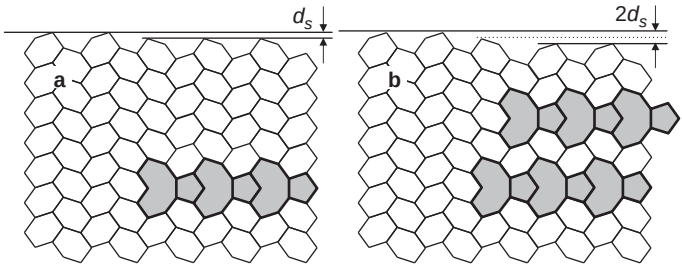

Fig. 15. Phason halfplanes in the ε_6-lattice. Offset d_s along the [0 0 1] direction due to the insertion of (a) a single and (b) two phason halfplanes.

3.2.1. Phason-plane strain field

Fig. 15(a) schematically depicts a phason halfplane, that is, a semi-infinite phason plane terminated in the bulk of the otherwise ideal ε_6-structure as represented by the alternating hexagon lattice. A comparison of the position of the upper limit of the structure at the leftmost and the rightmost parts of the figure reveals an offset d_s. This offset results from the difference in thickness (i.e., the extension along the [0 0 1] direction) of the ideal portion of the structure (left) and the part containing the phason halfplane (right). The offset can be quantified in terms of the edges of the hexagon lattice and amounts to $-c/2\tau^2(0\,0\,1)$ [37]. Fig. 15(b) shows the structure with two phason halfplanes inserted, the second one being "shorter" by one hexagon column. The upper right part of the structure is now again identically oriented as the initial structure and the total offset $2d_s = 2c/2\tau^2$ can directly be seen.

Comparing the numbers of (0 0 1) hexagon planes in the left and right parts of Fig. 15(b), one sees that two phason planes can be understood as a compacted combination of three hexagon planes. Since the thickness of the part containing the two phason halfplanes is smaller by $2d_s$, the thickness of a phason plane, d_p, can be calculated as $2d_p = 3d_h - 2d_s$, where $d_h = c$ is the thickness of a hexagon plane. With $d_s = c/2\tau^2$, we obtain $d_p = c\tau^2/2$ (see Appendix), which, with $c = 1.256$ nm for ε_6-Al–Pd–Mn, takes a value of 1.644 nm.

The offset d_s introduced by a phason plane can be interpreted as the vertical component of the phason-plane strain field. Since the phason plane turns hexagon columns into their alternate orientation, its strain field has in addition a lateral component corresponding to a translation of half a lattice constant along the [1 0 0] direction. The total phason-plane strain field can then be described by the displacement vector $\vec{r} = 1/2(1\ \ 0\ \ -1/\tau^2)$, which was experimentally verified by means of fringe-contrast analysis in TEM [37].

3.2.2. Related phases and phase transitions in terms of phason planes

In Section 2.2, we have introduced the fact that the ε_6-phase is the basic structure of a family of related phases, the ε-phase family. Fig. 4 shows examples of corresponding hexagon tilings. The ε_{28}-phase [Fig. 4(a)] is represented by a tiling which consists of hexagons and banana pentagons. The latter are thus structural elements of the ε_{28}-phase, while they are defects in the ε_6-phase.

The ε_{28}-phase can be considered as a structure consisting of a periodic stacking of phason planes. Other ε-phases consist of phason planes stacked with different periodicities, that is, with different amounts of hexagon rows between the phason planes. Generally, between the members of the ε-phase family, we can discriminate between phases with and without phason lines as structural elements. The phases ε_6 and ξ fall into the first category and the phases ε_{16}, ε_{22}, and ε_{28} into the second one. This concept can be expanded to include related monoclinic phases [31].

Phase transitions between ε-phases can be continuous, that is, of second order. For example, the transition from ε_6 to ε_{28} can occur by inserting a high density of phason lines and stacking the corresponding phason lines such that a periodicity of 5.80 nm results. Transitions from ε_6 to ξ occur via repetitive translation of phason lines with intermediate states of higher phason-line density [33]. Fig. 16 shows an example of a continuous transition from ε_6 to ε_{28}. The situation in Fig. 16(a) can be best interpreted as an ε_6-matrix with some phason-plane faults. The density of phason planes can be calculated according to $\rho = A/V = l_p t/a_x a_y t = l_p/a_x a_y$, where A is the total phason-plane area in the specimen volume V considered, l_p is the total length of phason planes in the image area $a_x, \cdot a_y$, and t is the specimen thickness. Figs 16(a)–16(d) show an increasing phason-plane density of $\rho = 2.83$, 6.63, 158 and $295 \times 10^6\ \mathrm{m}^{-1}$, respectively. The phason planes in Fig. 16(d) are quite regular and dense; they correspond to a lattice constant of about 10.2 nm. The phason-plane density of the ideal ε_{28}-phase is about twice as high as in Fig. 16d. It corresponds to $\rho = 3/c_{28} = 517 \cdot 10^6 \times\ \mathrm{m}^{-1}$, where $c_{28} = 5.80$ nm is the c-lattice constant of the ε_{28}-phase.

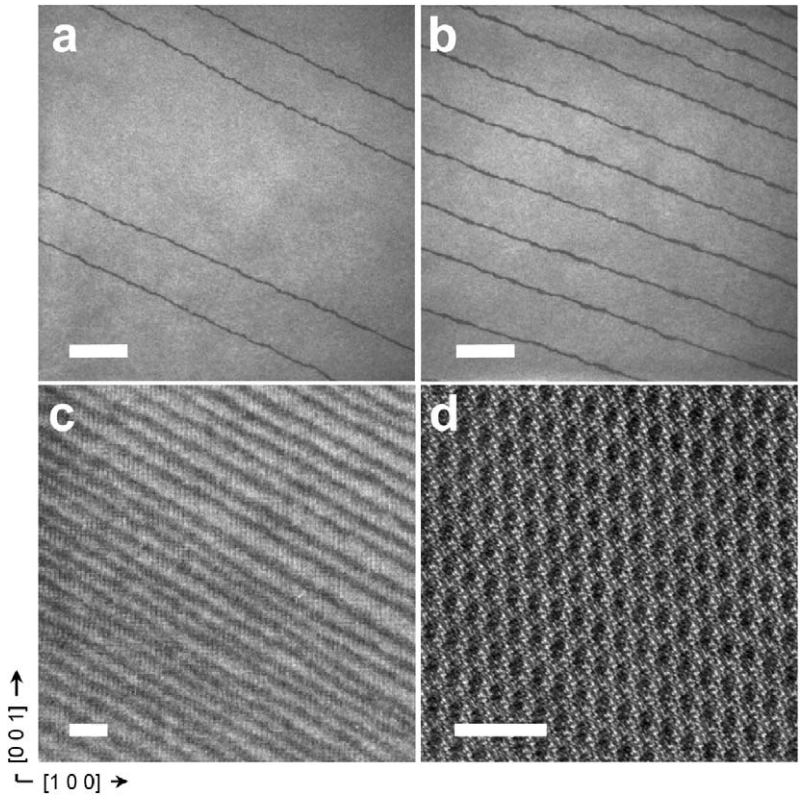

Fig. 16. Continuous transition from the ε_6-phase to the ε_{28}-phase. Scale bars: 200 nm (a, b) and 10 nm (c, d).

4. Metadislocations

4.1. History and basic features

Direct observation of metadislocations is possible by means of TEM through high-resolution or Bragg-contrast imaging. Fig. 1(a) depicts the first TEM micrograph ever taken of a metadislocation [1]. The metadislocation shown is imaged end-on, that is, the viewing direction in the electron microscope is parallel to the line direction. The metadislocation is embedded in the ε_{28}-Al–Pd–Mn phase, which is recognizable by the periodic stacking of phason planes in the outer image regions. At a distance from the metadislocation, the phason planes are approximately straight and perpendicular to the [0 0 1] direction. The metadislocation itself consists of a core (arrow), which is surrounded by a certain number of phason halfplanes. The present example has six associated phason halfplanes, which extend from the dislocation core to the right-hand side of the image. On the other side of the core, the metadislocation shows a region of pure ε_6-structure. The surrounding phason

planes bend around the core and, with increasing distance from the latter, narrow down the width of the pure ε_6-region, such that it takes a roughly triangular shape.

The overall appearance of the metadislocation resembles a dislocation in a simple metal but the differences are obvious: the apparent extension of the strain field of the metadislocation is larger by more than one order of magnitude, and the associated phasons are not inserted halfplanes like those of an edge dislocation in a simple metal, but consist of a locally transformed area. Historically, the first observed metadislocations in ε_{28}-Al–Pd–Mn were interpreted as defects in a structure of defects (Section 3.2) and were, therefore, termed "metadislocations" [1].

Fig. 17 shows a group of metadislocations in ε_{28}-Al–Pd–Mn at lower magnification in two-beam Bragg contrast. In Fig. 17(a), the metadislocations are imaged using a (0 0 6) reflection close to the (1 2 0) zone axis, at an angle of about 35° from their end-on orientation. Their linear character can clearly be seen. Fig. 17(b) shows the same group of metadislocations, imaged using the same

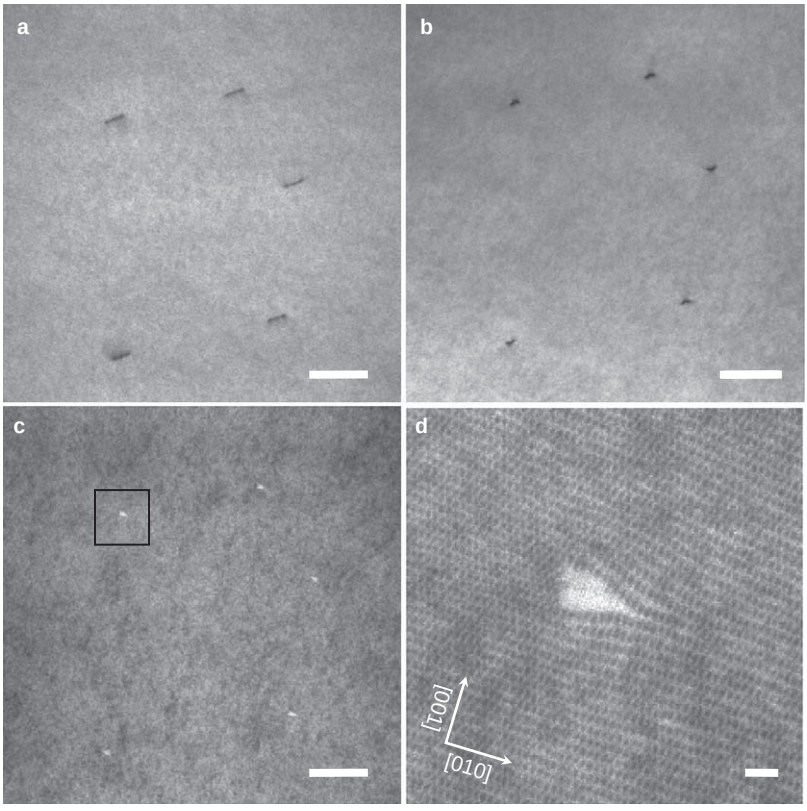

Fig. 17. Group of metadislocations in ε_{28}-Al–Pd–Mn. (a) At lower magnification in two-beam Bragg contrast using the (0 0 6) reflection for imaging close to the (1 2 0) axis and (b) close to the (0 1 0) zone axis. (c) Imaged under bright-field Laue conditions at the (0 1 0) zone axis. (d) Boxed area in (c) at higher magnification. Scale bars. 100 nm (a, b, c) and 10 nm (d).

reflection close to the (0 1 0) zone axis. They are now seen very close to the end-on orientation, and hence they appear as dark spots. Under Bragg conditions in Figs 17(a) and 17(b), the metadislocation contrast is very similar to that of normal dislocations in simple metals (see [38]). In Fig. 17(c), the metadislocations are shown under bright-field Laue conditions, that is using a symmetrical arrangement of reflections for imaging. Evidently, each dislocation position is decorated by a small bright contrast area. Fig. 17(d), finally, shows the boxed area in Fig. 17(c) at a higher magnification. The typical appearance of the metadislocation can now be seen [cf. Fig. 1(a)].

Fig. 18 depicts a metadislocation in ε_6-Al–Pd–Mn. The matrix structure entirely consists of flattened hexagons in alternating orientation. In this example, the six associated phason halfplanes stretch out to the right-hand side.

First characterizations of the Burgers vector of metadislocations were carried out by means of Bragg-contrast analysis [39]. Their Burgers vector direction was determined as parallel to the [0 0 1] direction. Since the line direction is parallel to the [0 1 0] direction, metadislocations are pure edge dislocations.

TEM micrographs of metadislocations in ε_6-Al–Pd–Mn at lower resolution are shown in Fig. 19. Fig. 19(a) is imaged under bright-field Laue conditions along the (0 1 0) zone axis. The metadislocation is seen on the left-hand side of the micrograph and terminates six phason halfplanes, imaged as dark lines on the light-gray background, which extend to the right-hand side. The lattice structure is not resolved and is seen as gray background. Fig. 19(b) shows the same sample area under two-beam bright-field conditions using the (0 0 6) reflection imaged close to the (1 2 0) zone axis. Under these conditions, the associated phason planes show fringe contrast.

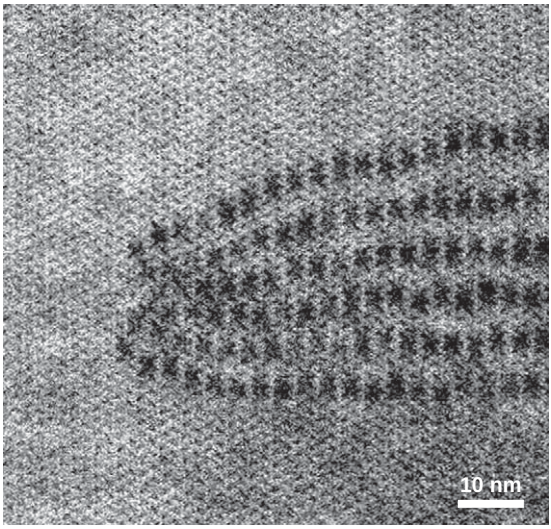

Fig. 18. Metadislocation with six associated phason halfplanes in ε_6-Al–Pd–Mn.

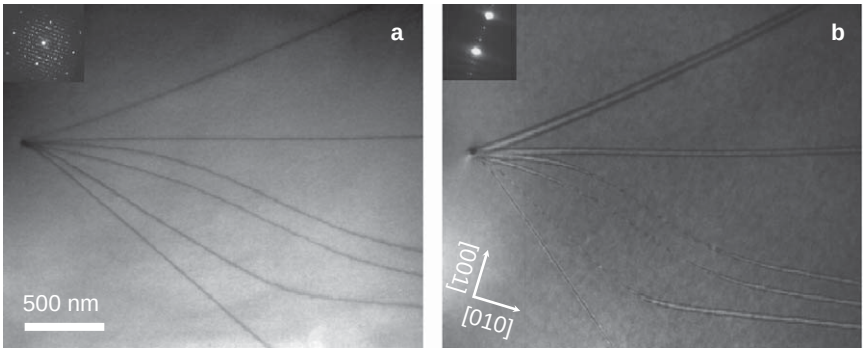

Fig. 19. Metadislocations in ε_6-Al–Pd–Mn at a low magnification. (a) Under bright-field Laue conditions along the (0 1 0) zone axis. (b) Under two-beam bright-field conditions using the (0 0 6) reflection imaged close to the (1 2 0) zone axis.

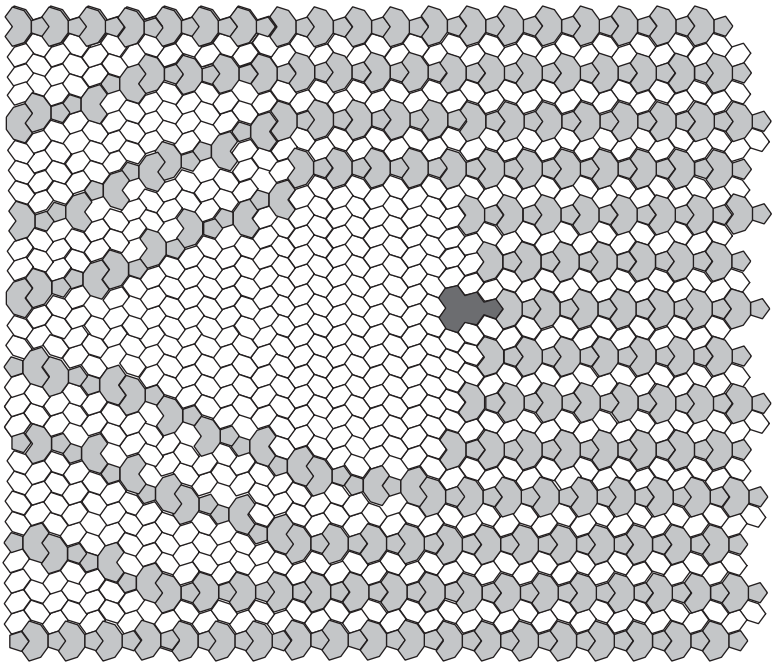

Fig. 20. Tiling representation of the metadislocation in Fig. 1(a). The metadislocation core is represented by a dark-gray tile. Six phason halfplanes are terminated at the right-hand side of the core.

4.2. Tiling description

Fig. 20 is a tiling representation of the metadislocation in Fig. 1(a). The metadislocation core is represented by a dark-gray tile. On the right-hand side,

one can see six phason halfplanes ending in the vicinity of the core. On the left-hand side of the core is an ideal ε_6-region, represented by alternating hexagons. As in the experimental image, the exterior phason planes bend around the dislocation core.

The tiling representation is very close to the experimental image and reproduces, besides the essential features, additional details such as the curvature of the phason planes. The latter, due to the mobility of the phason lines along the [0 0 1] direction, is rather arbitrary. The individual banana pentagons of the surrounding phason planes can be drawn in slightly different positions without changing the basic construction principle and, indeed, the curvature in the experimental image is smoother and extends over a larger distance along [1 0 0] than in the schematic representation.

The tiling representation shown includes non-essential features of the metadislocation, and in this sense it is held at a low degree of abstraction. Fig. 21(a) is a tiling representation of the metadislocation in the ε_{28}-structure at a higher degree of abstraction. The curvature of the phason planes is neglected but the essential features of the metadislocation, that is, the core tile, the six inserted phason halfplanes, and the surrounding ε_{28}-structure are present.

Fig. 21(b) is a tiling representation of a metadislocation in the ε_6-structure at the same level of abstraction. The essential features here are the core tile, the six inserted phason halfplanes, and the surrounding ε_6-structure. A comparison of figures reveals two essential facts: first, the construction principles of the metadislocation in the ε_6- and in the ε_{28}-structure are identical. The only difference is the surrounding matrix structure. Second, the metadislocations in the ε_6 and ε_{28} structures are complementary in character: one can consider the metadislocation in ε_6 [Fig. 21(b)] as being associated to a slab of ε_{28} in an ε_6-matrix and the metadislocation in ε_{28} [Fig. 21(a)] as being associated to a slab of ε_6 in an ε_{28}-matrix.

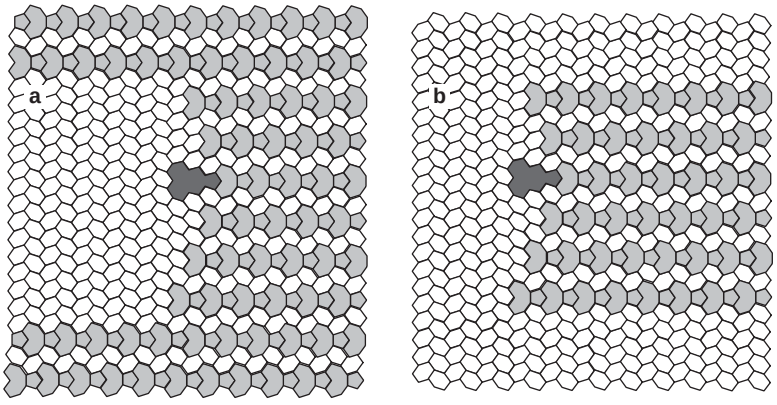

Fig. 21. Tiling representation at a higher degree of abstraction. (a) Metadislocation in the ε_{28}-structure. (b) Metadislocation in the ε_6-structure.

4.3. Burgers vector

Because metadislocations are connected to a number of associated phason halfplanes, their Burgers vector cannot be determined by means of a regular Burgers circuit [40]. The phason planes are not an element of the ideal structure of the ε_6-phase, and hence a comparison circuit for the metadislocation in ideal ε_6 cannot be performed. The same holds for the metadislocation in ε_{28}, since the associated slab of ε_6 is not present in the ideal ε_{28}-structure.

However, the hexagon tiling provides a set of vectors characteristic of the ideal structure, which can be used to perform a modified Burgers circuit. Fig. 22(a) shows a set of vectors in the (0 1 0) plane, which correspond to the edges of a regular pentagon and represent all edges present in the hexagon tiling. The vectors can be expressed as

$$\begin{aligned}
\vec{a}_1 &= a_0\begin{pmatrix}0\\1\end{pmatrix}, & \vec{a}_2 &= \frac{a_0}{2}\begin{pmatrix}\sqrt{\tau+2}\\ \tau-1\end{pmatrix},\\
\vec{a}_3 &= \frac{a_0}{2}\begin{pmatrix}\sqrt{3-\tau}\\ -\tau\end{pmatrix}, & \vec{a}_4 &= \frac{a_0}{2}\begin{pmatrix}-\sqrt{3-\tau}\\ -\tau\end{pmatrix},\\
\vec{a}_5 &= \frac{a_0}{2}\begin{pmatrix}-\sqrt{\tau+2}\\ \tau-1\end{pmatrix},
\end{aligned} \tag{2}$$

where the factor a_0 is the edge length of the hexagons. Fig. 22(b) depicts a circuit around the tile representing the core of a metadislocation with six associated phason halfplanes, using the vectors $\vec{a}_1$ to $\vec{a}_5$. Obviously, the circuit does not close. The closure failure indicated by the gray arrow corresponds to the Burgers vector. In terms of the vectors in eq. (2), the circuit reads $\vec{b}+\vec{a}_3+3\vec{a}_2+\vec{a}_4+3\vec{a}_5=0$, which yields

$$\vec{b} = -a_0\begin{pmatrix}0\\ 2\tau-3\end{pmatrix} = -a_0\begin{pmatrix}0\\ \tau^{-3}\end{pmatrix} \text{ (see Appendix).}$$

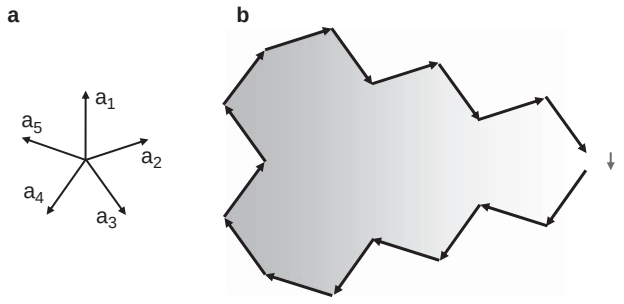

Fig. 22. (a) Basis vectors in the (0 1 0) plane. (b) Burgers vector determination by a circuit around the tile representing the core of a metadislocation with six associated phason halfplanes.

Hence, in the coordinate system of the ε_6-structure, the Burgers vector of the metadislocation is $\vec{b} = -c/\tau^4[0\,0\,1]$. With the lattice constant $c = 1.256$ nm for ε_6- and ε_{28}-Al–Pd–Mn, we obtain a Burgers vector length of 0.183 nm.

Two facts are noteworthy at this point. First, the Burgers vector of the metadislocation is a fraction of the lattice constant, that is the metadislocation is a partial dislocation in the ε_6 and ε_{28} structures. The length of the Burgers vector is of the same order as typical values found for simple metals, such as 0.29 and 0.26 nm in aluminum and copper, respectively. Hence, the elastic strain energy of the metadislocation is energetically acceptable, while the energy of a corresponding perfect dislocation would be unphysically high. Second, the ratio of the Burgers vector length and the lattice constant is irrational (recall that $\tau = 1/2(\sqrt{5}+1)$ is the irrational number of the golden mean). Therefore, unlike partials in simple metals, the Burgers vectors of which are always rational fractions of lattice distances, it is impossible to add up metadislocations in order to obtain an integer number of lattice translations. In Fe_3Al, for example, plastic deformation takes place by quadruplets of $1/4\langle 1\,1\,1\rangle$ partials [41]. Accordingly, the lattice translation adding up after the passing of four individual partials adds up to one lattice constant, such that the lattice becomes undistorted again. With metadislocations, this is only possible if networks including different metadislocation types are formed [42].

4.4. Metadislocation series

In simple metals, usually only one Burgers vector length exists for a given type of dislocation. This length is given by the distance of two minima in the corresponding gamma surface [43]. The gamma surface is basically determined by the lattice periodicity and structural details in the lattice planes. In CMAs, there are different length scales, which are related by irrational numbers. For example, the distance between the cluster centers (which is identical to the hexagon-tiling edge length a_0) is related to the c-lattice constant by $a_0 = c/\tau$. A result of this particular structural feature is that for a given Burgers vector direction, there are various local minima in the gamma surface. Hence, dislocations with different Burgers vector lengths can form.

In ε-Al–Pd–Mn, five different Burgers vector lengths for [0 0 1] metadislocations are experimentally found, which range from 0.070 to 0.480 nm [44]. Each Burgers vector length is associated with a certain number of phason halfplanes. Fig. 23 displays corresponding TEM micrographs, all taken along the [0 1 0] lattice direction. Fig. 23(a) is a low-resolution micrograph of a metadislocation with two associated phason halfplanes in ε_6-Al–Pd–Mn. The metadislocation is seen on the left-hand side of the micrograph and terminates two phason halfplanes, imaged as dark lines on the light-gray background, which stretch out to the right-hand side. The corresponding Burgers vector length is 0.489 nm. Fig. 23(b) is a micrograph of a metadislocation with four associated halfplanes. The associated phason halfplanes are not perpendicular to the [0 0 1] direction but are tilted downwards by 20–30°.

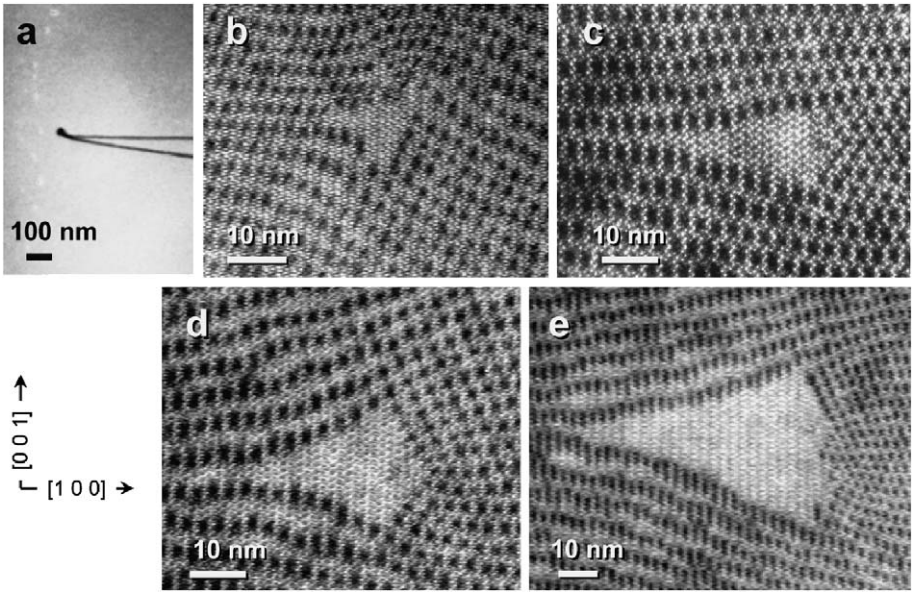

Fig. 23. Metadislocation series. TEM micrographs of metadislocations with (a) 2, (b) 4, (c) 6, (d) 10, and (e) 16 phason planes.

Table 1
Experimentally observed metadislocations with [0 0 1] Burgers vectors in ε_6- and ε_{28}-Al–Pd–Mn

N	b/c	b (nm)
2	$-\tau^{-2}$	−0.480
4	$+\tau^{-3}$	+0.296
6	$-\tau^{-4}$	−0.183
10	$+\tau^{-5}$	+0.113
16	$-\tau^{-6}$	−0.070

Note: N, number of associated phason halfplanes; b, Burgers vector length in terms of the c-lattice constant and actual value in the in ε_6- and ε_{28}-lattice.

The corresponding Burgers vector length amounts to 0.296 nm. Figs 23(c)–23(e) show metadislocations with 6, 10, and 16 associated phason halfplanes, with Burgers vector lengths of 0.183, 0.113 and 0.070 nm, respectively. In Table 1, all members of the metadislocation series, along with the corresponding Burgers vector lengths, are listed.

Tiling representations for the metadislocations with two, four, and ten associated phason halfplanes in ε_6-Al–Pd–Mn are displayed in Figs 24(a)–24(c), respectively. Each metadislocation core is represented by a characteristic tile, the area of which increases with increasing number of associated phason halfplanes.

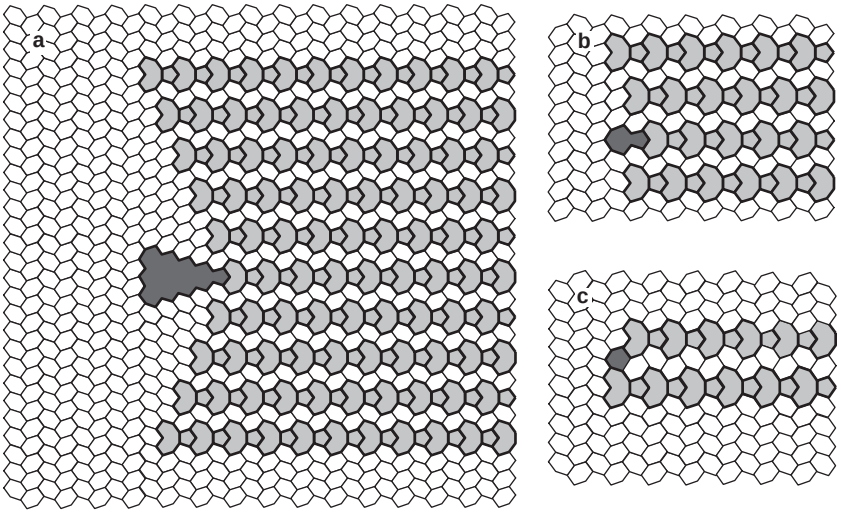

Fig. 24. Tiling representation of metadislocations with (a) ten-, (b) four-, and (c) two associated phason halfplanes in ε_6-Al–Pd–Mn.

Regarding the series of [0 0 1] metadislocations, the following facts are noteworthy:

- The numbers of associated phason halfplanes in the series take twice the values of the Fibonacci numbers 1, 2, 3, 5, and 8 (see Appendix).
- The Burgers vector lengths are related to each other by factors of $-\tau$. The negative sign of the factor results from Burgers circuits according to Fig. 22 around the characteristic tiles representing the core; this is discussed in Section 4.5.2.
- The sequences of associated phason halfplanes and Burgers vector lengths are opposed: with an increasing number of phason halfplanes, the Burgers vector lengths are decreasing.
- Experimentally, one finds that the different members of the metadislocation series are not evenly distributed but their number distribution shows a broad maximum. In deformed and undeformed ε-Al–Pd–Mn, most metadislocations found have six associated phason halfplanes. Metadislocations with ten halfplanes are observed almost as often, while those with four phason halfplanes are found considerably less frequently. Metadislocations with 16 phason halfplanes are even less frequently found and species with two halfplanes were only observed in very few occasions during an extensive number of experimental investigations. The frequency of occurrence of different metadislocation types considering their energy is discussed in Section 4.5.3.

4.5. Construction principles

We have seen in the previous sections that metadislocations are associated with a certain number of phason halfplanes. The latter are required to accommodate the core into the crystal lattice. In the following, we describe two different ways to construct metadislocations in terms of a tiling representation. This will enable the reader to comprehend the relation between the number of associated phason halfplanes and the Burgers vector length, as well as further characteristic properties of the individual metadislocations within the series.

4.5.1. Hexagon column arrangement

Fig. 25(a) shows the tile representing the core of a metadislocation with six associated phason halfplanes inserted in the ε_6-tiling. On the left and right of the core tile, the hexagons columns are arranged in an alternating sequence, which corresponds to the ideal ε_6-lattice. If we label the columns as shown in the figure, that is the columns with hexagons pointing downwards are labeled "*a*" and those with hexagons pointing upwards are labeled "*b*," the ideal ε_6-lattice corresponds to a column sequence given by *a–b–a–b–a–b–* …. The shape of the core tile requires that three columns of equal orientation are located above and below the core. Continuing our labeling throughout the figure, we have three *b* columns above the core and three *a* columns below (boxes). These sequences deviate from the ideal tiling and represent the structural defects necessarily connected to the core tile if phason planes are not involved. Now consider the effect of the insertion of a phason halfplane into the ε_6-tiling [Fig. 25(b)]. The column sequence above the phason halfplane contains two-neighboring *a* columns followed by an alternating order, while below, the sequence corresponds to the ideal ε_6-structure. Hence, a phason

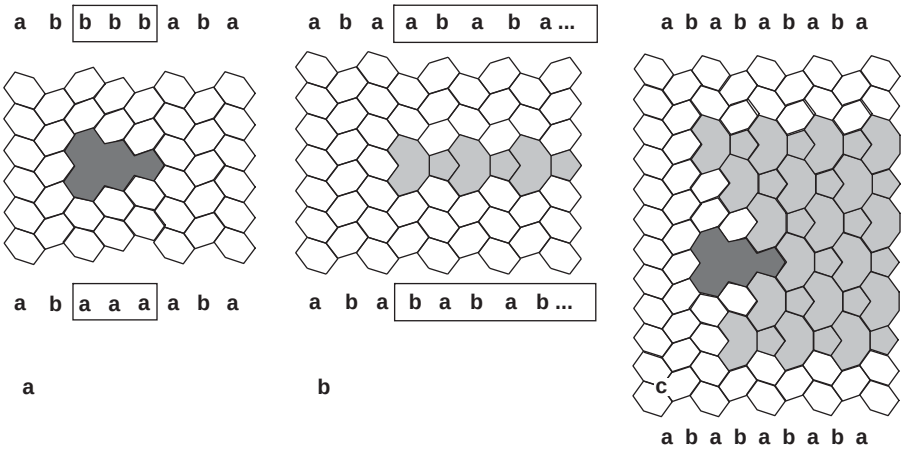

Fig. 25. Hexagon-column arrangement in the ε_6-tiling with the presence of (a) a metadislocation core, (b) a single phason plane, and (c) a combined arrangement of the latter (see text).

halfplane in the lattice has the effect of turning two equally oriented hexagon columns at its termination point into the correct order. Now consider a combination of Figs 25(a) and 25(b) and employ phason halfplanes to turn the columns at the core tile back into the correct order, such that, at a distance from the latter, the column sequence assumes the correct order of the ideal ε_6-structure. Since there are three equally oriented columns on each side of the core tile, six phason halfplanes are required in total to restore the correct order. Finding the required arrangement of phason halfplanes is an interesting geometrical puzzle, the solution of which is shown in Fig. 25(c) and corresponds to a metadislocation with six associated phason halfplanes. The latter is displayed here in compact form, with no hexagon rows between the phason halfplanes. This, however, does not change the principle. Arbitrary distances between the associated phason halfplanes can be chosen: As long as the lateral arrangement of phason halfplanes is maintained, the column sequence corresponding to the ideal ε_6-structure is obtained above and below the metadislocation.

The other metadislocations of the [0 0 1] series can be constructed in full analogy.

4.5.2. Construction via a modified Volterra process

In Section 3.2.1, we have quantified the strain field of a phason plane. This knowledge can be employed to develop a modified Volterra process for the construction of metadislocations. A conventional Volterra process for the construction of an edge dislocation, as employed in structurally simple crystals, involves cutting the crystal along a plane, which ends in the volume of the crystal, inserting or removing an atomic halfplane and subsequently relaxing the structure elastically. The modified Volterra process for metadislocations, on the other hand, comprises the removal of a slab of material of several nanometers in thickness rather than a single atomic halfplane. Subsequently, the gap is filled by another slab of structurally different material, which is closely related to the bulk material.

Fig. 26 illustrates this construction principle for a metadislocation with four associated phason planes in the ε_6-phase. From the ideal ε_6-structure (a), five hexagon halfplanes (gray) are removed (b). Then the gap is filled by four phason halfplanes (c). This slightly overcompensates the gap and hence leads to overlap of the tilings (arrow) since the four phason planes are slightly ''thicker'' than the five hexagon planes. Then the structure is elastically relaxed (d), which leads to some elastically distorted hexagon tiles and a central area that cannot be filled by regular tiles (dotted lines), where the dislocation core is located [cf. Fig. 24(b)]. Note that the overcompensation of the gap means that the net effect corresponds to the insertion of a thin layer of matter.

The Burgers vector of the so-constructed metadislocation is obtained by balancing the removed hexagon against the inserted phason halfplanes, which yields $-5d_\mathrm{h}+4d_\mathrm{p}$. With $d_\mathrm{h} = c$ and $d_\mathrm{p} = c\tau^2/2$ (Section 3.2.1), we obtain the Burgers vector c/τ^3. Analogously, we can construct the metadislocation with six associated phason halfplanes by removing eight hexagon and inserting six phason halfplanes, which yields $-c/\tau^4$. This exactly corresponds to the Burgers-vector length of a

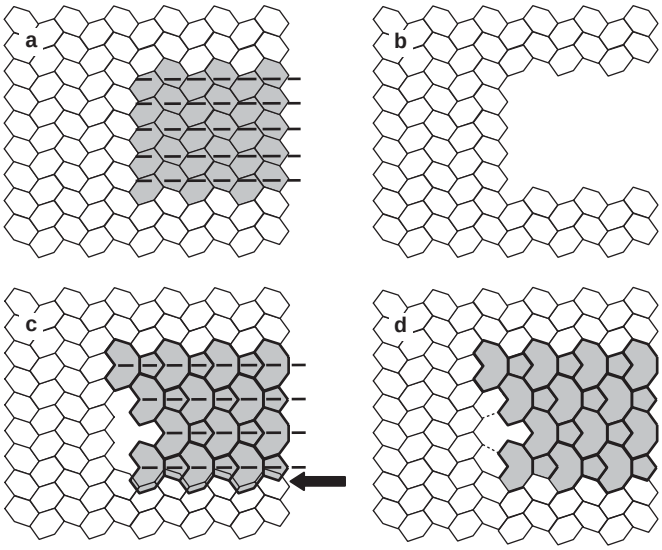

Fig. 26. Construction of a metadislocation with four associated phason halfplanes in the ε_6-phase by a modified Volterra process (see text).

Table 2
Parameters of Eq. (3) for the construction of metadislocations according to a modified Volterra process

p	h	b_p (nm)
2	3	−0.480
4	5	+0.296
6	8	−0.183
10	13	+0.113
16	21	−0.070

The constructed Burgers vector lengths b_p for ε_6- and ε_{28}-Al–Pd–Mn correspond to the experimental values (Table 1).

metadislocation associated to six phason halfplanes. The negative sign is due to the net removal of a thin layer of matter.

The process can be generalized as

$$b_p = c\left(\frac{\tau^2}{2}p - h\right), \tag{3}$$

where h is the number of hexagon halfplanes removed and p is the number of phason halfplanes, the metadislocation is associated with. Each member of the metadislocation series is represented by a doublet of numbers p and h, which constitutes its Burgers vector. The full series of metadislocations as experimentally observed is listed in Table 2 along with the corresponding parameter h.

As discussed in Section 4.4, the experimentally observed metadislocations correspond to double Fibonacci numbers $p = 2, 4, 6, 10, 16$. The numbers of corresponding hexagon planes is also a series of Fibonacci numbers $h = 3, 5, 8, 13, 21$. The construction correctly reproduces the sequence of Burgers vectors lengths, as well as the opposed sequence of numbers of associated phason halfplanes. The sign of the Burgers vectors alternately changes along the series; this is a direct consequence of the construction, as the inserted phason halfplanes alternately overcompensate or partially compensate the removed hexagon halfplanes.

Generally, the modified Volterra process is not limited to Fibonacci and double Fibonacci numbers. In principle, it can be performed with $p/2$ and m being any natural number. According to the large lattice parameters of the ε_6-structure, however, this may create huge lattice mismatches, connected to large Burgers vectors and high elastic energies (see Section 5.2).

4.5.3. Hyperspace projection

Engel and Trebin demonstrated [30] that all ε-phases (referred to as Ξ-phases in their paper) can be constructed by means of a projection formalism on the basis of a three-dimensional hyperspace. The result of the projection is a two-dimensional tiling in the (0 1 0) plane. These authors were able to reproduce the lattices of all ε-phases and their structural defects of phasonic type, that is, phason lines and phason planes.

Engel and Trebin performed an alternative Volterra construction in the three-dimensional hyperspace and a subsequent relaxation in the two-dimensional physical space, which leads to a metadislocation in the corresponding projected ε-phase. Fig. 27 shows a constructed metadislocation with six associated phason

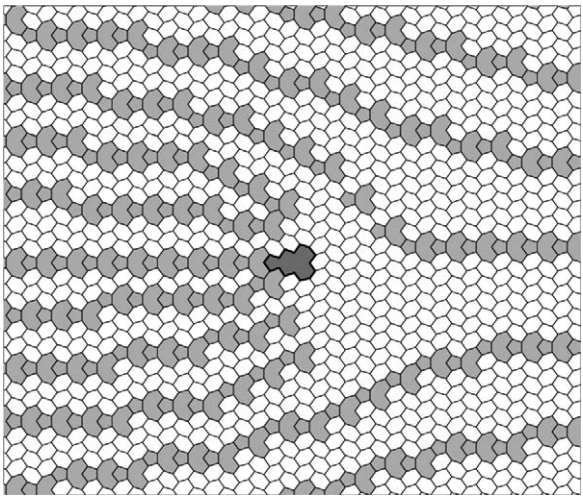

Fig. 27. Metadislocation with six associated phason halfplanes constructed by projection from a five-dimensional hyperspace (courtesy of M. Engel).

halfplanes, which perfectly corresponds to the experimental observations [Fig. 1(a)]. The other members of the metadislocation series (Section 4.4) can be obtained by varying the Burgers vector of the dislocation in hyperspace.

Moreover, the authors showed that there are metadislocation types with minimum total energy within the series. As shown in Table 1, the increasing number of associated phason halfplanes in a series is connected to an opposed sequence of Burgers vector lengths. Both attributes are connected to a certain energy cost – the length of the Burgers vector determines the elastic line energy of the dislocation according to eq. (1), and each phason halfplane is connected to an energy cost proportional to its area. Hence, there necessarily exists a type of metadislocation within the series, which is energetically preferred, that is, for which the elastic line energy and the phason-plane contribution balance to yield a minimum total energy. Engel and Trebin [30] demonstrated that this minimum depends on the ratio of the material-specific elastic constants c_{phon} and c_{phas} for the phonon and phason contribution, respectively. From the experimental fact that metadislocations with six associated phason halfplanes are most frequently observed in ε-Al–Pd–Mn [45], they concluded that $c_{\mathrm{phon}}/c_{\mathrm{phas}} = \tau^{10} \approx 123$.

5. Further aspects

5.1. Metadislocations as carriers of plastic deformation

5.1.1. Metadislocation loops

Dislocations are one-dimensional structural defects representing the boundary of an area over which a given displacement has occurred. Hence, a dislocation line evidently cannot end within an otherwise perfect region of crystal. It must terminate for instance at a free surface, another dislocation line, or a grain boundary [3]. Generally, a dislocation in a perfect and infinite crystal is a closed loop. Isolated segments observed experimentally are parts of loops arbitrarily cut out by the specimen surfaces. All current reports on metadislocations are focused on [0 1 0] segments. However, the above considerations hold for metadislocations as well, and hence the question for the remaining segments closing metadislocation loops has to be approached in order to obtain a complete view.

Fig. 28 is a two-beam bright-field TEM image of a ε_{28}-Al–Pd–Mn single crystal deformed to 8% strain. The micrograph was taken close to the (1 0 3) zone axis, which makes an angle of 90° with the [0 1 0] direction and of 32.5° with the [0 0 1] direction. The image shows a high density of elongated dislocation loops.

The habit planes of the dislocation loops are (0 0 1) planes. The long segments (black arrow) are parallel to the [0 1 0] direction and the short segments (white arrow) to the [1 0 0] direction.

The loops were identified as metadislocations loops [46]. Metadislocations, usually imaged along the [0 1 0] direction [see Fig. 1(a)], correspond to end-on observations of the long [0 1 0] segments. The loops are however completed by additional [1 0 0] segments. The aspect ratio of the [0 1 0] and [1 0 0] segments is very

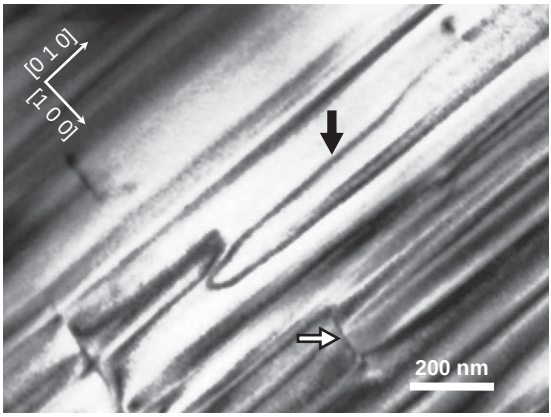

Fig. 28. Elongated dislocation loops in deformed ε_{28}-Al–Pd–Mn viewed along the [1 0 3] zone axis showing long [0 1 0] segments (black arrow) and short [1 0 0] segments (white arrow).

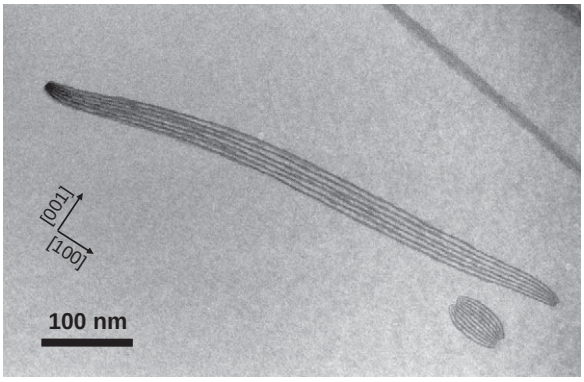

Fig. 29. Metadislocation loops in ε_6-Al–Pd–Mn sharing six and ten associated phason halfplanes.

large: The lengths of the short segments are of the order of 100 nm. This is consistent with the observation that these segments are usually not observed experimentally when images are taken along the [0 1 0] direction.

The loop nature of metadislocations can also be seen in images along the [0 1 0] direction. Fig. 29 is a TEM image of ε_6-Al–Pd–Mn. In the center of the image, two metadislocations are seen, which share six associated phason halfplanes. Obviously, the two metadislocations terminating the phason planes are segments of a loop, which has a habit plane close to (0 0 1). In the lower right corner, a smaller example of a metadislocation loop with ten associated phason planes is seen.

The important fact to note at this point is that, since metadislocation loops have [0 0 1] Burgers vectors, they are pure edge loops, also referred to as prismatic loops [3], that is, they possess only edge-type and no screw type segments.

5.1.2. Mode of metadislocation motion

In the previous section, we have identified metadislocations as loops with (0 0 1) habit planes and [0 0 1] Burgers vectors. They are pure edge loops, which can only expand and contribute to strain, if their segments move by climb. Glide motion of the segments would merely lead to unaltered movement of the loop along its glide cylinder, which does not contribute to strain.

So far, no direct observation of metadislocation motion, for instance by *in situ* tensile tests in a transmission electron microscope, has been reported. Therefore, there is as yet no direct experimental confirmation of whether metadislocations motion takes place by glide or climb. However, besides the strong evidence in favor of climb motion given above, there is also a potent argument against glide.

Consider a new tiling for the description of the phason lines. Fig. 30(a) depicts a metadislocation with six associated phason halfplanes [cf. Fig. 21(b)], but now the two tiles representing the phason lines, the banana and the attached pentagon, are replaced by three irregular hexagons (hatched area). This tiling is not very well suited to represent the structure of the material itself, since the additional vertices do not reflect positions of cluster centers but, on the other hand, it does have the advantage that the movement of every single vertex of the hexagon lattice can be traced during movements of phason lines or metadislocations.

Expressed in this new tiling, Fig. 30(b) shows a glide step (upward movement along [0 0 1]) of the metadislocation by one *c*-lattice constant. The initial position of all tiles is given by the black lattice [which is identical to that in Fig. 30(a)] and the tile representing the initial metadislocation-core position is shaded gray. The final positions are given by the gray lattice. Only those tiles of the final lattice, the position or shape of which is altered, are shown. Clearly, a very high number of

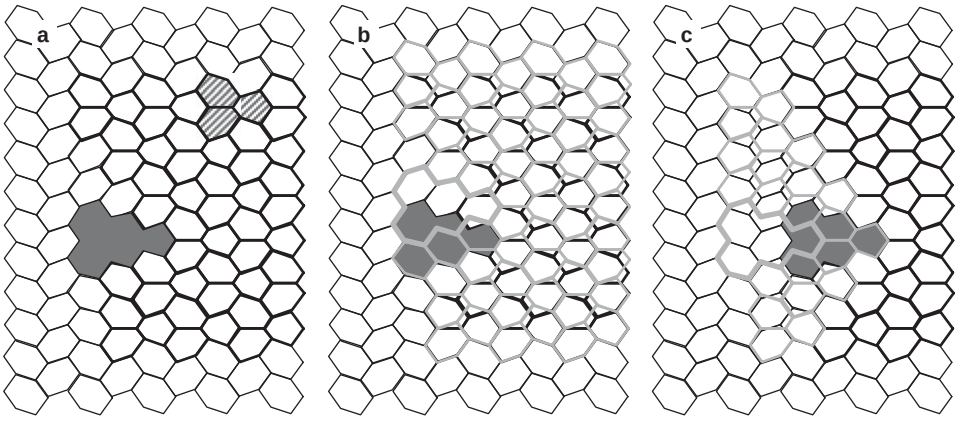

Fig. 30. (a) Metadislocation with six associated phason halfplanes represented by an alternative phason-line tiling (hatched area). (b) Glide step by one *c*-lattice constant. (c) Climb step by one *a*-lattice constant. Initial and final tile positions are shown in black and gray, respectively.

vertex flips is necessary to proceed from the initial to the final position. In fact, the number of vertex flips is approximately proportional to the area of the phason planes and hence diverges in an infinite crystal. This is simply due to the fact that, during glide motion, the associated phason halfplanes have to be dragged through the material along with the core.

Fig. 30(c) shows a climb step (movement along [1 0 0] to the left) of a metadislocation by one *a*-lattice constant. Again, the initial and final tiles are drawn in black and gray lines, respectively. For a climb step, a much smaller number of vertex jumps is necessary. The number of necessary vertex jumps is now limited to the core region and it is now finite, no matter how far the associated phason planes are extended. Since each vertex jump physically represents a number of local atomic movements (Section 3.1.2), climb motion obviously is connected with much less atomic rearrangement than glide motion.

However, long-range atomic transport is nevertheless required for the climb process because it is a non-conservative mode of dislocation motion. Depending on the direction of motion, either atoms or vacancies have to be moved to the dislocation-core region.

The need for atomic transport is not a principal objection against climb motion. Climb motion requires long-range atomic motion no matter whether it takes place in a CMA, a simple metal or even a quasicrystal. For the latter two types of materials, it has been demonstrated that climb takes place and can represent the primary mode of dislocation motion [47–49]. According to the above considerations, the condition for the preference of climb motion in the present material is apparent: Climb should be preferred if long-range atomic transport from or to the metadislocation core is energetically less costly than the numerous local atomic jumps necessary for the movement of the associated phason planes. Since the material is only ductile at high temperatures, where diffusive motion is greatly facilitated, this condition may readily be fulfilled. On the basis of these arguments, it is concluded that metadislocation motion takes place by pure climb [46].

The positive climb process requires long-range transport of matter and consumes vacancies. Continuous deformation will hence lead to a depletion of vacancies and eventually limit the effectiveness of the mechanism. Roitsch et al. [50] showed that besides the metadislocation loops, a second set of dislocations is involved in the deformation mechanism, which compensates the depletion of vacancies. The second set of dislocations consists of loops on (0 0 1) habit planes with [0 1 0] Burgers vectors [51]. These dislocations move by pure negative climb, that is, the expansion of the loops is connected to a production of vacancies, and hence the systems acts as a vacancy source. The interaction of the two loop systems in the form of vacancy exchange ensures continuous operation of the deformation mechanism.

This process, referred to as *complementary climb systems* [52] is conceptually identical to the mechanisms of basal-plane deformation in the hexagonal simple metals Zn and Be [47] and in decagonal Al–Ni–Co [53].

5.2. Elastic energy

In Section 4.5.2, a general construction scheme for metadislocations was introduced, which can be used to calculate the Burgers vector of any type of metadislocation, be it experimentally observed or hypothetical. In this section, we discuss the corresponding elastic strain energies estimated as $E \approx \mu b^2$ (Section 1). With a shear modulus of 30 GPa [54], we obtain about 10^{-9} J/m for a metadislocation with six phason halfplanes, which is comparable to that of a Shockley partial in copper (1.5×10^{-9} J/m). On the other hand, a perfect [0 0 1] dislocation in the ε_6-phase would have a very high elastic energy of 4.7×10^{-8} J/m.

Fig. 31 shows the elastic energies for experimentally observed and hypothetical metadislocations with $p/2$ and h being natural numbers. The grayscale of each box represents the logarithm of the elastic energy of the metadislocation corresponding to a (p, h) doublet, where the darkest gray corresponds to the lowest energy. We find a valley of low-energy values along a line, which is approximately diagonal in Fig. 31. Experimentally observed metadislocations are indicated by boxes with solid white outline. The boxes with broken white outline represent metadislocations that also possess relatively low energy, but which are not observed experimentally (e.g., those with 8, 12, or 14 associated phason halfplanes). In Fig. 32(a), the energies of metadislocations represented by boxed (p, h) doublets in Fig. 31 are shown in a bar graph. The gray bars represent the elastic energy of hypothetical metadislocations and the black bars represent the energy of those experimentally observed. Among the latter, the metadislocation with two associated phason halfplanes apparently has

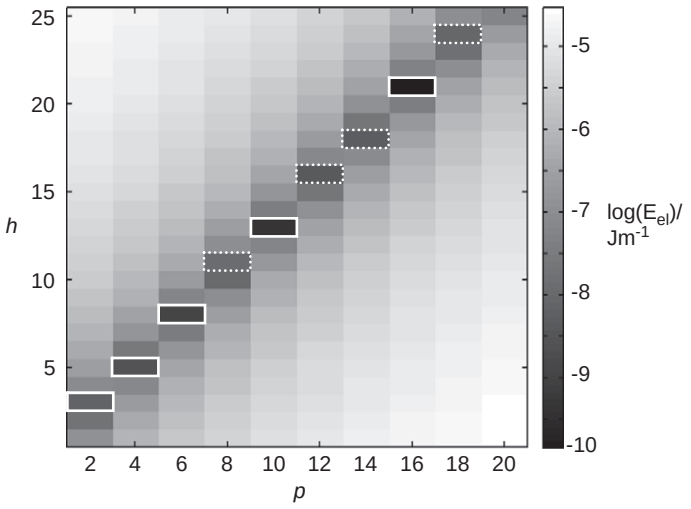

Fig. 31. Elastic strain energy of metadislocations represented by the parameters p and h. Experimentally observed metadislocations are marked by boxes with solid white outline, other hypothetical metadislocations are marked by boxes with broken white outline.

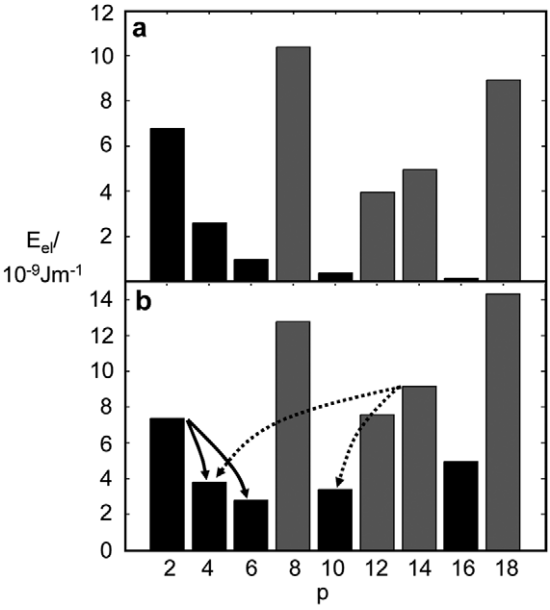

Fig. 32. Bar-graph representation of the energy of metadislocations represented by boxed (p, h) doublets in Fig. 31. Black bars represent the energy of metadislocations that were experimentally observed, gray bars represent other hypothetical metadislocations. (a) Elastic energy contribution. (b) Elastic energy plus fault-plane contribution. The solid and dotted arrows indicate metadislocation splitting and dissociation, respectively.

the highest elastic energy, even exceeding that of the hypothetical metadislocations with 12 and 14 phason planes. The metadislocations with higher numbers of associated phason halfplanes seem to be energetically favorable. This is due to the smaller Burgers vectors of the latter, which directly leads to a smaller elastic line energy. However there are additional energy factors which have not been accounted for in the above consideration, the most evident of which is the cost of the phason halfplanes associated with the metadislocation.

In Fig. 32(b), a corresponding contribution was taken into account, in a first approximation, as an additive energy term proportional to the number of associated phason halfplanes. Due to the lack of experimental data, the energy contribution of the additive term was adjusted such that the total energy reflects the experimental number-density distribution. Metadislocations with six phason planes, which are experimentally most frequently observed, have the lowest energy. Less frequently observed metadislocations with 16 and two phason planes have the highest elastic energies among the experimentally observed metadislocations. We furthermore find that the total energy of metadislocations with 12 and 14 phason halfplanes is very close or even smaller than that of the metadislocation with two phason halfplanes. The fact that they are nevertheless not experimentally observed may be due to reactions: metadislocations with 14 phason halfplanes, for example, may

dissociate into metadislocations with 10 and 4 phason halfplanes. This process is indicated in Fig. 32(b) by dotted arrows. This figure shows that the energy of two metadislocations with 10 and 4 phason halfplanes is lower than that of a metadislocation with 14 phason halfplanes at constant total number of phason halfplanes. On the other hand, metadislocation splitting increases the number of phason halfplanes and is indicated by solid arrows in Fig. 32(b). This process is discussed in detail in Section 5.3.

5.3. Metadislocation reactions

Splitting of perfect dislocations into partials is a phenomenon, which is commonly observed in various crystalline materials. Since metadislocations are partial dislocations *per se*, it may seem surprising that splitting of metadislocations into partials having smaller Burgers vectors is often observed, as well [42,55].

Fig. 33(a) shows a micrograph of two metadislocations associated with ten (1) and six phason planes (2), respectively which are mutually connected by six phason planes. Four phason planes are remaining; one is visible in the upper part of the micrograph and three are visible in the lower part. The situation is schematically depicted in Fig. 33(b) using triangles and lines representing metadislocations and phason planes, respectively. The number of phason planes associated to a metadislocation is denoted in the corresponding triangle, and an arrow indicates the length and direction of its Burgers vector. According to the opposite line directions of the metadislocations in Fig. 33(b), their Burgers vectors are oriented in the same direction and add up to $(0.113-(-0.183))\,\mathrm{nm} = 0.296\,\mathrm{nm}$ (Table 1), which corresponds to the Burgers vector of a metadislocation with four phason halfplanes [Fig. 33(c)]. Therefore, this situation can be interpreted in terms of metadislocation splitting: A metadislocation with four phason halfplanes has split into an equally oriented metadislocation with ten phason halfplanes and an inversely oriented metadislocation with six phason halfplanes. Due to the process of metadislocation splitting, the local elastic strain energy near the metadislocation cores is reduced. According to Frank's rule [40] $b_1^2 > b_2^2 + b_3^2$, where b_1 is the Burgers vector length of the initial dislocation and b_2 and b_3 are those of the products, the splitting is energetically favorable. Fig. 32(a) shows that the elastic energy of a metadislocation with four associated phason halfplanes is higher than the sum of those for metadislocations with six and ten phason halfplanes. On the other hand, splitting requires the creation of six local phason planes. This introduces additional fault-plane energy, which has to be balanced against the energy gain due to splitting.

Fig. 34 shows a more complex case of splitting into three metadislocations. A metadislocation with ten phason halfplanes (1) is connected with two metadislocations, each with six phason halfplanes (2 and 3). Two phason halfplanes leave the metadislocations at the right-hand side (4 and 5). Two additional phason planes seen in the micrograph (6 and 7) are not connected to the metadislocation arrangement. The net Burgers vector of the arrangement is $(-0.113–2\times 0.183)\,\mathrm{nm} = -0.480\,\mathrm{nm}$, which is equal to the Burgers vector of a

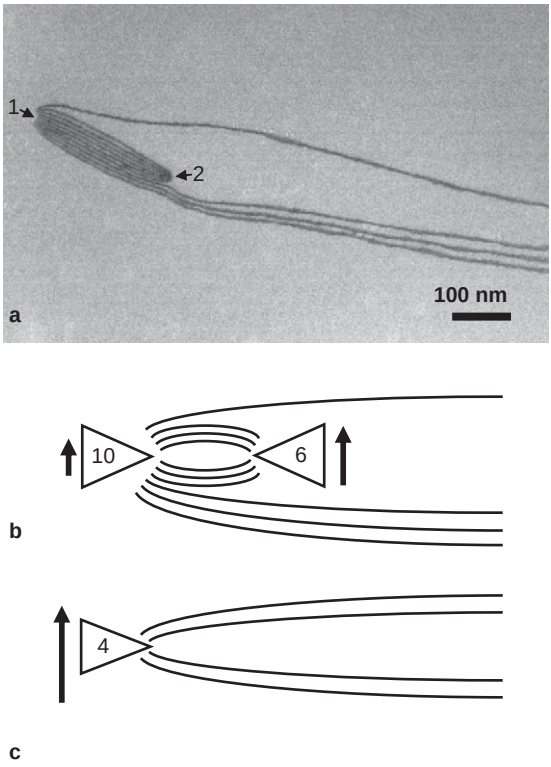

Fig. 33. Two metadislocations associated with ten (1) and six phason halfplanes (2), which are mutually connected by six phason planes. (a) TEM micograph. (b) Schematic representation in terms of triangles and lines, representing metadislocations and phason planes, respectively. The numbers in the triangles denote the number of associated phason halfplanes, the arrows indicate the lengths and directions of the Burgers vectors. (c) Corresponding schematic representation of a metadislocation with four associated phason halfplanes.

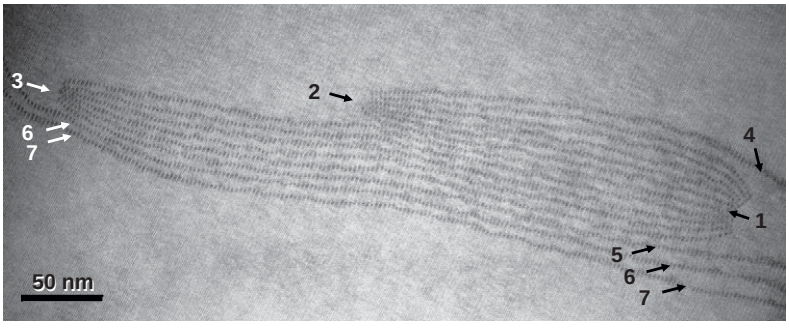

Fig. 34. Complex splitting into three metadislocations (see text).

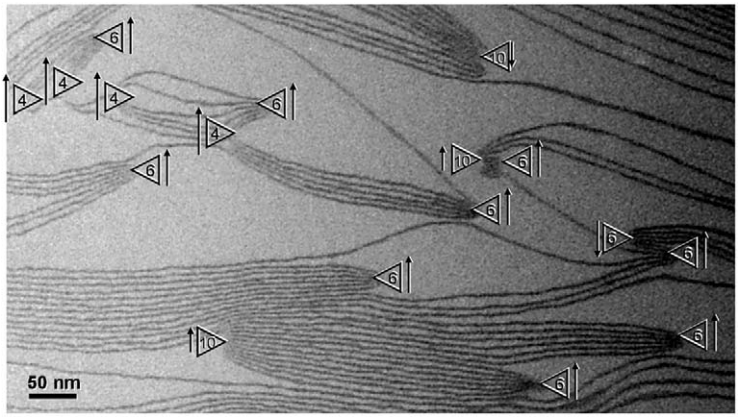

Fig. 35. Complex metadislocation network formed via the mutual interconnection by phason planes. The type and Burgers vector orientation of the metadislocations are indicated.

metadislocation associated with two phason halfplanes. Thus, Fig. 34 shows the splitting of a metadislocation associated with two phason halfplanes into three metadislocations with higher numbers of associated phason halfplanes, but shorter Burgers vectors. Metadislocation splitting into even higher numbers of partials is possible. For example, a metadislocation with two associated phason halfplanes may split into two metadislocations with 16 phason halfplanes, and three inversely oriented metadislocations with 10 phason halfplanes. Two extending phason halfplanes are left and the corresponding net Burgers vector has the length $(2 \times -0.070–3 \times 0.113)\,\text{nm} = -0.480\,\text{nm}$.

Fig. 34 discloses a further unique feature of metadislocations: The associated phason halfplanes can be connected to two or more other metadislocations and accordingly large networks of metadislocations can form. Fig. 35 shows a complex metadislocation network, formed by the mutual interconnection of metadislocations via their associated phason halfplanes. The type and Burgers vector orientation of the metadislocations are indicated. Notably, the Burgers vectors of most metadislocations are oriented in the same direction and add up to 2.781 nm, which corresponds to more than twice the *c*-lattice constant. Hence, metadislocation networks possess large net Burgers vectors, and their movement mediates high amounts of strain [55]. Therefore, they are highly effective means of plastic deformation.

5.4. Metadislocation-based phase boundaries

In some specific cases and orientations, the construction of phase boundaries between ε-phases is trivial since the corresponding lattice planes are congruent. This is the case, for example, for the (1 0 0) phase boundary between the ε_6- and ξ-phase [Fig. 4(d)], or (0 0 1) phase boundaries between any of the orthorhombic

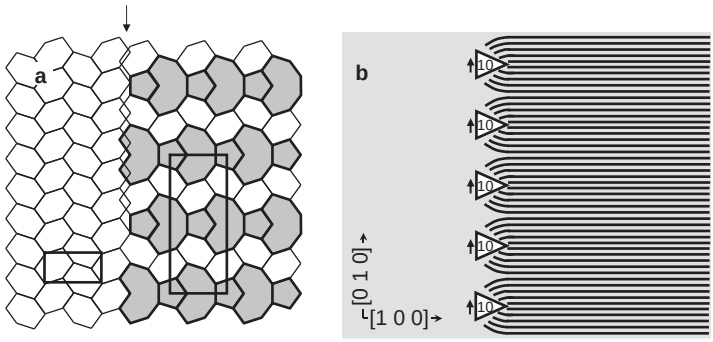

Fig. 36. (1 0 0) phase boundaries between the ε_6-structure and the ε_{28}-structure. (a) Tiling representation of a hypothetical direct boundary. (b) Construction by a periodic stack of identical metadislocations.

ε-phases (except the ξ-phase). The structure of (1 0 0) phase boundaries between orthorhombic ε-phases, however, involves metadislocations.

Let us consider a (1 0 0) phase boundary between ε_6 and ε_{28} phases. The lattice constants differ by a factor $3+\tau$ and the corresponding (1 0 0) planes are congruent over small distances of maximum $4c$ along the [0 0 1] direction [Fig. 36(a)]. In Section 4.2, we have seen that the phason halfplanes associated to a metadislocation can be regarded as a slab of inserted phase of a closely related structure. For example, for a metadislocation in the ε_6-structure, the associated phason halfplanes consist of a slab of ε_{28}-structure in an ε_6-matrix [Fig. 21(b)].

Accordingly, metadislocation arrangements can be used to construct a boundary between ε-phases with and without phason lines as structural elements. The simplest way to construct such a phase boundary is to arrange metadislocations of the same type periodically along the [0 0 1] direction, with all halfplanes stretching out to the same direction as schematically depicted in Fig. 36(b). The strain produced by a regular stack of metadislocations with 10 phason halfplanes can be expressed as $\varepsilon = b_{10}/l_{10}$, where b_{10} is the Burgers vector of a metadislocation with 10 phason planes and l_{10} is its extension in the c-direction. With $l_{10} = 5c(3+\tau)$ according to Fig. 24, we obtain a strain at the interface of $\varepsilon = 0.39\%$. If a phase boundary comprises different metadislocation types, that is different members of the metadislocation series (Section 4.4), the interface strain can be minimized since consecutive members of a metadislocation series have opposite Burgers vectors. For metadislocations of equal line direction (i.e., with phason halfplanes stretching out in the same direction), the interface strain caused by a given type of metadislocation can be compensated by including an appropriate number of other metadislocation types with opposite Burgers vector. Consider, for example, a phase boundary comprising metadislocations with six and ten associated phason halfplanes. Then the interface strain is given by $\varepsilon = (n_6 b_6 + n_{10} b_{10})/l$, where l is the length of the interface perpendicular to the line direction of the constituent metadislocations, and n_i and b_i ($i = 6, 10$), are the number and the Burgers vector length of the corresponding metadislocations, respectively. Since $b_{10} = b_6/\tau$, the

interface stress is fully compensated if,

$$n_{10} = \tau n_6. \tag{4}$$

This relation can, of course, be straightforwardly generalized to the case of more than two metadislocation types in the boundary.

Fig. 37 is a TEM micrograph of a phase boundary between ε_6- (upper left) and ε_{28}-Al–Pd–Mn (lower right). The boundary consists of metadislocations with six (white arrows) and ten (black arrows) phason planes, all extending to the lower right direction and aligned at a slight angle to the [0 0 1] direction. In the area shown, we find, $n_{10}/n_6 = 11/6 = 1.83$, which is close to the value of τ. In the limited image area full compensation according to eq. (4) cannot be fully achieved since τ is an irrational number. The actual interface strain in the micrograph, which comprises an interface length of about 450 nm, amounts to 0.03%.

Note that, for the sake of simplicity, we have argued that the structure in the lower right-hand side of the image is ε_{28}-Al–Pd–Mn. A closer inspection of this area reveals, however, that the phason-line density is lower than for ε_{28}, which indicates that a related phase with larger *c*-lattice constant exists here (Section 3.2.2). However, as long as the area contains a phase with phason lines as structural elements, this does not change the line of argumentation. Naturally, the distances between the metadislocation cores forming the boundary determine the *c*-lattice constant of the corresponding phase.

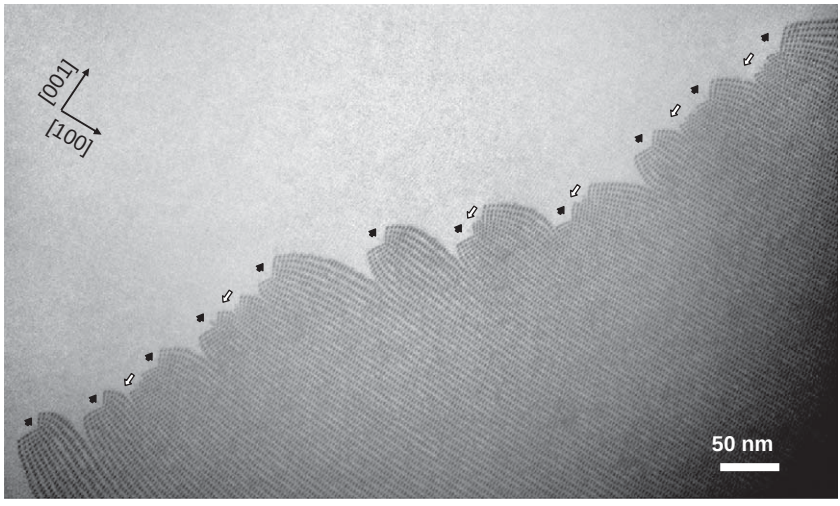

Fig. 37. TEM micrograph of a phase boundary between ε_6-Al–Pd–Mn (upper left) and ε_{28}-Al–Pd–Mn (lower right). The boundary consists of metadislocations with six (white arrows) and ten (black arrows) associated phason halfplanes.

6. Metadislocations in different crystal structures

The metadislocations discussed in the previous chapters were described in terms of the structure of orthorhombic ε-type phases, such as ε_6- and ε_{28}-Al–Pd–Mn. Indeed this particular type of metadislocation is critically related to characteristic structural features such as the distances and angles between the constituting clusters. Orthorhombic ε-phases derive from the basic binary Al_3Pd structure type [56], which has extensions into numerous ternary systems. Besides the system Al–Pd–Mn discussed above, in which the ε-phases have a stability range of up to about 6 at.% Mn [57], such phases also exist in the systems Al–Pd–Fe and Al–Pd–(Rh, Re, Ru, Co, Ir) ([32] and references therein). Furthermore, an isostructural phase exists in the system Al–Rh [58], which extends into the ternary systems with Cu and Ni ([32] and references therein). In all these systems, the structural conditions are such that metadislocations potentially exist. So far, their existence was experimentally confirmed in Al–Pd–Mn and, for Fe contents below about 3 at.%, in Al–Pd–Fe [59]. In Al–Rh–Ni, phason lines and phason planes were observed by Sun et al. [60]. To the best of our knowledge, corresponding microstructural investigations have not been undertaken as yet in all other ε-phase forming systems.

In the following section, it is shown that metadislocations exist is a wide range of CMAs other than ε-phases. To start with, we discuss metadislocations in monoclinic ε-phases. These are closely related to the orthorhombic ε-phases, and so are their metadislocations. In Sections 6.2 and 6.3, we proceed to structures more distantly related, for which the existence of metadislocations was theoretically predicted [46]. We show that metadislocations indeed exist in these systems, albeit in a different form than expected. In particular, the associated defects are not phason planes but different types of planar fault, which leads to a more general view of the characteristic features of metadislocations.

6.1. Metadislocations in ξ- and monoclinic ε-phases

Fig. 38(a) is a transmission electron micrograph of a metadislocation in $Al_{72.0}Pd_{22.8}Fe_{5.2}$. The metadislocation core is located in the lower left part of the image. It is associated with three planar defects extending to the upper right (dark contrast), which can be identified as phason planes.[2] The surrounding host structure is formed by a parallel arrangement of flattened hexagons and hence can be identified as a ξ-phase [Fig. 4(c)]. In the basis of the ξ-structure, the associated phason halfplanes are oriented approximately parallel to the (0 0 1) planes. Fig. 38(b) shows a tiling representation of the metadislocation. The host structure is given by parallel hexagons, representing the ξ-phase seen along the [0 1 0] direction. A Burgers circuit in terms of edges of the hexagon tiles around the

[2] Note that here the term ‘‘phason plane’’ is used in a more general sense than introduced in Section 3.1. The term is now used to refer to any lineup of phason lines that, to the eye, forms a continuous planar arrangement.

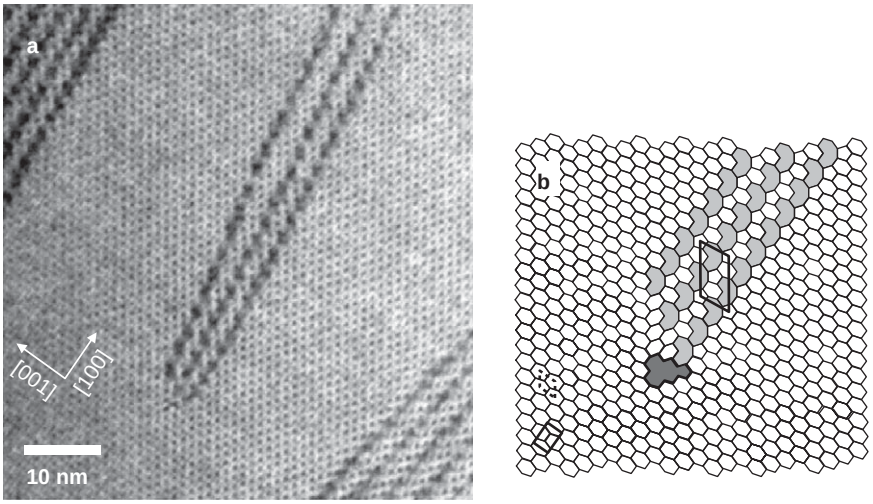

Fig. 38. Metadislocation in $Al_{72.0}Pd_{22.8}Fe_{5.2}$ associated with three planar defects in a ξ-host structure. (a) TEM micrograph. (b) Corresponding idealized tiling representation.

metadislocation core (Section 4.3) reveals a closure failure of $1/2\tau^4[1\,0\,1]$ in terms of the ξ-lattice, which corresponds to the metadislocations Burgers vector. The Burgers vector length is 0.179 nm.

The tiling representation in Fig. 38(b) is slightly idealized: the phason lines were ordered such that the phason planes are parallel to the (0 0 1) planes of the ξ-lattice. The group of phason planes can then be identified as a slab of monoclinic $(1, -1)$ phase (where the nomenclature of Heggen et al. [31] is used). The corresponding unit-cell projection is shown in Fig. 38(b). Comparing the tiles representing the metadislocation cores in the ξ-structure and of the metadislocation with six associated phason halfplanes in the ε_6-structure [Figs 38(b) and 20, respectively], one sees that the same polygon is used. In both cases the Burgers vector length, in terms of the edge length a_0 of the hexagons, is given by a_0/τ^3. The difference in Burgers vector length for ξ-Al–Pd–Fe and ε_6-Al–Pd–Mn (0.179 and 0.183 nm, respectively) is merely due to the slightly different lattice parameters of these phases. Accordingly, one expects that the metadislocation core structures in these phases are very similar.

Fig. 39(a) is a TEM micrograph of a metadislocation in a sample region of $Al_{72.0}Pd_{22.8}Fe_{5.2}$ with a high density of phason planes. The host structure can be identified as the monoclinic $(1, -1)$ variant of the ε_{22}-structure with additional local modulations [31]. The metadislocation core terminates three phason planes extending to the upper right part of the image. Below the core, a small region showing parallel flattened hexagons, that is of ξ-structure, is observed. The phason planes surrounding the metadislocation core are marked by white lines as a guide to the eye. Comparing Figs 38(b) and 39(b), one sees that for these metadislocations

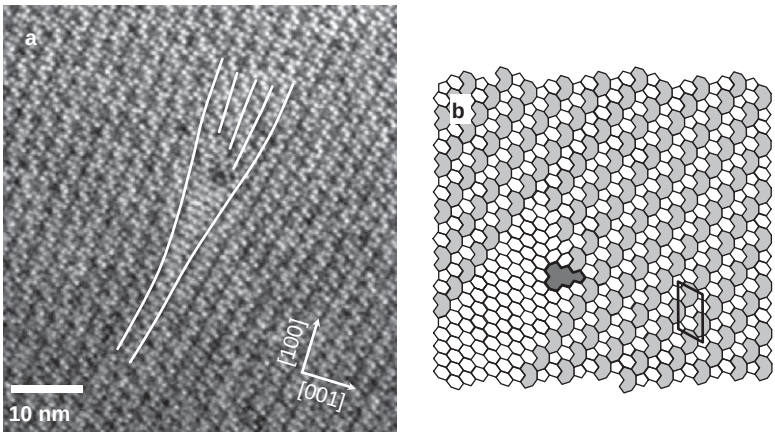

Fig. 39. Metadislocation in $Al_{72.0}Pd_{22.8}Fe_{5.2}$ in a sample region with a high density of phason planes. The host structure is the monoclinic $(1,-1)$ variant of the ε_{22}-structure. (a) TEM micrograph. (b) Corresponding idealized tiling representation. The crystallographic directions are indexed in the basis of the ξ-structure.

there is a complementarity similar the one found for metadislocations in the ε_6- and ε_{28}-structures (Section 4.2).

In complete analogy with the case of metadislocations in ε_6-Al–Pd–Mn (Section 4.4), series of metadislocations with other numbers of associated phason halfplanes can be constructed. Fig. 40 is a transmission electron micrograph showing two metadislocations in a sample region similar to that of Fig. 39(a). The left metadislocation is associated with five phason halfplanes and that on the right with eight phason halfplanes. In the areas directly below both metadislocation cores, regions of ξ-structure are identified.

The tiling representation of metadislocations with five associated phason halfplanes is shown in the ξ-structure [Fig. 41(a)] and in a region with a high density of phason planes [Fig 41(b)]. The tile representing the metadislocation core is identical in both cases and corresponds to that of a metadislocation with 10 associated phason planes in ε_6-Al–Pd–Mn [Fig. 24(a)]. The Burgers vector is $-1/2\tau^5[1\,0\,1]$ in terms of the basis of the ξ-lattice, corresponding to a length of a_0/τ^4. Analogously, metadislocations with one, two, and eight associated phason halfplanes can be constructed. The corresponding Burgers vectors are given in Table 3.

Thus, one can construct a sequence of metadislocations with increasing numbers of associated phason halfplanes. As in ε_6-Al–Pd–Mn, the Burgers vector lengths of the metadislocations in the sequence are related by factors of $-\tau$, and with increasing number of associated phason halfplanes, the Burgers vector length decreases. However, in the ξ-structure, the sequence of associated phason halfplanes is 1, 2, 3, 5, 8, … and it follows a Fibonacci sequence, whereas in ε_6 the sequence is 2, 4, 6, 10, 16, …, which follows a series of twice the Fibonacci numbers.

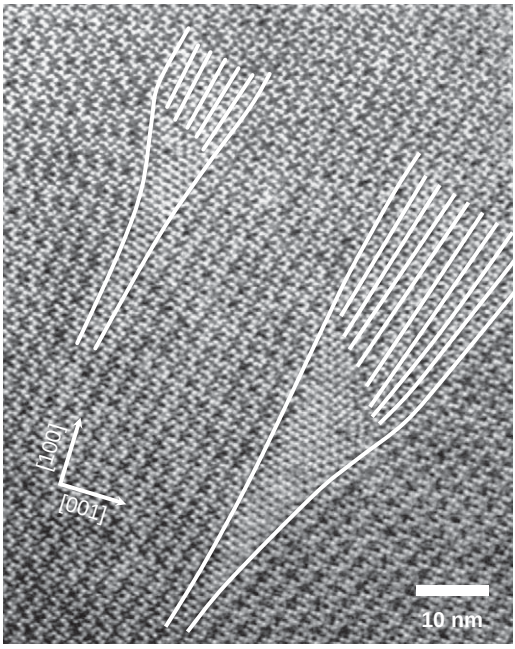

Fig. 40. Two metadislocations in a sample region similar to that of Fig. 39(a). The left metadislocation is associated with five phason halfplanes and the right one with eight phason halfplanes. The crystallographic directions are indexed in the basis of the ξ-structure.

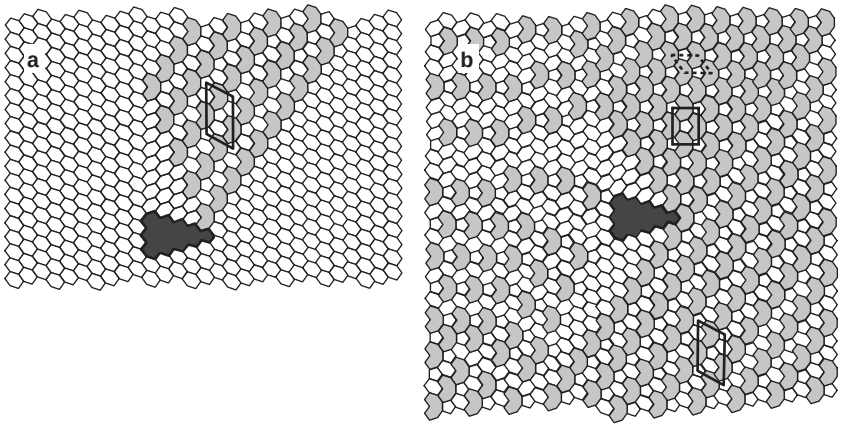

Fig. 41. Tiling representation of metadislocations with five associated phason halfplanes. (a) In the ξ-structure. (b) In a region with a high density of phason planes.

Table 3
Metadislocations in the ξ-structure

N	$\vec{b}$	b/a_0	b (nm)
1	$+1/2\tau^2[1\,0\,1]$	$+1/\tau$	+0.470
2	$-1/2\tau^3[1\,0\,1]$	$-1/\tau^2$	−0.290
3	$+1/2\tau^4[1\,0\,1]$	$+1/\tau^3$	+0.179
5	$-1/2\tau^5[1\,0\,1]$	$-1/\tau^4$	−0.111
8	$+1/2\tau^6[1\,0\,1]$	$+1/\tau^5$	+0.068

Note: N, number of associated phason halfplanes; $\vec{b}$, Burgers vector in the basis of the ξ-structure; and b, Burgers vector length in terms of hexagon edge length a_0 and absolute value.

The tiling representation of the associated phason halfplanes in Fig. 41 is different. While in Fig. 41(a) the respective area corresponds to a slab of monoclinic $(1,-1)$ phase, the area in Fig. 41(b) corresponds to the orthorhombic ε_{16} phase. This is merely a matter of representation and does not change the construction principle since phason lines can freely move along the [0 0 1] direction via local atomic jumps (Section 3.1.2).

There are obvious similarities between the metadislocations introduced in this section and those discussed before (Sections 4 and 5). However, a clear criterion to discriminate between the two types can be fixed via the structure type of the surrounding material: The metadislocations previously discussed form in orthorhombic structures like ε_6 and ε_{28}, while those introduced in this section form in structures that are monoclinic *or* possess an alternative monoclinic representation. The latter holds for ξ and ε_{16}, both of which can be described in terms of a monoclinic unit cell having half the volume of the orthorhombic alternative. Therefore, in the following, we refer to the previously discussed metadislocations and those introduced in this section as metadislocations in orthorhombic and monoclinic structures, respectively.

6.2. Metadislocations in Taylor phases

Taylor phases are based on binary Al_3Mn, the structure of which was firstly solved by Taylor [22]. The phase has ternary extensions into several systems (e.g., Pd, Ni, Fe) [61], all of which are referred to as Taylor- or T-phases. Binary Al_3Mn is a high-temperature phase, transforming to a triclinic variant below about 900 °C [62]. Addition of the third element Pd, Fe, or Ni stabilizes the T-phase, and hence the existence ranges of the ternary extensions extend to much lower temperatures.

T-Al–Mn–Pd has an orthorhombic structure with lattice parameters $a = 1.47$ nm, $b = 1.25$ nm, $c = 1.26$ nm [22,23,63], and 156 atoms per unit cell. Fig. 42(a) shows a projection of its unit cell along the [0 1 0] direction. The structure can be represented by a tiling consisting of flattened hexagons. Like the phase ε_6-Al–Pd–Mn, the T-phase structure is described in terms of tiles arranged in rows of

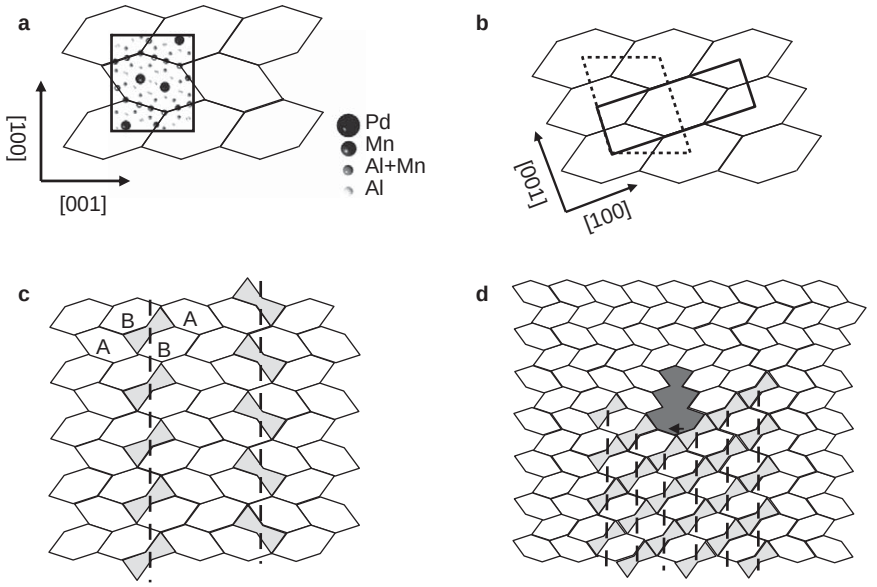

Fig. 42. (a) Projection of the unit cell of T-Al–Mn–Pd along the [0 1 0] direction and corresponding tiling description. (b) Tiling representation of the R-phase. (c) Phason lines (gray) forming (0 0 1) planes (broken lines). (d) Metadislocation with six associated phason halfplanes in the T-phase. The dark-gray tile represents the metadislocation core.

alternating orientation. Atomic columns containing Mn and Al are located at the vertices; edges and columns containing predominantly Pd and Mn are located in the hexagon centers. Fig. 42(b) represents the tiling of the R- or Robinson phase, which is structurally closely related to the T-phase [63,64] and can be represented by parallel rows of flattened hexagons. The dashed rectangle represents the orthorhombic unit cell. A monoclinic unit cell (dotted parallelogram) can, however, also be defined and can be interpreted in terms of a T-phase orthorhombic cell ''sheared'' along the [0 0 −1] direction. Fig. 42(c) shows phason lines (gray tiles) in a T-phase structure [65]. A single phason line exchanges the orientation of neighboring hexagon rows from B,A to A,B. Individual phason lines can line up along the [1 0 0] direction and form (0 0 1) phason planes [Fig. 42(c)]. As shown in Ref. [46], metadislocations in the T-phase can be constructed in full analogy with the ε-phases (Section 4.5). Fig. 42(d) shows a metadislocation in the T-phase with six associated phason halfplanes. The dark-gray tile represents the core of the metadislocation. Its Burgers vector is $\vec{b} = -c/\tau^4[0\,0\,1]$, which exactly corresponds to that of a metadislocation in ε_6-Al–Mn–Pd. Like for metadislocations in ε-type structures, a sequence of metadislocations with 2, 4, 6, 10, and 16 associated phason halfplanes can be constructed.

Plastically deformed single-crystalline T-Al–Mn–Pd samples exhibit a high density of metadislocations with a [0 1 0] line direction terminating planar defects with (1 0 0) habit planes. Fig. 43 shows a HAADF image of a (1 0 0) planar defect,

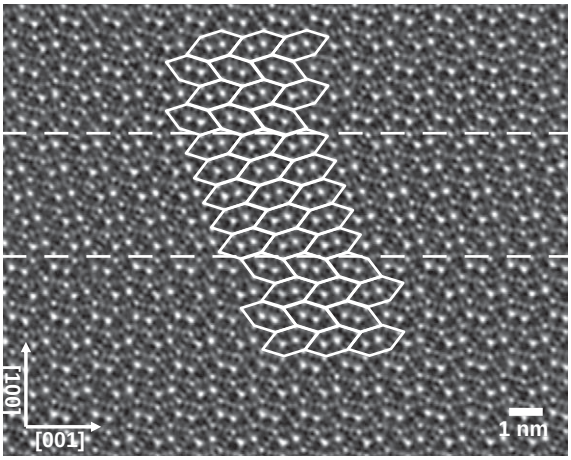

Fig. 43. High-resolution HAADF micrograph of a (1 0 0) planar defect in edge-on orientation located between the dashed lines, and superposed tilings for the T- and R-phases.

located between the dashed lines, in edge-on orientation. Bright dots correspond to atomic columns preferentially occupied by heavier atoms, that is, mainly Pd and Mn, and the micrograph can directly be compared to the tiling representation of T-Al–Mn–Pd (Fig. 42). In the upper and lower parts, the micrograph can be matched with the tiling representing the ideal T-phase, while the central part between the dashed lines requires a parallel arrangement of flattened hexagons, which corresponds to a slab of R-phase.

Fig. 44(a) shows a HAADF micrograph of a metadislocation in T-Al–Mn–Pd. The planar defect at the right-hand side, that is the slab of R-phase, is visible between the dashed lines. The metadislocation core is indicated by a polygon, which directly corresponds to the predicted polygon representing a metadislocation core [cf. Fig. 42(d)]. In addition three phason defects are visible at the left-hand side of the metadislocation core. Fig. 44(b) shows a full tiling representation of the defect.

It is obvious that the core structure of the experimental [Figs 44(a) and 44(b)] and predicted [Fig. 42(d)] metadislocation are represented by the same tile. Hence they both have the same Burgers vector. However, they are connected to different types of planar defects. While the metadislocation in Fig. 42(d) is associated with six phason planes, the metadislocation in Fig. 44(b) is associated with a slab of R-phase. The phason elements on the left-hand side of the metadislocation core change the stacking sequence of the ideal T-phase structure A,B,A,B,A to a sequence A,A,A,B,B. These additional defects are required to accommodate the symmetrical metadislocation core into the structure and have to move along with the latter. In other words, the three phason lines act as escort defects to the metadislocation core, which move ahead and clear the way for the latter. Upon movement, the metadislocation locally transforms the T-phase structure, leaving a slab of modified R-phase in its wake. Different types of metadislocations in T- and R-phase structures and their modes of motion are discussed in Section 6.4.

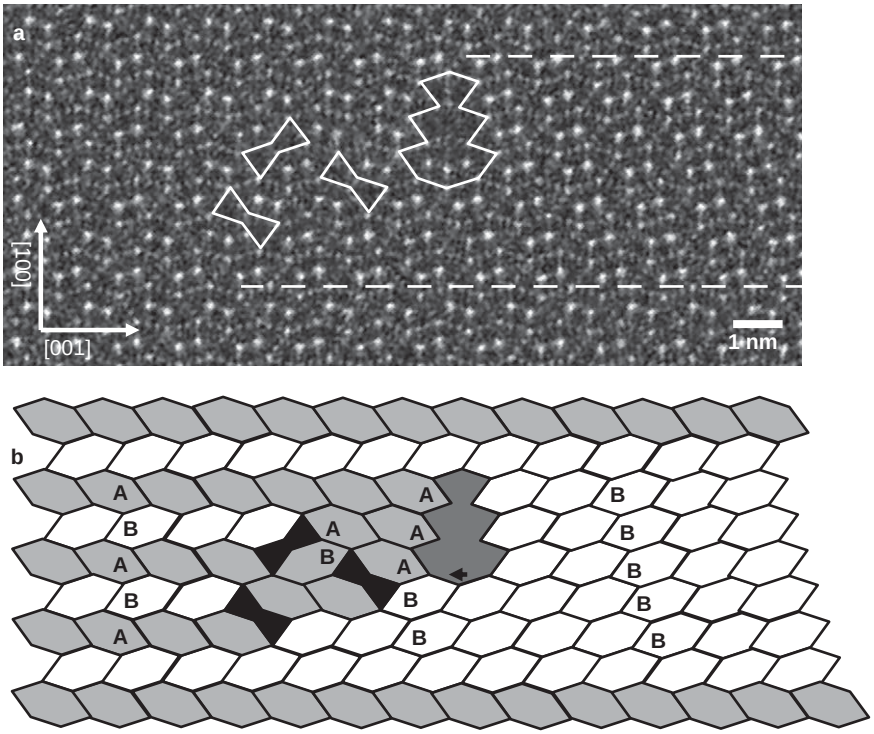

Fig. 44. Metadislocation in T-Al–Mn–Pd. (a) High-resolution HAADF micrograph. Dashed lines indicate the location of the slab of R-phase. The metadislocation core and three phason lines are highlighted. (b) Tiling representation of the defect.

6.3. Metadislocations in orthorhombic $Al_{13}M_4$ phases

The group of orthorhombic $Al_{13}M_4$ phases comprises *o*-$Al_{13}Co_4$ and *o*-$Al_{13}Fe_4$. *o*-$Al_{13}Co_4$ is an orthorhombic phase with space group $Pmn2_1$ and lattice parameters $a = 0.82\,\text{nm}$, $b = 1.23\,\text{nm}$ and $c = 1.45\,\text{nm}$ [66]. The main structural features are pair-connected pentagonal-prismatic channels extending along the [1 0 0] direction [66]. Within the (1 0 0) plane, the structure can be matched by a tiling consisting of regular pentagons and rhombs [46], as depicted in Fig. 45(a) where the rhombs are arranged in an antiparallel manner. The edges of the tiles correspond to atomic columns, which are predominately occupied by cobalt atoms. The orthorhombic unit cell is superimposed onto the tiling.

The structure of monoclinic *m*-$Al_{13}Co_4$ is homeotypic to that of monoclinic $Al_{13}Fe_4$ and structurally closely related to that of *o*-$Al_{13}Co_4$ [66–69]. The tiling description of *m*-$Al_{13}Co_4$ [Fig. 45(b)] is characterized by a parallel arrangement of the pentagon and rhomb elements. Phason lines [light-gray tiles in Fig. 45(c)] can be constructed by introducing an additional tile, a boat-shaped heptagon. The phason lines can arrange along the [0 1 0] direction, forming (0 0 1) planes [Fig. 45(c)].

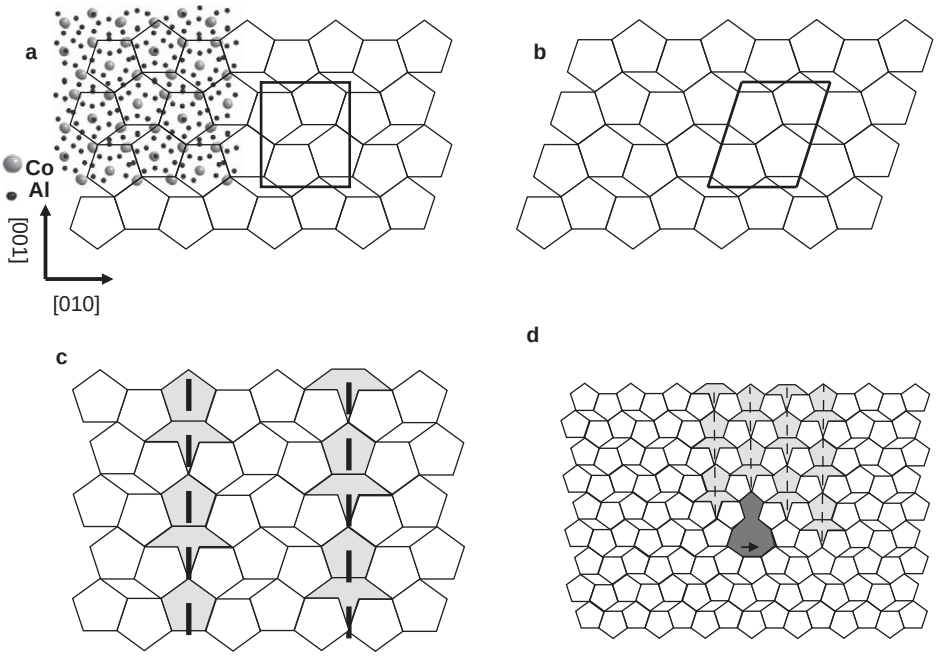

Fig. 45. (a) Projection of the unit cell of the o-$Al_{13}Co_4$ phase along the [1 0 0] direction and corresponding tiling description. (b) Tiling representation of the m-$Al_{13}Co_4$ phase. (c) Phason lines (gray) forming (0 1 0) planes (broken lines). (d) Metadislocation with four phason planes. The dark-gray tile represents the metadislocation core.

The phason planes can be used to construct a new type of metadislocation in $Al_{13}M_4$ [46]. Fig. 45(d) shows a hypothetical metadislocation with four associated phason planes. Its core is given by the dark-gray tile. The Burgers vector can be calculated as $\vec{b} = b/\tau^3[0\,1\,0]$. In analogy with the case of ε-type and T-phase structures, a sequence of metadislocations can be constructed.

In experimental investigations of plastically deformed $Al_{13}Co_4$ crystals, planar faults possessing (0 1 0) habit planes are not observed and phason planes, as depicted in Fig. 45(c), are not present. Instead, planar defects with (0 0 1) habit planes are found in high density [70] [Fig. 46(a)]. In the TEM micrograph, the planar defects are seen as parallel stripes covering the entire image area. The arrowhead in Fig. 46(a) points at a metadislocation terminating a planar defect. Most of the observed metadislocation line directions are parallel to [1 0 0]. Contrast-extinction experiments reveal that the metadislocation Burgers vectors and the displacement vectors of the associated planar defects are both parallel to the [0 1 0] direction. This shows that metadislocation glide on (0 0 1) planes is the basic mechanism of plastic deformation in $Al_{13}Co_4$. Fig. 46(b) is a HAADF micrograph of planar defects in edge-on orientation (arrows). Bright dots in the micrograph correspond to atom columns that are preferentially occupied by cobalt atoms and can be matched by the o-$Al_{13}Co_4$ tiling. As in the T-phase, the planar defects are

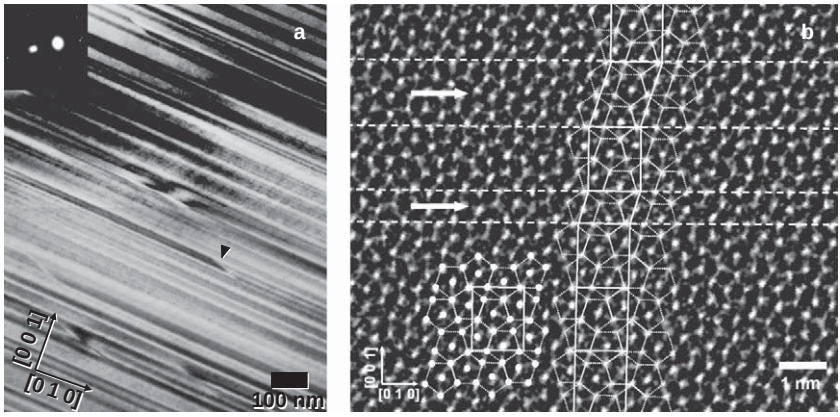

Fig. 46. (a) Bright-field TEM micrograph showing a high density of planar defects (parallel stripes) in a deformed *o*-$Al_{13}Co_4$ sample. The arrowhead points at a metadislocation terminating a planar defect. (b) High-resolution HAADF micrograph of planar defects in edge-on orientation (arrows) with superposed tilings for the *o*- and *m*-$Al_{13}Co_4$ structures.

slabs of the structurally related phase represented by a parallel tile arrangement. In this case, the latter correspond to the *m*-$Al_{13}Co_4$ phase.

Fig. 47(a) shows a high-resolution TEM micrograph of a metadislocation (central part of the image) in end-on orientation. The metadislocation terminates a (0 0 1) planar defect, that is, a structurally modified slab of *m*-$Al_{13}Co_4$ extending to the right-hand side of the image. The outline of the *o*-$Al_{13}Co_4$ unit cells is depicted by white rectangles. Rhomboids representing the unit cell of the monoclinic $Al_{13}Co_4$ phase are used to cover the structurally modified slab. Figs 47(b) and 47(c) show tilings corresponding to the arrangement of unit cells of *o*- and *m*-$Al_{13}Co_4$. In Fig. 47(b), the metadislocation-core tile is directly obtained as the area that cannot be filled using the regular tiles for *o*- or *m*-$Al_{13}Co_4$ and it is asymmetric. The core can be made mirror-symmetric by slight rearrangement of the tiles and the addition of an escort defect. Which tiling corresponds to the real structure cannot be decided on the basis of the available TEM micrographs. Both solutions however show that, again, this metadislocation differs from the predicted form [Fig. 45(d)] in the way it is associated with planar defects. It is not associated with phason planes but with a slab of a monoclinic *m*-$Al_{13}Co_4$ phase. However, the core structures of both metadislocations are described by tiles corresponding to the same Burgers vector.

6.4. Comparison of different types of metadislocations

In this section, different types of theoretically predicted and experimentally observed metadislocations are compared and their mode of motion is analyzed. Fig. 48 depicts the experimentally observed metadislocations in orthorhombic and monoclinic ε-phases, $Al_{13}M_4$- and T-phases. Their cores are represented by

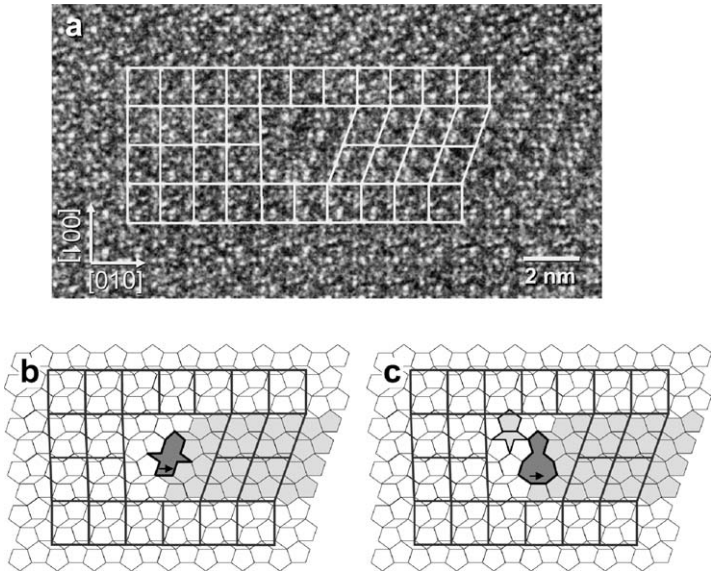

Fig. 47. Metadislocations in o-$Al_{13}Co_4$. (a) High-resolution TEM micrograph. The metadislocation terminates a (0 0 1) slab of m-$Al_{13}Co_4$ extending to the right-hand side of the image. White rectangles and rhombs represent the unit cell of the o- and m-$Al_{13}Co_4$ phases, respectively. Tilings of metadislocation core structures (b) without and (c) with escort defect. Both are compatible with the experimental image.

dark-gray polygons and their associated planar defects are shown in light gray. Their Burgers vectors are indicated by arrows. Figs 48(a) and 48(b) show metadislocations of the ε- and ξ-type, respectively. They are associated to six and three phason planes, which have (0 0 1) habit planes. The metadislocations move along the $\pm[1\,0\,0]$ direction (cf. Section 5.1.2). Their Burgers vectors are $1/\tau^4[0\,0\,1]$ and $1/2\tau^4[0\,0\,1]$, that is, the ε_6-type metadislocation moves by pure climb and, assuming movement in the habit plane of the associated phason halfplanes, the ξ-type metadislocation moves by a mixed glide and climb process. Fig. 48(c) shows a metadislocation in o-$Al_{13}Co_4$, which is associated to a (0 0 1) planar defect, that is, a slab of m-$Al_{13}Co_4$. This metadislocation moves along the $[0\,-1\,0]$ direction, which is parallel to its Burgers vector, that is, the $Al_{13}Co_4$-type metadislocation moves by pure glide. The same holds for the metadislocation in T-Al–Mn–Pd [Fig. 48(d)]. Upon movement, a slab of a modified phase is created in both cases. This mechanism resembles that of a shear transformation as observed in Laves phases, where moving dislocations introduce structurally modified slabs [71–73]. In the C14 Laves phase Cr_2Hf, for instance, dislocation motion creates a slab of the cubic C15 Laves phase within the C14 matrix [73]. The analysis of defect structures in T- and $Al_{13}M_4$-phases reveals that metadislocations are not necessarily associated to phason planes, but to a local structural transformation in a more general sense. In the case of T- and $Al_{13}Co_4$, the metadislocation mediates the local transformation to the closely related monoclinic R- and m-$Al_{13}Co_4$-phase, respectively.

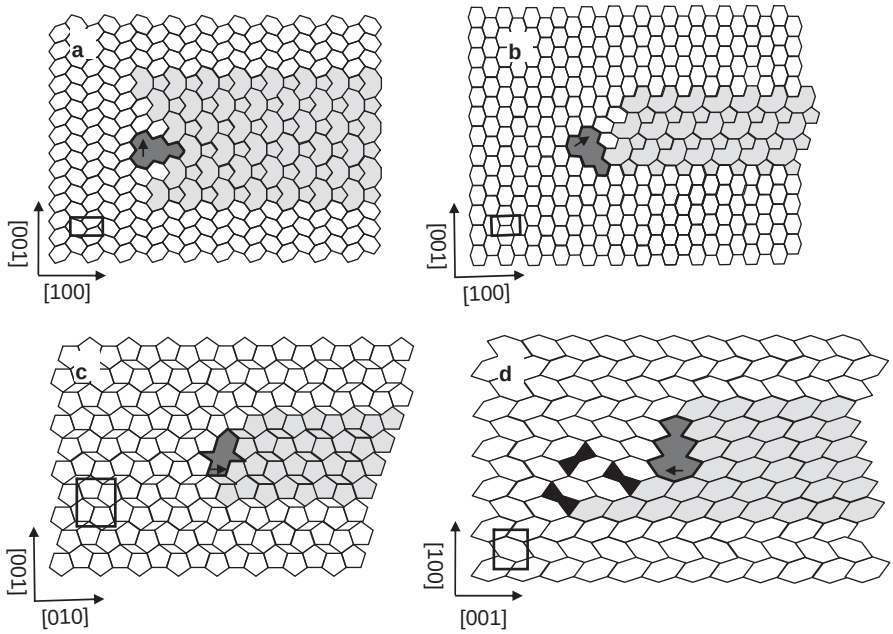

Fig. 48. Tiling representation of experimentally observed metadislocations in (a) orthorhombic ε-phases, (b) monoclinic ε-phases, (c) $Al_{13}M_4$- and (d) T-phases. The Burgers vectors are indicated by arrows (not to scale).

This generalization also includes the metadislocations in orthorhombic and monoclinic ε-phases, since the group of inserted phason halfplanes can, as demonstrated in Section 3.2.2, also be regarded as a slab of related ε-phase. In these terms, the metadislocation in the ε_6-phase [Fig. 21(b)] mediates the local transformation from ε_6 to ε_{28}, and in the complementary situation, the metadislocation in the ε_{28}-phase [Fig. 21(a)] mediates the local transformation from ε_{28} to ε_6. Similarly, as already discussed in Section 6.1, the metadislocations in the monoclinic ε-phases mediate local transformations from ξ to any of the ε-phases possessing phason lines as structural elements, or vice versa for the complementary case.

Fig. 49 presents different types of metadislocations with and without phason planes and demonstrates the generality of the construction principles. Figs 49(a)–49(d) show metadislocations in the T- and R-phase and Figs 49(e)–49(h) show metadislocations in the ε_6- and ξ-phase, respectively. On the left [Figs 49(a), 49(c), 49(e), and 49(g)], metadislocations with associated phason halfplanes are shown; on the right [Figs 49(b), 49(d), 49(f), and 49(h)], metadislocations associated with slabs of a structurally related phase (i.e., the R- and ξ-phases) are shown. Obviously, for this particular Burgers vector (as represented by the core tile) the number of associated planar defects depends on the host structure. In the present example, for the orthorhombic hosts ε_6 and T we find six associated planes (phason planes for ε_6 and layers of R-phase for T) and generally, for the members of the corresponding

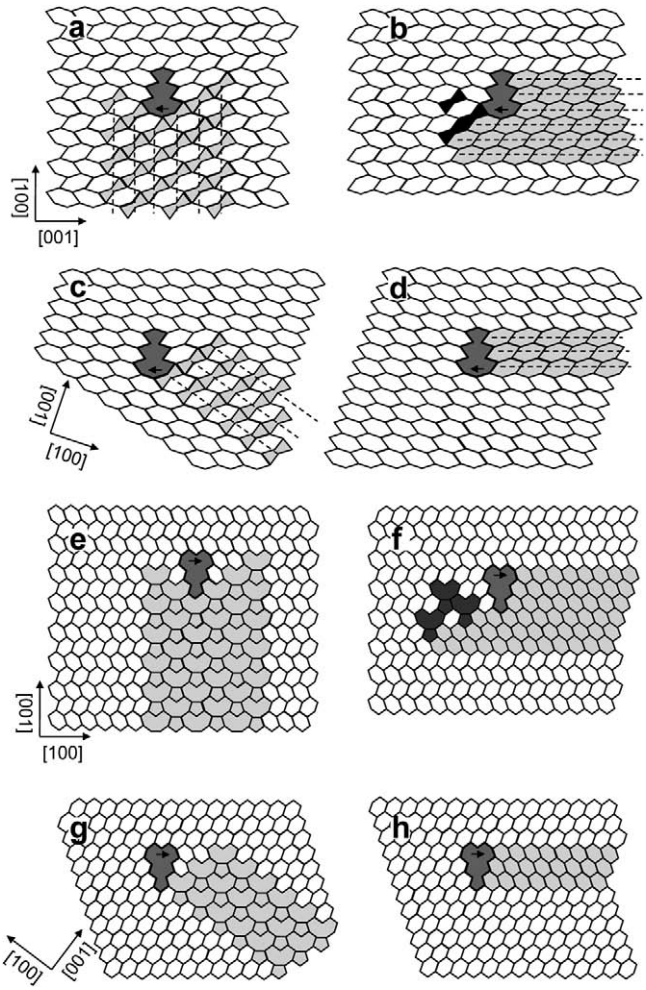

Fig. 49. Tiling representation of various possible metadislocations arrangements in different host structures. (a, b) In the T-phase. (c, d) In the R-phase. (e, f) In the ε_6-phase. (g, h) In the ξ-phase. The Burgers vectors are indicated by arrows (not to scale).

metadislocation series, double Fibonacci numbers. For the monoclinic hosts ξ and R, we find three associated planes (phason planes or layers of twinned structure) and generally single Fibonacci numbers for the corresponding metadislocation series. We find similar relations for orthorhombic and monoclinic $Al_{13}M_4$ (not shown).

The broad variety of constructible and observed metadislocations suggests a definition independent of their mode of motion and the type of associated planar defect: A metadislocation is a line defect with a Burgers vector corresponding to a

$1/\tau^n$ ($n = 1, 2, 3, \ldots$) fraction of the corresponding lattice constant, mediating a local transformation to a phase that is structurally related to the matrix and accommodates the irrational Burgers vector to the lattice. The metadislocation core region comprises structural features of both phases. This definition includes the experimentally observed dislocations in several CMAs like $Al_{13}Co_4$, ε_6- and ε_{28}-Al–Pd–Mn [1,42,44,46,55], ξ- and ε_{22}-Al–Pd–Fe [59], as well as several other ε-type phases [31,45].

Acknowledgments

The authors thank Holger Klein, Stefan Roitsch, Peter Schall, and Daniel Caillard for long lasting scientific cooperation and numerous stimulating discussions. The experimental work was carried out on single crystals grown by Carsten Thomas and Marita Schmidt. The work was financially supported by the 6th Framework EU Network of Excellence ''Complex Metallic Alloys'' (Contract No. NMP3-CT-2005-500140) and the Deutsche Forschungsgemeinschaft (PAK 36).

Appendix. Arithmetics of the golden mean τ

The golden mean, also referred to as golden ratio, is defined as follows: Two quantities are in the golden mean, if the ratio of the larger and the smaller one is equal to the ratio of their sum and the larger one, that is

$$\frac{a}{b} = \frac{a+b}{a}. \tag{A1}$$

Now, arbitrarily setting $a = \tau$ and $b = 1$, we directly obtain the constituting relation

$$\tau^2 = \tau + 1. \tag{A2}$$

Solving this equation for τ yields $\tau = 1/2(1 \pm \sqrt{5})$, the positive solution of which numerically amounts to about 1.6180. Eq. (A2) is also the generating polynomial of the Fibonacci recursion $F_{n+2} = F_{n+1} + F_n$, which defines the Fibonacci sequence. The first Fibonacci numbers F_n for $n = 0, \ldots, 8$, are 0, 1, 1, 2, 3, 5, 8, 13, and 21. The ratio of consecutive Fibonacci numbers converges and the limit for $n \to \infty$ approaches τ.

Eq. (A2) is a fundamental relation for the arithmetics of the golden mean. It has the consequence that a polynomial equation containing any power of τ can be reduced to a linear equation. The following relations, implying this property,

are highly convenient for calculating lattice distances, Burgers vectors, etc., in ε-type structures.

$$\begin{aligned}
 & \tfrac{1}{\tau} = \tau - 1 \\
\tau^2 = \tau + 1 \quad & \tfrac{1}{\tau^2} = -\tau + 2 \\
\tau^3 = 2\tau + 1 \quad & \tfrac{1}{\tau^3} = 2\tau - 3 \\
\tau^4 = 3\tau + 2 \quad & \tfrac{1}{\tau^4} = -3\tau + 5 \\
\tau^5 = 5\tau + 3 \quad & \tfrac{1}{\tau^5} = 5\tau - 8 \\
\vdots \quad & \vdots
\end{aligned}$$

Obviously, the coefficients on the right-hand sides of the equations follow a Fibonacci sequence, and their relation upon multiplication or division by τ can be generally expressed as

$$(n\tau + m)\tau = (n + m)\tau + n \tag{A3}$$

and

$$\frac{n\tau + m}{\tau} = m\tau + (n - m), \tag{A4}$$

respectively.

Another useful relation for calculating Burgers vectors in ε-type structures is

$$\tau\sqrt{3 - \tau} = \sqrt{\tau + 2}, \tag{A5}$$

the validity of which can be easily verified by the reader using Eq. (A1).

References

[1] H. Klein, M. Feuerbacher, P. Schall, K. Urban, Phys. Rev. Lett. 82 (1999) 3468.
[2] C.L. Jia, private communication (2008).
[3] J.P. Hirth, J. Lothe, Theory of Dislocations, Krieger Publishing, Malabar, FL, 1972.
[4] R.E. Smallman, R.J. Bishop, Modern Physical Metallurgy and Materials Engineering, Butterworth-Heinemann, Oxford, 1999.
[5] F.C. Frank, Acta Crystallogr. 4 (1951) 497.
[6] J. Heindl, W. Dorsch, H.P. Strunk, St. G. Müller, R. Eckstein, D. Hofmann, A. Winnacker, Phys. Rev. Lett. 80 (1998) 740.
[7] S. Muto, G. van Tendeloo, S. Amelinckx, Philos. Mag. B 67 (1993) 443.
[8] K. Urban, M. Feuerbacher, J. Non-Cryst. Solids 334 & 335 (2004) 143.
[9] J. Kepler, Harmonices Mundi 2 (1619).
[10] C. Janot, Quasicrystals: A Primer, Clarendon Press, Oxford, 1992.
[11] D. Shechtman, I. Blech, D. Gratias, J.W. Cahn, Phys. Rev. Lett. 53 (1984) 1951.
[12] F.C. Frank, J.S. Kasper, Acta Crystallogr. 11 (1958) 184.
[13] L. Pauling, Am. Sci. 43 (1955) 285.
[14] S. Samson, Acta Crystallogr. 19 (1965) 401.
[15] N. Tamura, Philos. Mag. 67 (1997) 337.
[16] G. Bergman, J.L.T. Waugh, L. Pauling, Acta Crystallogr. 10 (1957) 254.

[17] A.L. Mackay, Acta Crystallogr. 15 (1962) 916.
[18] M. Cooper, K. Robinson, Acta Crystallogr. 20 (1966) 614.
[19] S. Samson, Mater. Sci. Forum 22–24 (1987) 83.
[20] F. Edler, V. Gramlich, W. Steurer, J. Alloys Compd. 269 (1998) 7.
[21] F. Edler, Ph.D. thesis no. 12384, ETH Zuerich, Switzerland, 1997.
[22] M.A. Taylor, Acta Crystallogr. 14 (1961) 84.
[23] K. Hiraga, M. Kaneko, Y. Matsuo, S. Hashimoto, Philos. Mag. B 67 (1993) 193.
[24] M. Boudard, H. Klein, M. DeBoissieu, M. Audier, H. Vincent, Philos. Mag. A 74 (1996) 939.
[25] L. Beraha, M. Duneau, H. Klein, M. Audier, Philos. Mag. A 76 (1997) 587.
[26] M. Yurechko, B. Grushko, T.Y. Velikanova, K. Urban, in: T.Y. Velikanova (Ed.), Phase Diagrams in Materials Science, Materials Science International Services, Stuttgart, Germany, 2004.
[27] H. Klein, Ph.D. thesis, Inst. Nat. Polytech. de Grenoble, France, 1997.
[28] H. Klein, M. Durand-Charre, M. Audier, J. Alloys Compd. 296 (2000) 128.
[29] N. Shramchenko, F. Denoyer, Eur. Phys. J. B 29 (2002) 51.
[30] M. Engel, H.-R. Trebin, Philos. Mag. 85 (2005) 2227.
[31] M. Heggen, M. Engel, S. Balanetskyy, H.-R. Trebin, M. Feuerbacher, Philos. Mag. 88 (2008) 507.
[32] S. Balanetskyy, B. Grushko, T.Y. Velikanova, Z. Kristallogr. 219 (2004) 548.
[33] H. Klein, M. Audier, M. Boudard, M. de Boissieu, L. Beraha, M. Duneau, Philos. Mag. 73 (1996) 309.
[34] M. Heggen, L. Houben, M. Feuerbacher, 2009 (in preparation).
[35] P.D. Nellist, S.J. Pennycook, Ultramic 78 (1999) 111.
[36] R.E. Peierls, Proc. R. Soc. 52 (1940) 23.
[37] M. Feuerbacher, Acta Mater. 53 (2005) 3833.
[38] P.B. Hirsch, A. Howie, R. Nicholson, D.W. Pashley, M.J. Whelan, Electron Microscopy of Thin Crystals, Krieger Publishing, Malabar, FL, 1977.
[39] D.B. Williams, C.B. Carter, Transmission Electron Microscopy, Plenum Press, New York, 1996.
[40] D. Hull, D.J. Bacon, Introduction to Dislocations, Pergamon Press, Oxford, 1984.
[41] A. Brinck, C. Engelke, H. Neuhäuser, G. Molénat, H. Rösner, E. Langmaack, E. Nembach, Mater. Sci. Eng. 258 (1998) 32.
[42] M. Heggen, M. Feuerbacher, Mater. Sci. Eng. 400–401 (2004) 89.
[43] V. Vitek, Cryst. Latt. Def. 5 (1974) 11.
[44] H. Klein, M. Feuerbacher, Philos. Mag. 83 (2003) 4103.
[45] M. Engel, H.-R. Trebin, Philos. Mag. 86 (2006) 979.
[46] M. Feuerbacher, M. Heggen, Philos. Mag. 86 (2006) 985.
[47] G. Edelin, J.P. Poirier, Philos. Mag. 28 (1973) 1203.
[48] D. Caillard, G. Vanderschaeve, L. Bresson, D. Gratias, Philos. Mag. A 80 (2000) 237.
[49] M. Feuerbacher, P. Schall, Scr. Mater. 49 (2003) 25.
[50] S. Roitsch, Ph.D. thesis, RWTH Aachen, Aachen, 2008.
[51] M. Feuerbacher, D. Caillard, Acta Mater. 54 (2006) 3233.
[52] M. Feuerbacher, S. Roitsch, M. Heggen, 2009 (in preparation).
[53] P. Schall, M. Feuerbacher, K. Urban, Phys. Rev. B 69 (2004) 134105.
[54] M. Feuerbacher, H. Klein, K. Urban, Philos. Mag. Lett. 81 (2001) 639.
[55] M. Heggen, M. Feuerbacher, Philos. Mag. 86 (2006) 935.
[56] Y. Matsuo, K. Hiraga, Philos. Mag. Lett. 70 (1994) 155.
[57] M. Yurechko, B. Grushko, T. Velikanova, K. Urban, Phase Diagrams in Materials Science, MSI GmbH, 2002, p. 92.
[58] M. Yurechko, B. Grushko, T.Y. Velikanova, et al., Powder Metall. Met. Ceram. 40 (2001) 374.
[59] M. Feuerbacher, S. Balanetskyy, M. Heggen, Acta Mater. 56 (2008) 1849.
[60] W. Sun, Y.H. Chen, Z. Zhang, Philos. Mag. 87 (2007) 2815.
[61] S. Balanetskyy, G. Meisterernst, M. Heggen, M. Feuerbacher, Intermetallics 16 (2008) 71.
[62] A.J. McAlister, in: T.B. Massalski (Ed.), Binary Alloy Phase Diagrams, American Society for Metals, Metals Park, OH, 1986.
[63] H. Klein, M. Boudard, M. Audier, M. de Boissieu, H. Vincent, L. Beraha, M. Duneau, Philos. Mag. Lett. 75 (1997) 197.

[64] K. Robinson, Acta Crystallogr. 7 (1954) 494.
[65] L. Beraha, M. Duneau, H. Klein, M. Audier, Philos. Mag. A 78 (1998) 345.
[66] J. Grin, U. Burkhardt, M. Ellner, K. Peters, J. Alloys Compd. 206 (1994) 243.
[67] R.C. Hudd, W.H. Tailor, Acta Crystallogr. 15 (1962) 441.
[68] J. Grin, U. Burkhardt, M. Ellner, K. Peters, Z. Kristallogr. 209 (1994) 479.
[69] B. Grushko, R. Wittenberg, K. Bickmann, C. Freiburg, J. Alloys Compd. 233 (1996) 279.
[70] M. Heggen, D. Deng, M. Feuerbacher, Intermetallics 15 (2007) 1425.
[71] C.W. Allen, K.C. Liao, Phys. Status Solidi A 74 (1982) 673.
[72] P.M. Hazzledine, P. Pirouz, Scr. Metall. 28 (1993) 1277.
[73] M.F. Chisholm, S. Kumar, P. Hazzledine, Science 307 (2005) 701.

CHAPTER 95

Dislocations in Minerals

DAVID J. BARBER

Physics Centre, University of Essex, Colchester CO4 3SQ; Wolfson Centre for Materials Processing, Brunel University, Uxbridge, Middlesex UB8 3PH, UK

HANS-RUDOLF WENK

Department of Earth and Planetary Science, University of California, Berkeley, CA 94720, USA

GREG HIRTH

Department of Geological Sciences, Brown University, Providence, RI 02912, USA

and

DAVID L. KOHLSTEDT

Department of Geology and Geophysics, University of Minnesota, Minneapolis, MN 55455, USA

1572-4859, DOI: 10.1016/S1572-4859(09)01604-0

Dislocations in Solids
Edited by J. P. Hirth and L. Kubin

Contents

1. Introduction 173
2. Dislocation microstructures in different environments 175
   2.1. Dislocations and other defects introduced during growth and crystallization 175
   2.2. Deformation, slip, slip system analysis, Burgers vector 176
   2.3. Hardening 178
   2.4. Climb and recovery 178
   2.5. Recrystallization 182
   2.6. Preferred orientation 183
3. Dislocations in various minerals 184
   3.1. Halides 184
      3.1.1. Lithium fluoride 185
      3.1.2. Fluorite 185
      3.1.3. Halite 186
   3.2. Carbonates 187
      3.2.1. Occurrences and structures of carbonate minerals 187
      3.2.2. Calcite 188
      3.2.3. Dolomite 189
      3.2.4. Aragonite 190
   3.3. Oxides 191
      3.3.1. Corundum 192
      3.3.2. Hematite 193
      3.3.3. Ilmenite 193
      3.3.4. Periclase and wüstite (see also Section 3.8.1) 193
      3.3.5. Magnetite 195
      3.3.6. Spinel 195
      3.3.7. Perovskite (see also Section 3.8.5) 197
      3.3.8. Rutile 197
   3.4. Quartz 198
   3.5. Olivine 200
   3.6. Other silicates 203
      3.6.1. Garnet (see also Section 3.8.2) 203
      3.6.2. Orthopyroxene 204
      3.6.3. Clinopyroxenes 204
      3.6.4. Amphiboles 206
      3.6.5. Mica 207
      3.6.6. Sillimanite, Mullite 207
      3.6.7. Feldspars 207
   3.7. Sulfides 209
      3.7.1. Iron sulfides – general 209
      3.7.2. Pyrite 210
      3.7.3. Chalcopyrite 211
      3.7.4. Galena 211
      3.7.5. Sphalerite 213
      3.7.6. Pyrrhotite 214

3.8. High-pressure minerals 214
3.8.1. Magnesiowüstite (see also Section 3.3.4) 214
3.8.2. Majorite Garnet (see also Section 3.6.1) 215
3.8.3. Wadsleyite 215
3.8.4. Ringwoodite 215
3.8.5. $MgSiO_3$ perovskite and post-perovskite 216
3.8.6. Coesite 216
3.8.7. Stishovite 216
4. Simulations 216
5. Dislocation densities and strain energy 217
6. Conclusions 219
Acknowledgments 220
References 221

1. Introduction

Minerals are naturally occurring, macroscopically homogeneous chemical compounds with a regular crystal structure that form by a geological process. There are over 4000 different mineral species. In about 100 of these, dislocation structures have been studied in some detail. Minerals compose rocks. They also are synthesized for industrial applications. Dislocations and microstructures constitute a record of the various processes that formed and modified rocks and other geological materials. Study of the constituent minerals by geologists can constrain the conditions that have been experienced, for example, pressure, temperature, stresses. Understanding the rheology of crustal rocks is dependent on knowledge of the deformation behavior of their minerals. Correspondingly, the rheology of the zones in the mantle is strongly dependent on the plasticity of the high-pressure minerals in them [1,2]. In both cases, the chemical environment (especially water content) has an important influence on deformation behavior and anisotropy (e.g., fabric development).

Owing to space limitations, what follows is not a comprehensive review of what is known about dislocations in minerals; we are obliged to be selective and to feature mainly highlights. We also assume that readers will consult suitable texts concerning both the theory of dislocations (see [3] and see [4] for a more advanced treatment) and their characterization (see [5,6]).

The strain and contrast associated with large numbers of dislocations causes telltale broadening of X-ray diffraction peaks (see Section 5 in Ref. [7]) but techniques of much greater resolution are needed to image dislocations and microstructures directly. Probably, the first images of dislocations ever obtained were from a geological material – the mineral, halite (NaCl). These were obtained in 1905 when Seidentopf [8] examined naturally colored rock salt with an optical microscope. His observations (of dislocations decorated with sodium metal) predated the theoretical concept of a dislocation in an elastic medium [9] and the ideas that dislocations might play an important role in plastic deformation [10–13]. Thus, the significance of Seidentopf's results was not recognized. Much later, Rexer [14] inadvertently decorated dislocation lines in rock salt crystals with colloidal sodium. His work gave rise to the decoration methods used successfully to study dislocation behavior in alkali halides [15,16]). Fig. 1(a) shows an extensive decorated network. Decoration methods are of limited value in revealing dislocation microstructures, however, because a thermal treatment is usually required and this causes recovery. Exceptions are the print out effect in silver halides [18], the first direct observation of dislocations where they were properly identified, and olivine [19–21]. Olivine requires heat for the dislocations to become decorated but apparently at temperatures and times for which climb (see Section 2.4) is minimal. For an

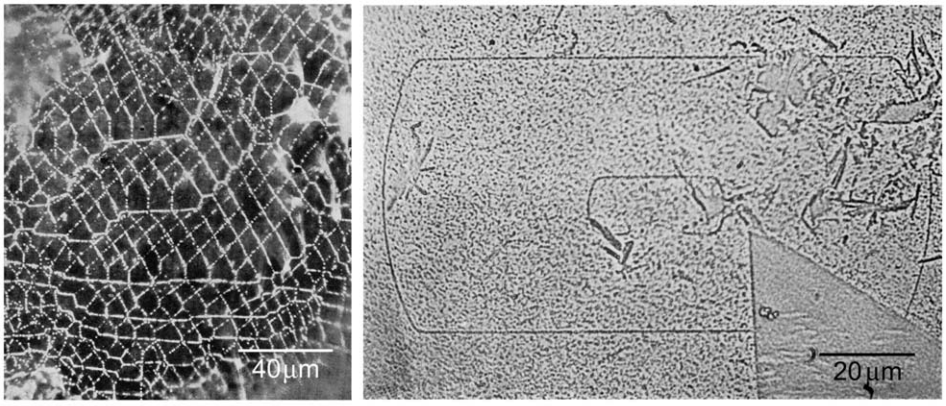

Fig. 1. (a) Dark-field optical micrograph of an extensive dislocation network in halite revealed by the decoration of the dislocations with colloidal silver [16]. (b) Optical phase image of growth steps, one unit cell high (0.79 nm) on the prism surface of a beryl crystal. The inner step joins a pair of opposite-handed screw dislocations, which are imaged as dots. The *c*-axis is almost parallel to the straight steps [17].

excellent report of early work on dislocations in many materials, including some minerals, see Amelinckx [5].

Growth twins in minerals, for example in calcite, have been known for centuries; observation of mechanical twinning also has a long history. But the dislocations often associated with both types of twinning remained undiscovered. The link between twinning and dislocations only emerged in the 1950s, after thin metal foils were first examined in the transmission electron microscope (TEM) by Hirsch et al. [22] and Bollmann [23]. Thereafter, the association was found in minerals that are well known for their twinning, like calcite (see [24]).

Although results from TEM studies on metals forged ahead of those from minerals prior to the widespread adoption of the ion-milling method [25,26], mineral crystals played key roles in earlier work. For example, Griffin [17] recognized groups of monomolecular surface steps on beryl crystals as indicative of the emergence of screw dislocations [Fig. 1(b)]. Some 20 years earlier, Honess [27] described various surface features that we now recognize as associated with dislocations, for example, tails or ''beaks'' extending from etch pits into the interiors of many mineral crystals (caused by dissolution following impurity atmospheres or decorating particles along dislocations). Dislocations in minerals can be preserved and locked against movement through geological times by the pinning of impurities or the segregation of a second phase [28]. In general, new dislocations must be nucleated for plastic deformation to proceed.

The study of dislocations by etch pitting was useful in early studies of plastic deformation. One of the best illustrations is the work of Gilman and Johnston [29] on synthetic lithium fluoride. Successful etch-pitting reagents were also devised for other minerals, such as halite [30] and olivine [31], but by then X-ray topography

[32] and TEM had emerged as preferable techniques because of their potential for obtaining images capable of providing 3-D information.

The first TEM studies of defects in minerals were mostly carried out on layer-structured crystals that could easily be cleaved to electron transparent thicknesses. These included mica [33], graphite [34], molybdenite [35,36], and talc [37]. The study of dislocation networks in talc [38] is an early milestone in dislocation analysis. Thereafter, the ion-milling method (and, more recently, the FIB (focused ion beam) technique) made it possible to investigate dislocations and other defects in a wide range of minerals, crustal rocks, and extraterrestrial materials.

The lunar samples returned by the Apollo 11 mission first demonstrated the value of ion-milling in TEM investigations of minerals. The resulting investigations helped convince geologists of the importance of detailed studies of microstructures and dislocations for the interpretation of the deformational and thermal history of geological materials. Various studies on lunar rock specimens (see [39–42]) made geologists, who already used SEM and EPMA, suddenly aware of the power of the TEM to analyze mineral microstructures, cosmic ray tracks, etc., leading to the acquisition of ion-milling equipment and TEMs by numerous laboratories. There followed a very active period during which many TEM papers were published detailing the relationships between microstructures, macroscopic properties, and mineral behavior. Although much progress was made [6], the boom in such studies was soon over and today only a few earth science laboratories work with the TEM, perhaps a reflection of the time-consuming nature of specimen preparation and the rigorous analytical approach required. There remains some interest in high-resolution imaging (HRTEM). Although, the latter supplies valuable information about stacking disorder, grain boundary structure, polytypism, and phase transformations [43], it seldom informs about dislocation behavior other than dissociation.

2. Dislocation microstructures in different environments

2.1. Dislocations and other defects introduced during growth and crystallization

Minerals form by various processes, embracing a wide range of temperatures. Those of sedimentary and low-temperature origin tend to start as poorly crystalline and often disordered solids. Unsurprisingly, dislocations are not usually observed in minerals in this state (e.g., geologically young dolomites). More equilibrated low-temperature minerals such as clays often show stacking defects but in general are not noted for significant numbers of dislocations. However, ancient calcian dolomites and other rhombohedral carbonates that exhibit compositional fluctuations producing lattice strain often contain collections of dislocations.

Mineral grains formed at higher temperatures by crystallization from melts, by phase transformations, or by reactions, generally contain ‘‘grown-in’’ dislocations. The densities of such dislocations are typically low to moderate (i.e., below about $10^4\,cm^{-2}$), unless special factors apply. Recrystallized grains are often dislocation-free. Most high temperature (HT) minerals have cooled over geologic times,

enabling equilibration, which favors low dislocation densities in the absence of subsequent deformation. An additional source of dislocations in any mineral that has cooled very rapidly can be the collapse of the lattice around clusters of point defects, especially vacancies.

Many minerals have ordered structures and they may exist in both ordered and disordered states. Ordering can occur when two different atomic species A and B utilize the same lattice sites and order is achieved when the two types of atoms occupy alternate adjacent sites, that is, ABABABA. Typically at high temperatures the site occupancy is random; ordering commences as the mineral cools. Because the ordering usually starts at many places simultaneously antiphase boundaries frequently occur where ordered domains impinge, for example, ABABA|ABABA (see p. 211 in Ref. [44]). Igneous rocks generally contain ordered minerals, whereas unmetamorphosed sedimentary rocks tend to contain disordered minerals. Generally speaking, order–disorder transitions do not appear to cause changes in the numbers of dislocations. Ordered structures, however, allow for a new type of dislocation, a superdislocation, which is a line defect of the both the A and B sublattices. Superdislocations in some structures are able to dissociate into superpartials.

An antiphase boundary (APB) is a type of stacking fault. Stacking faults also occur in materials that do not order, the simplest example being a fault in the normal close-packed layering in face-centered cubic metals, like copper, represented by CABCAB|ABCABC. Stacking faults, formed during crystal growth or as a result of deformation (slip), are bounded by partial dislocations.

2.2. Deformation, slip, slip system analysis, Burgers vector

Deformation is the main source of dislocations in rocks and minerals, although what is observed may have been modified subsequently. If the original deformation is brittle in nature there will be much cataclasis, but this may also generate dislocations because of the high stresses present at advancing crack tips. The detailed analysis of such cataclastic materials can be difficult even if subsequent annealing has occurred. Laboratory deformation of single crystal minerals has often been used to elucidate slip systems. The results must be applied with care when interpreting natural rock deformation because normally this has taken place at strain rates several orders of magnitude below those obtainable experimentally. Other considerations apply when interpreting natural shock deformation but here too laboratory experiments have played a useful role. Shock deformation effects in terrestrial and meteoritic minerals have been reviewed [45,46].

Plastic deformation creates many dislocations, possibly accompanied by effects such as twinning and kinking, grain boundary sliding, and competition from climb (see below). The first two processes can themselves add to the production of dislocations. Depending on the symmetry of the mineral, slip may proceed on one or on several planes. The slip planes in simple structures are close-packed planes or, in more complex structures, planes for which the breaking of bonds is relatively

easy and/or does not bring oppositely charged ions into closer proximity. The choice of slip direction is also governed by several structural considerations. In any case, too much energy is required for slip to occur simultaneously over a large area of slip plane and so instantaneously the slip is of limited extent – the boundary between slipped and unslipped material defines a dislocation in the atomic structure [44]. Slip occurs incrementally by the *glide* of dislocations across the slip planes. The motion of a dislocation out of its original slip plane can occur either by cross-slip onto an intersecting slip plane (provided there is a common slip direction) or by *climb* (if the diffusion of point defects is possible). Dislocations are typically curved, not straight, expanding from a small source under the action of applied stress. Where a dislocation is perpendicular to the direction of slip it is said to have edge character, where it is parallel it is screw-like (see [3] for an explanation); where it is neither, the dislocation is of mixed character. A slip system is specified in terms of a slip plane {h k l} and either a slip direction $\langle$ u v w $\rangle$ or the associated Burgers vector, if it is known. Table 1 lists the slip data for many important minerals and they will be discussed in later sections.

A dislocation is characterized by its Burgers vector, **b**. This is a measure of the local displacement of the lattice after a dislocation has passed through it. The Burgers vector is a translation vector of the unit cell. It determines whether, or how, a dislocation will interact with other dislocations. To analyze microstructures, to understand how they have formed and how they relate to macroscopic properties like texture, strength, etc., it is crucial to have complete information about dislocations (and other defects), slip systems, and Burgers vectors. Diffraction methods enable dislocations to be imaged, their properties identified and their Burgers vectors determined. X-ray topography and TEM are both suitable for this work; by comparing the visibility of dislocations in images recorded using several Bragg reflections in turn, one can ascertain Burgers vectors. TEM is the more widely applicable diffraction contrast method [158]: the conditions $\mathbf{g} \cdot \mathbf{b} = 0$ and $\mathbf{g} \cdot \mathbf{b} \times \mathbf{u} = 0$, where **g** is the diffraction vector and **u** is the direction of the dislocation, apply when a dislocation becomes invisible. Fig. 2 shows dark-field images of quartz with some dislocations in and out of contrast, depending on which **g** is used [151]. Analyzing dislocation strain fields by this method is dependent upon setting up ''two-beam conditions'' for imaging. This requires that there is only one strong electron reflection (only one reciprocal lattice vector **g** operating). Achieving and/or recognizing out-of-contrast conditions for a dislocation in a mineral is often not straightforward because (i) anisotropy in elastic properties may forbid complete invisibility and give residual contrast; (ii) crystal symmetry considerations can make it impossible to achieve two-beam conditions in certain crystal orientations with respect to the electron beam; (iii) radiation damage may decorate dislocations and this effect will be seen even when the dislocation's strain field does not interact with the electron beam [Fig. 2(b)]. Less widely used TEM techniques for characterizing Burgers vectors without any *a priori* assumptions are large angle convergent beam electron diffraction (LACBED), as first demonstrated by Carpenter and Spence [159] and Ishida fringes [6].

The characteristics of stacking faults and other defects can also be found using both diffraction contrast [6] and convergent beam techniques [160]. Simple stacking

Table 1
The main slip systems and Burgers vectors for major minerals

Mineral	Main slip systems		Known Burgers vectors (*is the shortest)	Reference(s)
	Low temperature	High temperature		
Carbonates				
Calcite	$\mathbf{r}^-$ $\{1\,0\,\bar{1}\,4\}\langle 2\,0\,\bar{2}\,\bar{1}\rangle$, $\mathbf{f}^-$ $\{\bar{1}\,0\,1\,2\}\langle 1\,0\,\bar{1}\,1\rangle$	$\mathbf{c}$ $(0\,0\,0\,1)\langle 2\,\bar{1}\,\bar{1}\,0\rangle$, $\mathbf{r}^-$ $\{1\,0\,\bar{1}\,4\}\langle 2\,0\,\bar{2}\,\bar{1}\rangle$, $\mathbf{f}^-$ $\{\bar{1}\,0\,1\,2\}\langle 1\,0\,\bar{1}\,1\rangle$	$\frac{1}{3}\langle 2\,0\,\bar{2}\,\bar{1}\rangle$, $\frac{1}{3}\langle 1\,0\,\bar{1}\,\bar{1}\rangle$, $\frac{1}{3}\langle 2\,\bar{1}\,\bar{1}\,0\rangle$*	[47–51]
Dolomite	$\mathbf{c}$ $(0\,0\,0\,1)\langle 2\,\bar{1}\,\bar{1}\,0\rangle$, $\mathbf{f}^-$ $\{\bar{1}\,0\,1\,2\}\langle 1\,0\,\bar{1}\,1\rangle$	$\mathbf{c}$ $(0\,0\,0\,1)\langle 2\,\bar{1}\,\bar{1}\,0\rangle$, $\mathbf{r}^-$ $\langle 1\,0\,\bar{1}\,4\}\langle 2\,0\,\bar{2}\,\bar{1}\rangle$, $\mathbf{f}^-$ $\{\bar{1}\,0\,1\,2\}\langle 1\,0\,\bar{1}\,1\rangle$	$\frac{1}{3}\langle 2\,\bar{1}\,\bar{1}\,0\rangle$*, $\frac{1}{3}\langle 2\,0\,\bar{2}\,\bar{1}\rangle$, $\frac{1}{3}\langle 1\,0\,\bar{1}\,\bar{1}\rangle$	[52–55]
Aragonite	$\{1\,0\,0\}[0\,0\,1]$, $\{1\,1\,0\}[0\,0\,1]$	$\{1\,0\,0\}[0\,0\,1]$, $\{1\,1\,0\}[0\,0\,1]$	$[0\,0\,1]$*	[56]
Felspars				
Plagioclase	–	$(0\,1\,0)[0\,0\,1]$, $(0\,0\,1)\langle 1\,1\,0\rangle$, $(0\,0\,1)[1\,0\,0]$, $(0\,1\,0)[1\,0\,0]$	$[0\,0\,1]$*, $[1\,0\,0]$	[57–62]
Alkali felspar	–	$(0\,1\,0)[0\,0\,1]$, $(0\,1\,0)[1\,0\,1]$, $(0\,0\,1)[1\,1\,0]$	$[0\,0\,1]$*, $\frac{1}{2}\langle 1\,1\,0\rangle$	[63–68]
Halides				
Halite (rock salt)	$\{1\,1\,0\}\langle 1\,\bar{1}\,0\rangle$	$\{1\,1\,0\}\langle 1\,\bar{1}\,0\rangle$, $\{1\,0\,0\}\langle 0\,\bar{1}\,1\rangle$, $\{1\,1\,1\}\langle 1\,\bar{1}\,0\rangle$	$\frac{1}{2}\langle 1\,1\,0\rangle$*	[69–71]
High-pressure phases				
Coesite	–	$(0\,1\,0)$ $[0\,0\,1]$	$[0\,0\,1]$, $[1\,0\,0]$*, $[1\,1\,0]$	[72]
Majorite	–	–	$\frac{1}{2}\langle 1\,1\,1\rangle$*, $\langle 1\,0\,0\rangle$	[73,74]
Magnesiowüstite	–	$\{0\,0\,1\}\langle 1\,\bar{1}\,0\rangle$, $\{1\,1\,0\}\langle 1\,\bar{1}\,0\rangle$	$\frac{1}{2}\langle 1\,1\,0\rangle$*	[75,76]
Post-perovskite	–	–	–	[77,78]
Ringwoodite	–	$\{1\,1\,1\}\langle 1\,\bar{1}\,0\rangle$, $\{1\,0\,0\}\langle 0\,\bar{1}\,1\rangle$	$\frac{1}{2}\langle 1\,1\,0\rangle$*	[79–81]
Stishovite	–	$(0\,0\,1)\langle 1\,0\,0\rangle$, $\{0\,1\,0\}\langle 1\,0\,0\rangle$, $\{1\,0\,0\}\langle 0\,0\,1\rangle$, $\{1\,1\,0\}\langle 1\,\bar{1}\,0\rangle$	$\langle 1\,0\,0\rangle$, $[0\,0\,1]$*, $\langle 1\,1\,0\rangle$, $\langle 1\,0\,1\rangle$	[82–84]
Wadsleyite	–	$\{1\,0\,1\}\langle 1\,1\,1\rangle$, $(0\,1\,0)[1\,0\,0]$, $\{0\,1\,1\}[1\,0\,0]$	$\frac{1}{2}\langle 1\,1\,1\rangle$, $[1\,0\,0]$*	[79,85,86]

Table 1. (*Continued*)

Mineral	Main slip systems		Known Burgers vectors (*is the shortest)	Reference(s)
	Low temperature	High temperature		
Olivine	(0 1 0)[0 0 1], {1 1 0}[0 0 1]	{0 *k* 1}[1 0 0], (0 1 0)[1 0 0]	[0 0 1]*, [1 0 0]	[87–93]
Sulfides				
Chalcopyrite	{1 1 2}⟨$\bar{3}$ 1 1⟩, (0 0 1) ⟨1 1 0⟩	{1 1 2}⟨1 1 $\bar{1}$⟩	$\frac{1}{2}$⟨$\bar{3}$ 1 1⟩, $\frac{1}{2}$⟨1 1 1⟩*	[94–97]
Pyrite	–	{1 0 0}⟨0 1 0⟩, {1 0 0}⟨0 1 1⟩	⟨0 1 0⟩*	[98–101]
Galena	{0 0 1}⟨1 1 0⟩	{0 0 1}⟨1 1 0⟩, {1 $\bar{1}$ 0}⟨1 1 0⟩	$\frac{1}{2}$⟨1 1 0⟩*	[102–105]
Sphalerite	{1 1 1}⟨1 $\bar{1}$ 0⟩	{1 1 1}⟨1 $\bar{1}$ 0⟩	$\frac{1}{2}$⟨1 1 0⟩*	[106]
Pyroxenes				
Orthorhombic	–	(1 0 0)[0 0 1]	[0 0 1]*, [0 1 0]	[107–112]
Monoclinic	–	(1 0 0)[0 0 1], {1 1 0}[0 0 1]	[0 0 1]*	[113–119]
Oxides				
Corundum	(0 0 0 1)⟨1 1 $\bar{2}$ 0⟩	(0 0 0 1)⟨1 1 $\bar{2}$ 0⟩, {1 0 $\bar{1}$ 1}⟨0 1 1 1⟩	$\frac{1}{3}$⟨1 1 $\bar{2}$ 0⟩*, $\frac{1}{3}$⟨0 1 1 1⟩	[120–126]
Hematite	(0 0 0 1)⟨1 1 $\bar{2}$ 0⟩, {1 1 $\bar{2}$ 0}⟨1 $\bar{1}$ 0 0⟩	(0 0 0 1)⟨1 1 $\bar{2}$ 0⟩, {1 1 $\bar{2}$ 0} ⟨1 $\bar{1}$ 0 0⟩	$\frac{1}{3}$⟨1 1 $\bar{2}$ 0⟩*, ⟨1 $\bar{1}$ 0 0⟩	[106,127,128]
Periclase, wüstite	{1 1 0}⟨1 $\bar{1}$ 0⟩	{1 1 0}⟨1 $\bar{1}$ 0⟩, {0 0 1}⟨1 $\bar{1}$ 0⟩	$\frac{1}{2}$⟨1 1 0⟩*	[129,75,130–134]
Perovskite	–	{1 1 0}⟨1 $\bar{1}$ 0⟩	$\frac{1}{2}$⟨1 $\bar{1}$ 0⟩*, [0 1 0]	[135]
Rutile	–	{1 0 1}⟨1 0 $\bar{1}$⟩, {1 1 0}[0 0 1]	[0 0 1]*	[136–139]
Spinel	{1 1 1}⟨1 $\bar{1}$ 0⟩, ({1 1 0}⟨1 $\bar{1}$ 0⟩ when nonstoichiometric)	{1 1 0}⟨1 $\bar{1}$ 0⟩	$\frac{1}{2}$⟨1 1 0⟩*	[140–149]
Magnetite	–	{1 1 1}⟨1 $\bar{1}$ 0⟩	$\frac{1}{2}$⟨1 1 0⟩*	[127,150]
Quartz	(0 0 0 1)⟨1 1 $\bar{2}$ 0⟩	(0 0 0 1)⟨1 1 $\bar{2}$ 0⟩, {1 0 $\bar{1}$ 0}[0 0 0 1], {1 0 $\bar{1}$ 0}[1 $\bar{2}$ 1 0], {1 0 $\bar{1}$ 0}[1 $\bar{2}$ 1 3]	$\frac{1}{3}$⟨1 1 $\bar{2}$ 0⟩*	[151–157]

Note: A dash means that either there is no activity or that there is no reliable data.

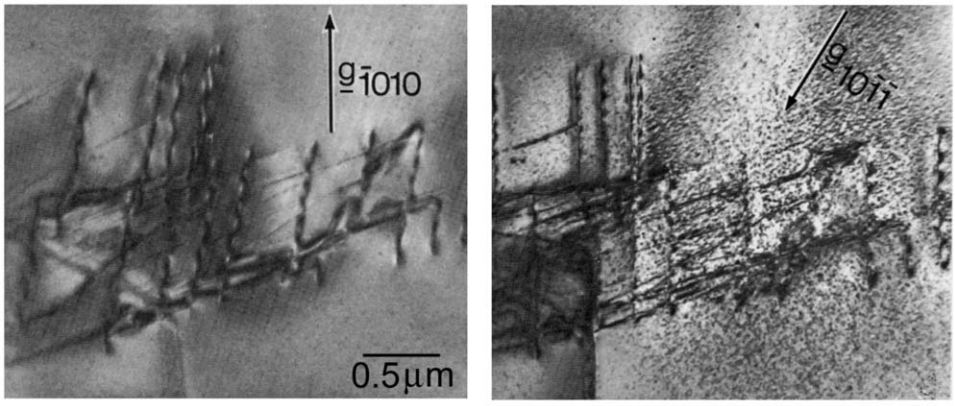

Fig. 2. Transmission electron micrographs of slip dislocations in quartz: (a) All in contrast, (b) some out of contrast (note spotty electron beam damage, typical of (''wet'') quartz after irradiation) [151].

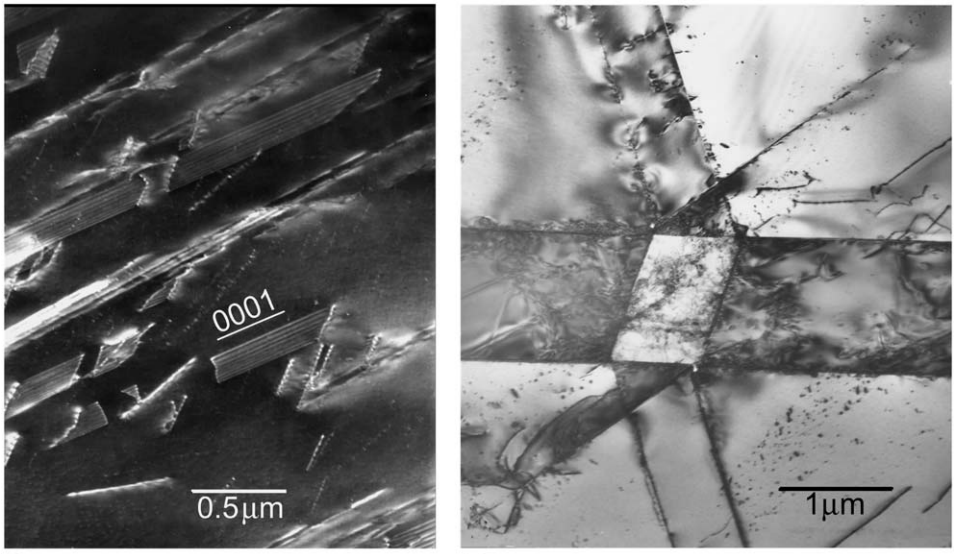

Fig. 3. Dislocations in carbonates: (a) Dark-field TEM image showing dislocations and stacking faults on the $\langle 2\,\bar{1}\,\bar{1}\,0\rangle$ planes generated by basal slip in a dolomite single crystal deformed at 420 °C [52]. (b) Dislocations associated with crossing mechanical twins in calcite (TEM, bright field) [161].

faults and other, more complex, planar faults commonly occur as a result of slip in minerals. Because the strain energy of a dislocation is proportional to $|\mathbf{b}|^2$, it can be energetically favorable for a dislocation to dissociate into two partials, $\mathbf{b}_1$ and $\mathbf{b}_2$, separated by a ribbon of stacking fault. Dissociation is favored in minerals where

cations in identical sites have large separations. Fig. 3(a) illustrates this behavior in experimentally deformed dolomite slipping on the basal plane, according to $\frac{1}{3}\langle 2\,\bar{1}\,\bar{1}\,0\rangle \rightarrow \frac{1}{3}\langle 1\,\bar{1}\,0\,0\rangle + \frac{1}{3}\langle 1\,0\,\bar{1}\,0\rangle$.

In addition to slip, mechanical twinning may occur as a deformation mechanism. Twin boundaries are often decorated with dislocations to relieve local strain [Fig. 3(b)].

2.3. Hardening

Much less is known about the hardening of minerals caused by plastic deformation than is the case for metals and alloys [162]. This is attributable to (i) the long-standing importance of understanding and optimizing the mechanical properties of metals, (ii) the poorly known and complex geological settings and conditions that pertained when rocks were deformed, and (iii) the comparatively few laboratory studies of mineral deformation. Nonetheless, we know from the stress–strain curves of minerals and rocks plastically deformed at low-to-moderate temperatures to moderate strains that the effect of strain is to increase resistance to further deformation, that is, to strengthen and harden the material. This hardening is largely due to (a) increased dislocation densities, formation of tangles of dislocations, etc., making the passage of newly nucleated dislocations more difficult and (b) a lack of activatable slip planes and slip systems. In the more ductile minerals strained to a few percent, cellular dislocation microstructures can develop that are similar to those seen in the stage III work hardening of metals [see p. 167 and Figs 11(b) and 12(b) in Ref. [163]]. Thus there are similarities in behavior, so mineralogists and geologists can look to the large literature on metals for help in understanding the microscopic behavior of minerals and rocks. Complications arise with minerals, however, because of the inability of many minerals to conform to the von Mises [164] criterion because of a symmetry-related lack of slip systems and hence their tendency to fracture. Nicolas and Poirier [165] give a good description of various hardening mechanisms and the role of climb and other processes in softening minerals, together with a discussion on how dislocation substructures relate to applied stress. Note that flow laws and hardening behavior have been quantified for only a few minerals.

2.4. Climb and recovery

Below temperatures where point defects are mobile, an edge dislocation and a mixed dislocation with an edge component are unable to move out of their glide planes (screws have no glide plane and so are not similarly confined). Interactions are therefore limited, being restricted to dislocations in a given glide plane unless a process like cross-slip is possible. But if point defects are mobile they can interact with a dislocation and gradually change its position: edges may move out of their glide plane; screws may become helices. Such effects are manifestations of a process called *climb*. Climb is the rearrangement and interaction of dislocations to reduce

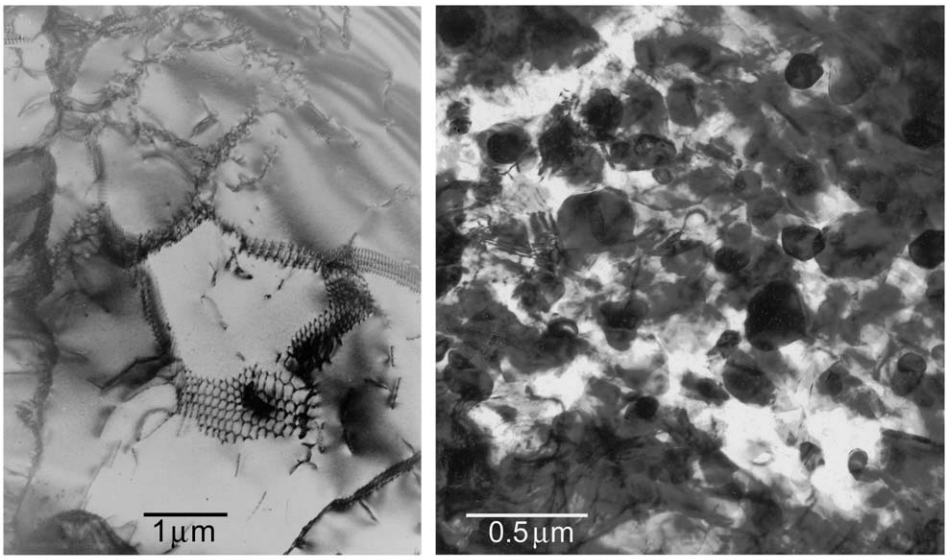

Fig. 4. Dislocations in naturally deformed quartz: (a) Micrograph showing sub-boundaries resulting from dislocation climb [166]. (b) Recrystallization with nucleation in regions of high dislocation density [167].

the stored elastic energy – i.e., it is partial equilibration. Climb only occurs at temperatures above $\sim 0.5\, T_m$, where T_m is the melting point in degrees Kelvin. Climb is only possible if all the relevant point defect species are mobile.

Annealing allows high-energy configurations of dislocations created by deformation to reduce their energies – by mutual annihilation, reactions, and climb. The dislocation density is reduced but all the dislocations are not eliminated; many will persist in the form of networks and other types of low-energy sub-boundaries and dislocation arrays. Fig. 4(a) illustrates the effect of climb in quartz.

2.5. Recrystallization

Recrystallization implies that a crystal or an existing grain structure is replaced with another. It is a solid-state process, driven by a need to reduce energy stored in the assembly and so it can proceed by more than one mechanism. The strain energy is directly proportional to the dislocation density [168,169]. Recrystallization occurs during diagenesis and metamorphism (a reduction of chemical free energy). The replacement of heavily deformed grains by new undeformed grains of the same type (giving a reduction of strain energy) is also known as recrystallization – short for *strain-induced recrystallization*. This process is a more drastic equilibration than can be achieved by climb. A wave of atomic rearrangement passes systematically through each heavily deformed grain, sweeping out any dislocations and generally leaving most grains free of dislocations and other extensive defects.

Where a completely new grain structure is formed the grain boundaries are almost all high angle ($>10^{\circ}$).

Static recrystallization is triggered when a heavily strained material is rapidly raised to a critical temperature. New dislocation-free grains are nucleated and swiftly grow by consuming heavily deformed material until they impinge on their neighbors. The resulting grain size depends on the relative successes of the two competing mechanisms, nucleation and growth. The equilibration to a new grain structure is catastrophic and *primary recrystallization*, the initial stage of generating the new grain structure, is complete within seconds if all the material is at the same temperature. *Grain growth and secondary recrystallization* take the form of some grain enlargement at the expense of much smaller grains, thus reducing total grain boundary area (and energy), together with some grain boundary flattening, equilibration at triple junctions, etc.

Although massive submicroscopic rearrangement has occurred, the macroscopic process described above is called static recrystallization, to distinguish it from *dynamic recrystallization*. The latter occurs while a material is under stress and being deformed at an elevated temperature, such that point defects are mobile and usually other stress-reducing mechanisms are also active (e.g., cross-slip, grain boundary sliding). Dynamic recrystallization causes some softening to mitigate the effects of the hardening that usually accompanies plastic deformation. It does so by providing new grains with relatively low-defect densities [165]. In metals, these are often elongate in the direction of the macroscopic deformation [170]; the same effect is seen in ductile minerals, for example, halite and calcitic marbles. Fig. 4(b) illustrates nucleation in regions of high dislocation densities in quartz [167]. The degree of softening during dynamic recrystallization is dependent on the strain rate and other factors because the new grains deform and acquire dislocations as they grow (e.g., see the case of olivine – [171,172]).

2.6. Preferred orientation

The macroscopic effects of the processes of pervasive deformation (and recrystallization) are the development of anisotropy in properties, due to preferred orientation or texture. Clearly, texture development is closely linked to movement of dislocations on slip planes and Taylor [173] introduced the first comprehensive theory to model texture development by slip that is still widely used. Interestingly, there is no mention of dislocations or slip systems in Sander's [174] famous treatise on fabric analysis. It was only through the classical ''Yule marble studies'' of Griggs and Turner that metallurgical concepts to link microscopic mechanisms with macroscopic properties, that is, the linkage of dislocations and texture patterns, became accepted in structural geology and have played a dominant role ever since (see [47,48]). The role of this micro–macro linkage is twofold: firstly, if slip systems of constituent minerals in rocks are known, we can predict the evolution of texture patterns during tectonic deformation in the crust (see [175]) or convection in the mantle (see [176,177]) and then use texture to interpret geological history or seismic

anisotropy. Secondly, if slip systems are not known, for example, because ultrahigh pressure phases cannot be quenched and studied by TEM, experimental texture patterns recorded *in situ* at highest pressures with diamond anvil cells can be used to infer slip systems (see, [178]). Not just deformation textures but also recrystallization textures can be related to dislocation structures, in terms of individual grain deformation that controls nucleation and growth [179]. There is no space here to discuss preferred orientation in minerals and several reviews exist [42,180,181]. In the next sections, we will look at dislocations in a variety of mineral systems and their variation with physical conditions, mainly temperature, strain rate, and pressure.

3. Dislocations in various minerals

Dislocations have been studied in many minerals of both geological and materials science interest. We review investigations on some mineral systems in considerable detail, without trying to achieve completeness. Slip systems and Burgers vectors of important minerals are summarized in Table 1. Many advances have been made since earlier reviews by Christie and Ardell [152] and McLaren [6]. Minerals are discussed in order of chemical groups, except for high-pressure minerals relevant for the deep earth; these are the subjects of the last section. We must mention briefly results that have relevance in other disciplines. For example, diamond and other various forms of carbon are very important technologically; a concise summary of relevant findings is given by Bernaerts and Amelinckx [182]. Ceramic materials are polymineralic and the microstructures of the constituent grains can strongly influence bulk properties [183]. Extraterrestrial materials, especially meteorites, embrace a wide range of minerals, sometimes with unique or unusual microstructures [184]. Recently, considerable attention has been given to dislocation structures in ice [185].

3.1. Halides

The susceptibility of halides to radiation damage and, for some also, to atmospheric attack, has meant that there are few direct observations of dislocations within them. Much of our knowledge comes from optical observations of surface slip traces, etch pits, and decorated dislocations. For a review of plastic deformation and dislocations in ionic crystals, see Castaing [186]. The highly ionic nature of halides imbues them with the interesting possibility of their dislocations being charged. Despite this, there has not been much research into the subject of charged dislocations since the earliest days and so there are relatively few definite results (but see 3.7.5). The most important halide minerals are cubic in structure. Only halite (NaCl), fluorite (CaF_2), and lithium fluoride (LiF) will be considered here, and the latter only because of early work that was very influential in the study of defects in nonmetals. For this reason, LiF is briefly considered first.

3.1.1. Lithium fluoride

Lithium fluoride is unimportant from the geological viewpoint but it has great value for optical components: lenses, prisms, windows, which transmit from the vacuum ultraviolet to the infrared and, when doped, as a laser material. Like halite, the LiF structure is cubic and has two interpenetrating face-centered cubic lattices, one of cations and one of anions. Studies of synthetic lithium fluoride using the etch-pitting method [187,188] were amongst the first to reveal the behavior of dislocations during plastic deformation. This ground-breaking work proved the main slip system to be $\{1\,1\,0\}\langle 1\,\bar{1}\,0\rangle$; it also demonstrated the glide and climb of dislocations, the expansion of surface half-loops under stress as well as the blocking of dislocations on one slip system by an orthogonal one.

3.1.2. Fluorite

The crystal structure of fluorite is most easily visualized as a primitive cubic lattice of fluorine ions with calcium ions at alternate body centers. Granular fluorite aggregate is a source for the chemical industry and large pure crystals have applications in modern optics.

Unlike the main minerals with the rock salt structure, fluorite cleaves on $\{1\,1\,1\}$ planes and slips on $\{1\,0\,0\}$ in the $\langle 0\,1\,\bar{1}\rangle$ direction [189]. Above 200 °C, slip on $\{1\,1\,0\}\langle 1\,\bar{1}\,0\rangle$ is also possible. Above 320 °C, polycrystalline plasticity is observed with the $\{1\,0\,0\}$ planes providing three independent slip systems and the $\{1\,1\,0\}$ planes giving two more [190]. Dislocations in fluorite have been studied by etch-pitting methods, and by TEM [191] but the latter is not without difficulty, since the mineral rapidly damages under electron and ion irradiation. A cubic symmetry void superlattice can be formed in TEM if the radiation flux is not restricted [192].

Possible core structures for dislocations gliding during $\{1\,1\,1\}$ slip have been considered with a view to possible charge effects [193,194]. A model of jogged dislocations with alternate positively and negatively charged segments to achieve overall neutrality was proposed [195]. Straight and jogged edge dislocations lying in $\{1\,0\,0\}$ have no intrinsic charge when moving; the anions must move normal to the Burgers vector, that is, along the dislocation [196,197]. A core model assumes a uniformly neutral edge dislocation at rest and atomistic movements that could operate to accommodate charge balancing during the glide of various types of dislocation. This has some similarities with the synchroshear mechanism for sapphire [198]. Straight edge and screw dislocations in the $\{1\,1\,0\}$ planes of the fluorite structure are uncharged [199]. Brantley and Bauer [197] examined various dislocation configurations in the fluorite structure for the presence of long-range electrostatic charge, assuming slip systems of the $\{0\,0\,1\}\ \langle 1\,1\,0\rangle$ type. They concluded that neither pure edge or screw dislocations, nor jogs and kinks on edge or screw dislocations necessarily give rise to charge. A long-range charge could be produced by adsorption or desorption of anions and cations. They also considered the possible effects on dislocation glide and the likelihood of charge transport by dislocations. Stacking fault energies for the $\{1\,0\,0\}$, $\{1\,1\,0\}$, and $\{1\,1\,1\}$ planes in CaF_2 were calculated and in all cases the energy was high so that only weak dissociation is to be expected [200].

Further ideas about the behavior of dislocations in fluorite can possibly be derived from the literature on oxides and oxide fuels [201], because some of these materials have the fluorite structure and they have been more widely researched than fluorite.

3.1.3. Halite

Halite (rock salt), NaCl, with the same cubic structure as LiF, deforms by slip easily and single crystals can sustain large strains provided failure by cleavage is suppressed. Halite has been studied extensively owing to its importance as a component of fault zones and oil traps in sedimentary basins, nuclear waste repositories, and a pressure medium for high-pressure experiments. Early studies often attributed deformation to twinning or kinking, but Pratt [69] showed that slip was the dominant mechanism. At low temperatures, $\{1\,1\,0\}\ \langle 1\,\bar{1}\,0\rangle$ is the principal slip system, with $\frac{1}{2}\langle 1\,1\,0\rangle$ as the Burgers vector. Each of the $\{1\,1\,0\}$ planes contains only one slip direction, so there are only two independent slip systems and the von Mises [164] criterion for plasticity in polycrystals is not met unless other systems are activated [70]. To a considerable degree, the mechanical properties of KCl (sylvite) are like those of halite.

Deformation and etch-pitting experiments on rock salt crystals have shown that both $\{1\,0\,0\}$ and $\{1\,1\,1\}$ slip can occur although electrostatic considerations make these planes less favored than $\{1\,1\,0\}$. Carter and Heard [71] deformed single crystals with various orientations at temperatures up to 500 °C at several strain rates and found that at room temperature $\{1\,1\,0\}$ slip was greatly favored but already at 300 °C $\{1\,0\,0\}$ and $\{1\,1\,1\}$ slip became equally active. The stress–strain curves and hardening behavior of pure halite resemble those of single crystals of fcc metals, with the three typical distinct stages [165, p. 225]. Duplex slip, glide polygonization and the creation of deformation bands characterize stage II. Cross-slip and the formation of dislocation tangles occur in stage III. X-ray topography was used to study the nature of deformation bands formed in stage II [202]. Possible hardening mechanisms have been investigated for several NaCl-type crystals, pure and doped [203]. The finding that the flow stress for the onset of stage III is thermally activated [204] led to the proposal and theoretical evidence that screw dislocations can dissociate in the $\{1\,1\,0\}$ planes and that cross-slip into $\{1\,0\,0\}$ requires stress-assisted, thermally activated recombination [205,206]. This suggests that cross-slip should be favored by increase in hydrostatic pressure [207].

As mentioned previously, the direct observation of dislocations in NaCl poses problems, although as mentioned in Section 1, the very first observations of dislocations were made using halite crystals some 100 years ago. About 50 years later, decorated dislocations in doped and thermally treated crystals provided much information [15,208]. Frank [209] studied theoretically the geometries of regular dislocation networks in the rock salt structure using Thomson's notation [210], while Amelinckx [5] found ways to analyze less regular networks. In the following years, most dislocation studies relied on the etch-pitting and stress-birefringence methods, which obviate the need for annealing. Fig. 5(a) shows $\{1\,1\,0\}\ \langle 1\,\bar{1}\,0\rangle$ slip bands in a lightly bent bar of halite, as revealed by the etch-pitting method. The

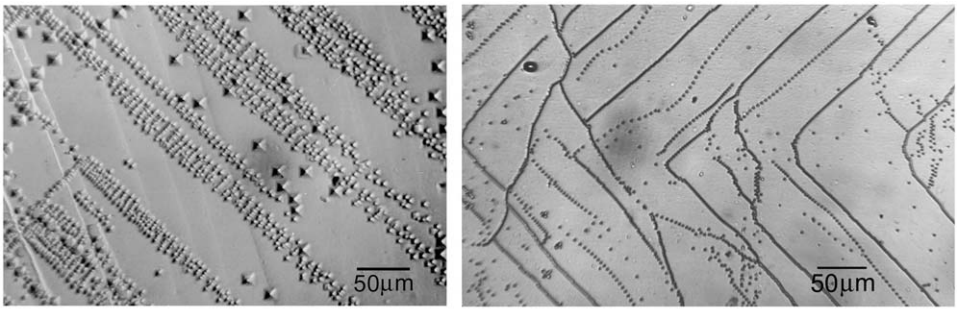

Fig. 5. Etch-pits marking the emergence sites of dislocations in halite: (a) Slip bands in a bent single crystal with glide polygonization in the bands (i.e., alignment perpendicular to the slip direction). The crystal was etched before and after bending; the larger etch-pits define where grown-in dislocations emerged at the surface. (b) Mostly tilt sub-boundaries formed by the annealing of a bent single crystal. The apices of the ''vees'' are aligned along the neutral axis of the bar (Barber, unpublished data).

dislocation density is locally very variable but it is approximately $10^6\,cm^{-2}$. Fig. 5(b) shows the etch-pit pattern due to edge dislocations arranged in low-angle tilt subgrain boundaries formed by the annealing of a strongly bent bar of halite. There is evidence for negatively charged dislocations in pure NaCl and positively charged OH-doped NaCl, after deformation by bending [211] with a Bauschinger effect, which is associated with the movement of charged dislocations.

The only report of TEM images of dislocations in deformed alkali halide crystals is by Hobbs and Goringe [212], who used special thin-sample preparation techniques, a TEM fitted with a liquid-He cooled stage and fast-emulsion photographic plates, the latter exposed using very low electron flux densities. Their diffraction contrast images lack any obvious signs of radiation damage and show $\langle 110 \rangle$ screw and $\langle 100 \rangle$ edge dislocations and tangles in KCl crystals deformed to 15% strain and $\langle 110 \rangle$ screws, and dipoles and debris in NaCl deformed to 10%.

3.2. Carbonates

3.2.1. Occurrences and structures of carbonate minerals

Rock-forming carbonate minerals at room temperature are rhombohedral (e.g., calcite and dolomite) or orthorhombic (e.g., aragonite). Calcite, $CaCO_3$, and the ordered double carbonate, dolomite, $CaMg(CO_3)_2$ predominate. High-temperature forms are often associated with rotational disorder of the carbonate groups [213]. Biogenic carbonates are predominately high magnesium calcite, dolomite, and aragonite. They importantly occur as very strong but lightweight protective constructions in the phyla *mollusca* and *echinodermata*. The fracture toughness of nacre is more than tenfold that of geological calcium carbonate [214]. Such biological constructions have, therefore, received attention from scientists interested in designing and making novel synthetic materials. Biogenic carbonates are

not considered here because of their diversity of both occurrence and structure and the current evidence that they lack grown-in dislocations and deform a brittle mode (their complex microstructures probably inhibit the nucleation of dislocations and hence their strength).

Calcite has trigonal symmetry, $R\bar{3}c$. The four-digit Miller–Bravais crystallographic indices used for calcite in this section refer to hexagonal axes and a (true) hexagonal structural cell. For this cell the calcite cleavage planes {**r**} have indices $\{1\,0\,\bar{1}\,4\}$ and the commonest twin planes {**e**} are $\{\bar{1}\,0\,1\,8\}$. Use of a true cell enables one to properly assign all reflections observed in X-ray and electron diffraction patterns to sets of planes with integer indices. Older literature mostly employs a rhombohedral cell, often the morphological (cleavage) cell containing $2CaCO_3$ molecules, which is not a true cell. Dolomite crystallizes in the point group $R\bar{3}$. Aragonite is the orthorhombic (Pcmn) polymorph of calcium carbonate. It is only a stable phase at high pressure, but notwithstanding this, the mineral occurs widely in marine sediments and in marine organisms, both skeletally and as nacre. For an earlier review of microstructures in carbonates see Wenk et al. [166].

3.2.2. Calcite

The plastic deformation of calcite usually involves both slip and twinning; both generate dislocations. Slip and twinning in rhombohedral carbonates have a preferred sense, that is, a definite direction of shear.

TEM results from the grains in naturally deformed calcites usually indicate that two or more deformation systems have operated, leading to complicated arrangements or tangles of dislocations. Even single crystals experimentally deformed to low strains generally contain complex dislocation configurations that defy analysis. A further handicap is the tendency of most calcite specimens to suffer electron beam damage, making it impossible to analyze dislocation properties from a set of images under various diffraction conditions. The eventual proof that the basal slip system can operate [49], subsequent to a long-held suspicion [50], necessitated the torsion at high temperature of a single crystal orientated to suppress the activation of all other slip systems.

Studies of limestones and marbles from various geological settings [215,216]) showed a fairly good correlation between the microstructures, metamorphic grade, and geologic history. For example, very high dislocations densities ($\sim 10^9\,\mathrm{cm}^{-2}$) were found in a deformed low-grade fine-grained limestone, whereas rocks of high metamorphic grade generally had lower dislocation densities. Greenschist facies samples could be distinguished from those of amphibolite facies on the basis of their microstructures. However, recovery was in evidence even in low-grade samples; as a consequence, the densities varied greatly between the grains in a fine-grained mylonite with a complex history. Dislocations in calcitic rocks clearly could move at much lower temperatures than in quartz rocks so that calcite was not suitable as an indicator of conditions in major tectonic events because of ease of subsequent recovery.

Analysis of TEM images of dislocations, together with structural considerations, indicate that the Burgers vectors for **r-**, **f-**, and **c-**slip are, respectively, $\frac{1}{3}\langle 2\,0\,\bar{2}\,\bar{1}\rangle$,

$\frac{1}{3}\langle 1\,0\,\bar{1}\,\bar{1}\rangle$, and $\frac{1}{3}\langle 2\,\bar{1}\,\bar{1}\,0\rangle$. There is no evidence for basal dislocations in calcite and marbles deformed at low temperatures. Activity on $(0\,0\,0\,1)$ $\langle 2\,\bar{1}\,\bar{1}\,0\rangle$ in high-temperature samples is characterized by many long straight screw dislocations. Slip on **r** in the negative sense occurs over a wide range of temperatures, as shown for single crystals [47] and for polycrystals [48,51]. Slip on **f** is also important, especially when twinning is less favored. The dislocations generated by both **r**- and **f**-slip do not have well-defined geometries. Those produced by **r-**slip are not crystallographically controlled; they tend to be strongly curved, are unregimented and seldom adhere strictly to their slip planes or form slip bands (this is in strong contrast to the situation for dolomite). The Burgers vectors are long (0.77 nm for **r-**slip and 0.81 nm for **f**-slip, but only 0.49 nm for **c**-slip). Despite the theoretical possibility of dissociation in the **r-**planes to partials with $\frac{1}{6}\langle 2\,0\,\bar{2}\,\bar{1}\rangle$ Burgers vectors and the creation of a stacking fault in the CO_3 lattice, there is no evidence for it.

Deformation twinning on both the **e-** and **r-**planes can produce several types of interaction and the generation of microcracks [161]. Twinning in calcite usually creates numerous dislocations, explaining why repeated twinning and detwinning is not possible [217,218]. Dislocations typically occur in the twin boundaries, within the twins and also external to them, especially when one twin impinges on another twin or an obstacle. Crossing twins [219] occur readily, producing rhombohedral channels, as first reported by Rose [220], after whom they are named. Stopping twins (these do not taper to a point) are common in polycrystals where many obstacles to propagation exist. Their terminations are important sites for dislocation nucleation and the initiation of microcracks (which themselves may create more dislocations).

In highly deformed calcite rocks **e**-twinning is usually profuse, which is consistent with their thermal history. Stress relief by twinning decreases as the temperature increases and in calcitic marbles deformed under suitable geological conditions, it is possible to find grains completely free of twins but with cell-like dislocation microstructures [Fig. 3(b)], resembling those observed in work-hardened metals.

3.2.3. Dolomite

The characteristics of dislocation configurations seen by TEM in dolomite are markedly different from those for calcite. In comparison, active slip systems for dolomite are more easily identified in deformed and unrecovered samples because dislocations tend to keep to their slip planes and frequently are geometrical in shape. Slip bands are common in experimentally deformed specimens. Because dolomite is an ordered mineral with a superlattice of both cations and anions (CO_3 groups), perfect dislocations in the structure are, *senso strictu*, superdislocations.

Examples of grown-in dislocations are found in ancient calcian dolomites and calcian ankerites. These minerals frequently exhibit fine-scale modulated microstrostructures with wavelengths commonly between 7.5 and 20 nm [221]. The modulations arise directly during growth, have been attributed to compositional or ordering fluctuations and superstructures [222,223], and are usually associated with a fine-scale growth banding closely perpendicular to the modulations [221]. The latter is a manifestation of plane concentric zoning and probably reflects small

compositional changes during growth [224]. The dislocations in these ancient dolomites and ankerites are oriented perpendicular to the growth zoning and thus roughly parallel to the modulations (Fig. 10-3 in Ref. [221]). They probably nucleated at the growing interface and being unable to terminate, traverse the growth sector.

Metamorphic dolomites can contain quite high dislocation densities, between 10^3 and $10^6\,cm^{-2}$. Evidence of recovery in the form of dislocation networks is commonly seen (see [225]). Generally speaking, there is a correlation of dislocation density with metamorphic grade: Crevola marble, a medium- to high-grade amphibolite facies rock [226] has a low dislocation density and is, therefore, suitable for deformation experiments [52]. To judge both from both experimental specimens and rocks, recovery does not appear to occur as readily as in calcite and so dolomite should be a better indicator of tectonic conditions. Fig. 5 illustrates microstructures in experimentally deformed single crystals. At low-temperature, dislocations are concentrated in bands [Fig. 6(a)]. At higher temperature, climb produces more open microstructures with loops [Fig. 6(b)].

Dolomite is much less prone to electron damage than calcite and so it is easier to determine Burgers vectors using diffraction contrast methods. The vectors for perfect dislocations are $\frac{1}{3}\langle 2\,\bar{1}\,\bar{1}\,0\rangle$ and $\frac{1}{3}\langle 2\,\bar{2}\,0\,1\rangle$. However, dislocation dissociation is also possible in dolomite; when it occurs in the basal planes, pairs of

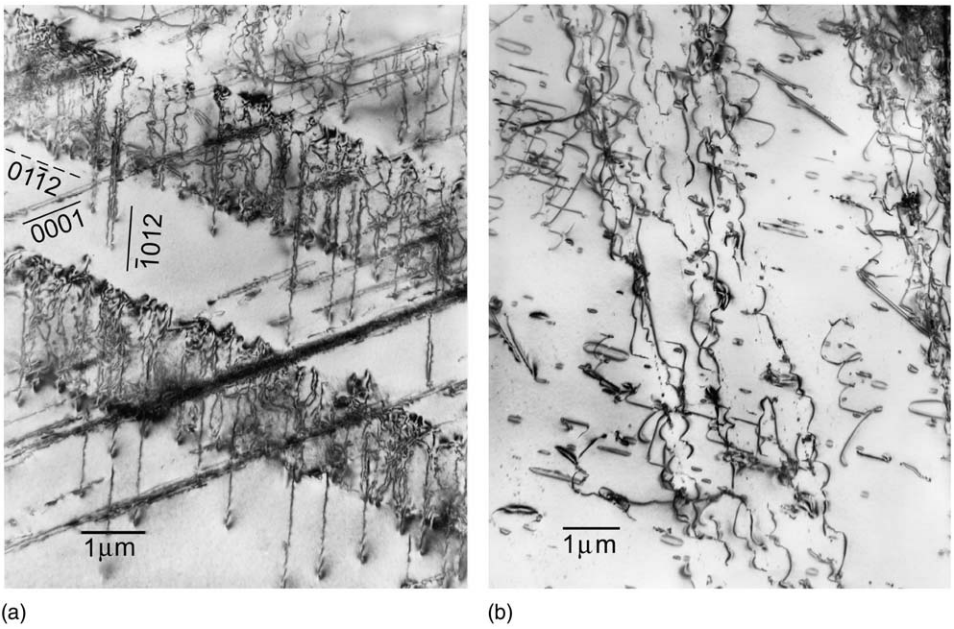

Fig. 6. TEM images of microstructures in experimentally deformed dolomite single crystals [52]: (a) At low-temperature dislocations are concentrated in slip bands. (b) At higher temperature climb and dislocation interactions produce dislocation loops.

superpartials separated by region of stacking fault are formed [53,225]. The Burgers vector of the basal partial dislocations is $\frac{1}{3}\langle 1\,0\,\bar{1}\,0\rangle$. Long ribbons of stacking fault can result from this dissociation in experimentally deformed dolomites [Fig. 3(a)]. The basal slip system is considered to be responsible for the unusual increase of strength with temperature demonstrable with single crystals [54,55]. Strengthening apparently occurs due to inability of basal dislocations to overcome obstacles because a mechanism (e.g., cross-slip) is lacking.

Dislocation dissociation accompanying slip on the **f**-planes presents more complex possibilities [53]. The slip directions and Burgers vectors lie along the intersection of two **f**-planes and therefore a superdislocation with a Burgers vector $\frac{1}{3}\langle 2\,\bar{2}\,0\,1\rangle$ can glide on two planes simultaneously in a vee-like configuration, or alternatively, as a closed rhombohedron-shaped loop using two planes of each orientation (this is known as pencil glide). If an **f**-slip dislocation dissociates to give partials of type $\frac{1}{6}\langle 2\,\bar{2}\,0\,1\rangle$ the passage of such a partial gives a fault in both the cation and CO_3 sublattices, resulting in what is normally called an APB. The diffraction contrast properties of such faults in practice, however, are not those expected for APBs. Therefore, they have been called complex stacking faults [53]. Usually many dislocation dipoles and small loops result from **f**-slip at moderate temperatures, on account of various interactions and the ease of cross-slip. When **f**-slip can occur, as in most grains in polycrystalline dolomite, it masks the increasing strength-with-temperature behavior associated with **c**-slip.

3.2.4. Aragonite

There are very few reports of observations of dislocations in either geological or biogenic aragonites although the slip systems are known (see Table 1) and {1 1 0} twinning occurs in both types. Studies of the aragonite→calcite transformation have shown that dislocation tangles and twins can serve as nucleation sites for calcite [227]. In an *in situ* TEM study of the transformation [228], there was no evidence of a martensitic mechanism [229] but the moving interphase boundary was seen to sweep away dislocations and twins. Recent interest in biomimetic materials has led to studies of the plasticity and microindentation of nacre. The results have provided new information about aragonite slip systems [56], but to date, no direct data about dislocation behavior.

3.3. Oxides

Several oxides that occur as significant minerals in nature are also important as ceramics or as components of ceramics, or as technological materials. Such materials are mostly synthesized for reasons of obtaining appropriate volume, mechanical properties or special geometry, control over impurities, and crystal defects, achieving functional doping, etc. These aspects of oxides will not be considered here. Bretheau et al. [129] carried out a comprehensive review (in French with an English summary) covering the properties and behavior of several technologically important oxides. The review points out that dislocation glide in oxides is not well documented and that

interpretations of observations from different oxides are often contradictory. Dislocation climb is the mechanism of interest at the elevated temperatures that are relevant to ceramics. To test possible theories, data about diffusing species are required and models of dislocation cores and jogs are necessary. Some methods of making core models have been proposed (see [230,231]), but generally these are lacking.

3.3.1. Corundum

Corundum, aluminum oxide (sapphire), α-Al_2O_3, has a crystal structure in which oxygen ions are close-packed and the aluminum ions occupy two-thirds of the octahedral interstices. The mineral is trigonal ($R\bar{3}c$) and the close-packed oxygen plane is basal, i.e. (0 0 0 1).

The extreme plastic anisotropy of sapphire was first reported by Wachtman and Maxwell [120] who detected basal creep in tensile specimens at 900 °C but found that when specimens with a *c*-axis were stressed in tension, no creep occurred until the temperature exceeded 1600 °C. The earliest TEM observations of dislocations in Al_2O_3 [232,233] used chemically thinned pure and doped synthetic sapphire and imaged various dislocations: sections of low-angle sub-boundaries and regular networks were seen in undeformed specimens while helices and loose networks were seen in specimens deformed in creep. Subsequent optical and TEM results established that slip is in the $\langle 1\,1\,\bar{2}\,0\rangle$ close-packed direction and the Burgers vector of the basal dislocations is $\frac{1}{3}\langle 1\,1\,\bar{2}\,0\rangle$. It was suggested that basal dislocations would need to glide by a mechanism of synchroshear involving dissociation of dislocations into quarter partials and the cooperative movements of anions and cations [198]. Further work showed that important additional slip systems for high temperatures are $\{1\,1\,\bar{2}\,0\}\langle 1\,\bar{1}\,0\,0\rangle$ [121,122] and $\{1\,0\,\bar{1}\,1\}\langle 0\,1\,\bar{1}\,1\rangle$, with a Burgers vector of $\frac{1}{3}\langle\bar{1}\,1\,0\,1\rangle$ [123–125]). Slip on $\{\bar{1}\,0\,1\,2\}\langle 1\,0\,\bar{1}\,1\rangle$, and possibly on $\{1\,0\,\bar{1}\,1\}\langle 1\,\bar{2}\,1\,0\rangle$ was also reported. TEM studies of the dislocations arrays around room temperature indentations showed that slip can also take place on the pyramidal planes $\{1\,1\,\bar{2}\,3\}$ in the $\langle 1\,\bar{1}\,0\,0\rangle$ direction, with the Burgers vector $\langle 1\,\bar{1}\,0\,0\rangle$ [126]. Basal twinning [126,234] and rhombohedral twinning are additional deformation mechanisms [235–237]. Both can occur at room temperature and rhombohedral twinning has been observed in deformation up to 1700 °C. Thermal shock often causes rhombohedral twinning.

Pletka et al. [238] examined various possible strengthening mechanisms in sapphire. The early stage of work hardening in pure samples deforming by basal slip is due to the formation of obstacles to dislocation glide in the form of many edge dipoles created by the trapping of dislocations on parallel planes [Fig. 7(a)]. As deformation proceeded further the dipoles were seen to break up by climb, forming small loops. When the rate of dipole accumulation became equal to the rate of their annihilation the rate of work hardening became zero. Several studies investigated the role of dislocations in the plastic deformation of Cr- and Ti-doped sapphire [238–241]. The effect of chromium concentration has little effect on dislocation multiplication mechanisms and dislocation velocities during basal slip between 900 and 1500 °C [242].

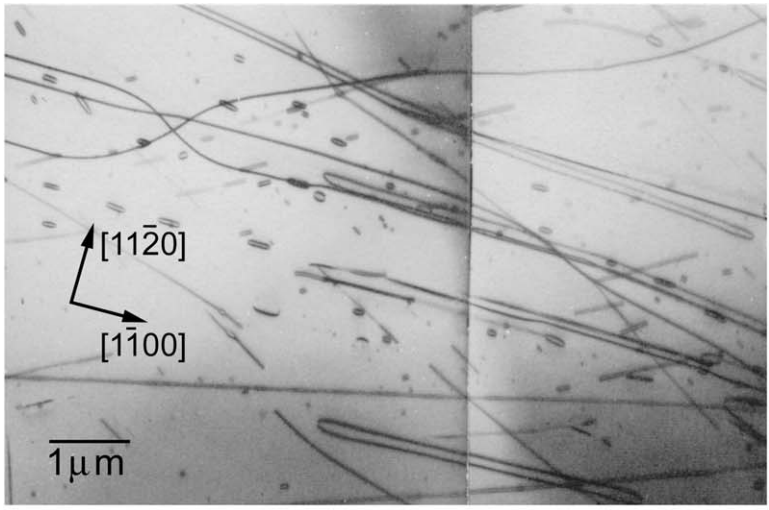

(a)

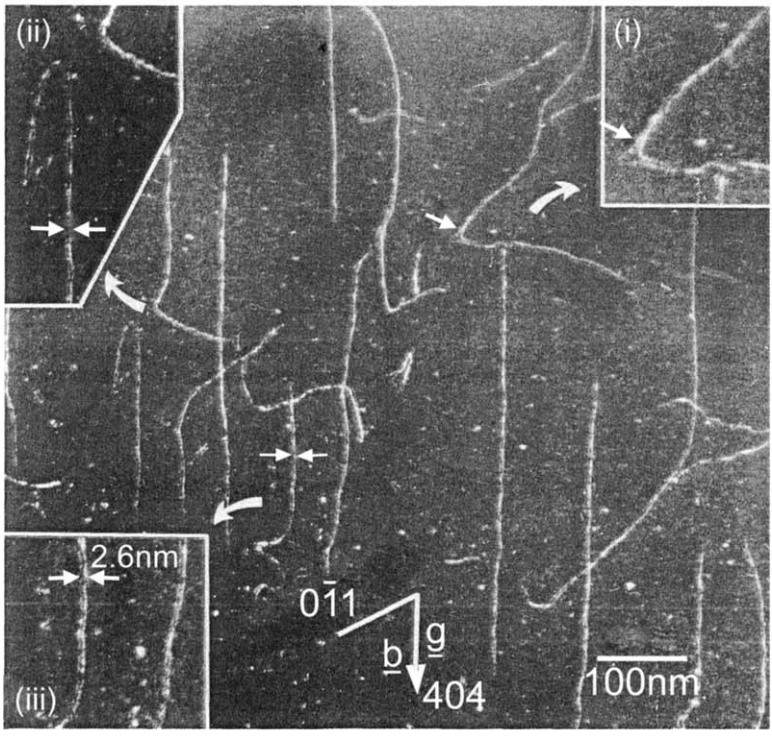

(b)

Fig. 7. Dislocation in oxides: (a) Bright field TEM image of dislocation microstructure consisting of long $\frac{1}{3}\langle 1\,1\,\bar{2}\,0\rangle$ edge dipoles, multipoles and debris of numerous small loops formed at the early stage of work hardening in corundum (sapphire), compressed at 1400 °C and deforming by basal slip; basal foil, $g = 3\,0\,\bar{3}\,0$ [238]. (b) Weak beam dark-field TEM image of a region in a spinel crystal deformed at 400 °C and slipping on {1 1 1} planes. The field is dominated by cross-slip of the $\frac{1}{2}\langle 1\,0\,1\rangle$ screw dislocations (vertical) on (0 1 0). All the dislocations are dissociated out of the primary slip plane but their widths vary (all the inserts have the same magnification) [146].

The slight dissociation possible for some dislocations in Al_2O_3 has been illustrated by several authors; two examples are: (a) the two arms of a $[1\,1\,\bar{2}\,0]$ dipole are each dissociated into two partials, the adjacent inner partials then annihilate to leave a wider ribbon of stacking fault, bounded by $\frac{1}{3}\langle 1\,0\,\bar{1}\,0\rangle$ partials [243]; (b) the dissociation of a dislocation with $\mathbf{b} = [0\,1\,\bar{1}\,0]$ into three partials that recombine where there is a change in angle [244].

3.3.2. Hematite

Hematite, α-Fe_2O_3, is a major ore mineral. It is isostructural with corundum and it seems reasonable to expect that it would slip on similar systems. There have been few deformation experiments on single crystals, however, and even fewer direct observations of dislocations in hematite.

At room temperature, the only easy deformation mechanisms in hematite appear to be twinning on the basal and pyramidal planes, $\{0\,1\,\bar{1}\,2\}$. Prismatic slip, $\{1\,1\,\bar{2}\,0\}\langle 1\,\bar{1}\,0\,0\rangle$, was shown to occur at 200 °C and above [106], although brittle fracture can still occur in tension at about 1200 °C in the absence of confining pressure [127]. At low strain rates, 25–700 °C and under confining pressure, hematite tested in compression was made to slip on $(0\,0\,0\,1)\langle 1\,1\,\bar{2}\,0\rangle$ and $\{1\,1\,\bar{2}\,0\}\langle 1\,\bar{1}\,0\,0\rangle$ [128]. There is TEM evidence for dislocations at twin interfaces and basal slip [245]. High-resolution TEM has been used to study symmetry and twinning in hematite [246,247] and intergrowths of hematite and magnetite [248,249] [Fig. 8(a)].

3.3.3. Ilmenite

Ilmenite, $FeTiO_3$, is also isostructural with corundum. Cations are ordered in alternate layers parallel to the close-packed oxygen layers, that is $(0\,0\,0\,1)$. Ilmenite is an important ore mineral for titanium. One might expect the same slip systems for ilmenite as with corundum. But similarly, slip on any plane transverse to the basal plane would require a perfect dislocation to have a large Burgers vector. Otherwise such slip would proceed by means of partials, generating regions of antiphase stacking, which would be likely only at high temperature. The mechanisms of plastic deformation of ilmenite have not been studied.

The interfaces between finescale exsolution lamellae of ilmenite in hematite have been investigated and most were shown to be coherent and dislocation free [251]. Due to differences in lattice parameters, dislocation arrays decorate the interface [Fig. 8(b)]. Contrast analysis revealed a hexagonal grid of rhombohedral dislocations [250] rather than dislocations with basal Burgers vectors [252]. The ordering phase transition in ferrian ilmenite from the high-temperature $R\bar{3}c$ disordered structure to a $R\bar{3}$ lower-temperature ordered structure results in the creation of twin domains [253,254]. No dislocations were involved.

3.3.4. Periclase and wüstite (see also Section 3.8.1)

Periclase, MgO, has the rock salt structure. It is rare in the Earth's crust but is thought to be a major component in the lower mantle in a solid solution with FeO (magnesiowüstite). As with NaCl, the easy glide plane at low temperature is the

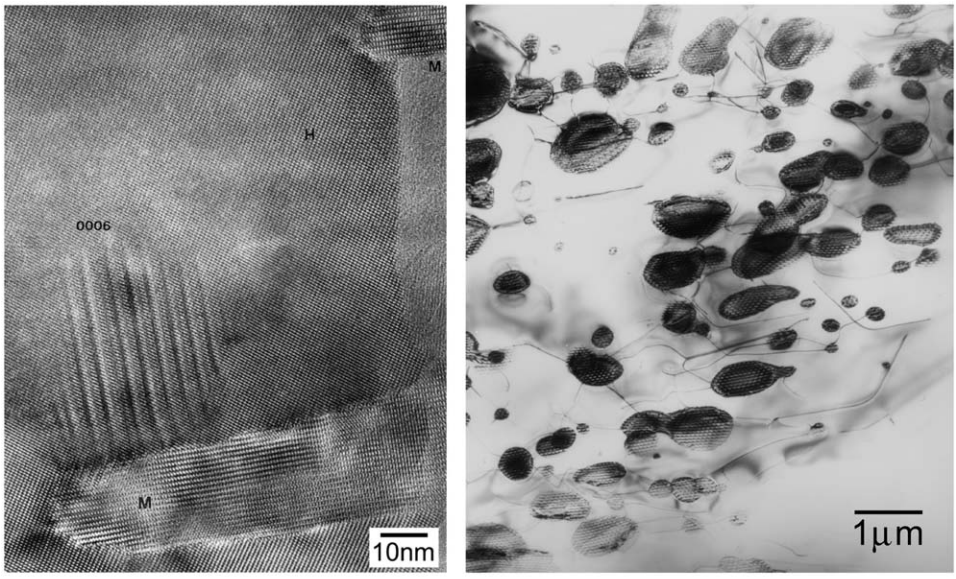

Fig. 8. TEM micrographs of dislocations in hematite intergrowths: (a). Magnetite-hematite intergrowth with zonal dislocation structures [249]. (b) Exsolution of ilmenite platelets in hematite. Ilmenite is decorated with a network of misfit dislocations to account for lattice strain caused by differences in lattice parameters [250].

electrically neutral plane, {1 1 0} and dislocations in MgO have Burgers vector $\frac{1}{2}\langle 1\,\bar{1}\,0\rangle$. At higher temperature, glide also occurs on $\{0\,0\,1\}\langle 1\,1\,0\rangle$ and $\{1\,1\,1\}\langle 1\,1\,0\rangle$. Dislocation structures formed during creep of MgO single crystals were investigated by etch-pitting [130,131]. Later work has relied more on TEM for the interpretation of microstructures [129]. Most of the plasticity of fine-grained polycrystalline MgO above 1000 °C was attributed to diffusional processes except for some evidence of dislocation glide [132,133]. Single crystal MgO shows plasticity due to slip on $\{1\,1\,0\}\langle 1\,\bar{1}\,0\rangle$ from below room temperature to moderate temperatures. Above 1200 °C, the $\{0\,0\,1\}\langle 1\,1\,0\rangle$ system is activated [134].

Wüstite, $Fe_{1-x}O$, with x commonly lying between 0.05 and 0.15, occurs as a phase in iron scale. The primary slip system is $\{1\,1\,0\}\langle 1\,\bar{1}\,0\rangle$, as in NaCl. A steady state can be attained in deformation experiments of polycrystalline FeO above 1000 °C and strain rates are proportional to the fourth power of stress, indicating that dislocation climb is active [127]. Diffusion creep is observed at yet higher temperatures. High strain experiments were performed in torsion and under confining pressure on magnesiowüstite aggregates by Heidelbach et al. [75] to investigate texture development and associated changes in mechanical behavior. The initial deformation texture was compatible with $\langle 1\,\bar{1}\,0\rangle$ dislocation glide on all three possible

slip systems: {1 1 1}, {1 1 0}, and {0 0 1} and this was confirmed by TEM results. The microstructure evolved into one of subgrains at a relatively low homologous temperature ($<0.5T_m$), which was possibly promoted by cross-slip between the active systems. Rotation of the subgrains ultimately led to a recrystallization texture. Dislocation creep and strain partitioning of olivine–wüstite aggregates deformed to large strains has been studied by Bystricky et al. [255].

3.3.5. Magnetite

Magnetite, Fe_3O_4, crystallizes in the inverse spinel-structure (cubic), with Fe^{3+} in the tetrahedral sites and both Fe^{2+} and Fe^{3+} in the octahedral sites (space group Fd3m). Many cationic substitutions occur. It is an important iron ore and occurs in many geological environments, as aggregates, veinlets, and inclusions.

There is relatively little information about dislocations in massive magnetite. Small crystals are usually dislocation-free: magnetosomes in magnetotactic bacteria are perfect single crystals [256]; the magnetites in the carbonates in the Martian meteorite, ALH84001, are also dislocation-free [257,258]. Preferred orientation measurements on magnetite ores deformed at 300 °C suggest the action of $\{1\,1\,1\}\langle 1\,\bar{1}\,0\rangle$ slip [150]. This mechanism was shown to be active at least up to 1000 °C [127].

3.3.6. Spinel

There is a large range of spinels, including magnetite as discussed above, but the most important, is the magnesium aluminate $MgO(Al_2O_3)_n$. Slip systems for this mineral have been researched thoroughly [140]. In stoichiometric samples ($n = 1$, i.e., $MgAl_2O_4$) deformed at high temperature (1800 °C), slip occurs on $\{1\,1\,1\}\langle 1\bar{1}0\rangle$ (glide of dislocations on the close-packed plane and direction) as predicted [141], and includes dissociation of $\langle 1\,1\,0\rangle$ dislocations into quarter partials [198]. One can deform spinel at temperatures below $0.5T_m$ if a uniaxial compressive stress is applied in the presence of a confining pressure [142]. Even deformation at room temperature is possible under special conditions [143]. Dislocation configurations associated with indentations made on spinel at room temperature have been studied by TEM [144,145].

Veyssière and Carter [146] deformed a stoichiometric single crystal of spinel along $\langle 1\,1\,0\rangle$ to cause primary slip on {1 1 1} with cross-slip occurring onto a {0 0 1} plane. Weak-beam imaging indicated that all dislocations associated with the primary slip plane were dissociated out of that plane, no matter what their character [Fig. 7(b)]. Deformation proceeded by gliding of the partials on parallel planes. The accompanying stacking faults have to migrate; this is achieved by a local shuffling of cations. Weak beam images of screw dislocations gave a stacking fault energy of $530 \pm 90\ \mathrm{mJ/m^2}$ for conservative dissociation on {0 0 1} at 400 °C.

The effect of cation vacancies in alumina-rich samples is to change the slip plane from {1 1 1} to {1 1 0}, with glide still in the $\langle 1\,1\,0\rangle$ direction [140,147–149]). Dissociation into quarter partial dislocations is again observed but with a larger separation [147].

3.3.7. Perovskite (see also Section 3.8.5)

Perovskite, $CaTiO_3$ is one of a large group of minerals with formula AA′BB″O3 owing to the ease of substitution of the cation species. The structure is unique in having a large cation site in 12-fold coordination. Perovskites have a cubic or cube-octahedral structure but symmetry is often reduced to tetragonal or orthorhombic by ordering or distortion [259]. There are many ''perovskites'' of scientific curiosity or industrial importance for devices (e.g., the ferroelectric tetragonal oxide $BaTiO_3$ and tetragonal/rhombohedral Pb(Ti, Zr)O_3). The perovskite structure also attracts much attention because of its associations with high-temperature superconductivity in compounds such as $YBa_2Cu_3O_6$. For geosciences, the perovskites (Mg, Fe)SiO_3 and $CaSiO_3$ are thought to be the main constituents of the lower mantle and control its rheology. Dislocations in these silicate perovskites will be discussed in the section on high-pressure minerals.

The easy glide systems in pseudo-cubic $CaTiO_3$ are $\{1\,1\,0\}\langle 1\,\bar{1}\,0\rangle$ and $\{0\,1\,0\}\langle 1\,0\,0\rangle$ [135]. Other slip systems can also be activated under special conditions, for example, $\{0\,0\,1\}\langle 1\,1\,0\rangle$ and $\{1\,1\,0\}\langle 0\,0\,1\rangle$. There is very little information about dislocations and microstructures in $CaTiO_3$ [260] but a large amount about them in other perovskites such as $SrTiO_3$. Dislocations in perovskites, including $SrTiO_3$, are widely observed to dissociate. Also a very marked flow stress anomaly in $SrTiO_3$ suggests that dislocations in the cubic perovskite structure may possess several core structures [261].

3.3.8. Rutile

The structure of rutile, TiO_{2-x}, is tetragonal, with a pseudo-hexagonal packing of oxygen ions in the (0 0 1) plane (space group $P4_2/mnm$). Rutile is commonly oxygen deficient. It is an ore for titanium and occurs in quartz veins in metamorphic rocks and as placer deposits.

The plastic behavior of rutile is surprising at first sight: (0 0 1) is not a slip plane at low to moderate temperatures and does not feature in the primary system at high temperatures, which is $\{1\,0\,1\}\langle 1\,0\,\bar{1}\rangle$ [136,137]. The secondary higher-temperature system is $\{1\,1\,0\}[0\,0\,1]$. Dissociated $\langle 1\,0\,\bar{1}\rangle$ dislocations and long stacking faults have been observed [138] but dislocations with [0 0 1] Burgers vectors are not dissociated [139]. The amount of dissociation appears to be associated with stoichiometry. Suzuki et al. [262] studied dislocation dissociations in rutile and isostructural SnO_2 by HRTEM and confirmed that [0 0 1] dislocations did not dissociate, while $\langle 1\,0\,1\rangle$ dislocations did. Furthermore, they observed edge dislocations with $\mathbf{b} = \langle 1\,0\,0\rangle$. These were found to dissociate on the $\{1\,0\,\bar{1}\}$ plane into sessile types by the reaction $[1\,0\,0] \rightarrow \frac{1}{2}[1\,0\,1] + \frac{1}{2}[1\,0\,\bar{1}]$.

3.4. Quartz

Quartz (SiO_2) is one of the most abundant minerals in the Earth's crust. Owing to its ubiquitous occurrence in zones of high strain tectonic deformation, its rheological properties are commonly used to model the mechanical behavior of

continental regions (see [263]). In addition, dislocation glide mechanics in quartz (specifically kink pair nucleation) have been applied to model the rheological evolution of grain scale asperities on faults during earthquakes [264].

The low-temperature polymorph (α-quartz) is trigonal ($P3_121$). The high-temperature polymorph (β-quartz; transition at 573 °C, increasing to ~900 °C at a pressure of 1.5 GPa) is hexagonal (P622). Low quartz is elastically very anisotropic, with a direction perpendicular to the negative rhomb $\{0\,2\,\bar{2}\,1\}$ almost twice as stiff as the direction perpendicular to the positive rhomb $\{2\,0\,\bar{2}\,1\}$. High quartz is fairly isotropic.

Dislocation imaging in quartz has a long history, but it was only with the development of ion beam thinning that dislocation microstructures could be quantified with TEM analysis [265]. Dominant slip systems in quartz have been studied by analysis of dislocations in deformed single crystals as well as experimentally and naturally deformed quartz rocks (quartzites). One of the first determinations of Burgers vectors identified $\mathbf{r} = \frac{1}{3}[2\,\bar{1}\,\bar{1}\,0]$ [151]. Contrast analysis is complicated by the fact that quartz undergoes rapid beam damage. Slip takes place mainly in **a**, **c**, and $\langle \mathbf{c}+\mathbf{a} \rangle$ directions on numerous low index planes containing these directions, but dominant under most conditions are $(0\,0\,0\,1)$ and $\{1\,0\,\bar{1}\,0\}$ planes [152]. Creep tests on wet synthetic crystals conducted at room pressure suggest a dominance of **c**-slip at low temperatures [153]. Furthermore, extrapolation of the temperature dependence for **c** and **a** slip to higher temperature indicates a transition from **c-** to **a-**slip (Fig. 9). Evidence for **a-**slip in quartz single crystals at lower temperatures has been reported (e.g., [154,155]) but the data are not unambiguous [153]. Recent high-pressure ($P = 1.5$ GPa) experiments on wet synthetic crystals do suggest that slip on $(0\,0\,0\,1)\ \frac{1}{3}\langle 1\,1\,\bar{2}\,0\rangle$ is easier than $\{1\,0\,\bar{1}\,0\}$ $[0\,0\,0\,1]$ at 600°C, and that the activity of **c-** and **a-**slip become similar at 900 °C, consistent with transitions in texture patterns observed in quartzite [156].

The effect of temperature on the microstructures and dominant slip systems determined from textures are similar for both experimentally and naturally deformed quartzites (see [266–269]). Inferences about slip systems from textures are not unequivocal, especially because many texture studies rely only on *c*-axis orientations and not the full orientation distribution. There are very few TEM investigations identifying dislocation geometries in natural quartzites. The newer studies are consistent with the concept that $(0\,0\,0\,1)\ \frac{1}{3}[2\,\bar{1}\,\bar{1}\,0]$ slip dominates at lower temperatures, with a transition to $\{1\,0\,\bar{1}\,0\}\ \frac{1}{3}\langle 1\,1\,\bar{2}\,0\rangle$ slip at intermediate temperatures (~900 °C in the laboratory, 500–600°C in the Earth) and finally $\{1\,0\,\bar{1}\,0\}$ $[0\,0\,0\,1]$ slip at temperatures above 600–700°C in the Earth [267]. Slip on the rhombohedral planes in **a** and **c** directions is also observed. The different transition temperatures observed for experiments and rocks recovered from natural settings are interpreted to reflect a kinetic trade-off between the temperature and strain rate. Experimental samples creep at rates 10^5–10^7 times faster than deformation occurs in the Earth.

Experimental data suggest that the displacive α–β transition may not strongly influence the dominant slip systems. This is not unexpected because the main basal and prismatic slip systems have "hexagonal" symmetry. However, textures are

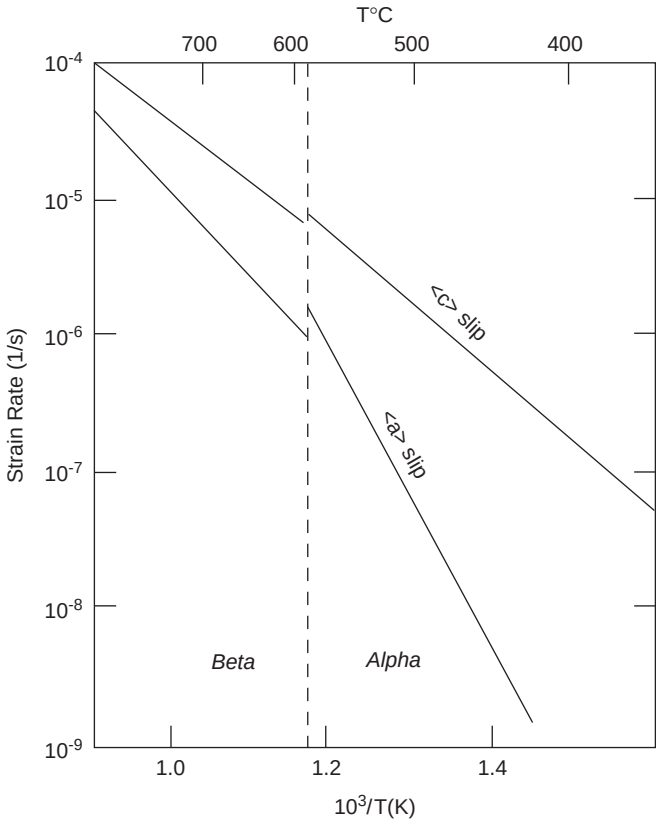

Fig. 9. Axial creep rates for wet synthetic quartz single crystals deformed in orientations to promote prism ⟨**c**⟩ slip and ⟨**a**⟩ slip [153].

distinctly trigonal in most natural quartz rocks, with very different orientation distributions for positive and negative rhombs (see [270]). The trigonal textures may arise for various reasons: conceivably rhombohedral slip systems are important. They may be due to mechanical Dauphiné twinning, which is geometrically a 180° rotation about the *c*-axis but achieved through slight structural distortions [271–273]. However, twins are rarely observed in natural quartzites in a wide range of conditions [263]. Interestingly, *in situ* heating experiments in the TEM documented the role of dislocations for the propagation of twins in the vicinity of the α–β transformation [274] [Fig. 10(a)]. Most natural quartzites are recrystallized, rather than plastically deformed and recrystallization under stress of this highly anisotropic material may induce the trigonality of the preferred orientation pattern [276–279].

The stress required for dislocation slip in quartz depends strongly on water fugacity. Under dry conditions, quartz is extremely strong, owing to the strongly covalent Si–O bonding. Dry gem-quality single crystals support stresses in excess of 1.0 GPa at a temperature of 1300°C ($\sim 0.8\, T/T_m$) and confining pressure of 0.3 GPa.

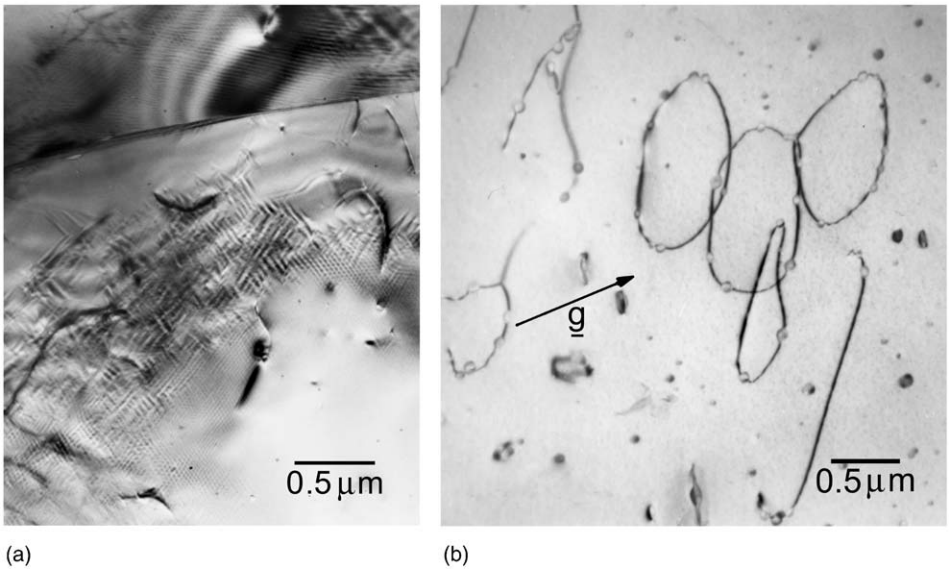

Fig. 10. TEM images of dislocation structures in quartz. (a) *In situ* heating experiment near the α–β phase transition with arrays of Dauphiné twins that are pinned by dislocations [274]. (b) Water bubbles in (“wet”) quartz are associated with dislocations, especially loops [275].

At these conditions, strain is accommodated dominantly by microcracking, and dislocation glide is largely isolated to crack tip regions [280]. By contrast, hydrothermally synthesized quartz crystals exhibit yield stresses in the range of 140 MPa at 750 °C [153,281,282]. The effect of water content on dislocation creep has also been documented for quartz aggregates, where creep rate is observed to increase approximately linearly with increasing water fugacity [283,284].

While the effects of water are well documented, and further substantiated by measurements of enhanced diffusion and dislocation recovery at high water fugacity [285,286], the mechanisms by which water (or hydrogen) influence dislocation mobility are still not well understood [287,288]. Some water is in the form of bubbles associated with dislocations [Fig. 10(b)] [275]. Microstructural evidence for enhanced dislocation climb, as well as rapid rates of dislocation recovery, suggest dislocation mobility is increased by enhanced diffusion rates under hydrous conditions [284,289,290]. However, climb was inhibited in deformation experiments on water-poor quartz, tested under P, T conditions that kept the residual water dissolved in the lattice and only basal and (**c**+**a**)-slip were rendered active, glide being aided by dislocation dissociation [157]. Enhanced diffusion rates under hydrous conditions are interpreted to result from an increase in the concentration of H-related defects with increasing pressure [290,291]. Such a process explains differences in the behavior of wet quartz at different water fugacities. However, the drastic changes in the behavior of dry quartz and quartz with $\sim$500 H/10^{6}Si may

represent true "hydrolytic weakening," where Si–O–Si bonds are hydrolyzed to form weaker Si–O–H–H–O–Si, lowering the Peierls barrier to dislocation glide [282].

Various TEM studies of quartz rocks illustrate systematic changes in microstructures with metamorphic grade and deformation conditions. Average dislocation densities range from $<10^7\,\mathrm{cm}^{-2}$ in high-temperature environments to $>10^9\,\mathrm{cm}^{-2}$ in heavily deformed cold-worked material (see [167,269,292,293]).

3.5. Olivine

Olivine, $(Mg_{1-x}Fe_x)_2SiO_4$, is the primary mineral in Earth's upper mantle with $x \approx 0.1$. The olivine crystal structure is orthorhombic in space group Pbnm. Deformation of olivine has been of long-standing interest, because this mineral is the major component of the Earth's upper mantle and controls its rheology. Furthermore, preferred orientation of olivine attained during mantle deformation by dislocation creep results in high and systematic seismic anisotropy [294,295], an observation that has been exploited by geophysicists to investigate the dynamics and kinematics of mantle convection.

The dominant slip systems in olivine at high temperatures (low differential stresses) are (0 1 0)[1 0 0] and (0 0 1)[1 0 0] with (0 1 0)[0 0 1] and (1 0 0)[0 0 1] playing a greater role at lower temperatures (high differential stresses) [87–89] (Fig. 11).

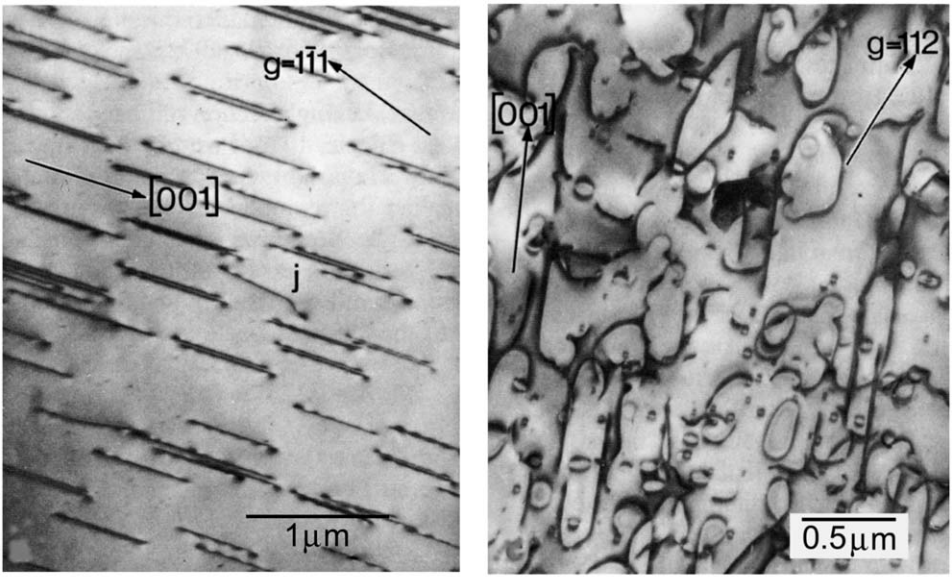

Fig. 11. Dislocation structures in experimentally deformed olivine. (a) Crystal deformed at 800 °C with [0 0 1] screws. (b) Dislocation loops in a crystal deformed at 100 °C. Also here $\mathbf{b} = [0\,0\,1]$, ref. [152].

However, TEM observations have revealed dislocations with [0 1 0] Burgers vectors as components of low-angle tilt boundaries [90], and high-resolution lattice fringe images demonstrated their dissociation into three or four partial dislocations [91] (Fig. 12). The transition between [1 0 0] and [0 0 1] dominated slip also occurs with increasing pressure [296]. At high temperatures, climb provides a portion of the strain as evidenced by analyses of the change of shape of single crystals deformed in compression [297] and by the kinetics of formation of low-angle tilt boundaries [90].

A substantial number of laboratory studies of the rheological behavior of olivine have been undertaken, both on single crystals and on polycrystalline samples [297–301]. These experiments demonstrate that the strength of olivine is sensitive not only to temperature and pressure but also to Fe content, oxygen fugacity, and water fugacity. In samples deformed under anhydrous conditions, four distinct deformation regimes have been identified: grain boundary diffusion creep, dislocation-accommodated grain boundary sliding, dislocation creep, and lattice friction creep. For samples deformed under hydrous conditions, the dislocation-accommodated grain boundary sliding regime appears to be absent, possibly because of the enhanced role of dislocation climb. In addition to temperature and pressure, ''water'' has a major effect on the strength of olivine. The water-weakening effect is associated with the introduction of hydrogen ions into olivine grains, analogous to doping a semiconductor material because olivine can be treated as a wide band gap semiconductor [298,302,303].

Transitions between slip systems have also been reported as a function of water fugacity. Five different regimes in stress – water fugacity space have been

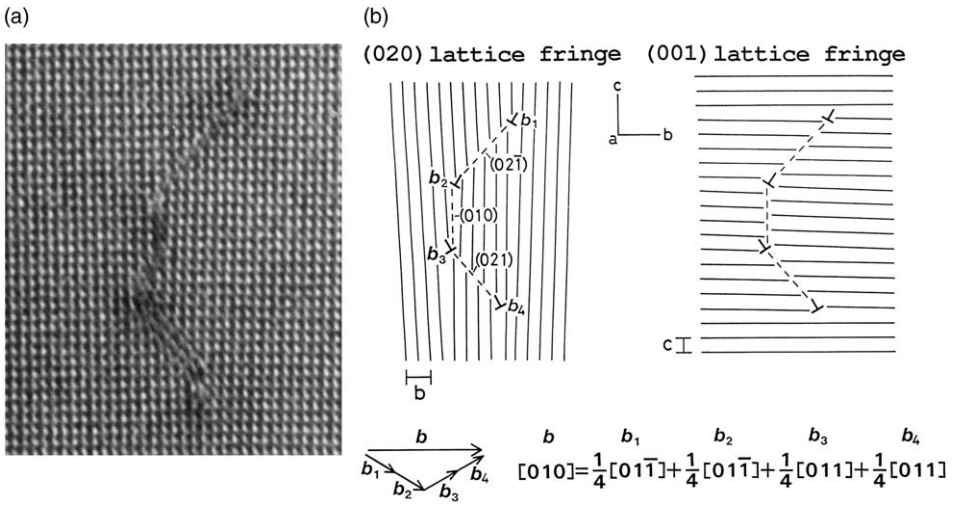

Fig. 12. HRTEM image of a dissociated dislocation with $\mathbf{b} = [0\,1\,0]$ in olivine grain from the Uenzaru peridotite in Japan [91]. The partial dislocations lie along [1 0 0]. Offsets in the lattice fringes are best viewed by observing the electron micrograph at an oblique angle. The schematic drawing illustrates (0 2 0) and (0 0 1) lattice fringes. The stacking faults lie on (0 1 0) and {0 2 1} planes. The dissociation reduces the elastic strain energy by a factor of ~ 3.

reported [92]: (0 1 0)[1 0 0] at low stress, low water content; (0 0 1)[1 0 0] at low stress, intermediate water content; (1 0 0)[0 0 1] at intermediate stress, high water content; (0 1 0)[0 0 1] at high stress, high water content; $\{0\,k\,l\}[1\,0\,0]$ at high stress, low water content. The relative roles of stress, water content, temperature, and pressure in the transitions between dominant slip systems is complex as it is not possible to vary one of these parameters without varying another. For example, to reach high water contents, it is necessary to go to high pressures [93]. Deformation at low stresses requires high temperatures, while deformation at high stresses requires high confining pressures and generally low temperatures.

3.6. Other silicates

3.6.1. Garnet (see also Section 3.8.2)

Garnets are cubic minerals with a wide range of chemical substitutions that occur in metamorphic rocks from the Earth's crust and as a volumetrically significant fraction of the upper mantle. Some end-members are almandine $Fe_3^{2+}Al_2(SiO_4)_3$, grossular $Ca_3Al_2(SiO_4)_3$, pyrope $Mg_3Al_2(SiO_4)_3$, and majorite $Mg_3MgSi(SiO_4)_3$. Some synthetic garnets are also important technologically. Gadolinium gallium garnet (GGG) thin films and yttrium aluminum garnet, YAG (the latter with various dopants, e.g., neodymium), have applications in magnetic bubble devices, and optical laser devices and waveguides, respectively. Some reports about growth-induced dislocations in these materials (see [304,305]) may have relevance to mineral garnets.

One of the earliest reports about dislocations in a natural garnet is that of Carstens [306] who studied Norwegian and Czech pyrope-rich garnets by etching them with hydrofluoric acid. Long etch channels extending from the surfaces, similar to those observed earlier [27], were attributed to deformation-induced dislocations. Tangled arrangements and cell structures were interpreted as indicators of dislocation creep.

TEM was used to elucidate the characteristics of dislocations in naturally deformed silicate garnets and olivines in garnet peridotites and silicate garnets in eclogites [307]. It was found that (i) dislocation densities in garnets from garnet-peridotites were always almost an order of magnitude less than those in the coexisting olivines; (ii) dislocation densities of garnets in eclogites that were within garnet peridotites were almost ten times greater than those in the garnets surrounding garnet peridotites. The Burgers vector, **b** was predominantly $\langle 1\,0\,0 \rangle$ for garnets with dislocation densities of 10^5–$10^6\,\mathrm{cm}^{-2}$, but **b** was $\frac{1}{2}\langle 1\,1\,1 \rangle$ for dislocation densities of 10^7–$10^8\,\mathrm{cm}^{-2}$.

Two very different but characteristic microstructures were identified in eglogites from the Alps [308]. One is indicative of only local microplasticity but overall brittle behavior, consisting largely of microfractures. The other, occurring more widely, was a dislocation microstructure that is the result of dislocation creep associated with dynamic recovery in the form of climb. Slip systems found to be operative were $\{1\,\bar{1}\,0\}\,\frac{1}{2}\langle 1\,1\,1\rangle$, $\{1\,1\,\bar{2}\}\,\frac{1}{2}\langle 1\,1\,1\rangle$, $\{1\,2\,\bar{3}\}\,\frac{1}{2}\langle 1\,1\,1\rangle$, $\{0\,1\,0\}\langle 1\,0\,0\rangle$, and $\{0\,1\,1\}\langle 1\,0\,0\rangle$.

Several analytical methods, including electron backscatter imaging and diffraction, were used to study elongate natural garnets that were deduced to have deformed at $\sim 700\,^{\circ}C$ [309]. In low strain regions, subgrains with small misorientation between neighbors were observed; boundary misorientations increased when approaching areas of higher strain. A polygonal microstructure was present in high strain areas.

With HRTEM, dissociations in a completely stoichiometric garnet were observed [310], contrary to the notion that dissociation is linked to traces of impurities. Parallel and narrow $\frac{1}{4}\langle 1\,1\,1\rangle$ partial dislocations were separated by stacking faults that corresponded to a low-energy configuration resulting from the occupancy of previously vacant dodecahedral and tetrahedral lattice sites.

3.6.2. Orthopyroxene

Enstatite-hypersthene, $(Mg,Fe)Si_2O_6$, the second most abundant mineral in upper mantle rocks, is orthorhombic (Pbca). Pyroxenes are chain silicates, with SiO_3 chains extending along the *c*-axis. Dislocations with [0 0 1] Burgers vectors dominate deformation with glide on the (1 0 0) and (0 1 0) planes [107–112]. There are also (1 0 0)[0 1 0] dislocations with a [1 0 0] line direction [311,312] [Fig. 13(a)]. The critical resolved shear stress (CRSS) for the (1 0 0)[0 0 1] slip system is significantly smaller than for (0 1 0)[0 0 1]. With a limited number of slip systems, it is inferred that climb

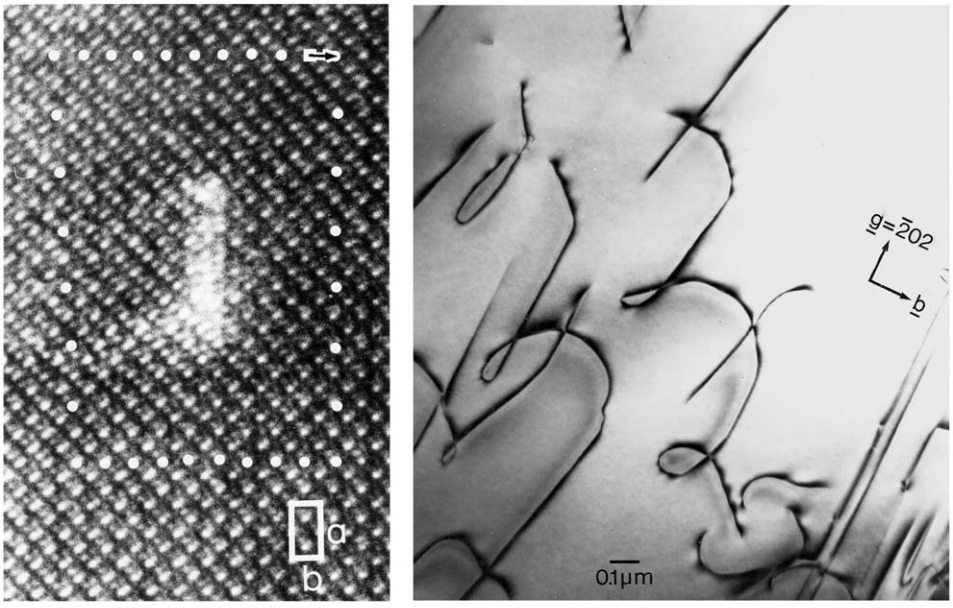

Fig. 13. (a) HRTEM image of a [0 1 0] edge dislocation in enstatite [311,312]. (b) TEM image of helix formation due to cross-slip of [0 0 1] screw dislocations in hornblende [313].

and grain boundary sliding must also be important deformation mechanisms in orthopyroxene rocks [314].

3.6.3. Clinopyroxenes

The clinopyroxenes are monoclinic: diopside $CaMgSi_2O_6$, augite $Ca(Mg,Fe)Si_2O_6$, and spodumene $LiAlSi_2O_6$ crystallize in space group C 2/c, pigeonite (Ca, Mg, Fe)Si_2O_6 and clinoenstatite $MgSiO_3$ in space group $P2_1/c$ and omphacite (Ca, Na) (Mg, Fe, Al)Si_2O_6 in P2/n.

Based on TEM analyses of experimentally deformed *diopside*, plastic deformation takes place by mechanical twinning on (1 0 0)[0 0 1] and (0 0 1)[1 0 0] with dislocation glide on (1 0 0)[0 0 1], (1 0 0)[0 1 0], and (0 1 0)[1 0 0] at temperatures of $<500\,^{\circ}C$ [113–119]. At higher temperatures, slip is activated on (1 0 0)[0 0 1], {1 1 0} $\frac{1}{2}\langle 1\,\bar{1}\,0\rangle$, {1 1 0}[0 0 1], (0 1 0)[0 0 1], (1 0 0)[0 1 0], and (0 1 0) $\frac{1}{2}$[1 0 1] [115,119,311, 312,315]. The easiest slip system appears to be (1 0 0)[0 0 1] at temperatures $500^{\circ} < T < 800^{\circ}C$, which alters to {1 1 0} $\frac{1}{2}\langle 1\,\bar{1}\,0\rangle$ and {1 1 0}[0 0 1] for $T > 800^{\circ}C$ [296,315].

Burgers vector and dislocation line analysis of naturally deformed *augite*-enstatite crystals indicate activation of many slip systems such as (1 0 0)[0 0 1], {1 1 0} $\frac{1}{2}\langle 1\,1\,0\rangle$, {1 1 0} $\frac{1}{2}\langle 1\,1\,2\rangle$, (1 0 0)[0 1 0], (0 1 0)[1 0 0], (0 1 0)$\langle 1\,0\,1\rangle$, and {1 1 0} $\langle 1\,1\,1\rangle$, the first two being the most active [311,312]. The study demonstrates that most dislocations are dissociated and stacking faults are produced that can be interpreted based on the complex structure of these chain silicates. In naturally deformed augite from a pyroxenite with lamellar exsolution $\frac{1}{2}$[1 0 1] dislocations in (0 1 0) combine single to double chains, yielding so-called chain multiplicity faults [316].

An interesting role of dislocations is in the stress-induced phase transformation of orthoenstatite to *clinoenstatite* [317–319].

As with other nominally anhydrous silicate minerals, the addition of a small amount of hydrogen in clinopyroxene results in a significant decrease in high-temperature viscosity, both in the diffusion creep regime and in the dislocation creep regime [119,320–322]. Compared to olivine, the dependence of creep rate on water fugacity is similar to that reported for olivine with an approximately linear relationship between creep rate and water fugacity [322]. However, in the dislocation creep regime, the dependence of creep rate on water fugacity is significantly larger for clinopyroxenes, for which creep rate increases roughly as the third power of water fugacity [321].

Omphacite is a clinopyroxene that can be disordered, but is rarely disordered in nature because it typically occurs in eglocite facies (metamorphic) rocks as a main phase with garnet. Mg and Al cations order convergently on the M1 positions of the monoclinic structure, leading to omphacite with the space group P2/n. The $\frac{1}{2}$[1 1 0] translational symmetry is lost in the ordering transition so that antiphase domains (APDs) with the displacement vector $\mathbf{R} = \frac{1}{2}$[1 1 0] can form [323,324].

Omphacite samples have been found to contain a range of crystal defects: free dislocations, deformation twin lamellae on (1 0 0), chain multiplicity faults parallel to (0 1 0), noncrystallographic faults terminating in dislocations, APDs, low-angle

grain boundaries, recrystallizing grains, exsolution lamellae [325]. Apart from the APDs and exsolution lamellae, all these defects result from deformation followed by or contemporaneous with recovery. The first determinations of the Burgers vectors of dislocations in omphacite were made by TEM by Van Roermund and Boland [326]. They identified the Burgers vectors [0 0 1], $\frac{1}{2}\langle 1\,1\,0\rangle$, and $\frac{1}{2}\langle 1\,1\,2\rangle$ (the latter at dislocation nodes) and concluded from the presence of many sub-boundaries that plastic deformation had been dominated by dislocation creep. These results and conclusions have been investigated in more detail in naturally deformed omphacites [327–330] and in experimentally deformed disordered (C2/c) omphacites [331].

Spodumene the lithium clinopyroxene has a Burgers vector {0 1 0} and a glide plane (1 0 0) [332]. In addition (1 0 0) twinning has been documented.

3.6.4. Amphiboles

Clinoamphiboles are monoclinic (C2/m) hydrous double-chain silicates that are common in metamorphic rocks. Dislocation structures have been studied in *hornblende* ($(Ca, Na, K)_{2-3}(Mg, Fe, Al)_5(OH, F)_2(Si, Al)_2Si_6O_{22}$) and *glaucophane* ($Na_2Mg_3Al_2(OH,F)_2Si_8O_{22}$).

Mechanical $(\bar{1}\,0\,1)$ $[\bar{1}\,0\,\bar{1}]$ twins have been identified in experimentally deformed hornblende single crystals, as well as dislocations on the (1 0 0)[0 0 1] slip system [333,334]. In hornblendes from naturally deformed rocks dislocations on {h k 0} planes were documented, mainly [0 0 1] screws [335–338]. A systematic investigation of dynamically recrystallized hornblende from a high-temperature shear zone discovered microstructures typical of dislocation creep, with subgrain boundaries and free dislocations [313]. The primary slip system is (1 0 0)[0 0 1] consistent with experimental results. Secondary, slip systems are (0 1 0)[1 0 0] and $\{1\,1\,0\}\frac{1}{2}\langle 1\,1\,0\rangle$. There is evidence for cross-slip of [0 0 1] screws producing helical microstructures [Fig. 13(b)]. Amphibole structures are intermediate between pyroxenes and sheet silicates and indeed "chain multiplicity faults" have been described [339] and transitional structures may be facilitated by movement of partial dislocations [340].

Studies of glaucophane from high-pressure–low-temperature metamorphic rocks reveal a variety of slip systems: (1 0 0)[0 0 1], {1 1 0}[0 0 1], (0 1 0)[1 0 0], $\{1\,1\,0\}\frac{1}{2}\langle 1\,1\,0\rangle$, and $(0\,0\,1)\frac{1}{2}\langle 1\,1\,0\rangle$ [341].

3.6.5. Mica

Micas are some of the earliest minerals where dislocations have been studied [33,342] using multiple beam interferometric techniques and imaging screw dislocations in the basal plane (0 0 1) of dioctahedral *muscovite* (C2/c) ($KAl_2(OH,F)_2AlSi_3O_{10}$). Burgers vectors were determined with TEM [343,344]) and X-ray transmission topography [345]: $\frac{1}{2}[1\,1\,0]$, $\frac{1}{2}[\bar{1}\,1\,0]$, and [1 0 0]. Dislocation microstructures play an important role in recrystallization of mica [346,347]) (Fig. 14). Experimental deformation of trioctahedral *biotite* (C2/m) ($K(Mg,Fe)_3(OH,F)_2AlSi_3O_{10}$) confirmed $\frac{1}{2}\langle 1\,1\,0\rangle$ and [1 0 0] as Burgers vectors [348].

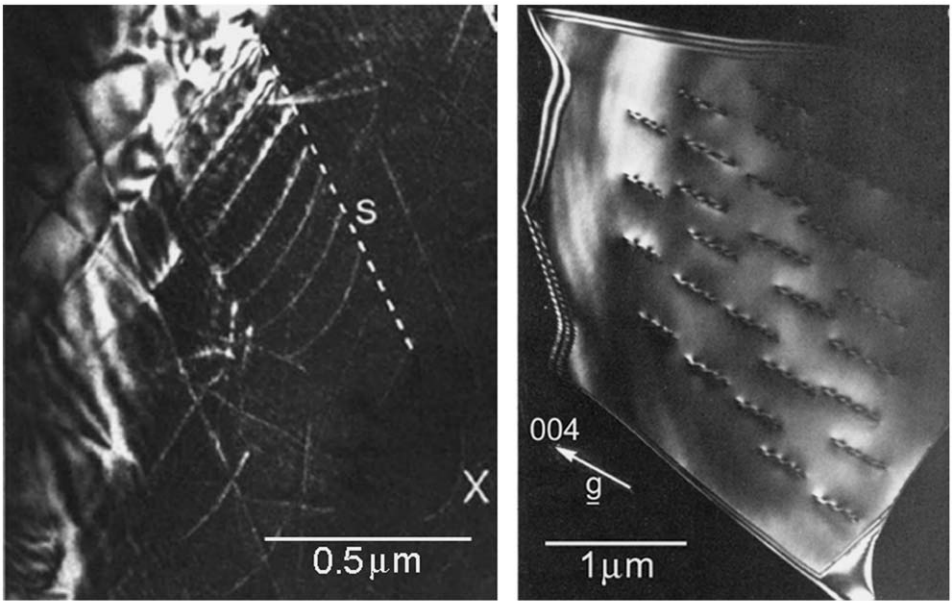

Fig. 14. (a) Weak beam dark-field image of dislocations in biotite. The trace of the slip plane (S) is indicated as well as dislocations bowing out (X). [346]. (b) Dark-field image of screw dislocations in sillimanite [350].

Mica minerals are also of industrial interest because of their unique electrical and thermal properties and dislocations are important [349].

3.6.6. Sillimanite, Mullite

Sillimanite and mullite are silicates with Si–Al tetrahedral chains. They occur in high-temperature metamorphic rocks and mullite is an important ceramic material. TEM analyses identify [0 0 1] as Burgers vector in sillimanite [350,351]. Dislocations are generally of screw type in the [0 0 1] direction [Fig. 14(b)] and sometimes are dissociated [352]. Dislocation-assisted high-temperature deformation has been documented in mullite [353]. The influence of dislocations and strain on the aluminosilicate phase transformations were investigated for kyanite [354].

3.6.7. Feldspars

Feldspars are the most abundant mineral in the Earth's crust and probably on the crusts of the Moon, Venus, and Mars as well. Feldspar compositions vary within two solid solutions, the alkali feldspars ($KAlSi_3O_8$–$NaAlSi_3O_8$) and plagioclase feldspars ($NaAlSi_3O_8$–$CaAl_2Si_2O_8$). Feldspars have two excellent cleavages, (0 0 1) and (0 1 0); these have also been identified as slip planes. All feldspars have low symmetry: C2/m for the high-temperature alkali feldspars high sanidine with complete disorder of Si and Al in tetrahedral sites above approximately 1000 °C

and partially ordered low-sanidine (orthoclase). Lower-temperature alkali feldspars albite and microcline are triclinic in the $C\bar{1}$ space group. (A centered unit cell is chosen to conform with the traditional morphologic unit cell and more or less parallel axes in all feldspar structures. Miller indices in this section all refer to the $c = 0.7$ nm albite unit cell unless indicated.) The Ca end member of plagioclase (anorthite) is in space group $P\bar{1}$ at temperatures below $\sim 250\,^{\circ}C$, and transforms to $I\bar{1}$ at higher temperatures due to positional disorder [355]. Feldspar structures of intermediate composition are extremely complex due to the competing forces of ordering (Al–Si) and exsolution (Na–K and Na–Ca). Many feldspars display complex microstructures with fine exsolution lamellae (perthite, peristerite, labradorite, bytownite), antiphase boundaries (anorthite) and pervasive twinning (microcline). There is a large literature on TEM studies of these microstructures. The investigations of dislocations are more sporadic and work has been reviewed by Tullis [57] and Gandais and Willaime [58]. While feldspars are major components of a large majority of igneous and metamorphic rocks they are generally quite undeformed and occur as porphyroclasts in a matrix of highly deformed quartz, calcite, and pyroxenes.

Experimental and microstructural studies of granitic rocks demonstrate that feldpars are stronger than quartz [286]. By contrast, plagioclase feldspar becomes a weak and interconnected phase controlling the rheology of more mafic gabbroic rocks [263], which are common in the lower continental crust and oceanic crust.

Analyses of dislocations in experimentally and naturally deformed feldspars by TEM indicate that the dominant slip plane is (0 1 0). The (0 1 0) plane may be favorable due to its low density of largely covalent Si(Al)–O bonds (2 per unit cell, [57–59]). With this criterion, other possible slip systems include (0 0 1), (1 1 0), and $(1\,0\,\bar{1})$ (with 4 Si(Al)–O bonds per unit cell), (1 0 0), and (1 1 1) (with six 4 Si(Al)–O bonds per unit cell). [0 0 1] is the dominant Burgers vector, which is supported by TEM analyses of experimentally and naturally deformed samples (see [60–62] but many other dislocations have also been identified.

Experimental studies of *alkali feldspars* in Westerley granite with ordered microcline [63,64] and disordered sanidine [65–68] show that (0 1 0)[0 0 1] slip is active in both. Other dislocations derive from (0 1 0)[1 0 1] [Fig. 15(a)], $(0\,0\,1)\frac{1}{2}[1\,1\,0]$, and $(1\,\bar{2}\,\bar{1})[1\,0\,1]$ slip. In naturally deformed alkali feldspars, subgrain formation was observed, indicative of climb [357–360]. It has been suggested that shear-induced mechanical Albite and Pericline twinning in potassium feldspar may facilitate ordering [361] but this has been disputed [362]. Dislocations have no effect on diffusion in alkali feldspar [363].

There is a considerable literature on dislocations in *plagioclase* but only few experimental studies. In single crystals deformed in orientations with high Schmid factor for both (0 1 0)[0 0 1] and $(0\,0\,1)\langle 1\,1\,0\rangle$ slip [356], dislocations from both systems are equally abundant [Fig. 15(b)]. This agrees with work by Marshall and McLaren [364,365]. High-temperature deformation of anorthite aggregates has been conducted at conditions near the transition from diffusion creep to dislocation creep mainly produces microstructures typical of diffusion creep [366–368]; intriguingly, samples deformed dominantly in the diffusion creep regime develop significant preferred orientation [369].

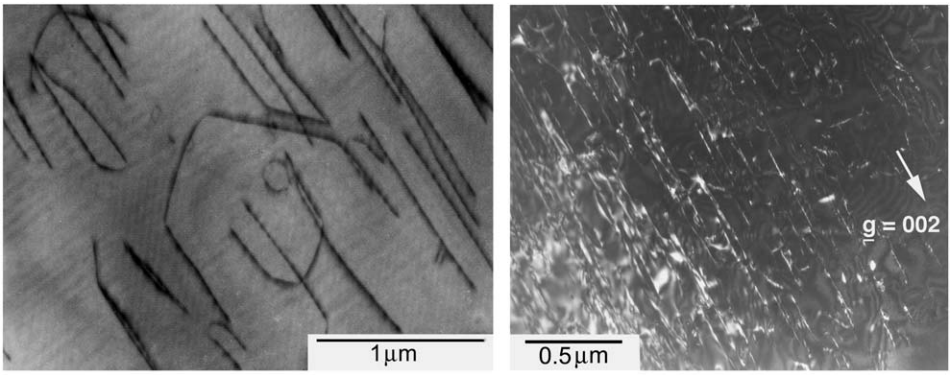

Fig. 15. (a) BF image of (0 1 0)[1 0 1] dislocations in experimentally deformed sanidine [58]. (b) Weak beam dark-field images of dislocations in experimentally deformed plagioclase favorably oriented for (0 1 0)[0 0 1] slip; **b** = [0 0 1] dislocations exhibit long screw components [356].

Many slip systems have been observed in naturally deformed plagioclase: in amphibolite (0 1 0)[1 0 0], (0 1 0)[1 0 1], (0 1 0)[2 1 0], (0 0 1) $\frac{1}{2}$[1 1 0], ($\bar{1}$ 1 $\bar{1}$) $\frac{1}{2}$[1 1 0], (0 0 1) $\frac{1}{2}$[1 $\bar{1}$ 0], (1 $\bar{1}$ $\bar{1}$) $\frac{1}{2}$[1 $\bar{1}$ 0], (1 1 $\bar{1}$) $\frac{1}{2}$[1 1 2], and (1 1 0) $\frac{1}{2}$[$\bar{1}$ $\bar{1}$ $\bar{1}$] [60,370], gabbro (0 1 0)[0 0 1], (0 0 1) $\frac{1}{2}$[1 1 0] [371], albite schist [1 0 0] [372]. Similar results were obtained in other studies (see [61,373]). TEM analysis of Burgers vectors in intermediate I$\bar{1}$ plagioclase (with $c = 1.4$ nm) shows dissociation of [1 0 0] dislocations: [1 0 0]→$\frac{1}{2}$[1 0 0]+$\frac{1}{2}$[1 0 0]; these partials would be unit dislocations in the C$\bar{1}$ structure ($c = 0.7$ nm).

Texture analysis and subgrain misorientations in both naturally and experimentally deformed plagioclase feldspar are also consistent with (0 1 0)[0 0 1] as an easy slip system [59,62,369,371,373–375]. Other studies suggested additional (0 1 0)[1 0 0] and (0 0 1)[1 0 0] slip (see [376–378]). Obviously, a polycrystalline aggregate cannot deform ductilely on a single slip system and other mechanisms including mechanical twinning, dynamic recrystallization, climb or grain boundary sliding have been observed to occur [379]. Subgrain misorientation axis data in porphyroclasts suggest a dominance of (0 1 0)[0 0 1] slip in porphyroclasts with dominant slip on (0 1 0)[1 0 0] and (0 0 1)[1 0 0] in matrix plagioclase. The relative importance of the [0 0 1] or [1 0 0] Burgers vectors may be a function of temperature, strain rate, H_2O activity, or confining pressure [376,367]. There is experimental evidence for mechanical twinning on the Albite and Pericline systems in plagioclase [380–382] but the significance for natural plagioclase is not clear [57].

3.7. Sulfides

Early investigations of the deformation modes of various sulfide minerals observed both plastic and brittle behavior [383–386]. Considerable subsequent work established slip and twinning mechanisms in several important sulfide ore

minerals [106]. We consider here only what is known about dislocations and related phenomena in the most important sulfides.

3.7.1. Iron sulfides – general

The crystal structures of iron sulfides are straightforward in principle but various aspects of some structures and their behavior are still uncertain. We emphasize that iron sulfides and iron oxides in natural rocks are often not in equilibrium.

3.7.2. Pyrite

The structure of pyrite, FeS_2 can be considered as a modified NaCl structure (cubic, Pa3): Fe atoms occupy fcc lattice positions; S–S covalently bonded pairs are also centered on fcc positions but they alternate in directionality. This alternation destroys the overall face-centered symmetry. Pyrite is stable up to 743 °C at which temperature it breaks down to pyrrhotite and sulfur [387]. The phase relationship between pyrite and the orthorhombic (Pmnn) polymorph, marcasite, is still enigmatic [388]. In marcasite, S–S pairs point in the same direction in each layer. This causes a distortion from cubic to orthorhombic. The **b** dimension of the marcasite unit cell is almost identical with the lattice parameter of pyrite. In the transformation of marcasite to pyrite an orientation relationship $\{0\,0\,1\}_P//\{1\,0\,1\}_M$, with $\langle 1\,0\,0\rangle_P//[0\,1\,0]_M$ is observed [389]. For the reverse transformation of pyrite to marcasite the similar atomic arrangement in pyrite $\{0\,0\,1\}$ and marcasite $\{1\,0\,1\}$ planes was mentioned [390].

Pyrite is usually considered to be hard and brittle, deforming by cataclasis up to 400 °C and 600 MPa confining pressure [391]. However, glide bands were revealed by metallographic methods on the surfaces of some natural samples [392,393], indicating plastic deformation. Van Goethem et al. [98] studied by TEM what they believed were translation faults in pyrite and concluded from their diffraction contrast analyses that the glide elements were $\{1\,0\,0\}\langle 0\,1\,1\rangle$. Plastic deformation can occur under confining pressure at elevated temperatures, predominately by slip on the $\{1\,0\,0\}\langle 0\,1\,0\rangle$ system [99–101]. The resulting dislocations tend to be dissociated into partials with colinear Burgers vectors of type $\frac{1}{2}[0\,1\,0]$. Planar defects formed in pyrite during growth lie parallel to the $\{1\,0\,0\}$ planes [394]. The faults were interpreted either as APBs with a displacement vector, **R** of type $\frac{1}{2}[1\,1\,0]$ [98], or as stacking faults with $\mathbf{R} = \pm 0.29\ [1\,1\,0]$ [394]. In natural pyrites perfect dislocations with $\mathbf{a}\langle 1\,0\,0\rangle$ Burgers vectors were identified. The Burgers vectors of partials bordering growth stacking faults are out of the defect plane, with the form $\mathbf{b} = \pm\mathbf{R} \pm \mathbf{a}\langle 1\,0\,0\rangle$, where **R**, the fault displacement vector, is **a**[0, 0.27, 0.5] [395].

The growth faults may correspond to marcasite lamellae in the pyrite [395,396]. Indeed HRTEM and electron diffraction revealed them as single $(1\,0\,1)$ layers of marcasite inserted between $(0\,0\,2)$ layers of pyrite [397]. Dislocation loops formed during the growth of pyrite also have the **a**[0, 0.27, 0.5] fault vector [101]. This translation was predicted as the most probable in a coincidence-site-lattice study [398].

A deformation mechanism map for pyrite in the range 0–743 °C [399] shows that pressure solution [102] and cataclastic flow are the dominant mechanisms operating at geological strain rates under low-grade metamorphic conditions. Diffusion creep occurs under high-grade conditions. Dislocation glide and power-law creep only occur at higher stresses, above ~400 °C and at fairly high strain rates. Table 1 lists the known slip systems for pyrite.

3.7.3. Chalcopyrite

Chalcopyrite (ccp) is a common accessory mineral in metamorphic and igneous rocks and is found in many types of ore deposits. It is tetragonal and can be envisaged as an ordered sphalerite structure. Both texture determinations and optical studies of deformed samples (see [103]) provided the first information about deformation mechanisms in chalcopyrite. Experimental deformation of chalcopyrite single crystals to low strains at 200 °C indicated slip on {1 1 2}, {1 0 0}, and (0 0 1) [94–96].

A comprehensive study of dislocation behavior established the existence of various slip systems (see Table 1) by applying stresses to crystals in different directions at different temperatures [97]. Deformation twinning according to $\{1\,1\,2\}\langle 1\,1\,\bar{1}\rangle$ also occurred, with high densities of screw-character twinning dislocation in the boundaries. At 200 °C $\{1\,1\,2\}\langle \bar{3}\,1\,1\rangle$ slip was the main mode of deformation, with perfect dislocations having $\frac{1}{2}\langle \bar{3}\,1\,1\rangle$ Burgers vectors, whereas at 400 °C the main slip system was $\{1\,1\,2\}\langle 1\,1\,\bar{1}\rangle$, with a Burgers vector of $\frac{1}{2}\langle 1\,1\,1\rangle$ for a perfect dislocation [Fig. 16(a)]. A marked change in slip mechanisms occurs in moving from 200 to 400 °C: coarse $\{1\,1\,2\}\langle \bar{3}11\rangle$ slip bands predominated at the lower temperature whereas homogeneously distributed dislocations were characteristic of deformation at 400 °C. Dislocations with $\frac{1}{2}\langle 1\,1\,1\rangle$ Burgers vectors were

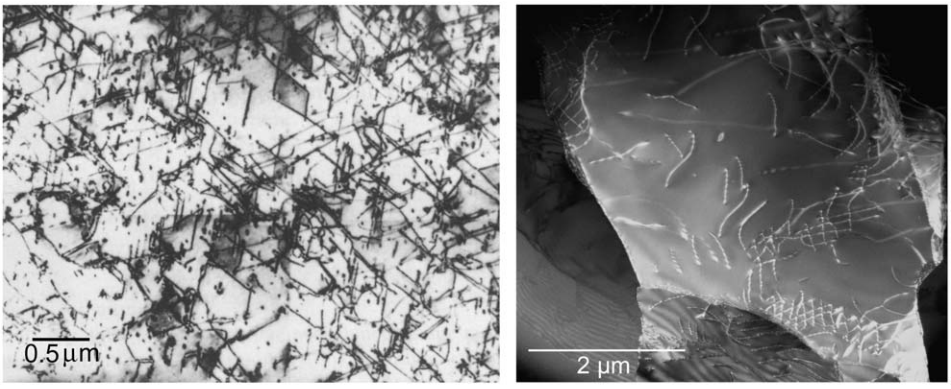

Fig. 16. (a) TEM image of dislocations in experimentally deformed chalcopyrite at 400 °C. Several screw dislocations are in contrast: $\mathbf{b} = \frac{1}{2}[\bar{1}\,\bar{1}\,\bar{1}]$ in (1 1 $\bar{2}$) planes (N 45°W), $\mathbf{b} = \frac{1}{2}[\bar{1}\,\bar{1}\,1]$ in (1 1 2) planes (N 65°E) and $\mathbf{b} = \frac{1}{2}[1\,\bar{1}\,0]$ (N 10°E) [97]. (b) Weak-beam dark-field TEM image of [1 0 0], [0 1 0], and [0 0 1] dislocations in stishovite deformed in a multianvil apparatus at 14 GPa and 1300 °C [84].

able to cross-slip by means of (1 1 0) planes. All the types of perfect dislocation were found to dissociate and many different dislocation reactions were also noted.

3.7.4. Galena

Galena, PbS, crystallizes in the cubic NaCl structure. The deformation of polycrystalline galena has been studied experimentally at temperatures up to 500 °C and strain rates down to $10^{-8}\,s^{-1}$ [102–105,400–402]. Atkinson [403] derived flow laws and calculated deformation maps for polycrystalline galena. According to the latter, dislocation glide is the predominant mechanism at low temperatures and high stresses. The slip systems are two of those found for NaCl, but unlike for NaCl, $\{0\,0\,1\}\langle 1\,1\,0\rangle$ is the primary system for galena whereas the primary system for NaCl, $\{1\,1\,0\}\langle 1\,\bar{1}\,0\rangle$, is secondary for galena. These systems have different CRSSs and very different dependences on temperature up to 400 °C [106]. When compression was applied along $\langle 1\,1\,1\rangle$ to achieve nonzero Schmid factors for $\{0\,0\,1\}\langle 1\,1\,0\rangle$ slip, dislocation glide was activated at low stresses, corresponding to CRSSs of 5–10 MPa at room temperature [104]. The strain in deformed polycrystalline specimens is usually distributed inhomogeneously, being largely concentrated in kink and deformation bands [404].

TEM studies of dislocations in deformed natural and synthetic galena show that Burgers vector of perfect dislocations is usually $\frac{1}{2}\langle 1\,1\,0\rangle$, as in NaCl. Up to 200 °C, slip on the {0 0 1} planes mostly involves edge dislocation dipoles and dislocations lying at 45° to their Burgers vector [405]. The density of dipoles increases as the test temperature is decreased. The numbers of "45° dislocations" is largest at low temperatures, which is consistent with the difficulty of activating $\{1\,1\,0\}\langle 1\,\bar{1}\,0\rangle$ slip. Dislocation segments inclined to the planes of the TEM specimens were observed to glide in {0 0 1}, {1 1 0}, and also {1 1 1} planes under thermally induced stresses [406], which can be attributed to the commonality of the Burgers vector for all three types of plane. This behavior is probably confined to elevated temperatures in bulk specimens. That the dissociation of dislocations is possible in galena is suggested by high-resolution TEM images of dislocations, lying in both {0 0 1} and {1 1 0} planes, separated by distances of 1 and 0.6 nm, respectively [407].

Many dislocation interactions occur when multiple slip systems operate, as in milled samples, variously resulting in dislocation annihilation, elimination of dipoles, new segments of dislocation and networks [408]. Some of the complex arrangements observed, for example, dislocation bundles winding around nodes, were attributed to the special conditions created during milling. Cross-slip was observed on {1 1 0} and {1 1 1} planes, giving rise to segments in the {0 0 1} planes and superjogs. Galena that had been naturally work hardened by tectonic events and then softened by annealing shows that rates of softening (due to both recovery and recrystallization) are temperature dependent and related to the amount of deformation [409].

3.7.5. Sphalerite

Sphalerite (zinc blende) is the cubic polymorph of zinc sulfide, ZnS, a II–VI semiconductor. The sulfur atoms form an fcc array and the zinc atoms fill half of the

tetrahedral interstices. Glide and dislocations in sphalerite have been researched both directly and indirectly, the latter because several important semiconductors like GaAs (III–V) and CdS (II–VI) are isomorphous with cubic ZnS. Many studies of defects in the III–V compounds have been carried out and so, by inference at least, various aspects of the behavior of the mineral sphalerite can be anticipated.

Sphalerite consists of alternate planes of Zn and S, stacked in a sequence represented by AaBbCcAa …., etc. Slip occurs on the $\{1\,1\,1\}$ planes, which are parallel to the stacking layers of atoms, and in the close-packed directions $\langle 1\,\bar{1}\,0\rangle$. The other deformation mode is $\{1\,1\,1\}\langle 1\,1\,\bar{2}\rangle$ twinning. Slip on the $\{1\,1\,1\}$ planes causes a flow of charge in the direction of slip [410], thought to occur because the dislocations are charged. Charged dislocations were predicted in ionic crystals many years ago; the electrical effects associated with dislocation motion in ZnS are strong evidence for such defects.

Sphalerite deformed at temperatures up to 500 °C and strain rates between 10^{-3} and $10^{-5}\,s^{-1}$ produced no twins in Fe-rich sphalerite [411,412] but abundant twinning in purer specimens [412], together with slip under all test conditions. The annealing of naturally and experimentally deformed sphalerites suggests that static recovery is possible above 300 °C and proceeds rapidly above 500 °C [412]. Recrystallization produces new grains with numerous growth twins.

The plastic deformation of ZnS indicates that dislocations glide between planes of aB type stacking and not between planes of Aa type [413]. This was determined from the direction of the current generated by slip in relation to the known absolute orientation of the crystal. Dislocation mobility in covalent semiconductors like ZnS is controlled by the high-friction Peierls regime [414]. As a consequence, dislocations with a $\frac{1}{2}\langle 1\,1\,0\rangle$ Burgers vector lie along $\langle 1\,1\,0\rangle$ atom rows of the $\{1\,1\,1\}$ glide planes and a dislocation glide loop consists of two types of segment, screw and 60°. In compound semiconductor one can also identify two types of 60° dislocation, depending on the nature of the atom species ending the associated extra half plane; these are α or β dislocations in the usual semiconductor terminology [415]. Dislocations are usually dissociated into two $\frac{1}{6}\langle 1\,1\,\bar{2}\rangle$ partials that bound a stacking fault; these partials are either 30 or 90° in character.

Because of the high lattice friction, dislocation glide in compounds like ZnS involves two steps [4]: the nucleation of a kink pair on the dislocation and the migration of these kinks along the line. Thereby the line is able to move smoothly. There are only small differences between the velocities of the various types of dislocations in ZnS [416], which contrasts with the findings for III–V semiconductors [417]. The dislocation mobility in ZnS is found to be greatly enhanced by electron radiation [416] although the Peierls regime still operates [418]. Apparently, the enhancement is due to the nonradiative recombination of charge carriers at electronic energy levels associated with the dislocations. The height of the Peierls barrier and the flow stress depends on the charge on dislocations; the latter is increased by illumination [419]. For this reason, ZnS shows a positive photoplastic effect, that is, there is an increase in the flow stress when the sample is illuminated. An after-effect is also found – the flow stress continues to increase after the illumination ceases [420].

3.7.6. Pyrrhotite

There is little information about dislocations in pyrrhotite, a mineral that can occur in several polymorphs, including monoclinic and hexagonal forms. Deformation experiments [103,391,412] at temperatures up to 500 °C to establish flow laws and to study textures have incidentally identified basal glide in hexagonal NC pyrrhotite. Fracturing contributes to deformation at low temperatures but decreases with temperature; twinning occurs above 200 °C.

3.8. High-pressure minerals

Samples of the Earth to a depth of about 400 km occur at the surface as xenoliths brought up from depth by volcanic eruptions. Minerals in the deeper interior are inaccessible to direct observation, but we know broadly about their conditions from geophysical data. One now can reproduce the high-pressure (>300 GPa) and high-temperature conditions (>5000 K) in the laboratory. With multianvil equipment, we can perform deformation experiments at pressures 25 GPa on a sample with a volume of about 5 mm^3 and a fair degree of control over the sample environment. At higher pressures, diamond anvil cells are used; and the diamond anvils not only exert pressure but also a compressive stress that deforms the material at pressure. Heat can be applied to a diamond anvil cell with a resistance furnace or laser irradiation [79]. Some materials can be quenched and investigated *ex situ* with the TEM. High-pressure minerals such as stishovite, majorite, and $MgSiO_3$ perovskite have been studied this way. But other minerals such as post-perovskite $MgSiO_3$ (a phase of the lowermost mantle) or ε-iron (composing the Earth's inner core) can only be examined *in situ* by optical, spectroscopic and X-ray diffraction techniques. The determination of slip systems can be inferred from texture patterns that develop during diamond anvil compression [421]. An alternative method is to predict deformation activity from first principles based on the Peierls–Nabarro model [422–424]. We review here briefly what is known about deformation mechanisms of minerals in the lower mantle [425].

3.8.1. Magnesiowüstite (see also Section 3.3.4)

Magnesiowüstite ($Mg_{0.8}Fe_{0.2}O$) is thought to be the second most abundant phase in the lower mantle and probably the weakest. Dislocation creep experiments produced textures consistent with slip on both {0 0 1} and {1 1 0} slip planes in the $\langle 1\,\bar{1}\,0\rangle$ direction [76]. The microstructures formed indicated that recovery rate was fast because dislocations were highly mobile and climbed rapidly. Subsequent high strain deformation experiments on aggregates to shear strains as large as $\gamma = 15.5$ produced first a deformation texture, compatible with dislocation glide in the $\langle 1\,\bar{1}\,0\rangle$ direction on all three probable slip systems {1 1 1}, {1 1 0}, and {0 0 1} and then transformed into a recrystallization texture [75]. Study of the dislocation microstructure by TEM confirmed the assignment of slip systems. It appeared that the formation of subgrains at relatively low homologous temperatures ($<0.5T_m$) was promoted by cross-slip of dislocations between the different glide planes.

3.8.2. Majorite Garnet (see also Section 3.6.1)

(Mg, Fe)SiO_3 garnet, that is majorite – a high-pressure phase of pyroxene, is believed to be a major constituent of the transition zone of the mantle. Majorite also occurs in impact melt veins in heavily shocked ordinary chondrites [426]. Majorite in shocked meteorites is cubic, apparently because they cool very quickly. Synthetic majorite transforms at around 1950 °C from the cubic phase to a tetragonal structure during its cooling [427]. Studies of majorite in the Tenham meteorite [73] and in the Acfer 90072 (shock grade S6) meteorite [74] have provided important indications about the origins of dislocations in the majorite grains. Dislocations with $\frac{1}{2}\langle 1\,1\,1\rangle$ and $\langle 1\,0\,0\rangle$ Burgers vectors may be largely the results of growth and not plastic deformation. Twin and tweed microstructures seen in synthesized majorite at 20 GPa and 1950–2000 °C are believed to form due to the cubic-tetragonal transition during quenching [427].

3.8.3. Wadsleyite

Wadsleyite (β-Mg_2SiO_4) is a high-pressure polymorph of forsterite. In wadsleyite deformed at pressures of 14 GPa and 1450 °C, dislocations with [1 0 0] Burgers vectors were identified, many in tangles, although creep had caused numerous dislocations to form walls [428]. In wadsleyite synthesized from forsterite in a multianvil apparatus and deformed in compression in another multi-anvil apparatus at 15–19 GPa and temperatures ranging from room temperature to 1800–2000 °C, TEM and LACBED studies identify [1 0 0], $\frac{1}{2}\langle 111\rangle$, [0 1 0], $\langle 1\,0\,1\rangle$, and [0 0 1] dislocations [85], the lattermost resulting from dislocations reactions, not slip. Wadsleyite is elastically almost isotropic but slip occurs predominately on planes that do not break Si–O bonds (e.g., (0 1 0) and (0 0 1)) and dislocation dissociation is crucial [86].

3.8.4. Ringwoodite

Ringwoodite, γ-Mg_2SiO_4, another high-pressure polymorph of olivine with spinel-structure is found in shocked meteorites [429] and believed to be present in the mantle transition zone. Like wadsleyite, β-Mg_2SiO_4, ringwoodite is a high-pressure phase of forsterite. Peierls–Nabarro modeling of dislocations at 20 GPa and 0 °K suggest that the Burgers vector for both {1 1 0} and {1 1 1} slip is $\frac{1}{2}\langle 1\,\bar{1}\,0\rangle$ [80]. This is compatible with *in situ* texture information at 6–10 GPa compared with polycrystal plasticity simulations [81]. The curvature of glide dislocations can be used as a method of estimating the resolved shear stress [430] in ringwoodite in multianvil deformation experiments.

3.8.5. $MgSiO_3$ perovskite and post-perovskite

Two important lower mantle minerals are $MgSiO_3$ perovskite and post-perovskite, the latter being a layered $CaIrO_3$-structured mineral [431] and thought to be the most important phase in the lowermost region (D″-layer). The slip planes for $MgSiO_3$ perovskite are {0 1 0} according to experiment [77] and theory [78]. For post-perovskite, theory suggests that the slip plane is {1 1 0} [78], but *in situ* experiments suggest that slip on (1 0 0) or (1 1 0) is dominating [178]. Simulations

based on the Peierls–Nabarro model provide models for the structure of dislocations cores in perovskite [432] as well as in post-perovskite [231].

3.8.6. Coesite

Coesite is a monoclinic silica mineral that exists at pressures above a few GPa and transforms to stishovite above about 10 GPa. Coesite was first identified as a natural phase at Meteor Crater, AZ [433] and coesite can assist in the recognition of meteorite impacts. The mineral occurs as a shock-induced phase in meteorites and tektites. It also is found in some high-pressure metamorphic rocks as in the Dora Maira massif of the Western Alps. A TEM study found Burgers vectors [1 0 0], [0 0 1], and [1 1 0], which correspond to **a** and **a**+**c** [72]. Twinning occurs on (0 2 1) [434].

3.8.7. Stishovite

Stishovite is the tetragonal silica polymorph with a rutile structure, stable at pressures in excess of 10 GPa. It was found in both terrestrial and meteoritic shocked samples and studied by TEM (see [432,435,436]). In experimentally deformed stishovite, Burgers vectors are $\langle 1\,0\,0\rangle$, $\langle 0\,0\,1\rangle$, $\langle 1\,1\,0\rangle$, and $\langle 1\,0\,1\rangle$ [82] comparable to rutile (Section 3.3.8). Stishovite experimentally deformed at 14 GPa and 1300 °C [83] shows evidence for slip in the $\langle 1\,0\,0\rangle$ directions on the (0 0 1), {0 1 0}, and {0 2 1} planes, and slip in the [0 0 1] direction (corresponding to the shortest Burgers vector) on {1 0 0}, {1 1 0}, and {2 1 0}, and in the direction $\langle 1\,1\,0\rangle$ on $\{1\,\bar{1}\,0\}$ [84] (Fig. 16b).

4. Simulations

Most dislocation studies in minerals rely on observations with the TEM as described in previous sections. These observations are used to determine the dislocation geometry, slip systems, and microstructural configurations. But simulations increasingly complement observations. These simulations are on two levels: To predict slip systems, atomistic simulations of generalized stacking faults (e.g., with density functional theory) are combined with a continuum-based description of the dislocation core within the framework of the Peierls–Nabarro model [422,423,437]. To investigate microstructural changes during deformation, for example, during hardening, a discrete dislocation dynamics model has been developed by metallurgists [438]. Both of these approaches are still restricted to single crystals and do not take dislocation interactions across grain boundaries into account.

The Peierls–Nabarro model has been used to determine properties of dislocation cores, the misfit energy and particularly changes with pressure. This is based on the assumption of a planar core which is the most able to glide. It has direct implications for slip systems. In order to move, a dislocation must overcome an energy barrier under an applied stress. The Peierls–Nabarro model has been used to constrain dislocation core sizes and Peierls stresses in several oxides and silicates relevant to the Earth's mantle, particularly periclase [439], olivine [440,441], ringwoodite [80],

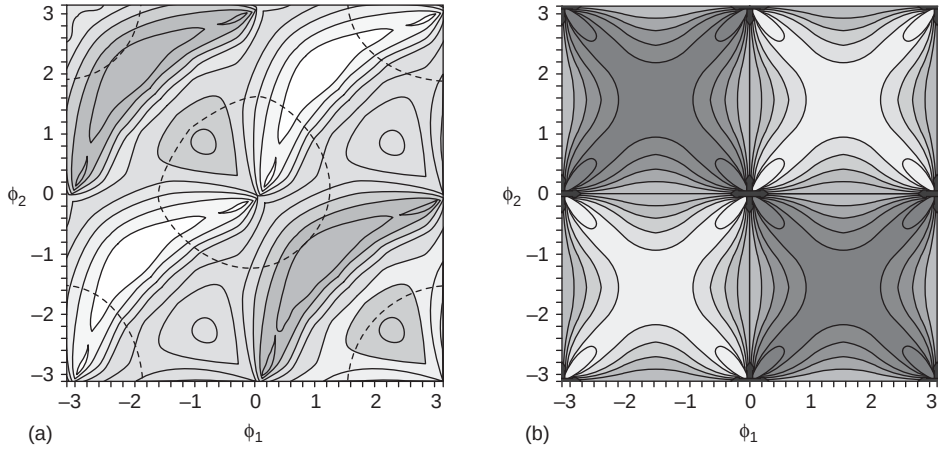

Fig. 17. Map of the interaction between dislocations in MgO as function of angles that define the orientation relative to the intersection of slip planes. Gray shades display interaction force (white attraction, black repulsion). (a) Lomer lock, (b) Hirth lock [443].

silicate perovskite [432], and silicate post-perovskite [442]. For olivine, the Peierls modeling explained why pressure affects some slip systems more than others [424].

Dislocation dynamics has been recently applied to minerals such as periclase [443] (Fig. 17) to explore the hardening in this material through interactions and reactions between dislocations gliding in noncoplanar slip systems and olivine [424]. Such simulations may in the future become important tools to predict plasticity based on dislocation geometry for a variety of conditions that cannot be explored experimentally.

5. *Dislocation densities and strain energy*

It is not easy to obtain an accurate estimation of dislocations densities from TEM images. X-ray topography is more reliable but is only applicable to materials with low dislocation densities. Fortunately, X-ray diffraction provides a way of estimating and monitoring dislocation densities and other defining parameters of microstructure. For example, a cellular dislocation microstructure gives an asymmetry in diffraction profiles according to Wilkens [444]. In recent years, analysis of diffraction peak profiles and line broadening [445,446] has emerged as a powerful tool for the determination of such parameters, although so far mostly applied to metals and composites (see [447,448]). The effect of dislocation contrast on line broadening has also been investigated [7].

As a result of this research, it is now recognized that various different properties of diffraction peak profiles address several microstructural parameters by modeling crystallite size and strain. These profile properties are peak broadening, asymmetric

peak shape, peak shift, and anisotropic broadening [449,450]. The method has been applied to the characterization of diamond/graphite [451] and forsterite [452] and it can be expected to be used increasingly.

The effect of dislocations on the reactivity of minerals has been investigated mainly for quartz with a few studies on feldspar and calcite, both experimentally and theoretically. The strain energy in a crystal lattice caused by dislocations can be described using ideal elastic behavior [4,453,454]. The increase in the internal energy of quartz caused by dislocations can be calculated by the following equation [453]:

$$\Delta E = D\left(\frac{\mu b^2}{8\pi K}\right)\ln\left(\frac{r_h^2 + d^2}{r_h^2}\right) \quad \text{with} \quad r_h^2 = \frac{\mu b^2 V}{8\pi^2 K \Delta H_{\mathrm{m}}} \tag{1}$$

and where symbols are (with values for quartz in parentheses): D, dislocation density (cm^{-2}); μ, shear modulus (44.4 GPa); V, molar volume (22.688 cm^3/mol); ΔH_{m}, enthalpy of melting (8.159 kJ/mol); b, magnitude of Burgers vector (0.4913–0.7304 nm); d, mean distance between dislocations $(1/D)^{1/2}$; K, constant related to the Burgers vector orientation, where $K = 1$ for a screw dislocation and $K = 1-v$ for an edge dislocation, where v is Poisson's ratio (0.007).

The internal energy is also dependent on the orientation of the dislocation relative to the Burgers vector. The equation assumes that the dependence is small, and is represented by the constant K [455]. Substituting the values into Eq. (1), one can calculate the increase in energy of quartz caused by a particular dislocation density on a particular slip system containing a certain type of dislocation. This equation indicates, even for a dislocation density as high as $10^{11}\,\mathrm{cm}^{-2}$, that the energy contributed to quartz is only 6% of the dissolution energy.

Dislocations may not contribute much to the bulk energy increase of a mineral, but they may nevertheless affect the reactivity by providing favorable areas for chemical processes such as precipitation and dissolution to occur. The local strain energy is more concentrated around the dislocations themselves, and is not distributed through the bulk crystal. Frank [456] has shown that the large amount of energy released locally at a dislocation site during dissolution decreases or eliminates the energy barrier (caused by the change in free surface energy) that prevents the removal of atoms. This may lead to regions where the reactivity is enhanced, potentially allowing also reactions other than dissolution to occur at higher rates [453,457]. For dissolution, it corresponds to etch pits, dissolution spirals, or hollow cores at dislocations.

An increase by 2 to 3 orders of magnitude in dislocation density has been shown to increase the dissolution rate by as much as a factor of 3 and this is highly significant for the stability and dissolution of quartz [458,459], of feldspars [363,460] and of carbonates [461]. Based on strain energy produced by dislocations in subgrain boundaries, Twiss [462] developed a theory to use the recrystallized grain size as a paleopiezometer.

Dissolution properties of minerals have some significant industrial applications. Concrete produced with highly deformed aggregate rocks such as mylonites, where

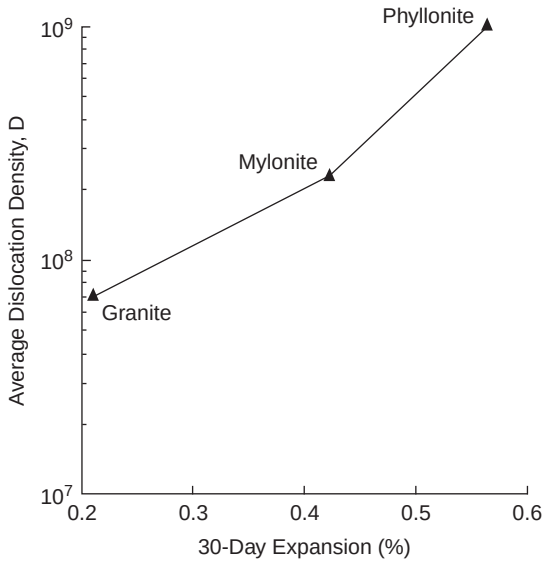

Fig. 18. Plot of the average 30-day expansion value of concrete samples with increasingly deformed granitic rock aggregate as function of average dislocation density in quartz [293].

quartz has high dislocation densities, are subject to the deleterious alkali silica aggregate reaction [293,463]. As the dislocation density increases by an order of magnitude, the expansion becomes threefold (Fig. 18). This causes ultimate fracture of the structure.

6. Conclusions

In spite of the enormous structural complexities, from triclinic plagioclase feldspar to piezoelectric trigonal quartz, from plasticity of ice at ambient conditions to post-perovskite deforming at highest pressures and temperatures in the lowermost mantle, from simple salt rocks to a polyphase material such as gneiss, dislocations in minerals are remarkably similar to those in metals and similar descriptions and interpretations apply. As in metals, dislocations are most relevant in the understanding of deformation processes. They provide the mechanism for deformation by slip that produces on the macroscopic scale preferred orientation and anisotropy. Dislocation microstructures are a driving force for recrystallization. They also play important roles in chemical reactions as well as in dissolution. Minerals compose rocks, and rock deformation is a key ingredient to understanding the dynamic earth, both mountain building and shearing in the crust as well as convection in the deep earth. Similar flow laws apply to metals and rocks because mechanisms are similar, even though timescales are entirely different. Geologic times and slow strain rates

compensate for the much slower dislocation mobility in minerals. Based on Orowan's equation, long-term deformation associated with mantle convection and flow in the crust is accommodated by dislocations with velocities in the range of 10^{-12}–10^{-13} m/s.

But minerals are not just significant in the context of geologic history. They are also important raw materials: most ceramics or their constituents are minerals: alumina, silica, perovskite, spinel. Cement minerals are extremely complex compounds and their strength and stability is of enormous technical importance. We are convinced that a close interaction between materials scientists, mineral physicists, and structural geologists will continue as an extremely stimulating endeavor. The investigation of dislocations remains an exciting field of research. Advanced experimental techniques allow for sophisticated imaging at all scales. Modeling of dislocation movements and dislocation interactions has become possible with high-speed computers.

This chapter of the last volume of *Dislocations in Solids* has been dedicated to dislocation in minerals. As we have shown, minerals were among the first materials in which dislocations were observed and with the advent of TEM and sample preparation techniques in the early 1960s a wide range of studies were undertaken to describe and quantify dislocation microstructures in the wide diversity of minerals. While compiling this review, what was perhaps the most striking revelation is what we still do not know: for example, the Burgers vectors in the common mineral–quartz, hardening behavior while undergoing high strains, the actual mechanism of recrystallization in many deformed rocks and the deformation of polymineralic aggregates, to name just a few. With such a rich background we are sure that future researchers will be inspired to continue investigating the roles of dislocations in minerals.

Acknowledgments

P. Cordier supplied reference material and reviewed our draft; we thank him for the invaluable help. W.F. Müller and W. Skrotzki provided micrographs. HRW acknowledges support from NSF (EAR-0337006). We are also indebted to the Editor, John Hirth for thoughtful comments that helped improve the manuscript.

References

[1] J.P. Poirier, Creep of Crystals, Cambridge University Press, Cambridge, UK, 1985.
[2] J.P. Poirier, Plastic Rheology of Crystals, in: T.J. Ahrens (Ed.), Minerals Physics & Crystallography: A Handbook of Physical Constants (AGU Reference Shelf No 2), American Geophysical Union, Washington, DC, 1995, p. 237.
[3] D. Hull, D.J. Bacon, Introduction to Dislocations, Pergamon Press, Oxford, 1984.
[4] J.P. Hirth, J. Lothe, Theory of Dislocations, McGraw-Hill, New York, 1968.
[5] S. Amelinckx, The Direct Observation of Dislocations, Solid State Physics 6, Academic Press, New York, 1964.

[6] A.C. McLaren, Transmission Electron Microscopy of Minerals and Rocks, Cambridge University Press, Cambridge, 1991.
[7] T. Ungár, A. Borbély, Appl. Phys. Lett. 69 (1996) 3173.
[8] H. Seidentopf, Phys. Zeit 6 (1905) 855.
[9] V. Volterra, Ann. Ec. Norm. Sup. 24 (1907) 400.
[10] L. Prandtl, Zeit. Angew. Math. Phys. 8 (1928) 85.
[11] E. Orowan, Z. Phys. 89 (1934) 605.
[12] M. Polanyi, Z. Phys. 89 (1934) 660.
[13] G.I. Taylor, Proc. R. Soc. A 145 (1934) 362.
[14] E. Rexer, Zeit. Phys. 78 (1932) 538.
[15] D.J. Barber, K.B. Harvey, J.W. Mitchell, Philos. Mag. 2 (1957) 704.
[16] S. Amelinckx, W. Dekeyser, Acta Metall. 6 (1958) 34.
[17] L.J. Griffin, Philos. Mag. 41 (1950) 196.
[18] J.M. Hedges, J.W. Mitchell, Philos. Mag. 44 (1953), 223, 357.
[19] D.H. Zeuch, Trans. Am. Geophys. Union 55 (1974) 418.
[20] D.L. Kohlstedt, C. Goetze, W.B. Durham, J.B. Vander Sande, Science 191 (1976) 1045.
[21] Y. Guéguen, Tectonophysics 39 (1977) 231.
[22] P.B. Hirsch, R.W. Horne, M.J. Whelan, Philos. Mag. Ser. 8 1 (1956) 677.
[23] W. Bollmann, Phys. Rev. 103 (1956) 1588.
[24] V.Z. Bengus, Sov. Phys. Cryst. 8 (1963) 322.
[25] M. Paulus, F. Reverchon, in: Le Bombardement Ionique. Proceedings of the Conference held at Bellevue, France, 1961 C.N.R.S., France, 1962, p. 223.
[26] D.J. Barber, J. Mater. Sci. 5 (1970) 1.
[27] A.P. Honess, The Nature, Origin and Interpretation of Figures on Crystals, Wiley, New York, 1927.
[28] R. Knipe, Tectonophysics 64 (1980) T11.
[29] J.J. Gilman, W.G. Johnston, in: R.M. Fisher (Ed.), Report on the Lake Placid Conference on Dislocations and Mechanical Properties of Crystals, Wiley, New York, 1957, p. 116.
[30] D.J. Barber, J. Appl. Phys. 33 (1962) 3141.
[31] M.W. Wegner, J.M. Christie, Contrib. Mineral. Petrol. 43 (1974) 195.
[32] A.R. Lang, in: S. Amelinckx, R. Gevers, G. Remaut, J. Van Landuyt (Eds.), Modern Diffraction and Imaging Techniques in Materials Science, North Holland, Amsterdam, 1980, p. 407.
[33] S. Amelinckx, Nature 169 (1952) 580.
[34] S. Amelinckx, P. Delavignette, J. Appl. Phys. 31 (1960a), 1691, 2126.
[35] S. Amelinckx, P. Delavignette, Nature 185 (1960b) 603.
[36] S. Amelinckx, P. Delavignette, in: J.B. Newkirk, J.H. Wernick (Eds.), Direct Observations of Imperfections in Crystals, Wiley-Interscience, New York, 1962, p. 295.
[37] S. Amelinckx, P. Delavignette, Philos. Mag. 5 (1960c) 533.
[38] S. Amelinckx, P. Delavignette, J. Appl. Phys. 32 (1961) 341.
[39] S.V. Radcliffe, A.H. Heuer, R.M. Fisher, J.M. Christie, D.T. Griggs, Science 167 (1970) 638.
[40] P.E. Champness, G.W. Lorimer, Contrib. Mineral. Petrol. 33 (1971) 171.
[41] J.M. Christie, J.S. Lally, A.H. Heuer, R.M. Fisher, D.T. Griggs, S.V. Radcliffe, Proc. 2nd Lunar Sci. Conf., Geochim. Cosmochim. Acta 1 (Suppl. 2) (1971) 69.
[42] H.-R. Wenk, M. Ulbrich, W.F. Müller, Proc. 3rd Lunar Sci. Conf., Geochim. Cosmochim. Acta 1 (Suppl. 3) (1972) 569.
[43] P.R. Buseck (Ed.), Minerals and Reactions at the Atomic Scale: Transmission Electron Microscopy, in: Reviews in Mineralogy, vol. 27, Mineralogical Society of America, Washington, DC, 1992.
[44] H.-R. Wenk, A. Bulakh, Minerals: Their Constitution and Origin, Cambridge University Press, Cambridge, 2004.
[45] D. Stöffler, F. Langenhorst, Meteoritics 29 (1994) 155.
[46] H. Leroux, Eur. J. Mineral. 13 (2001) 253.
[47] F.J. Turner, D.T. Griggs, H.C. Heard, Geol. Soc. Am. Bull. 65 (1954) 883.
[48] F.J. Turner, D.T. Griggs, R.H. Clark, R.H. Dixon, Geol. Soc. Am. Bull. 67 (1956) 1259.

[49] D.J. Barber, H.-R. Wenk, J. Gomez-Barreiro, E. Rybacki, G. Dresen, Phys. Chem. Miner. 34 (2007) 73.
[50] J.H.P. De Bresser, C.J. Spiers, Tectonophysics 272 (1997) 1.
[51] H.-R. Wenk, C.S. Venkitasubramanyan, D.W. Baker, Contrib. Mineral. Petrol. 38 (1973) 81.
[52] D.J. Barber, H.C. Heard, H.-R. Wenk, Mat. Sci. Eng. A 175 (1994) 83.
[53] D.J. Barber, H.-R. Wenk, Eur. J. Mineral. 13 (2001) 221.
[54] D.V. Higgs, J.W. Handin, Geol. Soc. Am. Bull. 70 (1959) 245.
[55] D.J. Barber, H.C. Heard, H.R. Wenk, Phys. Chem. Miner. 7 (1981) 271.
[56] C. Kearney, Z. Zhao, B.J.F. Bruet, R. Radovitsky, M.C. Boyce, C. Ortiz, Phys. Rev. Lett. 96 (2006) 255505.
[57] J. Tullis, Feldspar Mineralogy, in: P.H. Ribbe (Ed.), Reviews in Mineralogy, Vol. 2, Mineralogical Society of America, Washington, DC, 1983, p. 297.
[58] M. Gandais and C. Willaime, in: W.L. Brown (Ed.), Feldspars and Feldspathoids, NATO ASI Series C-137, Reidel, Dordrecht, 1984, p. 207.
[59] S. Ji, D. Mainprice, F. Boudier, J. Struct. Geol. 10 (1988) 73.
[60] T. Olsen, D. Kohlstedt, Phys. Chem. Miner. 11 (1984) 153.
[61] Y. Montardi, D. Mainprice, Bull. Mineral. 110 (1987) 1.
[62] S. Ji, D. Mainprice, J. Geol. 98 (1990) 65.
[63] J. Tullis, R.A. Yund, J. Geophys. Res. 82 (1977) 5707.
[64] J. Tullis, R.A. Yund, J. Struct. Geol. 2 (1980) 5707.
[65] E. Scandale, M. Gandais, C. Willaime, Phys. Chem. Miner. 9 (1983) 182.
[66] C. Willaime, M. Gandais, Bull. Soc. Fr. Mineral. Cristallogr. 100 (1977) 263.
[67] C. Willaime, J.M. Christie, M.-P. Kovacs, Bull. Mineral. 102 (1979) 168.
[68] Y. Zheng, M. Gandais, Philos. Mag. A 55 (1987) 329.
[69] P.L. Pratt, Acta Metall. 1 (1953) 103.
[70] G.W. Groves, A. Kelly, Philos. Mag. 8 (1963) 877.
[71] N.L. Carter, H.C. Heard, Am. J. Sci. 269 (1970) 193.
[72] F. Langenhorst, J.-P. Poirer, Earth Planet. Sci. Lett. 203 (2002) 793.
[73] M. Madon, J.-P. Poirier, Science 207 (1979) 66.
[74] V. Voegelé, P. Cordier, F. Langenhorst, S. Heinemann, Eur. J. Mineral. 12 (2000) 695.
[75] F. Heidelbach, I. Stretton, F. Langenhorst, S. Mackwell, J. Geophys. Res. – Solid Earth 108 (B3) (2003) 2154.
[76] I. Stretton, F. Heidelbach, S. Mackwell, F. Langenhorst, Earth Planet. Sci. 194 (2001) 229.
[77] H.-R. Wenk, I. Lonardelli, J. Pehl, J. Devine, V. Prakapenka, G. Shen, H.-K. Mao, Earth Planet. Sci. Lett. 226 (2004) 507.
[78] A.R. Oganov, R. Martonak, A. Laio, P. Raiteri, M. Parrinello, Nature 438 (2005) 1142.
[79] P. Cordier, H. Couvy, S. Merkel, D. Weidner, Plastic Deformation of Minerals at High Pressure: Multiscale Numerical Modelling, in: R. Miletich (Ed.), EMU Notes in Mineralogy, vol. 7, European Mineralogical Union, Vienna, 2005, p. 339.
[80] P. Carrez, P. Cordier, D. Mainprice, A. Tommasi, Eur. J. Mineral. 18 (2006) 149.
[81] H.-R. Wenk, G. Ischia, N. Nishiyama, Y. Wang, T. Uchida, Phys. Earth Planet. Inter. 152 (2005) 191.
[82] P. Cordier, T.G. Sharp, Phys. Chem. Miner. 25 (1998) 548.
[83] P. Cordier, D.C. Rubie, Mater. Sci. Eng. A 309 (2001) 38.
[84] M. Texier, P. Cordier, Phys. Chem. Miner. 33 (2006) 394.
[85] E. Thurel, P. Cordier, Phys. Chem. Miner. 30 (2003) 256.
[86] E. Thurel, J. Douin, P. Cordier, Phys. Chem. Miner. 30 (2003) 271.
[87] C.B. Raleigh, J. Geophys. Res. 73 (1968) 369.
[88] N.L. Carter NL, H.G. Avé Lallemant, Geol. Soc. Am. Bull. 81 (1970) 2181.
[89] C.B. Raleigh, S.H. Kirby, Min. Soc. Am. Spec. Pap. 3 (1970) 113.
[90] C. Goetze, D.L. Kohlstedt, J. Geophys. Res. 78 (1973) 5961.
[91] K. Fujino, H. Nakazaki, H. Momoi, S.I. Karato, D.L. Kohlstedt, Phys. Earth Planet. Inter. 78 (1993) 131.

[92] I. Katayama, H. Jung, S.I. Karato, Geology 32 (2004) 1045.
[93] D.L. Kohlstedt, H. Keppler, D.C. Rubie, Contrib. Mineral. Petrol. 123 (1996) 345.
[94] J.-J. Couderc, C. Hennig Michaeli, Phys. Chem. Miner. 13 (1986) 393.
[95] J.-J. Couderc, C. Hennig Michaeli, Philos. Mag. A 57 (1987) 301.
[96] C. Hennig Michaeli, H. Siemes, Tectonophysics 135 (1987) 217.
[97] C. Hennig Michaeli, J.-J. Couderc, Deformation Processes in Minerals, Ceramics and Rocks, The Mineralogical Society Series, Vol. 1. Unwin Hyman, London, 1990, p. 391.
[98] L. Van Goethem, J. Van Landuyt, S. Amelinckx, Am. Mineral. 63 (1978) 548.
[99] J.L. Graf, B.J. Skinner, J. Bras, M. Fagot, C. Levade, J.-J. Couderc, Econ. Geol. 76 (1981) 738.
[100] S.F. Cox, M.A. Etheridge, B.E. Hobbs, Econ. Geol. 76 (1981) 2105.
[101] C. Levade, J.-J. Couderc, J. Bras, M. Fagot, Philos. Mag. A 46 (1982) 307.
[102] K.R. McClay, J. Geol. Soc. Lond. 134 (1977) 57.
[103] B.K. Atkinson, Trans. Inst. Min. Metall. 83B (1974) 19.
[104] K.D. Lyall, M.S. Paterson, Acta Metall. 14 (1966) 371.
[105] H. Siemes, in: P. Paulitsch (Ed.), Experimental and Natural Rock Deformation, Springer, Berlin, Germany, 1970, p. 165.
[106] H. Siemes, Ch. Hennig-Michaeli, in: H.-R. Wenk (Ed.), Preferred Orientation in Deformed Metals and Rocks: An Introduction to Modern Texture Analysis, Academic Press, Orlando, FL, 1985, p. 335.
[107] D.L. Kohlstedt, J.B. Vander Sande, Contrib. Mineral. Petrol. 42 (1973) 169.
[108] A.C. McLaren, M.A. Etheridge, Contrib. Mineral. Petrol. 57 (1976) 163.
[109] L. Nazé, N. Doukhan, J.C. Doukhan, K. Latrous, Bull. Minéral. 110 (1987) 497.
[110] J.V. Ross, K.C. Nielsen, Tectonophysics 44 (1978) 233.
[111] J.M. Steuten, H.L.M. van Roermund, Tectonophysics 157 (1989) 331.
[112] J.-C. Van Duysen, N. Doukan, J.-C. Doukhan, Phys. Chem. Miner. 12 (1985) 39.
[113] C.B. Raleigh, J.L. Talbot, Am. J. Sci. 265 (1967) 151.
[114] H.G. Avé Lallemant, Tectonophysics 48 (1978) 1.
[115] N. Doukhan, J. Ingrin, J.-C. Doukhan, Terra Abstr. 3 (1991) 72.
[116] J.J. Kollé, J.D. Blacic, J. Geophys. Res. 88 (1983) 2381.
[117] S.H. Kirby, J.M. Christie, Phys. Chem. Miner. 1 (1977) 137.
[118] S.H. Kirby, A.K. Kronenberg, J. Geophys. Res. 89 (1984) 3177.
[119] J.N. Boland, T.E. Tullis, Geophys. Monogr. Am. Geophys. Union 36 (1986) 35049.
[120] J.B. Wachtman Jr., L.H. Maxwell, J. Am. Ceram. Soc. 37 (1954) 291.
[121] D.J. Gooch, G.W. Groves, J. Am. Ceram. Soc. 55 (1972) 105.
[122] D.J. Gooch, G.W. Groves, Philos. Mag. 28 (1973) 623.
[123] D.J. Gooch, G.W. Groves, J. Mater. Sci. 8 (1973) 1238.
[124] R.E. Tressler, D.J. Barber, J. Am. Ceram. Soc. 57 (1974) 1.
[125] R.E. Tressler, D.J. Michael, in: R.C. Bradt, R.E. Tressler (Eds.), Deformation of Ceramic Materials, Plenum Press, New York, 1975, p. 195.
[126] B.J. Hockey, in: R.C. Bradt, R.E. Tressler (Eds.), Deformation of Ceramic Materials, Plenum Press, New York, 1975, p. 167.
[127] Y. Hidaka, T. Anraku, N. Otsuka, Oxidation of Metals 58 (2002) 469.
[128] H. Siemes, B. Klingenberg, E. Rybacki, M. Neumann, W. Schafer, E. Jansen, K. Kunze, Ore Geol. Rev. 33 (2008) 255.
[129] T. Bretheau, J. Castaing, J. Rabier, P. Veyssière, Adv. Phys. 28 (1979)829, 835
[130] W. Hüther, B. Reppich, Philos. Mag. 28 (1973) 363.
[131] M. Hurm, B. Escaig, J. Phys. 34 (C9) (1973) 347.
[132] J.B. Bilde-Sörensen, J. Am. Ceram. Soc. 55 (1972) 606.
[133] M. Hurm, J. Phys. Paris 34 (C9) (1973) 347.
[134] S.M. Copley, J. Pask, J. Am. Ceram. Soc. 48 (1965) 139.
[135] J.P. Poirier, S. Beauchesne, F. Guyot, in: A. Navrotsky, D. Weidner (Eds.), Perovskite: A Structure of Great Interest to Geophysics and Materials Science, American Geophysical Union, Washington, D.C., 1989, p. 119.

[136] W.M. Hirthe, J.O. Brittain, J. Am. Ceram. Soc. 45 (1963) 546, 46, 411.
[137] K.H.G. Ashbee, R.E. Smallman, Proc. R. Soc. A 274 (1963) 195.
[138] K.H.G. Ashbee, R.E. Smallman, G.K. Williamson, Proc. R. Soc. A 276 (1964) 542.
[139] M.G. Blanchin, G. Fontaine, Phys. Status Solidi A 29 (1975) 491.
[140] L. Hwang, A.H. Heuer, T.E. Mitchell, in: R.C. Bradt, R.E. Tressler (Eds.), Deformation of Ceramic Materials, Plenum Press, New York, 1975, p. 257.
[141] J. Hornstra, J. Phys. Chem. Solids 15 (1960) 311.
[142] S.H. Kirby, P. Veyssière, Philos. Mag. A 41 (1980) 129.
[143] P. Veyssière, S.H. Kirby, J. Rabier, J. Phys., Paris 41 (1980) C6-115.
[144] P. Veyssière, J. Rabier, H. Garem, Philos. Mag. A 39 (1979) 815.
[145] N. Doukhan, J. Phys. Lett., Paris 40 (1979) 603.
[146] P. Veyssière, C.B. Carter, Philos. Mag. Lett. 57 (1988) 211.
[147] M.H. Lewis, Philos. Mag. 17 (1968) 481.
[148] K.C. Radford, C.W.A. Newey, Proc. Brit. Ceram. Soc. 9 (1967) 131.
[149] N. Doukhan, R. Duclos, B. Escaig, J. Phys. 34 (C9) (1973) 379.
[150] P. Müller, H. Siemes, Tectonophysics 23 (1974) 105.
[151] A.J. Ardell, J.M. Christie, J.W. McCormick, Philos. Mag. 29 (1974) 1399.
[152] J.M. Christie, A.J. Ardell, in: H.-R. Wenk (Ed.), Electron Microscopy in Mineralogy, Springer-Verlag, Berlin, Germany, 1976, p. 374.
[153] M. Linker, S. Kirby, A. Ord, J. Christie, J. Geophys. Res. 89 (1984) 4241.
[154] R.D. Baeta, K.H.G. Ashbee, Philos. Mag. 22 (1970) 601.
[155] J.D. Blacic, Tectonophysics 27 (1975) 271.
[156] J. Muto, J. Tullis, Eos Trans. AGU 88 (52) (2007) T13B-1338.
[157] P. Cordier, J.C. Doukhan, Philos. Mag. A 72 (1995) 497.
[158] P.B. Hirsch, A. Howie, R.B. Nicholson, D.W. Pashley, M.J. Whelan, Electron Microscopy of Thin Crystals, Butterworths, London, UK, 1965.
[159] R. Carpenter, J. Spence, Acta Cryst. A 38 (1992) 55.
[160] J.-P. Morniroli, P. Cordier, E. Van Cappellen, Jin Min Zuo, J. Spence, Microsc. Microanal. Microstruct. 8 (1997) 187.
[161] D.J. Barber, H.-R. Wenk, Phys. Chem. Miner. (1979).
[162] U.F. Kocks, H. Mecking, Prog. Mater. Sci. 48 (2003) 171–273.
[163] D.J. Barber, in: H.-R. Wenk (Ed.), Preferred Orientation in Deformed Metals and Rocks: An Introduction to Modern Texture Analysis, Academic Press, Orlando, FL, 1985, p. 149.
[164] R. von Mises, Zeit. Angew. Math. Mech. 8 (1928) 161.
[165] A. Nicolas, J.P. Poirier, Crystalline Plasticity and Solid State Flow in Metamorphic Rocks, Wiley, London, UK, 1976.
[166] H.-R. Wenk, D.J. Barber, R.J. Reeder, Carbonates: Mineralogy and Chemistry, in: R.J. Reeder (Ed.), Reviews in Mineralogy, Vol. 11, Mineralogical Society of America, Washington, DC, 1983, p. 301.
[167] N.A. Liddell, P.P. Phakey, H.-R. Wenk, in: H.-R. Wenk (Ed.), Electron Microscopy in Mineralogy, Springer Verlag, Berlin, Germany, 1976, p. 419.
[168] F. Haessner, Recrystallization of Metallic Materials, Riederer, Stuttgart, Germany, 1978.
[169] F.J. Humphreys, M. Hatherly, Recrystallization and Related Annealing Phenomena, Oxford University Press, Oxford, UK, 1995.
[170] G. Glover, C.M. Sellars, Metall. Trans. 4 (1973) 765.
[171] H.G. Avé Lallemant, N.L. Carter, Bull. Am. Geol. Soc. 81 (1970) 2203.
[172] J.-C.C. Mercier, in: H.-R. Wenk (Ed.), Preferred Orientation in Deformed Metals and Rocks: An Introduction to Modern Texture Analysis, Academic Press, Orlando, FL, 1985, p. 407.
[173] G.I. Taylor, J. Inst. Met. 62 (1938) 307.
[174] B. Sander, Einführung in die Gefügekunde der Geologischen Körper, Vol. 2, Springer, Wien, Austria, 1950.
[175] L. Ratschbacher, H.-R. Wenk, M. Sintubin, J. Struct. Geol. 13 (1991) 369.
[176] P.R. Dawson, H.-R. Wenk, Philos. Mag. A 80 (2000) 573.

[177] H.-R. Wenk, S. Speziale, A.K. McNamara, E.J. Garnero, Earth Planet. Sci. Lett. 245 (2006) 302.
[178] S. Merkel, A.K. McNamara, A. Kubo, S. Speziale, L. Miyagi, Y. Meng, T.S. Duffy, H.-R. Wenk, Science 316 (2007) 1729.
[179] H.-R. Wenk, G. Canova, Y. Brechet, L. Flandin, Acta Mater. 45 (1997) 3283.
[180] U.F. Kocks, C.N. Tomé, H.-R. Wenk, Texture and Ansiotropy, Cambridge University Press, Oxford, UK, 2000.
[181] H.-R. Wenk, Plastic Deformation of Minerals and Rocks, in: S.-I. Karato, H.-R. Wenk (Eds.), Reviews in Mineralogy, Vol. 51, Mineralogical Society of America, Washington, DC, 2002, p. 291.
[182] D. Bernaerts, S. Amelinckx, in: S. Amelinckx, D. van Dyck, J. van Landuyt, G. van Tendeloo (Eds.), Handbook of Microscopy, Vol. 3: Applications, in Materials Science, Solid State Physics and Chemistry, VCH, Weinheim, Germany, 1997, p. 437.
[183] T.E. Mitchell, A.H. Heuer, Dislocations in Solids, Vol. 12, Elsevier, Amsterdam, 2005, p. 339
[184] J.J. Papike (Ed.), Planetary Minerals, Reviews in Mineralogy, Vol. 36, Min. Soc. Am., Washington, DC, 1998.
[185] M. Montagnat, J. Weiss, J. Chevy, P. Duval, H. Brunjail, P. Bastie, J. Gil Sevillano, Philos. Mag. 86 (2006) 4259.
[186] J. Castaing, Ann. Phys. 6 (1981) 195.
[187] J.J. Gilman, W.G. Johnston, in: J.C. Fisher, W.G. Johnston, R. Thomson, T. Vreeland (Eds.), Conference on Dislocations and Mechanical Properties of Crystals, Lake Placid, NY, 1956, Wiley, New York, 1957.
[188] J.J. Gilman, W.G. Johnston, J. Appl. Phys. 30 (1959) 129.
[189] E. Schmid, W. Boas, Plasticity of Crystals, F.A. Hughes, London, UK, 1950.
[190] A.G. Evans, C. Roy, P.L. Pratt, Proc. Brit. Ceram. Soc. 6 (1966) 173.
[191] E. Schüller, S. Amelinckx, Naturwiss 47 (1960) 491.
[192] L.T. Chadderton, E. Johnson, T. Wohlenberg, Phys. Scr. 13 (1976) 127.
[193] S. Amelinckx, Nuovo Cim. Suppl. 7 (1958) 569.
[194] H. Blank, C. Ronchi, J. Nucl. Mater. 31 (1969) 1.
[195] A.G. Evans, P.L. Pratt, Philos. Mag. 20 (1969) 1213.
[196] K.H.G. Ashbee, F.C. Frank, Philos. Mag. 21 (1970) 211.
[197] W.A. Brantley, Ch.L. Bauer, Phys. Status Solidi B 40 (1970) 707.
[198] M.L. Kronberg, Acta. Metall. 5 (1957) 507.
[199] P.T. Sawbridge, E.C. Sykes, Philos. Mag. 24 (1971) 33.
[200] R.J. Gaboriaud, M. Boisson, J. Grilhe, J. Phys. C: Solid State Phys. 8 (1975) 3499.
[201] A.H. Heuer, R.J. Keller, T.E. Mitchell, in: D.J. Barber, P.G. Meredith (Eds.), Deformation Processes in Minerals, Ceramics and Rocks, Unwin Hyman, London, UK, 1990, p. 377.
[202] H. Strunk, Phys. Status Solidi A 11 (1972) K105.
[203] W. Skrotzki, P. Haasen, J. Phys. C3 (Suppl. 6) (1981) 119.
[204] J. Hesse, Phys. Status Solidi 9 (1965) 209.
[205] G. Fontaine, J. Phys. Chem. Solids 29 (1968) 209.
[206] G. Fontaine, P. Haasen, Phys. Status Solidi 31 (1969) K67.
[207] L.A. Davis, R.B. Gordon, Phys. Status Solidi 36 (1969) K133.
[208] S. Amelinckx, in Report on Conference on Dislocations and Mechanical Properties of Crystals, eds. J. C. Fisher, W. G. Johnston, R. Thomson and T. Vreeland, Lake Placid, N.Y., 1956 (Wiley, New York, 1957) p. 3.
[209] F.C. Frank, Report on Conference on Defects in Crystalline Solids, The Physical Society, London, UK, 1954.
[210] N. Thomson, Proc. R. Soc. B 66 (1953) 481.
[211] J.E. Caffyn, J.C. de Freitas, T.L. Goodfellow, Phys. Status Solidi B 9 (1965) 333.
[212] L.W. Hobbs, M.J. Goringe, Microscopie Électronique, Société Française de Microscopie Electronique, Paris, 1970, p. 289
[213] R.J. Reeder, Carbonates: Mineralogy and Chemistry, in: R.J. Reeder (Ed.), Reviews in Mineralogy, Vol. 11, Mineralogical Society of America, Washington, DC, 1983, p. 1.

[214] M. Sarikaya, K.E. Gunnison, M. Yasrebi, I.A. Aksay, in: M. Alper, P.D. Calvert, P.C. Rieke (Eds.), Materials Synthesis Utilizing Biological Processes, Materials Research Society Symposium Proceedings 174 (Materials Research Society, Pittsburgh, PA), p. 109.
[215] D.J. Barber, H.-R. Wenk, J. Mater. Sci. 8 (1973) 500.
[216] D.J. Barber, H.-R. Wenk, in: H.-R. Wenk (Ed.), Electron Microscopy in Mineralogy, Springer, Berlin, Germany, 1976, p. 428.
[217] R.E. Keith, J.J. Gilman, Acta Metall. 8 (1960) 1.
[218] V.I. Startsev, V.Z. Bengus, F.F. Lavrent'ev, L.M. Soifer, Kristallograhie 5 (1960) 737.
[219] R.W. Cahn, Philos. Mag. 3 (Suppl.) (1954) 363.
[220] G. Rose, Abh. Konig. Akad. Wiss. Berlin 23 (1868) 57.
[221] R.J. Reeder, Minerals and Reaction at the Atomic Scale: Transmission Electron Microscopy, in: P.R. Buseck (Ed.), Reviews in Mineralogy, Vol. 27, Mineralogical Society of America, Washington, DC, 1992, p. 381.
[222] R.J. Reeder, H.-R. Wenk, Geophys. Res. Lett. 6 (1979) 77.
[223] K. Reksten, Phys. Chem. Miner. 17 (1990) 266.
[224] R.J. Reeder, J.L. Prosky, J. Sediment. Petrol. 56 (1986) 237.
[225] D.J. Barber, H.C. Heard, M.S. Paterson, H.-R. Wenk, Nature 269 (1977) 789.
[226] V. Trommsdorff, H.-R. Wenk, Schweiz. Mineral. Petrogr. Mitt. 45 (1965) 551.
[227] S. Frisia-Bruni, H.-R. Wenk, J. Sediment. Petrol. 63 (1993) 1049.
[228] J.W. McTigue, H.-R. Wenk, Am. Mineral. 70 (1985) 1253.
[229] P. Gillet, M. Madon, Bull. Mineral. 105 (1982) 590.
[230] J.D. Gale, A.L. Rohl, Mol. Simul. 29 (2003) 291.
[231] P. Carrez, D. Ferré, P. Cordier, Nature 446 (2007) 68.
[232] D.J. Barber, N.J. Tighe, Philos. Mag. 11 (1965) 495.
[233] D.J. Barber, N.J. Tighe, Philos. Mag. 14 (1966) 531.
[234] K. Veit, Neues Jahrb. Mineral. Geol. Palaeontol. Beilageband 45 (1921) 121.
[235] E. Stofel, H. Conrad, Trans. AIME 227 (1963) 1053.
[236] R.L. Bertolotti, W.D. Scott, J. Am. Ceram. Soc. 54 (1971) 286.
[237] W.D. Scott, in: R.C. Bradt, R.E. Tressler (Eds.), Deformation of Ceramic Materials, Plenum Press, New York, 1975, p. 151.
[238] B.J. Pletka, T.E. Mitchell, A.H. Heuer, in: R.C. Bradt, R.E. Tressler (Eds.), Deformation of Ceramic Materials, Plenum Press, New York, 1975, p. 181.
[239] R. Chang, J. Appl. Phys. 31 (1960) 484.
[240] M.V. Klassen-Neklyudova, V.G. Govorkov, A.A. Urusovskaya, N.N. Voinova, E.P. Koslovskaya, Phys. Status Solidi 39 (1970) 679.
[241] K.C. Radford, P.L. Pratt, Proc. Brit. Ceram. Soc. 15 (1970) 185.
[242] M.C. Rodriguez, A. Munoz, J. Castaing, P. Veyssière, A.D. Rodriguez, J. Eur. Ceram. Soc. 27 (2007) 3317.
[243] T.E. Mitchell, B.J. Pletka, D.S. Philips, A.H. Heuer, Philos. Mag. 34 (1976) 441.
[244] J.B. Bilde-Sörensen, A.R. Tholen, J.J. Gooch, G.W. Groves, Philos. Mag. 33 (1976) 877.
[245] L.A. Bursill, R.L. Withers, Philos. Mag. 40 (1979a) 213.
[246] L.A. Bursill, J.L. Peng, Philos. Mag. Lett. A 60 (1989) 1.
[247] L.A. Bursill, J.L. Peng, X.D. Fang, Aust. J. Chem. 45 (1992) 1527.
[248] L.A. Bursill, R.L. Withers, J. Appl. Cryst. 12 (1979) 287.
[249] L.A. Bursill, P.J. Lin, in: J.N. Boland, J.D. FitzGerald (Eds.), Defects and Processes in the Solid State: Geoscience Applications, The McLaren Volume, Elsevier, Amsterdam, 1993, p. 447.
[250] J.S. Lally, A.H. Heuer, G.L. Nord, in: H.R. Wenk (Ed.), Electron Microscopy in Mineralogy, Springer Verlag, Berlin, Germany, 1976, p. 214.
[251] T. Kasama, U. Golla-Schindler, A. Putnis, Am. Mineral. 88 (2003) 1190.
[252] W.M. Cullen, M.J. Marcinkowski, E.S.P. Das, Surf. Sci. 36 (1973) 395.
[253] G.L. Nord Jr., Am. Miner. 74 (1989) 160.

[254] G.L. Nord Jr., Minerals and reactions at the atomic scale: Transmission electron microscopy, in: P.R. Buseck (Ed.), Reviews in Mineralogy, Vol. 27, Mineralogical Society of America, Washington, DC, 1992, p. 455.
[255] M. Bystricky, F. Heidelbach, S. Mackwell, Tectonophysics 427 (2006) 115.
[256] S. Mann, R.B. Frenkel, R.P. Blakemore, Nature 310 (1984) 405.
[257] K.L. Thomas-Keprta, D.A. Bazylinski, J.L. Kirschvink, S.J. Clement, D.S. McKay, S.J. Wentworth, H. Vali, E.K. Gibson, C.S. Romanek, Geochim. Cosmocim Acta 64 (2000) 4049.
[258] D.J. Barber, E.R.D. Scott, Proc. Natl. Acad. Sci. 99 (2002) 6556.
[259] A. Navrotsky, D.J. Weidner (Eds.), Perovskite: a Structure of Great Interest to Geophysics and Materials Science, American Geophysical Union, Washington, DC, 1989.
[260] H. Meisheng, H.-R. Wenk, D. Sinitsyna, Am. Mineral. 77 (1992) 359.
[261] D. Ferré, P. Carrez, P. Cordier, Phys. Rev. B 77 (2008) 1.
[262] K. Suzuki, M. Ichihara, S. Takeuchi, Philos. Mag. A 63 (1991) 657.
[263] R. Burgmann, G. Dresen, Ann. Rev. Earth Planet. Sci. 36 (2008) 531.
[264] J.R. Rice, N. Lapusta, K. Janjith, J. Mech. Phys. Solids 49 (2001) 1865–1898.
[265] A.C. McLaren, P.P. Phakey, J. Appl. Phys. 36 (1965) 3244.
[266] R. Heilbronner, J. Tullis, J. Geophys. Res. 111 (2006) B10202.
[267] V.G. Toy, D.J. Prior, R.J. Norris, J. Struct. Geol. 30 (2008) 602.
[268] G. Hirth, C. Teyssier, W.J. Dunlap, Int. J. Earth Sci. (Geol. Rundsch.) 90 (2001) 77.
[269] M. Stipp, H. Stuenitz, R. Heilbronner, S.M. Schmid, J. Struct. Geol. 24 (2002) 1861.
[270] J. Pehl, H.-R. Wenk, J. Struct. Geol. 27 (2005) 1741.
[271] A. Schubnikov, K. Zinserling, Z. Kristallogr. 83 (1932) 243.
[272] J. Tullis, T.E. Tullis, Am. Geophys. Union Monogr. 16 (1972) 67.
[273] H.-R. Wenk, I. Lonardelli, E. Rybacki, G. Dresen, N. Barton, H. Franz, G. Gonzalez, Phys. Chem. Miner. 33 (2006) 667.
[274] D.J. Barber, H.-R. Wenk, Phys. Chem. Miner. 17 (1991) 492.
[275] A.C. McLaren, J.D. Fitz Gerald, J. Gerretsen, Phys. Chem. Miner. 16 (1989) 465.
[276] W.B. Kamb, J. Geophys. Res. 66 (1961) 259.
[277] A.G. McLellan, J. Phys. C 11 (1978) 4665.
[278] M.S. Paterson, Rev. Geophys. Space Phys. 11 (1973) 355.
[279] I. Shimizu, J. Geophys. Res. 97 (1992) 4587.
[280] J.C. Doukhan, L. Trepied, Bull. Minéral. 108 (1985) 97.
[281] D.T. Griggs, J.D. Blacic, Science 147 (1965) 292.
[282] D.T. Griggs, Geophys. J. R. Astro. Soc. 14 (1967) 19.
[283] D.L. Kohlstedt, B. Evans, S.J. Mackwell, J. Geophys. Res. 100B (1995) 17587.
[284] G.C. Gleason, J. Tullis, Tectonophysics 247 (1995) 1.
[285] J. Farver, R.A. Yund, Chem. Geol. 90 (1991) 55.
[286] J. Tullis, Rev. Mineral. Geochem. 51 (2002) 51.
[287] A.K. Kronenberg, H-speciation and Chemical Weakening in Quartz, in: P.J. Heaney, C.T. Prewitt, G.V. Gibbs (Eds.), Reviews in Mineralogy, Vol. 29, Mineralogical Society of America, Washington, DC, 1994, p. 123.
[288] D.H. Mainprice, M.S. Paterson, J. Geophys. Res. 89 (1984) 4257.
[289] B.E. Hobbs, in: H.-R. Wenk (Ed.), Preferred Orientation in Deformed Metals and Rocks: An Introduction to Modern Texture Analysis, Academic Press, Orlando, FL, 1985, p. 463.
[290] M.C. Paterson, in: S.-I. Karato, M. Toriumi (Eds.), Rheology of Solids and of the Earth, Oxford University Press, Oxford, 1989, p. 107.
[291] P. Cordier, J.C. Doukhan, Eur. J. Mineral. 1 (1989) 221.
[292] T.G. Blenkinsop, M.R. Drury, J. Struct. Geol. 10 (1988) 673.
[293] H.-R. Wenk, P. Monteiro, K. Shomglin, J. Mater. Sci. 43 (2007) 1278.
[294] H.H. Hess, Nature 203 (1964) 629.
[295] J.P. Montagner, T. Tanimoto, J. Geophys. Res. 95 (1990) 4797.
[296] P. Raterron, E. Amiguet, J. Chen, L. Li, P. Cordier, Phys. Earth Planet Inter. 172 (2008) 74.
[297] W.B. Durham, C. Goetze, J. Geophys. Res. 82 (1977) 5737.

[298] S.J. Mackwell, D.L. Kohlstedt, M.S. Paterson, J. Geophys. Res. 90 (1985) 11319.
[299] Q. Bai, S.J. Mackwell, D.L. Kohlstedt, J. Geophys. Res. 96 (1991) 2441.
[300] P.N. Chopra, M.S. Paterson, J. Geophys. Res. 89 (1984) 7861.
[301] S.I. Karato, M.S. Paterson, J.D. Fitz Gerald, J. Geophys. Res. 91 (1986) 8151.
[302] S.I. Karato, in: S.D. Jacobsen, S. van der Lee (Eds.), Earth's Deep Water Cycle, AGU, Washington, DC, 2006, p. 113.
[303] D.L. Kohlstedt, Water in Nominally Anhydrous Minerals, in: H. Keppler, J.R. Smyth (Eds.), Reviews in Mineralogy and Geochemistry, Vol. 62, Mineralogical Society of America, Washington, DC, 2006, p. 377.
[304] W.T. Stacy, J.A. Pistorius, M.M. Janssen, J. Cryst. Growth 22 (1974) 37.
[305] C.-Z. Ge, N.-B. Ming, D. Feng, Philos. Mag. A 53 (1986) 285.
[306] H. Carstens, Contrib. Mineral. Petrol. 24 (1969) 348.
[307] J. Ando, K. Fujino, T. Takeshita, Phys. Earth Planet. Inter. 80 (1993) 105.
[308] V. Voegelé, P. Cordier, V. Sautter, T.G. Sharp, J.M. Lardeaux, F.O. Marques, Phys. Earth Planet. Int. 108 (1998) 319.
[309] C.D. Storey, D.J. Prior, J. Petrol. 46 (2005) 2593.
[310] F.M. Allen, B.K. Smith, P.R. Buseck, Science 238 (1987) 1965.
[311] J. Ingrin, N. Doukhan, J.-C. Doukhan, Eur. J. Mineral. 4 (1992) 1291.
[312] W. Skrotzki, Tectonophysics 229 (1994) 43.
[313] W. Skrotzki, Phys. Status Solidi A 131 (1992) 605.
[314] S.J. Mackwell, Geophys. Res. Lett. 18 (1991) 2027–2030.
[315] J. Ingrin, N. Doukhan, J.-C. Doukhan, J. Geophys. Res. 96 (1991) 14287.
[316] W. Skrotzki, Eur. J. Mineral. 13 (2001) 245.
[317] R.S. Coe, S.H. Kirby, Contrib. Mineral. Petrol. 52 (1975) 29.
[318] W.F. Müller, Neues Jahrb. Mineral. 2 (1974) 83.
[319] C.B. Raleigh, S.H. Kirby, N.L. Carter, H.G. Avé Lallemant, J. Geophys. Res. 76 (1971) 4011.
[320] M. Bystricky, S. Mackwell, J. Geophys. Res. 106 (2000) 13443.
[321] S. Chen, T. Hiraga, D.L. Kohlstedt, J. Geophys. Res. 111 (2006) B08203, doi:10.1029/2005JB003885.
[322] S. Hier-Majumder, S. Mei S, D.L. Kohlstedt, J. Geophys. Res. 110 (2005) B07406, doi:10.1029/2004JB003414.
[323] P.E. Champness, Am. Mineral. 58 (1973) 540.
[324] P.P. Phakey, S. Ghose, Contrib. Mineral. Petrol. 39 (1973) 239.
[325] W.F. Müller, G. Franz, Neues Jahrb. Mineral. Abh. 184 (2008) 285.
[326] H.L.M. Van Roermund, J.N. Boland, Tectonophysics 78 (1981) 403.
[327] H.L.M. Van Roermund, J.M. Lardeaux, Mineral. Mag. 55 (1991) 397.
[328] M. Buatier, H.L.M. Van Roermund, M.R. Drury, J.M. Lardeaux, Tectonophysics 195 (1991) 11.
[329] G. Godard, H.L.M. Van Roermund, J. Struct. Geol. 17 (1995) 1425.
[330] F.E. Brenker, D.J. Prior, W.F. Müller, J. Struct. Geol. 24 (2002) 1991.
[331] J. Zhang, H.W. Green II, K.N. Bozhilov, Earth Planet. Sci. Lett. 246 (2006) 432.
[332] J.-C. Van Duysen, J.-C. Doukhan, Phys. Chem. Miner. 10 (1984) 125–132.
[333] T.P. Rooney, R.E. Riecker, A.T. Gavasci, Geology 3 (1975) 364.
[334] D.J. Morrison-Smith, Am. Mineral. 61 (1976) 280.
[335] K.H. Brodie, Tectonophysics 78 (1981) 385.
[336] C. Biermann, H.L.M. van Roermund, Tectonophysics 95 (1983) 267.
[337] K.H. Brodie, E.H. Rutter, Adv. Phys. Chem. 4 (1985) 138.
[338] R.J. Cumbest, M.R. Drury, H.L.M. van Roermund, C. Simpson, Contrib. Mineral. Petrol. 101 (1989) 339.
[339] D.R. Veblen, P.R. Buseck, Am. Mineral. 66 (1981) 1107.
[340] J.E. Chisholm, J. Mater. Sci. 8 (1973) 475.
[341] B. Reynard, P. Gillet, C. Willaime, Eur. Mineral. 1 (1989) 611.
[342] N. Tolanski, C. Morris, Philos. Mag. 28 (1947) 137.
[343] S. Amelynckx, P. Delavignette, in: Proceedings of a Technical Conference on Direct Observations of Imperfections in Crystals, Missouri, 1962, 295–356.

[344] J. Demny, Z. Naturforsch. A 18 (1963) 1088.
[345] J.L. Caslavsky, K. Vedam, Philos. Mag. 22 (1970) 176–255.
[346] I.A. Bell, C.J.L. Wilson, Tectonophysics 78 (1981) 201.
[347] M.A. Etheridge, B.E. Hobbs, Contrib. Mineral. Petrol. 43 (1974) 111.
[348] R. Christoffersen, A.K. Kronenberg, J. Struct. Geol. 15 (1993) 1077.
[349] C.-L. Kuo, Y.-H. Huang, S.-J. Fan, J. Mater. Sci. 16 (1981) 877.
[350] H.-R. Wenk, Neues Jahrb. Mineral. Abh. 146 (1983) 1–14.
[351] D. Menard, J.C. Doukhan, J. Phys. 39 (1978) L19–L22.
[352] A. Lefevre, J. Paquet, Bull. Mineral. 106 (1983) 287–292.
[353] L. Taherabadi, J.E. Trujillo, T. Chen, J.R. Porter, M.L. Mecartney, J. Eur. Ceram. Soc. 28 (2008) 371–376.
[354] D. Menard, J.C. Doukhan, J. Paquet, Bull. Mineral. 102 (1979) 159–162.
[355] J.V. Smith, W.L. Brown, Feldspar Minerals, Vol. 1, Springer Verlag, Heidelberg, Germany, 1988.
[356] H. Stünitz, J.D. Fitz Gerald, J. Tullis, Tectonophysics 372 (2003) 215.
[357] G. Bossiere, A. Vauchez, Tectonophysics 51 (1978) 57.
[358] M. Sacerdoti, H. Labernardiere, M. Gandais, Bull. Mineral. 103 (1980) 148.
[359] J.-L. Vidal, L. Kubin, P. Debat, J.-C. Soula, Lithos 13 (1980) 247.
[360] S.K. Hanmer, J. Struct. Geol. 4 (1982) 197.
[361] H.L. Alling, J. Geol. 29 (1921) 193.
[362] R.A. Yund, J. Tullis, Contrib. Miner. Petrol. 72 (1980) 297.
[363] R.A. Yund, J. Quigley, J. Tullis, J. Metam. Geol. 7 (1989) 337.
[364] D.B. Marshall, A.C. McLaren, J. Mater. Sci. 12 (1977) 893.
[365] D.B. Marshall, A.C. McLaren, Phys. Chem. Miner. 1 (1977) 351.
[366] A. Dimanov, G. Dresen, X. Xiao, R. Wirth, J. Geophys. Res. 104 (1999) 10483.
[367] S. Ji, Z. Jiang, E. Rybacki, R. Wirth, D. Prior, B. Xia, Earth Planet. Sci. Lett. 222 (2004) 377.
[368] Z. Wang, G. Dresen, R. Wirth, Geophys. Res. Lett. 23 (1996) 3111.
[369] J. Gómez Barreiro, I. Lonardelli, H.-R. Wenk, G. Dresen, E. Rybacki E, Y. Ren, C.T. Tome, Earth Planet. Sci. Lett. 264 (2007) 188.
[370] T. Olsen, D. Kohlstedt, Tectonophysics 111 (1985) 107.
[371] D.M. Ague, H.-R. Wenk, E. Wenk, Geophys. Monogr. 56 (1990) 173.
[372] D.B. Marshall, C.J. Wilson, Contrib. Mineral. Petrol. 57 (1976) 55.
[373] S. Ji, D. Mainprice, Tectonophysics 147 (1987) 145.
[374] R. Kruse, H. Stünitz, K. Kunze, J. Struct. Geol. 23 (2001) 1781.
[375] J. Feinberg, H.-R. Wenk, G.R. Scott, P. Renne, Tectonophysics 420 (2006) 345.
[376] S. Ji, R. Wirth, E. Rybacki, Z. Jiang, J. Geophys. Res. 105 (2000) 16,651.
[377] Y. Xie, H.-R. Wenk, S. Matthies, Tectonophysics 370 (2003) 269.
[378] L. Mehl, G. Hirth, J. Geophys. Res. 113 (2008) B05202.
[379] J. Tullis, R.A. Yund, Geology 15 (1987) 606.
[380] I. Borg, J. Handin, Tectonophysics 3 (1966) 249.
[381] I. Borg, H.C. Heard, Contrib. Mineral. Petrol. 23 (1969) 128.
[382] D.B. Marshall, A.C. McLaren, Phys. Status. Solidi 41 (1977) 231.
[383] O. Mügge, Neues Jahrb.Mineral. (1898) 71.
[384] O. Mügge, Neues Jahrb. Mineral. (1920) 24.
[385] K. Veit, Neues Jahrb. Mineral. Beilageband 45 (1922) 121.
[386] M. Buerger, Am. Mineral. 13 (1928)1, 35
[387] G. Kullerud, H.S. Yoder, Econ. Geol. 54 (1959) 533.
[388] E.H. Nickel, Can. Mineral. 9 (1968) 311.
[389] M.E. Fleet, Can. Mineral. 10 (1970) 225.
[390] G. Brostigen, A. Kjekshus, Acta Chem. Scand. 24 (1970) 2983.
[391] B.K. Atkinson, Econ. Geol. 70 (1975) 473.
[392] A. Mookherjee, Econ. Geol. 66 (1971) 200.
[393] P. Natale, Soc. Ital. Mineral. Petrol. Rend. 27 (1971) 537.
[394] M. Fagot, C. Levade, J.-J. Couderc, J. Bras, Philos. Mag. A 38 (1978).

[395] M. Fayard, D. Gratias, R. Portier, Philos. Mag. A 41 (1980) 125.
[396] M.E. Fleet, P.J. MacLean, J. Barbier, Econ. Geol. Monograph 6 (1989) 356.
[397] I. Dodony, M. Posfal, P.R. Buseck, Am. Mineral. 81 (1996) 119.
[398] D. Gratias, R. Portier, M. Fayard, M. Guymont, Acta Cryst. A 35 (1979) 885.
[399] K.R. McClay, P.G. Ellis, Mineral. Mag. 47 (1983) 527.
[400] B.K. Atkinson, Econ. Geol. 71 (1976) 513.
[401] B.K. Atkinson, Phys. Chem. Miner. 2 (1978) 305.
[402] B.C. Salmon, B.R. Clark, W.C. Kelly, Econ. Geol. 69 (1974) 1.
[403] B.K. Atkinson, Geol. Foeren. Stockholm Foerh. 99 (1977) 186.
[404] K.R. McClay, B.K. Atkinson, Tectonophysics 39 (1977) 175.
[405] A. Foitzik, W. Skrotzki, P. Haasen, Phy. Status Solidi A 121 (1990) 81.
[406] A. Foitzik, P. Haasen, W. Skrotzki, Philos. Mag. A 64 (1991) 29.
[407] A. Foitzik, W. Skrotzki, P. Haasen, Mater. Sci. Eng. A 132 (1991) 77.
[408] C. Deeb, J. Castaing, P. Walter, P. Penhoud, P. Veyssière, P. Martinetto, Metall. Mater. Trans. A 35 (2004) 2223.
[409] R.L. Stanton, H.G. Willey, Econ. Geol. 65 (1970) 182.
[410] Y.A. Osip'yan, V.F. Petrenko, Zh. Eksp. Teor. Fiz. 69 (1975) 1362; Soviet Phys. JETP 42 (1975) 695.
[411] H.J. Saynisch, in: P. Paulitsch (Ed.), Experimental and Natural Rock Deformation, Springer, Berlin, Germany, 1970, p. 209.
[412] B.R. Clark, W.B. Kelly, Econ. Geol. 68 (1973) 332.
[413] C.C. Speake, P.J. Smith, T.R. Lomer, R.W. Whitworth, Philos. Mag. A 38 (1978) 603.
[414] C. Levade, J.-J. Couderc, A. Kara, Phys. Status Solidi 112 (1989) 89.
[415] H. Alexander, J. Phys. Colloques 40 (1979) C1-6.
[416] A. Faress, C. Levade, G. Vanderschaeve, Philos. Mag. A 68 (1993) 97.
[417] H. Steinhart, S. Schäfer, Acta Metall. 19 (1971) 65.
[418] C. Levade, G. Vanderschaeve, J. Cryst. Growth 197 (1999) 565.
[419] V.F. Petrenko, R.W. Whitworth, Philos. Mag. A 41 (1980) 681.
[420] A. Kara, J.-J. Couderc, C. Levade, G. Vanderschaeve, Phys. Status. Solidi 122 (1990) 545.
[421] H.-R. Wenk, I. Lonardelli, S. Merkel, L. Miyagi, J. Pehl, S. Speziale, C.E. Tommaseo, J. Phys. Cond. Matter. 18 (2006) S933.
[422] R. Peierls, Proc. Phys. Soc. 52 (1940) 34.
[423] F.R.N. Nabarro, Proc. Phys. Soc. Lond. 59 (1947) 256.
[424] J. Durinck, P. Carrez, P. Cordier, Eur. J. Mineral. 19 (2007) 631.
[425] P. Cordier, Plastic Deformation in Minerals and Rocks, in: S.-I. Karato, H.R. Wenk (Eds.), Reviews in Mineralogy and Geochemistry, Vol. 51, Mineralogical Society of America, Chantilly, VA, 2002, p. 137.
[426] B. Mason, J. Nelen, J.S. White, Science 160 (1968) 66.
[427] N. Tomioka, K. Fujino, E. Ito, T. Katsura, T. Sharp, T. Kato, Eur. J. Mineral. 14 (2002) 7.
[428] T.G. Sharp, G.Y. Bussod, T. Katsura, Phys. Earth. Planet. Sci. Int. 86 (1994) 69.
[429] D. Stöffler, K. Keil, E.R.D. Scott, Geochim. Cosmochim. Acta 55 (1991) 3485.
[430] P. Cordier, E. Thurel, J. Rabier, Geophys. Res. Lett. 29 (2002) 68.
[431] A.R. Oganov, S. Ono, Nature 430 (2004) 445.
[432] D. Ferré, P. Carrez, P. Cordier, Phys. Earth Planet. Inter. 163 (2007) 283.
[433] E.C.T. Chao, E.M. Shoemaker, B.M. Madsen, Science 132 (1960) 220.
[434] D. Jacob, P. Cordier, J.-P. Morniroli, H.-P. Schertl, Eur. J. Mineral. 20 (2008) 119.
[435] S.W. Kieffer, P.P. Phakey, J.M. Christie, Contrib. Mineral. Petrol. 59 (1976) 41.
[436] J.C. White, in: J.N. Boland, J.D. FitzGerald (Eds.), Defects and Processes in the Solid State: Geoscience Applications, The McLaren Volume, Elsevier, Amsterdam, 1993, p. 69.
[437] G. Schoeck, Acta Mater. 54 (2006) 4865.
[438] L.P. Kubin, B. Devincre, M. Tang, J. Comput. Aided Mater. Des. 5 (1998) 31.
[439] C.R. Miranda, S. Scandolo, Comput. Phys. Commun. 169 (2005) 24.
[440] J. Durinck, A. Legris, P. Cordier, Am. Mineral. 90 (2005) 1072.

[441] J. Durinck, B. Devincre, L. Kubin, P. Cordier, Am. Mineral. 92 (2007) 1346.
[442] P. Carrez, D. Ferré, P. Cordier, Philos. Mag. 87 (2007) 3229.
[443] P. Carrez, P. Cordier, B. Devincre, L.P. Kubin, Mater. Sci. Eng. A 400–401 (2005) 325.
[444] M. Wilkens, Phys. Status Solidi A 2 (1970) 359.
[445] T. Ungár, Acta Metall. 32 (1984) 333.
[446] N. Ji, J. Mater. Sci. 29 (1994) 1553.
[447] N. Ji, J.L. Lebrun, B. Marty, M. Bessiere, B. Chenal, J. Mater. Sci. Lett. 14 (1995) 674.
[448] J. Gubicza, L. Balogh, R.J. Hellmig, Y. Estrin, T. Ungár, Mater. Sci. Eng. A 400–401 (2005) 334.
[449] T. Ungár, Mat. Sci. Eng. A 309 (2000) 14.
[450] I. Groma, A. Borbély, Diffraction analysis of the Microstructure of Materials, Springer Series in Materials Science 68, Springer Verlag, Berlin, Germany, 2004, p. 285.
[451] C. Pantea, J. Gubicza, T. Ungár, G. Voronin, T.W. Zerda, Phys. Rev. B 66 (2002) 094106.
[452] K. Nyilas, H. Couvy, P. Cordier, T. Ungár, Z. Kristall. Suppl. 23 (2006) 135.
[453] A.E. Blum, R.A. Yund, A.C. Lasaga, Geochim. Cosmochim. Acta 54 (1990) 283.
[454] W. Bollmann, Crystal Defects and Crystalline Interfaces, Springer Verlag, Heidelberg, Germany, 1970.
[455] A.C. Lasaga, A.E. Blum, Geochim. Cosmochim. Acta 50 (1986) 2363.
[456] F.C. Frank, Acta. Crystall. 4 (1951) 497.
[457] S.L. Brantley, S.R. Crane, D.A. Credar, R. Hellmann, R. Stallard, Geochim. Cosmochim. Acta 50 (1986) 2349.
[458] R.P. Wintsch, J. Dunning, J. Geophys. Res. 90 (1985) 3649.
[459] M. Liu, R.A. Yund, J. Tullis, L. Topor, A. Navrotsky, Phys. Chem. Miner. 22 (1995) 67.
[460] G.R. Holdren, W.H. Casey, H.R. Westrich, M. Carr, M. Boslough, Chem. Geol. 70 (1988) 79.
[461] J. Schott, S. Brantley, D. Credar, C. Guy, M. Borcsik, C. Willaime, Geochim. Cosmochim. Acta 53 (1989) 373.
[462] R.J. Twiss, Pure Appl. Geophys. 115 (1977) 227.
[463] P.J.M. Monteiro, K. Shomglin, H.-R. Wenk, N.P. Hasparyk, ACI Mater. J. 98 (2001) 179.

CHAPTER 96

Dislocations in Colloidal Crystals

PETER SCHALL

Van der Waals-Zeeman Instituut, Universiteit van Amsterdam, Valckenierstraat 65, 1018 XE Amsterdam, The Netherlands

FRANS SPAEPEN

Harvard School of Engineering and Applied Sciences, Harvard University, 29 Oxford Street, Cambridge, MA 02138, USA

1572-4859, DOI: 10.1016/S1572-4859(09)01605-2

Dislocations in Solids
Edited by J. P. Hirth and L. Kubin

Contents

1. Introduction 235
2. Colloids 236
3. Colloidal crystals 237
4. Observation of dislocations 238
   4.1. Confocal microscopy 238
   4.2. Laser diffraction microscopy 240
5. Elasticity of dense colloidal systems 244
6. Misfit dislocations 247
   6.1. Lattice mismatch 247
   6.2. Critical thickness 248
   6.3. Dislocation density 249
   6.4. Dislocation offset 250
   6.5. Dislocation dynamics 250
7. Nucleation of dislocations 254
   7.1. Indentation experiment 254
   7.2. Strain distribution 254
   7.3. Nucleation kinetics 258
8. Conclusions and prospects 259
Acknowledgements 260
References 260

1. Introduction

Dislocations occur in lattices other than those of atomic-scale crystals. The best known examples, no doubt, are those in the experiments of Bragg and Nye with rafts of soap bubbles [1]. Their work illustrated the geometry and kinematics of the edge dislocations in these two-dimensional hexagonal lattices, and vividly revealed how macroscopic plastic deformation of crystals is effected by the motion of large numbers of such dislocations. Ahead of the definitive identification of moving dislocations in atomic crystals by electron microscopy [2], Bragg and Nye's experiments had convinced many of the reality and the potential of what had initially been a purely theoretical concept [3–5].

On a scale a thousand times smaller, particles in dense colloidal suspensions also form two- or three-dimensional lattices, both of which can contain dislocations. There is a fundamental difference between dislocations in two- and three-dimensional lattices. In the former case, dislocations are point defects, which can be in thermodynamic equilibrium and can lead to phase transformations. Their appearance into the hexagonal close-packed crystal leads to the loss of translational order and the formation of the hexatic phase. Their subsequent dissociation into disclinations leads to loss of the oriental order and formation of the liquid phase [6–8]. Colloidal systems are well suited for experimental exploration of two-dimensional dynamic systems [9,10], and the results have played an important role in the development of this field [11,12].

In this article, however, we discuss recent studies of dislocations in three-dimensional colloidal crystals. Such dislocations either are nonequilibrium growth defects, misfit dislocations, or are produced during plastic deformation. The first ones to observe and characterize such dislocations were Pieranski and coworkers [13,14]. Since then, the availability of new experimental tools, such as microlithography and confocal microscopy, has greatly expanded our capability to create and study three-dimensional colloidal crystals in three dimensions. One can now grow large single crystals on microlithographically prepared templates. Confocal microscopy has made it possible to track each individual particle in a colloidal system in space and time. As a result, these systems can be used as ''analog computers'' to simulate and study the dynamics of complex phenomena in crystals, liquids, and glasses. In this paper we review our recent study of the geometry, nucleation, and propagation of dislocations in large colloid single crystals. Even though our colloidal particles are hard spheres, the observed geometries can be described well by classic mechanics and even the kinetics correspond surprisingly well to those in atomic systems.

2. Colloids

Colloidal systems are suspensions of small particles, made of silica or a polymer, such as polymethylmetacrylate (PMMA) or polystyrene, in a fluid [15]. The fluid is usually a mixture prepared to match either the index of refraction or the density of the particles. The particles must be sufficiently small, so that their motion is primarily thermal in origin (Brownian motion) rather than due to, for example, gravity or convection. In the experiments discussed in this article, silica particles (diameter 1.55 μm, density 2.0 g/cm^3, and mass 3.9×10^{-15} kg) are suspended in a water–62.8 vol.% dimethylsulfoxide (DMSO) solution that matches the index of refraction of the silica and has a density of 1.10 g/cm^3. The average velocity of Brownian motion is given by:

$$\langle v_B \rangle = \sqrt{\frac{3k_B T}{m}}, \tag{1}$$

where k_B is Boltzmann's constant, T the temperature, and m the mass of the particle. For our case, this gives $\langle v_B \rangle = 2 \times 10^{-3}$ m/s. The gravitational settling velocity of the particle is given by

$$v_S = \frac{V_P \, \Delta\rho g}{6\pi r \eta}, \tag{2}$$

where V_P and r are, respectively, the volume and radius of the particle, $\Delta\rho$ is the density difference between particle and fluid, and η is the viscosity of the fluid, which is about 10^{-2} Pa s. This gives in our case $v_S = 10^{-6}$ m/s, which satisfies the condition for a colloidal particle. The index match makes the system optically transparent, which allows investigation by optical microscopy at large distances into the sample. Contrast between particle and solution is achieved by means of fuoroscein dye added to the solution. The index match also minimizes the van der Waals forces between the particles, which interact therefore like hard spheres.

Thermodynamically, an assembly of colloidal particles in the thermal bath of the solution has an equation of state similar to that of the ideal gas

$$\Pi = \rho k_B T Z, \tag{3}$$

where Π is the osmotic pressure, ρ the density of the particles, and Z a compressibility factor that depends on the packing fraction ($Z = 1$ at low density and diverges at the densest packing fraction) [16,17]. Since the particles interact with a central (spherically symmetric) potential, they form phases similar to those formed by atoms interacting with central potentials. In a hard-sphere system, the temperature is no longer a phase-controlling parameter, as can be seen from the following argument. To form a phase, the hard spheres must be confined to a finite volume. The controlling potential at constant volume is the Helmholtz free energy

$$F = U - TS, \tag{4}$$

where U and S are the energy and the entropy, respectively. Since the hard spheres only have kinetic energy, the internal energy of the system is

$$U = \frac{3}{2}RT, \tag{5}$$

and hence the Helmholtz free energy becomes

$$F = \left(\frac{3}{2}R - S\right)T. \tag{6}$$

Minimization of F, therefore, occurs by maximization of the entropy; temperature is not a controlling variable. The entropy, in turn, is controlled by the packing fraction of the particles. Fig. 1 shows a schematic phase diagram.

Computer simulations [18] and experiments on monodisperse colloids [19] established that volume fractions of coexisting liquid and crystalline phases are, respectively, 0.494 and 0.545. The liquid can be overcompressed to form a glass once it reaches a packing fraction of 0.58 [20]. That crystallization of hard spheres is also driven by maximization of entropy may seem paradoxical. To understand this, we consider a hard-sphere glass at its maximum packing fraction of 0.636 [21]. All spheres are jammed under this condition: none of them have any degree of freedom for motion. Although the structure is disordered, its positional entropy is small [22], and the entropy associated with local motion is zero. Since the packing fraction of the glass is well below that of a close-packed crystal (0.740), crystallization of the glass at constant volume produces a structure with zero positional entropy but with considerable local entropy.

3. Colloidal crystals

Colloidal crystals can have a large variety of structures that depend on the nature of the colloids (hard sphere, charged, mixed sizes, and charges) [23]. The equilibrium crystalline phase of single-sized hard spheres has the face-centered cubic structure. Its energy is only about $10^{-3}k_BT$ lower than that of the hexagonal close-packed crystal [24]. Equivalently, the stacking faults on the close-packed planes in both

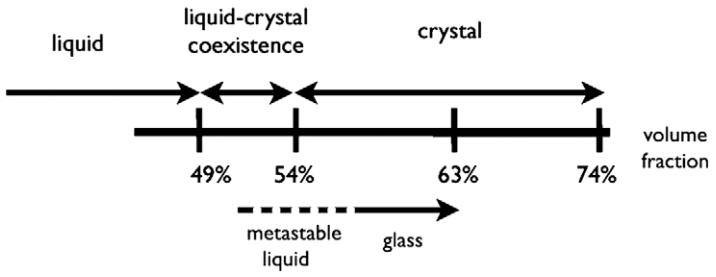

Fig. 1. Phase stability as a function of volume fraction for hard-sphere colloids.

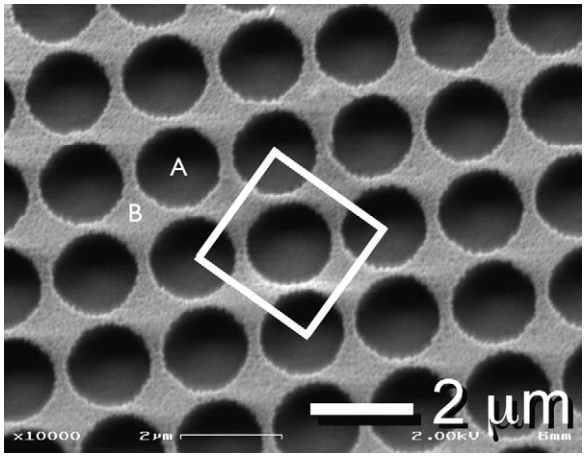

Fig. 2. PMMA template used for growth of face-centered cubic hard-sphere colloids in the (1 0 0) orientation.

structures have negligibly small energies. As a result, close-packed crystals grown in the laboratory by homogeneous nucleation from the liquid [25] or by sedimentation on a featureless plane surface consist of close-packed planes stacked randomly in the A, B, and C positions [see Fig. 3(D)]. Growth of single crystals requires special constraints, such as patterned templates [26]. Fig. 2 shows an example of a (1 0 0) template, microfabricated out of PMMA. Sedimentation onto this template occurs by growth of alternating layers aligned with the dimple positions (A) and the interstitial positions (B), which, ideally, produces a perfect single crystal [see Fig. 3(A)]. Occasionally, the crystals contains large stacking faults, as illustrated in Figs 3(B) and 3(C).

4. Observation of dislocations

4.1. Confocal microscopy

In a laser scanning confocal microscope [28], light is focused through a microscope objective where it excites fluorescence in the sample. The emitted light is retraced through the microscope and passed through a pinhole in the conjugate focal plane of the lit spot in the sample. This allows only light from that spot to pass; light from all other directions, for example from multiple scattering, is blocked. The light intensity is recorded by a detector and stored as the spot is scanned through the sample. The stored information can then be displayed directly as a three-dimensional image or can be processed into a reconstructed image, in which computer graphics is used to redraw the spheres. When the refractive index of the fluid is matched to that of the spheres, light can penetrate quite deeply into the sample with little scattering, so that tens of planes of a crystal can be imaged.

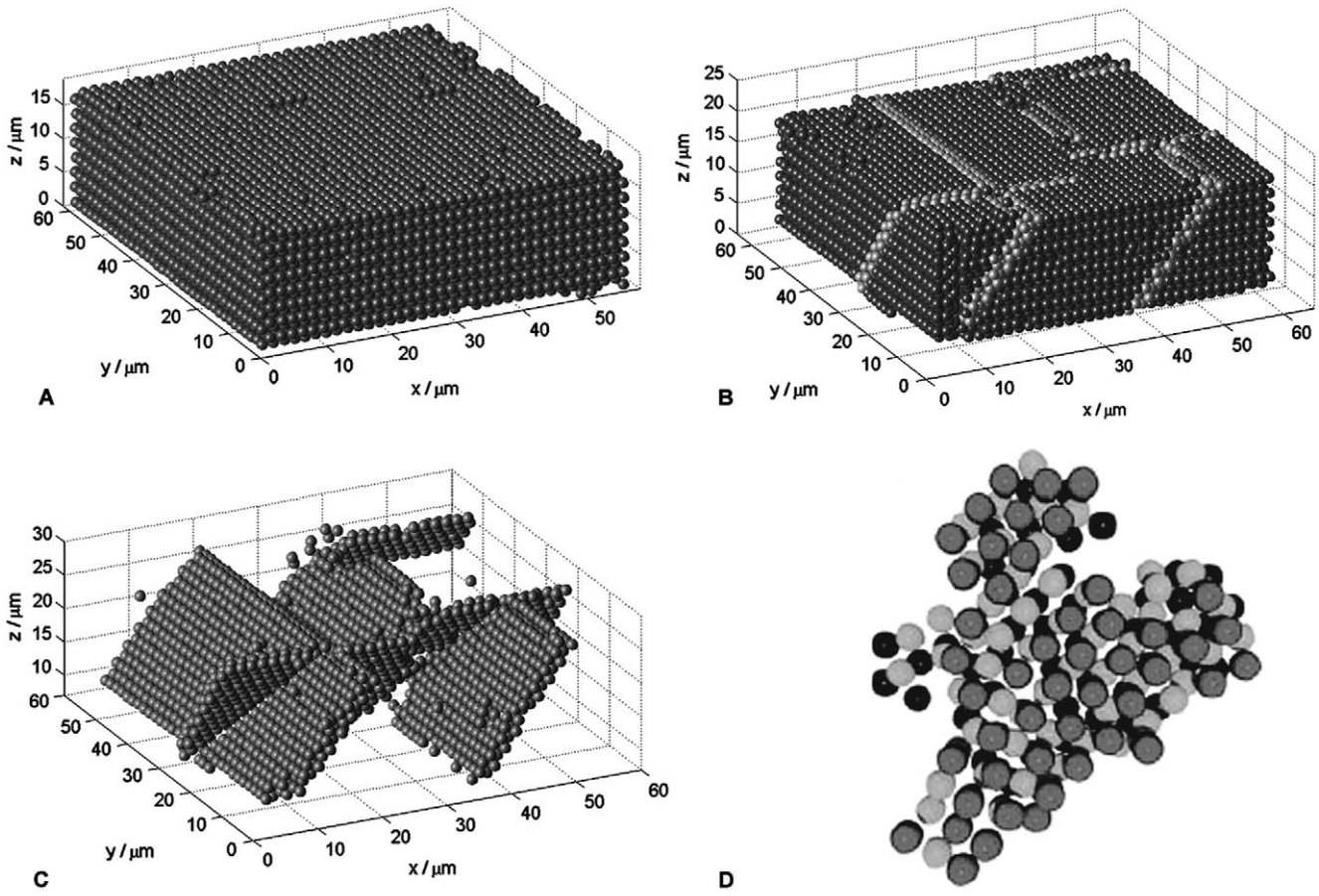

Fig. 3. Reconstructed confocal images of colloidal close-packed crystals. (A) Face-centered cubic crystal grown by sedimentation onto a (1 0 0) template. (B) Single crystal with stacking faults (between the gray spheres). (C) Just the gray spheres from part B: the stacking faults extend through the volume (from Schall et al. [27]). (D) Three consecutive, somewhat defective hexagonal close-packed layers in a small crystal nucleated from the liquid (from Gasser et al. [25]).

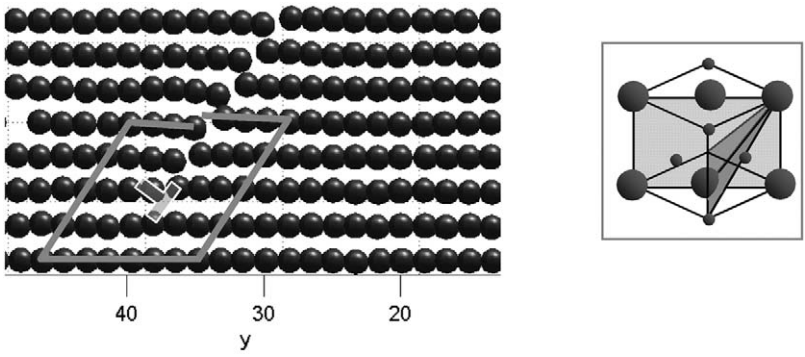

Fig. 4. Reconstructed image of a $(1\,\bar{1}\,0)$ plane in an fcc crystal (light shaded in the unit cell schematic on the right) intersected by a stacking fault on the (1 1 1) plane (dark shaded on the right), which ends in a Shockley dislocation with Burgers vector $1/6a[1\,1\,\bar{2}]$ (along the intersection of the two planes). After Schall et al. [27].

The lateral resolution (perpendicular to the optical axis) is about 200 nm, typical for optical microscopy. Because of limitations of the optics, the vertical resolution is only 500 nm. Application of image analysis techniques [29,30] improves the resolution for the location of the center of the particles by about an order of magnitude. A typical time to scan a stack of planes through a sample is a few seconds.

Dislocations can be identified in a 3D reconstructed image by the standard tracing of a Burgers circuit. Fig. 4 gives an example. The end of the stacking fault is a Shockley dislocation, the Burgers vector of which is $1/6a[1\,1\,\bar{2}]$, as identified by the closure failure of the circuit in the figure.

Dislocations can also be identified from the local coordination of the particles. Fig. 5 gives an example, taken during indentation of a crystal with a sewing needle, as an analog to nanoindentation of an atomic crystal. This leads to the nucleation of dislocations below the indenter, a full discussion of which is given in Section 8. The coordination of a particle is characterized by considering alignment of the vectors between it and its nearest neighbors. In the fcc structure, these form six aligned pairs; particles with this coordination are eliminated in Fig. 5. In the hcp structure, there are only three aligned pairs (in the basal plane). Particles with this coordination are the dark ones in Fig. 5. When they form two adjacent close-packed planes, they mark a stacking fault [also in Figs 3(C) and 3(D)]. Particles that fit neither coordination are the light ones in Fig. 5. When they line up at the edge of the stacking fault they demarcate the core of the partial dislocation line that has nucleated under the tip and has the stacking fault at its center.

4.2. Laser diffraction microscopy

In atomic crystals, dislocations were first imaged by the change in the diffraction conditions associated with their strain field. Because interatomic distances are on

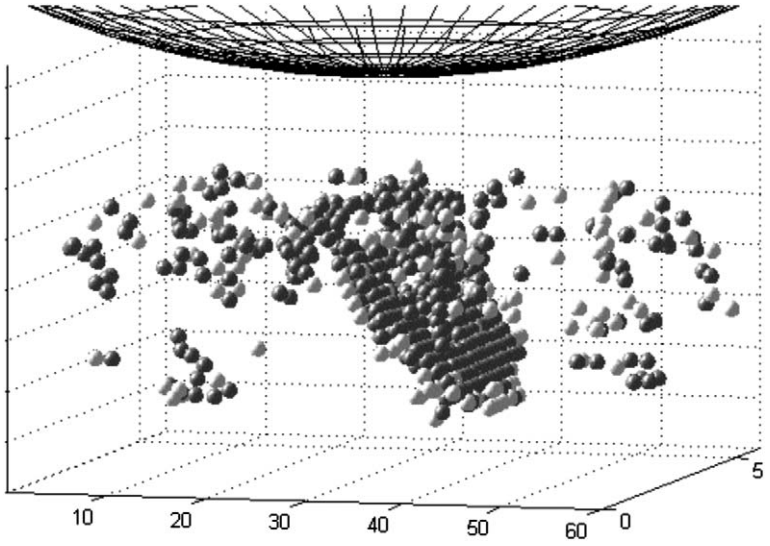

Fig. 5. Identification of a dislocation loop in a reconstructed image from a series taken during indentation of a (1 0 0) single crystal. Particles with fcc coordination have been removed. The dark particles have the hcp coordination, characteristic of the stacking fault. The light particles have neither of these coordinations. The light particles at the edge of the stacking fault trace out a nucleated dislocation loop. After Schall et al. [31].

the order of 0.1 nm, diffraction requires hard X-rays, as used in topography [32] or high-energy electrons, as in transmission electron microscopy [2]. The same can be done with colloidal crystals [27,33]. Since the interparticle distance is on the order of 1 μm, optical light can be used in a setup that is conceptually similar to that of an electron microscope. A quantitative difference, of course, is the relative curvature of the Ewald sphere: the ratio of the wavelength to the interparticle spacing is around unity for the colloids, whereas in the electron microscopy it is on the order of 0.01 (“flatter” Ewald sphere). A schematic diagram of the laser diffraction microscope (LDM) is shown in Fig. 6.

A He–Ne laser beam ($\lambda = 632$ nm), with wave vector $\mathbf{k}_0$, is aimed along the [1 0 0] direction of a single crystal grown on a (1 0 0) template with slightly mismatched (1.5%) lattice parameter. When the beam is exactly perpendicular to the template, a symmetric (1 0 0) diffraction pattern is observed. In Fig. 6, the sample is tilted slightly, so that the intensity of the (2 2 0) reflection, with wave vector $\mathbf{k}$, increases. When with the aid of a pair of lenses this reflection is projected onto a screen, a sharp image of the crystal is produced. Fig. 6(a) shows set of dark lines in the $(1\ \bar{1}\ 0)$ direction, perpendicular to the scattering vector $\mathbf{q} = \mathbf{k} - \mathbf{k}_0$, with $\mathbf{q} = \mathbf{g}_{220}$, the reciprocal lattice vector of the reflection. When the sample is tilted slightly, so that $\mathbf{q}$ deviates from $\mathbf{g}$ by the excitation vector $\mathbf{s} = \mathbf{q} - \mathbf{g}$, the contrast of the image inverts, which demonstrates that the lines in the images indeed result from lattice distortions. When the $(2\ \bar{2}\ 0)$ reflection is for imaging, these lines disappear and a new, perpendicular set appears [see Figs 9(c) and 9(d)]. Since lattice distortions are

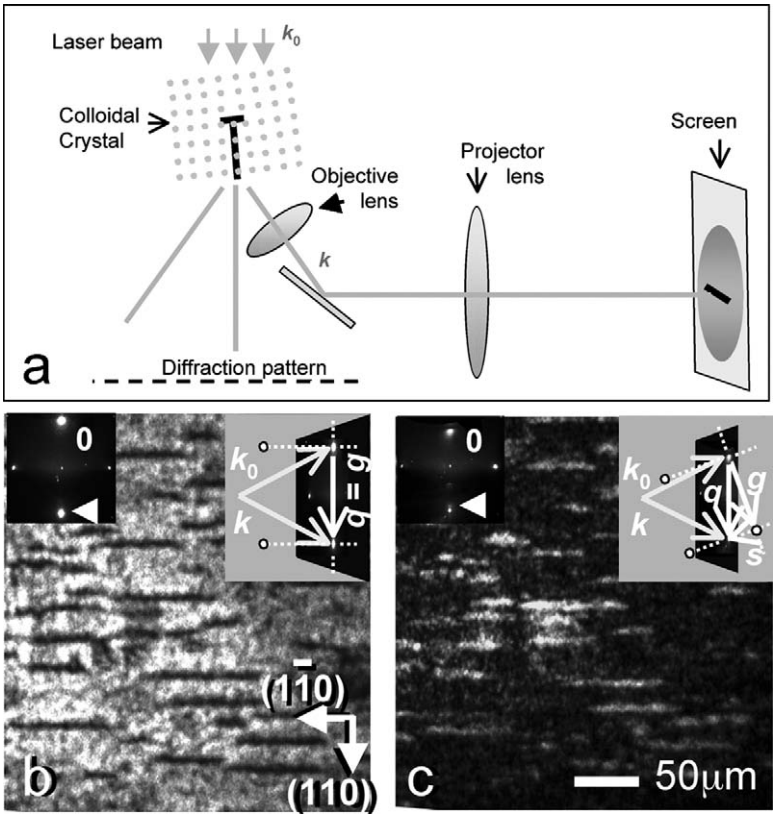

Fig. 6. Laser diffraction microscope (LDM) and images of dislocations in an fcc colloidal crystal. (a) Schematic diagram of the microscope. A laser beam with wave vector $\mathbf{k}_0$ passes through the crystal. A diffracted beam, with wave vector $\mathbf{k}$ is imaged on the screen with an objective and projector lens. (b and c) LDM images of dislocations. The upper left insets show the diffraction pattern (○: transmitted beam; arrow: the (2 2 0) diffraction spot used for imaging). These insets show the relation between the scattering vector $\mathbf{q} = \mathbf{k} - \mathbf{k}_0$ and the reciprocal lattice vector $\mathbf{g}$. In (c), the sample is tilted to produce an excitation error $\mathbf{s} = \mathbf{q} - \mathbf{g}$ that produces an inversion of the diffraction contrast. From Schall et al. [27].

visible only if they have a component in the direction of the scattering vector, the disappearance of the lines shows that the displacement fields are perpendicular to the lines and hence the lines represent edge dislocations. They are, in fact, misfit dislocations in the interface between the crystal and the template. These are discussed in more detail in Section 6.

When the particle positions in the strained lattice around a dislocation are known from confocal microscopy, one can test the contrast of the lines quantitatively, as illustrated by the example of Fig. 7. The amplitude of a point P in the image plane below a crystal is given by:

$$A = \sum_{\mathbf{x}_n} \exp(-2\pi i(\mathbf{k} - \mathbf{k}_0)\mathbf{x}_n), \tag{7}$$

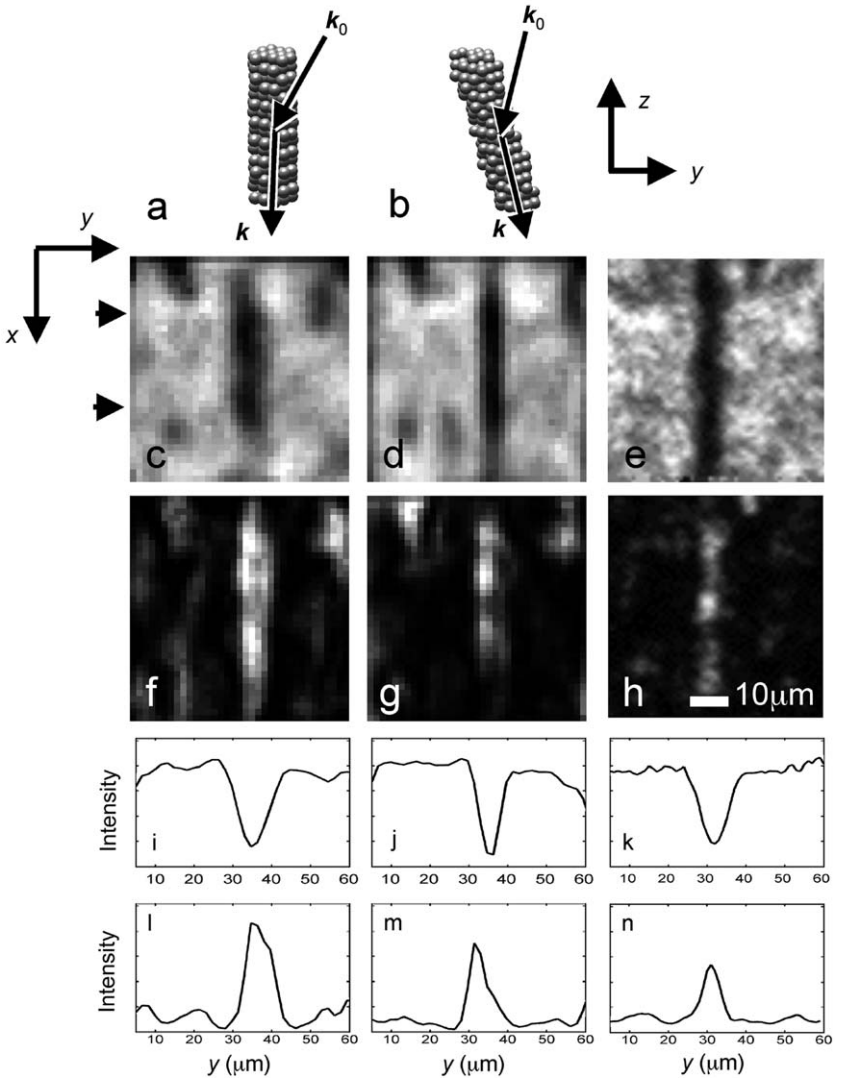

Fig. 7. Simulation of laser diffraction images of a dislocation. (a and b) Orientation of the incoming and scattered wave vectors with respect to the particle column, which contains a dislocation similar to that of Fig. 4 that runs along the *x*direction. (c and d) Images with zero excitation error calculated under conditions (a) and (b), respectively. (f and g) Images with excitation error $s = 0.12$ calculated under conditions (a) and (b), respectively. (e) Experimental image taken along a crystal orientation that maximizes the (2 2 0) diffracted intensity. (f) Experimental image taken for a crystal orientation slightly away from that of (e). (i–n) *x*-averaged intensity profiles of (c)–(h), respectively; for (c)–(e), the averaging is over the length between the arrows. From Schall and Spaepen [33].

where $\mathbf{x}_n$ are the positions of all particles in an imaging column parallel to $\mathbf{k}$, centered around P. The wave vector of the diffracted beam is given by:

$$\mathbf{k} = \mathbf{k}_0 + \mathbf{g} + \mathbf{s}, \tag{8}$$

where the reciprocal lattice vector is $\mathbf{g} = (1/d_0)(2\,2\,0)$ and the excitation error $\mathbf{s} = (1/d_0)(0\,0\,s)$, with d_0 the lattice constant. Fig. 7 shows two cases: one in which the diffracted beam is along the z-axis and the other in which it makes a 22.8° angle with this axis, in which case the incoming and diffracted beams make equal angles with the z-axis.

When the excitation error, $\mathbf{s}_z$, is small, the presence of the dislocation is revealed in the image as a dark line [Figs 7(c) and 7(d)]. These lines do not appear if $\mathbf{g} = (1/d_0)(\bar{2}\,2\,0)$ is used for the diffraction condition. This shows that the displacements of the dislocation strain field, which give rise to the contrast, are indeed perpendicular to the dislocation line, as expected for the Shockley partial dislocation of Fig. 4. The calculated images correspond closely to the experimental one [Fig. 7(e)], as illustrated also by the averaged intensity distributions of Figs 7(i)–7(k).

As the excitation increases, the contrast of the images inverts. Figs 7(f) and 7(g) show the images calculated for $s = 0.12$, which gives the strongest contrast inversion. Again, there is close correspondence with the experimental image of Fig. 7(h), as also illustrated by the averaged intensity distributions of Figs 7(l)–7(n).

The confocal and laser diffraction microscopies complement each other. The former has a resolution that allows a direct view of the particles, but its scope is limited in time and space (a $60\,\mu m \times 60\,\mu m \times 30\,\mu m$ volume in 2 s). The latter resolves only the strain field of the dislocations, but does so instantaneously for an area of $1\,mm \times 1\,mm$ and arbitrary thickness.

5. *Elasticity of dense colloidal systems*

Dense colloidal systems, such as liquids and glasses, are considered "soft" (or more accurately "compliant") matter: they have small but *nonzero* elastic moduli. Consider for simplicity first the equation of state, eq. (3), at low packing fraction, where it becomes that of an ideal gas:

$$\Pi V = k_B T, \tag{9}$$

where V is the volume per particle. Under isothermal conditions, the variations in osmotic pressure and volume are coupled by:

$$\Pi\, dV + V\, d\Pi = 0, \tag{10}$$

which gives for the bulk modulus:

$$K = \frac{d\Pi}{dV/V} = \Pi = \frac{k_B T}{V}. \tag{11}$$

Another way to look at this result is to consider the modulus as an energy density; in a hard-sphere colloidal system the only energy is k_BT (on the order of 10^{-21} J at room temperature) and the only volume is the volume per particle (on the order of 10^{-18} m^3 for densely packed, micrometer-size particles). As an aside: the moduli of ''hard'' (or more accurately ''stiff'') materials are on the order of 10^{11} Pa, which corresponds to an energy density of the cohesive energy (on the order of a few electron volts, or 10^{-19} J) per atomic volume (on the order of a few cubic angstroms, or 10^{-30} m^3).

For dense colloidal systems, such as crystals and glasses, however, in which the particle itself takes up most of the volume, a correction must be made. Simply put, the volume available that the particle can sample by Brownian motion, and that hence determines its entropy and free energy, is its *free volume*, i.e., the volume above that in its densest packed state. The packing fractions of colloidal crystals and glasses are usually a few percent below those of the closest packed crystal or glass (respectively 0.74 and 0.6366 for monodisperse systems). The appropriate volume to be used in the calculation of the energy density therefore is on the order of 10^{-20} m^3, which gives values for the bulk modulus on the order of 0.1–1 Pa. Accurate values for the modulus are obtained by using the compressibility factor Z, defined in eq. (3) [16,17].

Colloidal crystals and glasses are also ''solids'', in the sense that they have nonzero shear moduli. This can be seen by considering that the shear modulus, μ, is equal to the second derivative of the Helmholtz free energy density, F/V, with respect to the shear strain, γ:

$$\mu = \frac{1}{V}\frac{\partial^2 F}{\partial \gamma^2}. \tag{12}$$

In a hard-sphere system, according to eq. (6), this reduces to:

$$\mu = -\frac{T}{V}\frac{\partial^2 S}{\partial \gamma^2}. \tag{13}$$

Since in equilibrium, the entropy is at a maximum, its second derivative with respect to strain perturbations must be negative, which corresponds to stability with respect to shear and a positive shear modulus. A simple quantitative estimate of the entropy change in shear (i.e., at constant volume!) is difficult to make. Suffice it to say that, dimensionally, the energy density argument applies here as well and therefore a magnitude similar to that of the bulk modulus is expected.

Experiments bear this out. For example, the rheometric measurements of Mason and Weitz [34] of the frequency-dependent viscoelastic moduli of colloidal glasses give values on the order of 0.1–1 Pa for the storage moduli at low frequencies (static shear moduli). The methods discussed in this article also allow determination of the elastic moduli, albeit more indirectly. In Section 6 it is shown how a value of the shear modulus can be determined from the propagation of misfit dislocations. The calibration of such a measurement is based on the viscosity of the suspension fluid. It is also possible to determine the moduli from

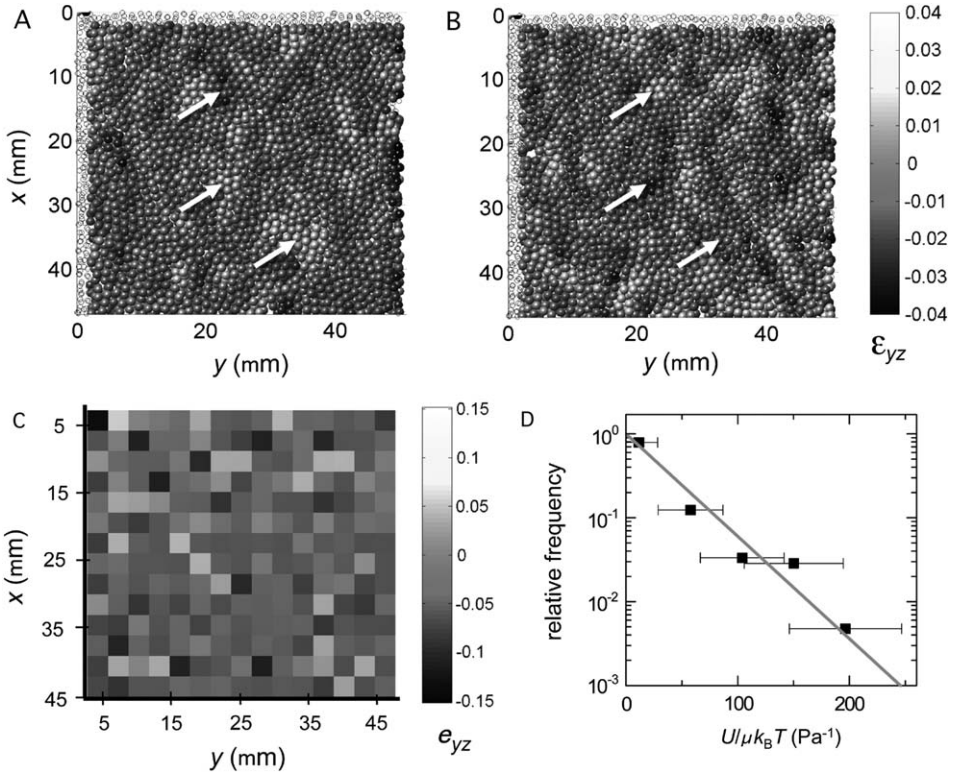

Fig. 8. Thermally induced strain fluctuations in a colloidal glass measured by confocal microscopy. (A and B) Distributions of the shear strain component ε_{yz} in a 3 μm thick x–y layer measured over two consecutive 2.5 min intervals. The arrows indicate regions in which the strain changed sign, demonstrating the presence of fluctuations. (C) Array of 3 μm × 3 μm squares, showing the incremental strain in 3 μm × 3 μm × 3 μm cells for the layer shown in (B). Each cell contains about nine particles. (D) Distribution of the normalized strain energies $E/\mu k_B T$, calculated from the strain values in (C). The squares at $23n$ Pa^{-1} ($n = 0, 1, 2, \ldots$) represent the relative frequency of the energy values in the range $[23n, 23(n+1)]$ Pa^{-1}. The error bars arise from the experimental uncertainty on the particle positions. The slope of the straight-line fit is −0.028 Pa. From Schall et al. [35].

the amplitude of thermal fluctuations (‘‘phonons’’) in a system in equilibrium [35], as described in the next paragraph. In that case, the calibration is from the thermal energy, $k_B T$.

Fig. 8 shows the local strain distribution in a slice through a colloidal glass as a function of time. The local time-dependent strain in a glass is calculated by following the particle trajectories and determining their relative displacements. First, the nearest neighbors of each particle are identified as those separated by a distance less than the first minimum in the pair distribution function. For each particle with center at $\mathbf{r}(t)$, the vectors to the nearest neighbors j at time t, $\mathbf{d}_j(t) = \mathbf{r}(t) - \mathbf{r}_j(t)$, are compared to their corresponding values at time $t-\Delta t$, $\mathbf{d}_j(t-\Delta t)$. The best affine deformation tensor, $\boldsymbol{\alpha}$, that transforms these nearest neighbor

vectors from the earlier time to t is determined by minimizing the mean square difference $\sum_j[\mathbf{d}_j(t-\Delta t)-\boldsymbol{\alpha}\mathbf{d}_j(t)]^2$ [36]. The symmetric part of $\boldsymbol{\alpha}$ is the strain tensor of the particle under consideration. Fig. 8 shows the distribution of the shear component ε_{yz}. The light and dark regions correspond to regions of positive and negative strains, respectively. Note that regions extend over several particles. Fluctuations are observed as the reversal of the sign of the shear in a region in consecutive measurements [Figs 8(A) and 8(B)]. That these are indeed thermal fluctuations can be checked by the relative frequency of their elastic energies. For this purpose, the strains in the slice of Fig. 8(B) were averaged (''coarse-grained'') over cells of $a = 3\,\mu\text{m}$ on a side. The contribution of this strain component to the elastic energy of each cell is, normalized by the shear modulus:

$$\frac{U}{\mu} = \frac{1}{2}(4\varepsilon_{yz}^2)a^3. \tag{14}$$

Fig. 8(D) shows that these energies obey an exponential distribution, as expected from thermal fluctuations:

$$f(U) = \exp\left(-\mu\frac{U}{\mu k_{\text{B}}T}\right). \tag{15}$$

The slope of the straight-line fit to the data corresponds to the shear modulus. That its value, $\mu = 0.028\,\text{Pa}$, is in line with other measurements and estimates confirms that indeed thermal fluctuations are being observed.

6. Misfit dislocations

6.1. Lattice mismatch

The lattice parameter of a colloidal hard-sphere crystal formed by sedimentation on a template depends on the size of the particles and the thickness of the crystal [27]. For example, silica particles with a diameter of $1.55\,\mu\text{m}$ and a size spread (''polydispersity'') of less than 3.5% form a perfect crystal on a (1 0 0) template with nearest neighbor distance $d_0 = 1.63\,\mu\text{m}$ (which corresponds to an fcc lattice parameter $a = 2.31\,\mu\text{m}$). The lattice spacing decreases slightly with increasing thickness due to the increasing pressure head.

When a crystal is grown on a template with a spacing different from the preferred lattice spacing, the mismatch is accommodated by a set of misfit dislocations. Fig. 9 shows the two perpendicular sets of edge dislocations, along the [1 1 0] and [1 $\bar{1}$ 0] directions, formed on a (1 0 0) template with a spacing that is $\varepsilon_0 = 1.5\%$ greater than that of the crystal. Confocal microscopy shows that they are Shockley partial dislocations like those of Fig. 4, with Burgers vectors $b = a/6\langle 1\,1\,2\rangle$. The in-plane component of these Burgers vectors, which accommodates the misfit, is $b\cos\alpha$, with $\alpha = 54.73^\circ$ and $\cos\alpha = 1/\sqrt{3}$.

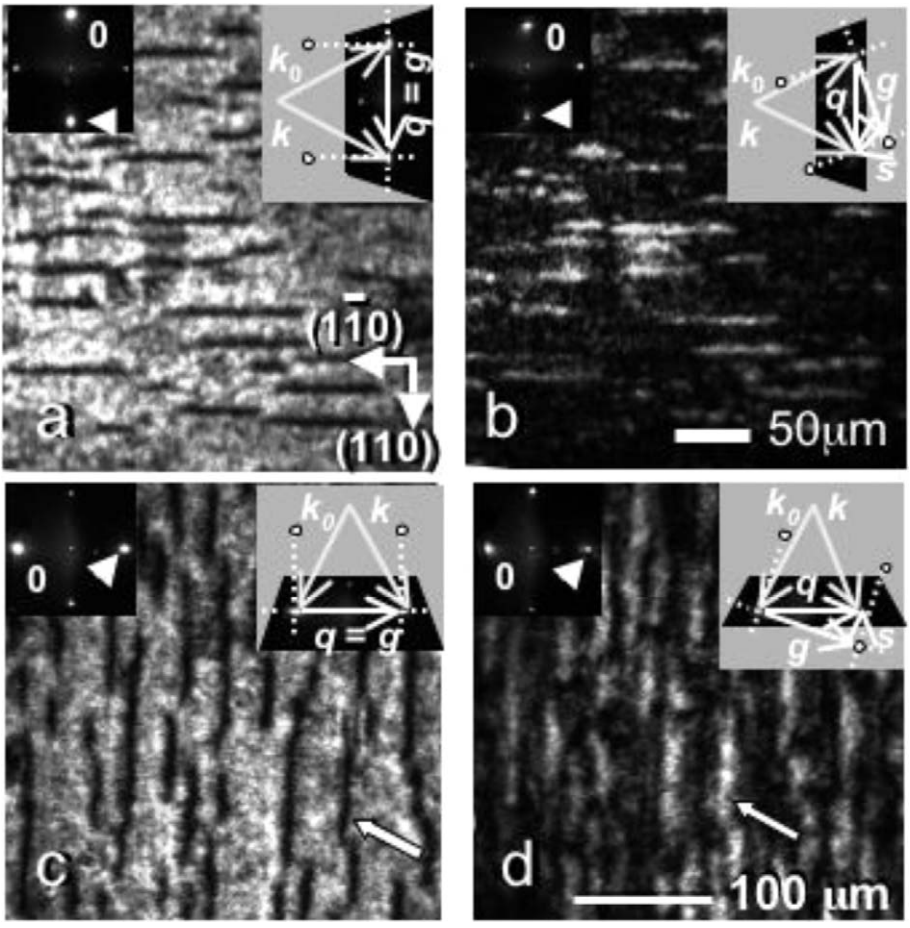

Fig. 9. Misfit dislocations at the interface of a colloidal crystal grown onto a (1 0 0) template with a lattice parameter that is 1.5% larger than that of the crystal. The images were made with the laser diffraction microscope (LDM), in bright (a and c) and dark (b and d) field contrasts. By changing the diffraction condition (insets), two perpendicular sets of dislocations are revealed. From Schall et al. [27].

6.2. Critical thickness

When the crystal grows on the template, no misfit dislocations are observed until it reaches a critical thickness $h_c = 22\,\mu m$. The physical basis of this critical thickness is well understood: only when sufficient strain energy is built up in the growing defect-free crystal does it become energetically favorable to trade off this energy against the line energy of the dislocations. The widely used one-dimensional, isotropic continuum models for epitaxial growth of thin films [37,38] can be applied to these colloidal crystals as well.

Consider a crystal of thickness h that contains a set of parallel misfit dislocations spaced Λ apart. The amount of strain relieved by these dislocations is

$$\varepsilon = \frac{b\ \cos\ \alpha}{\Lambda}. \tag{16}$$

The elastic energy per unit area in the partially strain-relieved crystal is

$$U_{\mathrm{el}} = \frac{1}{2} E \varepsilon_{\mathrm{el}}^2 h, \tag{17}$$

where $\varepsilon_{\mathrm{el}} = \varepsilon_0 - \varepsilon$ and E is Young's modulus. The energy per unit area associated with the dislocations is

$$U_{\mathrm{disl}} = \frac{1}{\Lambda} \frac{\mu b^2}{4\pi(1-\nu)} \ln \frac{R}{r_0}, \tag{18}$$

where μ is the shear modulus, ν the Poisson's ratio, R the range of the elastic field of the dislocation (taken to be the crystal thickness, h), and r_0 the effective core radius (taken to be $b/4$) [39]. When the total energy, $U_{\mathrm{el}} + U_{\mathrm{disl}}$ is minimized with respect to the dislocation spacing, this yields:

$$\frac{1}{\Lambda} = \frac{\varepsilon_0}{b\ \cos\ \alpha} - \frac{1}{4\pi(1-\nu)} \frac{\mu}{E} \frac{1}{\cos^2 \alpha} \frac{1}{h} \ln \frac{4h}{b}. \tag{19}$$

The critical thickness corresponds to an infinite spacing between the dislocations, or

$$h_{\mathrm{c}} = \frac{1}{4\pi(1-\nu)} \frac{\mu}{E} \frac{b}{\cos\ \alpha} \frac{1}{h} \ln \frac{4h_{\mathrm{c}}}{b}. \tag{20}$$

In an elastic isotropic continuum

$$\frac{E}{\mu} = 2(1+\nu). \tag{21}$$

These colloidal crystals are similar to their atomic counterparts, in that their Poisson ratio is close to 1/3 [24]. It can easily be checked that eq. (20) is satisfied by the experimentally observed value of $h_{\mathrm{c}} = 22\,\mu\mathrm{m}$.

6.3. Dislocation density

When the crystal exceeds its critical thickness, misfit dislocations nucleate and their density depends on the crystal thickness according to eq. (19). The crystal under consideration here was grown to a thickness of 30 μm, for which eq. (19), with the parameters used for the calculation of the critical thickness, yields a dislocation spacing $\Lambda = 152\,\mu\mathrm{m}$. This is considerably higher than the observed value $\Lambda = 53 \pm 10\,\mu\mathrm{m}$. Most likely, this discrepancy is the result of a decrease of the lattice parameter in the thicker crystal due to the increased pressure head. This increases the mismatch between the crystal and the template, and hence the strain

energy and the number of dislocations. An increase of 0.005 in the misfit strain suffices to explain the discrepancy.

6.4. Dislocation offset

As shown in the confocal image of Fig. 4, the core of the misfit dislocation is not located right at the interface, but a few particle layers ($\sim 3\,\mu m$) above it. This is the result of a balance between the attraction of the dislocation to the interface to relieve the strain in the crystal and the repulsion from an image dislocation that arises from the zero-displacement boundary condition at the interface.

Since the elastic energy, per unit area, in the crystal below the dislocations, located at a height z is

$$U_{el} = \frac{1}{2} E \varepsilon_0^2 z, \tag{22}$$

there is a force on each dislocation towards the interface equal to the vertical energy gradient:

$$F_{el} = \frac{1}{2} \Lambda E \varepsilon_0^2. \tag{23}$$

An image dislocation, located at $-z$ with the same in-plane Burgers vector, cancels the in-plane displacements at $z = 0$. The vertical repulsive force between the dislocations is

$$F_{rep} = \frac{\mu (b \cos \alpha)^2}{4\pi (1 - \nu) z}. \tag{24}$$

The balance of these forces gives the offset distance:

$$z_0 = \frac{(b \cos \alpha)^2}{2\pi (1 - \nu) \Lambda \varepsilon_0^2} \frac{\mu}{E}. \tag{25}$$

With the measured dislocation spacing, $\Lambda = 53\,\mu m$, and the parameters used in Section 6.2, this gives $z_0 = 2.1\,\mu m$, in good agreement with the observations.

6.5. Dislocation dynamics

Fig. 10 shows a sequence of laser microscopy images taken during the nucleation and growth of misfit dislocations. The starting time, t_0, for the observations was 14 h after the addition of a dose of particle to grow the crystal from its critical thickness of 22–30 μm. A number of dislocations are marked and their length as a function of time is plotted in Fig. 11(a). Note that dislocations 3 and 4 are not present at the beginning and hence their nucleation is observed.

The mechanism for the spreading of the dislocations is illustrated by the schematic of Fig. 11(b). Spreading is driven by the Peach–Koehler force on

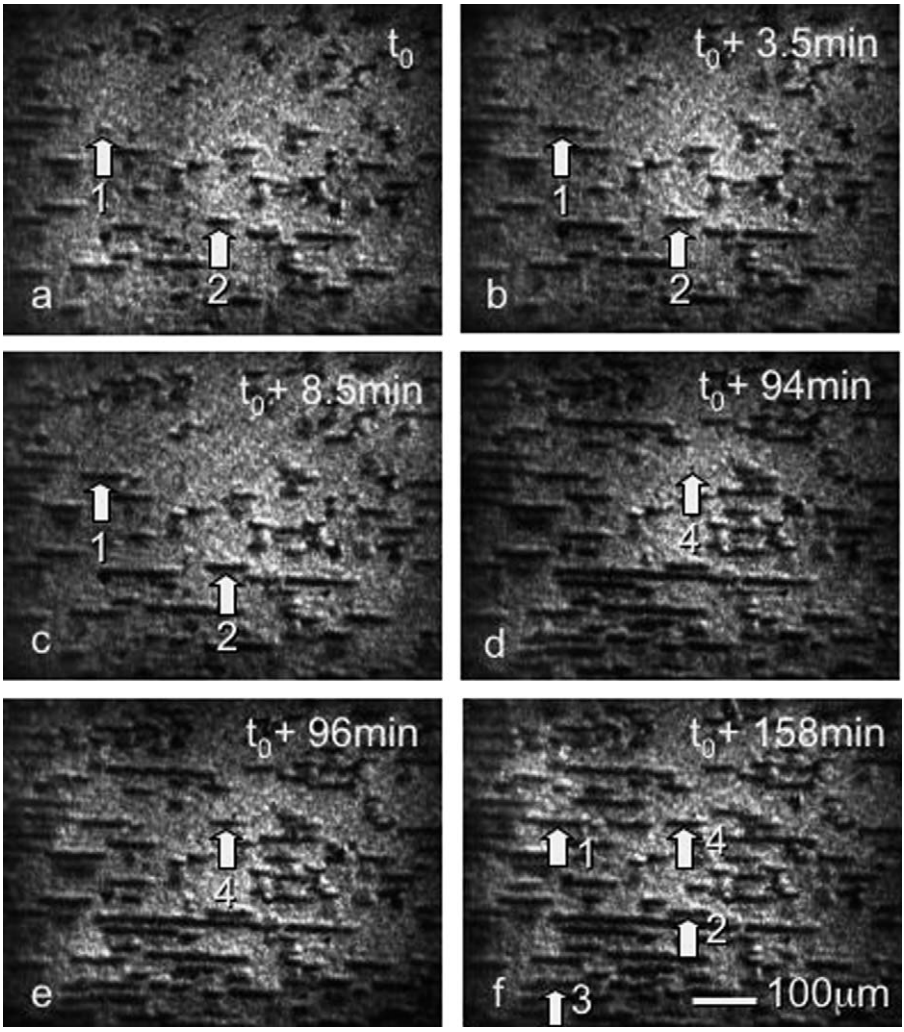

Fig. 10. The laser diffraction images taken at various times during the growth of misfit dislocations. The time t_0 corresponds to 14 h after the addition of a dose of particles to grow the crystal from 22 μm (critical thickness) to 30 μm. The numbers correspond to the dislocations whose length is plotted in Fig. 11(a). After Schall et al. [27].

the screw segment of the dislocation and is counteracted by the line tension of the dislocation being put down as well as the drag force on the screw segment.

The strained crystal is under a biaxial stress

$$\sigma = \frac{2\mu(1+\nu)}{(1-\nu)}\varepsilon_{\mathrm{el}}, \tag{26}$$

where $\varepsilon_{\mathrm{el}}$ is the elastic strain, given by $\varepsilon_0 - \varepsilon$, with ε equal to the strain relieved by the

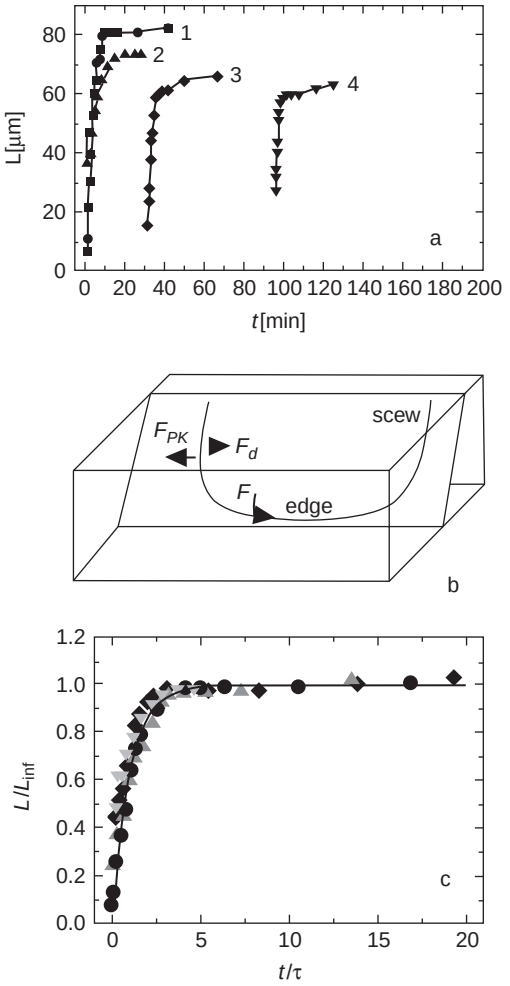

Fig. 11. (a) Length of four of the misfit dislocations as a function of time. (b) Schematic representation of the formation of the misfit dislocation at the interface. (c) Replotting of the data of (a) with respect to nucleation time and final length. The line is a fit to the prediction of the model, eq. (36), and the time axis has been rescaled with respect to the time constant of the model. From Schall et al. [27].

dislocations, as given by eq. (16). The Peach–Koehler force exerted by this stress on the screw segment of the dislocation of length h is then:

$$F_{\mathrm{PK}} = \frac{2\mu(1+\nu)}{(1-\nu)}\varepsilon_{\mathrm{el}} b \cos\alpha\, h. \tag{27}$$

The line tension has the classic form [39]

$$F_{\mathrm{l}} = \frac{\mu b^2}{4\pi(1-\nu)} \ln\frac{R}{r_0}. \tag{28}$$

The drag force is the result of the particles having to move through a medium with viscosity η, which makes it strictly *linear* with the dislocation velocity, v [14]:

$$F_{\mathrm{d}} = \gamma \frac{h}{\sin\,\alpha} v, \tag{29}$$

where the geometric factor arrives from the length of the dislocation and γ, the drag coefficient, is a geometrically scaled viscosity:

$$\gamma = \frac{\eta b^2}{4\pi r_0^2}. \tag{30}$$

The strain rate associated with the motion of the screw dislocations is given by the Orowan equation:

$$\frac{\mathrm{d}\varepsilon}{\mathrm{d}t} = \rho_{\mathrm{screw}} b\,\cos\,\alpha\, v, \tag{31}$$

where ρ_{screw} is the number of mobile screw dislocations per unit area of the film.

The velocity v is found from the force balance

$$F_{\mathrm{PF}} = F_{\mathrm{l}} + F_{\mathrm{d}}, \tag{32}$$

and inserted into eq. (31). This equation is integrated to give the time-dependent strain produced by the dislocations:

$$\varepsilon(t) = \varepsilon_{\mathrm{inf}}\left[1 - \exp\left(-\frac{t}{\tau}\right)\right], \tag{33}$$

where the asymptotic strain is

$$\varepsilon_{\mathrm{inf}} = \varepsilon_0 - \frac{1}{8\pi(1+\nu)} \frac{b}{h\,\cos\,\alpha} \ln\frac{R}{r_0}, \tag{34}$$

and the time constant is

$$\tau = \frac{\gamma(1-\nu)}{Eb^2\,\cos^2\alpha\,\sin\,\alpha\,\rho_{\mathrm{screw}}}. \tag{35}$$

Since the length, L, of edge dislocation deposited at the interface is proportional to the strain produced, its time dependence is the same as that of eq. (33), or

$$L(t) = L_{\mathrm{inf}}\left[1 - \exp\left(-\frac{t}{\tau}\right)\right], \tag{36}$$

where L_{inf} is the asymptotic length of the misfit dislocation.

In Fig. 11(c), the data of Fig. 11(a) are replotted to test the above result. By using a common origin and by normalizing the length to the asymptotic value, all the data can be collapsed onto a master curve. A fit of eq. (36) to this curve gives the time constant $\tau = 130 \pm 40$ s. This value can be used in eq. (35) to calculate the elastic modulus. The viscosity of the fluid is known [40], $\eta = 0.003$ Pa s, a typical value for simple fluids. The density of mobile screw dislocations was determined by counting the number of dislocations that was expanding, multiplying by two, and dividing

by the area of observation. This gave $\rho_{screw} = 3 \times 10^{-4}\,\mu m^{-2}$. With these values, eq. (35) yields $E = 0.3\,Pa$, consistent with other measurements of the stiffness of colloidal crystals.

Note that the critical thickness [eq. (20)] and the standoff distance [eq. (25)] depend on the *ratio* of two moduli, E/μ. The time constant for the spreading [eq. (35)], however, depends only on one modulus, which can be determined by knowledge of the viscosity of the fluid.

7. Nucleation of dislocations

7.1. Indentation experiment

Fig. 12 shows an experiment [31], analogous to nanoindentation of atomic crystals, in which an indenter is driven into a colloidal single crystal, grown on a (1 0 0) template, to observe the resulting dislocation dynamics by both confocal and laser diffraction microscopies. The indenter is simply a commercial sewing needle, which is produced with a hemispherical tip with a diameter of 40 μm. The ratio of the tip and particle radii is similar to that in nanoindentation experiments. The needle is attached to a piezoelectric drive and is moved at a rate of 3.4 μm/h.

The strain fields of the dislocations in Fig. 12 are revealed as dark images on a bright background in laser diffraction microscopy, as discussed in Section 4.2. Fig. 12(b) shows two fluctuations: they appear at 160 min and disappear at 220 min. Fig. 12(c) shows a dislocation loop that nucleates near the needle and eventually becomes detached from it [Fig. 12(d)]. The final configuration structure [Fig. 12(e)] is quite complex and needs to be analyzed on the particle scale.

Fig. 13 shows confocal images of the dislocations on the particle scale. As expected in a hard-sphere crystal, the defects that nucleate are stacking faults on {1 1 1} planes, each bounded by a Shockley partial dislocation. The fluctuations that lead up to the nucleation of the defect can be observed directly: the defect in Figs 13(b) and 13(e) disappears after about 5 min, and four more of these fluctuations are observed before the nucleation is successful and grows into a large dislocation loop [Figs 13(c and d) and 13(f and g)].

Fig. 13(i) shows the size of a subcritical ($r \sim 5\,\mu m$) and a supercritical ($r \sim 7\,\mu m$) dislocation loop. The critical radius for this loop is therefore $r_c \sim 6\,\mu m$.

7.2. Strain distribution

The strain in the crystal that results from the deformation can be calculated by a method [36] similar to that of Section 5, by minimizing the quantity $\sum_i (\mathbf{d}_i - \boldsymbol{\alpha}\mathbf{D}_i)^2$, where $\mathbf{d}_i$ are vectors between a particle and its 12 nearest neighbors, $\mathbf{D}_i$ are these vectors in the perfect fcc lattice, and $\boldsymbol{\alpha}$ is the optimal affine transformation tensor. The local strain tensor $\boldsymbol{\varepsilon}$ is the symmetric part of $\boldsymbol{\alpha}$. This tensor can be transformed

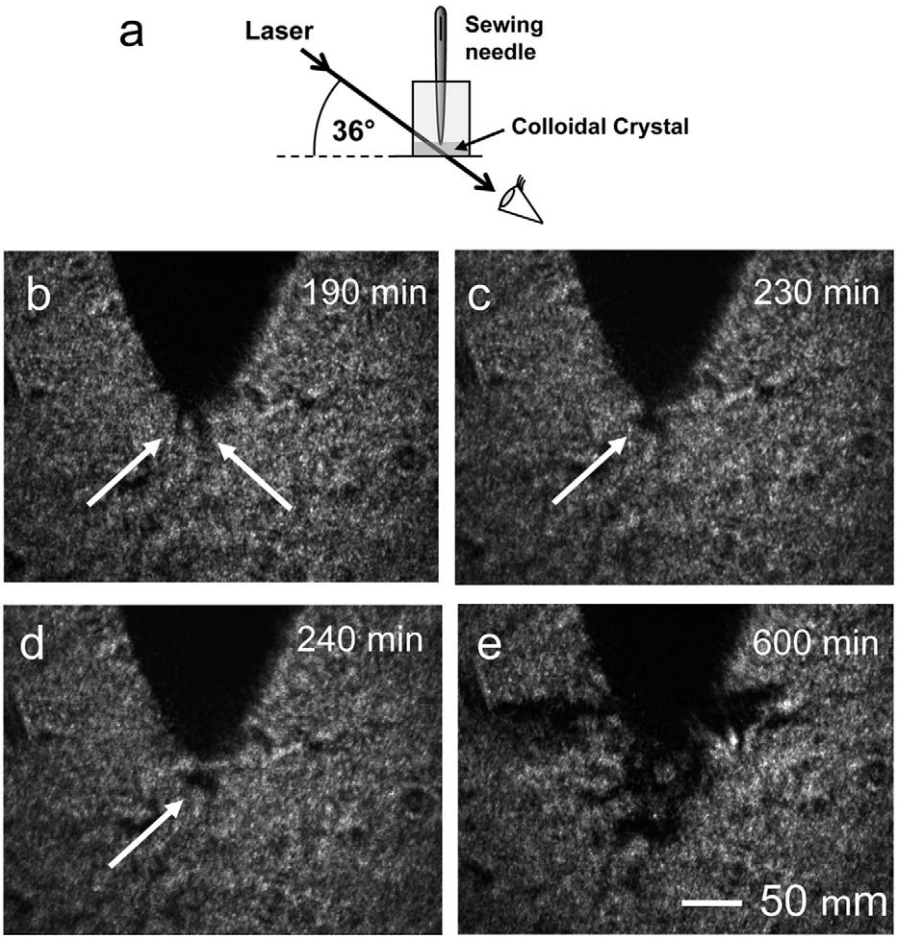

Fig. 12. Laser diffraction images of dislocations generated during indentation of a colloidal crystal with a sewing needle at 3.4 μm/h. (a) Schematic drawing of the indentation geometry. The line of sight makes a 36° angle with the template and corresponds to a ⟨1 1 1⟩ direction of the crystal. The dark regions indicated by arrows in (b) appeared at 160 min and persisted till 200 min. The arrows in (c) and (d) indicate a dislocation loop that became detached from the needle. (e) Final dislocation structure. From Schall et al. [31].

to a new coordinate system to give the resolved shear strains on a particular slip plane and along a particular direction.

Figs 14(a) and 14(b) show the resolved shear distribution during one of the subcritical fluctuations. The highest strain occurs 10 μm *below* the tip of the indenter. This value corresponds to about 0.8 times the contact radius of the needle at that stage, which is the location of maximum shear strain predicted by continuum theory [41,42]. A similar observation has been made in the indentation of a two-dimensional

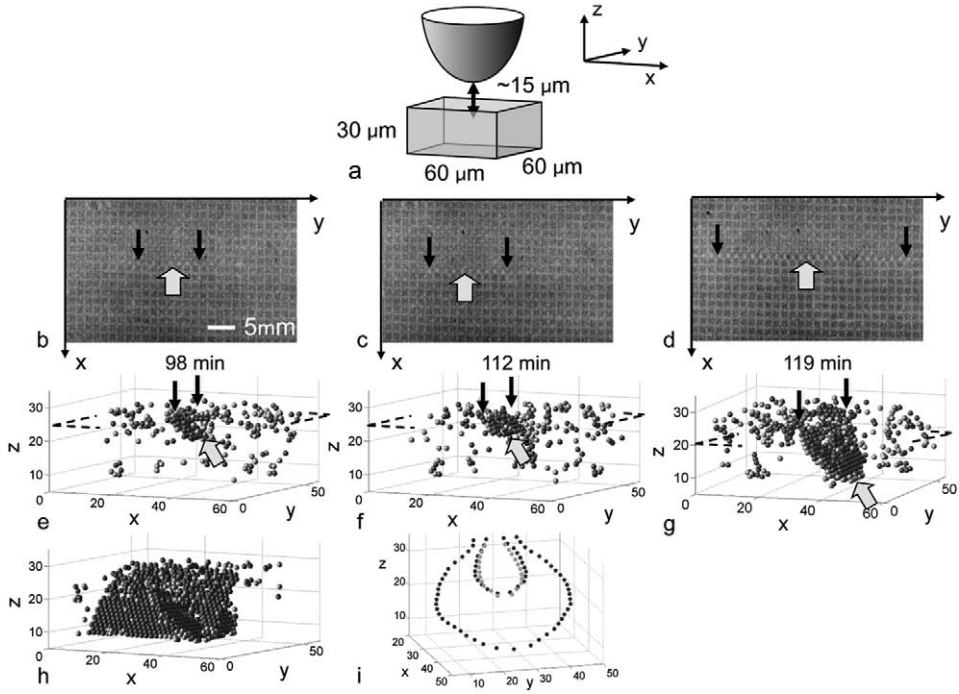

Fig. 13. Nucleation of dislocations in a colloidal crystal under a needle indenter, observed on the particle level by confocal microscopy. (a) Schematic diagram of the position of the needle with respect to the crystal imaged in (b)–(i). The x, y, and z-axes are, respectively, along the $[1\,\bar{1}\,0]$, $[1\,1\,0]$, and $[0\,0\,1]$ directions of the fcc lattice. (b–d) Confocal images of the defects, taken in a plane perpendicular to and 15 μm below the indenter. The defect indicated in (b) disappeared after a number of minutes. The defect indicated in (c) grew to that in (d). (e–g) Reconstructed images of the defects observed in (b)–(d). The particles are represented as in Fig. 5, which is the same as (g), with the position of the indenter marked as well. The dashed lines indicate the plane of the images. The arrows indicate the Shockley partials that bound a stacking fault on the $(1\,\bar{1}\,1)$ plane. (h) Reconstructed image of a second stacking fault, which nucleated on the intersecting $(\bar{1}\,\bar{1}\,1)$ plane at $t = 154$ min. (i) Traces of the dislocation lines that bound the stacking faults of (e)–(g). The lightest dots correspond to the subcritical defect in (e). The darker dots correspond to the two positions of the dislocation in (f) and (g) that nucleated successfully. These positions were determined from stacks of raw confocal images, such as those in (b)–(d). From Schall et al. [31].

bubble raft [43]. The shape of the region of highest strain in Fig. 14(a) has two lobes, and resembles that observed with the laser diffraction microscope in Fig. 12(b). Nucleation of the dislocations occurs entirely in this region.

After the dislocation nucleates, the strain distribution changes drastically. As Fig. 14(c) shows, the passage of the dislocation adds a negative strain, which makes nucleation of a second dislocation of this type unlikely until the indenter has produced more strain. On the intersecting glide plane, however, the resolved shear strain remains high [Fig. 14(d)], which can lead to the nucleation of a different dislocation loop, such as the one in Fig. 13(h).

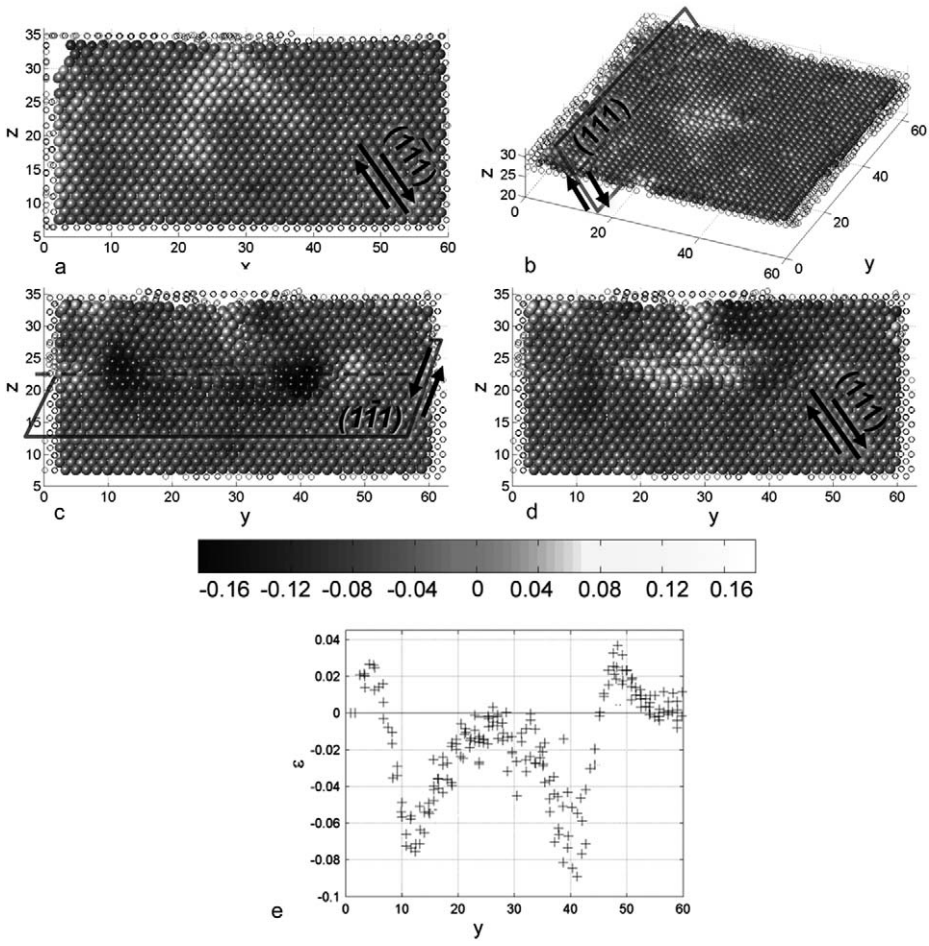

Fig. 14. Strain distribution during dislocation nucleation under an indenter. The grayscale indicates the level of the local resolved shear strain, $\gamma = 2\varepsilon_{ij}$, the sign of which is indicated by the arrows. In (a)–(c), the resolved shear stress is on the $(1\ \bar{1}\ 1)$ plane along the $[1\ \bar{1}\ \bar{2}]$ direction; in (d) it is on the $(1\ 1\ 1)$ plane in the $[1\ 1\ \bar{2}]$ direction. (a) and (b) correspond to a subcritical fluctuation at $t = 91$ min. (a) x–z plane (vertical), centered below the indenter tip at $y = 29\,\mu$m. (b) y–z plane (horizontal), located $10\,\mu$m below the needle at $z = 10\,\mu$m. (c) and (d) correspond to a just-nucleated dislocation loop at $t = 119$ min; both are y–z planes (vertical) at $x = 33\,\mu$m, which intersect the loop diametrically. (e) Plot of the resolved shear strain along the dashed line at $z = 23\,\mu$m in (c), for all particles within $1.6\,\mu$m of the line. From Schall et al. [31].

The distribution of the negative strain induced by the dislocation shown in Fig. 14(c) allows the dislocation line to be located with some precision. Fig. 14(e) is a plot of this strain along a line through the strain minima. The strain diverges on both sides of the dislocation and passes through zero at the dislocation core. The intersections are at $y = 7\,\mu$m and $y = 45\,\mu$m, exactly where the cores are located according to the confocal measurements of Fig. 13(i).

7.3. Nucleation kinetics

The energy required to create a dislocation shear loop of radius r is

$$U_{\text{loop}} = A\frac{\mu b^2 r}{2}\left[\ln\left(\frac{r}{b}\right) + B\right], \tag{37}$$

where $A = 5/4$ is a constant that accounts for the mixed edge-screw character of the loop and $B = 1.4$ [39]. The slip of the area inside the loop by the Burgers vector b allows the local shear stress τ that was present prior to nucleation to do work in the amount

$$W = \pi r^2 b\tau. \tag{38}$$

The total energy to be overcome in the nucleation process, $U = U_{\text{loop}} - W$, has a maximum, U_c, at the critical radius

$$r_c = \frac{A}{4\pi}\frac{1}{\gamma}b\left[\ln\left(\frac{r_c}{b}\right) + B + 1\right], \tag{39}$$

where the local elastic strain is introduced as $\gamma = \tau/\mu$. Insertion of experimental value of the critical radius, $r_c = 6\,\mu\text{m}$, in this equation gives $\gamma = 0.065$, in agreement with the average value of the high-strain region in Fig. 14(d). This corresponding value of the critical energy is

$$\frac{U_c}{\mu b^3} = \frac{A}{4}\left(\frac{r_c}{b}\right)\left[\ln\left(\frac{r_c}{b}\right) + B - 1\right], \tag{40}$$

which for the experimental critical radius gives a value of 4.5. The value of U_c can also be derived from the nucleation frequency

$$J = f_0 m \exp\left(-\frac{U_c}{k_B T}\right), \tag{41}$$

where m is the number of particles in the high-stress region where the nucleation can occur, and f_0 is the frequency with which the particles attempt the transformation. From the observed time between fluctuations the nucleation frequency is estimated at $J = 2\times10^{-3}\,\text{s}^{-1}$. The attempt frequency can be estimated from the time it takes a particle to move from the center to the edge of its free volume cage, estimated at $\delta = 0.08\,\mu\text{m}$. The time needed for a sphere of radius a to move diffusively over this distance through a viscous medium is [44]:

$$\tau = \frac{\pi\eta a\delta^2}{k_B T}, \tag{42}$$

where $\eta = 3\times10^{-3}\,\text{Pa}$ is the viscosity of the medium. This gives $\tau \sim 0.01\,\text{s}$ or $f_0 \sim 100\,\text{s}^{-1}$. The number of particles in the high-stress region is estimated, from Fig. 14(d), to be those in a cube of five particles on a side, or $m = 125$. This gives from eq. (41), $U_c = 16 k_B T$. Using the value for Young's modulus discussed in Section 6.5, $E = 0.3\,\text{Pa}$, and a Poisson ratio $\nu = 0.33$, the shear modulus can be estimated as $\mu = E/[2(1+\nu)] = 0.11\,\text{Pa}$, which gives $U_c/\mu b^3 = 0.7$. Given the

simplicity of both the nucleation theory and the estimation of the parameters, close agreement with the theory would fortuitous. The most important uncertainties that could account for factor of 6 discrepancy are the precise value of the shear modulus and the value of the attempt frequency.

8. Conclusions and prospects

That the classical theories and methods for observing and analyzing dislocations in atomic crystals can be carried over to a large extent to dislocations in colloidal crystals not only is intellectually satisfying, but also gives us confidence that these systems can be used to study complex processes in the deformation of crystals and glasses on a level that is otherwise hard to achieve. Indentation is such a complex process, and only the colloids allow direct observation of the attempts and eventual success of dislocation nucleation.

Other complex processes present themselves: the interaction of dislocations with each other and other crystal defects. Fig. 15 shows an example of twin boundary that can be grown on a specially designed template. Such boundaries are known to be very effective in the strengthening of materials [45], and colloidal crystals again offer an opportunity to observe the interaction between boundary and dislocation (pileup, decomposition, transmission, …) in a unique, direct fashion. Perhaps the most complex plastic deformation is that of amorphous materials. Here, the hard-sphere colloidal glasses allow direct observation of the local shear transformations that govern the plastic flow of these materials. That hard spheres make such

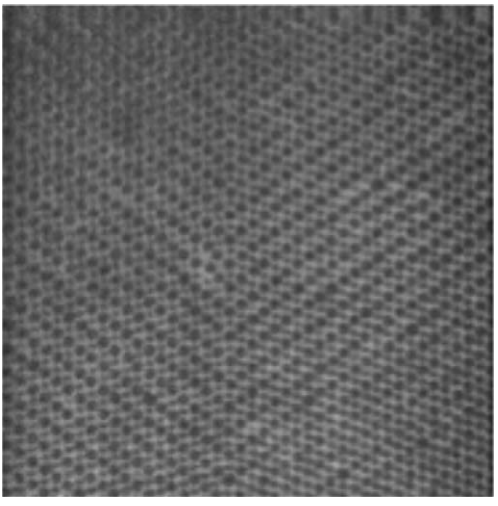

Fig. 15. Confocal microscopy image of a layer perpendicular to the Σ3 boundary between two twinned fcc crystals. The crystals were created by sedimentation onto a template composed of two {1 1 0} planes (C. Friedsam, D.A. Weitz, and F. Spaepen, unpublished data).

effective modeling systems is because many of the local rearrangements are governed by steric hindering, which is well modeled by the hard-sphere repulsion.

Acknowledgements

It is a pleasure to acknowledge the collaboration in this area with David Weitz, Itai Cohen, Ingo Ramsteiner, Claudia Friedsam, and Kate Jensen. The work has been supported by the Harvard Materials Research and Engineering Center of the National Science Foundation and by a Lynen Fellowship from the Alexander von Humboldt Stiftung. On this occasion, F.S. likes to thank John Hirth for many years of collegial friendship and for many enlightening discussions on the inexhaustible subject of dislocations.

References

[1] W.L. Bragg, J.F. Nye, Proc. R. Soc. A 190 (1947) 474.
[2] P.B. Hirsch, R.W. Horne, M.J. Whelan, Phil. Mag. 1 (1956) 677.
[3] G.I. Taylor, Proc. R. Soc. A 145 (1934) 660.
[4] E. Orowan, Z. Phys. 89 (1934) 634.
[5] M. Polanyi, Z. Phys. 89 (1934) 660.
[6] D.R. Nelson, B.I. Halperin, Phys. Rev. B 19 (1979) 2457.
[7] J.M. Kosterlitz, D.J. Thouless, J. Phys. C Solid State Phys. 6 (1973) 1181.
[8] D.R. Nelson, F. Spaepen, in: H. Ehrenreich, D. Turnbull (Eds.), Solid State Physics, vol. 42, Academic Press, New York, 1989, p. 1.
[9] C.A. Murray, D.H. Van Winkle, Phys. Rev. Lett. 58 (1987) 1200.
[10] K. Zahn, R. Lenke, G. Maret, Phys. Rev. Lett. 29 (1999) 2721.
[11] L. Radzihovsky, E. Frey, D.R. Nelson, Phys. Rev. E 63 (2001) 031503.
[12] D.R. Nelson, Defects & Geometry in Condensed Matter Physics, Cambridge University Press, Cambridge, 2002.
[13] P. Pieranski, Contemp. Phys. 24 (1983) 25.
[14] M. Jorand, F. Rothen, P. Pieranski, J. Phys. 46, C3 (1985) 245.
[15] P.N. Pusey, in: J.P. Hansen, D. Levesque, J. Zinn-Justin (Eds.), Liquids, Freezing and Glass Transition, Les Houches, Session LI, Elsevier, Amsterdam, 1991, p. 765.
[16] N.E. Carnahan, K.E. Starling, J. Chem. Phys. 51 (1969) 635.
[17] K.R. Hall, J. Chem. Phys. 57 (1972) 2252.
[18] W.G. Hoover, F.H. Ree, J. Chem. Phys. 49 (1968) 3609.
[19] P.N. Pusey, W. van Megen, Nature 320 (1986) 340.
[20] L.V. Woodcock, Ann. N.Y. Acad. Sci. 37 (1981) 274.
[21] J.L. Finney, Proc. R. Soc. A 319 (1970) 479.
[22] W. Kauzmann, Chem. Rev. 43 (1948) 219.
[23] M.E. Leunissen, C.G. Christova, A.P. Hynninen, C.P. Royall, A.I. Campbell, A. Imhof, M. Dijkstra, R. van Roij, A. van Blaaderen, Nature 437 (2005) 235.
[24] S. Pronk, D. Frenkel, J. Chem. Phys. 110 (1999) 4589.
[25] U. Gasser, E.R. Weeks, A. Schofield, P.N. Pusey, D.A. Weitz, Science 292 (2001) 258.
[26] A. van Blaaderen, R. Ruel, P. Wiltzius, Nature 385 (1997) 321.
[27] P. Schall, I. Cohen, D.A. Weitz, F. Spaepen, Science 305 (2004) 1944.
[28] V. Prasad, D. Semwogerere, E.R. Weeks, J. Phys. Condens. Matter 19 (2007) 113102.
[29] J.C. Crocker, D.G. Grier, J. Colloid Interface Sci. 179 (1996) 298.

[30] E.R. Weeks, J.C. Crocker, A.C. Levitt, A. Schofield, D.A. Weitz, Science 287 (2000) 627.
[31] P. Schall, I. Cohen, D.A. Weitz, F. Spaepen, Nature 440 (2006) 319.
[32] A.R. Lang, J. Appl. Phys. 29 (1958) 597.
[33] P. Schall, F. Spaepen, Int. J. Mater. Sci. (formerly Z. Metallk.) 97 (2006) 958.
[34] T.G. Mason, D.A. Weitz, Phys. Rev. Lett. 75 (1995) 2770.
[35] P. Schall, D.A. Weitz, F. Spaepen, Science 318 (2007) 1895.
[36] M.L. Falk, J.S. Langer, Phys. Rev. E 57 (1998) 7192.
[37] F.C. Frank, J.H. van der Merwe, Proc. R. Soc. A 198 (1949) 216.
[38] J.W. Matthews, A.E. Blakeslee, J. Cryst. Growth 27 (1974) 118.
[39] J.P. Hirth, J. Lothe, Theory of Dislocations, McGraw-Hill, New York, 1968.
[40] Y. Higashigaki, D.H. Christensen, C.H. Wang, J. Phys. Chem. 85 (1981) 2531.
[41] R.M. Davies, Proc. R. Soc. A 197 (1949) 416.
[42] K.L. Johnson, Contact Mechanics, Cambridge University Press, Cambridge, 1985.
[43] A. Gouldstone, K.J. Van Vliet, S. Suresh, Nature 411 (2001) 656.
[44] P.M. Chaikin, T.C. Lubensky, Principles of Condensed Matter Physics, Cambridge University Press, Cambridge, 1995.
[45] Y.H. Zhao, Y.T. Zhu, X.Z. Liao, Z. Horita, T.G. Langdon, Appl. Phys. Lett. 89 (2006) 121906.

Author Index

Abrosimov, N. 55
Aerts, E. 52
Ague, D.M. 209
Ahuja, R. 4, 6, 12, 14, 25
Albaret, T. 79
Alexander, H. 49–52, 54–55, 57, 71, 99, 213
Allem, R. 70
Allen, C.W. 164
Allen, F.M. 204
Alling, H.L. 208
Amelinckx, S. 51, 52, 53, 112, 173–175, 180, 184–186, 207, 210
Amiguet, E. 201, 205
Ando, J. 203
Anraku, T. 180, 193, 195
Antonangeli, D. 12–13
Aono, Y. 43
Arai, S. 65, 70, 72, 101
Ardell, A.J. 177, 180–181, 184, 198, 202
Argon, A.S. 56, 86
Arias, T.A. 3, 22, 25, 79–80
Arnaldsson, A. 85–90
Arsenlis, A. 3, 6, 11, 25, 37, 39
Asaoka, K. 65, 72
Ashbee, K.H.G. 180, 185, 197–198
Atkinson, B.K. 180, 210–212, 214
Audier, M. 116–119, 121–124, 129, 158–159
Avé Lallemant, H.G. 180, 183, 201, 204–205

Bacon, D.J. 135, 149, 173, 177
Badro, J. 12–13
Baeta, R.D. 180, 198
Bai, Q. 201
Baker, D.W. 179, 189
Balanetskyy, S. 118, 129, 154–155, 158, 167
Balogh, L. 217
Barber, D.J. 173–174, 178–181, 183, 186–192, 195, 199, 201
Barbier, J. 211
Barbieri, L. 58
Bartelt, M.C. 3, 6, 11, 37, 39
Barton, N. 199
Bastie, P. 184
Bauer, Ch.L. 185
Bazylinski, D.A. 195
Beauchamp, P. 78–90, 93, 99, 102
Beauchesne, S. 180, 197
Belak, J.F. 3, 8, 22–23, 36
Bell, I.A. 207–208
Benedict, L.X. 3, 22–23
Bengus, V.Z. 174, 189
Bennetto, J. 55
Beraha, L. 116–117, 119, 121–122, 124, 129, 158–159
Beraud, A. 12–13
Bergman, G. 114
Bernaerts, D. 184
Bertolotti, R.L. 192
Bessiere, M. 217
Bickmann, K. 161
Biermann, C. 206
Bilde-Sörensen, J.B. 180, 193, 195
Binetti, S. 74–76
Bishop, R.J. 111
Blacic, J.D. 180, 198–199, 204
Blakemore, R.P. 195
Blakeslee, A.E. 248
Blanchin, M.G. 180, 197
Blank, H. 185
Blech, I. 113
Blenkinsop, T.G. 200
Blum, A.E. 217–219
Blumenau, A.T. 103
Boas, W. 185
Boisson, M. 185
Boland, J.N. 180, 204–206
Bollmann, W. 174, 217
Bondarenko, V. 73
Borbély, A. 173, 217
Borcsik, M. 219
Borg, I. 209
Borisevich, A. 77
Boslough, M. 219
Bossiere, G. 208
Boudard, M. 116–119, 121–123, 129, 158–159
Boudier, F. 179, 208–209
Bowen, D. 22–23
Boyce, M.C. 179, 191
Bozhilov, K.N. 206

Bragg, W.L. 235
Brantley, S. 219
Brantley, S.L. 219
Brantley, W.A. 185
Bras, J. 180, 210–211
Brechet, Y. 3, 11, 184
Brenker, F.E. 206
Bresson, L. 146
Bretheau, T. 180, 191, 195
Brinck, A. 136
Brittain, J.O. 180, 197
Brochard, S. 81, 93, 95
Brodie, K.H. 206
Brostigen, G. 210
Brown, W.L. 207
Bruet, B.J.F. 179, 191
Brunjail, H. 184
Buatier, M. 206
Buerger, M. 209
Bulakh, A. 176–177
Bulatov, V.V. 3, 6, 8, 11, 22–23, 31, 37, 39, 55–56, 78, 86
Burgmann, R. 198–199, 208
Burkhardt, U. 161
Bursill, L.A. 193, 196
Buseck, P.R. 204, 206, 211
Bussod, G.Y. 215
Bystricky, M. 195, 205

Caffyn, J.E. 187
Cahn, J.W. 113
Cahn, R.W. 189
Cai, W. 3, 6, 11, 25, 37, 39, 55, 78
Caillard, D. 146
Campbell, A.I. 237
Canova, G.R. 3, 6, 11, 28, 37–39, 184
Carnahan, N.E. 236, 245
Carpenter, R. 177
Carr, M. 219
Carrez, P. 179, 192, 197, 214–218
Carstens, H. 203
Carter, C.B. 132, 180, 194, 196
Carter, N.L. 179, 183, 186, 205
Casey, W.H. 219
Caslavsky, J.L. 207
Castaing, J. 60, 62–63, 69, 180, 184, 191, 193, 195, 212
Černý, M. 91
Chadderton, L.T. 185
Chaikin, P.M. 258
Champier, G. 65
Champness, P.E. 174, 206
Chang, J. 55, 78
Chang, R. 192
Chao, E.C.T. 216
Chen, J. 67, 69, 201, 205
Chen, S. 205–206
Chen, T. 207
Chen, Y.H. 154
Chenal, B. 217
Chevy, J. 184
Chisholm, J.E. 206
Chisholm, M.F. 77, 164
Chopra, P.N. 201
Chow, P. 4, 12, 14, 25
Christensen, D.H. 253
Christensen, N.E. 4, 6, 14
Christie, J.M. 174, 177, 179–181, 184, 198, 202, 204, 208, 216
Christoffersen, R. 207
Christova, C.G. 237
Clark, B.R. 211, 213–214
Clark, R.H. 179, 183, 189
Clement, S.J. 195
Cockayne, D.J.H. 51–53
Coe, R.S. 205
Cohen, I. 239–242, 247–248, 251–252, 254–257
Cohen, M.L. 15
Condat, M. 3, 11
Conrad, H. 192
Cooper, M. 114
Copley, S.M. 180, 195
Cordier, P. 62, 64–66, 68, 90, 102, 177, 179–180, 192, 197, 199, 201, 204–205, 212, 214–218
Couderc, J.-J. 180, 210–211, 213–214
Couvy, H. 67, 69, 217
Cox, S.F. 180, 210
Crane, S.R. 219
Credar, D.A. 219
Crocker, J.C. 240
Csànyi, G. 79
Cullen, W.M. 193
Cumbest, R.J. 206
Cynn, H. 12

Das, E.S.P. 193
Dash, W.C. 50
Davies, R.M. 255
Davis, L.A. 186
Dawson, P.R. 183
Debat, P. 208
DeBoissieu, M. 116–118, 122–123
de Boissieu, M. 119, 121, 129, 158–159

De Bresser, J.H.P. 179, 188
Dederichs, P.H. 9
Deeb, C. 212
de Fouquet, J. 56
de Freitas, J.C. 187
Dekeyser, W. 173, 175
Delavignette, P. 52, 174
Dellby, N. 77
Demenet, J.L. 56, 60–62, 64–74, 83, 91–92, 94, 99, 101–102
Demny, J. 207
Denanot, M.F. 64–67
Deng, D. 162
Denoyer, F. 118
Desoyer, J.C. 73
Devincre, B. 3, 11, 217–218
Devine, J. 179, 216
De Vita, A. 79
de Wit, G. 66
Diaz de la Rubia, T. 3, 6, 11, 37, 39
Dijkstra, M. 237
Dimanov, A. 209
Ding, Y. 4, 12, 14, 25
Dixon, R.H. 179, 183, 189
Dodony, I. 211
Dorsch, W. 112
Douin, J. 179, 215
Doukan, N. 180, 204
Doukhan, J.C. 180, 199, 204–207
Doukhan, N. 180, 196, 204–205
Dresen, G. 179, 188, 198–199, 208–209
Drickamer, H.G. 59
Drozdov, N.A. 74
Drury, M.R. 200, 206
Duclos, R. 180, 196
Duesbery, M.S. 3, 22–23, 27, 58, 68, 70, 76, 82, 98, 104
Duffy, T.S. 184, 216
Duneau, M. 116–117, 119, 121–122, 124, 129, 158–159
Dunlap, W.J. 198
Dunning, J. 219
Durand-Charre, M. 118
Durham, W.B. 67, 173, 201
Durinck, J. 90, 214, 217
Duval, P. 184

Eckstein, R. 112
Edelin, G. 146
Edler, F. 115
Ellis, P.G. 211
Ellner, M. 161
Engel, M. 118, 129, 142–143, 155, 167
Engelke, C. 136
Eremenko, V.G. 55, 59–60
Eriksson, O. 4, 6, 12, 14
Escaig, B. 180, 195–196
Estrin, Y. 217
Etheridge, M.A. 180, 204, 207, 210
Evans, A.G. 185
Evans, B. 199
Eyidi, D. 67, 69

Fagot, M. 180, 210–211
Falk, M.L. 247, 254
Fan, S.-J. 207
Fang, X.D. 193
Farber, B.Ya. 56–57
Farber, D.L. 12–13
Faress, A. 213–214
Farver, J. 199
Fayard, M. 211
Feinberg, J. 209
Feng, D. 203
Ferré, D. 192, 197, 216–217
Feuerbacher, M. 111–112, 118, 128–131, 136, 143, 146–147, 149, 151, 154–155, 158–159, 161–162, 167
Figielski, T. 49, 54
Finney, J.L. 237
Fisher, E.S. 12–13, 26
Fisher, R.M. 174
Fitz Gerald, J.D. 199, 201, 209–210
Flandin, L. 184
Fleet, M.E. 210–211
Florando, J.N. 3, 6, 11, 37, 39
Foitzik, A. 212
Fontaine, G. 180, 186, 197
Frank, F.C. 112, 114–115, 185–186, 218, 248
Franz, G. 206
Franz, H. 199
Frauenheim, T. 103
Frederiksen, S.L. 3, 22, 25
Freiburg, C. 161
Frenkel, D. 237, 249
Frenkel, R.B. 195
Frey, E. 235
Friedman, L. 3, 11
Frisia-Bruni, S. 191
Fujino, K. 180, 201, 203, 215
Fujiwara, T. 83

Gaboriaud, R.J. 185
Gadaud, P. 56
Gale, J.D. 192
Gall, K. 95

Gallagher, C.J. 49
Gandais, M. 179, 208
Garem, H. 62, 64–65, 68, 73, 180, 196
Garnero, E.J. 183
Gasser, U. 238–239
Gavasci, A.T. 206
Ge, C.-Z. 203
Gehlen, P. 9
George, A. 49, 54, 65, 70–71
Gerretsen, J. 199, 201
Getting, I.C. 67
Ghoniem, N. 3, 11
Ghose, S. 206
Gibson, E.K. 195
Gillet, P. 191, 206
Gilman, J.J. 174, 185, 189
Gil Sevillano, J. 184
Gleason, G.C. 199
Glosli, J.N. 3, 22–23
Glover, G. 182
Godard, G. 206
Godet, J. 81, 93, 95
Goetze, C. 173, 180, 201
Golla-Schindler, U. 193
Gomez-Barreiro, J. 179, 188, 209
Gonzalez, G. 199
Gooch, D.J. 180, 192
Gooch, J.J. 193
Goodfellow, T.L. 187
Gordon, R.B. 186
Goringe, M.J. 187
Gottschalk, H. 57, 66
Gouldstone, A. 256
Govorkov, V.G. 192
Graf, J.L. 180, 210
Gramlich, V. 115
Gratias, D. 113, 146, 211
Grazhulis, V.A. 55
Green, H.W. 206
Gridneva, I.V. 59–60
Grier, D.G. 240
Griffin, L.J. 174–175
Griggs, D.T. 174, 179, 183, 189, 199
Grilhé, J. 93, 185
Grin, J. 161
Grosbras, P. 73
Groves, G.W. 179–180, 186, 192–193
Grushko, B. 118, 154, 161
Gu, H. 73
Gubicza, J. 217
Guéguen, Y. 173
Gumbsch, P. 15, 17
Guy, C. 219
Guymont, M. 211
Guyot, F. 180, 197

Haasen, P. 50–51, 53, 186, 212
Haessner, F. 182
Hall, K.R. 236, 245
Halperin, B.I. 235
Handin, J.W. 179, 190, 209
Hanmer, S.K. 208
Harvey, K.B. 173, 186
Hashimoto, S. 116, 158
Hasparyk, N.P. 219
Hatherly, M. 182
Hazzledine, P.M. 164
Heard, H.C. 179, 181, 183, 186, 189–191, 209
Hedges, J.M. 173
Heggen, M. 118, 129, 136, 143, 146, 149, 151, 154–155, 158–159, 161–162, 167
Heggie, M. 56
Heidelbach, F. 179–180, 195, 215
Heilbronner, R. 198, 200
Heindl, J. 112
Heinemann, S. 179, 215
Hellmann, R. 219
Hellmig, R.J. 217
Henkelman, G. 85
Hennig-Michaeli, Ch. 180, 193, 209, 211, 212
Hernandez, C. 5, 8
Hess, H.H. 200
Hesse, J. 186
Heuer, A.H. 174, 180, 184, 186, 192–196
Hidaka, Y. 180, 193, 195
Hier-Majumder, S. 205
Higashigaki, Y. 253
Higgs, D.V. 179, 190
Hill, M.J. 59, 69, 72
Hiraga, K. 116, 154, 158
Hiraga, T. 205–206
Hiratani, M. 3, 6, 11, 37, 39
Hirsch, P.B. 55–58, 132, 174, 177, 235, 241
Hirth, G. 198, 209
Hirth, J.P. 9, 32, 34, 111, 143–144, 173, 213, 217, 249, 252, 258
Hirthe, W.M. 180, 197
Ho, K. 79, 83
Hoagland, R. 9
Hobbs, B.E. 180, 199, 207, 210
Hobbs, L.W. 187

Hobgood, H.M. 102
Hockey, B.J. 180, 192
Hofmann, D. 112
Hohenberg, P. 4
Holdren, G.R. 219
Hollang, L. 30, 43
Holt, D.B. 49
Hommel, M. 30, 43
Hommes, G. 3, 6, 11, 37, 39
Honess, A.P. 174, 203
Hong, M.H. 102
Honnes, G. 3, 6, 11, 37, 39
Hoover, W.G. 35, 237
Horita, Z. 259
Horne, R.W. 174, 235, 241
Hornstra, J. 50–52, 77–81, 101, 180, 196
Howie, A. 132, 177
Hsiung, L.L. 3, 6, 11, 37, 39
Hüther, W. 180, 195
Huang, H. 3, 11
Huang, Y.-H. 207
Hudd, R.C. 161
Hull, D. 135, 149, 173, 177
Humphreys, F.J. 182
Hurm, M. 180, 195
Hwang, L. 180, 195–196
Hynninen, A.P. 237

Ichihara, M. 197
Imhof, A. 237
Ingrin, J. 180, 204–205
Ischia, G. 179, 216
Ismail-Beigi, S. 3, 22, 25
Ito, E. 215
Ito, K. 29
Iunin, Yu.L. 56–57
Izumi, S. 94–95

Jacob, D. 216
Jacobsen, K.W. 3, 22, 25, 83
Janjith, K. 198, 209
Janot, C. 113
Jansen, E. 180, 193
Janssen, M.M. 203
Jean, P. 65
Jenrich, U. 56
Ji, N. 217
Ji, S. 179, 208–209
Jiang, Z. 209
Joannopoulos, J.D. 79–80
Johansson, B. 4, 6, 12, 14
Johansson, S. 70
Johnson, E. 185
Johnson, K.L. 255
Johnston, W.G. 174, 185
Jones, R. 55–57, 103
Jónsson, H. 78, 83, 85–90
Joós, B. 58, 68, 70, 76, 82, 98, 104
Jorand, M. 235, 253
Jung, H. 180, 202
Jyobe, F. 104

Kamb, W.B. 199
Kamimura, Y. 79, 82
Kaminura, Y. 30
Kamiura, Y. 104
Kaneko, M. 116, 158
Kara, A. 213–214
Karato, S.I. 180, 201–203
Kasama, T. 193
Kasper, J.S. 114–115
Katahara, K.W. 12–13, 26
Katayama, I. 180, 202
Kato, T. 215
Katsura, T. 215
Kauzmann, W. 237
Kearney, C. 179, 191
Kedjar, B. 102
Keil, K. 215
Keith, R.E. 189
Keller, R.J. 186
Kelly, A. 179, 186
Kelly, W.B. 213–214
Kelly, W.C. 211
Kepler, J. 113
Keppler, H. 180, 202
Kieffer, S.W. 216
Kirby, S.H. 180, 196, 198, 201, 204–205
Kirchner, H.O.K. 30, 33, 83
Kirschvink, J.L. 195
Kitajima, K. 43
Kjekshus, A. 210
Klassen-Neklyudova, M.V. 192
Klein, H. 111–112, 116–119, 121–124, 129–131, 136, 147, 158–159, 167
Klepeis, J. 4, 6, 12
Klepeis, J.E. 4
Klingenberg, B. 180, 193
Knipe, R. 174
Kocks, U.F. 178, 184
Koelher, J.S. 66
Kohlstedt, D. 179, 208–209
Kohlstedt, D.L. 173, 179, 180, 199, 201–206, 208
Kohn, W. 4, 7

Koizumi, H. 33, 79, 82–84
Kolar, H.R. 57
Kollé, J.J. 180, 204
Koslovskaya, E.P. 192
Kosterlitz, J.M. 235
Kovacs, M.-P. 179, 208
Krause-Rehberg, R. 73
Krenn, C.R. 15
Krisch, M. 12–13
Krivanek, O.L. 77
Kronberg, M.L. 185, 192, 196
Kronenberg, A.K. 180, 199, 204, 207
Kruse, R. 209
Kubin, L.P. 3, 6, 11, 28, 37–39, 60, 62–63, 69, 208, 217–218
Kubo, A. 184, 216
Kullerud, G. 210
Kumar, S. 164
Kunze, K. 180, 193, 209
Kuo, C.-L. 207
Kuramoto, E. 29, 43
Kuroda, K. 70, 72, 101

Labernardiere, H. 208
Labusch, R. 55
Lagerlöf, O. 70
Laio, A. 179, 216
Lally, J.S. 174, 193, 196
Landa, A. 4, 6, 12
Lang, A.R. 174, 241
Langdon, T.G. 259
Langenhorst, F. 176, 179–180, 195, 215–216
Langer, J.S. 247, 254
Langmaack, E. 136
Lapusta, N. 198, 209
Lardeaux, J.M. 204, 206
Lasaga, A.C. 217–219
Latrous, K. 180, 204
Lavrent'ev, F.F. 189
Leach, A. 95
Lebedev, O.I. 103
Lebrun, J.L. 217
Le Donne, A. 74–76
Lee, B. 4
Lefevre, A. 207
Legris, A. 90, 217
Leibfried, G. 9
Leipner, H.S. 73
Lenke, R. 235
Leroux, H. 176
Leunissen, M.E. 237
Levade, C. 180, 210–211, 213–214
Levitt, A.C. 240
Lewis, M.H. 180, 196–197
Li, C. 81, 89
Li, G. 81, 89
Li, J. 55, 78–79, 83, 95
Li, L. 201, 205
Liao, K.C. 164
Liao, X.Z. 259
Liddell, N.A. 183, 200
Lin, P.J. 193, 196
Linker, M. 180, 198–200
Liu, M. 219
Lomer, T.R. 213
Lonardelli, I. 179, 199, 209, 214, 216
Long, N. 57
Lorimer, G.W. 174
Lothe, J. 34, 111, 143–144, 173, 213, 217, 249, 252, 258
Louchet, F. 54, 57
Lubensky, T.C. 258
Luo, W. 4, 12, 14, 25
Lupini, A.R. 77
Lyall, K.D. 180, 211–212

Mackay, A.L. 114
Mackwell, S.J. 179–180, 195, 199, 201–202, 204, 205, 215
MacLean, P.J. 211
Madon, M. 179, 191, 215
Madsen, B.M. 216
Maeda, K. 57, 104
Mainprice, D.H. 179, 199, 208–209, 215, 217
Manghnani, M.H. 12–13, 26
Mann, S. 195
Mao, H.-K. 4, 12, 14, 25, 179, 216
Marcinkowski, M.J. 193
Maret, G. 235
Marques, F.O. 204
Marshall, D.B. 209
Martin, R.M. 4, 6–7
Martinetto, P. 212
Martins, J.L. 4, 6–7
Martonak, R. 179, 216
Marty, B. 217
Marzegalli, A. 74–76
Mason, B. 215
Mason, T.G. 245
Matsuo, Y. 116, 154, 158
Matthews, J.W. 248
Matthies, S. 209
Maxwell, L.H. 180, 192

Mazot, P. 56
McClay, K.R. 180, 211–212
McCormick, J.W. 177, 180–181, 198
McKay, D.S. 195
McLaren, A.C. 173–174, 177, 180, 184, 198–199, 201, 204, 209
McLellan, A.G. 199
McNamara, A.K. 183–184, 216
McTigue, J.W. 191
Mecartney, M.L. 207
Mecking, H. 178
Mehl, L. 209
Mei S, S. 205
Meingast, R. 52
Meisheng, H. 197
Meisterernst, G. 158
Menard, D. 207
Meng, Q. 81, 89
Meng, Y. 184, 216
Mercier, J.-C.C. 183
Merkel, S. 184, 214, 216
Methfessel, M. 15, 17
Michael, D.J. 180, 192
Michel, J.P. 70
Michler, J. 58
Mikhnovich, V.V. 73
Milhet, X. 65, 67, 102
Mills, G. 83
Milman, Yu.V. 59–60
Min Zuo, Jin 177
Minari, F. 65
Ming, N.-B. 203
Minomura, S. 59
Miranda, C.R. 217
Mitchell, J.W. 173, 186
Mitchell, T.E. 180, 184, 186, 192–196
Miyagi, L. 184, 214, 216
Miyata, M. 83
Möller, H.J. 56
Molénat, G. 136
Momoi, H. 180, 201, 203
Montagnat, M. 184
Montagner, J.P. 200
Montardi, Y. 179, 208–209
Monteiro, P. 200, 219–220
Monteiro, P.J.M. 219
Mookherjee, A. 210
Moriarty, J.A. 3–9, 12, 15–18, 21–23, 26–31, 33, 36, 91
Morniroli, J.-P. 177, 216
Morris, J.W. 15
Morrison-Smith, D.J. 206
Moser, B. 58
Mrovec, M. 3, 22, 25, 31
Mügge, O. 209
Müller, P. 180, 195
Müller, St. G. 112
Müller, W.F. 174, 184, 205–206
Munoz, A. 193
Murfitt, M.F. 77
Murray, C.A. 235
Muto, J. 180, 198
Muto, S. 112

Nabarro, F.R.N. 214, 216
Nakazaki, H. 180, 201, 203
Natale, P. 210
Naumov, I. 4, 6, 12
Navrotsky, A. 219
Nazé, L. 180, 204
Needleman, A. 3, 11
Nelen, J. 215
Nellist, P.D. 77, 122
Nelson, D.R. 235
Nembach, E. 136
Neuhäuser, H. 136
Neumann, M. 180, 193
Newey, C.W.A. 180, 196
Nguyen-Manh, D. 3, 22, 25, 31
Nicholson, R.B. 132, 177
Nickel, E.H. 210
Nicolas, A. 178, 182, 186
Nielsen, K.C. 180, 204
Nikitenko, V.I. 56–57, 59–60
Nishiyama, N. 179, 216
Nord, G.L. 193, 196
Norris, R.J. 198
Nosé, S. 35
Nunes, R.W. 55
Nye, J.F. 235
Nyilas, K. 217

Occelli, F. 12–13
Oganov, A.R. 179, 216
Ohmura, T. 59–60, 62, 68
Olsen, T. 179, 208–209
Ono, S. 216
Oppelstrup, T. 3, 6, 11, 37, 39
Ord, A. 180, 198–200
Orlikowski, D. 12–13
Orowan, E. 173, 235
Ortiz, C. 179, 191
Osipyan, Y.A. 55

Otsuka, N. 180, 193, 195
Oueldennaoua, A. 70
Ourmazd, A. 56–57

Packeiser, G. 53
Pandey, K.C. 79
Pantea, C. 217
Paquet, J. 207
Parrinello, M. 179, 216
Parthasarathy, T.A. 5, 8
Pashley, D.W. 132, 177
Pask, J. 180, 195
Paterson, M.C. 199
Paterson, M.S. 180, 190, 199, 201–202, 211–212
Patrin, A.A. 74
Pauling, L. 114
Paxton, A.T. 15, 17
Payne, M.C. 79
Pedersen, A. 85–90
Pehl, J. 179, 199, 214, 216
Peierls, R.E. 125, 214, 216
Peng, J.L. 193
Penhoud, P. 212
Pennycook, S.J. 77, 122
Peter, K. 70
Peters, K. 161
Petrenko, V.F. 214
Pettifor, D.G. 3, 22, 25, 31
Phakey, P.P. 183, 198, 200, 206, 216
Philips, D.S. 193
Pichaud, B. 65
Pieranski, P. 235, 253
Pierce, T.G. 3, 6, 11, 37, 39
Pirouz, P. 56–57, 102, 164
Pistorius, J.A. 203
Pizzagalli, L. 78–95, 99, 102
Pizzini, S. 74–76
Pletka, B.J. 192–194
Pointikis, V. 3, 11
Poirier, J.-P. 146, 173, 178–180, 182, 186, 197, 215–216
Polanyi, M. 173, 235
Porter, J.R. 207
Portier, R. 211
Posfal, M. 211
Prakapenka, V. 179, 216
Prandtl, L. 173
Prasad, V. 238
Pratt, P.L. 179, 185–186, 192
Prior, D. 209
Prior, D.J. 198, 204, 206
Pronk, S. 237, 249
Prosky, J.L. 190
Pusey, P.N. 236–239
Putnis, A. 193

Quigley, J. 208, 219

Rabier, J. 49, 54, 60–76, 78–83, 91–92, 94, 99–102, 180, 191, 195–196, 216
Radcliffe, S.V. 174
Radford, K.C. 180, 192, 196
Radovitsky, R. 179, 191
Radzihovsky, L. 235
Raiteri, P. 179, 216
Raleigh, C.B. 180, 201, 204–205
Rao, S.I. 3, 5, 8, 22, 25, 31
Raterron, P. 201, 205
Ratschbacher, L. 183
Ray, I.L.F. 51–53
Ree, F.H. 237
Reeder, R.J. 183, 187, 189–190
Reksten, K. 189
Ren, Q. 82
Ren, Y. 209
Renault, P.O. 67, 69
Renne, P. 209
Reppich, B. 180, 195
Rexer, E. 173
Reynard, B. 206
Rhee, M. 3, 6, 11, 37, 39
Rice, J.R. 198, 209
Riecker, R.E. 206
Roberts, S.G. 58
Robinson, K. 114, 159
Rodriguez, A.D. 193
Rodriguez, C.O. 4, 6, 14
Rodriguez, M.C. 193
Rohl, A.L. 192
Romanek, C.S. 195
Ronchi, C. 185
Rooney, T.P. 206
Rose, G. 189
Rösner, H. 136
Ross, J.V. 180, 204
Rothen, F. 235, 253
Roundy, D. 15
Rowcliffe, D.J. 59, 69, 72
Roy, C. 185
Royall, C.P. 237
Ruban, A. 4, 6, 12
Rubie, D. 62
Rubie, D.C. 179–180, 202, 216
Rudd, R.E. 3–4, 8, 22–23, 36

Ruel, R. 238
Ruoff, A.L. 4, 6, 14
Rutter, E.H. 206
Rybacki, E.E. 179–180, 188, 193, 199, 209

Sacerdoti, M. 208
Saka, H. 65, 70, 72, 101
Salmon, B.C. 211
Samant, A.V. 102
Samanta, A. 95
Samson, S. 114–116
Samuels, J. 58
Sander, B. 183
Sander, W. 55
Sautter, V. 204
Sawbridge, P.T. 185
Saynisch, H.J. 213
Scandale, E. 179, 208
Scandolo, S. 217
Schafer, W. 180, 193
Schall, P. 111–112, 130–131, 146, 167, 239–243, 246–248, 251–252, 254–257
Schertl, H.-P. 216
Schäfer, S. 214
Schüller, E. 185
Schmid, E. 185
Schmid, S.M. 198, 200
Schoeck, G. 216
Schofield, A. 238–240
Schott, J. 219
Schubnikov, A. 199
Schwarz, K. 3, 11
Schweitz, J.Å. 70
Scott, E.R.D. 195, 215
Scott, G.R. 209
Scott, W.D. 192
Seeger, A. 23, 30, 43, 50–51
Seidentopf, H. 173
Seitz, F. 49
Sellars, C.M. 182
Semwogerere, D. 238
Sham, L. 4, 7
Sharp, T.G. 179, 204, 215–216
Shechtman, D. 113
Shen, G. 179, 216
Shimizu, I. 199
Shindo, D. 57
Shockley, W. 50, 54, 101
Shoemaker, E.M. 216
Shomglin, K. 200, 219–220
Shramchenko, N. 118
Shu, J. 4, 12, 14, 25
Sides, W.H. 77
Siemes, H. 180, 193, 195, 209, 211–212
Siems, R. 52
Simmons, J. 5, 8
Simpson, C. 206
Sinclair, J. 9
Sinitsyna, D. 197
Sintubin, M. 183
Skinner, B.J. 180, 210
Skrotzki, W. 186, 204–206, 212
Smallman, R.E. 111, 180, 197
Smith, B.K. 204
Smith, J.V. 207
Smith, P.J. 213
Söderlind, P. 3–9, 12, 14–18, 21–23, 26–31, 33, 36, 91
Soifer, L.M. 189
Soler, J.M. 81, 93
Soula, J.-C. 208
Spaepen, F. 239–243, 246–248, 251–252, 254–257
Speake, C.C. 213
Spence, J.C.H. 57, 177
Speziale, S. 183–184, 214, 216
Spiers, C.J. 179, 188
Stacy, W.T. 203
Stallard, R. 219
Stanton, R.L. 213
Starling, K.E. 236, 245
Startsev, V.I. 189
Steinhart, H. 214
Steurer, W. 115
Steuten, J.M. 180, 204
Stipp, M. 198, 200
Stofel, E. 192
Stöffler, D. 176, 215
Storey, C.D. 204
Streitz, F.H. 3, 8, 22–23, 36
Stretton, I. 179–180, 195, 215
Strunk, H.P. 112, 186
Stuenitz, H. 198, 200
Stünitz, H. 209–210
Sun, L. 3, 11
Sun, W. 154
Suresh, S. 256
Suzuki, K. 197
Suzuki, T. 29–30, 33, 59–60, 62, 68, 79, 82–84, 102
Sykes, E.C. 185
Szilagyi, Z.S. 77

Taherabadi, L. 207
Tailor, W.H. 161
Takeshita, T. 203

Takeuchi, S. 29, 100, 197
Talbot, J.L. 180, 204
Tamura, N. 114, 116
Tang, M. 3, 6, 11, 22–23, 28, 37–39, 217
Tanimoto, T. 200
Taylor, G.I. 173, 183, 235
Taylor, M.A. 116, 158
Texier, M. 179, 212, 216
Teyssier, C. 198
Thibault-Desseaux, J. 54
Thilly, L. 102
Tholen, A.R. 193
Thomas-Keprta, K.L. 195
Thomson, N. 186
Thouless, D.J. 235
Thurel, E. 179, 215–216
Tighe, N.J. 192
Tkachev, V.D. 74
Tokuoka, T. 102
Tomé, C.N. 184
Tome, C.T. 209
Tomioka, N. 215
Tommaseo, C.E. 214
Tommasi, A. 179, 215, 217
Tondellier, T. 62, 64–65, 68
Topor, L. 219
Toy, V.G. 198
Trebin, H.-R. 118, 129, 142–143, 155, 167
Trefilov, V.I. 59–60
Trepied, L. 199
Tressler, R.E. 180, 192
Trommsdorff, V. 190
Troullier, N. 4, 6–7
Trujillo, J.E. 207
Tullis, J. 179–180, 198–199, 207–210, 219
Tullis, T.E. 180, 199, 204–205
Turner, F.J. 179, 183, 189
Twiss, R.J. 219

Uchida, T. 179, 216
Ulbrich, M. 174, 184
Umeda, T. 65, 72
Umeno, Y. 91
Ungár, T. 173, 217
Urban, K. 111–112, 118, 130–131, 146–147, 167
Urusovskaya, A.A. 192

Vali, H. 195
van Blaaderen, A. 237–238
Van Cappellen, E. 177
Vanderbilt, D. 55
Van der Giessen, E. 3, 11
van der Merwe, J.H. 248
Vander Sande, J.B. 173, 180, 204
Vanderschaeve, G. 146, 213–214
Van Duysen, J.-C. 180, 204, 206
Van Goethem, L. 180, 210
Van Landuyt, J. 180, 210
van Megen, W. 237
van Roermund, H.L.M. 180, 204, 206
van Roij, R. 237
Van Tendeloo, G. 103, 112
Van Vliet, K.J. 256
Van Winkle, D.H. 235
Vauchez, A. 208
Veblen, D.R. 206
Vedam, K. 207
Veit, K. 192, 209
Velikanova, T.Y. 118, 154
Velikokhatnyi, O. 4, 6, 12
Venkitasubramanyan, C.S. 179, 189
Veyssière, P. 60, 62–63, 69, 180, 191, 193–196, 212
Vidal, J.-L. 208
Vincent, H. 116–118, 122–123, 158–159
Vitek, V. 3, 8, 18, 22–23, 25, 29, 31, 136
Vitos, L. 4, 6, 12
Voegelé, V. 179, 204, 215
Voinova, N.N. 192
Volterra, V. 173
von Mises, R. 178, 186
Voronin, G. 217

Wachtman, J.B. 180, 192
Walter, P. 212
Wang, C. 79, 83
Wang, C.H. 253
Wang, L. 67, 69
Wang, S. 102
Wang, Y. 67, 179, 216
Wang, Z. 73, 209
Wasmer, K. 58
Wasserbach, W. 41–42
Waugh, J.L.T. 114
Weber, E. 55
Weeks, E.R. 238–240
Wegner, M.W. 174
Weidner, D.J. 67
Weinberger, C. 3, 6, 11, 25, 37, 39
Weiss, J. 184
Weitz, D.A. 238–242, 245–248, 251–252, 254–257
Wenk, E. 209
Wenk, H.-R. 174, 176–177, 179, 181, 183–184, 187–191, 197, 199–201, 207–209, 214, 216, 219–220
Wentworth, S.J. 195

Wessel, K. 50, 71
Westrich, H.R. 219
Weygand, D. 3, 11
Whelan, M.J. 51, 132, 174, 177, 235, 241
White, J.C. 216
White, J.S. 215
Whitworth, R.W. 213–214
Wilkens, M. 217
Willaime, C. 179, 206, 208, 219
Willems, B. 103
Willey, H.G. 213
Williams, D.B. 132
Williamson, G.K. 180, 197
Wills, J.M. 4, 6–7, 12, 14
Wilson, C.J.L. 207–209
Wiltzius, P. 238
Winnacker, A. 112
Wintsch, R.P. 219
Wirth, R. 209
Withers, R.L. 193
Wittenberg, R. 161
Wohlenberg, T. 185
Woirgard, J. 56
Woodcock, L.V. 237
Woodward, C. 3, 5, 8, 22, 25, 31
Würthrich, C. 23

Xia, B. 209
Xiao, X. 209
Xie, Y. 209
Xu, G. 3, 11

Yacobi, B.G. 49
Yakimov, E. 55
Yamamoto, K. 70, 72, 101
Yamashita, Y. 57, 104
Yang, L.H. 3, 4–9, 15, 17–18, 21–23, 26–31, 33, 36, 81, 89, 91
Yasutomi, T. 102
Yip, S. 3, 8, 22–23, 31, 55–56, 78–79, 83, 86, 94–95
Yoder, H.S. 210
Yonenaga, I. 102
Yoo, C.-S. 12
Yund, R.A. 179, 199, 208–209, 217, 219
Yurechko, M. 118, 154

Zahn, K. 235
Zarudi, I. 70
Zbib, H. 3, 11
Zerda, T.W. 217
Zeuch, D.H. 173
Zhang, J. 206
Zhang, L.C. 70
Zhang, M. 102
Zhang, Z. 154
Zhao, Y.H. 259
Zhao, Z. 179, 191
Zheng, Y. 179, 208
Zhu, T. 95
Zhu, Y.T. 259
Zinserling, K. 199

Subject Index

ab initio 79, 80, 83
activation enthalpy 2, 5, 6, 22, 28, 29, 31–35, 37, 38, 40, 43, 44
Al_3Pd 116
albite 209
almandine 204
alumina 221
amphibole 207
anisotropy 178, 184, 200, 202, 220
anisotropy ratio 14
antiphase
– boundary 177, 192, 211
– domain 206
aragonite 179, 188, 192
atomistic 217
– calculations 79, 80, 93, 100, 101
– simulation 2, 5, 8, 10, 22, 24–27, 29, 31–35, 37, 44
augite 206
average structure 115, 116

banana pentagon 121–123, 125, 129, 134
basal-plane deformation 146
$BaTiO_3$ 111, 198
bcc screw dislocations at high pressure 27
Bergman cluster 114, 116
beryl 175
β-Al_3Mg_2 116
biogenic 188, 192
biotite 207, 208
bond reconstruction 55
Bragg contrast 130–132
– brittleness 189, 195, 210, 211
Brownian motion 236, 245
Burgers
– circuit 135, 138, 154
– vector 111, 112, 132, 135, 136, 139–141, 177
– vector length 136–138, 190
bytownite 209

calcite 175, 179, 181, 188, 189, 209, 219
carbon 185, 219
carbonate 179, 188, 219
cataclasis 177, 211
cement 221
ceramic 192, 193, 208
chain multiplicity fault 206, 207
chalcopyrite 180, 212
charge effects 186
clays 176
climb 100, 101, 145, 146, 164, 174, 177, 182, 183, 191, 201
– motion 145, 146, 164
– packing 114
clinoenstatite 206
clinopyroxene 206
closure failure 135, 155
cluster 114–118, 122–125, 136, 145, 154, 176
– substructure 113–117
coesite 179, 217
colloid 174, 236
– fluctuations 246
– modulus 244, 254
complementary climb systems 146
complex metallic alloy (CMA) 111–116
confining pressure 59–61, 64, 69, 103, 195–197, 210, 211, 238–240
confocal microscopy 238–240
continuous transition 129
convergent beam 178
core configuration 22, 23, 78, 82, 86, 91, 92, 97, 99, 104, 240
corundum 180, 193–195
crack tip 177, 201
creep 193, 196, 199, 201, 203, 206, 209, 211
– diffusion 206, 212
– power law 212
– rate 206
critical resolved shear stress (CRSS) 205, 213
critical thickness 248–250, 254
cross slip 65, 81, 100, 101, 184, 187, 192, 194, 197, 205, 207, 213, 215
crystal
– close-packed 238
– colloidal 237
– cubic 197, 211

– face-centered cubic (fcc) 51, 177, 239
– hexagonal 199
– orthorhombic 189, 198, 202, 205
– rhombohedral 188, 189
– structure 174
– symmetry 178, 189
– tetragonal 198
– trigonal 189, 193, 199
cut-and-projection formalism 121

dangling bond 55, 56, 79, 80, 82, 83, 87, 104, 105
dark-field 178, 181, 194, 208, 210, 212
Dauphiné twinning 200, 201
deformation band 187, 213
diagenesis 183
diamond 185
– anvil cell 185, 215
diffraction 240–244
– contrast 178, 188, 191, 199
diffusion 196, 201, 203
diopside 206
dislocation
– character 111
– charge 186, 188, 214
– climb 182, 191, 193, 203, 204, 210
– contrast 218
– core 50, 54–57, 71, 74, 79, 82, 83, 86, 91, 93, 94, 96–102, 111, 112, 130, 134, 140, 193, 217, 219, 249, 250, 257
– core energy 9, 22–28, 249
– core structure 9, 23, 25, 186
– creep 201, 202, 204, 206, 207, 209
– decoration 174, 185, 187
– density 176, 177, 184, 189, 202, 204, 218–220, 234, 249, 253
– dipole 193–195, 213
– dissociation 181, 193, 197, 201, 203, 216
– dynamics (DD) 2, 3, 5, 6, 10, 11, 22, 28, 34, 36–44, 250
– glide 178, 192, 193, 196, 206, 212
– loop 191, 193, 194, 201, 202, 211, 214
– misfit 142, 247–251
– mobility 56, 58, 66, 83, 89, 105, 201, 214, 253
– motion 125, 146, 164, 250
– nucleation 50, 60, 64, 94, 97, 98, 101, 104, 258
– tangles 182, 187, 188, 192
– velocity 2, 28, 35, 37–39, 41, 44, 193, 250
60° dislocations 60, 77, 83, 91, 95, 103
dissociated dislocation 54, 57, 63, 70, 71, 72, 77, 78, 83, 94, 97–105, 194, 210, 240
dissolution 175, 219, 220
dodecahedron 114–116
dolomite 176, 179, 181, 188, 190
domain 177

earthquake 199
edge dislocation 111, 131, 132, 140, 144, 182, 186, 205
effective shear modulus 14
eglogite 204, 206
elastic
– moduli 2–4, 6, 8, 12–14, 26, 27, 143, 244
– strain energy 111, 136, 147, 151, 247, 257
electronic-structure methods 2, 4, 6, 16
elementary kink 79
end-on orientation 111, 131, 132, 143, 163
enthalpy 219
enstatite 205, 206
epitaxy 238, 248
ε_6-Al-Pd-Mn, 116, 117, 118, 119
ε_{16}-Al-Pd-Mn 119
ε_{28}-Al-Pd-Mn 116, 119
ε-phase 116
etch channel 175, 204
etch-pit 175, 185–188, 196
exsolution 196, 206, 207, 209
extraterrestrial 176, 185

facies 206
feldspar 179, 208, 219
– alkali 179, 208, 209
– plagioclase 179, 208–210, 220
– potassium 209
– structure 209
ferroelectric 198
Fibonacci 142
– number 138, 142, 156, 166, 167
– recursion 167
– sequence 156, 167, 168
fivefold rotational axes 113, 114
flow law 182, 220
flow stress 40, 42, 44, 187, 198, 214
fluorite 185, 186
forsterite 216
fractional site occupation 115
Frank's rule 151
Friauf polyhedron 114, 115
fringe contrast 132
fringe-contrast analysis 129
fugacity 200, 201, 203, 206

gadolinium gallium garnet 204
galena 180, 213
gamma surface 136

garnet 204, 216
generalized stacking fault 1, 8, 12–21, 23–38, 40–44
giant unit cell 113
glaucophane 207
glide 145, 162, 164
– core 81–84, 93, 98, 102
– cylinder 145
– motion 145, 146, 250
– set 51–55, 58, 66, 70, 72, 73, 77, 78, 82, 98, 100, 101, 103
– step 145
gneiss 220
golden mean 115, 136, 167
grain
– boundary 176, 184, 217
– growth 184, 185
– sliding 177, 184, 203, 206, 210
– structure 183
granite 209, 220
Green's function boundary conditions (GFBC) 5, 8–10, 23–37, 44
grossular 204

halfplane 111
halides 179, 185
halite 174, 175, 179, 184, 185, 187
hard spheres 236–238, 245, 259
hardening 182, 187, 221
hematite 180, 195
hexagon 118, 119
– column 121, 122
– lattice 122, 123, 128, 145
– plane 119, 123, 129, 140, 142
– row 118, 129, 140, 159
– tiles 118
– tiling 119, 123, 129, 135
high-angle annular dark-field (HAADF) 122, 126, 160, 162
high pressure 2, 12, 174, 185, 198, 204, 215, 217
– experiments 199
– medium 187
– minerals 185
– phases 179
high resolution 176, 195, 203, 213
hollow dislocation 112
homologous temperature 197
hornblende 205, 207
high-resolution (transmission) electron microscopy (HREM, HRTEM) 67, 78, 102, 104, 112, 118, 119, 122, 126, 163, 176, 203, 205, 213
hydrogen 86, 96, 206
hydrolytic weakening 202
hydrostatic pressure 59, 60, 63, 64, 77, 91
hyperspace 142, 143
hypersthene 205

ice 185, 220
icosahedral 113–115
– cage 115
– cluster 113, 115
– coordination 113, 115
– group 114
– symmetric 114
icosahedron 114, 116
icosidodecahedron 114, 116, 117
ideal shear strength 2, 4, 6, 12, 15–18
igneous 177, 209, 212
ilmenite 180, 195
indentation 241, 254–258
inner cutoff radii 111, 249
in situ 185, 192, 216
– heating 200
– tensile test 145
interatomic potentials 2, 5, 7–8, 12, 44
interface strain 153, 247
intergrowths 195
intermetallic phase 112
ion-milling 175
ionic crystals 185, 214
irradiation 181, 186
irrational 115, 136, 153, 167
Ishida fringes 178

jog 186
– super 213

kink 125, 186, 199, 214
– band 213
– migration 57, 88–90, 102
– pair 56–58, 86, 89–91, 99
– pair formation energy 2, 5, 26–28, 31, 33, 37, 44
kinking 177, 187
kyanite 208

labradorite 209
large angle convergent beam electron diffraction (LACBD) 178, 216
large lattice parameters 111–113, 142
lattice fringe 203
Laue conditions 132
length scale 3–5, 11, 21, 111, 136
limestone 189

line direction 28, 35, 121, 125, 130, 132, 149, 152, 159, 162
lithium fluoride 185, 186
local order 113, 122
local transformation 164, 165, 167
loop 143–146

Mackay 114, 116, 118, 122
– cluster 114, 116
magnesiowüstite 179, 195, 196, 215
magnesium aluminate 197
magnetite 180, 195, 197
magnetosome 197
majorite 179, 204, 215, 216
mantle 202, 204, 205, 215–217, 221
marble 184, 189, 190
marcasite 211
metadislocation 111, 130–135
– core 133, 137, 146, 151, 153–156, 160, 167
– loop 143
– motion 145, 146
– network 151
– reaction 149
– series 136
– splitting 151
– type 136, 138, 143, 152, 153
metamorphic 183, 191, 207, 208, 212, 217
– grade 189, 202
meteorite 185, 216, 217
mica 175, 207, 208
microcline 209
microcracking 190, 201
misfit dislocation 242, 247–254
model generalized pseudopotential theory (MGPT) 5–6, 8–10, 12–14, 16–37, 44
modified Burgers circuit 135
modulus 244, 245, 247, 249, 253, 254, 258, 259
molybdenite 175
molybdenum (Mo) 4, 6–9, 11–31, 34–35, 37–39, 41–44
monoclinic 180, 206, 207
mullite 208
multianvil 212, 215, 216
multiscale modeling of plasticity 4, 36–45
muscovite 207
mylonite 219, 220

negative climb 146
neodymium 204
network 174, 175, 183, 187, 193, 213
non-conservative motion 146
– band method 84

olivine 174, 175, 180, 184, 202, 216, 217, 218
omphacite 206, 207
order 177, 206
ordering 206, 209
ore 212
– iron 195, 197
– titanium 195
orientation distribution 200
orthoclase 209
orthopyroxene 180, 205
orthorhombic 180
osmotic pressure 236, 244
oxides 180, 192–198, 217, 218

packing density 113, 114
parallel dislocation simulator (ParaDiS) 6, 11, 37–42, 44
partial dislocation 136, 149, 151, 177, 181, 195, 203, 205, 207, 210, 211, 214, 240, 247, 254
Peierls
– barrier 202, 214
– stress 2, 5, 22, 26, 28–32, 34, 35, 37–41, 44, 53, 56, 78–80, 83, 84, 86, 91, 95, 98, 101, 102, 217
– valley 65, 67, 68, 70, 72, 73, 78, 79
Peierls-Nabarro model 215–217
pentagon 114, 115, 119, 121, 122, 135, 145, 161
perfect dislocation 52–54, 63–65, 68–80, 86, 89, 91, 97–105, 65, 75, 80, 111, 112, 136, 149
periclase 180, 195, 196, 217
pericline 209
peridotite 203, 204
peristerite 209
perovskite 180, 197, 215, 216, 218, 221
perthite 209
phase boundaries 151–153
phase diagram 115
phase transformation 121, 129, 176, 192, 206, 208, 211
phason
– halfplane 113, 128–130, 132, 134–137
– line 121–125
– plane 126–129
– plane strain field 128, 129
phonon-drag mobility 5, 35, 36
phonons 246
photoluminescence 75
phyllonite 220
pigeonite 206
pinning 175
plagioclase 210
planar defect 154, 159, 160, 162–166
point defect 177, 178, 182, 183

polygonization 187, 188
polyhedra 114, 115
polymorph 199, 211, 213, 215–217
polytypism 176
positive climb 146
post-perovskite 179, 215, 216, 218
preferred orientation 184, 200, 202, 209, 220
prismatic loop 144
pyrite 180, 211
pyrrhotite 211, 215
pyrope 204
pyroxene 180, 205, 207, 209, 216

quarter partial 197
quartz 178, 180, 181, 183, 184, 198, 199, 209, 219–221
quartzite 199, 200
quasicrystal 113, 121, 122, 146

reactivity 219
recovery 182, 189, 191, 201, 204, 207, 215
rheology 174, 202, 209
recrystallization 183, 184, 200, 210, 213, 214, 220, 221
– dynamic 184
– static 184
– primary 184
– secondary 184
– strain induced 183
resolved yield stress 40–44
ringwoodite 179, 216, 217
rock 174, 176, 182, 203, 220
rock salt 174, 179
rose channels 190
rutile 180, 198, 217

sanidine 208
sapphire 186, 193
Schmid factor 209
screw dislocation 54, 59, 79–86, 88–93, 95, 96, 98, 101–103, 175, 182, 186, 194, 205, 208, 212
screw dislocation core 81, 91
screw type segment 144
sedimentary 176, 177
segment 143–145
semiconductor 50, 54, 55, 57, 91, 97, 102–104, 203, 214
sessile 198
shear modulus 111, 112, 147, 245
shear transformation 164
shock 177, 216, 217
shock deformation 177
Shockley partial 147
– dislocation 244, 247, 254
shuffle
– core 81–83, 93, 94, 98, 102, 104
– dislocation 51, 53, 54, 59, 70, 73, 76, 78, 79, 99–101
– set 51–55, 71, 74, 78, 81, 98, 100–103, 105
silica 221
silicate 198, 204–206, 208, 218
silicon 50, 51, 54–56, 58–61, 63, 65–67, 71, 78–80, 83–86, 91, 92, 94–97, 99, 101–105
sillimanite 208
silver halide 174
simulation 4, 8, 79, 86, 216, 217
single kink 57, 86, 87
slip
– direction 178
– plane 177, 182
– system 182, 185
softening 182, 184, 213
soccer ball 114
sphalerite 180, 212
spinel 180, 194, 221
– structure 197
split occupation 115
spodumene 206, 207
stability range 115, 154
stacking fault 19, 20, 22, 54, 101, 146, 177, 178, 181, 195, 197, 203, 205, 206, 211, 214, 217, 239–241, 254, 256
steric constraints 114, 115, 117
stiffness 254
stishovite 179, 212, 215, 217
stoichiometric 197, 205
strain
– energy 183, 203, 218, 219, 247, 257
– field 111, 129, 131, 140, 244–251, 253–258
subcluster 115
substructure 116
sulfide 180, 210
superconductivity 198
superdislocation 177, 190
superpartial 177
superstructure 190
synchroshear 186, 193

tantalum (Ta) 4, 6–9, 11–31, 33–42, 44
Taylor phase 158
texture 178, 184, 196, 199, 210, 215
thermal history 176

tiling 118–123, 125, 126, 129, 133, 134, 136, 137, 139
– representation 133, 134
T-phase 158–160, 162, 163
transmission electron microscopy (TEM) 54, 55, 58, 59, 64, 65, 67, 68, 71, 73, 78, 104, 111, 122, 175, 176, 178, 181, 185, 186, 188–197, 199–213, 215–218, 221, 242
twinning 175, 177, 187, 189, 193, 195, 206, 207, 209, 210, 212, 215
twins 190, 192, 200, 214, 216
– crossing 190

undissociated dislocation 67, 71, 73, 78
unstable stacking fault energy 21

vacancy 146, 177, 197
vacancy exchange 146
vacancy source 146
vanadium (V) 1, 4, 6, 7, 9, 12–16, 18, 20–23, 25, 26, 28, 29, 31, 32, 34, 38, 44
vertex flip 146
vertex jump 123–125, 146
Volterra 140, 142
Von Mises criterion 182, 187

wadsleyite 179, 216
water 174, 201, 203, 204, 206
work hardening 182, 193, 213
Wüstite 180, 195, 196

ξ-lattice 155, 156
ξ-phase 116, 118, 119, 154
ξ-structure 154, 155, 156
X-Ray 58, 66–69
– diffraction 215
– line broadening 174, 218
– topography 175, 178, 207, 218

yttrium aluminium garnet 204
Yule marble 184

zinc blende 213